J. Astrophys. Astr. (1990) **11**, 1–10

The in-Plane Motion of a Geosynchronous Satellite under the Gravitational Attraction of the Sun, the Moon and the Oblate Earth

K. B. Bhatnagar *Department of Mathematics, Zakir Hussain College, Delhi* 110006

Manjeet Kaur *Department of Mathematics, Mata Sundri College, New Delhi 110002*

Received 1989 June 20; accepted 1989 September 29

Abstract. The in-plane motion of a Geosynchronous satellite under the gravitational effects of the sun, the moon and the oblate earth has been studied. The radial deviation (Δr) and the tangential deviation ($r_c\Delta\theta$) have been determined. Here r_c represents the synchronous altitude. It has been seen that the sum of the oscillatory terms in Δr for different inclinations is a small finite quantity whereas the sum of the oscillatory terms in $r_c\Delta\theta$ for different inclinations is quite large due to the presence of the low-frequency terms in the denominator.

Key words: celestial dynamics—artificial satellites

1. Notations

C_i amplitude of *i*th oscillatory component in Equation (1)
D_i amplitude of *i*th oscillatory component in Equation (2)
r vector from centre of earth to the satellite
t time
α inclination of the satellite orbital plane to the reference plane
α_m inclination of the moon's orbital plane to the ecliptic
α_1 inclination of the reference plane to the ecliptic
α_0 steady-state value of α
ϕ orbital angle of the earth around the sun
θ orbital angle of the satellite around the earth
θ_m orbital angle of the moon around the earth
ψ satellite orbital regression angle
ψ_m lunar regression angle
ω_i oscillatory frequency of *i*th component in Equations (1) or (2)
G Universal gravitational constant = 6.668×10^{-8} dyne cm^2 gm^{-2}
J_2 coefficient due to the oblateness of the earth = 1.08219×10^{-3}
M_E mass of the earth = 600.06780×10^{25} gms
M_m mass of the moon = 7.380×10^{25} gms
M_s mass of the sun = ($332{,}946.8 \times M_E$) gms
R_0 mean earth radius = 6392.06 km
R distance between the centre of the sun to the centre of mass of the earth moon system = 1.4959965×10^8 km
ε obliquity = 23°27'

$\dot{\theta}_0^2$ $\simeq GM_E/r_c^3$
$\dot{\theta}_m$ moon's orbital rate = 0.22998 rad/solar day
$\dot{\psi}_m$ regression rate of the moon's orbital plane = -9.249×10^{-4} rad/solar day
$\dot{\psi}_0$ steady-state regression rate of the satellite
$\dot{\phi}$ earth's angular rate = 0.0172 rad/solar day
$\dot{\theta}_E$ earth's rotation rate = 6.3004 rad/solar day
r_c steady-state value of the synchronous altitude = 42296 km

2. Introduction

Frick & Garber (1962, Part III) have discussed the in-plane perturbations of a Geosynchronous satellite under the gravitational effects of the sun, the moon and the oblate earth. They have assumed that the sun, the moon, and the earth all lie in the plane of the ecliptic and the satellite's orbital plane and the reference plane coincide with the earth's equatorial plane. Bhatnagar & Mehra (1986, 1987) have also studied the motion of a Geosynchronous satellite under the combined gravitational effects of the sun (including its radiation pressure), the moon and the oblate earth (including its ellipticity). They have studied only the motion of the orbital plane of the satellite. It is shown that the orbital plane rotates with an angular velocity lying between 0.042°/year and 0.058 /year for a synchronous satellite. It is further observed that the regression period increases both as the orbital inclination and the altitude increase. Monica (1987) has shown that the major effect of the earth's equatorial ellipticity is to produce it change in the relative angular position Γ of the satellite as seen from the earth. In the present paper, we are studying the in-plane motion of a Geosynchronous satellite under the effects of the sun, the moon and the oblate earth. It has been assumed that the centre of the earth-moon system moves around the sun in a circle with constant angular velocity $\dot{\phi}$ in the plane of the ecliptic; the moon moves about the earth in a circle with constant angular velocity $\dot{\theta}_m$ in a plane at an angle of 5°8′ to the plane of the ecliptic and the earth is spinning about its axis. Further, the nominal orbit is also supposed to be circular. The nonlinear in-plane equations of motion have been made linear by applying the perturbation technique for determining the radial deviation Δr and the tangential deviation $r_c\Delta\theta$. The amplitudes of the oscillatory terms in Δr and $r_c\Delta\theta$ for different inclinations have also been determined.

3. Equations of motion

In Fig. 1, S represents the sun, E the earth, M the moon, P the satellite and G the mass-centre of the earth-moon system. Let

$$\mathbf{SE = R_E, SM = R_m, SP = r_s, SG = R,}$$

$$\mathbf{EP = r, EM = P_0, EG = P_E, MP = r_m.}$$

The circular motions of the bary-centre relative to the sun and of the moon around the earth give

$$\dot{\phi}^2 = \frac{GM_s}{R^3}, \frac{\dot{\theta}_m^2}{\mu} = \frac{GM_m}{P_0^3}$$

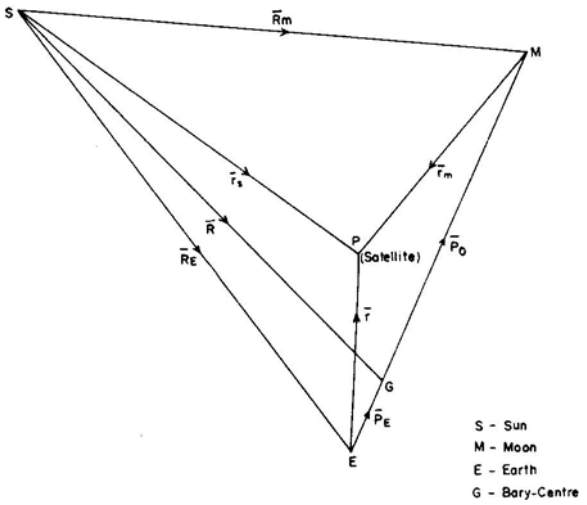

Figure 1, Configuration giving the position vectors of the sun, moon, earth and satellite.

where $\dot{\phi}$ = angular velocity of the earth around the sun;
$\dot{\theta}_m$ = angular velocity of the moon around the earth.

Proceeding as in Bhatnagar & Mehra (1986), the in-plane equations of motion of the satellite P are given by

$$(\ddot{r} - r\dot{\theta}^2) + \frac{GM_E}{r^2} = \xi + \sum_{i=1}^{127} C_i \cos \omega_i t, \tag{1}$$

$$\frac{\mathrm{d}}{\mathrm{d}t}(r^2\dot{\theta}) = \sum_{i=1}^{127} Di \sin \omega_i t, \tag{2}$$

where

$$\xi = -\frac{3GM_E}{8r_0^4} J_2 R_0^2 \{2 - 3\sin^2(\varepsilon - \alpha_1)\}(2 - 3\sin^2\alpha_0)$$
$$+ \frac{r_0\dot{\phi}^2}{8}(2 - 3\sin^2\alpha_0)(2 - 3\sin^2\alpha_1) + \frac{r_0\dot{\phi}_m^2}{16\mu}(2 - 3\sin^2\alpha_0)$$
$$\times (2 - 3\sin^2\alpha_1)(2 - 3\sin^2\alpha_m)$$

and

$$\mu = \frac{M_E + M_m}{M_m}.$$

All the notations used in the above equations are given in Section 1. Here r, θ determine the position of the satellite in the orbital plane shown in Fig. 2.

The amplitudes C_i, D_i are functions of any or all of the quantities α_0, α_1, α_m, r_0 and frequencies ω_i are linear combinations of $\dot{\theta}_0$, $\dot{\theta}_m$, $\dot{\phi}$, $\dot{\psi}_m$ and $\dot{\psi}_0$. The values of the frequencies ω_i and the amplitudes C_i, D_i (i =1 . . . 127) are not mentioned in this paper as these values cover about 45 pages. Their values can be obtained from the author on

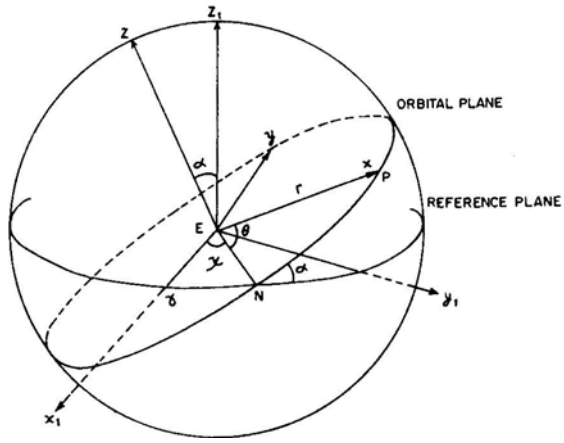

Figure 2. Parameters (r, θ, α, χ) representing the position of the satellite in space.

request. Out of 127 frequencies, the frequencies corresponding to i = 1, 2, 23, 24, . . . 32 are the low-frequency terms (Appendix 1); we have laid emphasis on these terms because of the presence of the factor $1/\omega_i$ which we obtain on integrating the equations of motion. For a synchronous satellite, the steady-state value r_o of r is replaced by r_c in our subsequent study.

4. Perturbation equations

The linearized technique used by Frick (1962, Part II) while determining the motion of a Geosynchronous satellite is not applicable for Equations (1), and (2), since we obtain time-variable coefficients in the final linearized equations. So we adopt a perturbation method as used by Frick (1962, Part III). Since for a synchronous satellite (Frick 1967),

$$\dot{\theta}_0 = \dot{\theta}_E - \dot{\psi}_0,$$

where $\dot{\theta}_E$ = earth's rotation rate = 6.3004 rad/solar day

and $\dot{\psi}_0$ = steady-state regression rate of the synchronous satellite

$= (-3.257 \times 10^{-4}) \cos \alpha_0$, rad/solar day.

This equation enables us to determine the value of the synchronous altitude for different inclinations ($0° \leqslant \alpha_0 \leqslant 90°$). Table 1 gives the differences to the synchronous altitude, 42296 km, corresponding to inclination $\alpha_0 = 0°$ for different inclinations. We may observe that the maximum change in the synchronous altitude is one and half kilometre at $\alpha_0 = 90°$.

Table 1. The difference in the value of the synchronous altitude corresponding to inclination zero (r_c = 42296.0 km).

α_0 (in deg)	0	10	20	30	40	50	60	70	80	90
Difference in r_c (in km)	0	.1	.1	.2	.4	.6	.8	1	1.3	1.5

Now, the perturbation relative to a synchronous orbit can be defined by the equations:

$$r = r_c + \Delta r$$
$$\dot{\theta} = (\dot{\theta}_E - \dot{\psi}_0) + \Delta\dot{\theta}.$$

Putting these in Equations (1) and (2), we get

$$\Delta\ddot{r} - 2r_c(\dot{\theta}_E - \dot{\psi}_0)\Delta\dot{\theta} - 3(\dot{\theta}_E - \dot{\psi}_0)^2\Delta r = \frac{r_c p_1}{8}\dot{\phi}^2 + \frac{r_c p_2}{16\mu}\dot{\theta}_m^2 + \left[\sum_{i=1}^{127} C_i \cos\omega_i t\right] r_0 = r_c,\ \dot{\theta}_0 = \dot{\theta}_E - \dot{\psi}_0 \tag{3}$$

$$\frac{d}{dt}[r_c^2\Delta\dot{\theta} + 2r_c(\dot{\theta}_E - \dot{\psi}_0)\Delta r] = \left[\sum_{i=1}^{127} D_i \sin\omega_i t\right] \qquad r_0 = r_c, \dot{\theta}_0 = \dot{\theta}_E - \dot{\psi}_0 \tag{4}$$

where

$$p_1 = (2 - 3\sin^2\alpha_0)(2 - 3\sin^2\alpha_1),$$
$$p_2 = (2 - 3\sin^2\alpha_0)(2 - 3\sin^2\alpha_1)(2 - 3\sin^2\alpha_m).$$

Equations (3) and (4) are two coupled linear differential equations with constant coefficients in variables Δr and $\Delta\theta$. After integrating Equation (4) we get

$$r_c^2\Delta\dot{\theta} + 2r_c(\dot{\theta}_E - \dot{\psi}_0)^2(\Delta r - \Delta r_0) = -\left[\sum_{i=1}^{127}\frac{D_i}{\omega_i}(\cos\omega_i t - \cos\omega_i t_0)\right] \qquad r_0 = r_c,\ \dot{\theta}_0 = \dot{\theta}_E - \dot{\psi}_0 \tag{5}$$

where at $t = t_0$ we suppose that

$$\theta = \theta_0, \quad \phi = \phi_0, \quad \theta_m = (\theta_m)_0, \quad \Delta r = \Delta r_0, \quad \Delta\dot{\theta} = 0.$$

It is necessary to assume a nonzero initial value Δr_0 of Δr since the effects of the sun and the moon may give an additional bias in the value of the synchronous radius.

Now we solve Equation (5) for $\Delta\theta$ and substitute its value in Equation (3) we get

$$\Delta\ddot{r} + (\dot{\theta}_E - \dot{\psi}_0)^2\Delta r = 4(\dot{\theta}_E - \dot{\psi}_0)^2\Delta r_0 + \frac{r_c p_1}{8}\dot{\phi}^2 + \frac{r_c p_2}{16\mu}\dot{\theta}_m^2 + \sum_{i=1}^{127} C_i\cos\omega_i t - \frac{2}{r_c}(\dot{\theta}_E - \dot{\psi}_0)\sum_{i=1}^{127}\frac{D_i}{\omega_i}(\cos\omega_i t - \cos\omega_i t_0). \tag{6}$$

Suppose at $t = t_0$, D $r = 0$ then solving Equation (6), we have

$$\begin{aligned}\Delta r = {} & [4 - 3\cos\dot{\theta}_0(t - t_0)]\Delta r_0 + \frac{1}{\dot{\theta}_0^2}\{1 - \cos\dot{\theta}_0(t - t_0)\}\frac{r_c p_1}{8}\dot{\phi}^2 \\ & + \frac{1}{\dot{\theta}_0^2}\{1 - t\cos\dot{\theta}_0(t - t_0)\}\frac{r_c p_2}{16\mu}\dot{\theta}_m^2 + \sum_{i=1}^{127}\frac{C_i}{\dot{\theta}_0^2 - \omega_i^2} \\ & \times\left[\cos\omega_i t - \cos\dot{\theta}_0(t - t_0)\cos\omega_i t_0 + \frac{\omega_i\sin\dot{\theta}_0(t - t_0)}{\dot{\theta}_0}\sin\omega_i t_0\right] \\ & + \frac{2}{r_c\dot{\theta}_0}\sum_{i=1}^{127}\frac{D_i}{\omega_i(\dot{\theta}_0^2 - \omega_i^2)}[\cos\omega_i t_0\{\dot{\theta}_0^2 - \omega_i^2(1 - \cos\dot{\theta}_0(t - t_0))\} \\ & - \dot{\theta}_0^2\cos\omega_i t - \dot{\theta}_0\omega_i\sin\dot{\theta}_0(t - t_0)\sin\omega_i t_0].\end{aligned} \tag{7}$$

Putting this value of Δr in Equation (5), we get

$$\Delta\dot{\theta} = -\frac{6\dot{\theta}_0}{r_c}[1-\cos\dot{\theta}_0(t-t_0)]\Delta r_0 - \frac{p_1}{4\dot{\theta}_0}\{1-\cos\dot{\theta}_0(t-t_0)\}\dot{\phi}^2$$
$$-\frac{p_2}{8\mu\dot{\theta}_0}\{1-\cos\dot{\theta}_0(t-t_0)\}\dot{\theta}_m^2 + \frac{2\dot{\theta}_0}{r_c}\sum_{i=1}^{127}\frac{C_i}{\dot{\theta}_0^2-\omega_i^2}$$
$$\times\left[\cos\dot{\theta}_0(t-t_0)\cos\omega_i t_0 - \cos\omega_i t - \frac{\omega_i}{\dot{\theta}_0}\sin\dot{\theta}_0(t-t_0)\sin\omega_i t_0\right]$$
$$+\frac{1}{r_c^2}\sum_{i=1}^{127} D_i\left[-\frac{\cos\omega_i t_0}{\omega_i}\left\{3+\frac{4\omega_i^2\cos\dot{\theta}_0(t-t_0)}{\dot{\theta}_0^2-\omega_i^2}\right\}\right.$$
$$\left.+\frac{4\dot{\theta}_0\sin\dot{\theta}_0(t-t_0)\sin\omega_i t_0}{\dot{\theta}_0^2-\omega_i^2} + \frac{\cos\omega_i t}{\omega_i}\left\{3+\frac{4\omega_i^2}{\dot{\theta}_0^2-\omega_i^2}\right\}\right]. \tag{8}$$

Equation (8) for $\Delta\dot{\theta}$ contains constant terms which would cause a steady-state increment in the angular rate relative to the desired synchronous conditions of the satellite. So we put these terms equal to zero and determine the value of Δr_0:

$$\Delta r_0 = -\frac{r_c p_1}{24\dot{\theta}_0^2}\dot{\phi}^2 - \frac{r_c p_2}{48\mu\dot{\theta}_0^2}\dot{\theta}_m^2 - \frac{1}{2r_c\dot{\theta}_0}\sum_{i=1}^{127}\frac{Di}{\omega_i}\cos\omega_i t_0. \tag{9}$$

Hence the complete solution for Δr, $\Delta\dot{\theta}$ are given by Equations (7) and (8) where Δr_0 is given by Equation (9). Equation (8) can be integrated and multiplied by r_c to obtain the tangential displacement of the satellite from its desired synchronous position:

$$r_c\Delta\theta = -6\dot{\theta}_0\left[(t-t_0)-\frac{\sin\dot{\theta}_0(t-t_0)}{\dot{\theta}_0}\right]\Delta r_0 - \frac{r_c p_1}{4\dot{\theta}_0}\left[(t-t_0)-\frac{\sin\dot{\theta}_0(t-t_0)}{\dot{\theta}_0}\right]\dot{\phi}^2$$
$$-\frac{r_c p_2}{8\mu\dot{\theta}_0}\left[(t-t_0)-\frac{\sin\dot{\theta}_0(t-t_0)}{\dot{\theta}_0}\right]\dot{\theta}_m^2 + 2\dot{\theta}_0\sum_{i=1}^{127}\frac{C_i}{\dot{\theta}_0^2-\omega_i^2}\left[\frac{1}{\dot{\theta}_0}\times\cos\omega_i t_0\sin\dot{\theta}_0\right.$$
$$\left.\times(t-t_0)-\frac{(\sin\omega_i t-\sin\omega_i t_0)}{\omega_i}+\frac{\omega_i}{\dot{\theta}_0^2}\sin\omega_i t_0\{-1+\cos\dot{\theta}_0(t-t_0)\}\right]$$
$$+\frac{1}{r_c}\sum_{i=1}^{127} D_i\left[-\frac{\cos\omega_i t_0}{\omega_i}\left\{3(t-t_0)+\frac{4\omega_i^2\sin\dot{\theta}_0(t-t_0)}{\dot{\theta}_0(\dot{\theta}_0^2-\omega_i^2)}\right\}\right.$$
$$\left.-\frac{4\sin\omega_i t_0}{\dot{\theta}_0^2-\omega_i^2}\cos\dot{\theta}_0(t-t_0)+\frac{3(\sin\omega_i t-\sin\omega_i t_0)}{\omega_i^2}+\frac{4\sin\omega_i t}{\dot{\theta}_0^2-\omega_i^2}\right]. \tag{10}$$

We observe from Equations (7), (9) and (10)that if the initial radius is corrected by an amount Δr_0 then the resulting variation in deviations Δr and $r_c\Delta\theta$ contain small it bias terms plus sinusoidal variations with angular frequencies of $\dot{\theta}_0$ and ω_i (i = … 127). However, as a result of the correction Δr_0 in the orbital radius there is no secular terms in the in-plane motion of the satellite. Hence the deviations of the satellite from the desired synchronous position are bounded and the satellite will remain essentially synchronous.

5. Results and discussion

5.1 *Case* 1: *Frick Case.*

From Equations (7), (9) and (10) Frick case can be deduced by putting

$$\alpha_0 = 0, \quad \alpha_m = 0, \quad \psi_0 = 0, \quad \psi_m = 0 \quad \text{and} \quad \varepsilon - \alpha_1 = 0,$$

so a modification to the initial radius r_c is required due to the attractions of the sun and the moon on the satellite. The magnitude of this correction depends on the initial position of the sun, the moon and the satellite relative to the earth and it can vary between –0.5017 km and 0.2477 km, being the maximum and minimum value of Δr_0 respectively. Moreover, the in-plane perturbations of the satellite caused by the attraction of the sun and the moon are in the form of small amplitudes oscillations which result in a maximum deviation from the desired synchronous position of about 72.66 km.

5.2 *Case* 2: *Orbit in any Plane*

From Equation (9) it is seen that because of the effects of the sun and the moon the initial value of r_c must be altered by an amount Δr_0 to eliminate the steady-state value of $\Delta\theta$. The magnitude of this correction is a function of the initial geometry of the sun-earth moon-satellite system as characterized by the angle φ_0 , $(\theta_m)_0$, θ_0, $(\psi_m)_0$ and ψ_0. For different orbital inclinations, the maximum possible negative value of Δr_0 occurs when θ_0 equals 90° and α_0, ϕ_0, $(\theta_m)_0$, $(\psi_m)_0$ and ψ_0 are all zero provided $\sum_{i=1}^{127} \frac{D_i}{\omega_i} < 0$. Under these conditions Δr_0 is given by

$$\Delta r_0 = -0.5197 \text{ km.}$$

On the other hand for different orbital inclinations, the maximum possible positive value of Δr_0 occurs when θ_0 equals 0^0 and α_0, ϕ_0, $(\theta_m)_0$,$(\psi_m)_0$ and ψ_0 are all zero Provided $\sum_{i=1}^{127} \frac{D_i}{\omega_i} < 0$. Under these conditions Δr_0 is given by

$$\Delta r_0 = 0.2278 \text{ km.}$$

Here the maximum possible negative value of the maximum possible positive value are slightly different (0.016 km) from Frick (1962) since he has not considered the inclination of the moon's orbital plane to the ecliptic (5°.8′).

5.3 *Case* 3: *Oscillation Amplitudes*

The amplitudes of the various oscillatory components in Equation (7) for Δr for different inclinations α_0 ($0° \leqslant \alpha_0 < 90°$) have been found. The graph of the arithmetic sum of all the 129 amplitudes involved in Δr is given in Fig. 3 for different inclinations of α_0. It shows that Δr_0 increases from 2.3522 km ($\alpha_0 = 0°$) to 8.052 km ($\alpha_0 = 80°$). The amplitudes of the various oscillatory components in Equation (10) for the tangential deviation have been found for different inclinations α_0($0° \leqslant \alpha_0 < 90°$). The graph of

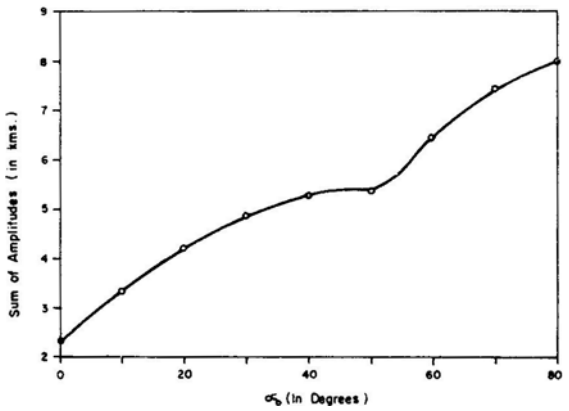

Figure 3. Sum of amplitudes in Δr for different orbital inclinations.

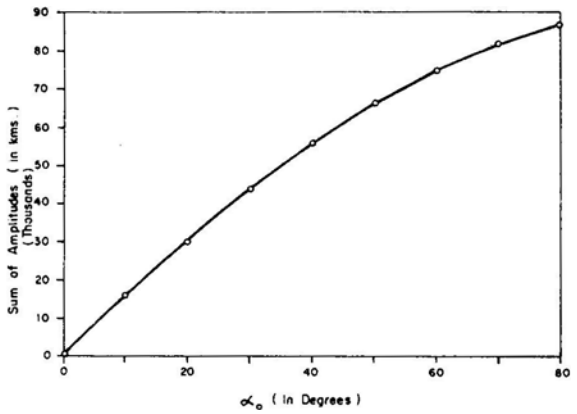

Figure 4. Sum of amplitudes in $r_c\Delta\theta$ for different orbital inclinations.

the arithmetic sum of all the 129 amplitudes involved in $r_c\Delta\theta$ is given in Fig. 4 for different inclinations of α_0. It shows that $r_c\Delta\theta$ increases from 1006.94 km to 87271.6 km (α_0 = 80°). Both Δr, $r_c\Delta\theta$ are not defined when α_0 = 90°. So the inplane perturbations of the satellite caused by the attraction of the sun and the moon and oblate earth are in the nature of large-amplitude oscillations because of the presence of low-frequency terms in the denominator and the orbital inclination α_0, whereas in Frick (1962) these perturbations are in the nature of small-amplitude oscillations which could result in a maximum deviation from the desired synchronous position of about 72.66 km as he has studied only one case, *i.e.*, when α_0 = 0° and in that case all the low frequency terms vanish.

Appendix 1

Low frequency terms ω_i (i =1, 2, 23, 24, . . ., 32)

$$\omega_1 = \dot{\psi}_0,$$

$$C_1 = -\frac{3r_c}{8}\dot{\phi}^2\left[\left\{1+\frac{\dot{\theta}_m^2}{2\mu\dot{\phi}^2}(2-3\sin^2\alpha_m)\right\}\sin 2\alpha_1 + 9K\sin 2(\varepsilon-\alpha_1)\right]\sin 2\alpha_0,$$

$$D_1 = 0.$$

$$\omega_2 = 2\dot{\psi}_0,$$

$$C_2 = \frac{3r_c\dot{\phi}^2}{8}\left[\left\{1+\frac{\dot{\theta}_m^2}{2\mu\dot{\phi}^2}(2-3\sin^2\alpha_m)\right\}\sin^2\alpha_1 - 9K\sin^2(\varepsilon-\alpha_1)\right]\sin^2\alpha_0,$$

$$D_2 = 0, \quad \text{where} \quad K = \frac{\dot{\theta}_0^2 J_2 R_0^2}{\dot{\phi}^2 r_c^2}.$$

$$\omega_{23} = \dot{\psi}_m - 2\dot{\psi}_0,$$

$$C_{23} = -\frac{3}{8}M_1\sin^2\alpha_0\sin\alpha_1\cos^2\frac{\alpha_1}{2}\sin^2\alpha_m,$$

$$D_{23} = 0.$$

$$\omega_{24} = \dot{\psi}_m - \dot{\psi}_0,$$

$$C_{24} = \frac{3M_1}{16}\sin 2\alpha_0(\cos\alpha_1 + \cos 2\alpha_1)\sin 2\alpha_m,$$

$$D_{24} = 0.$$

$$\omega_{25} = \dot{\psi}_m,$$

$$C_{25} = \frac{9}{16}M_1(2-3\sin^2\alpha_0)\sin 2\alpha_1\sin 2\alpha_m,$$

$$D_{25} = 0.$$

$$\omega_{26} = \dot{\psi}_m + \dot{\psi}_0,$$

$$C_{26} = -\frac{3}{16}M_1\sin 2\alpha_0(\cos\alpha_1 - \cos 2\alpha_1)\sin 2\alpha_m,$$

$$D_{26} = 0.$$

$$\omega_{27} = \dot{\psi}_m + 2\dot{\psi}_0,$$

$$C_{27} = \frac{3}{8}M_1\sin^2\alpha_0\sin\alpha_1\sin^2\frac{\alpha_1}{2}\sin 2\alpha_m,$$

$$D_{27} = 0.$$

$$\omega_{28} = 2\dot{\psi}_m - 2\dot{\psi}_0,$$

$$C_{28} = \frac{3}{8}M_1\sin^2\alpha_0\cos^4\frac{\alpha_1}{2}\sin^2\alpha_m,$$

$$D_{28} = 0.$$

$$\omega_{29} = 2\dot{\psi}_m - \dot{\psi}_0,$$

$$C_{29} = \frac{3}{8}M_1\sin 2\alpha_0\sin\alpha_1\cos^2\frac{\alpha_1}{2}\sin^2\alpha_m,$$

$$D_{29} = 0.$$

$$\omega_{30} = 2\dot{\psi}_m,$$

$$C_{30} = -\frac{9}{16} M_1 \sin^2 \alpha_0 \sin^2 \alpha_1 \sin^2 \alpha_m,$$

$$D_{30} = 0.$$

$$\omega_{31} = 2\dot{\psi}_m + \dot{\psi}_0,$$

$$C_{31} = -\frac{3}{8} M_1 \sin 2\alpha_0 \sin \alpha_1 \sin^2 \frac{\alpha_1}{2} \sin^2 \alpha_m,$$

$$D_{31} = 0.$$

$$\omega_{32} = 2\dot{\psi}_m + 2\dot{\psi}_0,$$

$$C_{32} = \frac{3}{8} M_1 \sin^2 \alpha_0 \sin^4 \frac{\alpha_1}{2} \sin^2 \alpha_m,$$

$$D_{32} = 0,$$

where

$$M_1 = \frac{r_c \dot{\theta}_m^2}{\mu}.$$

References

Bhatnagar, K. B., Mehra, M. *1986*, *Indian J. Pure Appl. Math.*, **17**, 1438,
Bhatnagar, K. B., Mehra, M. 1987, *Indian J. Pure Appl. Math.*, **18**, 461.
Frick, R. H., Garber, T. B. 1962, R-399-NASA.
Frick, R. H. 1967, R-454-NASA.
Mehra, M. 1987, *PhD Thesis*, Univ. Delhi.

J. Astrophys. Astr. (1990) **11**, 11–22

On the Effect of the Eccentricity of a Planetary Orbit on the Stability of Satellite Orbits

S. Ichtiaroglou & G. Voyatzis *Department of Physics, University of Thessaloniki, 54006, Greece*

Received 1989 May 11; accepted 1989 October 12

Abstract. The effect of the eccentricity of a planet's orbit on the stability of the orbits of its satellites is studied. The model used is the elliptic Hill case of the planar restricted three-body problem. The linear stability of all the known families of periodic orbits of the problem is computed. No stable orbits are found, the majority of them possessing one or two pairs of real eigenvalues of the monodromy matrix, while a part of a family with complex instability is found. Two families of periodic orbits, bifurcating from the Lagrangian points L_1, L_2 of the corresponding circular case are found analytically. These orbits are very unstable and the determination of their stability coefficients is not accurate, so we compute the largest Liapunov exponent in their vicinity. In all cases these exponents are positive, indicating the existence of chaotic motions.

Key words: celestial mechanics—periodic orbits—stability—Hill roblem

1. Introduction

The motion of a satellite in the gravitational field of Sun and a planet under the assumption that the solar parallax, the solar eccentricity and the satellite's inclination are zero, can be modelled by a limiting case of the three-body restricted problem, known as Hill's case (Hill 1886, see also Szebehely 1967, p. 602). One considers the usual circular restricted three-body problem with the two primaries P_1 and P_2 describing circular orbits around their centre of gravity and letting the body P_3 approach P_1 while the mass of P_1 tends to zero, one obtains by an appropriate enlargement of the vicinity of P_1 the nontrivial circular Hill (CH) problem. An extensive numerical investigation of the periodic orbits of the CH-problem and their stability has been carried out in a series of papers by Hénon (1969, 1970, 1974).

The elliptic Hill (EH) problem can be obtained by the same procedure if one considers that the body P_1 describes an elliptic orbit around P_2. Periodic orbits of the EH-problem can be found by continuation with respect to the eccentricity of the orbit of P_1 , of the periodic orbits of the CH-problem with period equal to $2k\pi$ where k is integer (Ichtiaroglou 1980). Three families of periodic orbits have been computed by Ichtiaroglou (1981) for values of the eccentricity e in the range $0 \leqslant e < 1$ for the pericentric and the apocentric case.

In this paper we determine the linear stability of all the known families of periodic orbits of the EH-problem. In Section 2 we define the model and give the equations of motion in a pulsating-rotating system of reference while in Section 3 the method of determining the linear stability of a periodic orbit is given and the stability coefficients of the periodic orbits of the three families a, g' and f_2 are presented. All orbits are found to be unstable, since the corresponding monodromy matrices possess in every case one or two pairs of real eigenvalues, while a part of family g' exhibits complex instability. In Section 4, two new families of periodic orbits which bifurcate from the Lagrangian points L_1 and L_2 are found analytically. These orbits possess very large stability coefficients and the method of computing them does not converge, so we compute the largest Liapunov exponent in their vicinity. All these exponents are found to be positive indicating the existence of chaotic motions in the neighbourhood of the periodic orbits.

2. The equations of motion

We consider a rotating system of reference whose origin coincides with the centre of mass of P_t and P_2 and its x-axis contains always these two bodies. In the following we use the normalization defined by the relations

$$k^2 = 1, \quad m_1 + m_2 = 1, \quad \dot{\theta}(0) = 1, \tag{1}$$

where k^2 is the gravitational constant, m_i is the mass of the body P_i and $\dot{\theta}(0)$ is the initial angular velocity of the rotating frame of reference. The equations of motion of the elliptic restricted problem are (Christides 1978).

$$\begin{aligned} \ddot{x}_1 - Q^2 x_1^{-3} &= -(1-\mu)^3 x_1^{-2}, \\ \ddot{x}_3 - 2Q x_1^{-2}\dot{y}_3 - Q^2 x_1^{-4} x_3 + 2Q x_1^{-3} y_3 \dot{x}_1 &= \Gamma, \\ \ddot{y}_3 + 2Q x_1^{-2}\dot{x}_3 - Q^2 x_1^{-4} y_3 - 2Q x_1^{-3} x_3 \dot{x}_1 &= \Delta, \end{aligned} \tag{2}$$

where x_i, y_i, are the coordinates of P_i,

$$\begin{aligned} \Gamma &= \mu(x_1 - x_3)\rho_{13}^{-3} - [\mu x_1 + (1-\mu)x_3]\rho_{23}^{-3}, \\ \Delta &= -[\mu\rho_{13}^{-3} + (1-\mu)\rho_{23}^{-3}]y_3, \\ \rho_{ij}^2 &= (x_i - x_j)^2 + (y_i - y_j)^2, \qquad \mu = m_1, \end{aligned} \tag{3}$$

and Q is the constant

$$Q = (1-\mu)P_\theta/\mu = \dot{\theta}x_1^2 = x_{10}^2 \tag{4}$$

where P_θ is the constant angular momentum of the system and $x_{10} = x_1(0)$.

Equation (2a) describes the elliptic motion of P_1 while (2b) and (2c) describe the motion of the body P_3. By making the substitution

$$\begin{aligned} x_3 &= x_1 + \mu^{1/3}\xi, \\ y_3 &= \mu^{1/3}\eta, \end{aligned} \tag{5}$$

and letting $\mu \to 0$, the equations of the EH-problem are obtained

$$\ddot{x}_1 = x_{10}^4 x_1^{-3} - x_1^{-2}, \tag{6}$$

and

$$\ddot{\xi} - 2x_{10}^2 x_1^{-2}\dot{\eta} + \xi(\rho^{-3} - 2x_1^{-3} - x_{10}^4 x_1^{-4}) + 2x_{10}^2 x_1^{-3}\dot{x}_1\eta = 0,$$
$$\ddot{\eta} + 2x_{10}^2 x_1^{-2}\dot{\xi} + \eta(\rho^{-3} + x_1^{-3} - x_{10}^4 x_1^{-4}) - 2x_{10}^2 x_1^{-3}\dot{x}_1\xi = 0, \tag{7}$$

where

$$\rho^2 = \xi^2 + \eta^2.$$

Equations (7) can be obtained by the time-dependent Hamiltonian

$$H = \tfrac{1}{2}(p_\xi^2 + p_\eta^2) + x_{10}^2 x_1^{-2}(\eta p_\xi - \xi p_\eta) - \rho^{-1} - x_1^{-3}(\xi^2 - \eta^2/2), \tag{8}$$

where x_1 is a periodic function of time, obtained as a solution of Equation (6) and

$$p_\xi = \dot{\xi} - x_{10}^2 x_1^{-2}\eta,$$
$$p_\eta = \dot{\eta} + x_{10}^2 x_1^{-2}\xi. \tag{9}$$

Equation (6) describes an elliptic motion of P_1 with eccentricity e and period T which are connected with the initial condition x_{10} by the relations (Ichtiaroglou 1980)

$$x_{10}^3 = 1 + e \tag{10}$$

and

$$T = 2\pi[(1-e)/(1+e)^3]^{1/2}. \tag{11}$$

Relations (10) and (11) hold when at $t = 0$ the two primaries are at periapsis. The corresponding relations for the apoapsis case can be obtained by substituting in (10) and (11)

$$e \to -e.$$

It is convenient thus to let the parameter e vary in the interval $(-1, 1)$, its negative values corresponding to the apocentric case.

3. Stability of periodic orbits

We introduce the vector $\bar{\eta}$ by the relations

$$\eta_1 = \xi, \qquad \eta_2 = \eta, \qquad \eta_3 = p_\xi \qquad \eta_4 = p_\eta.$$

The equations of motion (7) may be written in the form

$$\dot{\eta} = J\,\nabla H \tag{12}$$

where H is the Hamiltonian (8), $\nabla = \partial / \partial \eta_i$ and J is the 4×4 matrix

$$J = \begin{pmatrix} 0 & I \\ -I & 0 \end{pmatrix}. \tag{13}$$

$$\bar{\eta}_0(t+T) = \bar{\eta}_0(t) \tag{14}$$

be a periodic solution of Equations (12) with period T and let $\bar{\varphi}$ be a small variation around this solution. The corresponding variational equations are

$$\dot{\bar{\varphi}} = JS\bar{\varphi} \tag{15}$$

where $s(t)$ is the symmetric periodic matrix with elements

$$S_{ij} = (\partial^2 H / \eta_i \partial \eta_j)_0. \tag{16}$$

In Equation (16), subscript 0 indicates that the corresponding expression is to be evaluated on the periodic solution (14). A solution $\bar{\varphi}$ W of the variational Equations (15) is given by

$$\bar{\varphi}(t)=\Delta(t)\ \bar{\varphi}\ (0) \tag{17}$$

where $\Delta(t)$ is the matrizant of the system (15). The matrix $\Delta(T)$ is the corresponding monodromy matrix and its eigenvalues determine the stability of the periodic orbit (14) (Hadjidemetriou 1977). A(T) is a symplectic matrix, so its eigenvalues form reciprocal pairs

$$\lambda, \quad 1/\lambda, \qquad \mu, 1/\mu. 1$$

The periodic orbit is stable if and only if all four eigenvalues lie on the unit circle in the complex plane. Following Broucke (1969), we define the stability coefficients a_1, a_2 by the relations

$$a_1 = -(k_1 + k_2),$$
$$a_2 = 2 + k_1 k_2, \tag{18}$$

where k_1, k_2 are the stability indices

$$k_1 = \lambda + 1/\lambda,$$
$$k_2 = \mu + 1/\mu. \tag{19}$$

The periodic orbit is stable when the following inequalities hold

$$D = a_1^2 - 4a_2 + 8 > 0, \qquad k_1^2 < 4, \qquad k_2^2 < 4. \tag{20}$$

Broucke (1969) (see also Howard & McKay 1987, Hadjidemetriou 1979) showed that there are seven possible types of stability corresponding to seven distinct regions on the (a_1, a_2) plane defined by the straight lines

$$a_2 = 2a_1 - 2, \tag{21}$$

$$a_2 = -2a_1 - 2, \tag{22}$$

and the parabola

$$a_1^2 - 4a + 8 = 0, \tag{23}$$

as shown in Fig. 1, where the corresponding positions of the eigenvalues on the complex plane are shown for each region. The orbit is stable when a_1, a_2 lie in region 1. Region 2 ($D < 0$) corresponds to complex instability (*e.g.* Pfenniger 1985). The stability coefficients a_1, a_2 can be computed from the elements of the monodromy matrix $\Delta(T)$ by the relations

$$a_1 = -\text{trace}\ \Delta(T),$$
$$a_2 = b_{12} + b_{13} + b_{14} + b_{23} + b_{24} + b_{34},$$

where

$$b_{ij} = \begin{vmatrix} \Delta_{ii} & \Delta_{ij} \\ \Delta_{ji} & \Delta_{jj} \end{vmatrix}.$$

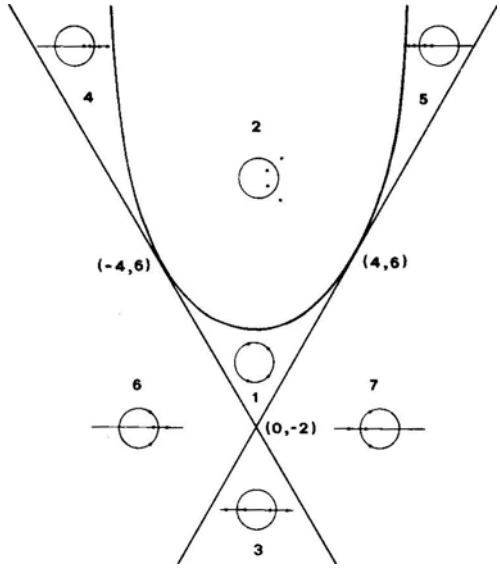

Figure 1. Broucke's seven stability regions on the (a_1, a_2) plane.

In the case of CH-problem ($e = 0$), x_1 is a constant, so the Hamiltonian (8) is time-independent and it is an integral of motion for the system. The existence of an integral of motion results to a pair of unit eigenvalues of the monodromy matrix and the stability of the orbit (under perturbations with respect to the initial conditions) is characterized by the stability index a (Hénon 1965) where

$$a = \tfrac{1}{2} \text{ trace } \Delta(T)$$

and the corresponding orbit is stable when $|a| < 1$. The stability coefficients a_1, a_2, for $e = 0$ are related to a by the relations

$$a_1 = -2(1+a), \qquad a_2 = 2(1+2a), \tag{24}$$

and the corresponding point in Fig. 1 lies on the line (22). In the case of the double-period bifurcation of family f_2, instead of a, the parameter

$$a' = \tfrac{1}{2} \text{ trace } \Delta(2T) = \tfrac{1}{2} \text{ trace } \Delta^2(T) = 2a^2 - 1$$

must be used in (24).

By continuing a $2\kappa\pi$–periodic orbit of the CH-problem for $e \neq 0$, the double unit eigenvalue of $\Delta(T)$ gives rise to a pair of distinct eigenvalues λ, $1/\lambda$ since Hamiltonian (6) is not anymore an integral of motion. It can be shown (Hadjidemetriou 1982) that this double eigenvalue is of mixed kind in the sense of Krein theory (Yakubovich & Starzhinskii 1975, p. 162), so λ, $1/\lambda$ in general move out of the unit circle along the real axis generating instability.

Numerical results showed that this is not the case for the apocentric parts of families a and g′, where the double unit eigenvalue gives rise to a pair of complex conjugates on the unit circle. The orbits however are unstable, since the other pair of eigenvalues is real.

Three families of periodic orbits of the EH-problem are known, which are named a, g′, and f_2 after their corresponding bifurcation family of the CH-problem (Hénon 1969). These families consist of periodic orbits which are symmetric with respect to the ξ–axis. The initial conditions ξ_0 , $\dot{\eta}_0$ and the evolution of the orbits have been given elsewhere (Ichtiaroglou 1981). In Figs 2 and 3 diagrams of ξ_0 and $\dot{\eta}_0$ versus e are presented for the above three families.

(a) *Family a*: This family bifurcates from a periodic orbit of family a of the CH-problem with period 2π. The corresponding stability index is $a = 71.0$ so it is expected that at least for small eccentricities the orbits will be unstable. In Table 1 the stability coefficients and the corresponding region of Fig. 1 in which each orbit belongs are given. In Fig. 4 the corresponding diagram in the (a_1, a_2) plane is presented. Eigenvalues μ, $1/\mu$ are always real while $\mu \to \infty$ as $e \to 1$. The other pair λ, $1/\lambda$ lies on the unit circle, except for the part $0 < e < 0.4$.

(b) *Family g′*: The bifurcation orbit for this family lies in family g′ of the CH-problem. Its period is also 2π and its stability index is $a = -241.7$ In most of the pericentric part both pairs of eigenvalues are real and in most of the apocentric part one pair is real while the other lies on the unit circle. For $0.7 < e < 0.755$ there is a part

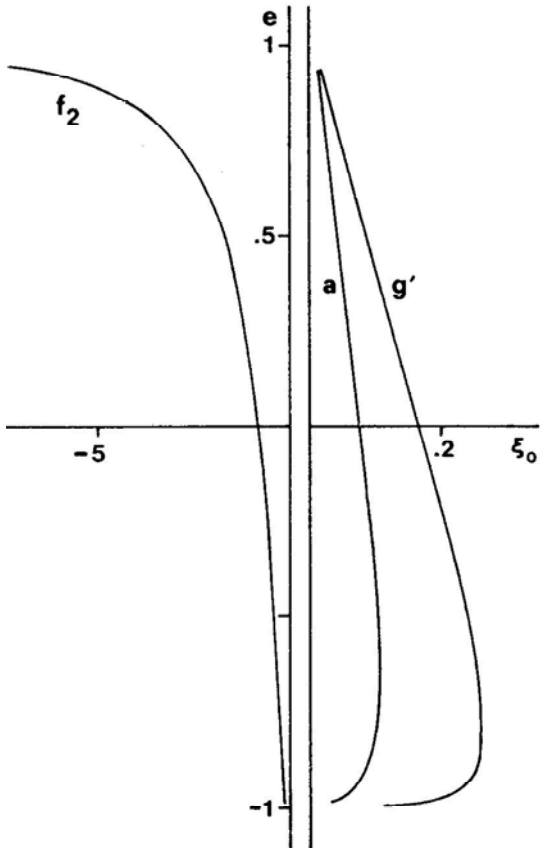

Figure 2. Initial position ξ_0 versus e for families a, g′ and f_2.

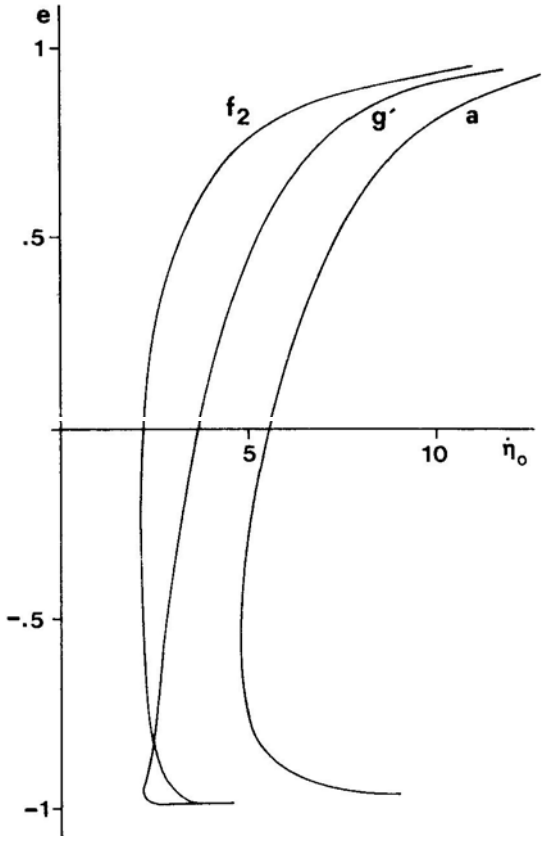

Figure 3. Initial velocity $\dot{\eta}_0$ versus e for families a, g′ and f_2.

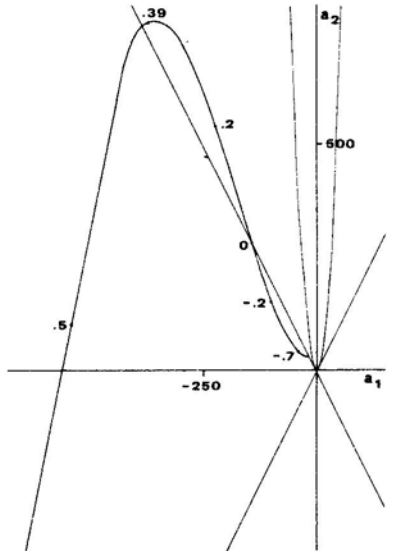

Figure 4. Stability diagram for family a.

Table 1. Stability coefficients of family a.

e	a_1	a_2	Region
−.94	−18.4	30.2	6
−.90	−22.3	33.1	6
−.70	−39.2	43.0	6
−.50	−58.0	63.9	6
−.30	−82.6	110.4	6
−.20	−98.7	150.0	6
0	−144.0	286.0	
.20	−222.1	538.8	4
.30	−286.0	697.2	4
.50	−541.2	101.2	6
.60	−852.7	−1697.8	3

Table 2. Stability coefficients of family g′.

e	a_1	a_2	Region
−.90	3533.6	2466.8	7
−.80	5735.6	11973.9	7
−.60	2392.8	3443.4	7
−.40	1192.2	235.1	7
−.20	712.9	−641.8	7
0	481.4	−964.8	
.20	351.1	−1149.3	3
.40	261.0	−1174.0	3
.60	160.0	−203.1	7
.70	67.2	1064.4	5
.71	53.8	1105.7	2
.72	39.2	1077.8	2
.73	23.1	947.6	2
.75	−14.0	177.0	2
.76	−35.7	−619.5	3
.80	−155.8	−10433.2	3

with complex instability. In Table 2 the stability coefficients are given while Fig. 5 presents the corresponding stability diagram.

In Table 3 we present the initial conditions for the orbits with complex instability which have not been presented elsewhere.

(c) *Family f_2*: Family f of CH-problem consists exclusively of stable orbits around P_1 but it does not contain a member with period $2k\pi$ for any integer k. Family f_2 of EH-problem bifurcates from a periodic orbit of f with period π, which is considered as written two times. The pair of unit eigenvalues however moves out of the unit circle for $e \neq 0$, so the continuation with respect to e gives no stable orbits. It must be noted that the stability coefficients of the orbits in this family are the same for the pericentric and the apocentric part. There is a sudden variation of stability for $|e| > 0.9$. The stability coefficients for this family are given in Table 4 while in Fig. 6 the stability diagram is shown.

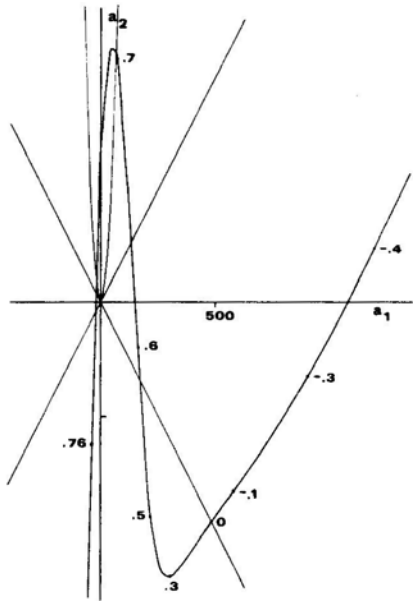

Figure 5. Stability diagram for family g'.

Table 3. Initial conditions for orbits of family g' with complex instability.

e	ξ	$\dot{\eta}$
.710	.046570	6.585264
.720	.045351	6.673609
.730	.044133	6.765350
.750	.041704	6.960076

Table 4. Stability coefficients for family f_2.

e	a_1	a_2	Region
0	−1.76	1.52	
.2	−1.68	1.27	6
.4	−1.85	0.22	6
.6	−3.35	−4.85	6
.8	−11.02	−35.99	3
.9	−32.08	−117.30	3
.96	−106.76	−203.15	6
.97	−149.23	−118.08	6
.98	−233.54	276.92	6
.99	−484.48	2599.40	4

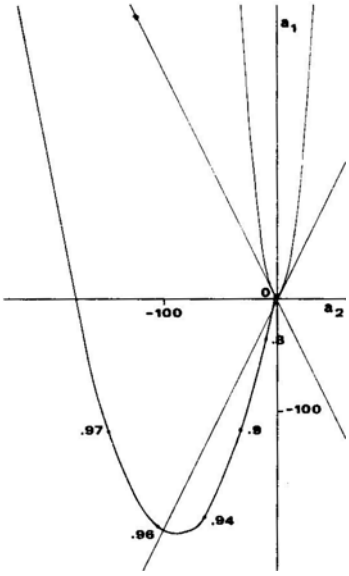

Figure 6. Stability diagram for family f_2. The values of a_1, a_2 are the same for the pericentric and the apocentric case.

4. Two families of rectilinear periodic orbits

We seek for a rectilinear solution of Equations (7) with $\eta = \dot{\eta} = 0$. The second Equation (7) yields

$$\dot{\xi} / \xi = \dot{x}_1 / x_1,$$

that is

$$\xi = c x_1. \tag{25}$$

Substituting (25) into the first Equation of (7) and taking into account Equation (6) we obtain

$$c = \pm\ 3^{-1/3}.$$

So the EH-problem admits the periodic solutions

$$=\xi = \pm\, 3^{-1/3}\, x_1, \qquad \eta = 0 \tag{26}$$

For $e = 0$ the above solutions correspond to the two collinear Lagrangian points L_1 and L_2 of the CH-problem (Hénon 1969). The value of the stability index at these points is (Charlier 1927, p.121 after Hénon 1969)

$$a = 1006.8.$$

So the orbits of the families (26) are very unstable for at least small *e.* It turns out that the orbits possess large stability coefficients for all values of *e* and the accuracy of the method presented in Section 3 is poor. In order to estimate the stability of the periodic orbits, we computed the largest Liapunov exponent σ (*e.g.*Lichtenberg & Lieberman

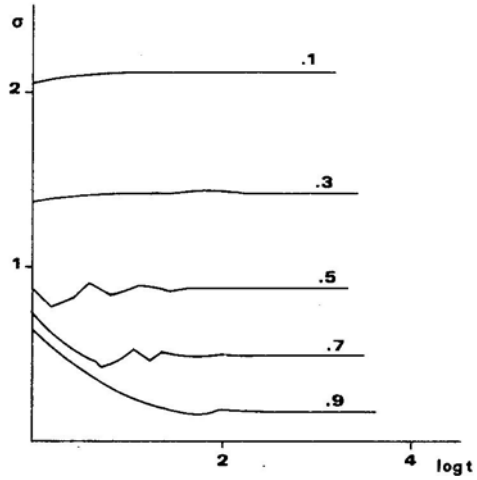

Figure 7. Largest Liapunov exponent σ versus log *t* for the rectilinear periodic orbits.

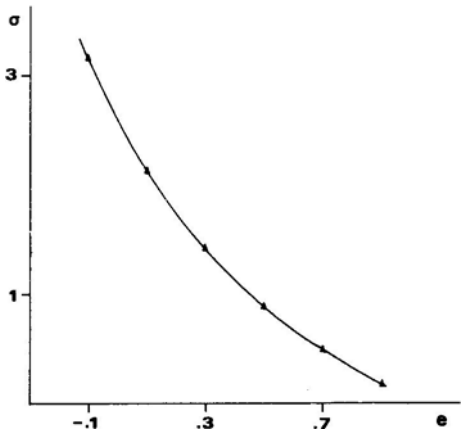

Figure 8. Largest Liapunov exponent a versus *e* for the rectilinear periodic orbits.

1983, p. 262) in the vicinity of these orbits. In Fig. 7 we give the computed a versus log *t*, where *t* is the computation time and in. Fig. 8 the computed exponents versus *e* are shown for $-0.1 < e < 0.9$. In every case the exponents are positive and large—of the order of 1 compared to the corresponding *a* of the chaotic regions in the Henon-Heiles system which are of the order of 0.1 (Benettin *et al.* 1976)—indicating the existence of chaotic regions in the vicinity of the periodic orbits (26).

5. Conclusions

In this paper we use the model of the elliptic Hill problem to study the effect of the eccentricity of a planet's orbit on the stability of the orbit of a satellite. Two of the periodic orbits of the corresponding circular case which have been used as bifurcation

orbits are unstable while the corresponding orbit of family f is stable. The existence of a double unit eigenvalue of the monodromy matrix in the circular case, which is of the mixed kind in the sense of Krein's theory indicates the generation of instability for $e \neq 0$ also for the continuation of this latter orbit and numerical investigation confirmed that this is indeed the case. Of course we cannot preclude the existence of stable periodic orbits in the EH-problem, but this seems to be improbable, at least for orbits with low multiplicity (orbits with less than three intersections of ξ-axis during a semiperiod). The period in the corresponding stable parts of families g and g' of the CH-problem varies in the interval $0 < T < 2.30206$ (Hénon 1969), so, in order to continue periodic orbits of these parts in the EH-problem, one has to consider them as written at least four times.

Two families of rectilinear periodic orbits which have been found analytically are also unstable and the computation of positive Liapunov exponents indicates the existence of chaotic motions in their vicinity.

References

Benettin, G., Galgani, L., Strelcyn, J.-M. 19 76, *Phys. Rev. A,* **14**, 2338.

Broucke, R. A. 1969, NASA Tech. Report 32–1360.

Charlier, C. L. 1927, *Die Mechanik des Himmels,*. 2. Auflage, Vol II, Walter de Gruyter, Berlin.

Christides, T. 1978, *PhD Thesis,* Univ. of Thessaloniki.

Hadjidemetriou, J. D. 1977, *Lectures* on *Periodic Orbits and their Stability,* Universite de Paris VI.

Hadjidemetriou, J. D. 1979, in *Instabilities in Dynamical Systems,* Ed. V. Szebehely, D. Reidel, Dordrecht, p. 135.

Hadjidemetriou, J. D. 1982, *Cel. Mech.,* **27**, 305.

Henon, M. 1965, *Ann. Ap.,* **28**, 992.

Welton, M. 1969, *Astr. Astrophys.,* **1**, 223.

Henon; M. 1970, *Astr. Astrophys.,* **9**, 24.

Henon, M. 1974, *Astr. Astrophys.,* **30**, 317.

Hill, G. W. 1886, *Acta Math.*, **8**, 1.

Howard, J. E. & Mackay, R. S. 1987, *J. Math. Phys.,* **28**, 1036.

Ichtiaroglou, S. 1980, *Astr. Astrophys.,* **92**, 139.

Ichtiaroglou, S. 1981, *Astr. Astrophys.,* **98**, 401.

Lichtenberg, A. J., Lieberman, M. A. 1983, *Regular and Stochastic Motion,* Springer-Verlag, New York.

Pfenniger, D. 1985, *Astr. Astrophys.,* **150**, 97.

Szebehely, V. 1967, *Theory of Orbits,* Academic Press, New York.

Yakubovich, V. A., Starzhinskii, V. M. 1975, *Linear Differential Equations with Periodic Coefficients,* Vol. I, J. Wiley & Sons, New York.

J. Astrophys. Astr. (1990) **11**, 23–28

The Magnetohydrodynamics of Stellar Structures

G. S. Dubey, U. S. Pandey* & J. P. Singh** *Department of Physics, G.S. Degree College, Samodhpur, Jaunpur, 223102*

L. K. Singh & S. N. Singh *Physics Department, Avadh University, Faizabad, U.P.*

Received 1989 June 6; accepted 1989 October 16

Abstract. The equation governing the equilibrium of a centrally-symmetric, self-gravitating distribution of matter is obtained by assuming that matter is described by magnetofluid and it is shown that the equation of stellar structure described by an ideal fluid is recovered when magnetic field **h** is vanishing.

Key words: relativity —magnetohydrodynamics—stellar structure

1. Introduction

Central symmetry about a point implies that there exists a coordinate system in which the line-element ds^2 has the property of being the same at all points at the same 'radial distance' from the centre of symmetry. We have chosen 'polar' spatial coordinates r, θ, φ with the origin located at the centre of symmetry. We have considered centrally-symmetric and static gravitational fields in the presence of magnetofluid.

The use of classical magnetohydrodynamics has been much successful in astrophysical systems like magnetic variable stars, sunspots and spiral arms (Alfvén 1950; Chandrasekhar 1961; Cowling 1962). But regime of astronomy mostly deals with the supremacy of gravitational attraction over all other forces. One needs, then, a theory of relativistic magnetohydrodynamics (RMHD). The important contributions to RMHD are due to Coburn (1963), Taub (1970) and Greenberg (1971). Lichnerowicz (1967) gives an elegant account of RMHD field equations and has established the existence and uniqueness of solutions. These equations were used by Yodzis (1971) to get an idea of magnetic effect in galactic cosmogony, gravitational collapse and pulsar theory. With this impetus, the study of the magnetohydrodynamics of stellar structures may be of current interest from both theoretical and observational viewpoints.

In this paper we have derived the relativistic magnetofluid equation of stellar structure in Section 2, the Schwarzschild solution for homogeneous masses for vanishing magnetic field **h** and magnetized version of Schwarzschild solution in Section 3. Concluding remarks are given in the last section.

* Department of Physics, University of Gorakhpur, 273009.
** Department of Physics, Rastriya Degree College, Jamuhai, Jaunpur.

2. Relativistic magnetofluid equation of stellar structure

The centrally-symmetric and static line element (Bose 1980) is described by

$$ds^2 = B(r)dt^2 - A(r)dr^2 - r^2(d\theta^2 + \sin^2\theta\, d\varphi^2). \tag{1}$$

We assume that matter is described by perfect magnetofluid. Perfect magnetohydrodynamics (Lichnerowicz, 1967) is characterized by the properties of a perfect fluid with infinite electrical conductivity and vanishing electric field **e** = 0. The electromagnetic field is reduced to a magnetic field **h** with respect to the velocity of the considered fluid. One assumes that permeability μ of the medium is constant. The energy-momentum tensor of such a fluid is given by

$$T_{\mu\nu} = (p+\rho)u_\mu u_\nu - pg_{\mu\nu} + \mu[(u_\mu u_\nu - \tfrac{1}{2}g_{\mu\nu})|\mathbf{h}|^2 - h_\mu h_\nu] \tag{2}$$

where

$$u_\mu h^\mu = 0, \qquad |\mathbf{h}|^2 = -h_\mu h^\mu \geqslant 0 \tag{3}$$

and u^μ being the four-velocity of the fluid with

$$u_\mu u^\mu = 1. \tag{4}$$

Maxwell equations under perfect magnetohydrodynamic approximation are expressed by

$$(u^\mu h^\nu - u^\nu h^\mu)_{;\mu} = 0. \tag{5}$$

Total pressure P and the energy-density W are written as

$$P = p + \tfrac{1}{2}\mu|\mathbf{h}|^2,$$
$$W = \rho + \tfrac{1}{2}\mu|\mathbf{h}|^2. \tag{6}$$

In view of Equation (6), Equation (2) takes the form

$$T_{\mu\nu} = (P+W)u_\mu u_\nu - Pg_{\mu\nu} - \mu h_\mu h_\nu. \tag{7}$$

For this spacetime $R_{0i}=0$ (i= 1, 2, 3) and nonvanishing four-velocity component is

$$u_0 = (B)^{1/2}. \tag{8}$$

Combining Equation (8) with (2) and assuming that P, W and **h** de[p]end on $r=x^1$ one obtains from $T^{\mu\beta}_{;\beta} = 0$ as

$$T^{\mu\beta}_{;\beta} = \frac{1}{\sqrt{-g}}\frac{\partial}{\partial x^\beta}(\sqrt{-g}\,T^{\mu\beta}) + \Gamma^\mu_{\nu\beta}T^{\nu\beta} = 0$$

or

$$-g^{\mu\nu}\frac{\partial P}{\partial x^\nu} + \Gamma^\mu_{\nu\beta}(P+W)u^\nu u^\beta - \frac{\mu}{\sqrt{-g}}\frac{\partial}{\partial x^\nu}(\sqrt{-g}\,h^\mu h^\nu) - \mu\Gamma^\mu_{\sigma\beta}h^\sigma h^\beta = 0. \tag{9}$$

By making use of Equation (8), the second term becomes $(P + W)\,\Gamma^\mu_{00}$ and $\Gamma^\mu_{00} = -\tfrac{1}{2}g^{\mu\nu}\,\partial g_{00}/\partial x^\nu$. Now, Equation (9) reduces to

$$-g^{\mu\nu}\frac{\partial P}{\partial x^\nu} - \frac{1}{2}g^{\mu\nu}\left(\frac{P+W}{B}\right)\frac{\partial B}{\partial x^\nu} - \frac{\mu}{\sqrt{-g}}\frac{\partial}{\partial x^\nu}(\sqrt{-g}\,h^\mu h^\nu)$$
$$-\frac{1}{2}\mu g^{\mu\nu}\left(\frac{\partial g_{\sigma\nu}}{\partial x^\beta} + \frac{\partial g_{\nu\beta}}{\partial x^\sigma} - \frac{\partial g_{\sigma\beta}}{\partial x^\nu}\right)h^\sigma h^\beta = 0. \tag{10}$$

Further contraction by $g_{\mu\alpha}$ gives

$$\frac{\partial P}{\partial x^\alpha}+\frac{1}{2}\left(\frac{P+W}{B}\right)\frac{\partial B}{\partial x^\alpha}+g_{\mu\alpha}\frac{\mu}{\sqrt{-g}}\frac{\partial}{\partial x^\nu}(\sqrt{-g}h^\mu h^\nu)$$

$$+\frac{\mu}{2}\left(\frac{\partial g_{\sigma\alpha}}{\partial x^\beta}+\frac{\partial g_{\alpha\beta}}{\partial x^\sigma}-\frac{\partial g_{\sigma\beta}}{\partial x^\alpha}\right)h^\sigma h^\beta=0. \quad (11)$$

For this case it can easily be shown that

$$h^0=h^2=h^3=0 \quad \text{and} \quad h^1\neq 0.$$

From Maxwell Equations (5) and (3), one obtains

$$\frac{|\mathbf{h}|_{,1}}{|\mathbf{h}|}+\frac{2}{r}=0. \quad (12)$$

Integrating the above equation we have

$$|\mathbf{h}|=\frac{D}{r^2}. \quad (13)$$

Here D is a constant of integration. The Equation (11) for $\alpha = 0$ merely re-expresses the time independence of P and becomes trivial. For $\alpha = 2$ and $\alpha = 3$, corresponding derivatives of P vanish, showing that P possesses central symmetry. For $\alpha = 1$, Equation (11) is non-trivial and yields

$$P'+\left(\frac{P+W}{2}\right)\frac{B'}{B}-\frac{1}{2}\mu|\mathbf{h}|^2\frac{3B'}{B}+\frac{2}{r}\mu|\mathbf{h}|^2=0 \quad (14)$$

which is the condition satisfied by $B(r)$ in magnetohydrostatic equilibrium. It may be inferred from Equation (14), when magnetic field is absent, that the equation satisfied by $B(r)$ in hydrostatice-quilibrium is

$$\frac{B'}{B}=-\frac{2p'}{p+\rho}. \quad (15)$$

By inserting the expression for $T_{\mu\nu}$ and T into the Einstein equation we obtain

$$R_{\mu\nu}=8\pi[(P+W)u_\mu u_\nu-\tfrac{1}{2}g_{\mu\nu}(W-P)-\mu h_\mu h_\nu-\tfrac{1}{2}g_{\mu\nu}\mu|\mathbf{h}|^2]. \quad (16)$$

From it, we derive

$$\frac{1}{2}\left(\frac{R_{00}}{B}+\frac{R_{11}}{A}\right)+\frac{R_{22}}{r^2}=8\pi W. \quad (17)$$

Further simplification leads to

$$\frac{A'}{rA^2}-\frac{1}{Ar^2}+\frac{1}{r^2}=8\pi W \quad (18)$$

which can be rewritten in the form

$$\left(\frac{r}{A}\right)'=1-8\pi r^2 W. \quad (19)$$

The solution of the above differential equation is

$$A(r)=\left(1-\frac{2M(r)}{r}+\frac{C}{r}\right)^{-1} \tag{20}$$

where C is a constant of integration and

$$M(r)=4\pi\int_0^r r^2\,W(r)\,\mathrm{d}r. \tag{21}$$

The boundary condition that $A(r)$ is nonzero at the origin follows from Equation (17) so that the constant C must be zero. Hence

$$A(r)=\left(1-\frac{2M(r)}{r}\right)^{-1}. \tag{22}$$

From the '22 component' of the Einstein equation, we obtain

$$R_{22}=1-\frac{r}{2A}\left(\frac{B'}{B}-\frac{A'}{A}\right)-\frac{1}{A}=4\pi r^2[(W-P)+\mu|\mathbf{h}|^2]. \tag{23}$$

By eliminationg A and B and using Equations (14) and (22), one may obtain relativistic magnetofluid equation of stellar structure

$$-r^2\frac{\mathrm{d}P}{\mathrm{d}r}=(P+W-3\mu|\mathbf{h}|^2)\,[M(r)+4\pi r^3P-4\pi r^3\,\mu|\mathbf{h}|^2]\times\left(1-\frac{2M(r)}{r}\right)^{-1}+2r\mu|\mathbf{h}|^2. \tag{24}$$

It is concluded from Equation (24) that, when magnetic field is absent, one may obtain the equation of stellar structure when the matter is described by an ideal fluid as

$$-r^2\frac{\mathrm{d}P}{\mathrm{d}r}=(p+\rho)\,[M(r)+4\pi r^3\,p]\left(1-\frac{2M(r)}{r}\right)^{-1}. \tag{25}$$

Once the appropriate boundary conditions are specified, Equation (24) together with Equation (21) supplemented by the equation of state of matter, provides a system of equations from which stellar structure could be calculated.

3. Magnetized version of Schwarzschild solution for homogeneous masses

We assume an equation of state

$$W = \text{constant throughout the stat.} \tag{26}$$

Equation (2) yields

$$M(r)=\frac{4\pi}{3}\,Wr^3 \tag{27}$$

and the stellar structure Equation (24) reduces to

$$-\frac{\mathrm{d}P}{\mathrm{d}r}=(P+W)-3\mu|\mathbf{h}|^2)\frac{4\pi r}{3}(W+3P-3\mu|\mathbf{h}|^2)\left(1-\frac{8\pi}{3}\,Wr^2\right)^{-1}+\frac{2}{r}\,\mu|\mathbf{h}|^2. \tag{28}$$

For vanishing magnetic field, we obtain

$$-\frac{dp}{dr}=\frac{4\pi r}{3}(p+\rho)(3p+\rho)\left(1-\frac{8\pi}{3}\rho r^2\right)^{-1}. \tag{29}$$

By expressing the energy-density W in terms of star's mass M and radius R, one may obtain

$$M=M(R)=\frac{4\pi}{3}WR^3 \quad \text{and} \quad A(r)=\left[1-\frac{2Mr^2}{R^3}\right]^{-1}. \tag{30}$$

We see that at the star's radius $r = R$ the above solution matches with the corresponding expression for the Schwarzschild exterior solution. One can easily obtain the solution of Equation (25) subject to the condition that the pressure p vanishes at the star's radius R. In the limit of vanishing magnetic field **h**, p turns out to be

$$p(r)=\frac{3M\left(1-\frac{2M}{R}\right)^{1/2}-\left(1-\frac{2Mr^2}{R^3}\right)^{1/2}}{4\pi R^3\left(1-\frac{2Mr^2}{R^3}\right)^{1/2}-3\left(1-\frac{2M}{R}\right)^{1/2}}. \tag{31}$$

However, when the magnetic field is present, one may obtain from Equation (14) as

$$\frac{B'}{B}=-\frac{2\left[P'+\frac{2}{r}\mu|\mathbf{h}|^2\right]}{P+W-3\mu|\mathbf{h}|^2}. \tag{32}$$

We determine the function $B(r)$ from Equations (28), (30) and (32). In the limit of vanishing magnetic field and to the boundary condition that at $r = R$, $B(r)$ matches the corresponding expression $\left(1-\frac{2M}{R}\right)$ for Schwarzschild exterior solution, one obtains

$$B(r)=\frac{1}{4}\left[3\left(1-\frac{2M}{R}\right)^{1/2}-\left(1-\frac{2Mr^2}{R^3}\right)^{1/2}\right]^2. \tag{33}$$

4. Concluding remarks

We have derived relativistic magnetofluid equations of stellar structure (RMESS) by assuming that matter is described by perfect magnetofluid. The general formalism developed here may be used to study the different stellar structures using the appropriate boundary conditions and equation of states.

Acknowledgements

The authors are thankful to Professor R. M. Misra for encouragement and useful discussions during these investigations. GSD is thankful to University Grants Commission, New Delhi for providing research assistance. The authors are thankful to two referees for correcting our equations, constructive criticisms and useful suggestions.

References

Alfvén, H. 1950, *Cosmical Electrodynamics*, Clarendon Press, Oxford.
Bose, S. K. 1980, *An Introduction to General Relativity*, Wiley Eastern Ltd, New Delhi.
Chandrasekhar, S. 1961, *Hydrodynamic and Hydromagnetic Stability*, Clarendon Press, Oxford.
Coburn, N. 1963, *Relativistic Fluid Mechanics and Magnetohydrodynamics*, Academic Press, New York.
Cowling, T. G. 1962, *Rep. Prog. Phys.*, **25**, 000.
Greenberg, P. J. 1971, *Astrophys. J.*, **164,** 589.
Lichnerowicz, A.1967, *Relativistic Hydrodynamics and Magnetohydrodynamics*, W. A. Benjanin, New York.
Taub, A. H. 1978, *Ann. Rev. Fluid Mech.*, **10**, 301.
Yodzis, P. 1971, *Phys. Rev.*, **D3**, 2941.

J. Astrophys. Astr. (1990) **11**, 29–35

The Newtonian Forces in the Kerr Geometry*

Sandip K. Chakrabarti *Tata Institute of Fundamental Research, Homi Bhabha Road, Colaba, Bombay 400005*

A. R. Prasanna *Physical Research Laboratory, Navarangpura, Ahmedabad 380009*

Received 1989 June 12; accepted 1989 October 16

Abstract. We study the properties of the 'Newtonian forces' acting on a test particle in the field of the Kerr black hole geometry. We show that the centrifugal force and the Coriolis force reverse signs at several different locations. We point out the possible relevance of such reversals particularly in the study of the stability properties of the compact rotating stars and the accretion discs in hydrostatic equilibria.

Key words: black holes—accretion discs—stability

In spite of the beautiful description of physics through geometry expressed by Einstein's general relativity seventy-five years ago, and its resurrection during the last twenty-five years, a large percentage of physicists still feel comfortable to discuss the dynamics of a particle in terms of the 'Newtonian forces' such as the centrifugal force, Coriolis force *etc.* which are introduced in the early stages of one's education. Although Einstein's description of the motion of the particles in a given curved spacetime in terms of their geodesics is very general, understanding the 'physical significance' of the various terms that occur in the equation giving the total acceleration is not always possible. However, it has been shown (Abramowicz, Carter & Lasota 1988, hereinafter referred to as ACL) recently that in a conformally projected three-geometry of the four-dimensional manifold where the null lines of the four-geometry are the geodesics, a reference frame exists where the total force acting on a test particle may be split into the gravitational, the centrifugal and the Coriolis terms. This is called the Optical Reference Geometry (ORG).

In this paper we present and analyze these forces in the Kerr geometry, which is the most general solution that represents the spacetime outside a compact rotating object. We show, however, that these forces do not always have the 'Newtonian' behaviour.

The frame of reference as expressed in ORG is obtained through the decomposition,

$$\mathrm{d}s^2 = \Phi[\tilde{g}_{ik}\mathrm{d}x^i\mathrm{d}x^k - (\mathrm{d}t + 2\alpha_i\mathrm{d}x^i)^2] \tag{1}$$

which on comparison with $\mathrm{d}s^2 = g_{\alpha\beta}\mathrm{d}x^\alpha\mathrm{d}x^\beta$ for the Kerr metric yields on the equatorial plane (in Boyer–Lindquist coordinates),

$$\tilde{g}_{rr} = r^3/[(r-2)\Delta], \quad \tilde{g}_{\phi\phi} = r^2\Delta/(r-2)^2, \quad \Phi = (1-2/r), \quad \Delta = r^2 - 2r + a^2,$$

* Received honourable mention in the 1989 Gravity Research Foundation essay competition.

and

$$\alpha_\phi = a/(r-2). \tag{2}$$

Here, a is the Kerr parameter.

If we now consider a test particle in motion, the forces acting on it as expressed by the ACL equation are given by,

$$m\Phi(f_i - 2\alpha_i f_0) = p^j \tilde{\nabla}_j p_i + 1/2 m^2 \partial_i \Phi + 2Ep^j \omega_{ij}, \tag{3}$$

where, $p^t = \Phi p^i$, is the 3-momentum in the projected conformal space (ORG) and $\tilde{\nabla} j$ is the covariant derivative with respect to the 3-metric $\tilde{g}_{ik}$. The three terms on the right-hand side may be interpreted as the contributions from the centrifugal force, the gravitational force and the Coriolis force respectively provided a negative sign is taken throughout to match the conventional direction for gravitational force (one identifies the gravitational potential= – Φ/2). With this convention one can see that in Kerr geometry, various quantities take the form

$$\begin{aligned} \omega_{r\phi} &= -a/(r-2)^2, \\ p^\phi &= El(r-r_l)(r-2)/[r^2\Delta], \\ r_l &= 2(1-a/l). \end{aligned} \tag{4}$$

Here, E and l are the conserved specific energy and the specific angular momentum of the test particle respectively: $E = u_t$ and $l = u_\phi/u_t$, where u_ϕ and u_t are the covariant components of the four velocity and m is the mass of the test particle. In the absence of a better word, we shall call r 'the p^ϕ reversal radius' as the sign of p^ϕ changes at this location. In the Schwarzschild geometry (a =0), it is observed (Abramowicz & Prasanna 1989, hereinafter AP) that the centrifugal force (Coriolis force is identically zero) *reverses sign* at the circular photon orbit (r =3) which is the minimum of the proper circumferential radius $\tilde{r}$ of the projected orbit in the ORG defined by,

$$\tilde{r}^2 = \tilde{g}_{ik} \tilde{\delta}^i \tilde{\delta}^k \tag{5}$$

where $\tilde{\delta}^i$ is the azimuthal (spacelike) Killing vector satisfying the Killing equation, $\tilde{\nabla}_{(i}\tilde{\delta}_{j)}$

As this quantity is independent of the orbital angular momentum of the particle it is useful to relate it to another well-known quantity of the same dimension λ (Chakrabarti 1984, 1985; also see Abramowicz 1983 where λ. was used for some co-ordinate transformation), defined as $\lambda^2 = 1/\Omega$, Ω being the angular velocity of the test particle ($= u^\phi/u^t$). In the present case one has,

$$\tilde{r}^2 = r^2\Delta/(r-2)^2, \tag{6a}$$

$$\lambda^2 = r^2\Delta/[(r-r_l)(r-r_\Omega)] = (r^3 + a^2 r - alr_l)/(r-r_l). \tag{6b}$$

Notice that in both *2.*[2] and the force components, the angular momentum of the particle appears in the combination '*al*' or '*al*', indicating the nature of the angular momentum coupling and the importance of the relative signs of the combination. Also, $r_\Omega = 2(1 - a\Omega)$. Among the most important properties of λ^2, one notes that it *becomes equal to* r^2 *in the Schwarzschild geometry; the supremum* (*infimurn*) *of its minima coincides with the last circular photon orbit for the prograde (retrograde) motion*, (Chakrabarti, 1985) and itself and its derivative diverge at the 'p^ϕ reversal radius' $r = r_i$. Expressing the

force components explicitly in terms of p^{ϕ} one finds,

$$F_{\rm cf} = r^2 p^{\phi 2}[r(r-2)(r-3)-2a^2]/[m(r-2)^4]$$
$$= E^2 l^2 [r(r-2)(r-3)-2a^2](r-r_l)^2/[r(r-2)(r-r_-)(r-r_+)]^2, \quad (7)$$

$$F_{\rm g} = -m/r^2(1-2/r)^{-1}, \quad (8)$$

$$F_{\rm co} = 2aErp^{\phi}/[m(r-2)^3]$$
$$= 2alE^2(r-r_l)/[r^2(r-2)^2(r-r_-)(r-r_+)]. \quad (9)$$

Since the gravitational force F_g is independent of the angular momentum of the particle, we shall be primarily concerned with the centrifugal force $F_{\rm cf}$ and the Coriolis force $F_{\rm co,}$ Here r_- and r_+ denote the inner and the outer event horizons respectively. Notice that both the centrifugal and the Coriolis forces are zero everywhere on the 'p^{ϕ} reversal radius' $r = r_l$ *except* when $r_i = r_-$, *i.e.*, $2a/l = r_+$ and $r_l = r_+$, *i.e.*, $2a/l = r_-$. *Otherwise on the event horizons both the force components diverge. They also diverge on the ergosurface.* In addition, the centrifugal force vanishes at $r = r_\infty$ where $r_\infty(r_\infty - 2)(r_\infty - 3) = 2a^2$. [The reason for calling these locations r is that the geodesic curvature $\mathscr{R}$ g ∞ r at these points (AP)].

To illustrate how the forces behave we draw in Figs 13 $F_{\rm cf,}$ $F_{\rm co}$, and $F_{\rm sum} = F_{\rm cf} + F_{\rm co}$ respectively for the test particles with $a/l = -0.3$ and 0.3 shown in dashed and solid curves respectively. The Kerr parameter a was chosen to be 0.95 throughout. One notes that for both the values, $a/l = \pm$ 0.3, $F_{\rm cf}$ changes sign (Fig. la) at $0 < r_\infty < r_-$, at $r^- < r_\infty < r_+$, and also at $r_\infty > 2$. It also vanishes without changing sign at $r = r_l$ (= 1.4 for a/l=0·3, 2.6 for $a/l = -$ 0.3). Fig. lb shows in detail the region outside the ergosphere and particularly the locations of r_∞ and r_l . $F_{\rm cf}$ diverges at $r = 0$, $r = r_\pm$ and $r = 2$. The Coriolis force $F_{\rm co}$ changes sign (Fig. 2) at $r=r_\pm$, $r= r_{l\,,}$ The sum of these two angular momentum-dependent forces $F_{\rm sum}$ similarly reverses sign at several different places (Fig. 3). At the points where $F_{\rm sum}$ changes sign, only force acting on the particle is due to gravity, albeit the presence of rotation. To show the behaviour of $F_{\rm sum}$ over a large range of $a/1$ ratio, the contours of $F_{\rm sum} = 0$ are plotted in the 'r–a/l' plane in Fig. 4a. One notices that among other things, $F_{\rm sum}= 0$ on the straight line $r = 2(1- a/1)$, except at $2a/l=r_\pm$.

Consider now a fluid configuration (say, an accretion disc surrounding the Kerr hole or a compact rotating object such as a neutron star) in hydrostatic equilibrium which constitutes a collection of such test particles. The stability of this configuration is determined by the condition

$$F(l, r) + G(r) = 0. \quad (10)$$

Here, $F(l, r)$ contains the forces which explicitly depend upon the angular momentum of the particle and $G(r)$ denote all the forces including gravity, which are independent of the angular momentum of the particle. When some test matter of angular momentum $l_0 = l(\mathrm{r_0})$ is displaced from its original position r_0 to a new position $r_o + \delta r$, where the angular momentum of the matter is $l_o + \delta l$, the perturbation of the total force is

$$\delta T = [F(l_1, r_1) + G(r_1)] - [F(l_0, r_1) + G(r_1)] = -\frac{\partial F}{\partial l}\frac{\partial l}{\partial r}\delta r. \quad (11)$$

Since in the stable situation, the displaced matter must come back to its original

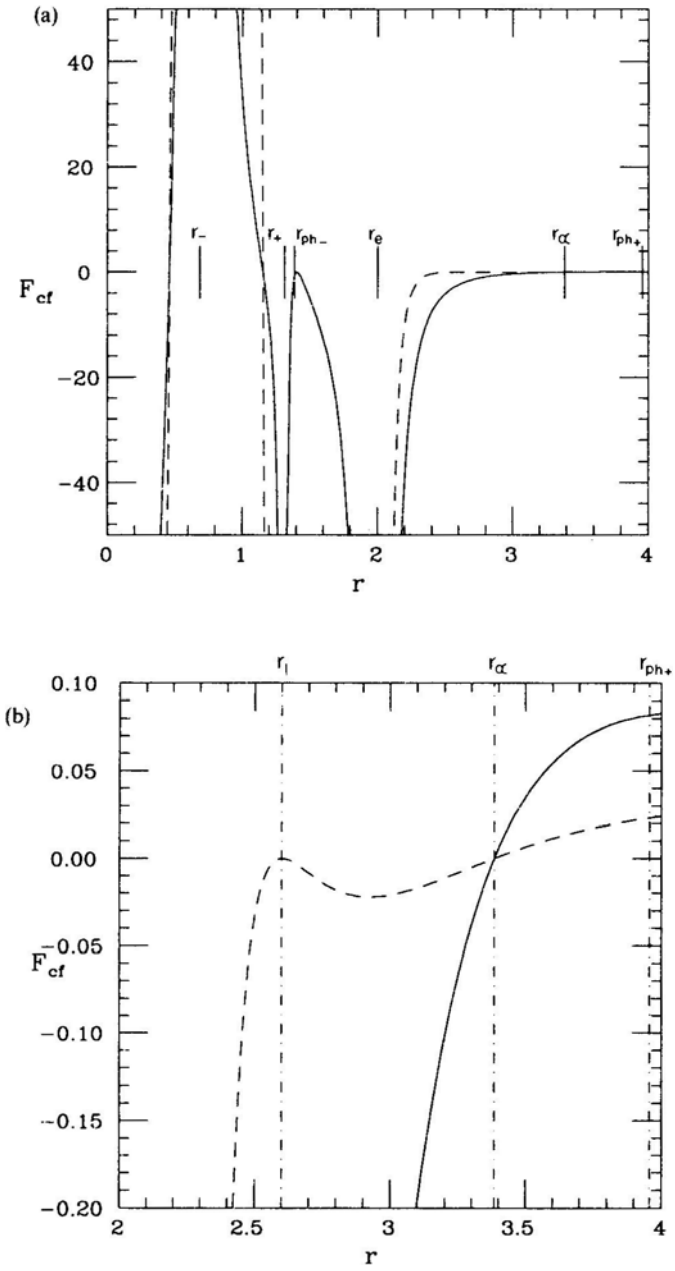

Figure 1. (a) The variation of the centrifugal force F_{cf} as a function of the radial distance on the equatorial plane in the Kerr geometry with angular momentum parameter a = 0.95. The solid curve is for a/l= –0.3 and the dashed curve is for a/l = 0.3. Various geometrical important locations are indicated by the vertical solid lines. They are from the left to the right r_{-}, the inner horizon, r_+ the outer horizon, r_{ph-}, the inner photon orbit, r_c, the ergosphere and r_{ph+}, the outer photon orbit. Also shown is r_∞ outside the horizon where the geodesic curvature $\mathscr{R}$ diverge. (b) An expanded view of the region outside the ergosphere of (a). In addition to r_∞ where F_{cf} vanishes independent of the angular momentum of the particle, we show the 'p^ϕ reversal radius' r_l.

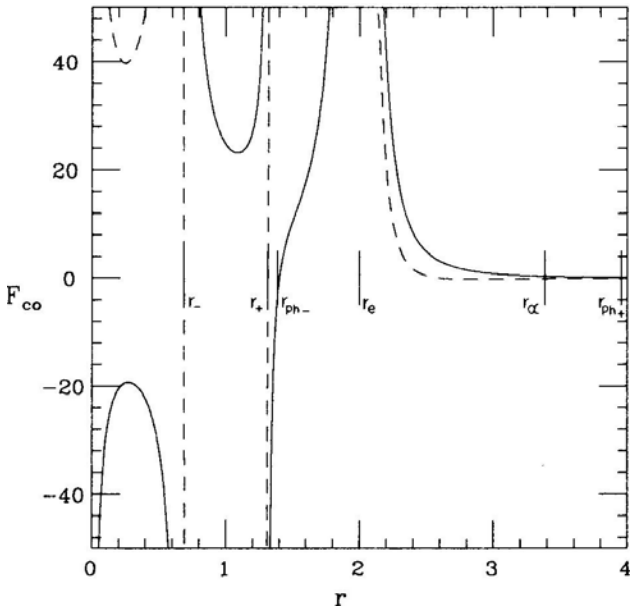

Figure 2. A figure similar to Fig. la showing the variation of the *Coriolis* force F_{co}.

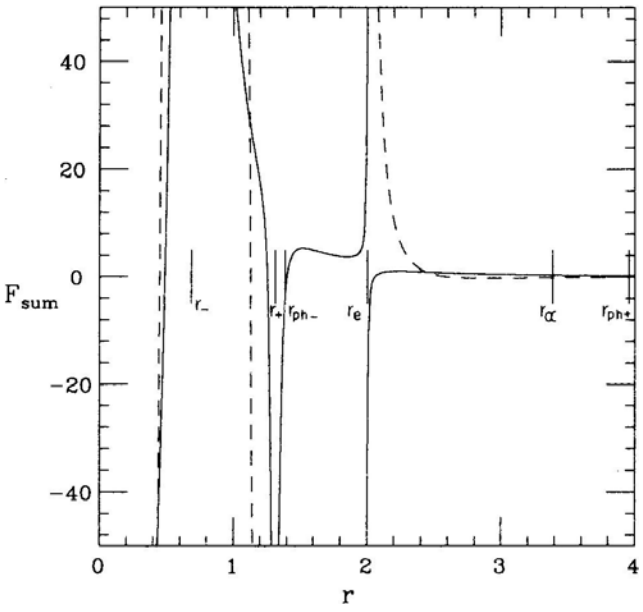

Figure 3. A figure similar to Fig. la showing the variation of the *total* angular-momentum-dependent force F_{sum} acting on the test particle.

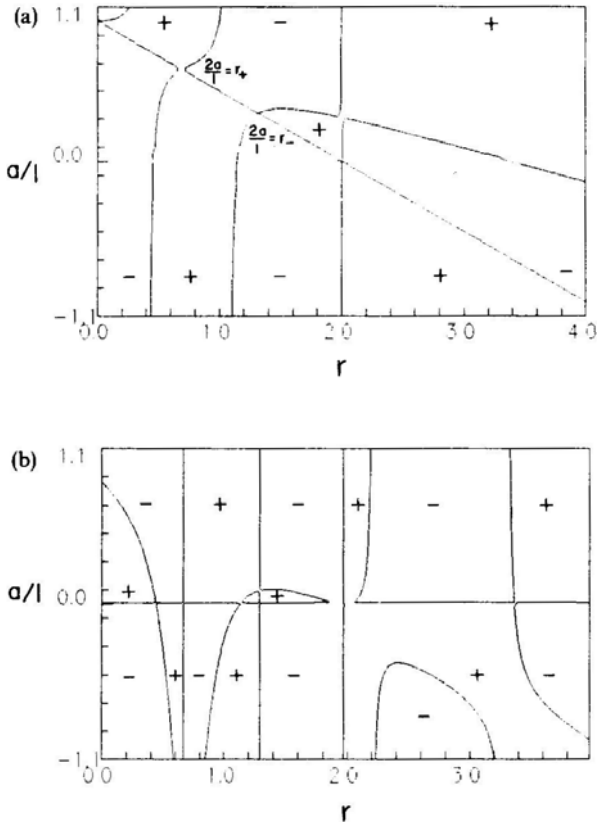

Figure 4. (a) The contours of $F_{\rm sum}$= 0 are shown in the '*r*–*a*/*l*' plane. The signs + and – indicate the outward and the inward directed force respectively. Notice that the $F_{\rm sum}$ vanishes everywhere on the $r = r_l$ line (the so-called 'p^{ϕ} reversal radius') except where $2a/l=r_{\pm}$. (b) The contours of $\partial F_{\rm sum}/\partial l=0$ separating the regions where the Rayleigh criterion for stability of a rotating configuration reverses sign. The signs +and – indicate the signs of $\partial l/\partial r$ which are required for the configuration to be stable under axisymmetric perturbation.

Position, $\partial T/\partial r <0$, *i.e.*,

$$\frac{\partial F}{\partial l}\frac{\partial l}{\partial r} > 0.$$

In the present situation, $F(l, r) = F_{\rm sum}$. The gradient $\partial F_{\rm sum}/\partial l$ need not be positive everywhere as in the Newtonian case. Indeed, this quantity reverses its sign several times inside as well as outside the horizon. Fig. 4b shows its behaviour for a large range of *a*/*l* ratio. Only the contours of $\partial F_{\rm sum}/\partial l =0$ are shown and the sign of the gradient $\partial l/\partial r$ which keeps the equilibrium configuration stable are noted. The important conclusion of this exercise is that the familiar Rayleigh criterion of stability, namely, $\partial l/\partial r>0$ does not hold everywhere in the Kerr geometry.

The importance of the reversals of the gradient of the angular momentum distribution could be significant, particularly, in the study of the structure of the compact stars and the geometrically thick accretion discs. In these cases the complete solution has to be obtained fully self-consistently by solving Einstein's equations in the

presence of the gravitating matter. The fact that $F_{\rm sum}$ points *inwards* in some region may be the cause of the observation of Chandrasekhar & Miller (1974) who show that in the context of general relativity, the ellipticity of a rotating homogeneous Maclaurin spheroid first increases and then decreases in the course of its collapse if the total angular momentum and the mass are kept fixed. Equivalently, if a compact star accretes mass and angular momentum (as is believed to be the case for the millisecond pulsars), it is not necessary that the star becomes progressively unstable, since addition of angular momentum does not always imply enhancement of centrifugal force. In fact the star may pass through some stable phase beyond the well-known marginal configuration in which the angular velocity at the outer surface is equal to the Keplerian velocity. A complete study is essential to settle this important issue. Our result, presented here at the test particle level, can only give guidance as to what to expect. Recently, Abramowicz & Miller (1989) consider this aspect, and show that the Chandrasekhar and Miller result for slowly rotating bodies may be explained within the framework of the general discussion of rotational effects in a strong gravitational field as given by AP.

References

Abramowicz, M. A. 1983, *Astrophys. J.*, **254**, 784.
Abramowicz, M. A., Carter, B., Lasota, J. P. 1988, *Gen. Rel. Graw.*, **8**, 1173.
Abramowicz, M. A., Prasanna, A. R. 1989, *Mon. Not. R. Astron. Soc*, (to appear) (AP).
Abramowicz, M. A., Miller, J, 1989, *Mon. Not. R. Astr. Soc.*, (to appear).
Chakrabarti, S. K. 1984, *Active Galactic Nuclei*, Ed. J. E. Dyson, Manchester Univ. Press.
Chakrabarti, S. K. 1985, *Astrophys. J.*, **288**, 1.
Chandrasekhar, S., Miller, J. C. 1974, *Mon. Not. R. Astr. Soc.*, **167**, 63.

J. Astrophys. Astr.(1990) **11**, 37–42

Emission Spectrum of Hot R OB Star MV Sgr*

N. Kameswara Rao *Indian Institute of Astrophysics, Bangalore 560034*

L. Houziaux *Instut d' Astrophysique, Universite de Liège, Liege, Belgium*

Sunetra Giridhar *Indian Institute of Astrophysics, Bangalore 560034*

Received 1989 August 23; accepted 1989 October 18

Abstract. The new spectroscopic observation of MV Sgr obtained at ESO in 1987 July shows enhanced emission lines of He I λ3889, [S II] λ4068 relative to the observations discussed by Jeffrey *et al.* (1988). The presence of [S II] λ4068 indicates the presence of planetary-nebulae-like envelope around the star. Although the radial velocity of the absorption lines and Fe II emission lines do agree with the velocity given by Jeffrey *et al.*, the [S II] λ4068 and probably He I emission lines appear to behave differently.

Key words: stars, R CrB type—stars, nebulosities—stars, individual

1. Introduction

MV Sgr is one of the hot R CrB stars with $T_{\rm eff}$ = 15400 ± 400 K (Drilling *et al.* 1984) which shows light variations of R CrB type with magnitude range 12–16. The spectrum near maximum light has been described by Herbig (1964, 1975) who discovered the presence of emission lines mostly due to Fe II in addition to a hydrogen-deficient B-typestar absorption spectrum. The emission lines consisting of Hα, Fe II, He I, Si II, N I and O I dominate the red part of the spectrum which led Herbig to propose that the Fe II emission is associated with gaseous component that has excitation temperature substantially lower than the colour temperature of the B star. In the ultraviolet (UV), the low-excitation lines mainly due to Fe II, Si II, C I, O I, AI II exist in absorption (Rao & Nandy 1982) indicative of the low temperature gas seen against the continuum of the B-type star. Moreover, Rao & Nandy (1982) also reported variability in the strengths of these circumstellar absorption lines.

Recently higher resolution blue spectra obtained around light maximum have been analysed by Jeffrey *et al.* (1988) who find that the photospheric spectrum is hydrogen-deficient by about the same degree as the helium star HD 124448, but is under-abundant in metals N, Si by 1 dex and carbon is underabundant by 2 dex relative to HD 124448. Their CASPEC spectrum obtained with ESO 3.6 metre telescope when the star was about a magnitude fainter showed more emission-line activity. They also discovered that the Fe II emissions are split with peak separation of 68.2 km s^{-1} and FWHM of 131 ±18 km s^{-1}. The central minimum of the emission is nearly at line

* Based on observations collected at the European Southern Observatory, La Silla, Chile.

centre and therefore the mean emission-line centre gives a radial velocity very close to the one given by the absorption lines. MV Sgr also seems to show variability in the emission lines of Hα, He I. In this paper we describe the emission line spectrum which showed many interesting changes relative to that described by Jeffrey *et al.* (1988).

2. Observations

The observations were obtained in 1987 July 30, with ESO 1.5 metre spectrographic telescope using the Boller & Chivens spectrograph and a CCD detector combination giving a dispersion of 39 Å mm^{-1} in the blue which corresponds to 0.58 Å per pixel. The wavelength region covered was from λ3705 to λ4300. The wavelength calibration was done with He-Ar source which was observed just after the stellar exposure. The flux calibration was done using three Standard stars, Kopff 27, LTT 7987 and LTT 9239. The spectrum reductions were done using the MIDAS package at ESO, Garching. The flux-calibrated spectrum is shown in Fig. 1.

It appears that these observations have been obtained when the star was slightly below maximum light (*i.e.* at $m_v \sim 13.2$) according to AAVSO visual estimates (Mattei 1989, Personal communication).

3. Results and discussion

The spectrum is mostly dominated by absorption lines predominantly due to He I, O II and N II. Several of the early members of He I triplet series have emission components emerging through the absorption *e.g.* λ4026. Some of these identifications are shown in the figure. Incidentally, Jeffrey *et al.* (1988) have reported that nearly all He I lines are found in absorption including λ3889 (their Table 2) whereas our spectrum (Fig. 1) shows He I λ3889 very strongly in emission.

3.1 *Radial Velocities*

The wavelength calibration of our spectrum is done using the He–Ar comparison source. A third degree polynomial fits the 22 comparison lines across the spectrum with a standard deviation of 0.087 Å corresponding to 6.4 km s^{-1} at 4100 Å. We have measured the radial velocity of 14 stellar absorption lines(12 He I, one N II, one CII) which show that the radial velocity of MV Sgr on JD 2447006.7 as – 95 ± 8 (s.d.) km s^{-1}. This value is in good agreement with the measurements of Jeffrey *et al.* (1988). They derive – 91 ± 7 km s^{-1} using 9 lines on JD 2445153.2 and – 96 ± 4 km s^{-1} using 4 lines on JD 2446163.7 which indicates no large-scale radial velocity variations.

We could measure only one interstellar line of Ca II at λ3933 which gives a radial velocity +19 km s^{-1} in good agreement with + 20 km s^{-1} obtained by Jeffrey *et al.* (1988).

3.2 *The Emission Lines*

As mentioned by Jeffrey *et al.* (1988) and also by Herbig (1975), the emission lines are mostly due to Fe II, Ti II, Ca II, Si I *etc.* All the lines in Table 6 of Jeffrey *et al.* (1988)

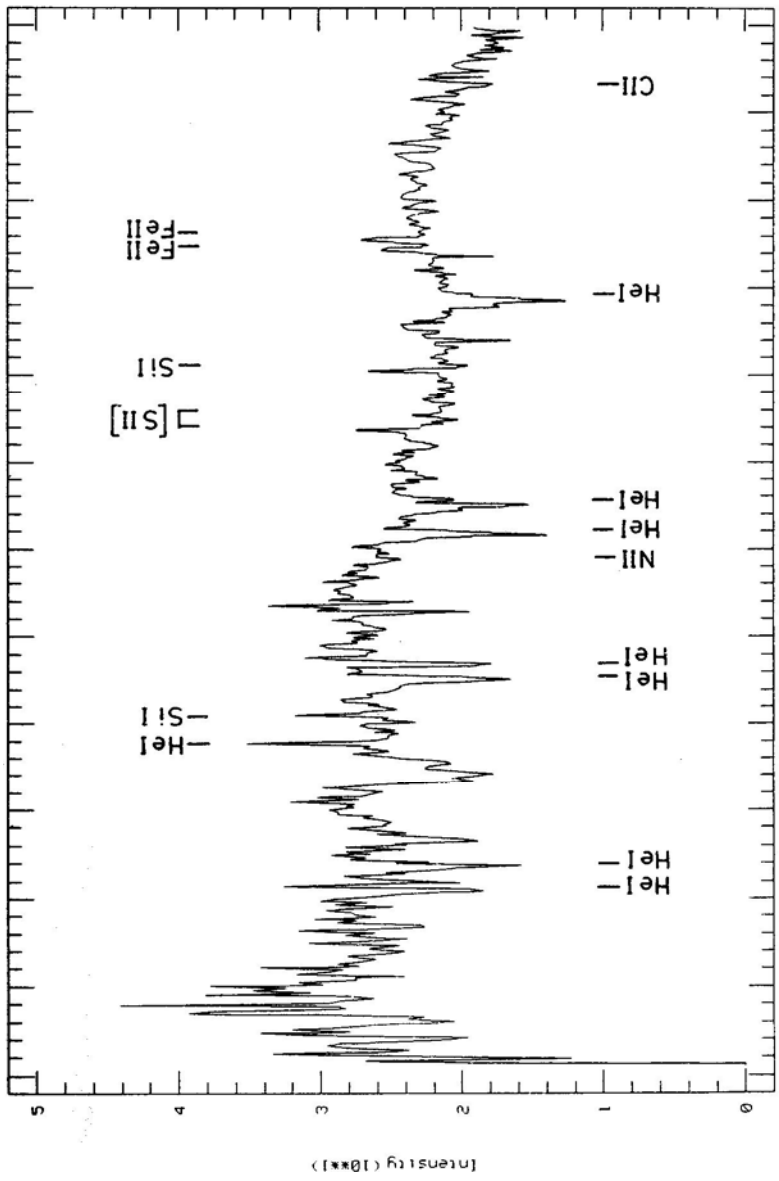

Figure 1. Flux-calibrated spectrum of MV Sgr in the wavelength region 3705 Å to 4300 Å.

which occur in this wavelength range of λλ3705–4300 Å are present in our spectrum. In addition, we see He I λ 3889 line very strongly in emission. It is actually the strongest emission feature in the spectrum. The emission features of Si I multiplet No. (2) at λ4102.9, λ3905.5 are also strong but the intensity ratio is not 1:81 as expected from the log*gf* values (Wiese, Smith & Miles 1969) but appears more like 1:1 probably reflecting the optical depth effects. There is a strong emission feature at λ4068.19 that was not mentioned by Jeffrey *et al.* (1988) and could be identified with [S II] λ4068.62. The other line of [S II] doublet at λ4076.22 is expected to be 5 times weaker, also seems to be present but it is on the red wing of the absorption feature at λ4075 (CII + O II (1)).

Earlier Herbig (1964) had identified the emission feature at λ6715 as due to [S II] λ6717, λ6731, although he did not mention these features in the description of his 1973 Aug. spectra (Herbig 1975). Examination of the prints of these spectra (EC 11629) kindly sent by Herbig does show presence of weak emission feature at λ6718. Since the [S II] lines seem to be present, we looked for the presence of other nebular lines at λ6548 and 16583 of [N II] and [O II] λλ7320, 30. There again is a weak feature at λ6548. The 16583 feature is blended with the line listed by Herbig at λ6586.2 as exceedingly broad emission due to Fe II (–) (an unclassified strong line of Fe II) and the absorption lines of λλ6578, 82 of C II.

There is a feature at λ7330 corresponding to [O II]. The other line of the doublet at λ7320 is blended with the broad emission λ7323.6. The possible presence of [O I] λ6300 ha been commented on by Herbig (1975).

According to Jeffrey *et al.* (1988) the FWHM of Fe II emission lines is 131 ± 18 km s^{-1}, this corresponds to 3–4 pixels on our spectrum. A comparison of the λ4068 feature (also 13889) with Fe II lines at λ4173.4, λ4178.9 does indicate that λ4068 is sharper than Fe II lines. Thus the presence of λ4068.62 [S II] does confirm the presence of the nebular lines from a low-density nebula.

3.3 *Radial Velocities of Emission Lines*

We list in Table 1 the radial velocity of some of the emission lines and their fluxes (measured above the continuum).The radial velocities of Fe II, Si I, Ca II are consistent with absorption velocity –95 k m s^{-1}. Jeffrey *et al.* (1988) find the mean of 31 emission lines as – 81 ± 17 (s.d.) km s^{-1} and Herbig (1975) finds from the measurement of 11 relatively unblended emissions a value of –96 ± 13 (s.d.) km s^{-1}. Thus, the radial velocity of the emitting material Fe II, Si I, Ca II etc is essentially the same as that of the star.

However, the two strong emission lines of [S II] 14068.22 and He I λ3889 show a radial velocity quite different from the stellar velocity. One possibility is that the He I line may be superposed on a strong underlying stellar absorption line that could displace the centre of emission. At the position of the nebular line 14068 no strong absorption is seen in the tracing of HD 124448 (Westin 1980).

The radial velocities of other strong He I emission lines in the red region as calculated from the measured wavelengths of Herbig (1975) indicate that these radial velocities are similar to the radial velocity measured for λ3889 by us (Table 1). However, Hα radial velocity seems to be consistent with – 96 km s^{-1} stellar velocity. The central emission in He I λ4026 is red-shifted to – 3.4 km s^{-1} although the absorption core gives a radial velocity of —92 km s^{-1}.

Table 1. Radial velocities and fluxes of emission lines.

Wavelength	Radial Velocity km s^{-1}	F 10^{-12} erg s^{-1} cm^{-2}	Wavelength Å	Radial Velocity km s^{-1}	F 10^{-12} erg s^{-1} cm^{-2}
He I			[S II]		
3888.65	−42	12.6	4068.62	−32	5.2
5875.62	−56*		4076.22		1.4
6678.15	−26*				
7281.35	−32*				
Fe II			Si I		
4173.45	−124	7.0	3905.53	−90	5.1
4178.86	−96	9.6	4102.03	−80	6.8
4233.17	−121	4.1			
4258.15	−83	4.5			
			Ca II		
			3968.47	−90	

* From Herbig (1975); λ7065.4 is probably blended with Fe. II.

Thus, there is a possibility that the nebular velocity might be different from that of the star. However, this is based on almost a single line of [S II], although in He I lines the emission component also seems to agree with the radial velocity. Further confirmation with better observations are essential.

3.4 *Discussion*

The nebular lines might be strong in our 1987 July spectrum because the stellar continuum was fainter than on the other occasions. There is also a possibility that emission lines have varied in strength. Jeffrey *et al.* (1988) found that the relative strength of the He I λ6678 to Hα was the reverse of that given by Herbig's observation *i.e.* He I was stronger than Hα.

The description of emission spectrum and infrared excess in MV Sgr is similar to that of the high luminosity B supergiants in LMC which show doubling in emission lines of Fe II, He I, Si II, in addition to the nebular lines of [N II] and [S II] (Zickgraf *et al.* 1986). In MV Sgr, the ratio of the [S II] line 24068 to $\lambda\lambda$6717 + 31 apears to be greater than one.

The presence of the [S II], [N II] and [O II] lines in MV Sgr indicates the existence of a low-density planetary nebula around the star. Then the question would be whether the star of T_{eff} ~ 15400 K and log g ~ 2.5 could photoionize the nebula and sustain it. The temperature is apparently too low for photoionization. It is however possible that the photoionization could have occurred at an earlier time when the star was hotter.

Further observations are essential, particularly during a light minimum to establish the nature of the nebulosity and radial velocity differences among emission lines in MV Sgr.

Acknowledgement

We would like to thank Prof. G. H. Herbig for sending the prints of his spectra to one of us (NKR). NKR would also like to thank ESO, Garching for their hospitality during

his visit there and for letting him use their facilities. We would like to thank J. Mattei of AAVSO for sending the visual observations of MV Sgr.

References

Drilling, J. S., Schönberner, D., Heber, U., Lynas-Gray, A. E. 1984, *Astrophys. J.*, **278,** 224.
Herbig, G. H. 1964. *Astrophys. J.*, **140**, 1317.
Herbig, G. H. 1975, *Astrophys. J.*, **199**, 702.
Jeffrey, C. S., Heber, U., Hill, P. W., Pollacco, D. 1988, *Mon. Not. R. astr. Soc*, **231**, 175.
Rao, N. K., Nandy, K. 1982, *J. Astrophys. Astr.*, **3**, 79.
Westin, B. A. M. 1980, *Astr. Astrophys.*, **81**, 74.
Wiese, W. L., Smith, M. W., Miles, B. M. 1969, NSRDS-NBS 22, Vol. II.
Zickgraf, F. J., Wolf, B., Stahl, O., Leitherer, C, Appenzeller, I. 1986, *Astr. Astrophys.*, **163,** 119.

J. Astrophys. Astr. (1990) **11,** 43–48

The Chromospherically Active Solar-Type Spectroscopic Binary HD 191262

R. F. Griffin* *The Observatories, Madingley Road, Cambridge, England CB3 0HA*

F. C. Fekel† *Department of Physics & Astronomy, Vanderbilt University, Nashville, Tennessee 37235, U.S.A.*

Received 1989 August 7; accepted 1989 October 23

Abstract. HD 191262 is a double-lined spectroscopic binary consisting of two slightly unequal solar-type stars in an orbit' with a period of 5.43435 days. The system is both synchronized and circularized and is probably at least as old as the Sun. The inclination of the system is about 45°.

Key words: spectroscopic binary—radial velocities—orbit—HD 191262

1. Introduction

HD 191262 is an eighth-magnitude star in the northeast corner of the constellation Aquila, about 7° north-following Altair. It is listed in the *Henry Draper Catalogue* (Cannon & Pickering 1923) with spectral type G5; no modern magnitude or type has been published to our knowledge, but good photographic magnitudes on the International scale were given by Beer, Redman & Yates (1954) as $m_{pv=}$ 7.93, m_{pg} = 8.54.

2. The nature of HD 191262

The catalogue by Beer, Redman & Yates was used as the basis for a radial-velocity survey of late-type stars in the + 15° Selected Areas at Cambridge in the late 1960s—one of the first large programmes undertaken with the then newly developed photoelectric radial-velocity spectrometer (Griffin 1967). One of the very few stars that were observed on that programme but did not feature in the published results (Griffin 1971) was HD 191262: it failed to give a recognizable 'dip' in the trace when it was observed in 1969. Stars that had given no result with the radial-velocity spectrometer were placed on the programme for an observing run which Dr G. A. Radford (then a graduate student) and R.F.G. had at the Isaac Newton telescope at Herstmonceux in 1974; a classification-dispersion (60 Å mm^{-1}) spectrogram was taken of HD 191262

* Guest Investigator, Palomar Observatory; Visiting Observer, Dominion Astrophysical Observatory, Victoria, and at the Geneva Observatory's 'Coravel' at Haute-Provence.

† Visiting Astronomer, Kitt Peak National Observatory, [U.S.] National Optical Astronomy Observatories, operated by the Association of Universities for Research in Astronomy, Inc., under contract with the [U.S.] National Science Foundation

on 1974 April 7. The spectrum was classified by Radford as G3 V, with very broad lines, which would explain the difficulty in measuring the velocity. R.F.G. made a further attempt to obtain a result on HD 191262 with the radial-velocity spectrometer in 1975, but again without success.

Recalling the characteristics of the object some years later in connection with Dr B. W. Bopp's interest in FK Corn stars, R.F.G. suggested the object to Dr Bopp, who in turn persuaded F.C.F. (who was about to have an observing run at the Kitt Peak 84-in coudé) to observe it. A CCD spectrum taken on 1983 July 12 disclosed that the absorption lines were not broad but double. In the light of that discovery a fresh effort this time successful, was made with the Cambridge radial-velocity spectrometer in 1983 August, and before the month was half gone a preliminary orbit had been obtained. The spectrometer was still the same instrument as before, but various improvements (notably a new photomultiplier of the Rb–Cs type developed by EMI) had enabled *SIN* ratios to be increased since the earlier attempts, and a correct knowledge of the nature of the features to be looked for in the trace was a distinct advantage. Indeed, with hindsight it was possible to measure velocities, of a sort, from the 1975 trace.

3. Radial velocities and orbit

Radial-velocity measurements of HD 191262 have continued up to the time of writing, and altogether 51 photoelectric observations have now been made. All but seven of them are at double-lined phases. The majority of them have been made, more easily than at Cambridge, with newer radial-velocity spectrometers at which R.F.G has enjoyed visiting-observer privileges; Fig. 1 shows a trace obtained with the Palomar spectrometer (Griffin & Gunn 1974). Furthermore, 16 observations have been made at double-lined phases at Kitt Peak National Observatory with the coudé spectrograph of the 84-inch telescope fed by the auxiliary telescope system. Those observations were obtained with a Texas Instruments CCD and were usually centred at λ6430 Å. They have a resolution of 0.2 Å and cover a wavelength range of 90 Å. The velocities were determined by cross-correlation techniques; the zero-point was set by the use as a reference star of μ Her, which was assumed to have a radial velocity of – 15.6 km s^{-1} (Wilson 1953). All of the radial-velocity data are listed in Table 1.

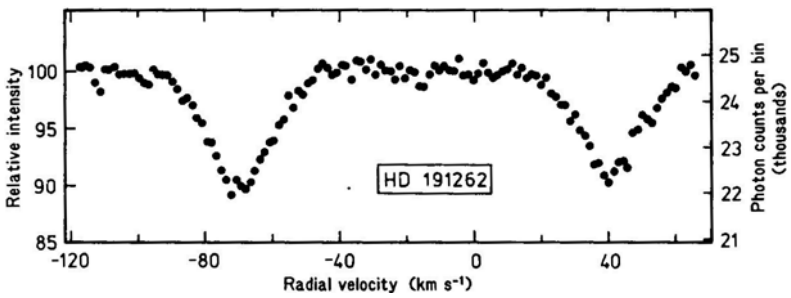

Figure 1. Radial-velocity trace of HD 191262, obtained with the Palomar spectrometer on 1983 October 15.

Table 1. Radial-velocity measurements of HD 191262.

Date			HMJD	Velocity Prim. km s^{-1}	Velocity Sec. km s^{-1}	Phase	(O−C) Prim. km s^{-1}	(O−C) Sec. km s^{-1}	Source*
1975	Aug	26.002	42650.002	−61.2:	+27.9:	530.587	0.0	−3.4	Cambridge
1983	July	12.373	45527.373	+34.0	−65.0	0.065	−0.5	−0.2	Kitt Peak
	Aug	2.063	548.063	+22.2	−52.7	3.872	−0.4	+0.1	Cambridge
		2.981	548.981	+35.4	−69.8	4.041	−1.8	−2.4	Cambridge
		3.922	549.922	−2.7:	−27.8:	.215	+0.4	−0.8	Cambridge
		4.937	550.937	−60.2	+29.1	.401	−1.2	0.0	Cambridge
		6.979	552.979	−15.3		.777			Cambridge
		11.886	557.886	−39.3	+10.6	5.680	−1.3	+2.6	Cambridge
		16.037	562.037	−67.4	+33.7	6.444	−1.6	−2.2	Cambridge
		20.945	566.945	−46.4	+16.6	7.347	−0.4	+0.6	Cambridge
	Sept	5.883	582.883	−14.2		10.280			Cambridge
		18.257	595.257	−65.3	+35.4	12.557	+0.4	−0.4	Kitt Peak
		18.869	595.869	−40.7	+12.0	.669	+0.5	+0.8	Cambridge
		19.886	596.886	+19.4	−47.1	.857	+0.9	+1.6	Cambridge
		21.200	598.200	+29.0	−58.5	13.098	0.0	+0.7	Kitt Peak
	Oct	13.166	620.166	+20.3	−48.8	17.141	+1.0	+0.7	Palomar
		14.249	621.249	−44.6	+14.2	.340	−0.7	+0.2	Palomar
		15.115	622.115	−69.7	+40.1	.499	−0.6	+0.9	Palomar
		24.203	631.203	+11.6	−41.4	19.171	+1.0	−0.7	Victoria
1984	Apr	21.466	45811.466	−46.3	+14.4	52.343	−1.6	−0.3	Kitt Peak
		22.472	812.472	−68.2	+38.7	.528	+0.1	+0.3	Kitt Peak
		23.456	813.456	−28.7	−0.8	.709	+0.2	+0.3	Kitt Peak
		24.491	814.491	+28.5	−58.3	.899	0.0	+0.4	Kitt Peak
	May	31.467	851.467	−31.0	+0.3	59.703	−0.3	−0.4	Kitt Peak
	June	1.437	852.437	+24.9	−54.6	.882	+0.1	+0.4	Kitt Peak
	Aug	27.244	939.244	+18.7	−48.0	75.856	+0.5	+0.4	Kitt Peak
	Sept	4.927	947.927	−65.9	+39.0	77.453	+0.9	+2.1	Cambridge
		29.249	972.249	+32.7	−64.1	81.929	−1.0	−0.2	Kitt Peak
	Oct	1.233	974.233	−29.1	−1.3	82.294	+0.7	−1.1	Kitt Peak
	Nov	30.120	46034.120	−36.8	+7.6	93.314	−0.6	+1.4	Palomar
	Dec	1.125	035.125	−69.9	+39.7	.499	−0.8	+0.5	Palomar
		2.149	036.149	−35.9	+5.9	.687	−0.2	+0.2	Palomar
		10.718	044.718	−15.0		95.264			Cambridge
		14.730	048.730	+38.4	−69.1	96.003	−0.6	+0.2	Cambridge
1985	Sept	28.923	46336.923	+36.8	−68.5	149.034	−1.0	−0.5	Cambridge
	Oct	22.819	360.819	−63.0	+34.5	153.432	+1.1	+0.2	Cambridge
		24.850	362.850	+3.5	−36.3	.805	+0.1	−2.8	Cambridge
1986	May	27.053	46577.053	−14.5		193.222			Cambridge
	Aug	23.085	665.085	−63.5	+34.4	209.421	−1.0	+1.8	Coravel
		23.935	665.935	−64.2	+32.8	.577	−1.4	−0.1	Coravel
		24.970	666.970	−16.1		.768			Coravel
		25.904	667.904	+35.2	−65.5	.940	0.0	−0.1	Coravel
		27.985	669.985	−39.3	+9.1	210.323	−0.5	+0.2	Coravel
		28.868	670.868	−68.3	+38.4	.485	+0.5	−0.6	Coravel
	Oct	14.198	717.198	+38.2	−68.6	219.010	−0.7	+0.5	Kitt Peak
	Nov	23.102	757.102	−46.7	+18.2	226.353	+1.0	+0.4	Palomar
		26.077	760.077	+28.6	−59.2	.901	−0.3	−0.1	Palomar
1987	June	26.401	46972.401	+38.9	−67.5	265.972	+0.8	+0.9	Kitt Peak
	Oct	17.801	47085.801	+13.0		286.839	−0.6		Coravel

Table 1. Continued.

Date	HMJD	Velocity Prim. km s^{-1}	Velocity Sec. km s^{-1}	Phase	(O−C) Prim. km s^{-1}	(O−C) Sec. km s^{-1}	Source*
1988 Mar 15.203	47235.203	−42.4	+12.3	314.331	−1.0	+0.9	Coravel
Oct 21.131	455.131	+0.8	−31.7	354.801	−1.2	+0.4	Kitt Peak
Nov 2.836	467.836	+20.3	−50.4	357.139	+0.6	−0.5	Coravel
3.835	468.835	−38.8		.323	+0.1		Coravel
3.846	468.846		+8.5	.325		−1.0	Coravel
5.789	470.789	−37.9	+7.7	.682	−0.6	+0.3	Coravel
6.845	471.845	+23.0	−53.5	.877	−0.6	+0.3	Coravel
1989 Mar 25.177	47610.177	−41.2	+13.0	383.332	+0.4	+1.4	Coravel
26.181	611.181	−67.3	+38.5	.516	+1.5	−0.4	Coravel
27.189	612.189	−31.9	−0.4	.702	−0.8	−1.5	Coravel
28.168	613.168	+24.1	−54.7	.882	−0.7	+0.3	Coravel
29.177	614.177	+33.6	−63.8	384.068	−0.6	+0.6	Coravel
30.160	615.160		−14.8	.249			Coravel
Apr 11.525	627.525	−67.8	+37.8	386.524	+0.7	−0.8	Kitt Peak
28.121	644.121	−62.4	+32.6	389.578	+0.3	−0.2	Coravel
29.151	645.151		−15.3	.767			Coravel
May 1.139	647.139	+21.6	−50.6	390.133	+0.4	+0.7	Coravel
2.140	648.140	−37.6	+7.7	.317	−0.3	+0.4	Coravel
3.113	649.113	−69.0	+40.1	.496	+0.1	+0.9	Coravel

* Sources: Cambridge: 36-inch telescope and radial-velocity spectrometer (Griffin 1967), Kitt Peak: Coudé feed and Coudé spectrograph of the 84-inch telescope (see text), Palomar: 200-inch telescope and radial-velocity spectrometer (Griffin & Gunn 1974), Victoria: 48-inch telescope and radial-velocity spectrometer (Fletcher *et al.* 1982), Coravel: 1m Geneva telescope and 'Coravel' radial-velocity spectrometer at Haute-Provence (Baranne, Mayor & Poncet 1979).

In the derivation of the orbit from the material in Table 1 it was found appropriate to weight the Cambridge observations 0.3, all others having weight 1. All the data except those from Kitt Peak were obtained by comparing the velocity of HD 191262 directly with that of the reference star λ Lyr, following the standard Cambridge procedure (Griffin 1969), and no relative adjustment of the Kitt Peak measurements proved necessary. The orbit has no significant eccentricity, so we have assumed it to be exactly circular. It is illustrated in Fig. 2 and has the following elements:

$P = 5.434350 \pm 0.000011$ days
$T_0 = \text{MJD } 46548.676 \pm 0.002$
$\gamma = -15.03 \pm 0.07$ km s^{-1}
$a_1 \sin i = 4.04 \pm 0.01$ Gm
$K_1 = 54.04 \pm 0.14$ km s^{-1}
$a_2 \sin i = 4.05 \pm 0.02$ Gm
$K_2 = 54.23 \pm 0.25$ km s^{-1}
$f(m_1) = 0.0890 \pm 0.0007\ M_\odot$
$q = 1.004 \pm 0.004\ (= m_1/m_2)$
$f(m_2) = 0.0900 \pm 0.0012\ M_\odot$
$e \equiv 0$
$m_1 \sin^3 i = 0.359 \pm 0.003\ M_\odot$
ω is undefined
$m_2 \sin^3 i = 0.357 \pm 0.003\ M_\odot$

The true period (in the rest frame of the system) is 5.434622 + 0.000011 days. The r.m.s. radial-velocity residual for an observation of unit weight is 0.7 km s^{-1} for each component.

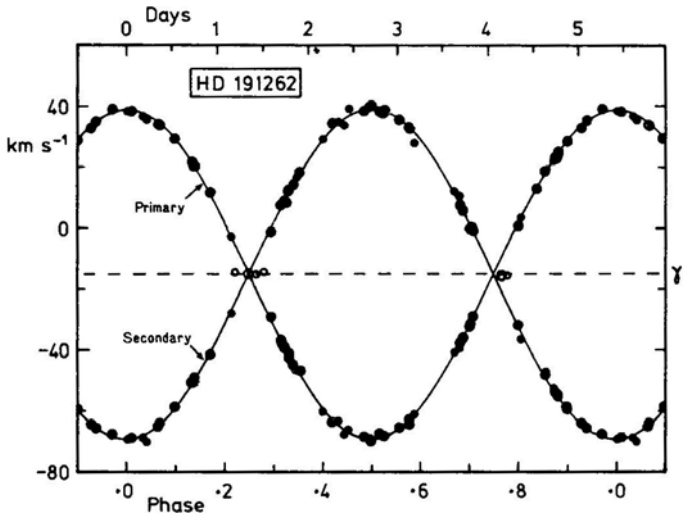

Figure 2. The computed orbit of HD 191262, with the measured radial velocities plotted. Observations made at Cambridge, which are less accurate than those made elsewhere, are represented by smaller dots. Open symbols indicate blended observations, which were not used in the solution of the orbit.

4. Spectroscopy

Strassmeier *et al.* (1988) listed HD 191262 as a chromospherically active binary candidate. Recently, Strassmeier *et al.* (1990)—not the same consortium—obtained a spectrum of it showing both components to have Ca II H and K in emission, confirming it as a chromospherically active binary and suggesting it to be an early-type BY Draconis variable. They found the absolute emission-line fluxes to be similar to those of other field G-dwarf binaries which have periods of a few days.

A spectrum of the λ6707 Å lithium region was obtained at Kitt Peak on 1989 April 12. There is no evidence of a lithium absorption line in either component above the detection limit of 5 mÅ equivalent width. From the curves of growth given by Pallavicini, Cerruti-Sola & Duncan (1987), that limit corresponds to a lithium abundance of $\log n(\mathrm{Li}) \lesssim 1.1$ on a scale of $\log n(\mathrm{H}) = 12$.

5. Discussion

For stars of any given temperature, the lithium abundance progressively decreases with time (Herbig 1965) and can therefore serve as an indicator of stellar age. Cayrel, Cayrel de Strobel & Campbell (1984) found the solar lithium abundance (expressed in the same way as that of HD 191262 above) to be 1.15 from a spectrum of Ceres. They also determined abundances in the range 2.2 to 2.5 for several Hyades stars with temperatures similar to that of the Sun. Thus it seems likely that HD 191262 is substantially older than the Hyades and is perhaps the Sun's age or older. Another indication that HD 191262 is substantially older than the Hyades may be provided by the fact that its orbit is circularized at a period near which a Hyades member (vB 121;

see Griffin & Gunn 1978) still has a quite eccentric orbit, although Zahn & Bouchet (1989) have recently cast doubt upon the age-dependence of the cut-off period of orbit circularization.

The mass ratio of the components is seen from the orbital elements to differ from unity by 0.4 per cent ± 0.4 per cent. The difference in mass is therefore not of high statistical significance, but its sign is supported by the fact that the component which is the primary according to its mass also gives a slightly stronger dip on radial-velocity traces than the other. For the eight Palomar traces the mean ratio of the 'equivalent widths' of the dips is 1.08 ± 0.03; it corresponds (like the mass ratio) to a difference of less than one subtype in the spectral type. The sum of the equivalent widths is about 4.8 km s^{-1}, which in a Hyades star would correspond to a (B — V) colour of $0^m.61$ and a type of about G1 V. The discrepancy from the observed type of G3 V is quite plausible: the lines in the spectrum of HD 191262 could easily be weaker than those of Hyades stars of the same temperature, since the general metal abundance of HD 191262 may be appreciably smaller on account of its much greater age.

The minimum masses, $m \sin^3 i$, shown by the orbit solution are only about a third of the actual masses expected for this pair of solar-type stars; they show, therefore, that $\sin^3 i \sim$, so sin i 0.7 and i 45°: eclipses are not to be expected. The line widths seen on Palomar radial-velocity traces and in the Kitt Peak spectra are compatible with the projected rotational velocities of about 6.5 km s^{-1} expected on the basis of synchronous rotation.

R.F.G. is very grateful to the Palomar, Geneva, Dominion Astrophysical and European Southern observatories for the use of their equipment, and to the UK SERC for defraying the costs of visits there; F.C.F. is similarly grateful to Kitt Peak National Observatory. We thank Dr B. W. Bopp for putting us in touch with one another over HD 191262.

References

Baranne, A., Mayor, M., Poncet, J.-L. 1979, *Vistas Astr.*, **23**, 279.
Beer, A., Redman, R. 0., Yates, G. G. 1954, *Mem. Roy. astr. Soc.*, **67**, 1.
Cannon, A. J., Pickering, E. C. 1923, *Ann. Marv. Coll. Ohs.*, **98**, 153.
Cayrel, R., Cayrel de Strobel, G., Campbell, B. 1984, *Astrophys. J.*, **283**, 205.
Fletcher, J. M., Harris, H. C., McClure, R. D., Scarfe, C. D. 1982, *Publ. astr. Soc. Pacific*, **94,** 1017.
Griffin, R. F. 1967, *Astrophys. J.*, **148**, 465.
Griffin, R. F. 1969, *Mon. Not. R. astr. Soc.*, **145**, 163,
Griffin, R. F. 1971, *Mon. Not. R. astr. Soc.*, **155**, 1.
Griffin, R. F., Gunn, J. E. 1974, *Astrophys. J.*, **191**, 545.
Griffin, R. F., Gunn, J. E. 1978, *Astr. J.*, **83**, 1114.
Herbig, G. H. 1965, *Astrophys. J.*, **141**, 588.
Pallavicini, R., Cerruti-Sola, M., Duncan, D. K. 1987, *Astr. Astrophys.*, **174**, 116.
Strassmeier, K. G., Hall, D. S., Zeilik, M., Nelson, E., Eker, Z., Fekel, F. C. 1988, *Astr. Astrophys. Suppl.*, **72**, 291.
Strassmeier, K. G., Fekel, F. C., Bopp, B. W., Dempsey, R. C., Henry, G. W. 1990, *Astrophys. J. Suppl.*, in press.
Wilson, R. E. 1953, *General Catalogue of Stellar Radial Velocities*, Carnegie Institution of Washington, Washington, D.C.
Zahn, J.-P., Bouchet, L. 1989, *Astr. Astrophys.*, **223**, 112.

J. Astrophys. Astr. (1990) **11**, 49–66

Relativistic Magnetofluid Disc with nonzero Radial Velocity in Schwarzschild Geometry

P. Bhaskaran & A. R. Prasanna *Physical Research Laboratory, Ahmedabad 380009*

Received 1989 June 30; accepted 1989 October 25

Abstract. In this paper we consider the equilibrium of a magnetofluid disc in Schwarzschild background with an external magnetic field, having the azimuthal and the radial components of the flow velocity nonzero. The electrical conductivity σ of the fluid is taken to be finite and thus the solution for the electromagnetic field is required to satisfy the Ohm's law too with the four-current having only J^{ϕ} and J^{t} nonzero. The various physical parameters that have to correlate for possible equilibrium configurations are identified and their respective magnitudes estimated. It is found that for a given angular momentum distribution the inner edge of the disc can reach well within the usual $6m$ limit only when the surface magnetic field of the central object is not too high when the matter density at the outer edge of the disc and the accretion rate are taken with reasonable limits.

Key words: accretion discs—magnetohydrodynamics, relativistic

1. Introduction

The study of axisymmetric stationary fluid configuration around compact objects has been one of the continued interests for over two decades mainly in the context of models presumed for high-energy astrophysical sources wherein accretion is the main mode of energy production by the central engine. However in many of the standard models (Abramowicz, Jaroszynsk & Sikora 1978; Kozlowski, Jaroszynski & Abramowicz 1978) the flow is restricted to the azimuthal component only with the inherent assumption that the radial and the meridional components are negligible in comparison with the azimuthal one. Recently Kuwahara (1988) has studied the relativistic accretion tori around Schwarzschild blackhole considering all the three components of flow velocity to be nonzero and has found that though the radial and the meridional velocities play a minor role in the structure of the tori, they play an important role in determining the accretion rate and the angular momentum transport due to shear stress. However, in our opinion, the story is yet incomplete as these discussions neglect completely the role of electromagnetic fields that could coexist with any such fluid configurations. As the gravitational potential particularly in the inner regions could be very high the matter would be at sufficiently high temperature and thus be in plasma form, and the motion of plasma would necessarily generate currents which could give rise to electromagnetic fields apart from the source fields that would naturally exist when the central compact object is a neutron star, Thus, while

considering models for astrophysical scenario it is important to consider electromagnetic fields coexisting with the given gravitational field and hence develop the dynamical equations for a self-consistent magnetofluid in the presence of gravitational, electromagnetic and centrifugal forces. With this in mind a general programme of studying plasma discs around compact objects in curved spacetime was set up quite sometime ago by Prasanna (1982), and more recently (Prasanna & Bhaskaran 1989) the general framework in the linearised Kerr geometry was formulated.

In the case when the rotation of the central source is neglected (*i.e.* restricting to Schwarzschild background) it was shown that there can exist possible equilibrium solutions for an incompressible fluid disc when the motion is restricted to the azimuthal component alone (Prasanna & Bhaskaran 1989; Bhaskaran & Prasanna 1989). The importance of considering the magnetic fields was easily realized by the fact that the inner edge of the disc can now reach almost upto $3m$ ($m = MG/c^2$) whereas one knows that in the pure Schwarzschild geometry the inner edge is necessarily beyond $6m$.

Presently we shall consider the structure of the disc when both the radial and the azimuthal velocity components are nonzero and the associated electromagnetic field being self-consistent, for finitely conducting disc, in the absence of toroidal magnetic field.

2. Formalism

The present discussion being for the case of a plasma disc with finite conductivity and having only the coefficient of bulk viscosity to be nonzero ($\eta_b \neq 0$) with the central compact object static ($a = 0$) the system of governing equations are given by the continuity equation

$$\left(\rho+\frac{\bar{p}}{c^2}\right)\left[\frac{\partial V^r}{\partial r}-\frac{2m}{r^2}\left(1-\frac{2m}{r}\right)^{-1}V^r+\frac{2}{r}V^r\right]+V^r\frac{\partial}{\partial r}\left(\rho-\frac{\bar{p}}{c^2}\right)$$
$$=-\frac{1}{c^2u^{t^2}}\{F^t{}_kJ^k-2(F_{rk}V^r+F_{\phi k}V^\phi)u^{t^2}J^k\}, \tag{2.1}$$

the momentum equation

$$\left(\rho+\frac{\bar{p}}{c^2}\right)u^{t^2}\left[V^r\frac{\partial V^r}{\partial r}+\frac{mc^2}{r^2}\left(1-\frac{2m}{r}\right)-\frac{3m}{r^2}\left(1-\frac{2m}{r}\right)^{-1}(V^r)^2\right.$$
$$\left.-(r-2m)\sin^2\theta(V^\phi)^2\right]+\left(1-\frac{2m}{r}\right)\frac{\partial\bar{p}}{\partial r}=\left(F^r{}_k-F^t{}_k\frac{V^r}{c}\right)\frac{J^k}{c}, \tag{2.2}$$

$$\left(\rho+\frac{\bar{p}}{c^2}\right)u^{t^2}[-\sin\theta\cos\theta V^{\phi^2}]+\frac{1}{r^2}\frac{\partial\bar{p}}{r\theta}=F^\theta{}_k\frac{J^k}{c}, \tag{2.3}$$

$$\left(\rho+\frac{\bar{p}}{c^2}\right)u^{t^2}\left[V^r\frac{\partial V^\phi}{\partial r}+\frac{2}{r}\left(1-\frac{2m}{r}\right)^{-1}\left(1-\frac{3m}{r}\right)V^rV^\phi\right]=\left(F^\phi{}_k-F^t{}_k\frac{V^\phi}{c}\right)\frac{J^k}{c}, \tag{2.4}$$

and the Maxwell's equations

$$-\frac{1}{r^2\sin\theta}\left(1-\frac{2m}{r}\right)\frac{\partial}{\partial\theta}(\sin\theta B_\phi)=J^r, \tag{2.5}$$

$$\frac{1}{r^2}\frac{\partial}{\partial r}\left[\left(1-\frac{2m}{r}\right)B_\phi\right]=J^\theta, \tag{2.6}$$

$$\frac{1}{r^4\sin\theta}\frac{\partial}{\partial\theta}\left[\frac{B_r}{\sin\theta}\right]-\frac{1}{r^2\sin^2\theta}\frac{\partial}{\partial r}\left[\left(1-\frac{2m}{r}\right)B_\theta\right]=J^\phi, \tag{2.7}$$

$$\frac{1}{r^2}\frac{\partial}{\partial r}(r^2E_r)-\frac{1}{r^2\sin\theta}\left(1-\frac{2m}{r}\right)^{-1}\frac{\partial}{\partial\theta}(\sin\theta E_\theta)=J^t, \tag{2.8}$$

$$\frac{\partial E_\theta}{\partial r}-\frac{\partial E_r}{\partial\theta}=0, \tag{2.9}$$

$$\frac{\partial B_r}{\partial r}+\frac{\partial B_\theta}{\partial\theta}=0, \tag{2.10}$$

and the Ohm's law

$$J^i=\sigma F^i{}_k u^k. \tag{2.11}$$

As the toroidal component of the magnetic field has been assumed to be zero ($B_\phi = 0$), Equations (2.5) and (2.6) give

$$J^r=0, \quad \text{and} \quad J^\theta=0. \tag{2.12}$$

Using these conditions in Equation (2.11) we are led to the relation between E and B fields:

$$E_r=B_\theta\frac{V^\phi}{c} \quad \text{and} \quad E_\theta=-B_r\frac{V^\phi}{c} \tag{2.13}$$

whereas from Equation (2.4) we get the equation for V^ϕ

$$\frac{\partial V^\phi}{\partial r}+\frac{2}{r}\left(1-\frac{2m}{r}\right)^{-1}\left(1-\frac{3m}{r}\right)V^\phi=0 \tag{2.14}$$

whose solution is given by

$$V^\phi=\frac{L(\theta)}{r^2}\left(1-\frac{2m}{r}\right). \tag{2.15}$$

The θ dependence of V^ϕ may be obtained through consistency conditions for defining J_ϕ and J^t through Ohm's law and this requires $L(\theta)=L/\sin^2\theta$. Thus we have for the azimuthal component of the velocity the structure

$$V^\phi=\frac{L}{r^2\sin^2\theta}\left(1-\frac{2m}{r}\right). \tag{2.16}$$

Using this V^ϕ in Equation (2.13) and substituting so obtained E_r and E_θ in Equation (2.9) (which says curl $E = 0$) we will then have two equations for B_r and B_θ which may be solved to get the general solutions

$$B_r=-Ar^{k-1}\left(1-\frac{2m}{r}\right)^{-k/2}\sin^{k-1}\theta\cos\theta, \tag{2.17}$$

$$B_\theta=Ar^k\left(1-\frac{3m}{r}\right)\left(1-\frac{2m}{r}\right)^{-\frac{k}{2}-1}\sin^k\theta, \tag{2.18}$$

and consequentlythe electric field is given by

$$E_r = \frac{AL}{c} r^{k-2}\left(1-\frac{3m}{r}\right)\left(1-\frac{2m}{r}\right)^{-\frac{k}{2}} \sin^{k-2}\theta, \tag{2.19}$$

$$E_\theta = \frac{AL}{c} r^{k-3}\left(1-\frac{2m}{r}\right)^{-\frac{k}{2}+1} \sin^{k-3}\theta\cos\theta, \tag{2.20}$$

with A and k being arbitrary constants. Using these E and B fields one can calculate the nonzero current components J^ϕ and J^t given by

$$J^\phi = -\frac{\sigma}{r^2\sin^2\theta} B_\theta V^r u^t, \tag{2.11}$$

$$J^t = -\sigma\left(1-\frac{2m}{r}\right)^{-1} V^\phi V^r B_\theta u^t. \tag{2.22}$$

Thus we have solved for the electromagnetic field and the azimuthal velocity exactly leaving behind the equation of continuity and the two momentum equations and part of the Ohm's law concerning J^ϕ and J^t, as given in Equations (2.21) and (2.22). Consistency of Equations (2.21) and (2.22) with the Maxwell's Equations (2.7) and (2.8) lead us to the exact solution for V^r as given by

$$V^r u^t = -\frac{c^2}{4\pi\sigma}\frac{1}{r^2}\left\{km+(2-k)(r-2m)\left[1+\cot^2\theta\left(1-\frac{3m}{r}\right)^{-1}\right]\right\} \tag{2.23}$$

wherein

$$u^t = \left(1-\frac{2m}{r}\right)^{-1/2}\left(1-\frac{V^2}{c^2}\right)^{-1/2}, \qquad V^2 = V^{(r)^2} + V^{(\phi)^2} \tag{2.24}$$

the parentheses around an index indicating the local Lorentz component. Expressing the remaining equations in terms of local Lorentz components (Prasanna & Bhaskaran 1989) we now have the system

$$\left(\rho+\frac{\bar{p}}{c^2}\right)\left[\frac{\partial V^{(r)}}{\partial r}+\frac{2V^{(r)}}{r}\right]+V^{(r)}\frac{\partial}{\partial r}\left(\rho-\frac{\bar{p}}{c^2}\right)=\frac{2\sigma}{c^4}u^t V^{(r)^2} B^2_{(\theta)}\left(1-\frac{V^{(\phi)^2}}{c^2}\right), \tag{2.25}$$

$$\left(\rho+\frac{\bar{p}}{c^2}\right)\left(1-\frac{V^2}{c^2}\right)^{-1}\left[V^{(r)}\frac{\partial V^{(r)}}{\partial r}+\frac{mc^2}{r^2}\left(1-\frac{2m}{r}\right)^{-1}\left(1-\frac{V^{(r)^2}}{c^2}\right)-\frac{1}{r}V^{(\phi)^2}\right]+\frac{\partial\bar{p}}{\partial r}$$

$$=-\frac{\sigma}{c^2}u^t B^2_{(\theta)} V^{(r)}\left(1-\frac{V^{(\phi)^2}}{c^2}\right), \tag{2.26}$$

and

$$\left(\rho+\frac{\bar{p}}{c^2}\right)\left(1-\frac{V^2}{c^2}\right)^{-1} V^{(\phi)^2}\cot\theta+\frac{\partial\bar{p}}{\partial\theta}=-\sigma u^t V^{(r)} B_{(r)} B_{(\theta)}\left(1-\frac{V^{(\phi)^2}}{c^2}\right), \tag{2.27}$$

wherein

$$V^{(r)} = \left(1-\frac{2m}{r}\right)^{-1} V^r,$$

$$V^{(\phi)} = r\sin\theta\left(1-\frac{2m}{r}\right)^{-1/2} V^{\phi},$$

$$B_{(r)} = \frac{1}{r^2\sin\theta} Br,$$

$$B_{(\theta)} = \frac{1}{r}\left(1-\frac{2m}{r}\right)^{1/2}\frac{B_\theta}{\sin\theta}. \tag{2.28}$$

From equations (2.25) and (2.26) one can easily obtain the relation

$$\left(\rho+\frac{\bar{p}}{c^2}\right) r^2 V^{(r)} = C_1\left(1-\frac{2m}{r}\right)^{-1}\left(1-\frac{V^2}{c^2}\right)$$

which indeed is the relativistic generalization of the equation for the accretion rate and thus one has

$$\left(\rho+\frac{\bar{p}}{c^2}\right)\left(1-\frac{2m}{r}\right)\left(1-\frac{V^2}{c^2}\right)^{-1} r^2 V^{(r)} = -\dot{M} \tag{2.29}$$

the parameter C_1 being identified with $-\dot{M}$, may be a function of θ. With this we now have just two equations and two unknowns in p and ρ.

$$\left(\rho+\frac{\bar{p}}{c^2}\right)\left(1-\frac{V^2}{c^2}\right)^{-1}\left\{-\frac{c^2}{2}\left(1-\frac{2m}{r}\right)\frac{\partial}{\partial r}\left[\left(1-\frac{2m}{r}\right)^{-1}\left(1-\frac{V^2}{c^2}\right)\right]\right\}+\frac{\partial\bar{p}}{\partial r}$$

$$= -\frac{\sigma}{c^2}u^t B_{(\theta)}^2 V^{(r)}\left(1-\frac{V^{(\phi)^2}}{c^2}\right) \tag{2.30}$$

and Equation (2.27). Using Equation (2.29), they may be written as

$$\frac{\dot{M}c^2}{2}\frac{1}{r^2 V^{(r)}}\frac{\partial}{\partial r}\left[\left(1-\frac{2m}{r}\right)^{-1}\left(1-\frac{V^2}{c^2}\right)\right]+\frac{\partial\bar{p}}{\partial r} = -\frac{\sigma}{c^2}B_{(\theta)}^2 V^{(r)}u^t\left(1-\frac{V^{(\phi)^2}}{c^2}\right), \tag{2.31}$$

$$-\frac{\dot{M}V^{(\phi)^2}\cot\theta}{r^2 V^{(r)}}\left(1-\frac{2m}{r}\right)^{-1}+\frac{\partial\bar{p}}{\partial\theta} = -\sigma B_{(r)}B_{(\theta)}V^{(r)}u^t\left(1-\frac{V^{(\phi)^2}}{c^2}\right). \tag{2.32}$$

The integrability condition for p viz. $\frac{\partial\bar{p}}{\partial\theta}$ (2.31) $\frac{\partial\bar{p}}{\partial r}$ (2.32) would give a differential equation for $\dot{M}$ and thus one can in principle have a complete set of solution for $\dot{M}$, $\bar{p}$ and ρ.

Special Case: thin disc approximation $\theta = \pi/2$. With this we have

$$V^{(\phi)} = \frac{L}{r}\left(1-\frac{2m}{r}\right)^{1/2},$$

$$u^t V^{(r)} = -\frac{c^2}{4\pi\sigma}\left(1-\frac{2m}{r}\right)^{-1}\left\{\frac{km}{r^2}+\frac{1}{r}(2-k)\left(1-\frac{2m}{r}\right)\right\},$$

$$B_{(\theta)} = Ar^{k-2}\left(1-\frac{2m}{r}\right)^{-\frac{k+1}{2}}\left(1-\frac{3m}{r}\right),$$

$$\frac{\partial\bar{p}}{\partial\theta} = 0,$$

and

$$\frac{d\bar{p}}{dr} = -\frac{\dot{M}c^2}{r^2 V^{(r)} u^t}\frac{d}{dr}\left[\left(1-\frac{2m}{r}\right)^{-1/2}\left(1-\frac{V^2}{c^2}\right)^{1/2}\right] - \frac{\sigma}{c^2}B_{(\theta)}^2 V^{(r)} u^t\left(1-\frac{V^{(\phi)^2}}{c^2}\right), \tag{2.33}$$

which on integration gives after using Equation (2.29) again the equation for ρ

$$\rho c^2 = (k-2)\dot{M}(4\pi\sigma)\int\left(1-\frac{2m}{r}\right)^{-1/2}\frac{\left(1-\frac{V^2}{c^2}\right)^{1/2}dr}{[km+(2-k)(r-2m)]^2}$$
$$-\frac{1}{4\pi}\int\frac{B_{(\theta)}^2}{r^2}[km+(2-k)(r-2m)]\left(1-\frac{2m}{r}\right)^{-1}\left(1-\frac{V^{(\phi)^2}}{c^2}\right). \tag{2.34}$$

For different values of k one can evaluate the density profiles and consequently the pressure profile from Equation (2.29) for a given $\dot{M}$ the accretion rate.

3. Structure of the magnetic field

In order to get the structure of the complete magnetic field inside and outside the disc one has to consider a proper solution for a poloidal magnetic field in the Schwarzschild background. Using the general approach of Ginzburg & Ozernoi (1964), Prasanna & Varma (1977) have expressed the vacuum solution of a magnetic field dipolar at infinity as given by

$$B_{(r)} = -B_0\left[\ln\left(1-\frac{2m}{r}\right)+\frac{2m}{r}\left(1+\frac{m}{r}\right)\right]\cos\theta, \tag{3.1}$$

$$B_{(\theta)} = B_0\frac{m}{r}\left(1-\frac{2m}{r}\right)^{1/2}\left[\left(1-\frac{2m}{r}\right)^{-1}+\ln\left(1-\frac{2m}{r}\right)+1\right]\sin\theta. \tag{3.2}$$

Demanding the continuity of the magnetic field lines across the disc through matching Equations (2.17) and (2.18) with Equations (3.1) and (3.2) one can express the constant A in terms of the constant $B_0 = (3\mu/4m)$. Approximating from the expression for the dipole moment of a magnetized star at its surface having surface field strength B_S and the radius R we can use for B_0 the expression $(3B_s/4)$ $(R/m)^3$, R the radius being expressed in the units of $m=MG/c^2$. Figs l(a) and (b) show a typical profile of the magnetic field structure without and with the disc. For the purpose of illustration the meridional structure of the disc is presumed to extend to about 15° on either side of the equatorial plane.

4. Results and discussion

The integration of the equation for the density (2.34) involves a boundary condition as well as the knowledge of the accretion rate $\dot{M}$ and of the electrical conductivity σ. While the second term can be integrated analytically for different values of k, the first term can be integrated numerically and thus the profiles of density and pressure be

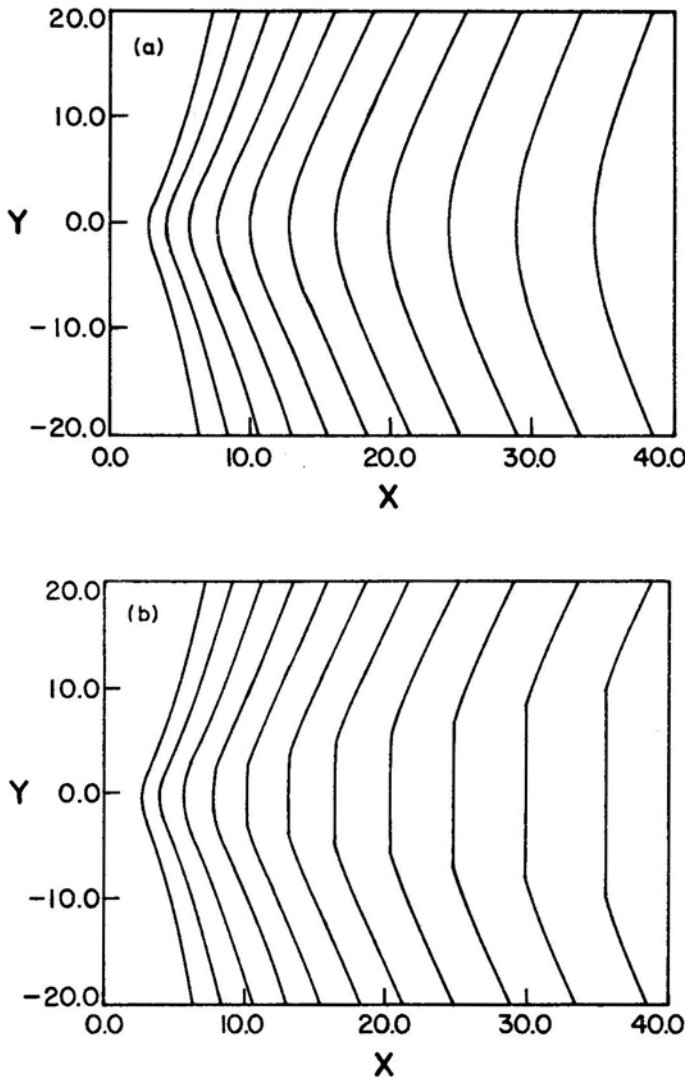

Figure 1. Structure of magnetic field lines (a) without the disc and (b) with the disc.

obtained. One other factor to be kept in mind is that the velocity should not exceed c and this restriction for the Schwarzschild geometry imposes the restriction on the constant angular momentum $l=L/cm$ to be less than $3\sqrt{3}$. As the formation of the disc is through accretion (normally from the companion of the compact star in a binary) of matter flowing in through the inner Lagrange point, for any realistic model one should have the outer edge of the accretion disc located at a distance r_b less than b_1 the distance of L_1 from the centre of the primary (the compact object). Using the approximate relation as given by Plavec & Kratochvil (Franck, King & Raina 1985)

$$b_1 = (0.5 - 0.227 \log q)a \tag{4.1}$$

with q being the mass ratio M_2/M_1 and a the distance between the centres of the two

stars, one can work out for a typical binary with the period-mass relation

$$4\pi^2 a^3 = G(M_1 + M_2)M_\odot P^2$$

P being the binary period. If $M_1 \sim 2M_\odot$ and $M_2 \sim 1\ M_\odot$ and $P \sim 10$ days (typical for X-ray binary) $a \simeq 2 \times 10^5$ km and $b_1 \sim 1.13 \times 10^5$ km. With this in mind we chose $r = 50\ m$ ($m = MG/c^2$) which places the disc around the primary well within the Roche lobe. As the constant k in our expression for the electromagnetic field was kept free we can now choose some typical values for k and then integrate for the density.

(a) $k = 2$:

$$B_{(\theta)} = A\left(1-\frac{3m}{r}\right)\left(1-\frac{2m}{r}\right)^{-3/2}$$

$$E_{(r)} = \frac{AL}{cr}\left(1-\frac{3m}{r}\right)\left(1-\frac{2m}{r}\right)^{-1}$$

$$\rho c^2 = \frac{A^2}{4\pi}\frac{1}{12}\left[19-\frac{90m}{r}+\frac{108m^2}{r^2}\right]\left(1-\frac{2m}{r}\right)^{-3}+\frac{A^2}{4\pi}\frac{L^2}{m^2c^2}\frac{1}{16}\left[\frac{72m^4}{r^4}+\frac{48m^3}{r^3}-\frac{88m}{r}+33\right]\left(1-\frac{2m}{r}\right)^{-2}+\frac{A^2}{4\pi}\frac{L^2}{m^2c^2}\frac{11}{8}\ln\left(1-\frac{2m}{r}\right)-C_2$$

(b) $k = 0$:

$$B_{(\theta)} = \frac{A}{r^2}\left(1-\frac{3m}{r}\right)\left(1-\frac{2m}{r}\right)^{-1/2}$$

$$E_{(r)} = \frac{AL}{cr^3}\left(1-\frac{3m}{r}\right)$$

$$\rho c^2 = \frac{-2\dot{M}c^2}{4(c^2/4\pi\sigma)}\int\frac{1}{r^2}\left(1-\frac{2m}{r}\right)^{-5/2}\left(1-\frac{V^2}{c^2}\right)^{1/2}dr-\frac{A^2}{4\pi}\frac{1}{480\,m^4}\left[864\left(\frac{m}{r}\right)^5-180\left(\frac{m}{r}\right)^4+40\left(\frac{m}{r}\right)^3+30\left(\frac{m}{r}\right)^2+30\left(\frac{m}{r}\right)+15\ln\left(1-\frac{2m}{r}\right)\right]-\frac{A^2}{4\pi}\frac{L^2}{m^2c^2}\frac{m^2}{3r^6}\left[\left(1-\frac{3m}{r}\right)^2+\frac{6m}{7r}\left(1-\frac{3m}{r}\right)+\frac{6m^2}{23r^2}\right]-C_2$$

(c) $k = -2$:

$$B_{(\theta)} = \frac{A}{r^4}\left(1-\frac{3m}{r}\right)\left(1-\frac{2m}{r}\right)^{1/2}$$

$$E_{(r)} = \frac{AL}{cr^5}\left(1-\frac{3m}{r}\right)\left(1-\frac{2m}{r}\right)$$

$$\rho c^2 = \frac{4\dot{M}c^2}{(c^2/4\pi\sigma)}\int\frac{\left(1-\frac{2m}{r}\right)^{-1/2}\left(1-\frac{V^2}{c^2}\right)^{1/2}dr}{(4r-10m)^2}-\frac{A^2}{4\pi}\frac{2m}{9r^4}\left[\left(1-\frac{3m}{r}\right)^2+\frac{3m}{5r}\left(1-\frac{3m}{r}\right)+\frac{9}{55}\frac{m^2}{r^2}\right]+\frac{A^2}{4\pi}\frac{L^2}{m^2c^2}\frac{2m^3}{11r^{11}}\left[\left(1-\frac{3m}{r}\right)^2\left(1-\frac{11m}{6r}\right)+\frac{m}{2r}\left(1-\frac{3m}{r}\right)\left(1-\frac{22m}{13r}\right)\right.$$

$$+\frac{3m^2}{26r^2}\left(1-\frac{11m}{7r}\right)\Bigg]+\frac{A^2}{4\pi}\frac{1}{2r^8}\left\{\left(1-\frac{3m}{r}\right)^2\left(1-\frac{16m}{r}\right)\right.$$
$$\left.+\frac{2m}{3r}\left(1-\frac{3m}{5r}\right)\left(1-\frac{8m}{5r}\right)-\frac{m^2}{5r^2}\left(1-\frac{16m}{11r}\right)\right\}$$
$$-\frac{A^2}{4\pi}\frac{L^2}{m^2c^2}\frac{2m^2}{5r^{10}}\left\{\left(1-\frac{3m}{r}\right)^2\left[1-\frac{40m}{11r}+\frac{10m^2}{3r^2}\right]\right.$$
$$\left.+\frac{6m}{11r}\left(1-\frac{3m}{r}\right)\left[1-\frac{10m}{3r}+\frac{110m^2}{39r^3}\right]+\frac{3m^2}{r^2}\left[\frac{1}{220}-\frac{2}{143}\frac{m}{r}+\frac{1}{91}\frac{m^2}{r^2}\right]\right\}-C_2$$

(d) $k = 1$:

$$B_{(\theta)}=\frac{A}{r^3}\left(1-\frac{3m}{r}\right)$$
$$E_{(r)}=\frac{AL}{cr^4}\left(1-\frac{3m}{r}\right)\left(1-\frac{2m}{r}\right)^{1/2}$$
$$\rho c^2=\frac{3\dot{M}c^2}{(c^2/4\pi\sigma)}\int\frac{\left(1-\frac{2m}{r}\right)^{-1/2}\left(1-\frac{V^2}{c^2}\right)^{1/2}dr}{(3r-4m)^2}+\frac{A^2}{4\pi}\frac{1}{m^6}\left\{-\frac{9}{16}\left(\frac{m}{r}\right)^8+\frac{3}{28}\left(\frac{m}{r}\right)^7\right.$$
$$-\frac{1}{48}\left(\frac{m}{r}\right)^6-\frac{1}{80}\left(\frac{m}{r}\right)^5-\frac{1}{128}\left(\frac{m}{r}\right)^4-\frac{1}{192}\left(\frac{m}{r}\right)^3-\frac{1}{256}\left(\frac{m}{r}\right)^2-\frac{1}{256}\left(\frac{m}{r}\right)$$
$$\left.-\frac{1}{512}\ln\left(1-\frac{2m}{r}\right)\right\}-\frac{A^2}{4\pi}\frac{L^2}{m^2c^2}\frac{1}{96r^6}\left[1-\frac{27m}{5}\frac{}{r}+\frac{81m^2}{11}\frac{}{r^2}\right]$$
$$-\frac{A^2}{4\pi}\frac{1}{2r^6}\left[1-\frac{36m}{7}\frac{}{r}+\frac{54m^2}{8}\frac{}{r^2}\right]+\frac{A^2}{4\pi}\frac{3L^2}{m^2c^2}m^2\left\{\frac{1}{8r^8}\left(1-\frac{3m}{r}\right)^2\left(1-\frac{16m}{9}\frac{}{r}\right)\right.$$
$$\left.-\frac{m}{12r^9}\left(1-\frac{3m}{r}\right)\left(1-\frac{8m}{5r}\right)+\frac{m^2}{5r^2}\left(1-\frac{16m}{11}\frac{}{r}\right)\right\}-C_2$$

wherein the constant C_2 is evaluated through the boundary condition.

Fixing L and obtaining A through B_s the assumed surface magnetic field of the compact star one can obtain the relation between ρ_0 and $\dot{M}$ through the boundary condition that the pressure in the disc at the outer edge is equal to the magnetic pressure at that point plus one-third the energy density at that point

$$(\rho)_{rb}=(\rho_M)_{rb}+\frac{\rho_0 c^2}{3}$$

by using Equation (2.29). Hence fixing one of them the other may be evaluated and subsequently the density and the corresponding pressure profiles are obtained. The set of results are presented in tables and figures as detailed below.

Table (1) gives the approximate position of the inner edge X_A as a function of the angular momentum l for different values of k. As shown in the corresponding Figs 2(a)–(c), the pressure profiles for $k = 2$ and 0 decrease inwards for $l=3\sqrt{3}$, whereas for $k= -2, -1$ there is no such pathology, and the pressure has a reasonable profile

decreasing outwards and saturating as one moves away from the inner edge. As is evident from the table for k =0 and 2, the inner edge stays quite far away from 3m for l = 3, $\sqrt{3}$ whereas for lower values of l the inner edge can reach farther inwards. Figure 2(d) gives a typical density profile for k = – 2, for different values of l, which however are not significantly different.

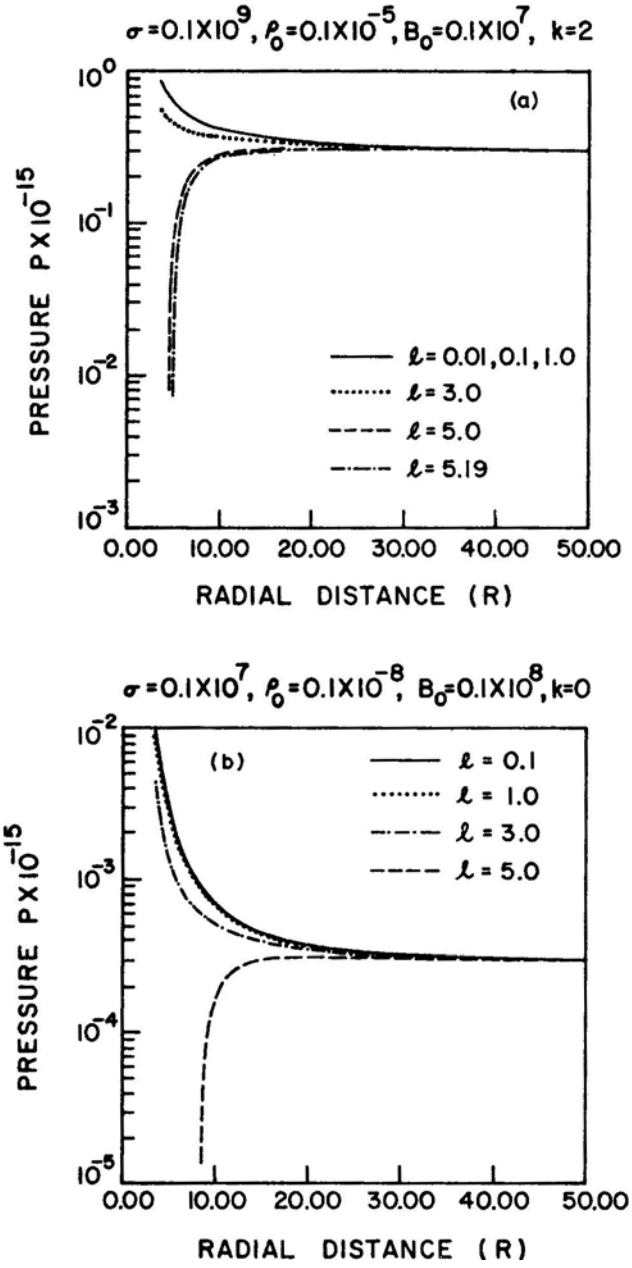

Figure 2. (a)–c) Pressure profiles and (d) density profiles for different l.

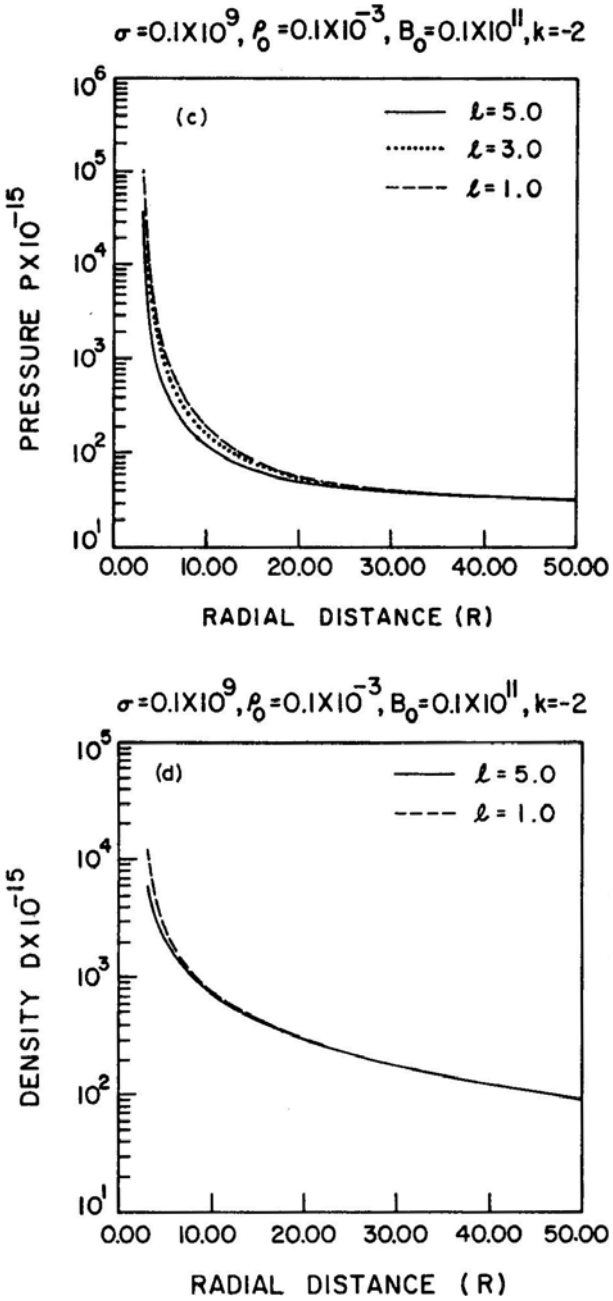

Figure 2. Continued.

Table (2) gives the positions of inner edge as a function of the conductivity σ which seems to have a minimum plausible value of 10^3. As k changes from 2 to – 2, one sees the minimum allowed σ for reasonable pressure profiles is about 10^3 which also depends on correlated values of B_0 and ρ_0. Figs 3(a) and (b) show the typical profiles for pressure and density as a function of σ.

Table 1. Position of inner edge for different values of *l*.

k	l	σ	B_0	ρ_0	$\dot{M}$	X_A
0	0.1×10^{0}	0.1×10^{7}	0.1×10^{8}	0.1×10^{-8}	0.1348×10^{13}	3.5
	0.1×10^{1}				0.1348×10^{13}	3.5
	0.3×10^{1}				0.1350×10^{13}	3.5
	0.5×10^{1}				0.1354×10^{13}	8.4
2	0.1×10^{-1}	0.1×10^{9}	0.1×10^{7}	0.1×10^{-5}	0.2808×10^{12}	3.5
	0.1×10^{0}				0.2808×10^{12}	3.5
	0.3×10^{1}				0.2808×10^{12}	3.5
	0.5×10^{1}				0.2813×10^{12}	4.5
	0.519×10^{1}				0.2823×10^{12}	4.9
-2	0.1×10^{0}	0.1×10^{9}	0.1×10^{11}	0.1×10^{-3}	0.2667×10^{16}	3.1
	0.1×10^{1}				0.2668×10^{16}	3.1
	0.3×10^{1}				0.2672×10^{16}	3.1
	0.5×10^{1}				0.2680×10^{16}	3.1
-1	0.1×10^{0}	0.1×10^{9}	0.1×10^{7}	0.1×10^{-5}	0.2008×10^{14}	3.1
	0.1×10^{1}				0.2008×10^{14}	3.1
	0.3×10^{1}				0.2011×10^{14}	3.1
	0.5×10^{1}				0.2017×10^{14}	3.1

Table 2. Position of inner edge for different values of a

k	l	σ	B_0	ρ_0	$\dot{M}$	X_A
2	1.0	0.1×10^{4}	0.1×10^{9}	0.1×10^{-5}	0.2814×10^{17}	5.6
		0.5×10^{4}			0.5628×10^{16}	3.5
		0.1×10^{6}			0.2814×10^{15}	3.5
0	1.0	0.1×10^{4}	0.1×10^{11}	0.1×10^{-3}	0.1589×10^{21}	28.8
		0.5×10^{4}			0.2717×10^{20}	9.5
		0.8×10^{4}			0.1690×10^{20}	3.5
		0.1×10^{5}			0.1350×10^{20}	3.5
-1	5.0	0.1×10^{9}	0.1×10^{7}	0.1×10^{-3}	0.2017×10^{16}	3.1
		0.1×10^{7}			0.2017×10^{18}	3.1
		0.1×10^{5}			0.2026×10^{20}	3.1
		0.1×10^{4}			0.2754×10^{21}	3.1
-2	5.0	0.5×10^{4}	0.1×10^{11}	0.1×10^{-3}	0.5522×10^{20}	13.1
		0.7×10^{4}			0.3888×10^{20}	3.1
		0.1×10^{5}			0.2701×10^{20}	3.1
		0.1×10^{7}			0.2680×10^{18}	3.1
-1	5.0	0.1×10^{4}			0.2754×10^{21}	3.1
		0.1×10^{5}			0.2020×10^{20}	3.1
		0.1×10^{6}			0.2017×10^{19}	3.1
		0.1×10^{7}			0.2017×10^{18}	3.1

Table (3) shows the possible permitted values of *1*, and Bo for different k and ρ_0. Again for k = 0, – l and –2 if ρ_0, is less than some critical value for the same *1*, σ and B_0, the inner edge cannot reach beyond 6m. Figs 4(a) and (b) show the pressure profiles for k= – 2, – 1 whereas 4(c) gives the density profiles for k= – 2.

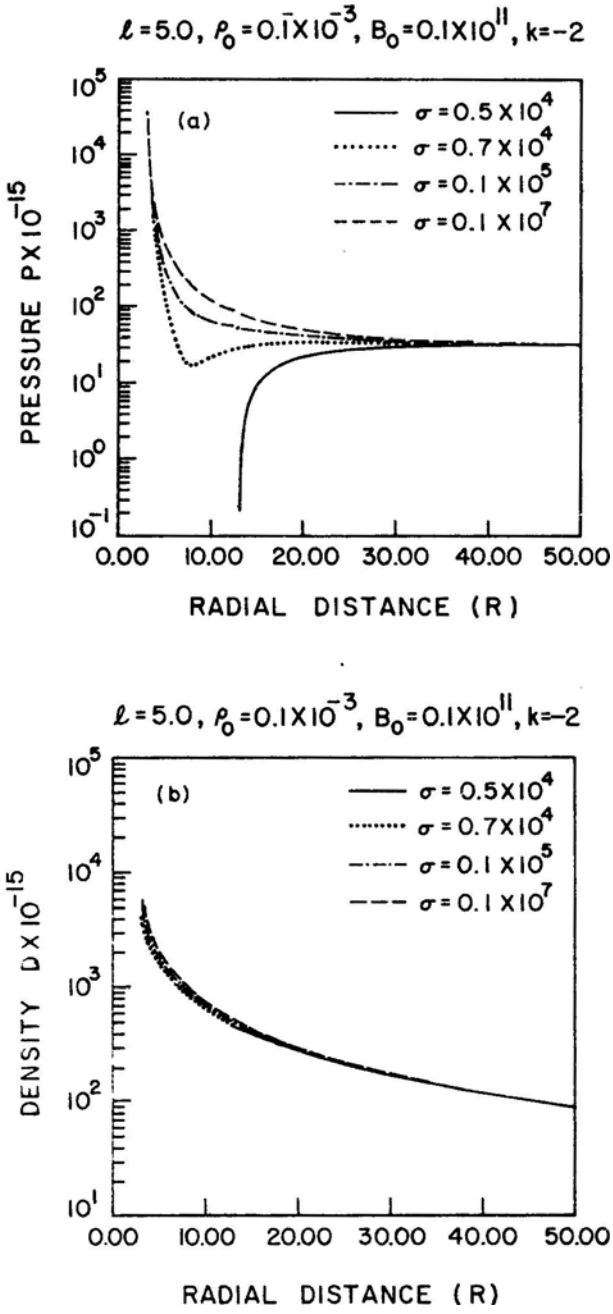

Figure 3. (a) Pressure profiles and (b) density profiles for different *p*.

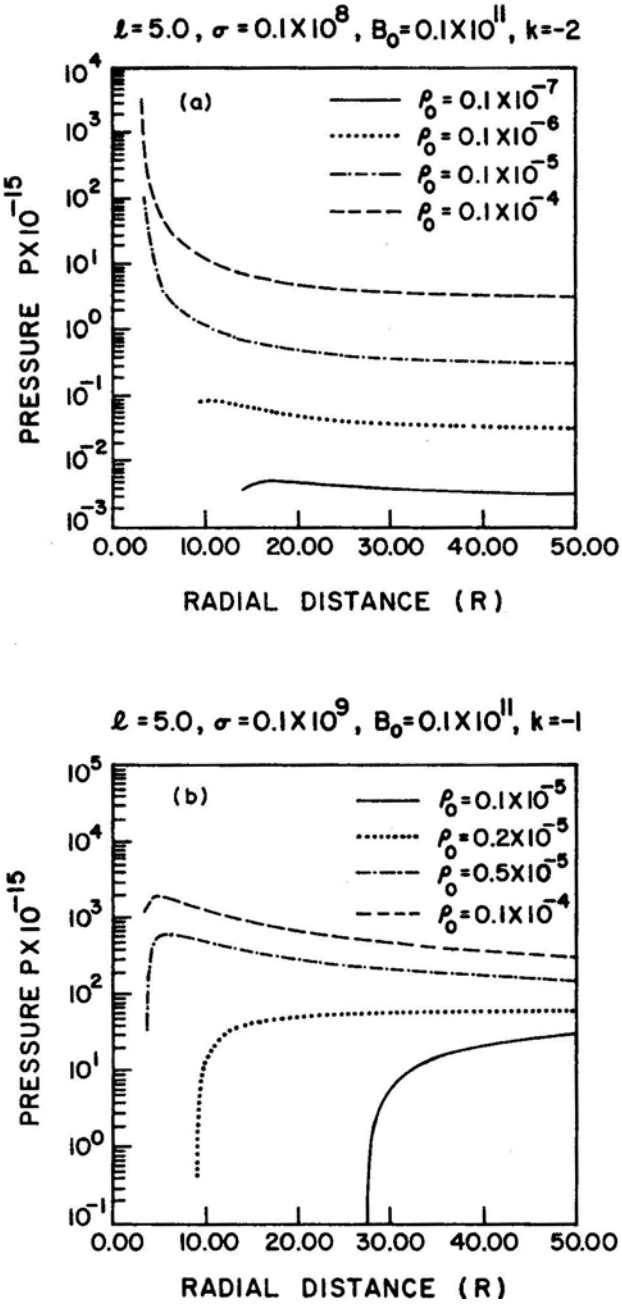

Figure 4. (a) and (b) Pressure profiles and (c) density profiles for different ρ_0.

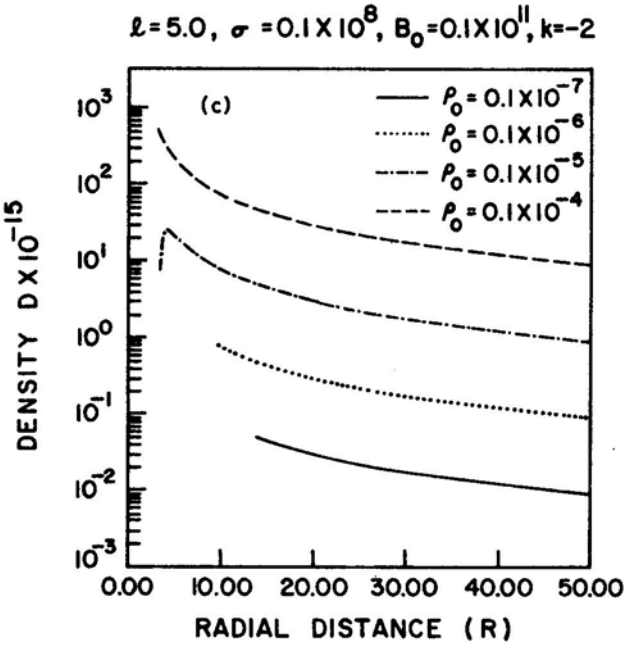

Figure 4. Continued.

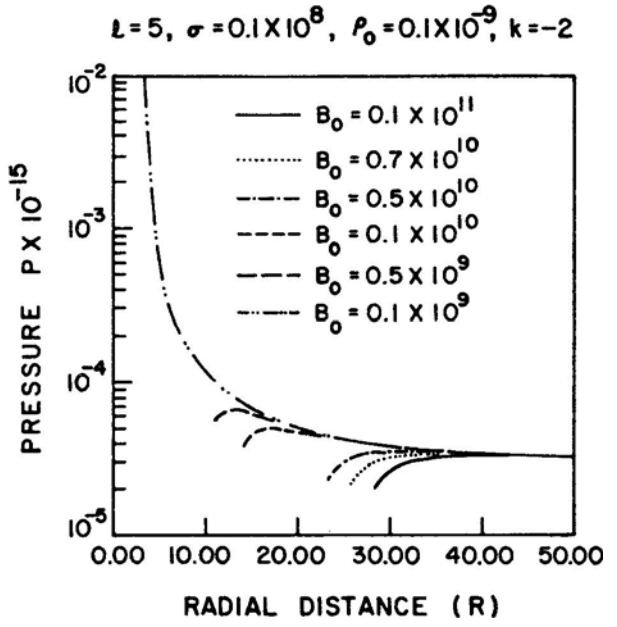

Figure 5. Pressure profiles for different *B*o.

Table 3. Position of inner edge for different values of ρ_0.

k	l	σ	B_0	ρ_0	$\dot{M}$	X_A
2	1.0	0.1×10^{9}	0.1×10^{11}	0.1×10^{-3}	0.3335×10^{14}	3.5
				0.1×10^{-2}	0.2861×10^{15}	3.5
				0.1×10^{-1}	0.2814×10^{16}	3.5
2	1.0	0.1×10^{9}	0.1×10^{6}	0.1×10^{-5}	0.2808×10^{12}	3.5
				0.1×10^{-7}	0.2808×10^{10}	3.5
				0.1×10^{-8}	0.2808×10^{9}	3.5
				0.1×10^{-11}	0.2814×10^{6}	3.5
0	1.0	0.1×10^{7}	0.1×10^{8}	0.1×10^{-8}	0.1348×10^{13}	3.5
				0.1×10^{-9}	0.1348×10^{12}	3.5
				0.1×10^{-10}	0.1348×10^{11}	3.5
				0.7×10^{-11}	0.9440×10^{10}	7.8
				0.5×10^{-11}	0.6743×10^{10}	9.5
0	1.0	0.1×10^{7}	0.1×10^{5}	0.1×10^{-17}	0.1351×10^{04}	17.5
				0.1×10^{-16}	0.1348×10^{05}	3.5
				0.1×10^{-14}	0.1348×10^{07}	3.5
−1	5.0	0.1×10^{9}	0.1×10^{11}	0.1×10^{-5}	0.2017×10^{14}	27.4
				0.2×10^{-5}	0.4055×10^{14}	9.0
				0.5×10^{-5}	0.1008×10^{15}	3.4
				0.1×10^{-4}	0.2017×10^{15}	3.1
−2	5.0	0.1×10^{8}	0.1×10^{11}	0.1×10^{-7}	0.2680×10^{13}	14.1
				0.1×10^{-6}	0.2680×10^{14}	9.2
				0.1×10^{-5}	0.2680×10^{15}	3.3
				0.1×10^{-4}	0.2680×10^{16}	3.1
−2	5.0	0.1×10^{8}	0.1×10^{7}	0.1×10^{-13}	0.2680×10^{7}	3.3
				0.1×10^{-12}	0.2680×10^{8}	3.1
				0.1×10^{-11}	0.2680×10^{9}	3.1

Table (4) gives the variation with respect to the magnetic field and as may be seen the magnetic fields cannot be higher than a critical value for reasonable pressure behaviour. For instance with $k = -1$, $l = 5$, and $\sigma = 10^8$ if $B_0 \sim 10^{11}$ the inner edge can reach upto 3.1 m, but still the pressure at that point shows an abrupt decrease from the steady value. However for $B_0 \sim 10^{10}$, one can have a reasonable pressure profile with $X_A \sim 3m$. Fig. 5 shows the pressure profiles for $k = -2$ and different B_0 wherein a plausible equilibrium configuration occurs only for $B_0 \sim 10^8$ and for any higher value the pressure decreases at the inner edge.

Thus as may be seen from the set of tables and figures a possible disc-like equilibrium structures exist only for a right combination of k, l, σ, B_0 and ρ_0. For a given magnetic field B_0 and angular momentum l the density at the outer edge has to be reasonably high if one wants a disc-like configuration. For example, with $B_0 \sim 10^7$ if the disc inner edge has to reach up to $\sim 3m$ (within $6m$, where GTR influence would be strong) then $\rho_0 \gtrsim 5 \times 10^{-10}$ g cm^{-3} or 5×10^{21} particles m^{-3} with the corresponding accretion rate $\dot{M} \gtrsim 7 \times 10^{11}$ g cm^{-3} $\simeq 10^{-14} M_\odot$ yr^{-1}.

In conclusion we can say that accretion discs around very compact objects (radius $< 3m$) can be sustained provided one has a certain amount of magnetic field associated

Table 4. Position of inner edge for different values of B_0.

k	l	σ	B_0	ρ_0	$\dot{M}$	X_A
−1	5.0	0.1×10^9	0.1×10^{11}	0.1×10^{-2}	0.2017×10^{17}	3.1
			0.5×10^{11}		0.2017×10^{17}	3.1
			0.1×10^{12}		0.2017×10^{17}	3.1
			0.5×10^{12}		0.2017×10^{17}	40.0
−1	5.0	0.1×10^9	0.1×10^8	0.1×10^{-8}	0.2017×10^{11}	3.1
			0.5×10^8		0.2017×10^{11}	3.1
			0.1×10^9		0.2017×10^{11}	3.1
			0.5×10^9		0.2017×10^{11}	40.9
−1	5.0	0.1×10^9	0.1×10^9	0.1×10^{-9}	0.2017×10^{10}	27.4
			0.1×10^8		0.2017×10^{10}	3.1
			0.5×10^8		0.2017×10^{10}	3.8
−1	5.0	0.1×10^9	0.1×10^{11}	0.1×10^{-3}	0.2017×10^{16}	3.1
			0.5×10^{11}		0.2017×10^{16}	3.8
			0.1×10^{12}		0.2017×10^{16}	27.4
−2	5.0	0.1×10^5	0.1×10^{11}	0.1×10^{-3}	0.2701×10^{20}	3.1
			0.5×10^{11}		0.2701×10^{20}	3.1
			0.1×10^{12}		0.2701×10^{20}	6.2
			0.5×10^{12}		0.2701×10^{20}	12.1
			0.1×10^{13}		0.2701×10^{13}	14.9
−2	5.0	0.1×10^8	0.1×10^{10}	0.7×10^{-9}	0.2683×10^{11}	25.6
			0.5×10^{10}		0.2682×10^{11}	23.3
			0.1×10^{10}		0.2680×10^{13}	14.1
			0.5×10^9		0.2680×10^{11}	11.0
			0.1×10^9		0.2680×10^{11}	3.3
−2	5.0	0.1×10^8	0.1×10^{13}	0.1×10^{-4}	0.2681×10^{16}	20.3
			0.5×10^{12}		0.2681×10^{16}	16.4
			0.1×10^{12}		0.2681×10^{16}	9.2
			0.5×10^{11}		0.2681×10^{16}	6.3
			0.1×10^{11}		0.2681×10^{16}	3.1

with the compact object which may be either due to the intrinsic field like in a neutron star or due to ring currents just outside the event horizon, which smoothly joins with the disc field existing due to the currents within the disc. It is very interesting to note that for possible stable configurations having reasonable accretion rate a *disc close to the surface* of a highly compact star ($R \sim 3m$) is possible only when the surface magnetic field strength is lower than $\sim 10^{10}$ G. It may also be noted, that though the bulk viscosity coefficient does contribute through the nonzero radial velocity term, it does not seem to be very effective at this stage of calculations.

References

Abramowicz, M. A., Jaroszynski, M., Sikora, M. 1978, *Astr. Astrophys.*, **63**, 22.
Bhaskaran, P., Prasanna, A. R., 1989, *Astrophys. Sp. Sci.*, (in press).
Franck, J., King, A. R., Raina, D. J. 1985, *Accretion in Binary System*, Cambridge Univ. p. 56.

Ginzburg, V. L., Ozernoi, I. M. 1965, *Sov. Phys.*, **20**, 689.
Kozlowski, M., Jaroszynski, M., Abramowicz, M. A. 1978, *Astr. Astrophys.*, **63**, 209.
Kuwahara, F. 1988, *Prog. Theo. Phys.*, **80**, 449.
Prasanna, A. R. 1982, *Gravitation and Relativistic Astrophysics*, World Scientific.
Prasanna, A. R., Bhaskaran, P. 1989, *Astrophys. Sp. Sci.*, **153**, 201.
Prasanna, A. R., Varma, R. K. 1977, *Pramana*, **8**, 229.

J. Astrophys. Astr. (1990) **11,** 67–72

Estimation of the Dissociation Energy of CO^+ from Spectroscopic Data

R. R. Reddy & R. Viswanath *Department of Physics, Sri Krishnadevaraya University, Anantapur 515003*

Received 1989 June 16; accepted 1989 November 3

Abstract. The potential energy curves for the $X^2\,\Sigma^+$ and $B^2\,\Sigma^+$ states of CO^+ have been constructed by the Rydberg–Klein–Rees (RKR) method as modified by van der Slice *et al.* The dissociation energy is estimated to be 7.70±0.19 eV by the method of curve fitting using the five parameter Hulburt–Hirschfelder's function. The estimated value is in good agreement with the value (7.839 eV) given by Misra *et al.* Carefull observation of the results reveals that accurate D_0 value for CO^+ is 8.33 eV.

Key words: CO^+ molecule—RKRV potential energy curves—dissociation energy—curve fitting method

I. Introduction

The band spectrum of the CO^+ molecule consists of four electronic systems in the region 11760 and 55560 cm^{-1} (at 8500 A and 1800 Å). These systems are due to the $B^2\Sigma^+ - X^2\Sigma^+$ (first negative), $B^2\Sigma^+ - A^2\Pi_I$, $A^2\Pi_i - X^2\Sigma^+$ (Comet-tail), and $c^2\Delta_r - A^2\Pi_i$ transitions respectively. The most prominent bands of CO^+ are observed in the tail of Comet (Herzberg 1950; Narahari Rao 1950; Price, Sulzmann & Penner 1971; Whipple 1978; Misra *et al.* 1987). The existence of CO^+ has been observed in Comets (Wurm 1943; Price, Sulzmann & Penner 1971), Meteors (Milliman 1972) and in the ionosphere of Venus (Bauer 1979).

Wilkinson (1963) has pointed out that a knowledge of ionization potentials and dissociation energies is important to astrophysical as well as many physical and chemical problems. In order to estimate molecular abundances and interpret dissociation equilibria and ionization processes in stellar and planetary atmospheres, precise dissociation energies and ionization potentials of certain astrophysically important molecules are necessary. The values of dissociation energies (D_e) of CO^+ obtained from different methods have been reported by various investigators as shown in Table 1. The present investigation deals with the estimation of the value of D_e by the method of curve-fitting using the potential energy curve and the molecular constants reported by Misra *et al.* (1987) recently. Bagare & Murthy (1978) have evaluated D_e of CO^+ by curve-fitting method using three parameter Lippincott potential function and the estimated value (9.3 eV) is very high. The recent molecular constants on CO^+ (Misra *et al.* 1987) and no report on the molecular properties of $B^2\Sigma^+$ state, initiated the present authors to take up this work.

Table 1. Values of the dissociation energy and ionization potential for the ground state of CO^+.

Investigator	Method	D_e(eV)	IP(eV)
Herzberg (1950)	Cycle	8.334	27.90
Biskamp (1933)	Linear extrapolation	9.90	
Asundi (1943)	Collision Data	9.20	
Huber & Herzberg (1979)	$D_O(CO)+IP(C)-IP(CO)$	8.338	26.80
Recommended values by Gaydon (1968)	—	8.34	
Misra *et al.* (1987)	Spectroscopic	7.839	
Bagare & Murthy	Curve fitting	9.30	

2. Evaluation of dissociation energy

In the curve-fitting procedure, an empirical potential function which gives the best reproduction of RKRV curve is chosen. In this potential function, the turning points evaluated by the RKRV potential energy curve are substituted with different values of D_e. By this procedure energy values $U(r)$ for various vibrational levels are calculated. These values are compared with experimental energy values $G(v)$. The value of D_e for which the best fit is obtained is taken to be the value of the dissociation energy for that state of the molecule.

We have chosen five-parameter Hulburt–Hirschfelder function in the case of CO^+, as this function is seen to be superior to other functions (Steele, Lippincott & van der Slice 1962). The deviation of the calculated energy value from the experimentally observed value is found to be minimum, only when the above potential function is chosen.

Experimentally observed vibrational levels are used to construct the RKRV potential energy curve. For the known vibrational levels, the Rydberg-Klein-Rees (RKR) method gives the turning points by

$$r_{\pm} = [(f_v/g_v)+f_v^2]^{1/2} \pm f_v.$$

Here f_v and g_v are calculated by the procedure of van der Slice *et al.* (1960). The molecular constants used in the present study (Misra *et al.* 1987) are listed in Table 2. The computed values of the turning points are given in Table 3 for the $B^2\Sigma^+$ and $X^2\Sigma^+$ states of CO^+. The modified Jarmain turning points are given for comparison. The turning points and the extrapolated energy values are also listed in Table 3.

The RKRV turning points are used in the Hulburt–Hirschfelder potential function (1941) and the value of D_e is varied until the best fit to the true potential energy curve is

Table 2. Molecular constants for $X^2\Sigma^+$ and $B^2\Sigma^+$ states of CO^+.

State	T_e(cm^{-1})	ω_e(cm^{-1})	$\omega_e X_e$(cm^{-1})	B_e(cm^{-1})	α_e(cm^{-1})	r_e(Å)
$B^2\Sigma^+$	45876.38	1734.48	27.76	1.79980	0.02999	1.16863
$X^2\Sigma^+$	0.0	2214.27	15.20	1.97695	0.018975	1.11504

Table 3. Potential energy curves for the electronic states of CO^+ molecule.

V	U (cm^{-1})	RKRV		Modified Jarmain method	
		r_{min} (Å)	r_{max} (Å)	r_{min} (Å)	r_{max} (Å)
		$X^2\Sigma^+$ State			
0	1103.33	1.0705	1.1650	1.0708	1.1649
1	3287.20	1.0411	1.2057	1.0417	1.2054
2	5440.67	1.0222	1.2360	1.0229	1.2357
3	7562.74	1.0076	1.2621	1.0081	1.2619
4	9656.41	0.9956	1.2859	0.9955	1.2658
5	11718.69	0.9852	1.3081	0.9844	1.3084
6	13750.56	0.9760	1.3292	0.9742	1.3300
7	15752.03	0.9678	1.3496	0.9646	1.3510
⋮	⋮	⋮	⋮		
73	80634.65	0.5877	4.9079	—	—
		$B^2\Sigma^+$ State			
0	860.30	1.1195	1.2267	1.1203	1.2263
1	2539.26	1.0881	1.2763	1.0900	1.2755
2	4162.70	1.0684	1.3148	1.0705	1.3138
3	5730.62	1.0533	1.3492	1.0547	1.3483
4	7243.02	1.0408	1.3814	1.0408	1.3811

achieved (Reddy, Reddy & Rao 1985; Reddy, Reddy & Rao 1986a; Reddy, Reddy & Rao 1986b). In Table 4, the energy values obtained by using Hulburt–Hirschfelder potential function for CO^+ are compared, with those obtained by using experimental data, *i.e.*, $G(v)$. The average percentage deviation of $U(r)$ values from $G(v)$ is also given.

Table 4. Energy values from the Hulburt—Hirschfeldcr function for CO^+.

r(Å)	Observed	Calculated $U(r)$ in (cm^{-1})		
	$G(v)$ cm^{-1}	$D_e = 7.86$ eV	$D_e = 7.84$ eV	$D_e = 7.82$ eV
1.0705	1103.33	1106.86	1103.37	1099.88
1.0411	3287.20	3295.72	3285.34	3274.95
1.0222	5440.67	5448.80	5431.63	5414.45
1.0076	7563.74	7564.70	7540.86	7517.01
0.9956	9656.41	9642.18	9611.79	9581.40
0.9852	11718.69	11680.10	11643.28	11606.46
0.9760	13750.56	13677.62	13634.51	13501.40
0.9678	15752.03	15633.99	15584.71	15535.43
1.1650	1103.33	1107.55	1104.06	1100.57
1.2057	3287.20	3301.52	3291.12	3280.71
1.2360	5440.67	5469.62	5452.30	5435.14
1.2621	7563.74	7612.84	7588.85	7564.85
1.2859	9656.41	9732.22	9701.55	9670.87
1.3081	11718.69	11828.66	11791.38	11754.09
1.3292	13750.56	13902.85	13859.02	13815.20
1.3496	15752.03	15955.70	15905.41	15855.13
Average per cent deviation		0.5384	0.4448	0.5115

3. Results and discussion

The inherent error in H–H function is 2 per cent (Steele *et al.* 1962). The error involved in evaluation of D_e is the average percentage deviation plus the inherent error in the potential function. The *Do* value of 7.70 ± 0.19 eV for CO^+ is in good agreement with the value 7.839 eV recommended by Misra *et al.* (1987). Here $D_o = D_e - G(v)$; Bagare & Murthy (1978) have evaluated the D_e value of CO^+ as 9.30 ± 0.35 eV using Lippincott three-parameter potential function. The function leading to the smallest deviation determined the dissociation energy of the molecule. The minimum deviation obtained in their study is 0.68. Moreover, the inherent error in Lippincott potential function is 3 per cent. They have used the molecular constants reported by Biskamp (1933) and Narahari Rao (1950). The minimum deviation in the present study is 0.44. Recently reported molecular constants (Misra *et al.* 1987) are utilized for the evaluation of D_e.

The reported D_e values of CO^+ (Table 1) vary between 7.83 eV to 9.90 eV. We have to judge which value is more probable, as follows.

Given the D_o (11.09 eV) value of CO (Huber & Herzberg 1979), the D_o value of CO^+ (7.70 eV) and the ionization potential of carbon atom (Gaydon 1968), the ionization potential of CO can be evaluated. As the ionization potential of carbon is less than that of the oxygen atom, the process of ionization in the CO molecule probably may be regarded as the loss of an electron from the carbon atom.

The difference between the bond energies of CO + and CO is given by the relation

$$D_o\,(CO^+) - D_e\,(CO) = I(C) — I\,(CO) \simeq 2.7 \text{ eV}$$

which is consistent with the ionization of a bonding electron. It expresses that CO^+ has one bonding electron less than CO and so one would expect $D_o(C0^+)$ will less than D_o(CO). Because the force constants for CO and CO + are 18.99 and 19.77 Mdyn cm^{-1}, respectively, the CO bond is less stronger than CO + bond. As a consequence, the ionization potential of *I*(CO) must be greater than that of *I*(C). So, the ionization potential of the CO molecule is

$$I(CO) = I(C) + D_o(CO) - D_o(CO^+)$$

$$= 11.258 + 11.09 - 7.70 = 14.648 \text{ eV},$$

which is in close agreement with the value of 14.013 eV given by Huber & Herzberg (1979). The difference between the estimated *I*(CO) and *I*(CO) given by Huber and Herzberg is 0.635 eV. If we add this value to the curve-fit estimate of $D_o(CO^+)$, then one obtains 8.335 eV. Except $D_o(CO^+)$ in the above equation, all values are experimentally determined. Hence, addition of the difference to the curve-fit estimate of $D_o(CO^+)$ is reasonable. If the value of $D_o(CO^+)$ suggested by Bagare & Murthy (1978) is inserted in the above equation, one obtains *I*(CO)= 13.048 eV. This value is significantly smaller than the value (14.013 eV) recommended by Huber & Herzberg (1979). So our estimate of $D_O(CO^+)$ appears better than that of Bagare & Murthy (1978).

There are other ways of estimating the dissociation energy of the molecule. If a few experimental values for $(v+1)4 \leftarrow v$ transitions are available, linearly extrapolating the equation

$$G(v) = \tfrac{1}{2}\,[G(v+1) - G\,(v-1)]$$

$$= \omega_e - 2\omega_e X_e(v + \tfrac{1}{2})$$

to $\Delta G(v) = 0$ gives $v = v_c$; v_c may also be obtained from $v_c = (\omega_e/2\omega_e X_e) - (1/2)$. This value, inserted in the equation

$$G(v) = \omega_e(v_c + ½) - \omega_e X_e(v_c + ½)^2 + \ldots$$

yields an estimate of $G(v)$. This value is equal to the dissociation energy (D_e) of the molecule. Employing the above method, one obtains v_c = 73 and D_e = 80634.65 cm^{-1}. Gaydon suggested that the Brige-Sponer (1926) extrapolation (above method) gives an upper limit to the dissociation energy for covalent molecules and a lower limit to molecules where the ionic forces predominate. The probable error in this method is ± 20 per cent. Here CO^+ is considered as covalent because its electronegativity difference is 1.0. Considering the above statement, Birge & Sponer (1926) extrapolation gives an upper limit in this case and the error is 20 per cent (i.e. 16126.93 cm^{-1}). So the probable exact value here is 80634.65 –16126.93 = 64507.72 cm^{-1}/7.99 eV. Hildenbrand & Murad (1969) suggested that D_e value may also be evaluated from

$$D_e = \omega^2_e/(5.33\ \omega_e X_e - 2B_e)$$

$$= 63623.92\ cm^{-1}/7.89\ eV.$$

The values obtained from the above two methods are in reasonable agreement with the value obtained from curve fitting. The relationship between $\Delta G(v)$ and the observed vibrational levels is found to be linear in the case of CO^+. Thus, the Birge-Sponer extrapolation is fairly satisfactory.

The exact $D_o(C0^+)$ value may be estimated with the following relation

$$D_o(CO^+) — Do(CO) = I(C) — I(CO).$$

If $D_o(CO^+)$ = 8.338, $D_o(CO)$=11.09, $I(C)$ = 11.258 and $I(CO)$ =14.013 (all are in eV), then the equation is accurately balanced. It is hence concluded that the accurate value of $D_o(CO^+)$ is 8.338 eV, in close agreement with the value estimated here.

Acknowledgements

This work was supported by Indian Space Research Organization (ISRO), Department of Space, Government of India. One of the author's (RRR) wishes to express his thanks to ISRO for their financial support.

References

Asundi, R. K. 1943, *Proc. Indian Acad. Sci.,* **A18**, 8.

Bagare, S. P., Murthy, N. S. 1978, *Proc. Indian Acad. Sci.,* **A87**, 211,

Bauer, S. M. 1979, *Science*, **205**, 110.

Birge, R. T., Sponer, H. 1926, *Phys. Rev.*, **28**, 259.

Biskamp, H. 1983, Z. Phys., **86**, 33.

Gaydon, A, G. 1968, *Dissociation Energies and Spectra of Diatomic Molecules*, 3edn, Chapman and Hall, London.

Herzberg, G. 1950, *Spectra of Diatomic Molecules*, D. Van Nostrand, New Jersey.

Hildenbrand, D. L., Murad, E. J. 1969, *J. Chem. Phys.,* **51,** 807.

Huber, K. P., Herzberg, G. 1979, *Constants of Diatomic Molecules,* Van Nostrand, New York.

Hulburt, H. M., Hirschfelder, J. **0.** 1941, *J. Chem. Phys.,* **9,** 61.

Milliman, P. M., 1972, *Plasma to Planet,* Wiley-Inter Science, New York.
Misra, P., Ferguson, D. W., Narahvi Rao, K., Willians, Jr. W., Mathews, C. W. 1987, *J. molec. Spectrosc.*, **125**, 54.
Narahari Rao, K. 1950, *Astrophys. J.,* **111**, 306.
Price, P. L., Sulzniann, K. G. P., Penner, S. S. 1971, *J. quantit. Spectrosc. radiat. Transfer,* **11**, 427.
Reddy, R. R., Reddy, A. S. R., Rao, T. V. R. 1985, *Pramana,* **25**, 187.
Reddy, R. R., Reddy. A. S. R., Rao, T. V. R. 1986a, *Proc. Indian Natl. Sci. Acad.,* **52A**, 653.
Reddy, R. R., Reddy, A. S. R., Rao, T. V. R. 1986b, *J. quantit. Spectrosc. radiat. Transfer,* **35**, 167.
Steele, D., Lippincott, E. R., van der Slice, J. T. 1962, *Rev. Mod. Phys.,* **34**, 239.
van der Slice, J. T., Mason, E. A., Maisch, W. G., Lippincott, E. R. 1960, *J. molec. Spectrosc.,* **5**, 83.
Whipple, F. L. 1978, *Cosmic Dust,* Wiley-Inter Science, New York.
Wilkinson, P. G. 1963, *Astrophys. J.,* **138**, 778.
Wurm, R. 1943, *Vierteljahreshchr, Astr. Ges.,* **78**, 18.

The search for such a steady signal of high energy neutrinos from SN1987A is continuing in many large scale experiments and an upper limit on this flux has been reported by Oyama *et al*, (1987). Here we report the search for neutrinos of energy > 1 GeV from SN1987A in phase I and phase II of the nucleon decay experiments being operated at KGF (12.9°N, 78.3°E) in India.

2. The experiment and results

The KGF detectors are essentially calorimeters with alternating layers of proportional counters of wall thickness 2.3 mm and iron absorbers (Krishnaswamy *et al.* 1982, 1986). The counter layers are crossed to enable three-dimensional reconstruction of the tracks. The other relevant details of the two detectors are given in Table 1.

The basic trigger is a five-fold coincidence of any 5 layers (with at least one counter per layer) out of 11 consecutive layers. In addition there is a special 2-layer coincidence with at least 2 counters per layer to record tracks with large zenith angles. Thus the detector covers almost all the directions in space except for a narrow band between zenith angles (θ) 87° and 93°. This small gap in acceptance due to the triggering criteria is taken into account in the estimate of exposure. The trigger threshold is $\simeq$100 MeV for both the detectors.

At such large depths the majority of events recorded are due to atmospheric muons which have a steep zenith angular distribution (Fig. 1 for Phase II) with negligible flux beyond 60°. On the other hand, the muons produced in ν-interactions in the surrounding rock are nearly isotropic so that a clear separation is possible between these two sources of muons. However, we have to restrict the angular regions to 60°–120° and 65°–115° for Phase I and II detectors respectively in view of the fact that up and down sense of motion could not be obtained due to the slow response of counters employed here. In spite of these angular cuts, as shown in Fig. 2, the source

Table 1. Specific details of the KGF nucleon decay detectors.

Description	Phase I	Phase II
Depth	2.3 km (7000 hg cm^{-2})	2.0 km (6045 hg cm^{-2})
No. of proportional counter layers	34	60
Detector size	6 m × 4 m × 3.8 m	6 m × 6 m × 6.4 m
Thickness of absorber plates (iron)	12 mm	6 mm
Angular resolution	1° for full tracks 4° for 1 m tracks	1° for full tracks 4° for 1 m tracks
Zenith angle region for this study	82°–120°	82°–115°
Live-time (1987 Feb 23 to 1989 March 29)	535 d	658 d

The search for such a steady signal of high energy neutrinos from SN1987A is continuing in many large scale experiments and an upper limit on this flux has been reported by Oyama *et al*, (1987). Here we report the search for neutrinos of energy > 1 GeV from SN1987A in phase I and phase II of the nucleon decay experiments being operated at KGF (12.9°N, 78.3°E) in India.

2. The experiment and results

The KGF detectors are essentially calorimeters with alternating layers of proportional counters of wall thickness 2.3 mm and iron absorbers (Krishnaswamy *et al.* 1982, 1986). The counter layers are crossed to enable three-dimensional reconstruction of the tracks. The other relevant details of the two detectors are given in Table 1.

The basic trigger is a five-fold coincidence of any 5 layers (with at least one counter per layer) out of 11 consecutive layers. In addition there is a special 2-layer coincidence with at least 2 counters per layer to record tracks with large zenith angles. Thus the detector covers almost all the directions in space except for a narrow band between zenith angles (θ) 87° and 93°. This small gap in acceptance due to the triggering criteria is taken into account in the estimate of exposure. The trigger threshold is $\simeq$100 MeV for both the detectors.

At such large depths the majority of events recorded are due to atmospheric muons which have a steep zenith angular distribution (Fig. 1 for Phase II) with negligible flux beyond 60°. On the other hand, the muons produced in ν-interactions in the surrounding rock are nearly isotropic so that a clear separation is possible between these two sources of muons. However, we have to restrict the angular regions to 60°–120° and 65°–115° for Phase I and II detectors respectively in view of the fact that up and down sense of motion could not be obtained due to the slow response of counters employed here. In spite of these angular cuts, as shown in Fig. 2, the source

Table 1. Specific details of the KGF nucleon decay detectors.

Description	Phase I	Phase II
Depth	2.3 km (7000 hg cm^{-2})	2.0 km (6045 hg cm^{-2})
No. of proportional counter layers	34	60
Detector size	6 m × 4 m × 3.8 m	6 m × 6 m × 6.4 m
Thickness of absorber plates (iron)	12 mm	6 mm
Angular resolution	1° for full tracks 4° for 1 m tracks	1° for full tracks 4° for 1 m tracks
Zenith angle region for this study	82°–120°	82°–115°
Live-time (1987 Feb 23 to 1989 March 29)	535 d	658 d

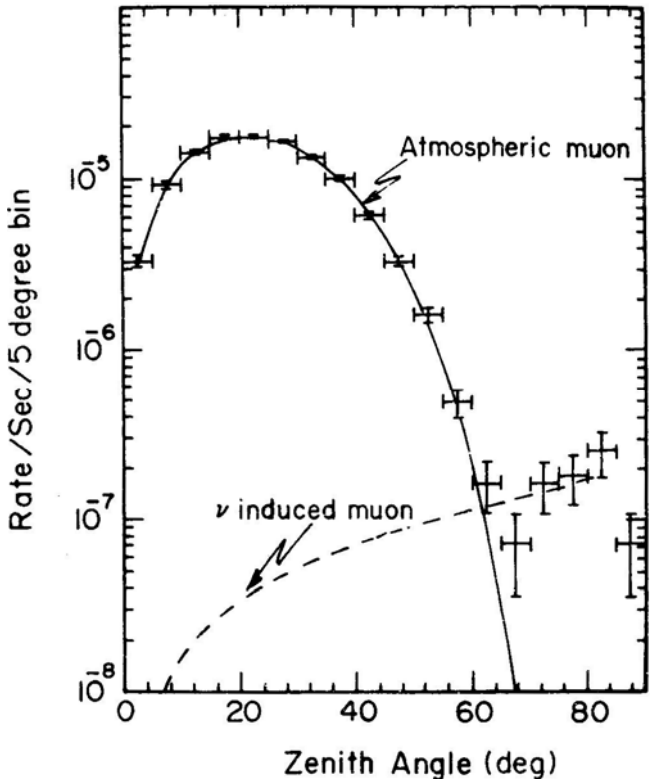

Figure 1. The zenith angular distribution of atmospheric and neutrino-induced muons in the Phase II detector at the depth of 6045 hg cm^{-2} in Kolar Gold Fields. The solid curves show the rates expected on the basis of past experiments in the case of atmospheric muons and calculations in the case of neutrino-induced muons. Beyond 65° the rate of neutrino-induced muons remains almost constant; that of atmospheric muons falls off rather steeply and is negligible. The distribution is similar for Phase 1 at 7000 hg cm^{-2} the cutoff angle being 60°.

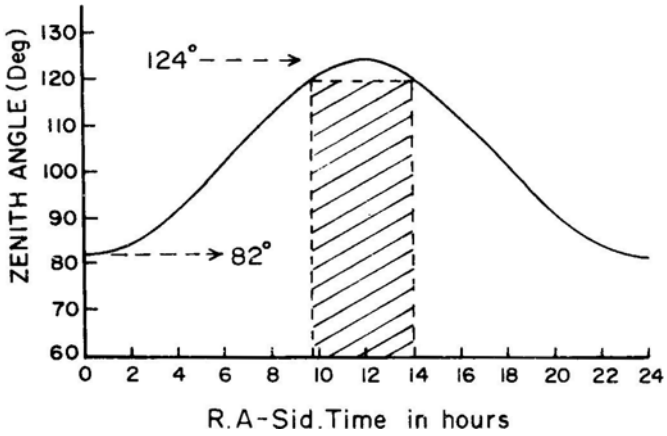

Figure 2. The zenith angle θ of SN**1987A** as a function of (RA – Siderial Time) at Kolar Gold Fields (12.9°N, 78.3°E). The hatched region shows the 'off-time' per 24 siderial hours. It can be seen that the source remains in the accepted angular region ($60° < \theta < 120°$) for more than 70 per cent of a siderial day.

SN1987A remains within view for > 70 per cent of the time due to the equatorial latitude of the detectors and the large declination of SNI987A.

A majority of these muons have track lengths > 3 m inside the detector and their angles arc known to an accuracy better than 1°; only 10 per cent of the events have track lengths 1 m–3 m and their angular resolution is correspondingly poorer. Combining this with the dispersion in the production angle in *v*-interactions as well as the subsequent multiple Coulomb scattering of muons in rock, we estimate that the secondary muon could deviate from the original direction of the neutrinos by $\simeq 4°$. We thus use a cone of half angle of 8º so that > 95 per cent of the muons from the source direction will be included in the sample.

A total of 80 *v*-induced muons recorded since the supernova burst until 1989 March are plotted in Fig. 3 in equatorial coordinates. Each of them in turn is plotted twice in the two hemispheres due to the ambiguity on the sense of motion. Also shown in this figure are the location of SN1987A with an angular window of radius 8º around it.

As seen in Fig. 3. no muon has been recorded within the 8º window around SN1987A in a total exposure of 83 m^2 yr. This corresponds to an upper limit of 8.8 $\times 10^{-14}$ cm^{-2} s^{-1} (90% C.L.) for the flux of muons ($E_\mu > 500$ MeV) coming from the direction of SN1987A.

3. The analysis and conclusions

The above result has been converted into upper limits on the corresponding neutrino flux and luminosity as follows.

1. The zenith angle θ of the source at siderial time t_s and the corresponding effective area $A(t_s)$ presented by the detector to the source are calculated as a function of siderial time t_s. The effect of triggering criteria and the zenith angle cut to suppress atmospheric muons are taken into account in this calculation.

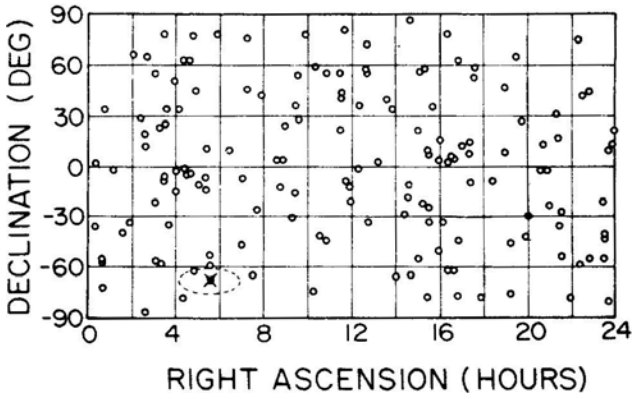

Figure 3. The celestial plot of the 80 large-angle ($\theta > 60º$) muons seen in Phases I and II of the KGF nucleon decay experiment. Since 'Up-Down' information is not available for these tracks, each event it shown twice corresponding to two opposite directions in the celestial sphere. The position (marked by a X) of SN1987A and a window of radius 8^0 around this source are also shown.

2. The differential spectrum of the neutrinos (ν)* at production in the source, is assumed to be $F(E_\nu)\mathrm{d}E_\nu = CE_\nu^{-(\gamma+1)}\mathrm{d}E_\nu$, the neutrinos having energies up to a maximum energy E_{cutoff}.

3. The muon produced in the charged current neutrino interaction is required to have a minimum energy of 500 MeV before entering the detector to satisfy the event selection criterion of a minimum pathlength of 1 m inside the detector. Thus the threshold energy E_{th} for the neutrino is $\simeq 1$ GeV.

4. The following quantities are calculated as a function of neutrino energy E_ν ($E_{\mathrm{th}} < E_\nu < E_{\mathrm{cutoff}}$) and the zenith angle θ of the neutrino.

(i) We define a restricted range R (E_μ) in rock of the muon such that a muon with an initial energy E_μ will have a residual energy E_{th}(= 500 MeV) after traversing R (E_μ). The average energy E_μ of the muon in a charged current interaction of the neutrino and hence R (E_μ) are found.

(ii) Next we compute the probability P_{SUT} (E_ν, t_s) that the neutrino from the source survives without absorption in the earth and enters a rock shell of thickness R (E_μ) surrounding the detector at siderial time t_s.

For these calculations we have assumed the ν-cross-sections $\sigma(E_\nu)$ and average E_μ/E_ν ratios of Quigg *et al.* (1986). Use of average E_μ/E_μ values to determine muon energy gives only negligible errors as checked in a few cases by using the actual y distribution.

5. The number of muons from the direction of the source entering the detector is then,

$$M = \int_0^{T_s} \int_{E_{\mathrm{th}}}^{E_{\mathrm{cutoff}}} F(E_\nu)\, P_{\mathrm{sur}}(E_\nu, t_s)\, \sigma(E_\nu)\, N_{\mathrm{AV}}\, R(E_\mu)\, A(t_s)\, \mathrm{d}E_\nu\, \mathrm{d}t_s$$

where T_s = Actual run-time of detector in siderial hours and N_{AV} = Avogadro number. Equating M to the number of events seen (=2.3 for 90% C.L.) will determine the normalization constant C in $CE^{-(\gamma+1)}$. From this we obtain the neutrino flux

$$\left\{ \int_{E_{\mathrm{th}}}^{E_{\mathrm{cutoff}}} F(E_\nu)\, \mathrm{d}E_\nu \right\}$$

and the luminosity

$$\left\{ 4\pi D^2 \int_{E_{\mathrm{th}}}^{E_{\mathrm{cutoff}}} F(E_\nu)\, E_\nu\, \mathrm{d}E_\nu \right\}$$

which are shown in Fig. 4 as a function of E_{cutoff} for various values of γ. The source distance D is taken as 50 kpc.

In this study we have used only the average range-energy relation for the muon *viz.* $-\mathrm{d}E/\mathrm{d}x = a + bE$ with increasing a and b as a function of energy. The effect of fluctuations in the energy loss of muons is small for $\gamma = 1.1$ and even for the largest γ (= 1.9) the maximum contribution to muon intensity comes from the region of few hundred metres of the rock surrounding the detector; for these overburdens fluctuations are small (<10 per cent).

* Throughout this paper ν means ν_μ and $\nu\mu$. We do not consider ν_e and ν_e since they contribute only a very small and negligible fraction to the type of events considered here.

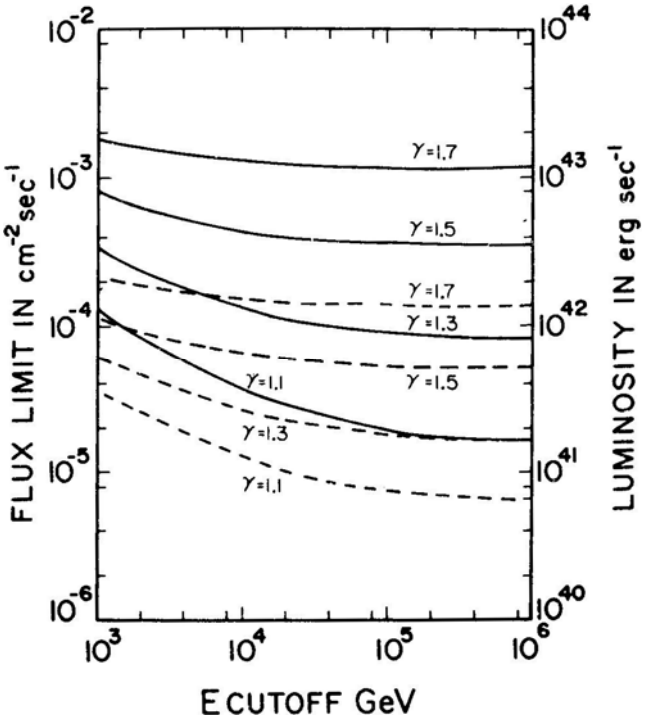

Figure 4. The 90 per cent confidence limits on the neutrino flux (solid lines and left vertical scale) and neutrino luminosity (dashed lines and right vertical scale) of SN1987A corresponding to the result of zero signal in KGF nucleon decay experiments. The values of γ correspond to the assumed differential spectrum $F(E)\,\mathrm{d}E = CE^{-(\gamma+1)+1)}\,\mathrm{d}E$ and the horizontal scale to the maximum energy E_{cutoff} of the neutrinos from the source.

Our neutrino energy threshold of 1 GeV is low compared to that (1.7 GeV) of Oyama *et al.* (1987). The present result corresponds to the period upto 1989 March beginning from the supernova burst whereas the result of Oyama *et al.* covers a 6-month period from the burst. Moreover, the intervals of observation in each day do not exactly match due to the location of detectors and different zenith angular cuts for event selection. Thus these two experiments correspond to different intervals and duration in real time. However, our results agree within a factor of 2. These results give sufficiently stringent limits on the neutrino luminosities to rule out some of the models (Gaisser & Stanev 1987) of acceleration mechanism in supernovae which predict neutrino luminosities $> 10^{43}$ erg s^{-1}.

Acknowledgements

We thank Messrs B. Satyanarayana, S. D. Kalmani, P. S. Murthy, R. Nagaraj and L. V. Reddy for able assistance in maintenance and data collecting. We are thankful to the Ministry of Education for partial financial support. The co-operation of the officers and other staff of the Bharat Gold Mines Ltd of KGF at all stages of the experiment is gratefully acknowledged.

References

Aglietta, M. A., Badino, G., Bologna, G., Castagnoli, C., Castallina, A., Dadykin, V. L., Fulgione, W., Galeotti, P., Kalchukov, F. F., Kortchaguin, V. B., Kortchaguin, P. V., Malguin, A. S., Ryassny, V. G., Ryazhkaya, O. G., Saavedra, O., Talochkin, V. P., Trinchero, G., Vernetto, S., Zatsepin, G. T., Yakushev, V. F. 1987, *Euro. Phys. Lett.*, **3**, 1315, 1321.

Alexeyev, E. N., Alexeyeva, L. N., Krivoscheina, I. V., Volchenko, V. I. 1987, Proc XXII Rcontre De Moriond, **1**, 739.

Bionta, R. M., Blewitt, G., Bratton, C. B., Casper, D., Ciocio, A., Claus, R., Cortez, B., Crouch, M., Dye, S. T., Errede, S., Foster, G. W., Gajewski, W., Ganezer, K. S., Goldhaber, M., Haines, T. J., Jones, T. W., Kielczewska, D., Kropp, W. R., Learned, J. G., Losecco, J. M., Mathews, J., Miller, R., Mudan, M. S., Park, H. S., Price, L. R., Reines, F., Schultz, J., Seidel, S., Schumand, E., Sinclair, D., Sobel, H. W., Stone, J. L., Sulak, L. R., Svaboda, R., Thornton, G., Van der Velde, J. C., Wuest, C. 1987, *Phys. Rev. Lett.*, **58**, 1494.

Blandfold, R. D., Ostricker, J. P. 1980, *Astrophys. J.*, **237**, 793.

Cavallo, G., Pacini, F. 1980, *Astr. Astrophys.*, **88**, 367.

Gaisser, T. K., Stanev, T. 1987, *Phys. Rev. Lett.*, **58**, 1695.

Ginzburg, V. L., Ptuskin, V. S. 1984, *J. Astrophys. Astr.*, **5**, 99.

Gunn, J. E., Ostricker, J. P. 1969, *Phys. Rev. Lett.*, **22**, 728.

Hirata, K., Kajita, T., Koshiba, M., Nakahata, M., Oyama, Y., Sato, N., Suzuki, A., Takita, M., Totsuka, Y., Kifune, T., Suda, T., Takahashi, K., Tanimori, T., Miyano, K., Yamada, M., Beier, E. W., Fieldscher, L. R., Kim, S. B., Mann, A. K., Newcomer, F. M., Van Berg, R., Zhang, W., Cortez, B. G. 1987, *Phys. Rev. Lett.*, **58**, 1419.

Krishnaswamy, M. R., Menon, M. G. K., Mondal, N. K., Narasimham, V. S., Sreekantan, B. V., Hayashi, Y., Ito, N., Kawakami, S., Miyake, S. 1982, *Phys. Lett.*, **115B**, 349.

Krishnaswamy, M. R., Menon, M. G. K., Mondal, N. K., Narasimham, V. S., Sreekantan, B. V., Hayashi, Y., Ito, N., Kawakami, S., Miyake, S. 1986, Il *Nuovo Cim.*, **9C**, 167.

Oyama, Y., Hirata, K., Kajita, T., Koshiba, M., Nakahata, N., Sato, N., Suzuki, A., Takita, M., Totsuka, Y., Kifune, T., Suda, T., Nakamura, K., Takahashi, K., Tanimori, T., Miyano, K., Yamada, M., Beier, E. W., Fieldscher, L. R., Kim, S. B., Mann, A. K., Newcomer, F. M., Van Berg, R., Zhang, W., Cortez, B. G. 1987, *Phys. Rev. Lett.*, **59**, 2604.

Quigg, C., Reno, M. H., Walker, T. P. 1986, *Phys. Rev. Lett.*, **57**, 774.

J. Astrophys. Astr. (1990) **11**, 81–123

An Atlas of the Optical Spectrum of Supernova 1987A in the Large Magellanic Cloud

V. J. Mclntyre, A. C. Gilmore & J. B. Hearnshaw *Mount John University Observatory* and *Department of Physics, University of Canterbury, Private Bag, Christchurch, New Zealand*

Received 1989 September 18; accepted 1989 November 7

Abstract. Photographic spectra of SN1987A in the LMC have been obtained from 1987 February 25 to 1988 June 30. Microdensitometer tracings of these have been reduced to intensity and corrections for instrumental response have been applied to the spectra. This paper presents these data in an atlas format, discusses the reduction procedures in detail, and presents radial velocity measurements of selected lines in the spectra.

Key words: Supernovae, general—Supernovae, individual (SN1987A)—optical spectroscopy

1. Introduction

Immediately following the announcement of its discovery by Ian Shelton (Kunkel & Madore 1987), spectroscopic observations of SN1987A were begun at Mt John University Observatory (MJUO), and continued on a regular basis for the next twelve months. Thepurpose of this paper istopresent aphotographic atlasofthesupernova's optical spectrum covering about the first thirteen months of evolution. Similar spectroscopic monitoring programmes have been carried out at other observatories (Menzies *et al.* 1987; Hanuschik & Dachs 1987; Phillips *et al.* 1988; Ashoka *et al.* 1987) and the observations made at MJUO are intended to complement these although with some differences. In particular, the Mt John spectra are photographic while the first three groups listed above used solid-state cameras or spectrophotometers. Also, because of Mt John's southerly position (44°S), the supernova could be observed year round at favourable airmasses. Some of the observations shown here have been published previously (Hearnshaw *et al.* 1988), but not in fully-reduced form. Hearnshaw *et al.* also presented radial velocity measurements of the spectra and a determination of the distance to SN1987A; further radial velocity measurements are shown here.

2. Observations

The observations were made using red (IIIaF) and blue (IIaO, IIIaJ) emulsions at medium dispersion. The spectra were digitized, reduced to intensity, adjusted for the

Wavelength-dependent response of the emulsions, and compiled into the atlas plots shown in the Appendix.

In the year following the supernova's outburst, 108 'red' plates and 103 'blue' plates were taken. A journal of the observations presented in the atlas is shown in the Appendix. At first, observations were made on every clear night, but after about 1987 July 31 the frequency was decreased to two plates (one red and one blue) per week, until 1988 March 13. A few additional observations were made during 1988 June. The Boller and Chivens spectrograph (similar to that described in Taylor & Schmidt 1975) was used with an 80 μm slit, attached to either the 0.61 m Boller and Chivens or 1.0 m McLellan telescopes at Mount John University Observatory. The 'red' exposures were made of the second-order red spectrum at a dispersion of 90 Å mm^{-1}. A yellow (Corning CS 3-71) filter ($\lambda_{cutoff} \simeq 4750$ Å) was used for order separation. The wavelength resolution of the spectrograph was 1.6 Å for the red spectra. The 'blue'exposures were third order blue spectra, at 60 Å mm^{-1}, through a clear quartz filter (used to preserve collimator focus). The resolution was 1.1 Å. The emulsions used were mainly Kodak IIIaF (red-sensitive) and IIaO (blue-sensitive), but the earliest blue plates were Kodak IIIaJ emulsion.

Initially, plates were hypersensitized by baking in nitrogen to remove water and other impurities from the emulsion, but this produced such high fog levels that a change was made to soaking in hydrogen at room temperature. This method gave plates with very low fog levels, and a reasonable increase in speed. For a period near maximum light, (1987 May 4-September 7) the IIIaF plates were not hypersensitized. A number of different emulsion batches were used (see Table 1). The spectra were widened by scanning the image across the slit a number of times. Typically two or three separate spectra were exposed on each plate. A helium-argon comparison lamp was used for wavelength calibration of each exposure. Each plate was calibrated by spot sensitometer exposures, using a 'Kitt Peak' design of sensitometer (see Schoening 1976 for a description). Red plates were calibrated at 6500 Å (using an interference filter with a bandpass of 114 Å FWHM), blue plates at 4500 Å (65 ÅFWHM).

3. Reduction procedures

From each plate the most suitable spectrum was chosen, and converted into digital form with the microcomputer-controlled Joyce-Loebl Mk III CS microdensitometer of the Physics Department. The chosen photographic spectra were all traced at 25 μm per step, using a 25 μm wide slit on the emulsion. This corresponds to a pixel size of 2.3 Å for the digitized 'red' spectra and 1.5 Å for the 'blue' spectra. For each tracing,

Table. 1. Photographic emulsions and batches.

Blue			Red		
Emulsion	Batch	Dates	Emulsion	Batch	Dates
IIIaJ	HD2G0	Feb 25–Mar 4	IIIaF	HD1F1	Feb 25–Aug 5
IIaO	HD3H5	Mar 6–July 7	IIIaF	HD1E7	Aug 7–Jun 10
IIaO	HD2H5	July 9–Sep 17			
IIaO	HD1F7	Sep 26–June 30			

three consecutive scans were made: one each of the spectrum, the comparison lines (on one side of the supernova spectrum) and the 'fog' (an unexposed section of the plate). No fixed-height slits were used, but the microdensitometer's deckers were adjusted so that its slit covered only the central 3/4 of the spectrum. The procedure of widening the spectra by trailing and setting the deckers to cut off the edges of the spectrum produced a nearly uniform density over the length of the scanning slit.

Dispersion solutions were obtained by least-squares fitting of a third order polynomial to selected comparison lines. Because only one set ofcomparison lines was used, there existed the possibility of systematic errors in the wavelength of each pixel due to misalignment of the spectrum and positioning errors in the microdensitometer. However, tests showed these to be less than 1.0 Å (Mclntyre 1988). The combined uncertainties in the wavelength of a given pixel from random and systematic sources are approximately 1.5–2.0 Å for red plate spectra and 0.7–1.0 Å for blue spectra, which corresponds to less than one pixel in both cases.

Each plate was calibrated by means of a 4×4 array of spots of known intensity ratios exposed on the same plate by the spot sensitometer. These spots were traced with the microdensitometer and characteristic curves were produced for 71 of the plates, 44 being red plates and 27 blue. Comparing characteristic curves revealed variations between different batches of the same emulsion and different curves for hypered and unhypered plates, though differences in treatment times did not show up clearly. The curves were grouped together on the basis of emulsion, batch and hypersensitization, and mean characteristic curves were drawn. Typical mean characteristic curves are shown in Fig. 1. Pairs of (density, log (exposure)) values were taken from each mean curve, and used in transforming the spectra from density to intensity with the Physics Department's spectrum analysis program ATLAS running or the University of Canterbury's VAX 8350 computer.

The transformation to intensity is only approximate, because the emulsion contrast (*i.e.* the slope of the straight-line part of the characteristic curve,) changes with wavelength. This effect is described for different emulsions in: Latham (1968) and Zichová *et al.* (1984) (IlaO); Clowes (1983) and Aoki & Watanabe (1987) (IIIaJ); Eccles *et al.* (1983) and Aoki & Watanabe (1987) (IIIaF). The effect on the spectrum is particularly marked in the case of IIIaF, where differences in contrast cause the change in shape of the white-light spectra in Fig. 2. As the light source is unchanged between exposures, one would expect the derived intensity distribution to be the same for all exposures. However this will only be achieved if the characteristic curve is known for all wavelengths, and all pixels are transformed using the curve appropriate to their wavelength. An approximation to this would be to make calibration exposures at more than one wavelength (*e.g.* 5000, 5500 and 6500 Å for IIIaF) and interpolating between curves. Latham (1968) finds that (for IIaO) this method should yield intensities with uncertainties of ~ 5 per cent, given consistent exposure and development techniques. However this was not practicable for the present work as the plates were only large enough for one set of sensitometry spots.

4. Flat-fielding

Because the spectra showed interesting features at the ends of the orders, an attempt was made to correct the spectra for the response of the film, to restore the true line

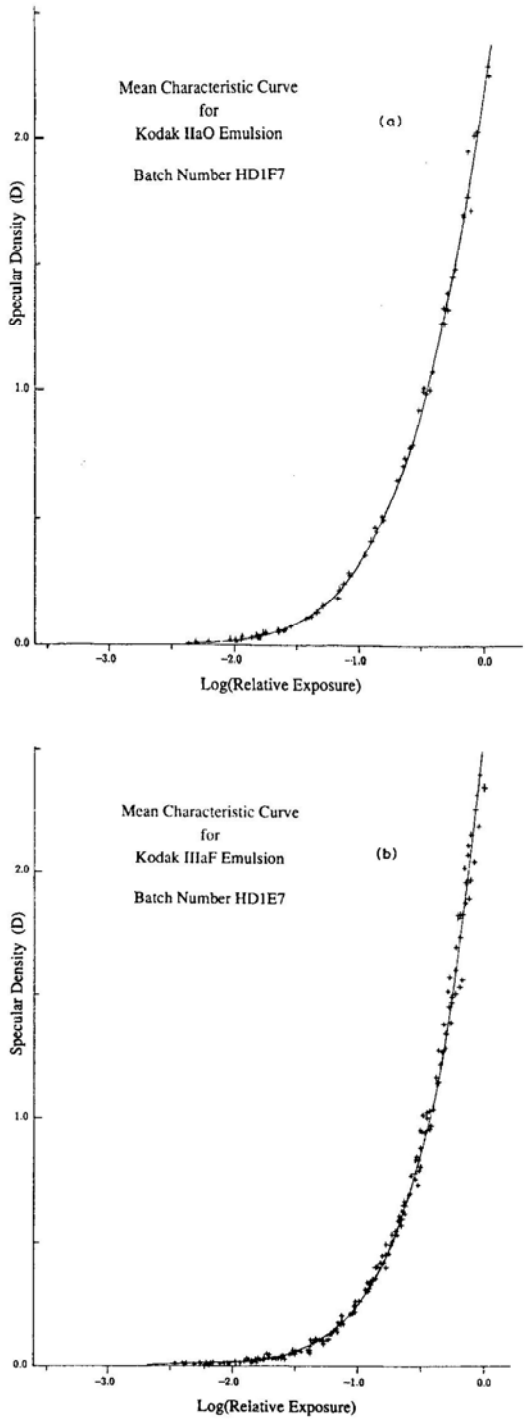

Figure 1. Mean characteristic curves for (a) a bath of 'blue' and (b) a batch of 'red' plates. The points are measured data, and the smooth curve the mean.

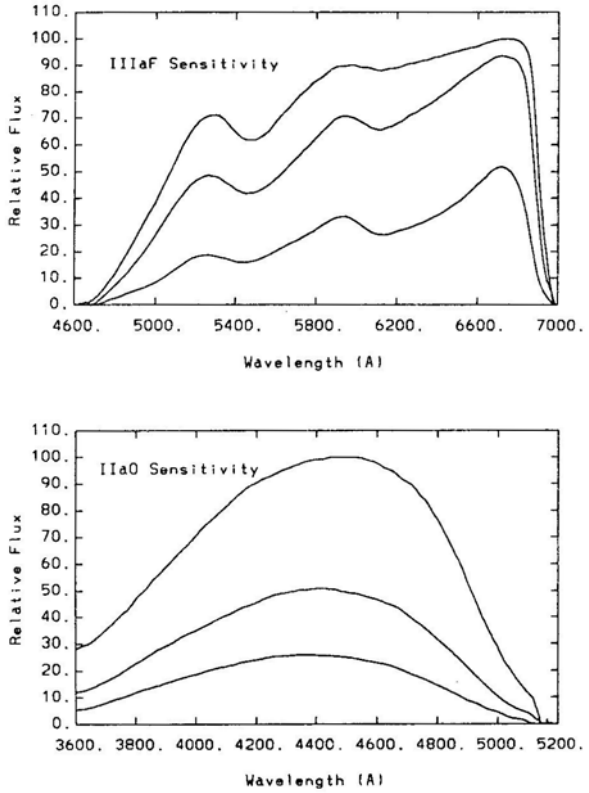

Figure 2. Flatfield spectra for different exposures. The plots are scaled relative to the largest value of the most heavilyexposed spectrum in each. For the blue spectra, the centre spectrum received 50 per cent of the exposure given the top spectrum, and the bottom spectrum 25 per cent. The relative exposures of the red spectra are unknown.

profiles in regions where the instrument response was changing rapidly with wavelength.

After light with a flux distribution $F(\lambda)$ passes the slit of the spectrograph it is dispersed and the spectrum is then recorded by the photographic plate. However the throughput of the spectrograph and the emulsion's sensitivity to light changes with wavelength (represented by a function $R(\lambda)$) as shown in Fig. 2. The intensities derived from the densities on the plate are related to the product of the two functions, $F(\lambda)R(\lambda)$. In stellar spectroscopy, the wavelength region of interest is usually so small that $R(\lambda)$ is nearly constant over a line.However,to get aclear picture of the spectrum over a large range of wavelength, it is necessary to correct for the "response function' of the spectrograph and emulsion.

There are two approaches to this. Firstly, one can determine $R(\lambda)$ explicitly, for example with a spectrosensitometer as shown in Zichová *et al.* (1984). A rather simpler method is to take a 'flat-field' spectrum of an optical continuum source. If the colour temperature of this source is similar to that of the object under study, dividing the observed spectrum $F(\lambda)R(\lambda)$ by the flat field will produce a better representation of the true spectrum $F(\lambda)$ with a flattened continuum. If an exact match is not possible, the

Flat-field can be transformed so that it approximates one obtained by exposure to a source of the correct colour temperature. For this work, once the flat field frames were reduced to intensity they were transformed to the blackbody temperature adopted for the supernova in the following way. Firstly the flat field was divided by a blackbody function with the same colour temperature as the continuum source, and then it was multiplied by a blackbody function corresponding to the colour temperature of the supernova. The resulting flatfield was used to divide supernova spectrum tracings to obtain the 'true' spectrum, as shown in Fig. 3.

The best results were obtained by dividing each supernova spectrum by flat field of similar density. Flat field spectra were only available from one batch each of IIaO, IIIaJ and IIIaF so there is some uncertainty arising from sensitivity differences between batches. However this will probably be small, as the mean characteristic curves changed relatively little from batch to batch.

An ordinary battery-powered flashlight was used as the continuum source in producing the flat-fields shown in Fig. 2, after attempts to set up a 100-W lamp as an artificial star failed. The light source was set up inside the dome, several feet from the spectrograph and aimed so that the ground glass window normally used by the comparison lamp was evenly illuminated. The comparison lamp was reinstalled between flashlight exposures, and comparison exposures were made. Placement of the flashlight relative to the spectrograph, and exposure times, were determined by trial and error. Development procedures were the same as for all other plates.

The flashlight was used for flatfielding because:

1. white dwarf flux standards such as LTT 3218 and LTT 4364 (used by Menzies *et al.* (1987) as their flux standard) are too faint to observe with the Boller and Chivens spectrograph from Mount John;

2. ordinary stars bright enough to work with that have colour temperatures similar to that of the supernova (about 5500 K) have too many absorption lines (*i.e.* are not continuum sources); and

3. O or B supergiants (which are basically continuum sources) could not be used as they did not give effective cancellation of the system response function R. The reason for this was that the systematic intensity errors arising from the use of a monochromatic density-to-intensity calibration curve were different for sources of different colour temperature. Small differences between the supernova and the continuum source could be accomodated bychanging the effectivetemperature ofthe flatfield spectra(as described above); the systematic errors would still cancel adequately. This was not the case for spectra of hot stars, however.

The temperature of the supernova's photosphere is known from photometric studies, so the value used for the colour temperature of the flashlight light is of some importance in producing realistic spectra. It was not possible to determine it experimentally (with a bolometer, for example), but an estimate could be made using spectral emissivity tables in Weast (1982). From these data the temperature appeared to be in the range 2700–3000 K (see Fig. 4). A temperature of 5500 K was adopted for the supernova, which is the value obtained by Blanco *et al.* (1987) between 25 and 100 days after outburst. By dividing some supernova spectra by flatfields which had been transformed to 5500 K from temperatures ranging from 2700 to 3000 K, and comparing with other optical spectra (those of Menzies *et al.* (1987) and Phillips *et al.* (1988)) as well as comparing blue and red spectra from the same night in the overlap region 4700–5200 Å, a value of 3000 K was chosen as being the most suitable

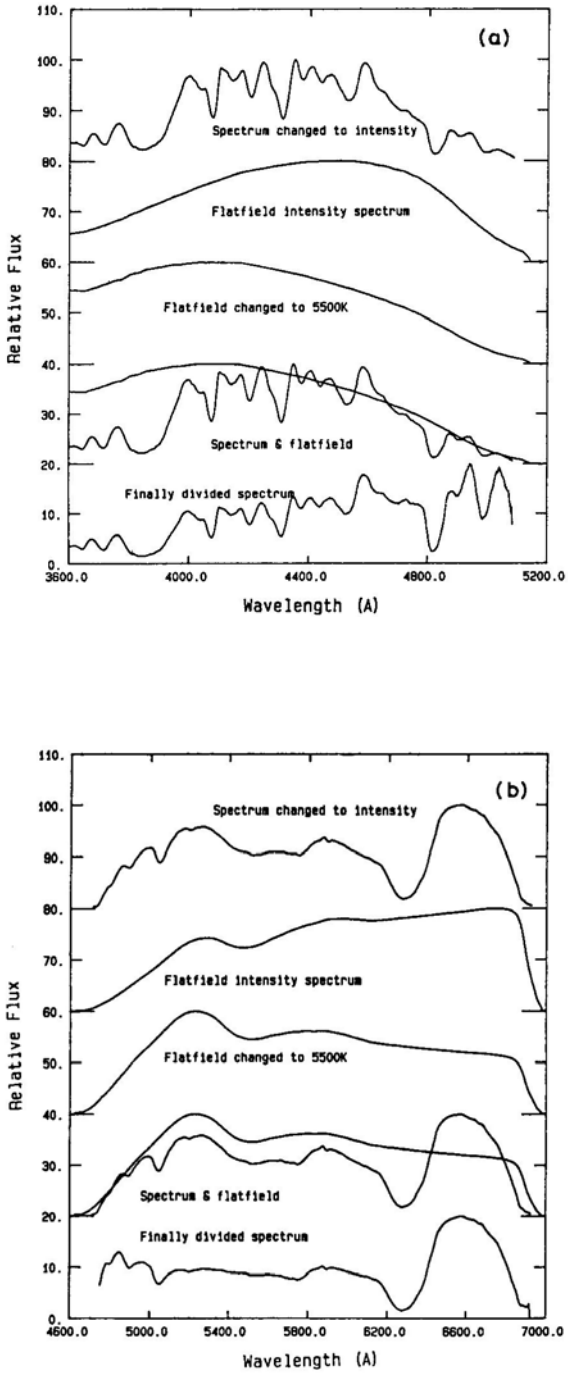

Figure 3. The spectrum-division process, for (a) red and (b) blue spectra. Each spectrum has been scaled to cover a range of 20 units on the vertical axis.Note the marked effect of the division upon the ends of the spectra.

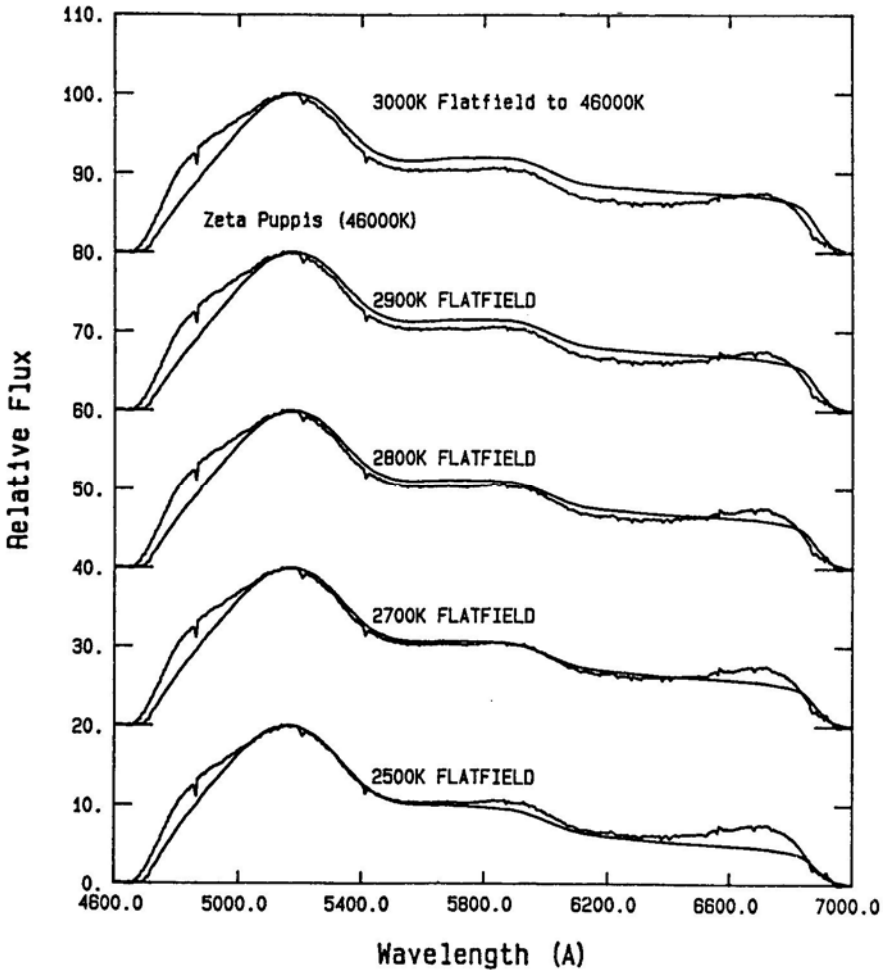

Figure 4. Tests plots showing the effect of transforming the colour temperature of a 'continuum' source's spectrum. Shown here are the results of transforming one of the 'flat field' frames of Fig. 2 from temperatures between 3000 K and 2500 K to the temperature of the star ζ Puppis (46000 K). The spectrum of ζ Puppis is distinguishable by the presence of absorption lines.

temperature for the flashlight. This may seem rather high and is possibly an overestimate of the flashlight temperature. However this value gave the best representation of the spectra at the orders' ends, and the most satisfactory agreement of the blue and red spectra across the overlap region.

5. The spectra

The spectra obtained are shown in the Appendix. Each spectrum is scaled relative to the maximum intensity within it so that the spectrum covers a range of 10 units of the vertical scale. The spectra have been arbitrarily shifted in the vertical direction. Long

tick marks denote the zero-intensity level for each spectrum. Times of observation (midway through the exposure) are shown in Universal Time (UT).

The spectra obtained for this work compare fairly well with those obtained with solid-state detectors (Menzies *et al.* 1987; Phillips *et al.* 1988), but there are two significant shortcomings with the red plate spectra.

First, there is the reproduction of the Hα emission profile. Because of the limited dynamic range of photographic emulsions, Hα quickly reaches saturation in the centre of the emission and the line profile becomes distorted. This effect is especially noticeable in spectra taken during the 'supernebular' phase (later than about August 1987) but happened at almost all phases of evolution. However, it cannot really be avoided as the Hα emission must be over exposed in order to get any detail in the rest of the spectrum. Where the profile is highly saturated, it has been plotted with a dashed line.

The other problem is that some red spectra suffer from contamination by scattered light from the comparison lamp. Fortunately,this only occurs for the two helium lines (5875.7 and 6678.1 Å) which are by far the strongest in the comparison spectrum, and by placing the comparison lines further from the spectrum (using wider deckers in the spectrograph), and making the comparison exposure first, the problem can be avoided. The wider comparison line spacing was adopted from about 1987 July 1, and the problem is restricted to some of the early (February–June) spectra. Not all the spectra on a given plate suffered from contamination, and where possible an uncontaminated spectrum has been chosen. The comparison lines are much narrower than any supernova spectral features, so contamination by the He 6678.1 Å comparison line is readily distinguished from the fine structure in the red wing of Hα that appeared in the first few months of the supernova's evolution (Hanuschik & Dachs 1987; Hanuschik *et al.* 1988).In Fig. A2 all features caused by comparison line contamination have been marked with an asterisk (∗).

A more general problem is that the division process amplifies the intrinsic noise at the less exposed ends of each spectrum by the same amount as the signal. This means that the red spectra are noisiest at the blue end (the sharp cutoff at the red end makes it easier to exclude 'noise' features from the spectra). For the blue spectra, the noise is greatest at the red end, as can be seen in Fig. 3. The intrinsic noise of the spectra was reduced by averaging over a number of pixels. This means some resolution is lost—for the smoothed blue spectra, the wavelength resolution is ~ 7 Å, and for the red spectra the limit is about 10 Å.

Finally, it should be recognized that the spectra in both colours have not been properly corrected for atmospheric extinction, and are not absolutely calibrated spectrophotometry. The flat field spectra are unaffected by atmospheric extinction, so when the spectra are divided, extinction effects are exaggerated. The temperature adopted for the (flashlight) continuum source probably compensates somewhat for this, in that the rather high colour temperature adopted means the intensities at the blue end of a flat field spectrum transformed to the supernova's colour temperature will be lower than for a flat field transformed from a lower temperature. Correspondingly, after division the blue-wavelength intensities in the supernova spectrum will be greater than otherwise. Note that the same colour temperature for the supernova (5500 K) has been used in the flat-field correction at *all* epochs. From comparisons between spectra taken on successive nights and between two divided spectra produced from the same original but divided with different flatfields, the uncertainty in the

derived intensities is at most 20–30 per cent of the maximum intensity over most of a given spectrum, the uncertainty being greatest at the ends of the spectrum. Great care must be exercised, therefore, in comparing the relative strengths of features more than 500 to 1000 Å apart, especially those close to the ends of the spectrum. However, flat-fielding was essential for the monitoring of the profiles and positions (for radial velocity determinations) ofindividual lines. It was unable to restore accurate relative intensities of widely separated features in the supernova's spectrum.

6. Absorptions in Hα emission profile

The spectra taken on 1987 February 25 and 27 shown in Appendix and Fig. 5 show pronounced absorption features in the Hα emission profile. The absorptions are narrow (~ 35 Å FWHM, equivalent to 1600 km s^{-1}) compared to the other spectral features at the time (~ 15000 km s^{-1}), and appear to vary on a timescale of a few hours. The greatest variation is the change from one absorption to two features, between February 25 and 28. The absorptions are not seen at later dates, partly because the blueshifted Hα absorption moves to longer wavelengths and the relevant part of the spectrum becomes almost completely dark. It should be emphasized that these absorptions are not scratches or other plate faults: the bands are plainly visible on the photographic emulsion.

Similar features are seen at some other observatories. Phillips *et al.* (1987) show a narrow absorption in the Hα peak ('2D-fruitti' spectra, 5 Å resolution) on February 27

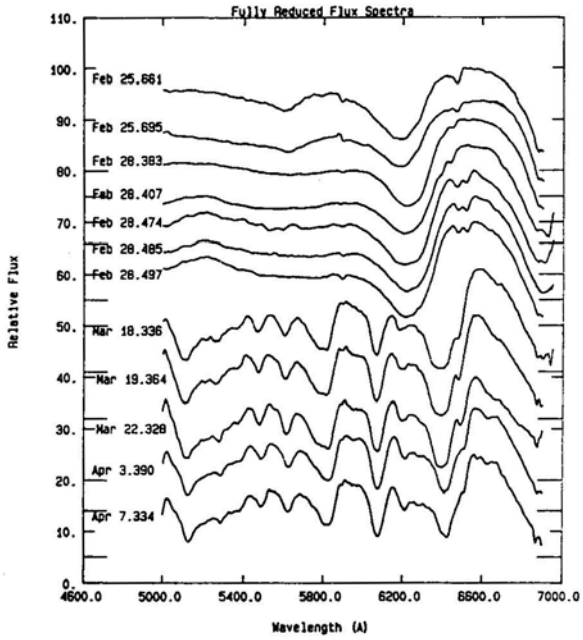

Figure 5. Anomalous absorptions in Hα, from 1987 February and the 'Bochum event' of 1987 March-April. The spectra have been reduced in the same manner as those in Appendix. The February 25.695 spectrum has a slight contamination at 5890 Å from the comparison lamp.

at 6447 A and on February 28 at 6478°Å, but nothing appears in their (17 Å resolution) CCD spectrum of February 25.1. A spectrum taken at February 26.03, shown by Ashoka *et al.* (1987) shows evidence oftwo absorptions near 6500 Å. Unpublished raw spectra of 0.9 Å resolution obtained at Mt Stromlo Observatory on February 27 and March 6 (M. Dopita & S. Ryder, personal communication) show a number of narrow absorption lines in the Hα peak and near 5900 Å. However neither Hanuschik & Dachs (1987), nor Menzies *et al.* (1987) show any sign of these features. The Bochum group's spectra probably have a resolution of ~ 13 Å, the SAAO spectra have 7 Å resolution. Finally, high signal-to-noise spectra with 10 Å resolution reported by Tyson & Boeshaar (1987) show only marginal evidence of weak absorptions in the Hα emission on February 25–28.

No satisfactory identification of these absorptions has been found so far, though there area number of possibilities. First and most obviously, is that they are produced by terrestrial water vapour. Curcio *et al.* (1964) show atmospheric water vapour produces two fairly strong bands centred on 6479 and 6517 Å, in good agreement with the wavelengths of the observed features. However there are a number of difficulties with this explanation. Firstly, another H_2O band of similar strength centred on 5942 Å is not visible in the Mt John spectra, although they are in the Mt Stromlo data, and the narrow absorptions in these particular spectra may well be due to water vapour. Also, water vapour is rarely seen at this resolution (1.6 Å on the photographic plate), and the absorptions are strong enough (equivalent with W ~ 3 Å) that it is difficult to attribute them to water vapour, even allowing for blending of individual lines in the water bands by the low resolution. The two nights in question were not unusually humid, about 70 per cent on the 25th and 80 per cent on the 27th, these latter spectra being taken through thin cloud. Changing humidity and cloud conditions could conceivably account for some of the variations in the absorptions, but not without difficulty. Finally, test spectra of ζ Puppis taken on 'damp' and 'dry' nights failed to show any signs of water vapour bands. It would seem therefore, that the equipment used in this work cannot reliably detect atmospheric water vapour bands, even under favourable conditions.

Other explanations involve some phenomenon in or around the supernova—the rapid variations rule out interstellar absorptions; also there are no known diffuse interstellar bands (Herbig 1975) in the wavelength interval the absorptions covered. If the absorptions are intrinsic to the supernova, they are still difficult to understand. Their narrowness relative to the other spectral lines suggests they could be formed by a blob of gas or thin circumstellar shell with a characteristic thickness of a few light hours. A blob of ejecta in front of the bulk of the material would absorb over a small range of velocities (depending on how much of the supernova's disc it covers). This could produce absorptions with the correct widths, but is unlikely to form lines as strong as those observed. Secondly, the material would presumably be mainly hydrogen, and the absorptions are only about 4000 km s^{-1} blue ward of Hα, implying a much slower expansion (along the line of sight) than the bulk of the ejecta.

The absorption widths are much greater than the UV emission lines observed by IUE (Panagia *et al.* 1987), which have been ascribed to the relic of the red supergiant wind. Absorption lines from this relic wind would be even narrower, as only the material within the solid angle subtended by the supernova would be visible. It is therefore difficult to explain the absorptions as due to a circumstellar shell of material, unless they are composed of a number of blended lines.

7. Radial velocities

The radial velocities measured from the spectra are presented in Tables 2 and 3. The same data appear in graphical form in Figs 6–9. These include data from Hearnshaw *et al.* (1988), with numerous additions and some corrections. As before the data refer to the deepest minima of the absorptions and are quoted in the LMC rest frame.Blended features are represented by mean wavelengths weighted by the *gf*-values of the component transitions. The uncertainties are of order 200 km s^{-1}, although some of the earlier data measured from broad absorption troughs are more uncertain, up to 500 kms^{-1} for Hα.

Most of the velocity curves continued to decline slowly. The velocities of the Balmer lines at day 490 were 2300kms^{-1} (Hβ), 2000 kms^{-1} (Hγ) and 1900kms^{-1} (Hδ). Hα declined more slowly than the other Balmer series lines, falling to approximately 3800km s^{-1} by day 490.The iron lines, FeII '4565' and 5018 Å, reached velocities of 2700 and 2300 kms^{-1} by day 250, which have remained roughly constant since then. The line identified by Ashoka *et al.* as Fe II 4565, a blend of Fe II lines, may in fact be Ba II 4554, as proposed byWilliams (1987). If so, the velocities in Table 3 are too large by ~700 kms^{-1}. Phillips *et al.* (1988) adopt the barium identification, and our data are in agreement with theirs if the 700 kms^{-1} adjustment is made. However, Stathakis (1989) identifies the emission peak which appeared in 1987 November to the red of this absorption as Mg Ib 4571 Å, so there may be a significant magnesium component in the absorption trough.

Table 2. Velocities measured from red plates (all velocities are in km s, measured in rest frame of SN).

Days since Feb 23.32	H Alpha (Emn)	H Alpha (Absn)	NaID (Emn)	NaID (Absn)	MgIb (Absn)	Fe5018 (Absn)
2.341	-287	18156	1999	16154	.	.
5.055	1085	15739	528	18589	10654	.
5.154	1998	16072	341	18997	9898	.
5.165	207	15666	7	19461	9924	.
5.177	536	16338	374	19674	10499	.
9.106	307	13701	879	7141	7482	7518
11.116	-973	12874	751	6021	6456	6111
13.171	-332	11542	60	5563	5922	6071
17.028	-270	10150	-25	4826	5145	4421
17.036	-743	10102	-1140	5007	5148	.
19.077	-472	9969	-154	4969	4739	4546
19.093	-1247	9379	-1121	5016	4638	.
23.016	-972	8533	-1082	4711	4450	3714
24.044	-1064	8172	-940	4646	4140	3584
25.013	-1201	8335	-148	4941	3830	3552
26.034	.	8195	.	.	.	.
27.008	-177	7803	-431	5131	3777	3271
27.018	-1567	8041	-1603	3949	4000	3139
29.049	-1064	8004	-1377	4642	3830	3369
30.197	-195	7708	-635	4717	3360	2829
32.128	-763	7507	-585	4401	3177	2467
32.146	-1430	7513	-1334	4298	3543	.

Table 2. Continued.

Days since Feb 23.32	H Alpha (Emn)	H Alpha (Absn)	NaID (Emn)	NaID (Absn)	MgIb (Absn)	Fe5018 (Absn)
38.047	-1338	7112	-1753	3769	3150	2827
39.058	-744	7112	-1467	4157	3150	2780
41.061	-607	7875	-1265	3708	3320	2505
42.042	-437	6849	-1504	4004	3210	2631
43.014	-561	6873	-914	4017	3110	2675
46.056	-314	7054	-943	3918	2888	2537
46.068	-698	6917	-1226	3532	2930	2465
46.984	-561	6433	-635	4389	2780	2420
48.044	-348	6443	-751	4133	3029	2486
48.057	-652	6526	-1463	4201	3170	2289
51.043	-561	6589	.	.	.	.
52.158	.	6327	-1442	4130	.	2830
53.086	-150	6213	-680	4780	3210	2693
54.033	-607	6312	-881	3785	2970	2250
55.024	-927	6136	-1561	4130	3039	2482
67.142	-927	5427	-718	4388	3024	2342
68.009	-790	5591	-1028	4405	2880	2332
70.110	-836	5363	-707	4671	3120	2454
71.083	-1201	5363	-1169	4581	2710	2253
73.193	-881	5299	-939	4377	2710	2340
74.020	-1247	5235	-1000	4575	2780	.
75.010	-1110	5363	-1292	4675	2750	.
75.972	-1201	5299	-1158	4743	2650	.
76.991	-1658	5171	-1252	4682	2740	.
77.988	-1110	5171	-852	4489	2940	2200
79.118	-652	5171	-1030	4525	3115	2183
79.968	-744	5038	-1050	4687	3185	2368
79.976	.	5299	.	.	.	.
88.966	-515	5171	-872	4789	2818	2224
95.008	-790	5038	-1231	5044	2656	2233
97.048	-1247	.	-1119	4828	2725	1994
97.056	-790	5130	-1150	5244	3158	2394
97.995	-881	5102	-1282	5123	2941	2362
99.111	-927	.	-1142	4998	2688	2130
102.037	-927	4974	-1249	5136	2813	2104
103.043	-1201	5038	-887	5123	2503	2058
106.345	-199	4943	-1091	5133	2589	2090
106.357	-58	5102	-1031	5835	2484	2066
107.163	-1384	4910	-1151	5639	2767	2068
108.107	-698	5256	-1208	5354	2418	2071
109.063	-698	5190	-1108	5571	2264	2108
111.014	-835	4938	-1317	5367	2346	1989
114.008	-835	5048	-877	5860	2241	2044
117.410	-927	5103	-927	6187	1874	2195
118.470	-972	4943	-1465	5980	2299	2022
119.447	-927	4933	-1171	5883	2250	2136
130.218	-515	5217	-732	6076	2177	2618
132.031	-515	5061	-1173	5986	2060	2344

Table 2. Continued.

Days since Feb 23.32	H Alpha (Emn)	(Absn)	NaID (Emn)	(Absn)	MgIb (Absn)	Fe5018 (Absn)
133.063	-835	5031	-934	5800	1964	1877
136.097	-790	5037	-1272	5720	1714	2250
152.143	-561	4974	-948	5749	2236	2238
153.452	-378	5247	-1151	5950	2015	2082
155.078	-790	5319	-1062	6091	1919	2146
156.165	-927	5235	-1280	6007	1916	2215
156.208	-743	5584	-847	5752	1980	2181
167.417	-1429	5372	-990	6019	2096	2545
168.294	-652	5288	-1283	5817	1885	2390
171.386	-1155	5344	-1312	5946	1967	2540
171.413	-1475	4911	-1304	5868	1804	2478
175.194	-1475	5131	-947	6145	2079	2297
176.295	-1292	5040	-1144	5891	1852	2378
177.243	-1064	4924	-1249	5930	1874	2282
189.069	-1155	5058	-1135	5787	1636	2195
196.212	-1203	5189	-1085	5809	2120	2255
198.320	-1247	5052	-1047	5647	1685	2202
206.281	-708	5009	-923	5524	1806	2369
206.318	-951	5167	-1063	5245	1868	2219
215.311	-562	5062	-840	4901	2622	2291
217.252	-1292	4713	-1135	5390	2648	2320
230.171	-727	4686	-840	4964	2375	2016
238.276	-1091	4784	-1029	4877	2856	2311
240.354	-1375	4812	-1023	5011	2701	2308
243.336	-1123	4580	-1060	5059	2668	2163
250.236	-873	4850	-968	4947	3106	2308
256.310	-924	4713	-813	4633	3202	2411
257.293	-794	4623	-913	4888	2734	2176
265.254	-1045	4670	-912	4647	2915	2160
266.324	-801	4527	-744	4813	2933	2163
267.079	-1096	4819	-943	4846	2862	2507
268.130	-793	4769	-804	4731	2584	2227
269.069	-640	4692	-1148	4485	2795	2111
274.297	-576	4450	-692	4397	2923	2160
286.283	-641	4385	-891	4535	2973	2365
293.173	-601	4416	-900	4406	2935	2194
306.265	-781	4243	-712	4422	2802	2156
307.128	-872	4352	-862	4261	3080	2519
313.241	-465	4484	-1010	4397	3020	2232
321.149	-390	4444	-841	4440	2778	2075
330.274	-760	4159	-1008	4226	3025	2178
340.163	-742	4274	-1069	4212	2889	2103
348.283	-614	4325	-899	4382	3321	2356
350.229	-919	4210	-1033	4148	2915	2220
361.133	-305	4263	-678	4390	3132	2058
378.224	-282	4211	-664	4341	.	2155
383.335	-200	4211	-664	4193	.	2263
472.150	-177	3640	-578	3674	.	2466

Table 3. Velocities measured from blue plates (all velocities are in km s, measured in rest frame of SN).

Days since Feb 23.32	H Beta (Absn)	H Gamma (Absn)	H Delta (Absn)	Fe4565 (Absn)
2.256	13369	13241	.	.
5.132	13151	11466	10859	.
5.227	11834	11121	10957	.
9.078	9979	8857	8168	7337
11.185	8784	7927	7833	6511
13.149	7945	7409	8096	6070
17.085	7709	7324	7711	5595
18.020	7849	7685	8022	5783
19.037	7565	7213	7915	5344
23.067	7292	6977	7340	5425
24.018	7140	6526	7144	5229
25.033	7083	6336	7171	5277
26.013	7058	6470	6935	4896
27.045	6825	6544	7811	5504
29.018	6600	6088	6820	5009
30.338	6104	6005	6925	4895
31.408	.	6018	6828	5216
32.112	5738	6043	6610	4820
38.092	5723	5768	6817	4794
39.027	6045	6403	7336	5341
39.043	.	6262	7564	5147
41.121	5887	5691	6148	4902
42.018	5671	5654	6670	4718
43.065	.	5910	6945	4933
46.031	5633	5750	6791	4717
47.024	.	5488	6926	4648
51.080	5316	5709	6877	4565
52.018	5977	5602	6650	4740
53.122	.	5535	6815	4576
53.999	.	5626	6589	4597
54.998	.	5573	6512	4608
67.133	.	5393	6389	4207
68.030	.	5072	6456	4025
70.020	3897	3889	6521	4264
71.113	4204	4295	6560	4202
73.144	4156	5400	6352	3962
74.054	3490	4547	6485	4070
75.034	3584	3803	6100	3957
76.033	3670	4403	6375	3965
77.010	3976	4747	6471	3986
78.020	3633	4179	6096	3983
79.041	2793	4552	6429	3855
80.004	3703	4117	6047	3838
80.070	2959	4501	6165	3690
88.927	3902	4009	6178	3543
97.963	3968	3819	5284	3386
99.148	4317	3980	5177	3461

Table 3. Continued.

Days since Feb 23.32	H Beta (Absn)	H Gamma (Absn)	H Delta (Absn)	Fe4565 (Absn)
102.038	3964	3799	5218	3212
103.088	4094	3830	5065	3564
106.247	4088	3868	4507	3556
108.020	4036	3615	4217	2877
111.047	4050	3577	3937	3153
113.968	3953	3525	3638	2959
117.453	3853	3404	3632	2985
118.426	3926	3613	3599	3173
119.474	3923	3573	3593	3132
132.074	3827	3495	3321	2937
133.039	3673	3279	3535	2948
135.954	3787	3489	3291	2811
146.444	3794	3406	3283	2770
152.020	3751	3690	3126	3092
153.405	3777	3205	3209	2810
155.020	3729	3288	3189	2870
156.003	3746	3234	3049	2805
157.151	3824	3258	3054	2833
165.170	3658	3187	3268	2791
168.379	3655	3192	3146	2958
171.372	3667	3178	3085	2611
175.415	3655	3060	3080	2815
176.237	3482	3334	3139	2698
177.362	3586	3090	3038	2660
182.428	3511	3115	3228	2813
188.268	3491	3268	3100	2698
189.118	3557	3017	2782	2561
196.156	3436	2743	2784	2595
206.237	3592	2969	2661	2728
215.347	3744	3174	2958	2937
216.103	3420	2901	2618	2746
221.383	3310	2861	2732	2970
230.128	3367	2703	2642	2625
238.335	3353	2794	2664	2860
240.308	3422	2861	2664	2716
243.374	3267	2718	2678	2623
250.213	3411	2762	2393	2576
256.350	3258	2548	2355	2645
257.215	3196	2659	2436	2589
265.320	3267	2713	2277	2873
266.263	3013	2670	2632	2654
267.144	3171	2701	2409	2911
268.072	3029	2875	2330	2548
269.128	3146	2642	2334	2764
274.273	3065	2683	2371	2630
286.318	3087	2653	2230	2708
293.110	2819	2607	2142	2712
307.211	2904	2622	2367	2659

Table 3. Continued.

Days since Feb 23.32	H Beta (Absn)	H Gamma (Absn)	H Delta (Absn)	Fe4565 (Absn)
313.127	2914	2369	2461	2693
330.119	2631	2343	2157	2670
340.211	2690	2320	1994	2705
348.197	2760	2326	2093	2640
350.113	2584	2377	2105	2656
361.261	2740	2466	2116	2616
378.306	2586	2480	2109	2853
472.083	2358	2086	2021	2807
490.074	2401	2023	1765	2629
492.387	2185	1913	1867	2741

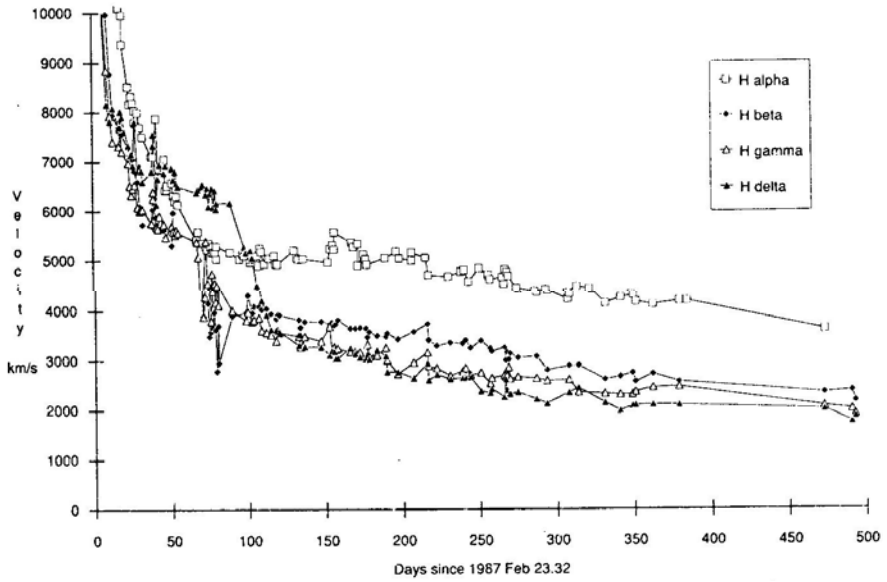

Figure 6. Balmer line absorption velocity curves for the first 500 days of SN1987A's evolution. For clarity the vertical scale has been expanded and some of the early Hα data have been omitted.

Two velocity curves exhibit peculiar behaviour. The sodium D line velocities (Fig. 8) declined rapidly until about day 50, then increased to a maximum of ~6000 kms^{-1} near day 150. Finally the curve declined again, from day 250 its behaviour precisely tracking that of Hα, with almost identical velocities. Similar behaviour is observed by Phillips *et al.* (1988), up to day 131. It appears to stem from the asymmetry of the sodium absorption profile in this period, possibly due to blending. The Mg I b line (Fig, 9) has a similarly interesting velocity curve, which fell quickly to ~ 3000 km s^{-1}, levelled out briefly, then fell again at day 100 to level out at about 2000 km s^{-1}. Between days 200 and 250, the velocities increased again to near 3000 km s^{-1},

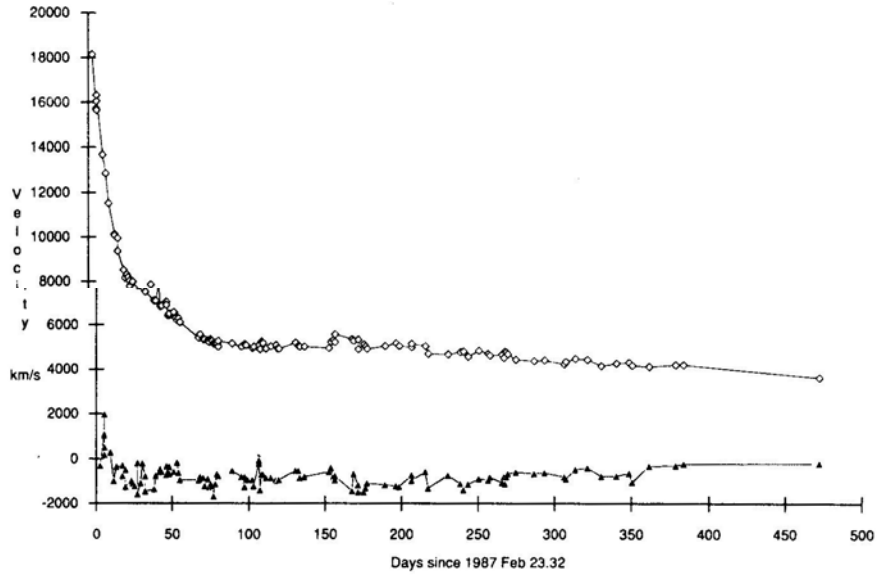

Figure 7. Hα velocity data — emission peak (triangles) and absorption trough (diamonds).

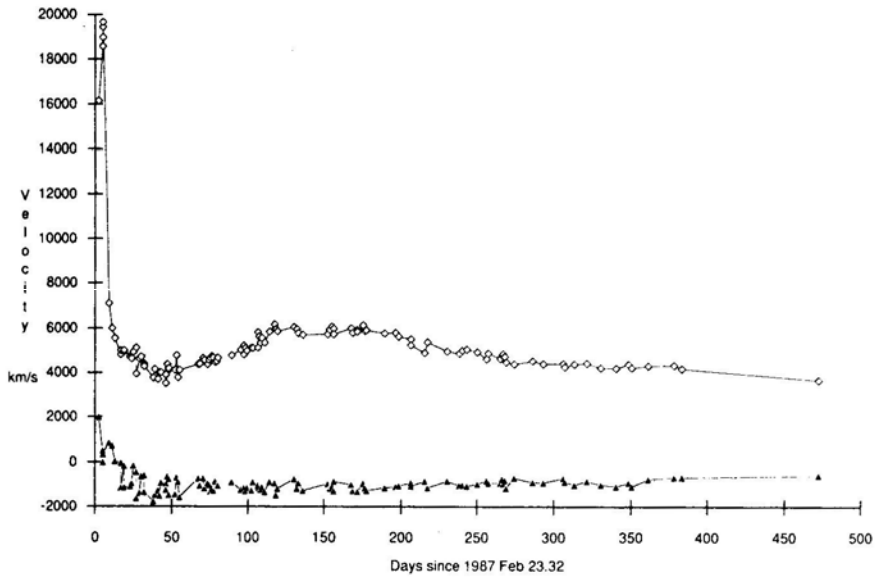

Figure 8. Sodium D line velocity date emission peak (triangles) and absorption through (diamonds).

remaining constant on average thereafter . The declining velocity phases seem to be consistent with the decreasing density(and therefore optical depth) of the ejecta, which allows progressively slower-moving levers to be seen. The velocity curve's unusual behaviour between days 200 and 250 was caused by the line blending with other absorptions, however. Multiple components(probably three) became apparent in 1987

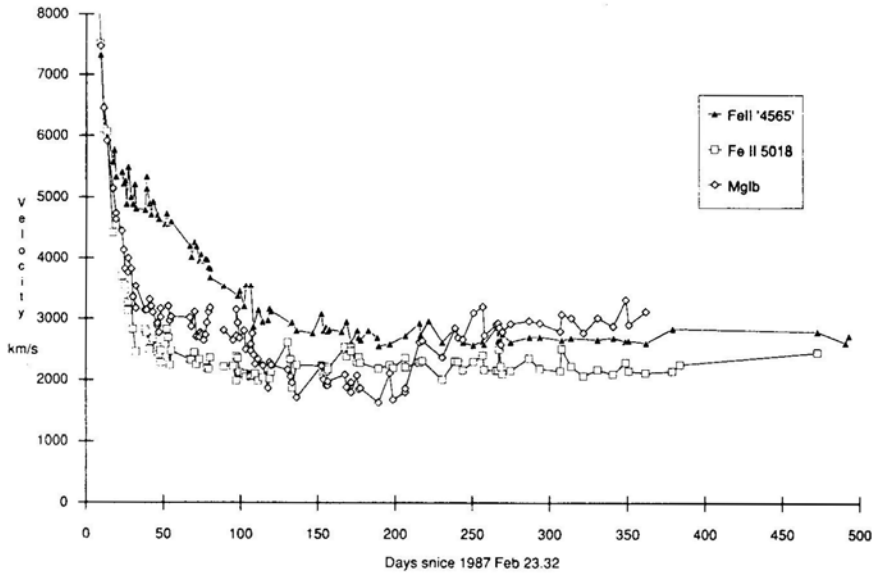

Figure 9. Absorption line velocity data for the 'metal' lines—Fe II and Mg I.

August. By October one of these had declined and the line became flat-bottomed, appearing to be composed of two absorptions. Thereafter the shorter-wavelength line increased in intensity, drawing the absorption minimum to the blue, and giving higher radial velocities. Another absorption, to the blue of the magnesium line, grew stronger and began to blend with the Mg feature during 1987 December and 1988 January. After 1988 February, blending had increased to the point where the two features formed a broad trough, making accurate velocity measurements impossible.

The Mg I b line may also have been misidentified—Williams (1987) considers it to be Fe II 5169 Å, and there may also be a third line involved: Fosbury *et al.* (1987) find hat on 1987 March 3 the line is consistent with contributions of 40% from Fe II 5169, 50 per cent Ti II 5185, and 5per cent Mg I b. Adopting the Fe II identification produces velocities about 500 km s^{-1} smaller; giving close agreement with the Fe II 5018 Å data over the first 120 days of evolution, and also after about day 250. Such agreement would be expected as both transitions arise in the same level of the Fe II ion, and should be formed in the same layer of the supernova's atmosphere. The divergence of the curves between days 120 and 250 might then be attributed to the appearance of another absorption to the red of the Fe II line, which then either is overpowered by Fe II , or declines intrinsically.

The emission line velocities were measured by finding the peak of the emission, or if the line was saturated, the centre of the emission was measured, at a range of intensities. If the (saturated) line was asymmetrical, the centroid nearest the steeper wing of the line was chosen. A surprising result of these measurements was that the Hα and Na I D emission lines were *redshifted* relative to the supernova rest frame. The shift was small compared with the width of the lines—for Hα the shift is ~ 1/8 of the full width at half maximum in the supernebular phase, and a smaller fraction at earlier stages. The emission-line velocity measurements are more uncertain than the absorptions—for Hα the errors are ± 500 km s^{-1} over most of the period, although the

earliest measurements (when the line was extremely broad) are uncertain by up to 1000 km s^{-1}.The sodium line velocities are known to ~ ± 300 km s^{-1}. Nevertheless, significant redshifts were observed from about day 30, to day 350. Thereafter the Hα redshift appears to decline, but the Na I D velocity does not change noticeably.

The redshift of Hα is also detected by Phillips *et al*. (1988). Although our redshifts are generally larger, the average difference being about 600 km s^{-1}, the uncertainty ranges probably still overlap, except in the first 20 days or so. Redshifts are also observed at other wavelengths. Stathakis (1989) shows the emission profile at 4520 Å as redshifted Mg I b 4517 Å. In the infrared (1–5 μm), Oliva et al. (1987) reported redshifts of 500–1000 km s^{-1}, which are uncorrelated with optical depth. Similar shifts were seen at ~ 20 μm by Haas *et al*. (1987). Not all the emission lines are redshifted, however, Measurements of the forbidden oxygen lines at ; $\lambda\lambda$ 6300 and 6360 Å in our spectra showed these lines were not shifted from their LMC rest wavelengths, in agreement with Stathakis (1988).

There are two possible systematic effects which could produce emission-line redshifts in our spectra, which we consider briefly here. Photographic saturation could bias the measurements, but velocities derived from under-exposed spectra in which Hα was not saturated, differed by only 100 km s^{-1} or so, well within the measurement uncertainty. Secondly, the microdensitometer's response to a large density step function is a somewhat rounded step, which could shift the peak redward (the plates were traced from blue to red). However this is probably a small effect and does not account for the shift observed in the weaker Na I D emission.

Two astrophysical interpretations of the redshifts have been proposed. One (Hearnshaw *et al*. (1988)) is that the expansion is not spherically symmetric, which is consistent with the polarization data of Jeffery (1987) and Cropper *et al*. (1987), and the speckle interferometry observations of Karovska *et al*. (1988). In addition, Phillips & Heathcote (1989) interpret the 'Bochum event' emission features that appeared on the wings of the H0 emission (and a number of other emission features in the optical and near IR) in 1987 March as evidence for a non-spherical emitting region. However departures from spherical symmetry do not explain the unshifted [O I] lines, whose strength and width (~2500 km s^{-1}) imply they originate from the supernova ejecta. An alternative explanation proposed by Witteborn *et al*. (1989) is that proportionately more backscattered radiation reaches the observer, biasing the line profile to the red. This explains unshifted lines as coming from the outer (low-density) regions of the ejecta where the optical depth is small enough to allow the passage of forward-scattered radiation.

References

Ashoka, B. N., Anupama, G. C., Prabhu, T. P., Giridhar, S., Gosh, K. K., Jain, S. K., Pati, A. K., Kameswara Rao, N. 1987, J. Astrophys. Astr., **8**, 195.

Aoki, T., Watanabe, T. 1987, in *Proc. IAU Workshop Astrophotography*, Ed. S. Marx, Springer-Verlag, Berlin, p. 56.

Blanco, V. M., Gregory, B., Hamuy, M., Heathcote, S. R.. Phillips, M. M., Suntzeff, N. B., Terndrup, D. M., Walker, A. R., Williams, R. E., Pastoriza, M. G., Storchi-Bergmann. T., Matthews, J. 1987, *Astrophys. J*., **320**, 589.

Clowes, R. G. 1983, *Amer. astr. Soc. Photo-Bull*., **32**, 14.

Cropper M, Bailey, J., McCowage, J., Cannon, R. D., Couch, W. J., Walsh, J. R., Staede, J. O., Freeman, F. 1987, *Mon. Not. R. astr. Soc*, **231**, 695.
Curcio, J. A., Drummeter, L. F., Kenestric, G. L. 1964, *Applied Optics*, **3**, 1401.
de Jager, C. 1980, *The brightest stars*, Geophys. and Astrophys. Monographs, Vol. 19, D. Reidel, Dordrecht, pp. 67–70.
Eccles,M. J, Sim, M. E., Tritton, K. P.1983, *Low light level detectors in astronomy*, Cambridge Univ. Press, p. 24.
Fosbury, R. A. E., Danziger, I. J., Lucy, L. B., Gouiffes, C, Christiani, S. 1987, in *Proc. ESO Workshop on SN* 1987*A*, Ed. I. J. Danziger, ESO, Garching bei München, p. 139.
Hanuschik, R. W., Dachs, J. 1987, in *Proc. ESO Workshop on SN* 1987*A*, Ed. I. J. Danziger, ESO, Garching bei München, p. 153.
Hanuschik, R. W. Thimm, G., Dachs, J. 1988, *Mon. Not. R. astr. Soc*, **234,** 41P.
Hearnshaw, J. B., Mclntyre, V. J., Gilmore, A. C. 1988. *J. Astrophys. Astr*., **9**, 93.
Herbig, G. H. 1975, *Astrophys. J.*, **196**, 129.
Jeffery, D. J. 1987, *Nature*, **329**, 419.
Karovska, *et al.* 1988, *IAU Circ. No.* 4604.
Kunkel, W., Madore, B. 1987, *IAU Circ. No.* 4316.
Latham, D. W. 1968, *Astr. J.*, **73**, 515.
McIntyre, V. J. 1988, *MSc Thesis*, Univ. Canterbury, New Zealand.
Menzies, J. W., Catchpole, R. M., van Vuuren, G., Winkler, H., Laney, C. D., Whitelock, P. A., Cousins, A. W. J., Carter, B. S., Marang, F., Lloyd Evans, T., Roberts, G., Kilkenny, D., Spencer Jones, J., Sekiguchi, K., Faireil, A. P., Wolstencroft, R. 1987, *Mon. Not. R. astr. Soc*, **227**, 39P.
Oliva, E., Moorwood, A. F. M., Danziger, I. J. 1987, *ESO Messenger*, **50**, 18.
Panagia, N., Gilmozzi, R., Casatella, A., Wamsteker, W., Kirshner, R. P., Sonneborn, G. 1987, *IAU Circ. No.* 4514.
Phillips, M. M., Heathcote, S. R., Hamuy, M., Navarrete, M. 1988, *Astr. J.*, **95**, 1087.
Phillips, M. M., Heathcote, S. R. 1989, *Publ. astr. Soc. Pacific*, **101**, 137.
Schoening, W.E.,1976, *Amer. Astr. Soc. Photo-Bull*, **11**, 8.
Stathakis, R. 1988, *AAO Newsletter*, **45**, 1.
Stathakis, R. 1989, *AAO Newsletter*, **49**, 5.
Taylor, D. J., Schmidt, E. G. 1975, *Publ.astr. Soc. Pacific*, **87**, 357.
Tyson, J. A., Boeshaar, P. C. 1987, *Publ. astr. Soc. Pacific*, **99**, 905.
Weast, R. C. 1982, *C. R. C. Handbook of Chemistry and Physics*, 63rd Edn, C. R. C. Press, Cleveland, Ohio.
Williams, R. E. 1987, *Astrophys. J. Lett.*, **320**, L117.
Witteborn, F. C, Bregman, J. D., Wooden, D. H., Pinto, P. A., Rank, D. M., Woosley, S. E., Cohen, M. 1989. *Astrophys. J. Lett.*, **338**, L9.
Zichová, O., Zicha, J, Honsa, J. 1984. in *Astronomical Photography* 1984, *Occas. Rep. of R. O. E.*, Eds M. E. Sim & K. Ishida No. 14.

Appendix

Atlas of Spectra of SN 1987a

The ‘blue’ spectra cover the period 1987 February 25 to 1988 June 30, whereas the ‘red’ spectra cover the period 1987 February 25 to 1988 June 10. The microdensitometer tracings have been converted to intensities and ‘flat fielded’ as described in the text. Contaminations of the spectra by light from comparison lamp are indicated by an asterisk (∗) in the ‘red’ spectra. Overexposed portions of Hα line are shown by dotted lines.

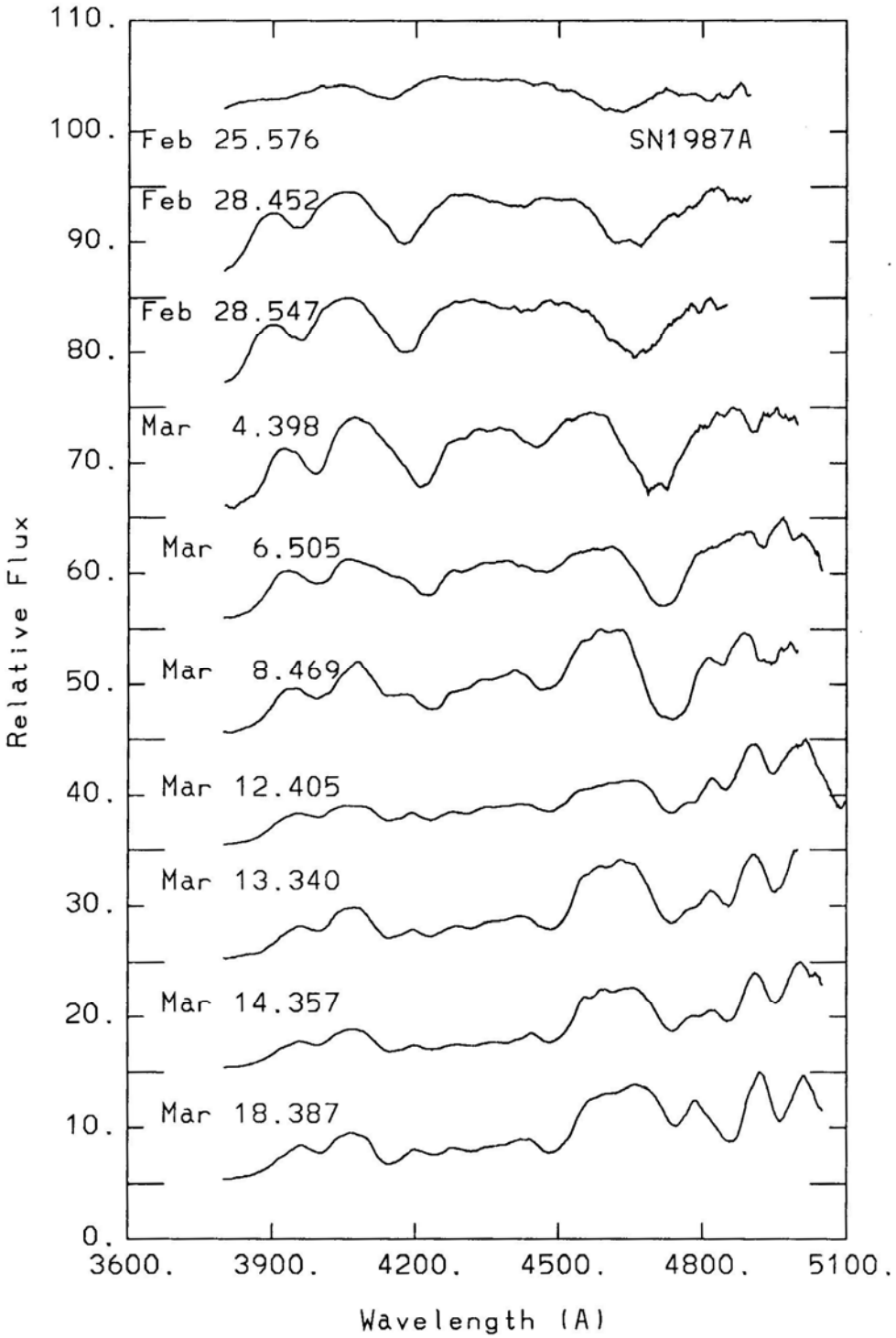
110.
100.
90.
80.
70.
60.
50.
40.
30.
20.
10.
0.
Relative Flux
Feb 25.576
SN1987A
Feb 28.452
Feb 28.547
Mar 4.398
Mar 6.505
Mar 8.469
Mar 12.405
Mar 13.340
Mar 14.357
Mar 18.387
3600.
3900.
4200.
4500.
4800.
5100.
Wavelength (A)

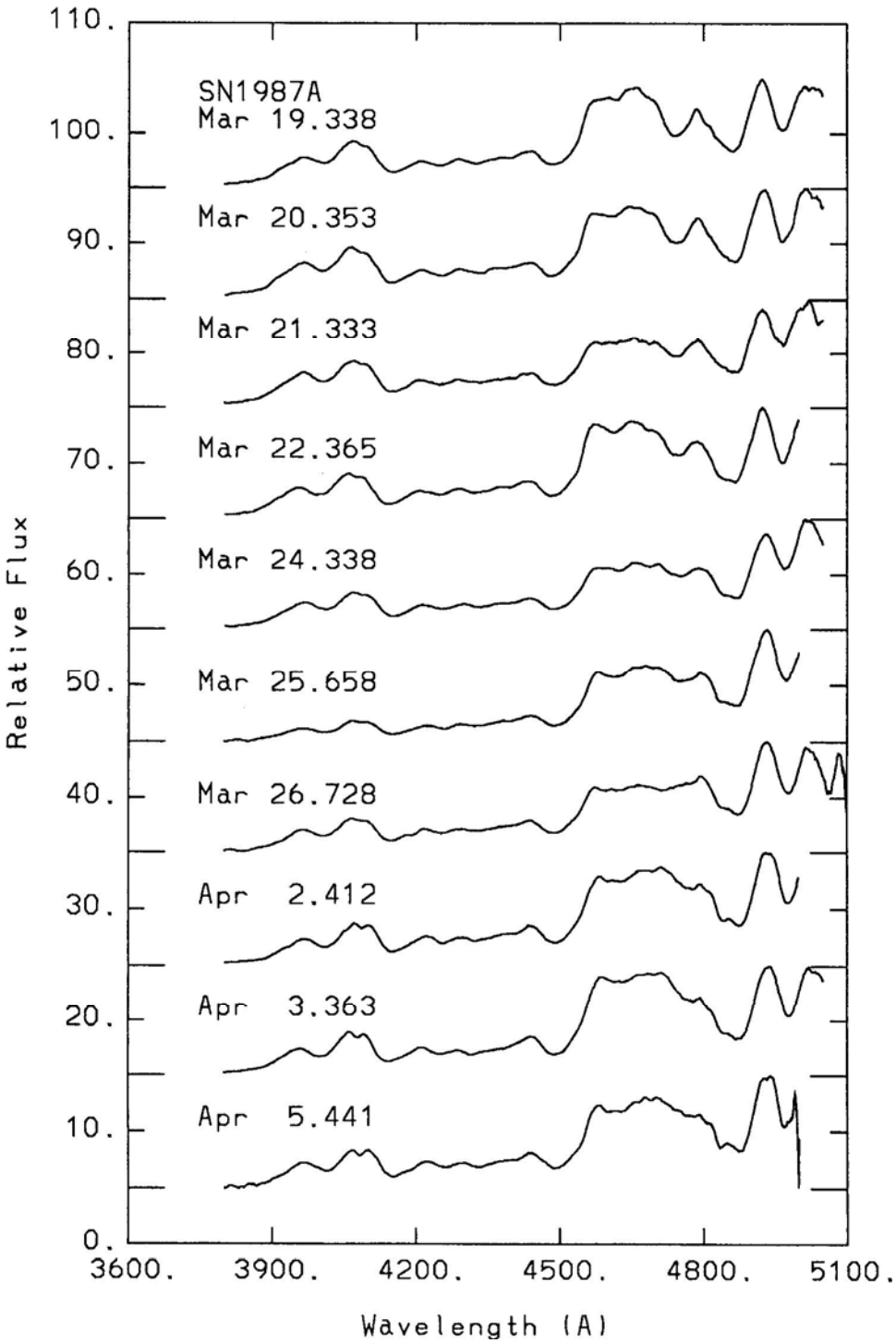
SN1987A
Mar 19.338
Mar 20.353
Mar 21.333
Mar 22.365
Mar 24.338
Mar 25.658
Mar 26.728
Apr 2.412
Apr 3.363
Apr 5.441
Relative Flux
0.
10.
20.
30.
40.
50.
60.
70.
80.
90.
100.
110.
3600.
3900.
4200.
4500.
4800.
5100.
Wavelength (A)

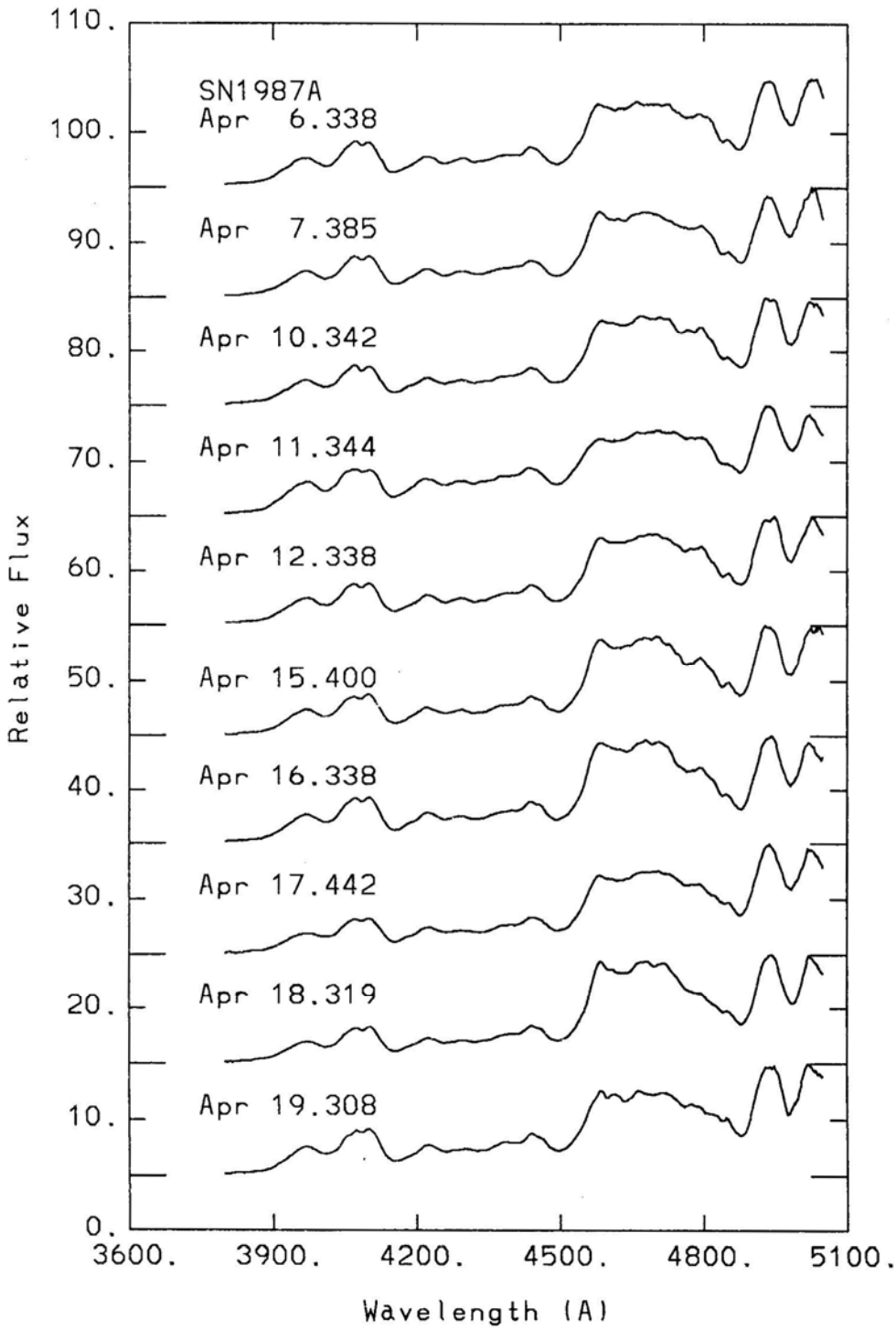
SN1987A
Apr 6.338
Apr 7.385
Apr 10.342
Apr 11.344
Apr 12.338
Apr 15.400
Apr 16.338
Apr 17.442
Apr 18.319
Apr 19.308
Relative Flux
110.
100.
90.
80.
70.
60.
50.
40.
30.
20.
10.
0.
3600.
3900.
4200.
4500.
4800.
5100.
Wavelength (A)

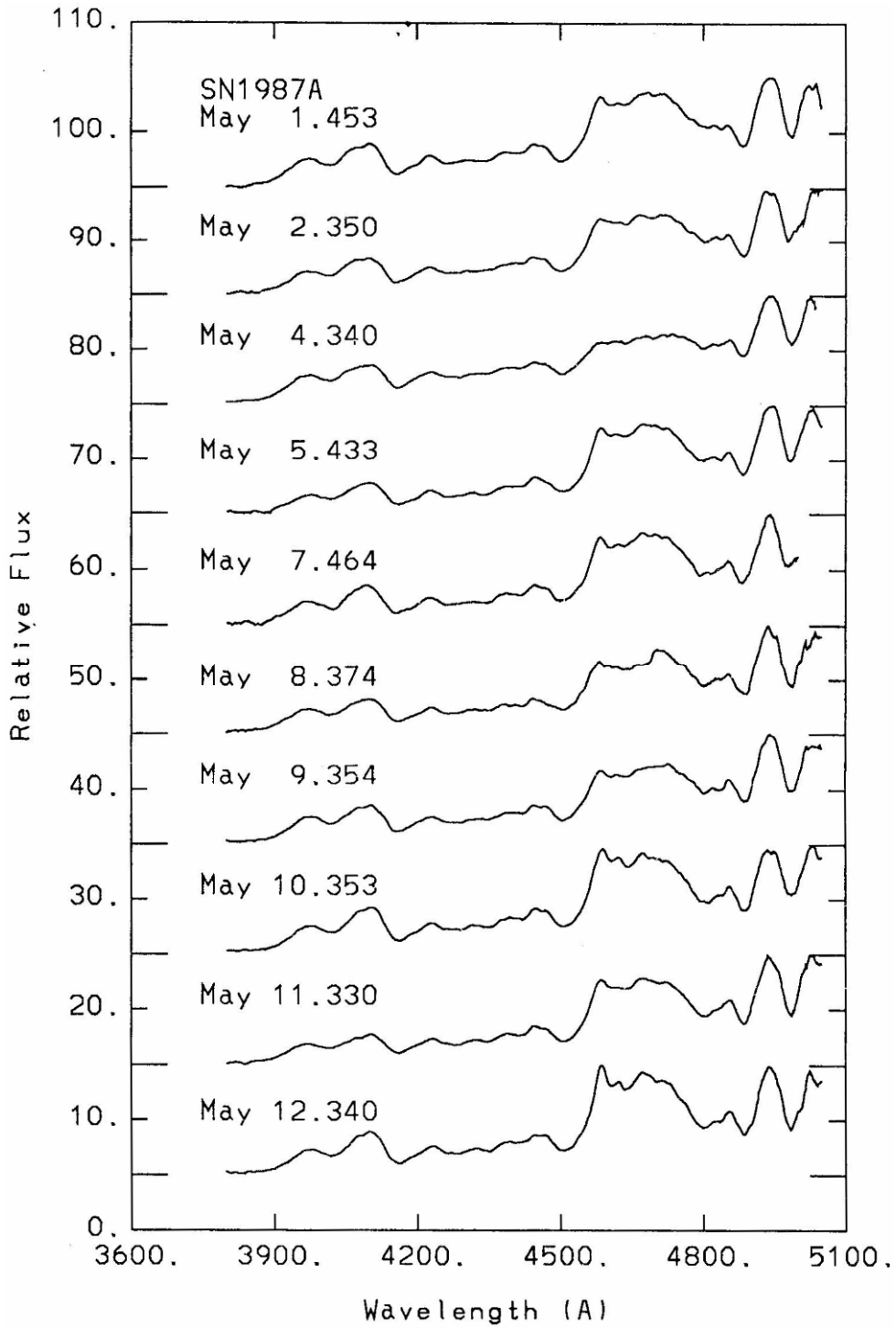
SN1987A
May 1.453
May 2.350
May 4.340
May 5.433
May 7.464
May 8.374
May 9.354
May 10.353
May 11.330
May 12.340
Relative Flux
110.
100.
90.
80.
70.
60.
50.
40.
30.
20.
10.
0.
3600.
3900.
4200.
4500.
4800.
5100.
Wavelength (A)

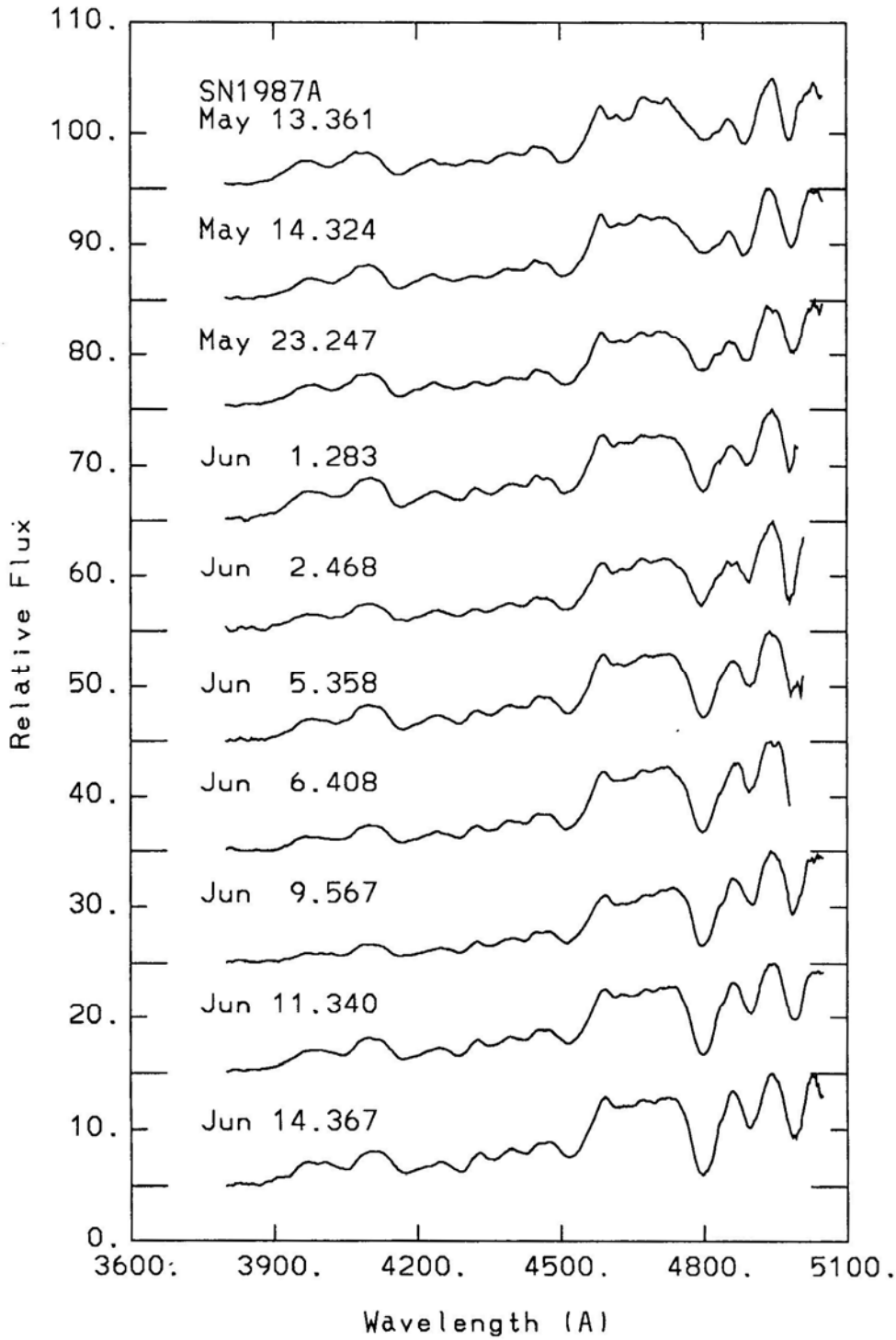
SN1987A
May 13.361
May 14.324
May 23.247
Jun 1.283
Jun 2.468
Jun 5.358
Jun 6.408
Jun 9.567
Jun 11.340
Jun 14.367
Relative Flux
Wavelength (A)
110.
100.
90.
80.
70.
60.
50.
40.
30.
20.
10.
0.
3600.
3900.
4200.
4500.
4800.
5100.

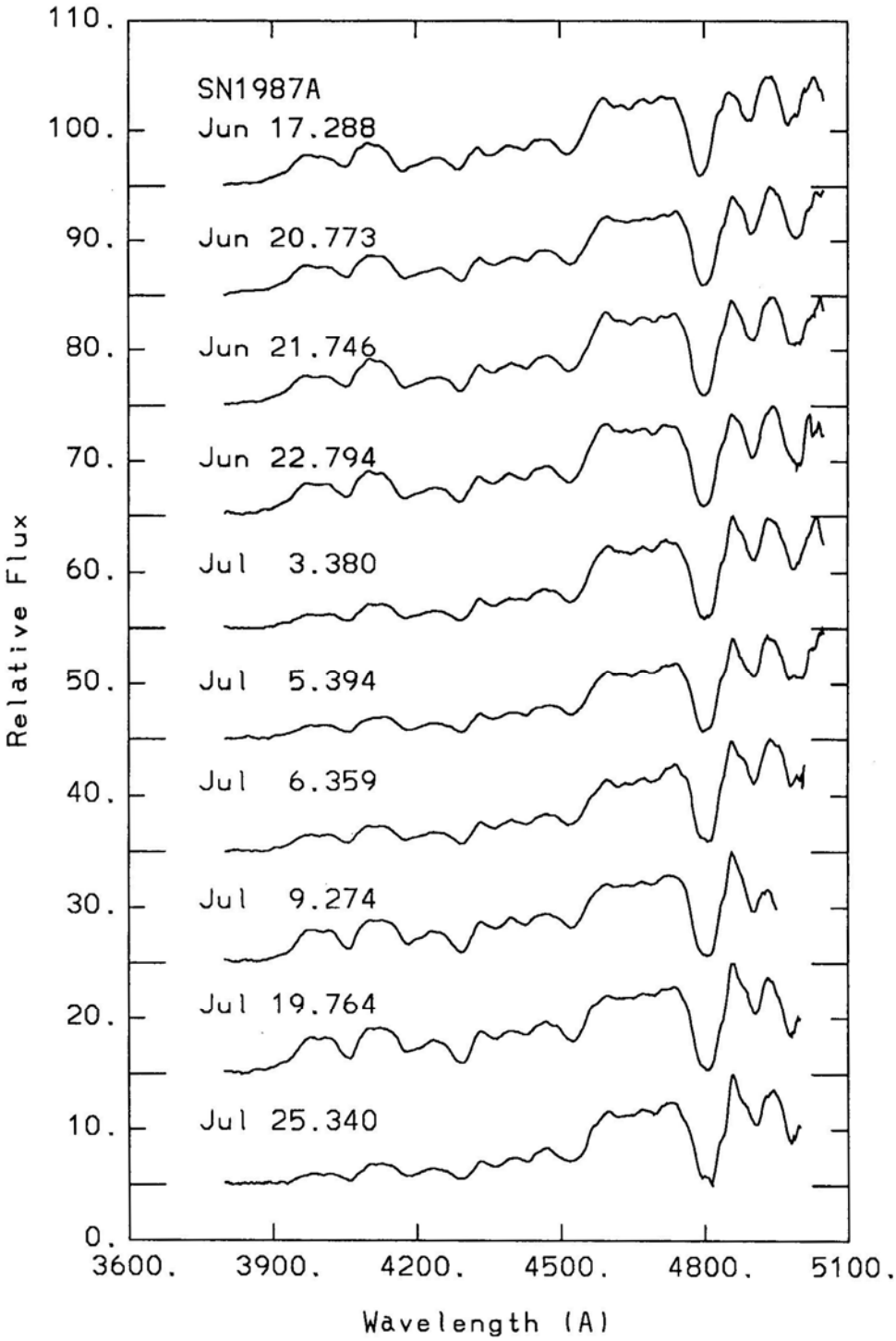
SN1987A
Jun 17.288
Jun 20.773
Jun 21.746
Jun 22.794
Jul 3.380
Jul 5.394
Jul 6.359
Jul 9.274
Jul 19.764
Jul 25.340
Relative Flux
110.
100.
90.
80.
70.
60.
50.
40.
30.
20.
10.
0.
3600.
3900.
4200.
4500.
4800.
5100.
Wavelength (A)

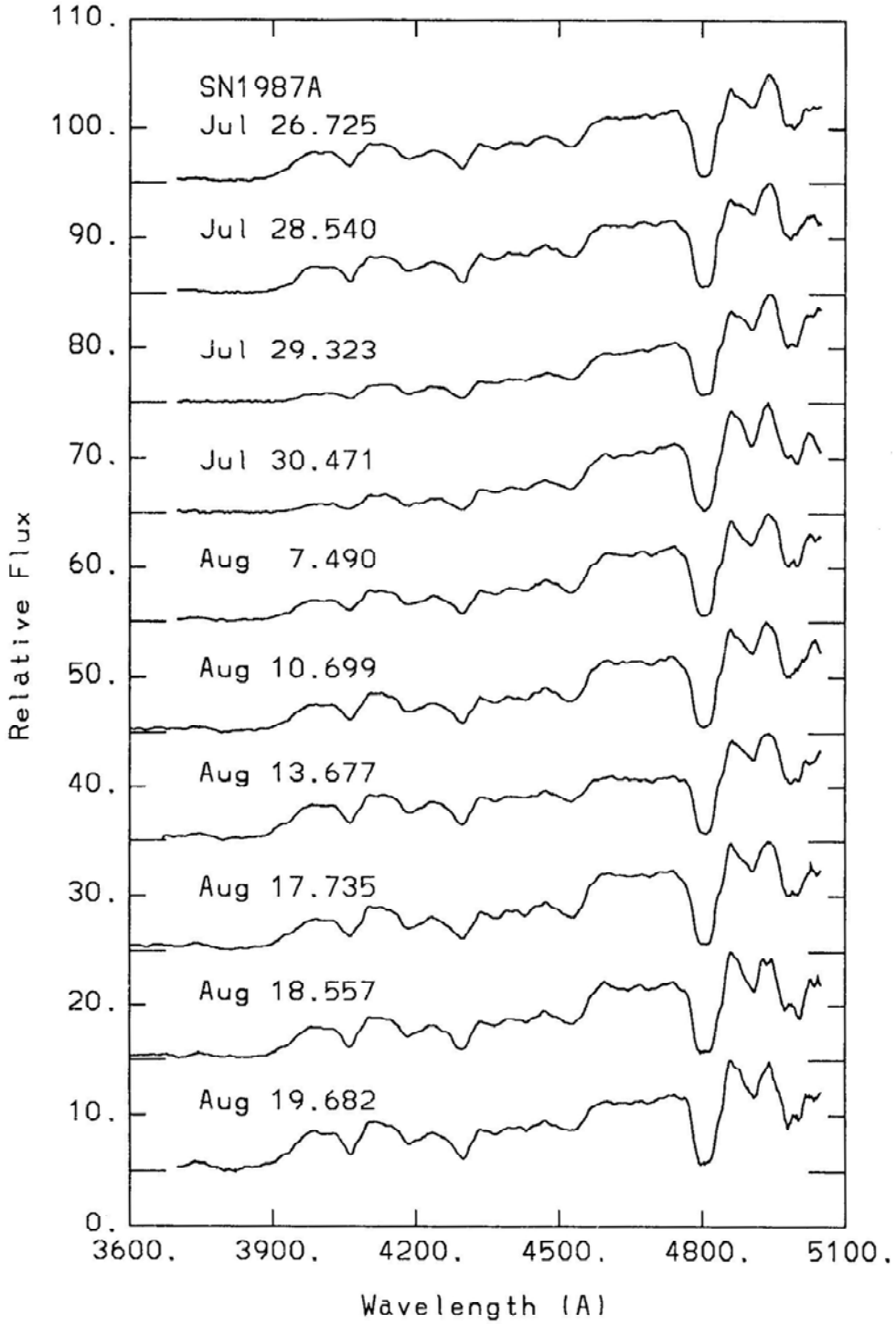
SN1987A
Jul 26.725
Jul 28.540
Jul 29.323
Jul 30.471
Aug 7.490
Aug 10.699
Aug 13.677
Aug 17.735
Aug 18.557
Aug 19.682
Relative Flux
Wavelength (A)
110.
100.
90.
80.
70.
60.
50.
40.
30.
20.
10.
0.
3600.
3900.
4200.
4500.
4800.
5100.

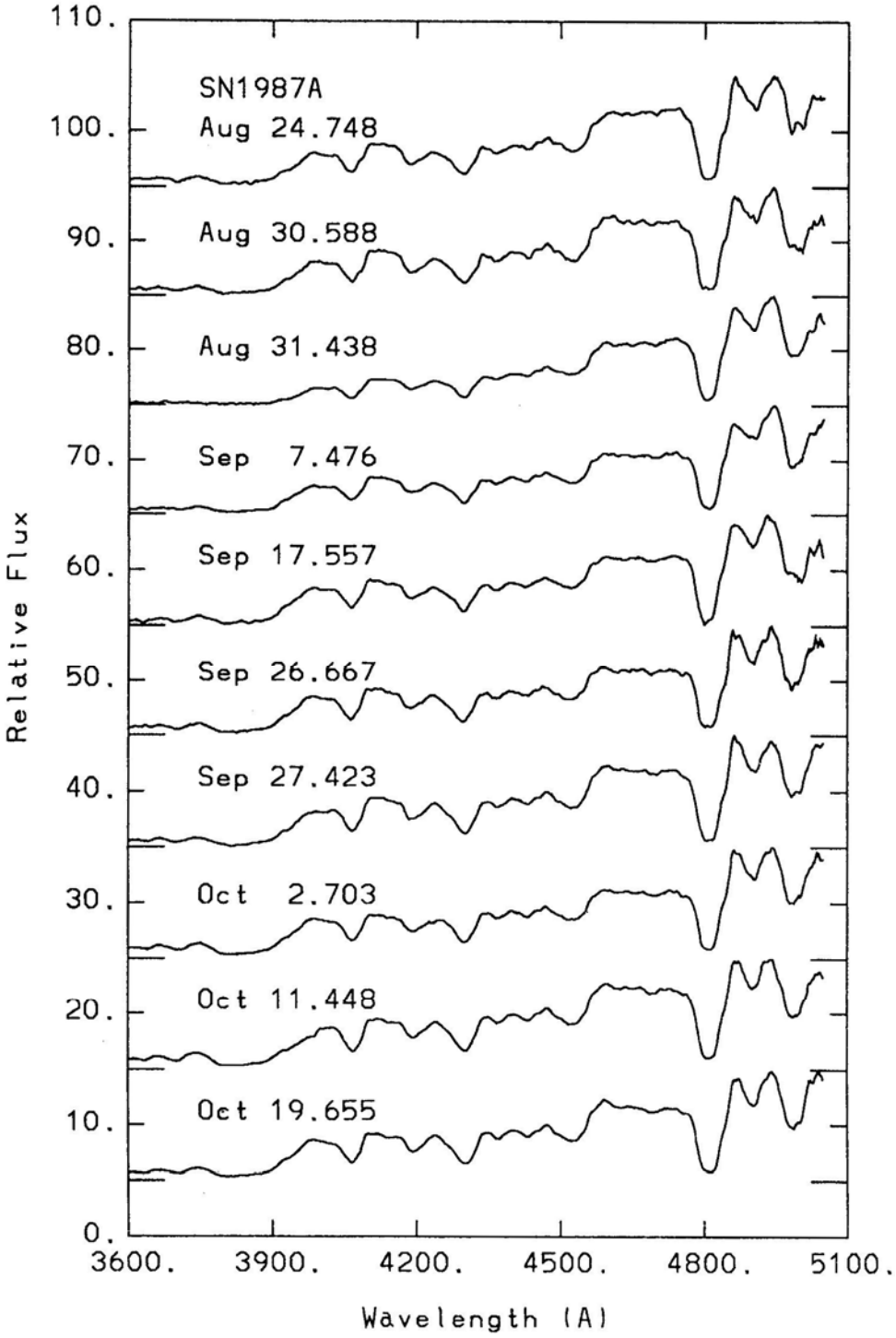
SN1987A
Aug 24.748
Aug 30.588
Aug 31.438
Sep 7.476
Sep 17.557
Sep 26.667
Sep 27.423
Oct 2.703
Oct 11.448
Oct 19.655
Relative Flux
Wavelength (A)
110.
100.
90.
80.
70.
60.
50.
40.
30.
20.
10.
0.
3600.
3900.
4200.
4500.
4800.
5100.

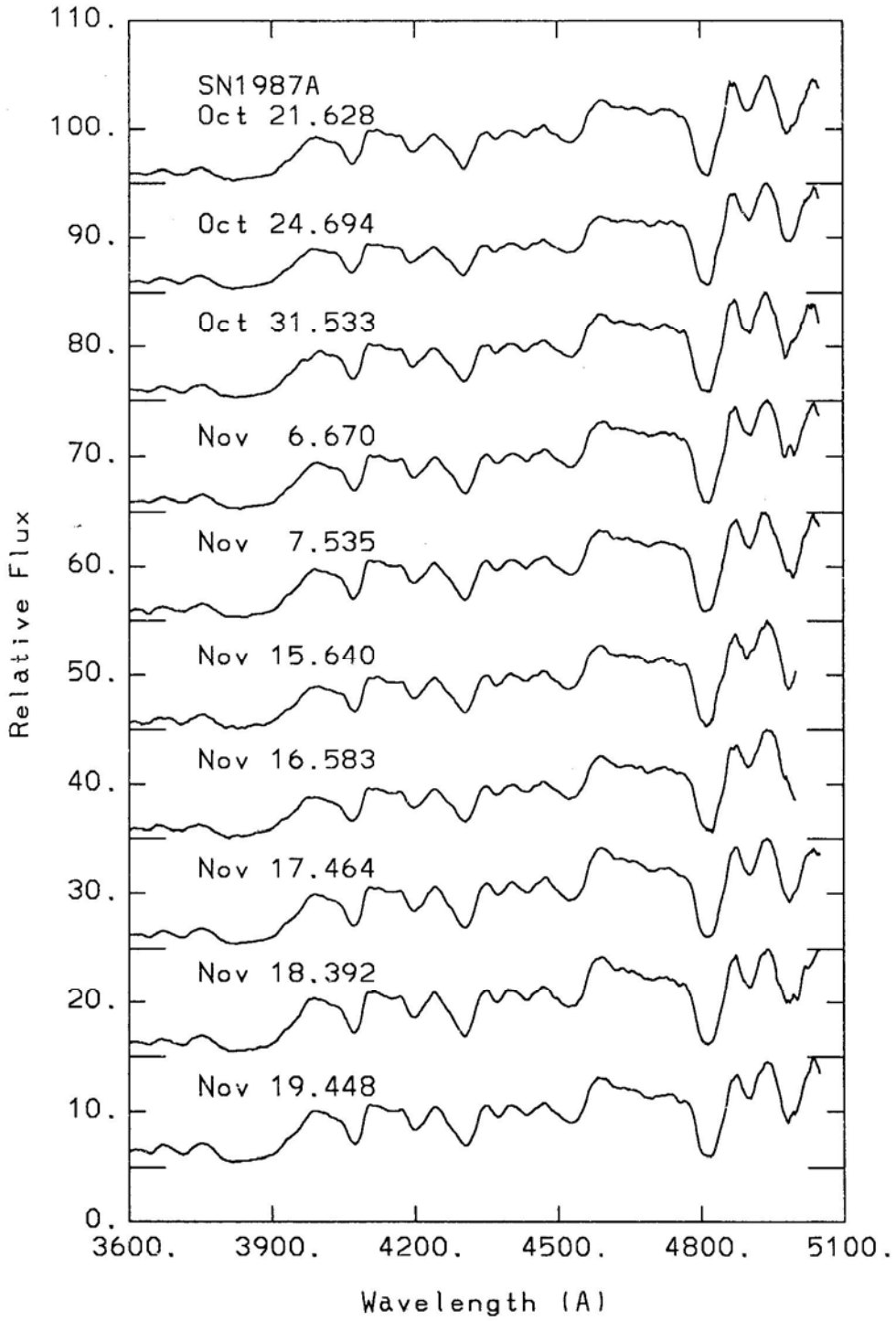
SN1987A
Oct 21.628
Oct 24.694
Oct 31.533
Nov 6.670
Nov 7.535
Nov 15.640
Nov 16.583
Nov 17.464
Nov 18.392
Nov 19.448
Relative Flux
Wavelength (A)
110.
100.
90.
80.
70.
60.
50.
40.
30.
20.
10.
0.
3600.
3900.
4200.
4500.
4800.
5100.

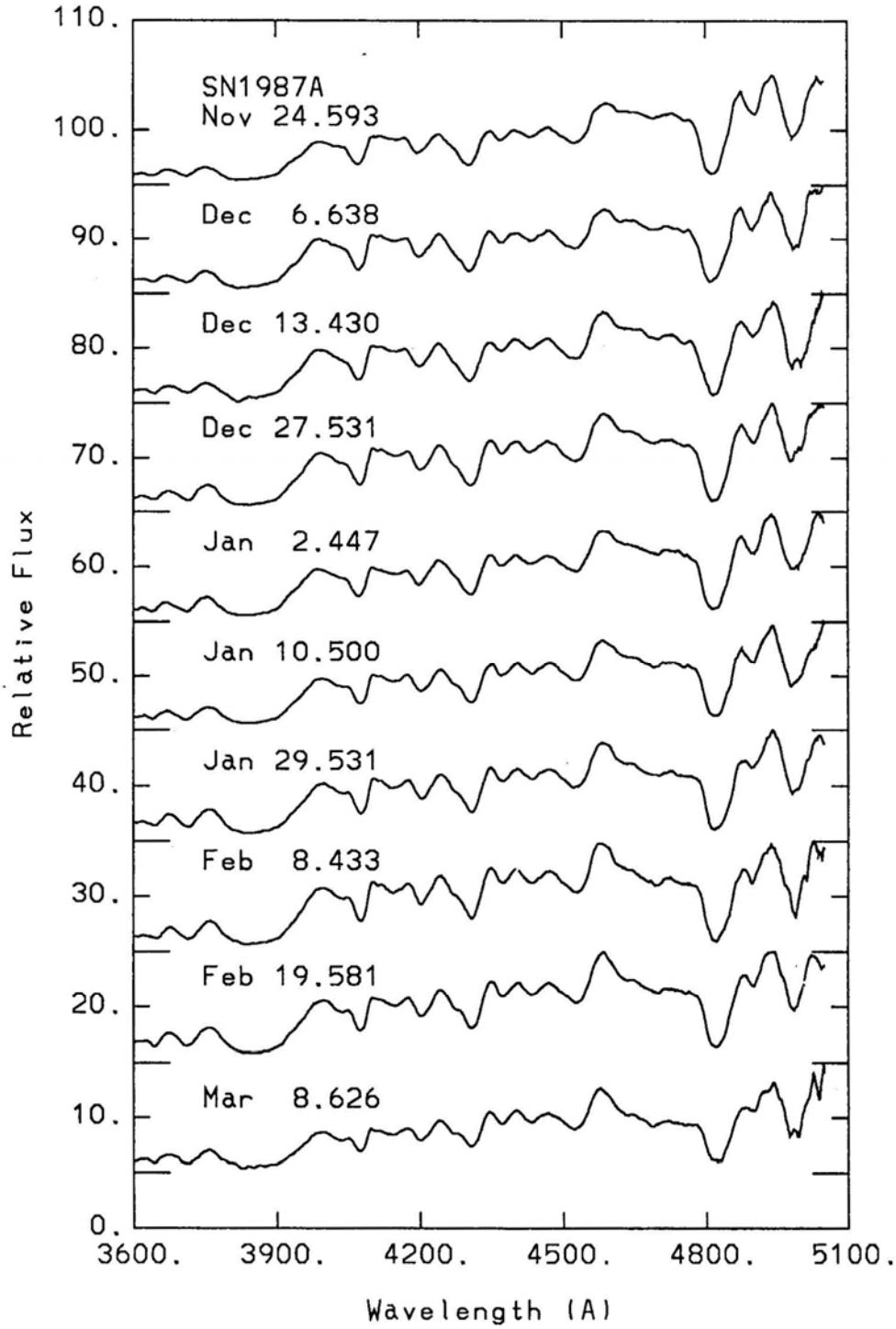
SN1987A
Nov 24.593
Dec 6.638
Dec 13.430
Dec 27.531
Jan 2.447
Jan 10.500
Jan 29.531
Feb 8.433
Feb 19.581
Mar 8.626
Relative Flux
Wavelength (A)
110.
100.
90.
80.
70.
60.
50.
40.
30.
20.
10.
0.
3600.
3900.
4200.
4500.
4800.
5100.

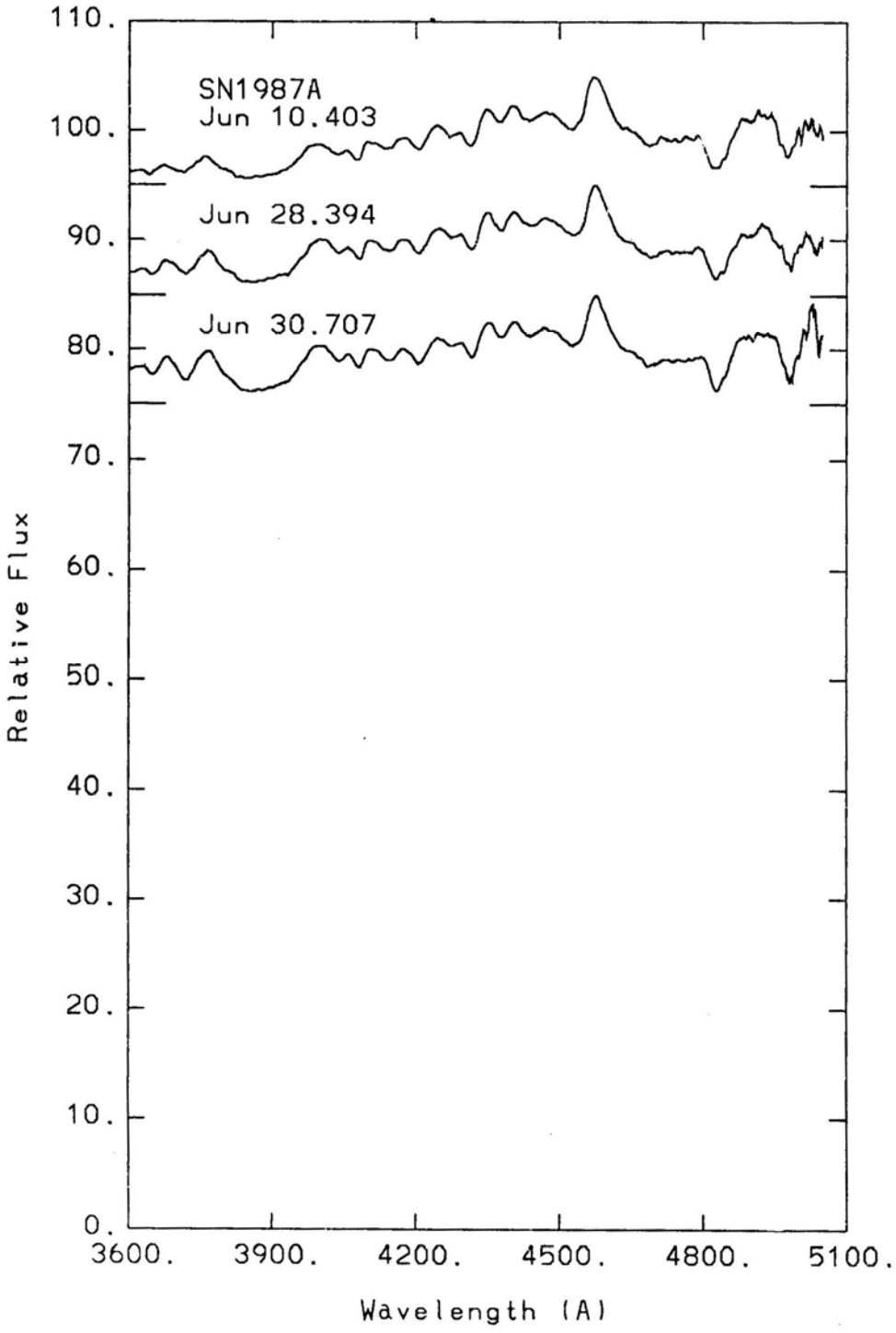
SN1987A
Jun 10.403
Jun 28.394
Jun 30.707
Relative Flux
110.
100.
90.
80.
70.
60.
50.
40.
30.
20.
10.
0.
3600.
3900.
4200.
4500.
4800.
5100.
Wavelength (A)

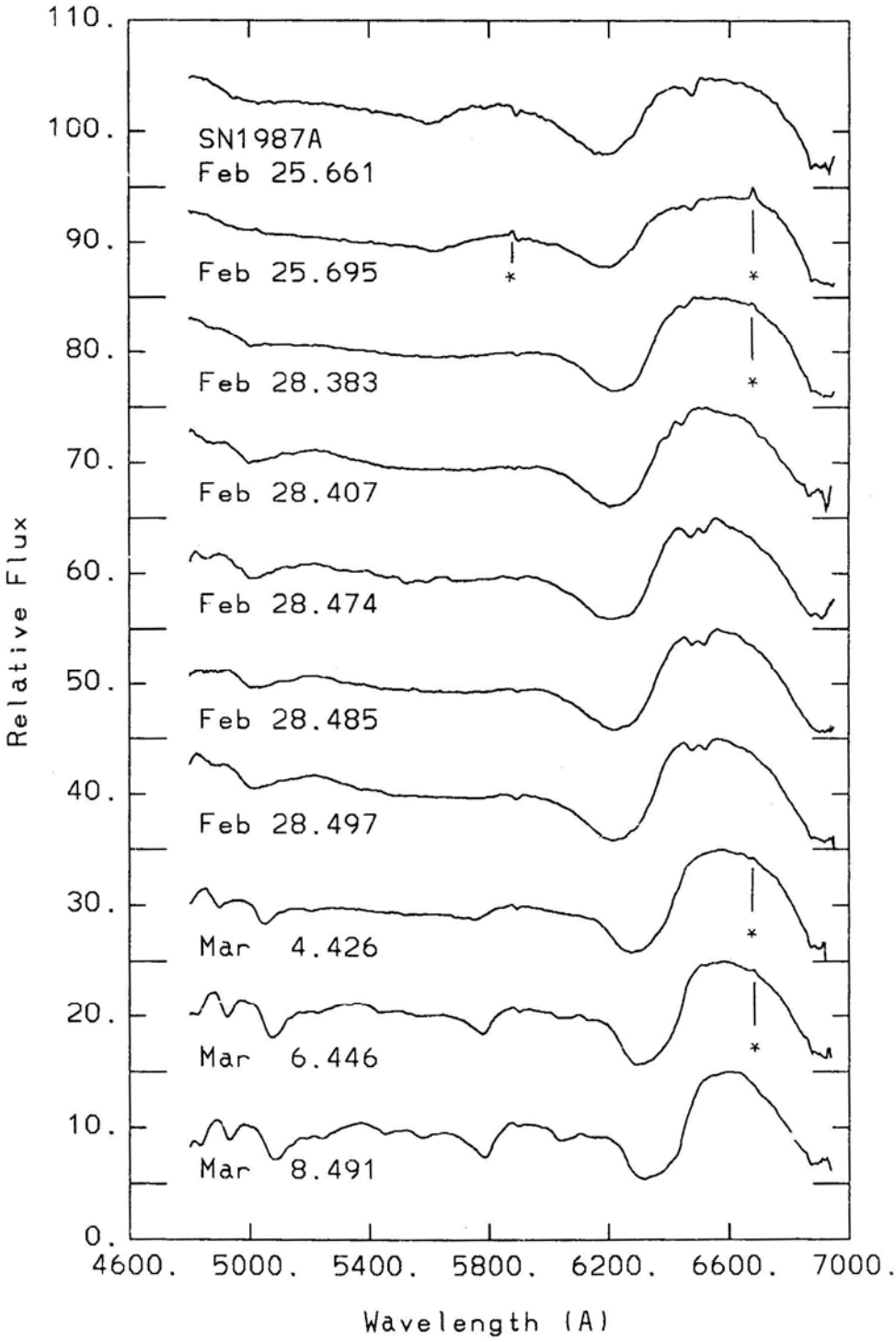
110.
100.
90.
80.
70.
60.
50.
40.
30.
20.
10.
0.
SN1987A
Feb 25.661
Feb 25.695
Feb 28.383
Feb 28.407
Feb 28.474
Feb 28.485
Feb 28.497
Mar 4.426
Mar 6.446
Mar 8.491
*
Relative Flux
4600. 5000. 5400. 5800. 6200. 6600. 7000.
Wavelength (A)

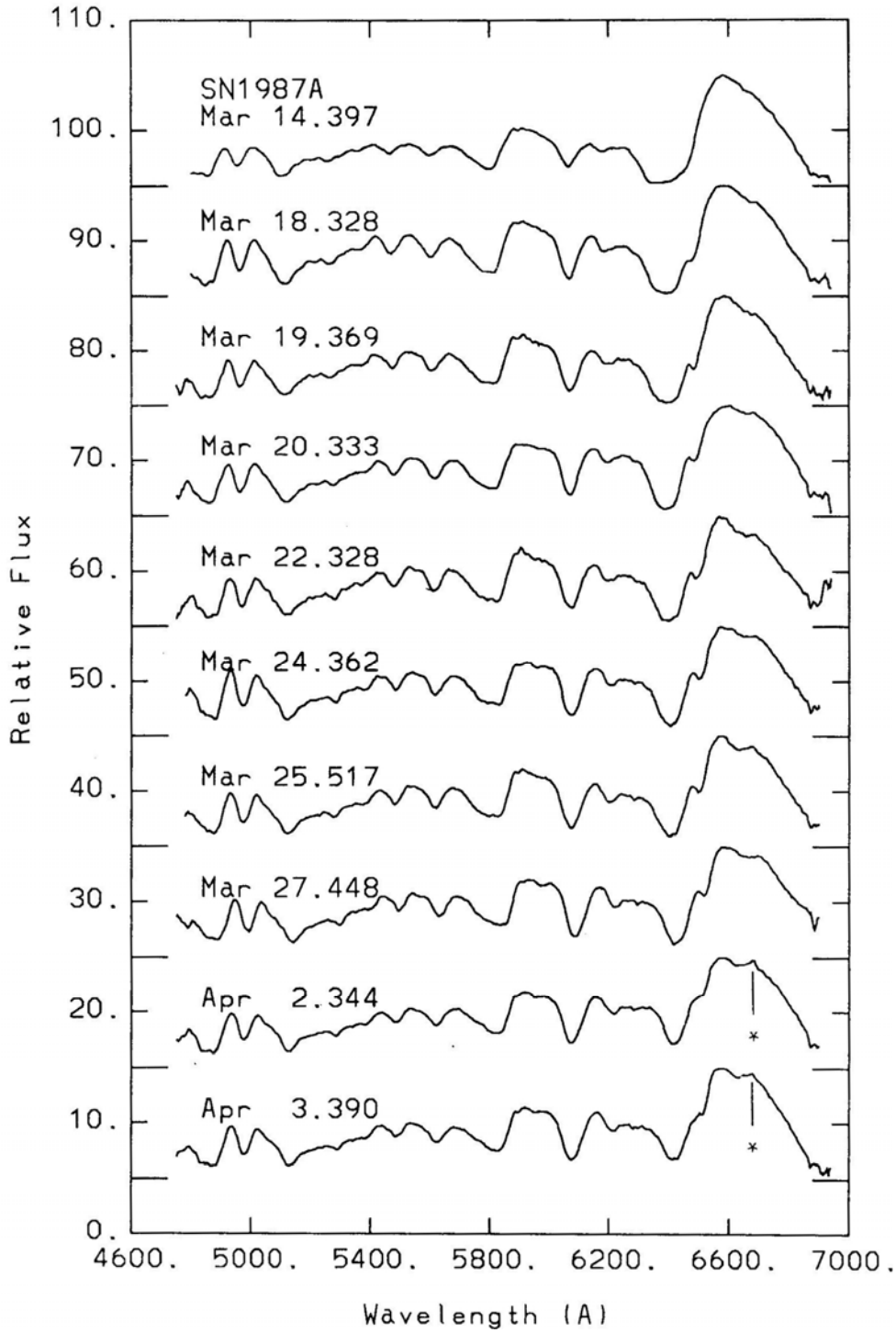
SN1987A
Mar 14.397
Mar 18.328
Mar 19.369
Mar 20.333
Mar 22.328
Mar 24.362
Mar 25.517
Mar 27.448
Apr 2.344
Apr 3.390
Relative Flux
Wavelength (A)
110.
100.
90.
80.
70.
60.
50.
40.
30.
20.
10.
0.
4600.
5000.
5400.
5800.
6200.
6600.
7000.

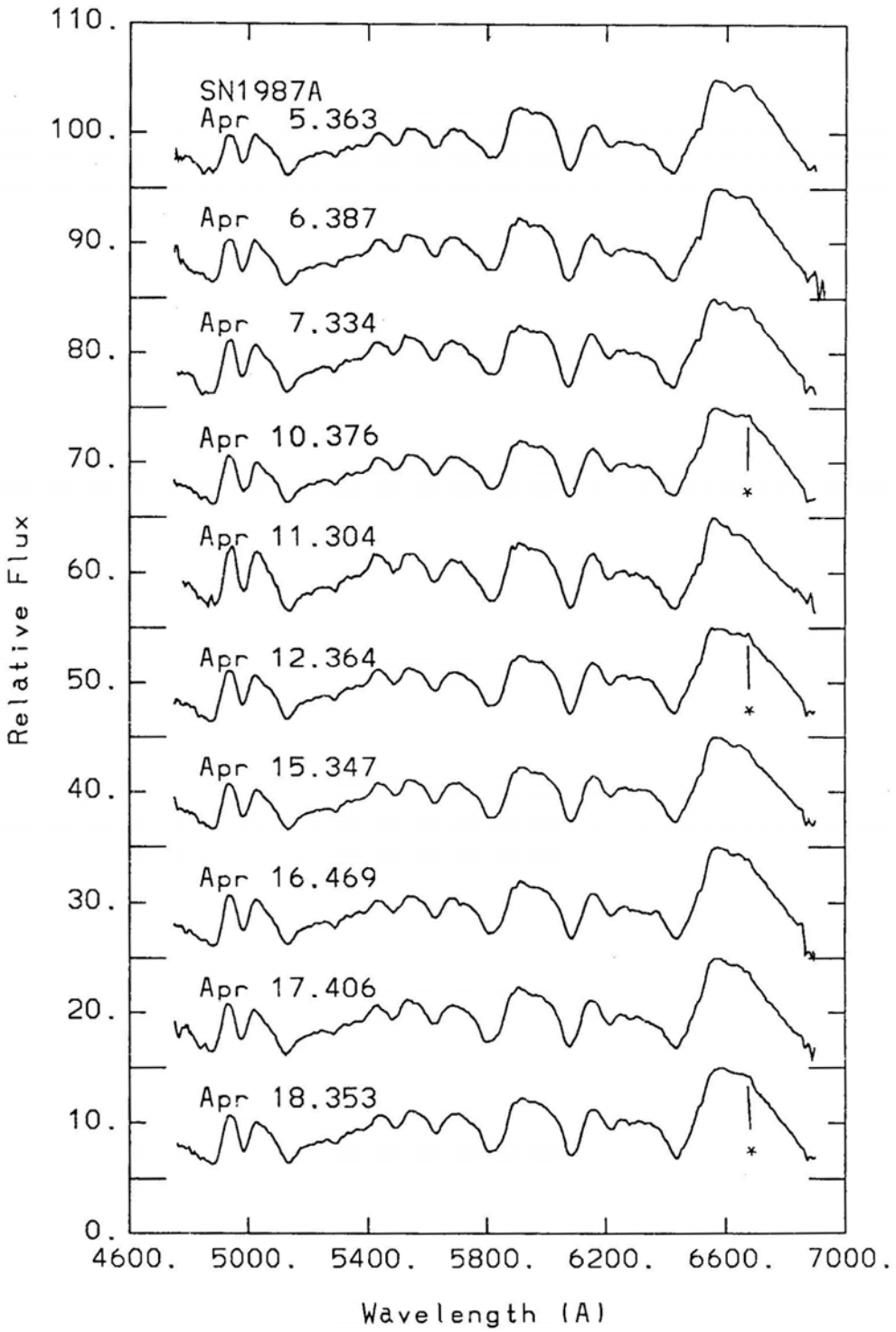
SN1987A
Apr 5.363
Apr 6.387
Apr 7.334
Apr 10.376
Apr 11.304
Apr 12.364
Apr 15.347
Apr 16.469
Apr 17.406
Apr 18.353
Relative Flux
Wavelength (A)
110.
100.
90.
80.
70.
60.
50.
40.
30.
20.
10.
0.
4600.
5000.
5400.
5800.
6200.
6600.
7000.

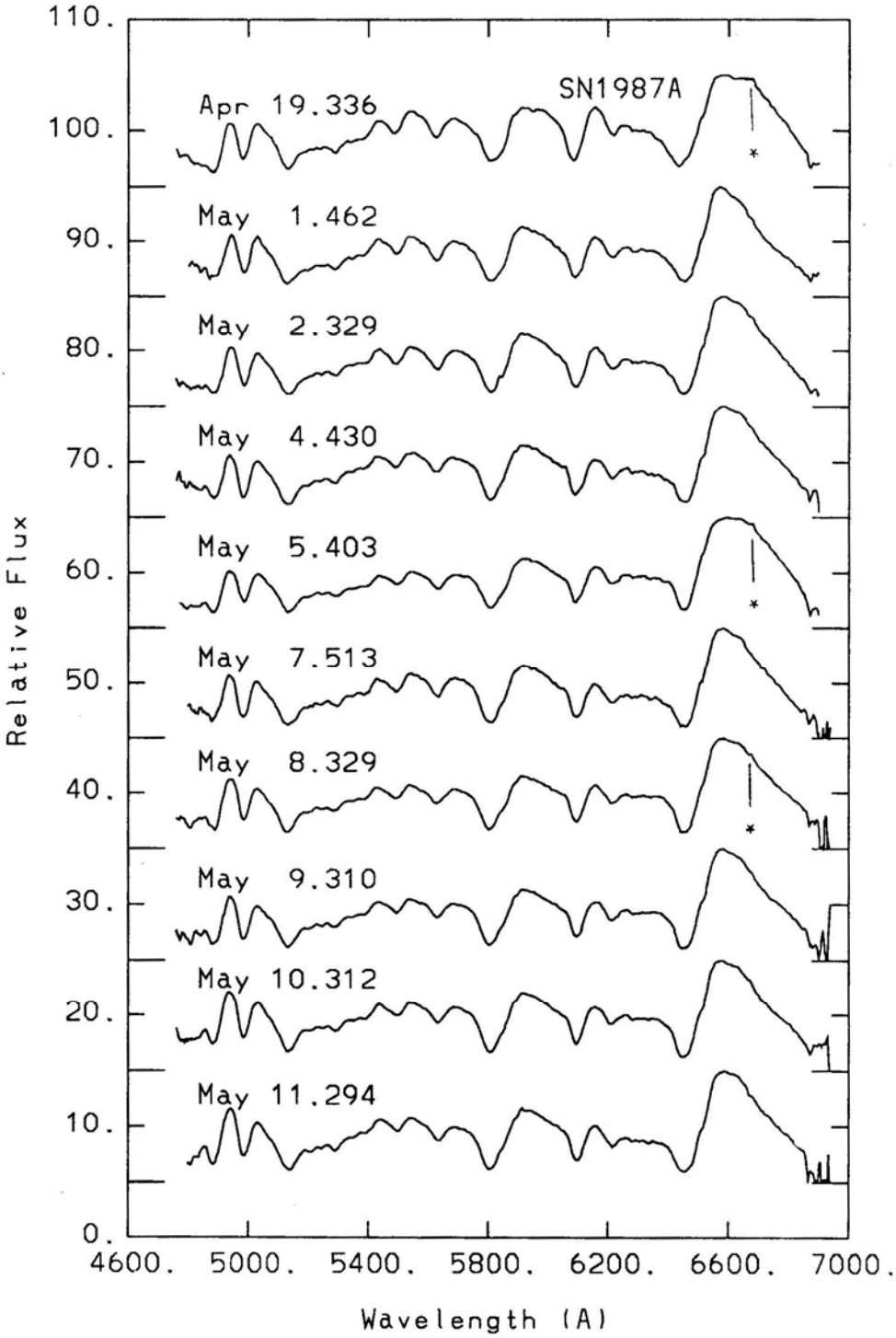
SN1987A
Apr 19.336
May 1.462
May 2.329
May 4.430
May 5.403
May 7.513
May 8.329
May 9.310
May 10.312
May 11.294
Relative Flux
Wavelength (A)
110.
100.
90.
80.
70.
60.
50.
40.
30.
20.
10.
0.
4600.
5000.
5400.
5800.
6200.
6600.
7000.

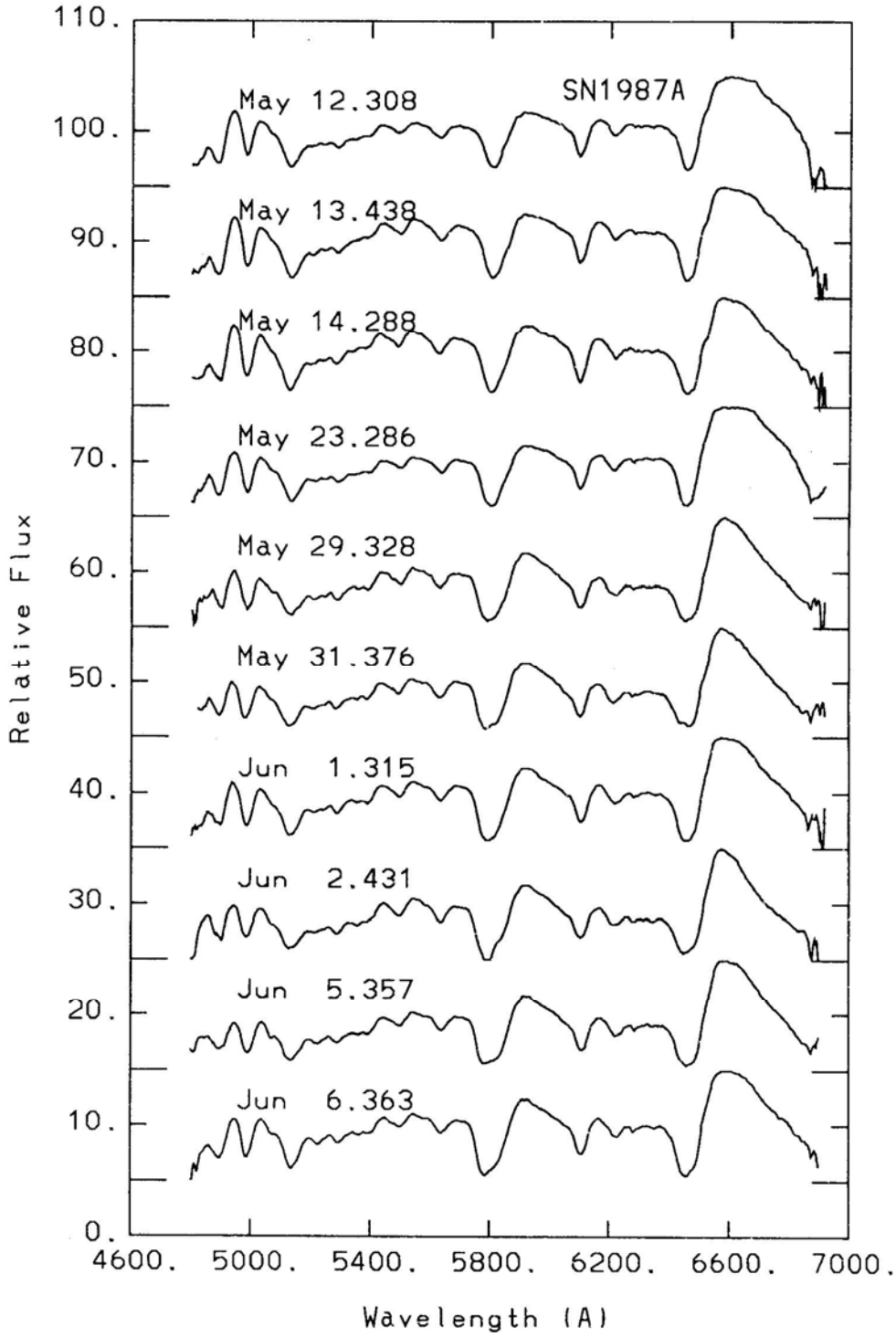
SN1987A
May 12.308
May 13.438
May 14.288
May 23.286
May 29.328
May 31.376
Jun 1.315
Jun 2.431
Jun 5.357
Jun 6.363
Relative Flux
Wavelength (A)
110.
100.
90.
80.
70.
60.
50.
40.
30.
20.
10.
0.
4600.
5000.
5400.
5800.
6200.
6600.
7000.

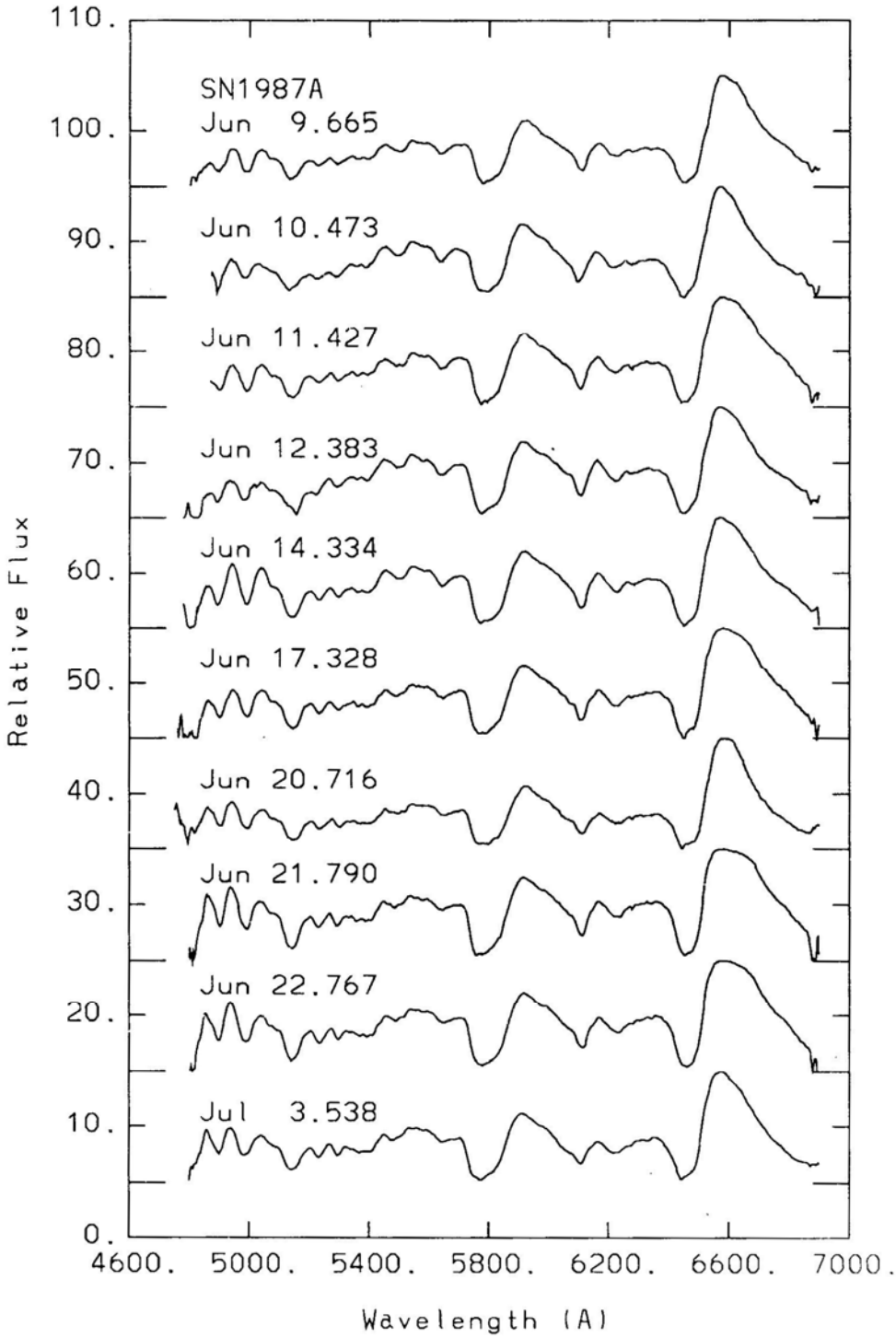
SN1987A
Jun 9.665
Jun 10.473
Jun 11.427
Jun 12.383
Jun 14.334
Jun 17.328
Jun 20.716
Jun 21.790
Jun 22.767
Jul 3.538
Relative Flux
Wavelength (A)
110.
100.
90.
80.
70.
60.
50.
40.
30.
20.
10.
0.
4600.
5000.
5400.
5800.
6200.
6600.
7000.

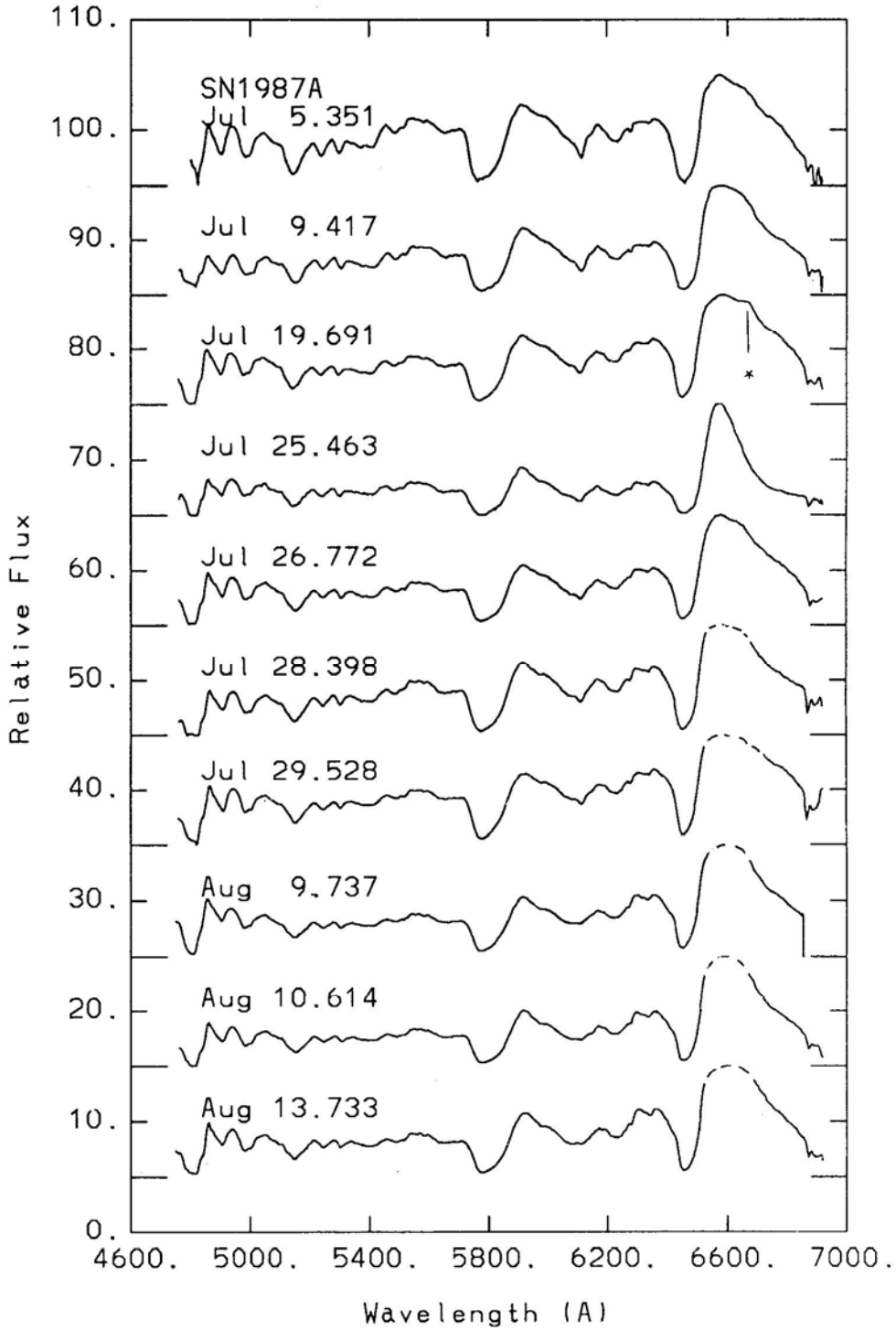
SN1987A
Jul 5.351
Jul 9.417
Jul 19.691
Jul 25.463
Jul 26.772
Jul 28.398
Jul 29.528
Aug 9.737
Aug 10.614
Aug 13.733
Relative Flux
Wavelength (A)
110.
100.
90.
80.
70.
60.
50.
40.
30.
20.
10.
0.
4600.
5000.
5400.
5800.
6200.
6600.
7000.

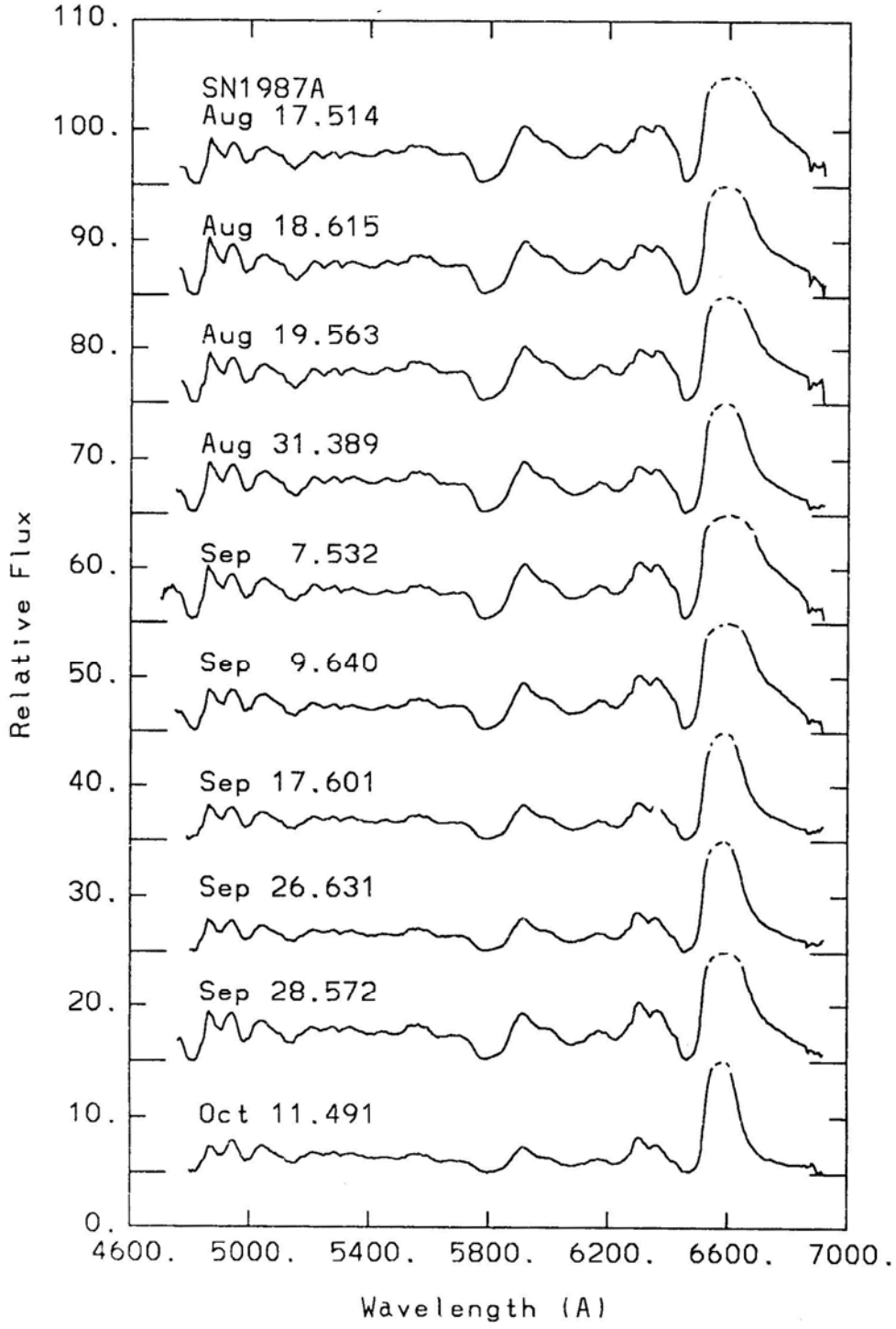
SN1987A
Aug 17.514
Aug 18.615
Aug 19.563
Aug 31.389
Sep 7.532
Sep 9.640
Sep 17.601
Sep 26.631
Sep 28.572
Oct 11.491
Relative Flux
Wavelength (A)
110.
100.
90.
80.
70.
60.
50.
40.
30.
20.
10.
0.
4600.
5000.
5400.
5800.
6200.
6600.
7000.

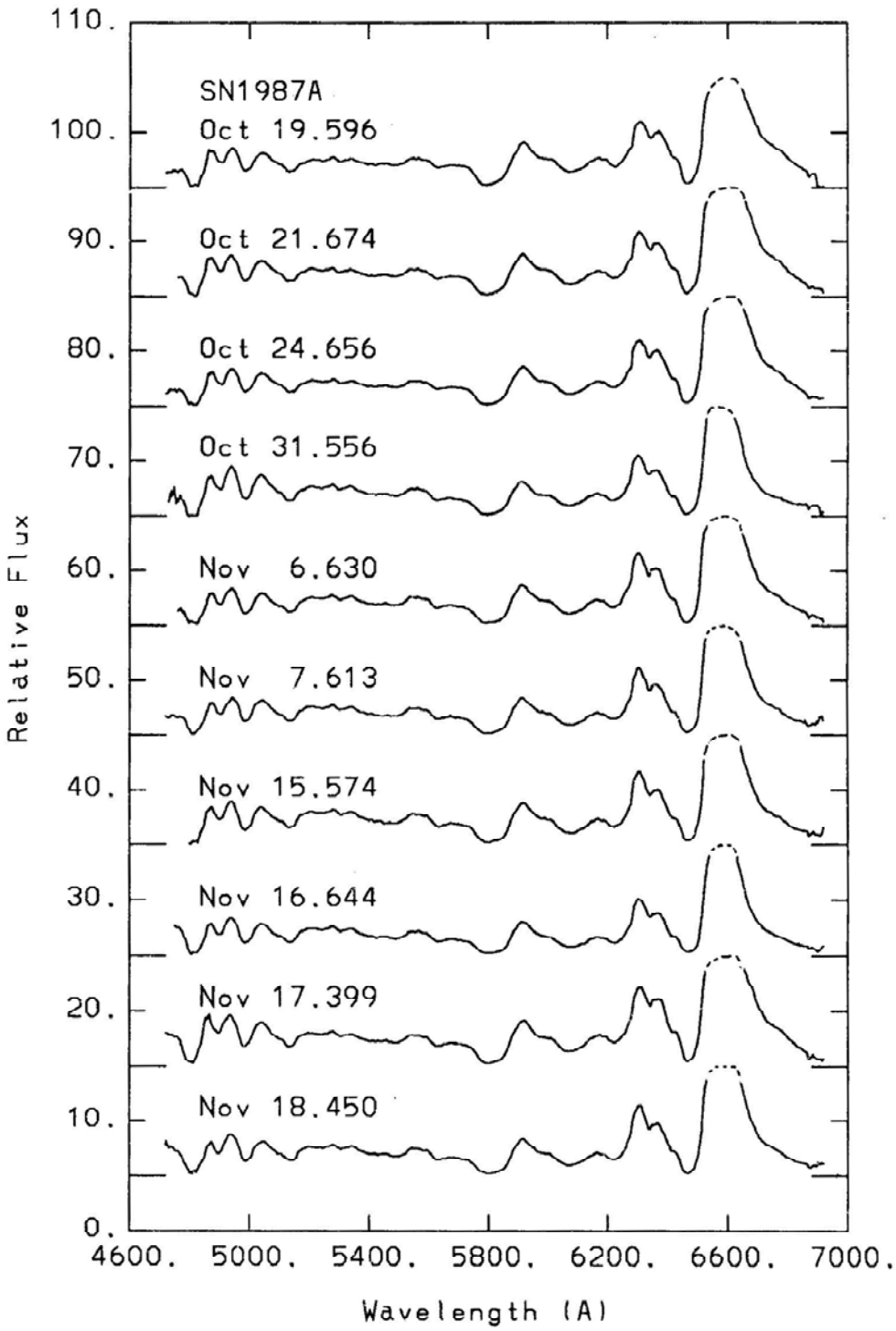
SN1987A
Oct 19.596
Oct 21.674
Oct 24.656
Oct 31.556
Nov 6.630
Nov 7.613
Nov 15.574
Nov 16.644
Nov 17.399
Nov 18.450
Relative Flux
Wavelength (A)
110.
100.
90.
80.
70.
60.
50.
40.
30.
20.
10.
0.
4600.
5000.
5400.
5800.
6200.
6600.
7000.

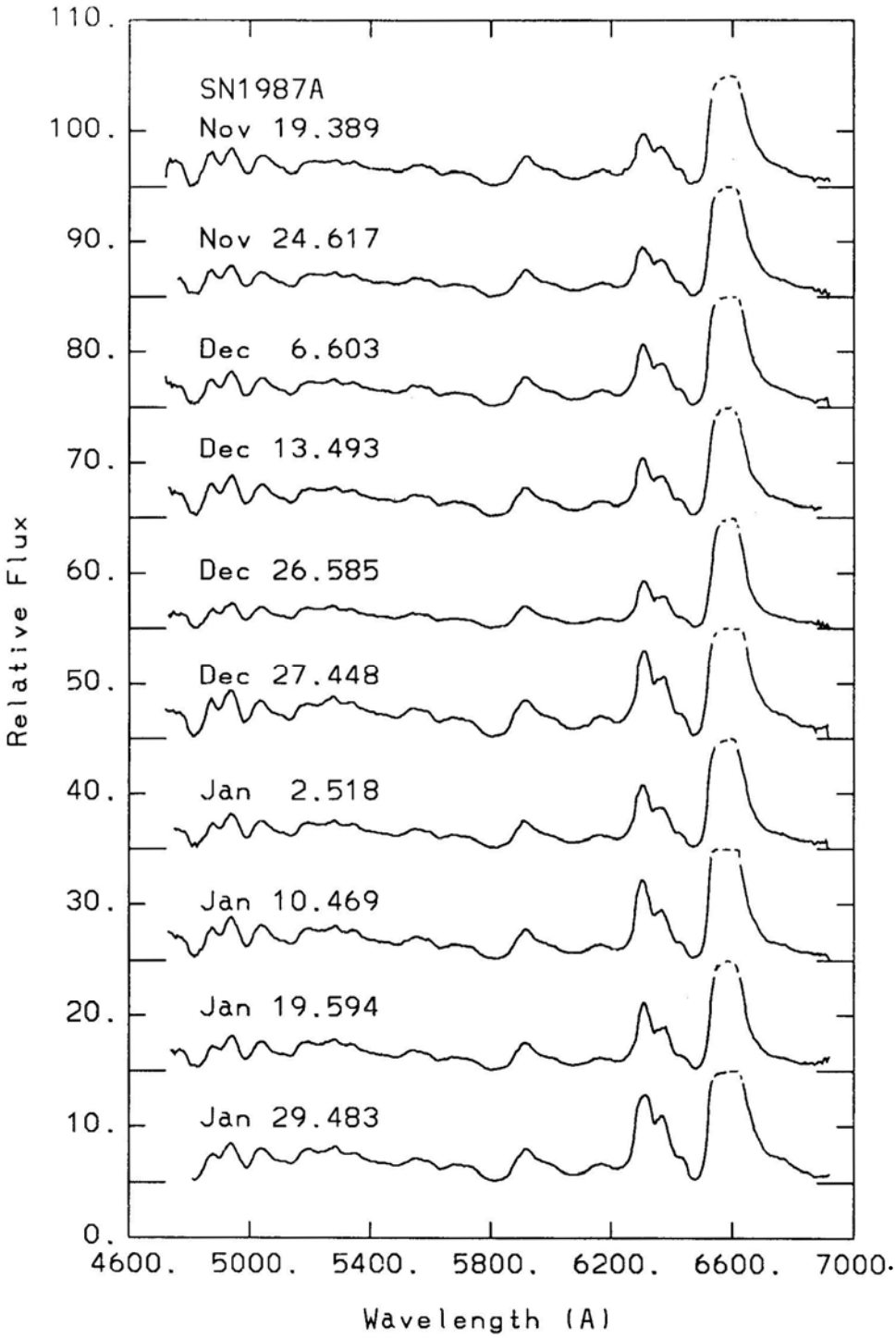
SN1987A
Nov 19.389
Nov 24.617
Dec 6.603
Dec 13.493
Dec 26.585
Dec 27.448
Jan 2.518
Jan 10.469
Jan 19.594
Jan 29.483
Relative Flux
Wavelength (A)
110.
100.
90.
80.
70.
60.
50.
40.
30.
20.
10.
0.
4600.
5000.
5400.
5800.
6200.
6600.
7000.

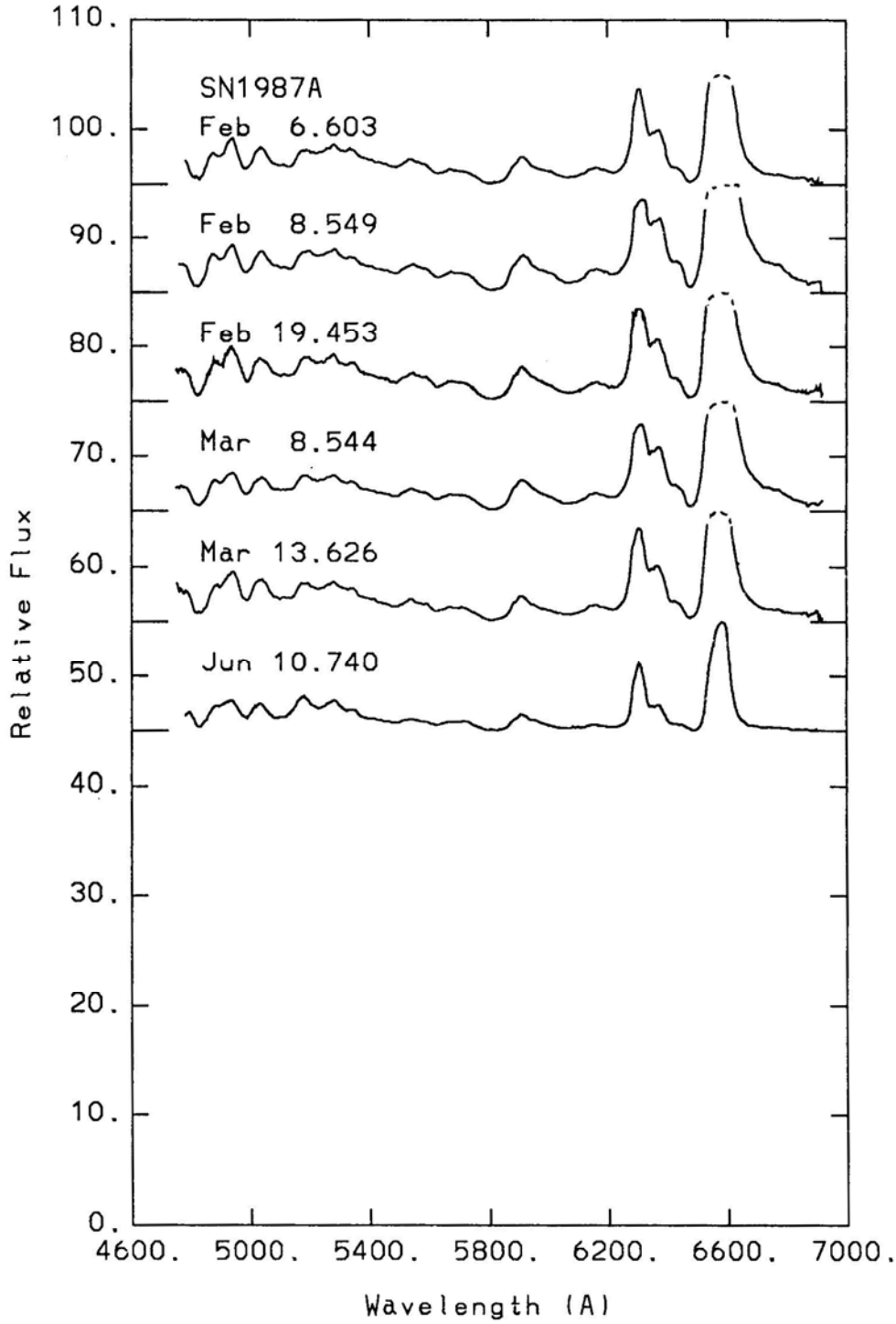
SN1987A
Feb 6.603
Feb 8.549
Feb 19.453
Mar 8.544
Mar 13.626
Jun 10.740
Relative Flux
Wavelength (A)
110.
100.
90.
80.
70.
60.
50.
40.
30.
20.
10.
0.
4600.
5000.
5400.
5800.
6200.
6600.
7000.

J. Astrophys. Astr. (1990) **11,** 125–140

On the Morphology of Supernova Remnants with Pulsars

D. Bhattacharya* *Raman Research Institute, Bangalore 560080*

Received 1989 August 30; accepted 1989 November 19

Abstract. One of the intriguing aspects of supernova remnants is their morphology. While the majority of them look like hollow shells, a few, called plerions, are centrally filled like the Crab nebula, and some have a shell-plerion combination morphology. The centrally-filled component in these remnants is believed to be powered by a central pulsar. In this paper we present results of model calculations of the evolution of surface brightness and morphology of supernova remnants containing pulsars. We discuss how the morphology of a supernova remnant will depend on the velocity of expansion, the density of the ambient medium into which it is expanding, and the initial period and magnetic field strength of the central pulsar.

Key words: Supernova remnants, evolution—Supernova remnants, morphology—plerions—pulsars.

1. Introduction

Detailed radio observations over the past two decades have established that there are at least three distinct types of supernova remnants (SNRs). The vast majority of them have the appearance of hollow "shells" with hardly any central emission (*e.g.* Tycho's SNR, SNR 1006 etc.). Another class of SNRs are centrally-filled with no limb brightening. These have come to be known as "plerions", the Crab nebula is a prime example of this morphology. The third category contains SNRs of a "hybrid" nature—a shell surrounding a centrally condensed nebula. These are commonly referred to as "combination remnants". The SNR G 326.3–1.8 is an example of this class. Of the ~ 150 SNRs so far identified in our galaxy the relative numbers in the above three categories are roughly in the ratio 10:1:1 respectively (Weiler & Sramek 1988; Green 1988).

The reason for the occurrence of the three distinct types of SNRs has been debated in the literature. It is now widely accepted that a filled-centre nebula is powered by a central pulsar, although in many cases the pulsar may not be beamed towards us. A pronounced shell emission is believed to be the result of the interaction of the supernova ejecta with the interstellar medium. By extension, the presence of an active pulsar at the site of the supernova explosion would naturally account for the hybrid

* Present Address: Astronomical Institute, University of Amsterdam, Roetersstraat 15, 1018 WB Amsterdam, The Netherlands.

appearance of some SNRs. This still leaves unaccounted why the majority, viz. the shells, have hollow interiors. The explanation often invoked is that the shells and the plerions are the remnants of different types of supernova. Shklovskii (1980) suggested that plerions are produced by type II supernovae which leave behind pulsars, while shells are the result of type I supernovae which according to current models leave no stellar remnants. Although it is reasonable to associate plerions with supernovae that leave behind pulsars, it is not obvious that the hollow shells do not harbour central pulsars. In any case, it is difficult to identify the majority of shells with type I supernovae for the following reason. Recent studies of supernova statistics indicate that the Galactic rates of supernovae of type Ia, type Ib and type II are in the ratio 3:4:11 (van den Bergh, McClure & Evans 1987). If the progenitors of type Ib supernovae are massive stars as argued by van den Bergh (1988) then they, too, might leave behind neutron stars. Thus, the hollowness of the interiors of most SNRs can not, in all cases, be attributed to the absence of central neutron stars.

This led Radhakrishnan and Srinivasan (1983) to argue that the hollow shells should be understood in terms of their central pulsars having rather long initial periods. Srinivasan, Bhattacharya & Dwarakanath (1984) showed that the paucity of luminous plerions is, indeed, consistent with most pulsars being born spinning rather slowly. Although the hollow shells and the hybrid SNRs found a natural explanation in this scheme, the intriguing question as to why the classical plerions like the Crab nebula, 3C 58 etc. show no limb brightening remained open. Could it be that the plerions and the shells are merely manifestations of different stages of evolution of SNRs with central pulsars? Although such a suggestion was made by Lozinskaya (1980) it has not been examined in detail.

In this paper we wish to report the results of a simple model calculation which elucidates this question. Our aim is to obtain a qualitative understanding of the general trends of evolution, rather than to build detailed quantitative models. The problem we have studied is the following. Let there be an active pulsar at the centre of an expanding shell of supernova ejecta. The relativistic wind from the pulsar will produce a central synchrotron nebula, and the interaction of the ejecta with the interstellar medium will result in radio emission. By assuming these two components to evolve independent of each other, the radio morphology of the SNR at various times can be inferred by comparing the surface brightness of the shell and that of the central plerion. In the next section the analytical method adopted to compute the surface brightness of the two components is briefly outlined. In Section 3 the results for a Crab-like central pulsar are discussed. The dependence of SNR morphology on the characteristics of the central pulsar is discussed in Section 4. It has now become quite clear from observations that supernova remnants may expand in media of different densities, and also have different blast energies. The role of the ambient density in determining the surface brightness and morphology of a supernova remnant is discussed in Section 5.

2. The approach

The morphology of a supernova remnant which has both shell and plerionic components of emission depends on the relative surface brightness of the two. To study the evolution of the morphology, therefore, we have followed the evolution of both

these components of composite SNR models, in which the shell emission forms at the outer edge of the plerionic nebula.

2.1 *The Plerionic Component*

A detailed theoretical model for the evolution of a pulsar-produced nebula was first constructed by Pacini & Salvati (1973). They derived analytical results for the evolution of the spectral luminosity of a uniformly expanding spherical bubble in which a central pulsar continuously injects magnetic field and relativistic particles. We have used the same formalism in our model calculations, with modifications appropriate for a bubble that undergoes deceleration at late times due to interaction with the surrounding medium. According to this model, the surface brightness of the plerion at a given time is determined by: (a) the initial period P_0 and the magnetic field B of the pulsar, and (b) the expansion velocity $v(t)$ of the nebula. Detailed analytical expressions for the luminosity evolution in the decelerated phase can be found in Reynolds & Chevalier (1984) and Bhattacharya (1987). A more accurate numerical treatment of this phase has been made by Bandiera, Pacini & Salvati (1984), and also Reynolds & Chevalier (1984). For the present model calculations, we feel that it is sufficient to follow the analytical approach.

2.2 *The Shell Component*

The radio emission of the shell component is believed to originate due to the interaction of the supernova ejecta with the interstellar medium. Unfortunately, no reliable analytical method exists for the computation of the evolution of the radio luminosity. The first quantitative model for the radio emission of a shell remnant was due to Gull (1973). He studied the numerical evolution of hydrodynamical models of supernova remnants, and showed that a certain fraction of the blast wave energy goes into turbulence at the interface between the shocked interstellar matter and the supernova ejecta. These turbulent cells can amplify the magnetic field by stretching and twisting the field lines, and also accelerate relativistic particles by the "Fermi process". Under the assumption that an equipartition is reached between the energy densities in turbulence, magnetic field and relativistic particles, one may then calculate the evolution of the radio luminosity of the shell. The surface brightness at a given time will be a function of the ejected mass $M_{\rm ej}$, the ambient density n_0 and the blast energy $E_{\rm tot} \equiv \frac{1}{2} M_{\rm ej} v_{\rm i}^2$, where $v_{\rm i}$, is the initial velocity of expansion. This model explains fairly well the evolution of radio luminosity of young supernova remnants like Cas A and Tycho's SNR (Gull 1973,1975; Braun, Gull & Perley 1987). Detailed models of particle acceleration, if included, also leads to similar results (Scott & Chevalier 1975; Cowsik & Sarkar 1984). It is likely that in some cases shock acceleration may also be an important source of relativistic particles in the shell. Unfortunately there is as yet no complete theory for the origin of these high-energy particles. In this paper we have used Gull's models to estimate the radio luminosity of the shell component of the SNR.

To build the final model, we have combined the evolution of the shell and the plerionic components with a common expansion velocity. The SNR is assumed to be a

spherical bubble of radius R at a time t, where

$$R(t) = v_i t \qquad \text{if} \quad M_{sw}(t) < M_{ej}$$

and

$$R(t) = v_i t_0 (t/t_0)^{0.4} \qquad \text{if} \quad M_{sw}(t) > M_{ej}.$$

Here M,(t) is the swept up mass: $M_{sw}(t) = \frac{4\pi}{3} R^3(t) n_0 \, m_p$, and t_0 is the time at which $M_{sw}(t) = M_{ej}$; m_p is the proton mass. This model for expansion is based on asymptotic slopes, and is admittedly crude. The $t^{0.4}$ expansion law is appropriate for the so-called Sedov phase of evolution, but numerical calculations (*e.g.* Fabian, Brinkmann & Stewart 1983) show that the Sedov phase begins when $M_{sw} \gtrsim 5 M_{ej}$, and is fully established only after $M_{sw} > 19 M_{ej}$. This is likely to introduce an uncertainty of a factor ~ 2 in the estimate of to mentioned above. The shell emission is assumed to be confined to within a thickness $\Delta R = \delta \cdot R(t)$ at the outer edge. In the calculations reported here, we have used a constant value of $\delta = 0.2$[†]. The cavity interior to the shell is assumed to be filled by the plerionic nebula.

It should be mentioned that due to the simple relation adopted between the expansion rate of the shell and the plerionic components of the remnant, this model cannot treat the case of a large amount of slow-moving material in the interior of the supernova ejecta, a scenario discussed in detail by Reynolds & Chevalier (1984).

As mentioned above, we are interested in studying the evolution of the SNR for different values of blast energy (E_{tot}), ambient density (n_0) and ejected mass (M_{ej}). However, Gull's (1973) calculations were done for a particular choice of these parameters. To use these results for other values of E_{tot}, n_0 and M_{ei}, we adopted the following scaling procedure:

(a) From the results presented graphically by Gull (1973), we expressed the dimensionless quantities E_{rel}/E_{tot} and $B_s(M_{ej} l n_0 E_{tor})^{1/2}$ as a function of the dimensionless mass ratio parameter x, defined as $x = \frac{4\pi}{3} R^3(t) m_p n_0 / M_{ej}$, where E_{rel} is the energy content in relativistic particles, B_s the magnetic field in the shell region and m_p the proton mass. These relations were expressed in best-fit polynomial form.

(b) From the radius *vs* time relation in our model we computed $x(t)$, and using the above relations we obtained $E_{rel}(t)$ and $B_s(t)$ for any desired value of E_{tot}, n_0 and M_{ej}. These were then used to compute the radio luminosity of the shell component as a function of time.

The relativistic particles responsible for the synchrotron radiation from both the shell and the plerionic components were assumed to be injected with a power-law energy distribution of the form $N(E) \propto E^{-\gamma}$, with the value of γ chosen to be 1.6 for the plerionic component (in analogy with the Crab Nebula), and 2.3 for the shell component (as in an average shell remnant).

Given the assumptions and the method outlined above, one can now follow the evolution of the surface brightness of the idealized composite SNR. We compute, as a function of time, the surface brightness of the plerionic component averaged over the

[†]This estimate of shell thickness is likely to be poor in late phases of the evolution, and when the pulsar power is small. In reality, the relative size of the pulsar bubble and the outer shock may vary with time in a complicated manner, as suggested by Reynolds & Chevalier (1984). However, we shall adopt the (simpler) model described above, in order to keep the problem tractable.

projected "disc", and that of the shell component averaged over the projected bright "ring" at the edge of the plerionic "disc".

3. Results

Fig. 1 illustrates the evolution of the surface brightness for the following parameters.

initial velocity = 10_4 km s^{-1}

density of ISM = 1 atom cm^{-3}

initial period of PSR = 16 ms

magnetic field = 3.7×10^{12} G

The parameters of the pulsar have been chosen to be that of the Crab pulsar, often assumed to be the prototype of a young pulsar. Again, the initial velocity of the ejecta and the density of the ISM are "standard-values". As expected, the surface brightness of the shell (broken line) increases to reach a maximum at a time ~ t_0 when deceleration sets in. The rapid decline at $t > 3000$ yr is an artefact of the extrapolation of the polynomial fit to Gull's models. The evolution of the plerion is shown as the solid line. The change of the rate of decline of the surface brightness at $t = t_0$ and $t = \tau_0 (\equiv P_0 / 2\dot{P}_0)$, the initial characteristic slow-down timescale, are due to the deceleration of the walls of the cavity and the decline in the pulsar luminosity respectively. In reality the transition between these different phases will be smooth and gradual.

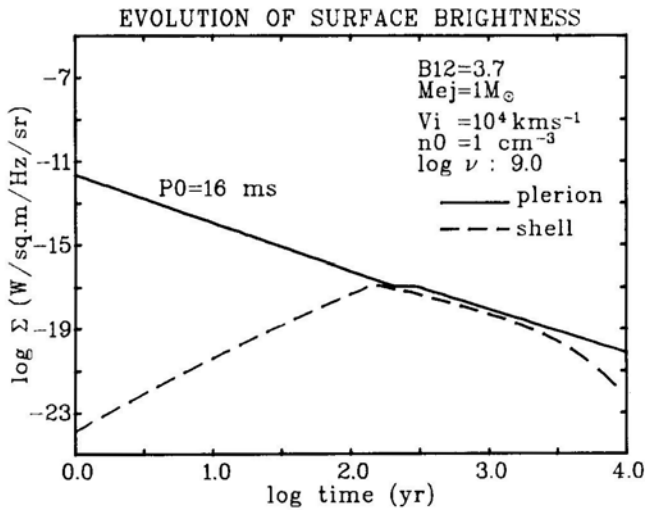

Figure 1. Evolution of the 1 GHz surface brightness of the plerionic component (solid line)and the shell component (dashed line) of a supernova remnant harbouring a Crablike pulsar and expanding in a uniform medium of density 1 Hatom cm^{-3}.10^{12} B12 gauss is the surface dipole magnetic field of the pulsar and P0 is its initial rotation period. Mej is the mass in the ejecta, Vi the initial velocity of expansion, and n0 the density of the ambient medium, ν is the assumed frequency of observation in Hz. A fairly strong shell component is expected, resulting in a combination morphology of the remnant. The rapid drop of the shell surface brightness at ages exceeding ~ 3000 yr is an artifact due to the extrapolation of the polynomial relations used to fit Gull's (1973) models.

As we see from this figure, once the shell emission builds up to its peak value its surface brightness remains comparable to that of the central plerionic component. Thus, after a few hundred years the remnant will have a combination morphology. Although the surface brightnesses plotted in Fig. 1 have been computed at 1 GHz, the morphology will be roughly the same also at lower observing frequencies. Quantitatively, the ratio of the surface brightness of the shell to that of the plerion will be larger at lower frequencies owing to the fact that the spectral index of the shell is usually larger than that of the plerion.

The most striking feature of the above figure is that although the central pulsar has the same period and magnetic field as the Crab pulsar, the morphology of the remnant is very different from that of the Crab nebula which shows no pronounced limb brightening. In our opinion, the reason for this is the following. One of the most remarkable properties of the Crab nebula is its very small expansion velocity ~ 1700 km s^{-1}. All available evidence indicates that the ejecta have not yet decelerated; if anything, there was a post supernova acceleration of the filaments. To see the effect of such a small initial velocity of expansion on the morphology of the remnant we have repeated the calculations for a slowly expanding remnant and the results are shown in Fig. 2. We see that in this case even after the shell builds up, its surface brightness will be about two orders of magnitude smaller than that of the plerion. A recent lunar occultation observation of the Crab nebula (Agafanov *et al.* 1987) confirms the earlier observations that the spectrum steepens significantly near the outer edge of the nebula. The surface brightness of this steeper spectral component is ~ 1 per cent that of the relatively flat spectrum plerion. This is consistent with the expectations based on Fig. 2.

To summarize, our calculations indicate that bright plerions like the Crab and 3C 58 which show hardly any limb brightening may be the remnants of rather low

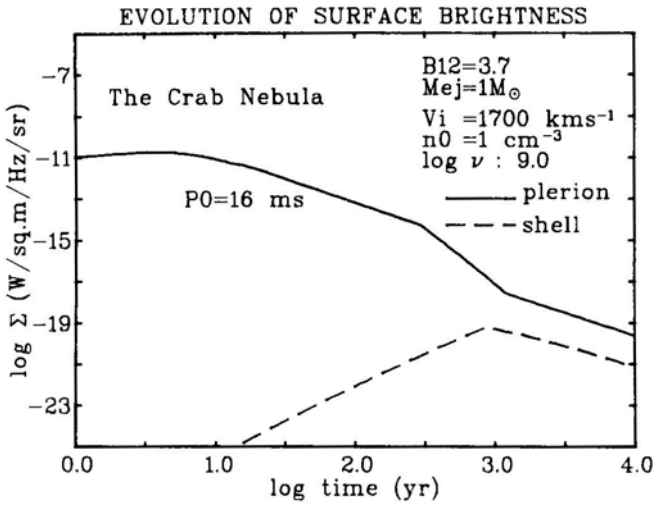

Figure 2. Evolution of the shell and the plerionic components of the Crab nebula, expanding with a small velocity ~ 1700 km s^{-1}. The plerionic component dominates the emission at all times; the maximum contribution of the shell component being ~ 1%, in agreement with recent lunar occultation observations (Agafanov et al. 1987) of the Crab nebula. See caption of Fig. 1 for explanation of legends.

energy Supernovae. The paucity of such objects is consistent with the fact that the estimates of the kinetic energy of the ejecta in most extragalactic Supernovae is $\sim 10^{51}$ ergs, rather than 10^{49} ergs estimated for SN 1054 from the Crab nebula. In view of this, in the remainder of the discussion we shall adopt the standard value of $E_{\rm tot} \sim 10_{51}$ erg.

4. Dependence of the morphology on pulsar parameters

Although the kinetic energy of the ejecta in most Supernovae may be a Standard number, the parameters of the pulsar and the interstellar medium into which the ejecta expand are not. First we will discuss how the morphology of an SNR depends on the properties of the central pulsar.

Even though the Crab pulsar is often taken to be the prototype of young pulsars there is mounting evidence that this may not be so. A careful analysis of the statistics of plerions (Srinivasan *et al.* 1984) and a study of the distribution of the periods and period derivatives of pulsars (Vivekanand & Narayan 1981; Narayan 1987) both suggest that the majority of pulsars may be born with rather long spin periods compared to the Crab pulsar. In addition the distribution of the derived magnetic fields of pulsars reveals a spread of over two orders of magnitude. As was mentioned before, both the initial period and the magnetic field have an important influence on the surface brightness of the plerions produced by the pulsars. This is illustrated in the next two figures. In Fig. 3 the surface brightness of the plerions produced by pulsars with three different initial periods is compared with that of the shell; the blast energy and the density of the interstellar medium are the same as in Fig. 1 (10^{51} erg and 1 atom cm^{-3} respectively). As can be seen, the central nebula produced by a 100 ms pulsar never gets nearly as bright as the shell. Such remnants, once they build up, will have the morphology of a hollow shell. Interestingly, this is nearly true even if the initial period of the pulsar is very small. The nebula produced by a 3 ms pulsar, though very bright initially, will become less luminous than that produced by a 16 ms pulsar. Consequently, the remnant will have a combination morphology with a dominant shell component. The reason for this is that a very fast pulsar deposits most of its energy rather quickly when the size of the cavity is rather small. Because of this the adiabatic losses are more severe and reduce the energy content at late times considerably. Consequently, the luminosity of the plerion is less than that of, for example, a 16 ms pulsar. At lower frequencies the shell will be even brighter relative to the plerion. Thus only when the initial characteristics of the central pulsar are similar to that of the Crab pulsar will the remnant have a hybrid radio morphology with a strong plerionic component. If the initial period of the pulsar is very small, then the pressure of the pulsar bubble will *accelerate* the ejecta, increasing the kinetic energy of expansion. This will result in the shell component being even brighter relative to the plerion.

Fig. 4 shows the evolution of the surface brightness for three different values of the surface magnetic field of the pulsar; the initial period is assumed to be 16 ms for all the pulsars. We see that if the surface magnetic field of the pulsar is very large then at late times the plerion it produces becomes less bright than one produced by a pulsar with a lower magnetic field. Again the basic reason is more severe adiabatic losses at early times. However, if the magnetic field is *very* small then the plerion never builds up to a

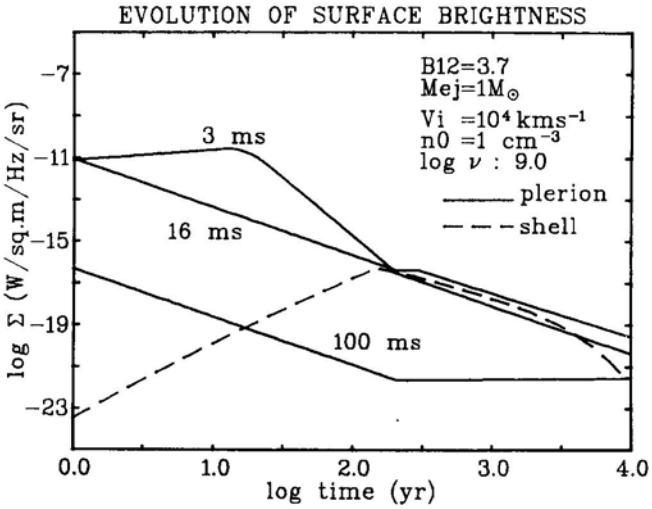

Figure 3. Dependence of the SNR morphology on the initial spin period of the central pulsar. Plerionic components produced by pulsars with initial periods 3, 16 and 100 ms are shown. An ambient density of 1 H atom cm^{-3} has been assumed. The ratio of the surface brightness of the plerion to that of the shell attains a maximum value when the timescale for the ejecta to decelerate matches the initial spindown timescale of the central pulsar. See caption of Fig. 1 for explanation of legends.

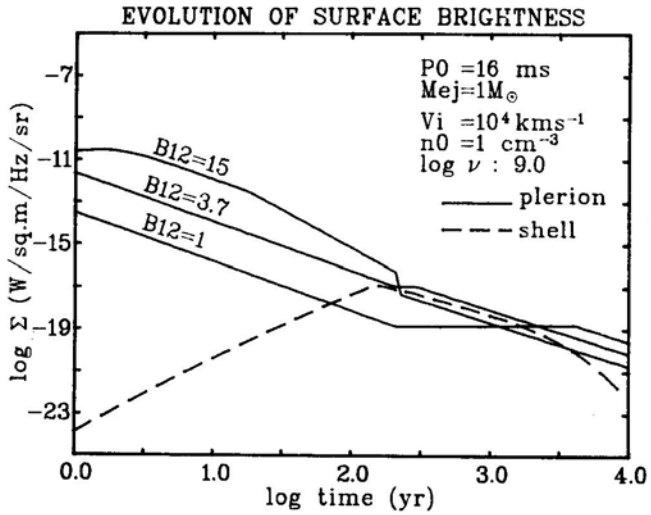

Figure 4. Evolution of the shell and the plerionic component of an SNR for three different values of the magnetic field of the central pulsar. See caption of Fig. 1 for explanation of legends.

high enough surface brightness to compete with the shell. Thus as in the case with different initial periods, the remnant is expected to have a hybrid morphology with a strong plerionic component only if the magnetic field of the central pulsar has a value similar to that of the Crab pulsar ($\sim 4 \times 10^{12}$ G).

The evolutionary model considered above is relevant for the early phase of development of supernova remnants, upto an age of $\sim 10^4$ yr. When the remnant

becomes very old, many other physical processes may significantly influence its morphology. For example, it has been suggested (Shull, Fesen & Saken 1989) that in remnants of age $\gtrsim 10^5$ yr, the pulsar may move and catch up with the decelerated shell, and re-energize it by supplying relativistic particles. The resultant morphology in this case may turn out to be quite complicated, CTB 80 being an example.

5. The role of the interstellar density

One of the major factors determining the evolution of supernova remnants is the density of the ISM into which it expands. Traditionally, in this context it is generally assumed that the particle density of the ISM is of the order of 1 atom cm^{-3}. There is mounting evidence that this not a good assumption.

The standard model of the ISM that emerged from 21 cm observations is the so-called "two component" model in which small cool clouds are in pressure equilibrium with a warm diffuse intercloud medium of density $n_0 \sim 0.3$ cm^{-3} (Spitzer 1978). It is this intercloud medium in which most supernova remnants are assumed to evolve. While the existence of such a warm medium is well established, its filling factor is still very controversial. Recent ultraviolet and X-ray observations (Rogerson *et al.* 1973; Jenkins & Meloy 1974; York 1974; Cowie & Songaila 1986) have revealed the presence of a medium of much lower density and higher temperature ($n_0 \sim 3 \times 10^{-3}$ atoms cm^{-3}, $T \sim 10_6$ K). The existence of such a "Coronal gas" had, in fact, been predicted by Spitzer (1956). According to some authors (*e.g.* McKee & Ostriker 1977) this gas may have a filling factor ~ 70 per cent, but this, too, is very uncertain and controversial. Nevertheless it is important to examine how a supernova remnant will evolve in such a low density medium. It has been poirted out by several authors (Lozinskaya 1979; Srinivasan & Dwarakanath 1982 and several others) that a shell remnant expanding in a low-density medium will turn on later, and its peak luminosity will be smaller compared to one expanding in a denser medium. A low-density ambient medium also has an important effect on the plerion. Since deceleration will set in much later, the adiabatic losses of the energy in relativistic particles and magnetic fields will be severe for much longer.

Quite apart from the coronal gas there are reasons to expect that some fraction of Supernovae with massive progenitors may go off in low-density regions. In recent years it has been established that massive stars lose a significant amount of mass by means of high-velocity stellar winds. Such a stellar wind is expected to excavate a cavity in the original interstellar medium. The interior of such a bubble is likely to have a density ~ 0.01 atom cm^{-3} and its radius can be $\gtrsim 10$ pc (Weaver *et al.* 1977). If such a bubble remains stable till the star eventuall, explodes, then the ejecta will initially expand in a low-density medium before encountering the interstellar medium.

Keeping all this in mind we have repeated the evolutionary calculation for lower values of the ambient density. Fig. 5 shows the model evolution in a stellar wind bubble with the characteristics mentioned above. As expected, the shell emission turns on later, and the peak surface brightness is smaller than that in Fig. 3. In spite of this the plerionic component does not dominate at late times. This is a direct consequence of the free expansion phase lasting longer in a low density medium. This trend will be the same, of course, in the coronal gas.

Fig. 5 also illustrates the fact that at a given age a supernova remnant expanding in a low-density medium is much less bright than its counterpart in a higher-density medium. Consequently, given a detection limit for surface brightness, the lower the ambient density, the shorter will be the observable lifetime of the supernova remnant. This has an important implication for the derived birthrates of the supernova remnants and we will discuss this a little later.

The morphology of a supernova remnant expected under different conditions is briefly summarized in Table 1. As we can see, very fast pulsars produce very bright plerionic nebulae which at late times evolve into shell remnants. Crab-like pulsars, on the other hand, produce long-lived and bright plerions. For standard explosion energies ($\sim 10^{51}$ erg) such plerions are expected to be surrounded by shell components of comparable brightness.

After the shell emission builds up, the relative contrast between the brightness of the shell and that of the plerionic component (and hence the final morphology of the SNR) is not as strongly dependent on the ambient density as the surface brightness itself is. The highest value of $\Sigma_{\rm plerion}/\Sigma_{\rm shell}$ obtains when the initial spindown timescale τ_0 of the central pulsar roughly equals the deceleration timescale t_0, which is different in different media. If the central pulsar is fast, and if the remnant is expanding in a low-density medium, the shell component will become more dominant at late times. However, since in a low-density medium the lifetime of a supernova remnant is small, and the shell turns on later, this late phase of evolution will be detectable only for a short time; consequently for most of its lifetime the remnant will have a plerionic appearance. It seems therefore that while a shell or a combination morphology of a supernova remnant may be expected under a wide variety of circumstances, there appear to be only two ways to make a purely plerionic nebula: either the kinetic energy of expansion must be very low—like in the Crab nebula, or the ambient medium must

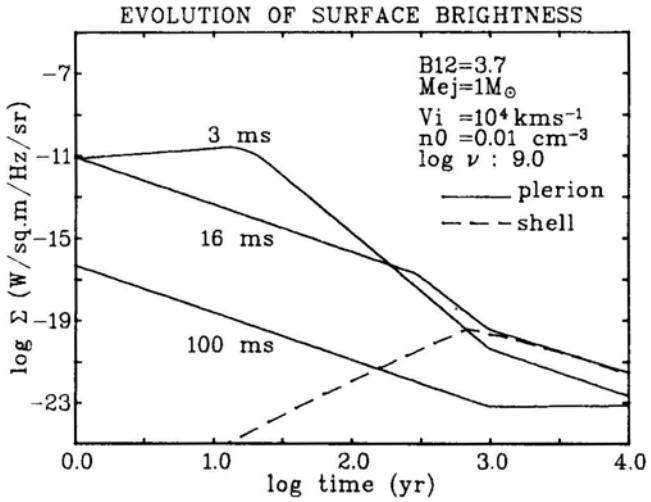

Figure 5. Same as Fig. 3, but for an ambient density of 0.01 H atom cm^{-3}, appropriate for a stellar wind bubble. The shell emission turns on later, and reaches a smaller peak surface brightness than in Fig. 3. Yet the plerionic component does not dominate at late times because of the prolonged phase of free expansion during which adiabatic losses are severe. See caption of Fig. 1 for explanation of legends.

Table 1. SNR morphology expected under different conditions.

Pulsar's initial spin		Strong Explosion $E_{tot} \sim 10^{51}$ erg	Weak Explosion $E_{tot} \sim 10^{49}$ erg
Fast	($P_0 \lesssim 5$ ms)	Very bright plerion ⇒ Shell	"Pulsar-driven" bright plerion⇒ shell
Medium	($P_0 \sim 20$ ms)	Bright plerion ⇒ combination	Bright plerion
Slow	($P_0 \sim 100$ ms)	Weak plerion ⇒ shell	Weak plerion ⇒ combination

have a very low density, which will keep the morphology "plerionic" for most of the detectable lifetime of the SNR. Of course, the characteristics of the central pulsar must be appropriate for producing a strong plerionic component.

6. Discussion

We wish to illustrate a few specific cases where the morphology and the surface brightness (or the limit to it) of supernova remnants seem to be best understood in terms of their evolution in media of low density.

6.1 *Absence of SNRs around Young Pulsars*

In a recent high frequency survey by Clifton & Lyne (1986) three pulsars with spindown ages ~ 20,000 yrs were discovered (PSR1737–30, PSR1800–21, and PSR 1823–13). A subsequent sensitive search with the VLA for supernova remnants around these pulsars have placed stringent upper limits on the surface brightness of possible emission surrounding these pulsars (Braun, Goss & Lyne 1989). Using our simple model it is possible to estimate the expected surface brightness of the supernova remnants around these pulsars for different values of the ambient density. We find that in all the three cases the limit of the surface brightness set by the VLA observations can be reconciled only if the ambient density is assumed to be less than or equal to 0.01 atom cm^{-3}, for standard values of the explosion energy.

6.2 *The Supernova Remnant MSH 15-52*

Another likely case of evolution in a tenuous medium is that of the supernova remnant MSH 15–52. This remnant harbours a pulsar (PSR 1509–58) with a spindown age of ~ 1600 years, but has a rather large diameter (~ 30 pc). The standard "Sedov" age of the SNR is ~ 10^4 yr (Seward *et al.* 1984). In radio the remnant has the morphology of a hollow shell, but there is a bright X-ray plerion surrounding the pulsar. The relevant properties of this SNR are listed in Table 2.

Table 2. Properties of SNR MSH 15–52.

		Ref.
Angular Diameter	: 30 arcmin	1
Flux (1 GHz)	: 70 Jy	2
Σ of the shell region	: 8×10^{-20} W m^{-2} Hz^{-1} sr^{-1} at 1 GHz	1
Distance	: 4.2 kpc	3
X-ray luminosity of the plerion	: 5×10^{16} erg s^{-1} Hz^{-1} at 4 keV	4
PSR 1509–58		
Period	: 150 ms	5
Period derivative	: 1.54×10^{-12} s s^{-1}	5
Derived Magnetic Field	: 1.5×10^{13} gauss	
Spindown age	: 1600 yr	

References:
1 Caswell, Milne & Wellington 1981
2 Weiler 1983
3 Caswell, Murray, Roger, Cole and Cooke 1975
4 Seward, Harnden, Szymkowiak and Swank 1984
5 Weisskopf et al. 1983

Different explanations offered for the discrepancy between the apparent ages of the pulsar and the supernova remnant include:

1. chance superposition of the pulsar on the supernova remnant (van den Bergh & Kamper 1984),
2. late turn-on of a ~ 10^4-year-old neutron star as a pulsar due to magnetic field growth (Blandford, Applegate & Hernquist, 1983), and
3. a fast expansion of the SNR to its presently observed size in ~ 1600 years (Srinivasan, Dwarakanath & Radhakrishnan 1982; Seward *et al.* 1984).

The last alternative requires a low ambient density around the supernova. This is, in fact, quite likely since this SNR is in the vicinity of a complicated OB association indicating that the progenitor of the supernova might have been a massive star with a strong stellar wind, which could have created a large low-density bubble around itself.

We wish to argue that all the gross properties of this supernova remnant are consistent with the hypothesis that it initially expanded in a low-density stellar wind bubble. If the density of the external medium is 0.01 cm - ^{3}, then the observed size of the remnant can easily be reconciled with an age ~ 1600 years if the mass ejected was ~ 2 $M_\odot$ and the initial expansion velocity ~ 12000 km s^{-1}. The expected surface brightness of the shell is also consistent with this choice of initial parameters (see Fig. 6). What remains to be explained is why there is no detectable radio plerion although there is a fairly luminous X-ray plerion. As has been argued before, the clue resides in the initial rotation period of the pulsar. We see from Fig. 7 that the observed X-ray luminosity can be well understood if the initial period was ~ 6 ms. Given such a fast pulsar in a rapidly expanding cavity the low radio surface brightness of the plerion is to be expected. As can be seen from Fig. 6, the expected radio surface brightness will be < 10^{-23} Wm^{-2} Hz^{-1} sr^{-1}, well below the level of detectability. Of course, given that this is a very-high-field pulsar, even a somewhat slower pulsar will produce a weak radio plerion (see Fig. 4). Therefore, in our opinion, the only reasonable way to

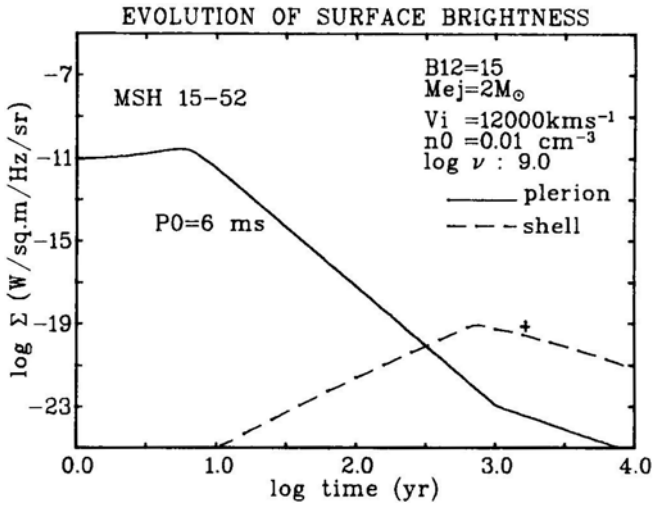

Figure 6. A model evolution of the shell and the plerionic components of the supernova remnant MSH 15–52. It is assumed that the remnant is expanding in a stellar wind bubble. The observed value of Σ is shown by a " + " mark. See caption of Fig. 1 for explanation of legends

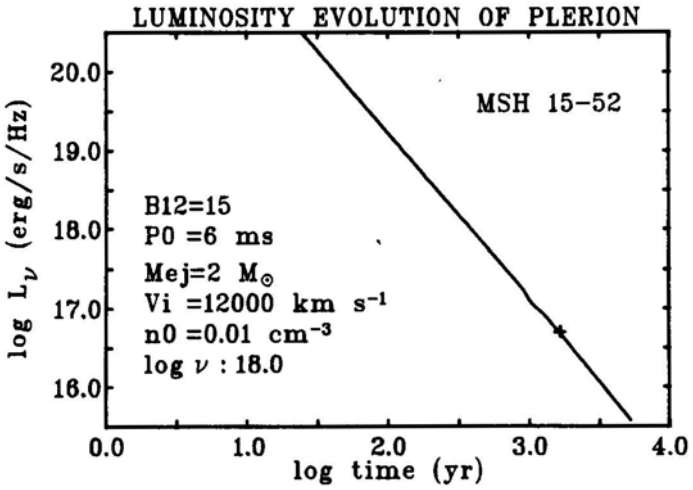

Figure 7. A model evolution of the X-ray luminosity of the plerionic component of the supernova remnant MSH 15–52. The observed X-ray luminosity is indicated by the " + " mark. See caption of Fig. 1 for explanation of legends.

reconcile a bright X-ray plerion and the absence of a radio plerion is to invoke an initial rapid expansion phase.

7. Conclusions

The important points that emerge from the above discussions are:

1. In many cases the morphology of a SNR harbouring a pulsar is likely to be that of a hollow shell. Indeed, the conditions in which a detectable plerionic component is

expected are quite restricted. Thus, the hope that the presence of a pulsar in a SNR should be revealed by means of the plerion it creates (Radhakrishnan & Srinivasan 1980) may, in most cases, not be realized in practice. An immediate implication of this is the following.

2. A good fraction of shell SNRs may, in fact, have pulsars in them, and more and more of them will be classified as combination remnants as the dynamic range of the observations improve in the future.

3. The SNR Birthrate: An obvious implication of the above is that the birthrate of shell SNRs must be nearly equal to the pulsar birthrate, if not more. There has been a long-standing controversy in this regard. While the present estimate of the pulsar birthrate is about one in ~ 40 years (see, *e.g.* Narayan 1987), the "standard" estimate of SNR birthrate is one in ~ 80 years (Clark & Caswell 1976).

A possible resolution of this disagreement is suggested by another important point raised in the above discussion. We have seen that in some cases the observed characteristics of supernova remnants have to be understood in terms of the ambient medium being of rather low density. It has also been argued that in a good fraction of cases a supernova is expected to go off in a low-density medium, namely, the interior of a stellar wind bubble created by the progenitor star. Some SNRs should also evolve in the very tenuous coronal gas.

As has been discussed by many authors (*e.g.* Lozinskaya 1979; Higdon & Lingenfelter 1980; Tomisaka, Habe and Ikeuchi 1980; Srinivasan and Dwarakanath 1982), and also pointed out above, a low ambient density significantly reduces the detectable lifetime of a supernova remnant, and appropriate allowance has to be made for this in deriving the birthrate of SNRs. This can be done in the following manner (see Lozinskaya 1979). If f_w and f_c represent the "filling factors" of the "warm" medium (of density ~ 0.3 atom cm^{-3}) and the coronal gas (of density ~ 3×10^{-3} atom cm^{-3}) respectively ($f_w + f_c = 1$), and f_b represents the fraction of SNRs expanding in stellar wind bubbles, then the inverse birthrate τ_{SNR} would be given by:

$$\tau_{SNR} = [f_b t_b + (1 - f_b)(f_w t_w + f_c t_c)]/N_{SNR}$$

where N_{SNR} is the number of shell SNRs (since most of the evolved remnants are expected to have a shell morphology) detected above a certain limit of surface brightness, and t_w, t_c and t_b are the "lifetimes" of these SNRs above this level of surface brightness in the corresponding media. According to Clark & Caswell (1976), the sample of galactic supernova remnants is reasonably complete above a surface brightness $\Sigma = 10^{-20}$ W m^{-2} Hz^{-1} sr^{-1} at 408 MHz. Their catalogue contains 71 shell SNRs above this limit. Using our models, we estimate the lifetimes t_w and t_b above this limit to be ~ 5300 yr and ~ 850 yr respectively. A supernova remnant evolving in the coronal gas would never become brighter than this limit, and the value of t_c can be taken to be zero. If the fraction of SNRs evolving in stellar wind bubbles is insignificant, *i.e.* $f_b \simeq 0$, then the inverse birthrate τ_{SNR} derived from the above expression lies in the range 76–23 yr for a corresponding range of 0–70 per cent for the filling factor f_c of the coronal gas. On the other hand, if we assume that ~ 50 per cent SNRs evolve in stellar wind bubbles, for example (*i.e.* $f_b \sim 0.5$), then τ_{SNR} will lie in the range 43 to 17 yr for f_c in the above range.

Acknowledgements

The author would like to thank R, A. Chevalier for his comments on the manuscript. This paper is based on a part of the doctoral thesis submitted to the Indian Institute of Science, Bangalore. Some of the above results were presented at the 1988 Bad Honnef workshop on "Supernova Shells and Their Birth Events" (Srinivasan & Bhattacharya 1988).

References

Agafanov, M. I., Aslanyan, A. M., Gulyan, A. G., Ivanov, V. P., Martirosyan, R. M., Stankevich, K. S., Stolyarov, S. P.,1987, *Sov. Astr.,* **31**, 31.
Bandiera, R., Pacini, F., Salvati, M., 1984, *Astrophys. J.,* **285**, 134.
Bhattacharya, D., 1987, *Ph. D. Thesis,* Indian Institute of Science, Bangalore.
Blandford, R. D., Applegate, J. H., Hernquist, L., 1983, *Mon. Not. R. astr. Soc,* **204**, 1025.
Braun, R., Goss, W. M., Lyne, A. G., 1989, *Astrophys. J.,* **340**, 355.
Braun, R, Gull, S. F., Perley, R. A., 1987, *Nature,* **327**, 395.
Caswell, J. L, Milne, D. K., Wellington, K. J., 1981, *Mon. Not. R. astr. Soc,* **195**, 89.
Caswell, J. L., Murray, J. D., Roger, R. S., Cole, D. J., Cooke, D. J., 1975, *Astr. Astrophys.,* **45**, 239.
Clark, D. H., Caswell, J. L, 1976, *Mon. Not. R. astr. Soc,* **174**, 267.
Clifton, T. R., Lyne, A. G., 1986, *Nature,* **320**, 43.
Cowie, L. L., Songaila, A., 1986, *Ann. Rev. Astr. Astrophys.,* **24**, 499;
Cowsik, R., Sarkar, S., 1984, *Mon. Not. R. astr. Soc,* **207**, 745.
Fabian, A. C, Brinkmann, W., Stewart, G. C, 1983, in: IAU Symposium 101: *Supernova Remnants and their X-ray Emission,* eds. J. Danziger and P. Gorenstein, D. Reidel, Dordrecht, p. 119.
Green, D. A, 1988, *Astrophys. Sp. Sci.,* **148**, 3.
Gull, S. F., 1973, *Mon. Not. R. astr. Soc,* **161**, 47.
Gull, S. F., 1975, *Mon. Not. R. astr. Soc,* **171**, 237.
Higdon, J. C, Lingenfelter, R. E., 1980, *Astrophys. J.,* **239**, 867.
Jenkins, E. B., Meloy, D. A., 1974, *Astrophys. J.,* **193**, L121.
Lozinskaya, T. A., 1979, So*v. Astr.,* **23**, 506.
Lozinskaya, T.A.,1980, *Sov. Astr.,* **24**, 407.
McKee, C. F., Ostriker, J. P., 1977, *Astrophys. J.,* **218**, 148.
Narayan, R., 1987, *Astrophys. J.,* **319**, 162.
Pacini, F., Salvati, M., 1973, *Astrophys. J.,* **186**, 249.
Radhakrishnan, V., Srinivasan, G., 1980, *J. Astrophys. Astr.,* **1**, 25.
Radhakrishnan, V., Srinivasan, G., 1983, in: IAU Symposium 101: *Supernova Remnants and their X-ray Emission,* eds. J. Danziger and P. Gorenstein, D. Reidel, Dordrecht, p. 421.
Reynolds, S. P., Chevalier, R. A., 1984, *Astrophys. J.,* **278**, 630.
Rogerson, J. B., Spitzer, L., Drake, J. F., Dressler, K., Jenkins, E. B., Morton, D. C, York, D. G., 1973, *Astrophys. J.,* **181**, L97.
Scott, J. S., Chevalier, R. A, 1975, *Astrophys. J.,* **197**, L5.
Seward, F. D., Harnden, F. R., Szymkowiak, A., Swank, J., 1984, *Astrophys. J.,* **281**, 650.
Shklovskii, I. S., 1980, *Publ. Astr. Soc Pacific,* **92**, 125.
Shull, J. M., Fesen, R. A., Saken, J. M., 1989, *Astrophys J.,* **346**, 860.
Spitzer, L., 1956, *Astrophys. J.,* **124**, 20.
Spitzer, L., 1978, *Physical Processes in the Interstellar Medium,* Wiley, New York.
Srinivasan, G., Bhattacharya, D.,1988, in: *Supernova Shells and their Birth Events,* ed. W. Kundt, Springer-Verlag, p. 15.
Srinivasan, G., Bhattacharya, D., Dwarakanath, K. S., 1984, *J. Astrophys. Astr.,* **5**, 403.
Srinivasan, G., Dwarakanath, K. S., 1982, *J. Astrophys. Astr.,* **3**, 351.
Srinivasan, G., Dwarakanath, K. S., Radhakrishnan, V., 1982, *Curr. Sci,* **51**, 596.

Tomisaka, K., Habe, A., Ikeuchi, S., 1980, *Prog. Theor. Phys.,* **64**, 1587.
van den Bergh, S., 1988, *Astrophys. J.,* **327**, 156.
van den Bergh, S., Kamper, K. W., 1984, *Astrophys. J.,* **280**, L51.
van den Bergh, S., McClure, R. D., Evans, R., 1987, Astrophys. *J.,* **323**, 44.
Vivekanand, M., Narayan, R., 1981, *J. Astrophys. Astr.,* **2**, 315.
Weaver, R., McCray, R., Castor, J., Shapiro, P., Moore, R., 1977, *Astrophys. J.,* **218**, 377.
Weiler, K. W., 1983, in IAU Symp. 101: *Supernova Remnants and their Xray Emission,* ed. P. Gorenstein and J. Danziger, D. Reidel, Dordrecht, p. 299.
Weiler, K. W., Sramek, R. A., 1988, *Ann. Rev. Astr. Astrophys.,* **26**, 295.
Weisskopf, M. C, Elsner, R. F., Darbro, W., Leahy, D., Naranan, S., Sutherland, P. G., Grindlay, J. E., Harnden, F. R., Seward, F. D., 1983, *Astrophys. J.,* **267**, 711.
York, D. G., 1974, *Astrophys. J.,* **193**, L127.

J. Astrophys. Astr. (1990) **11**, 141–150

Scope of High-Frequency Time Keeping in Searches for Short-Period Gamma-Ray Sources

M. L. Sapru, A. K. Tickoo, I. K. Kaul, S. K. Kaul, C. L. Bhat,
R. K. Kaul, H. S. Rawat, V. K. Senecha, R. C. Rannot & H. Razdan
Bhabha Atomic Research Centre, Nuclear Research Laboratory, Srinagar 190006, Kashmir

Received 1989 July 25; accepted 1989 December 9

Abstract. This paper presents a novel technique to derive the absolute time of occurrence of an event with an accuracy of < 200 μs by adapting the HF time synchronization technique to correct for the aging rate and the frequency drift of a temperature-controlled quartz frequency standard. The propagation delay suffered by the HF time signals has been estimated by monitoring the clock error with respect to time signals from five broadcast stations located at distances in the range 500–3700 km from Gulmarg. Using simulated data, we further show the viability of this technique in permitting periodicity searches on timescales of $\geqslant$ 5 milliseconds in cosmic gamma-ray data.

Key words: time keeping—gamma-ray sources—atmospheric Cerenkov technique

1. Introduction

The atmospheric Cerenkov technique (Jelly 1967; Weekes 1988) provides the only viable method of studying very high energy γ rays (10^{11} –10^{13} eV) from celestial objects, inspite of the constraint of a low duty cycle ($\leqslant$10 per cent) imposed on this technique by the need to operate on clear, moonless nights. However, the gray signals are quite weak in this energy range, corresponding to a flux of typically < 1 photon m^{-2} $week^{-1}$, and the sensitivity of most of the present generation γ-ray telescopes is such that long exposure spells, of upto a few months per source, are generally required to retrieve a d.c. signal with a good statistical significance. In addition, while searching for bursts of γ-ray emission, a supplementary stipulation, apart from good counting statistics, is to seek a near simultaneity of the cosmic event at two or more suitably separated geographical locations, which requires timing the event aboslute epoch to at least tens of milliseconds accuracy. Likewise, in case of periodic sources like pulsars and X-ray binary systems, the otherwise long signal recovery time can be substantially decreased by folding the event arrival times with the characteristic rotation/orbital period of the candidate source and performing a phase analysis (or a Rayleigh power test where the exact source period is unknown). Here the source emission appears as a significant enhancement in one or a few phase bins over the otherwise large albeit phase-uniform, cosmic-ray-produced background events. Such a data-folding operation again demands very accurate time keeping so as to

prevent phase wandering and consequent smearing of the phase distribution of the signal photons. Quantitatively, the accuracy in time, Δt, needed to allow the folding of a dataset of duration t seconds, is related to the source period p by

$$\Delta t/t = (p/t)\Delta\phi \tag{1}$$

where $\Delta\phi$ is the desired width of the phase bin. Thus, for a generally preferred value $\Delta\phi$ = 0.1, for example, the time accuracy required for a 120 day data sample is only ~ 1.6 $\times 10^{-4}$ s s^{-1} for a signal modulated at the 4.8 h orbital period of Cygnus X-3 but ~ 10^{-10} s s^{-1} for the suggested pulsar period of ~ 12.6 ms in this system (Chadwick *et al.* 1985).

A time accuracy of the order of ~ 10_{-10} ss^{-1} demands the use of atomic time standards but they are difficult to maintain and expensive to replace. The general practice, therefore, is to use temperature-controlled crystal oscillators as local frequency standards and to regularly correct for frequency drift and aging of the oscillator by slaving the clock to more accurate time-markers provided by satellite timing receivers (Putkovich 1981; Jain *et al.* 1981), TV synchronization systems (Kovacevic *et al.* 1981; Lake 1981) and high frequency time signals. The first two techniques are favoured by some g-ray astronomers (Ramana Murthy 1981; De Jager *et al.* 1988) as they are rather straightforward to implement and lead to a higher accuracy in absolute time ($\leqslant 30\mu$s). However, both the methods are comparatively expensive and suffer from the disadvantage of not being as universally available as the HF timing transmissions. As the HF transmission is generally received via the ionospheric F layer(s), the accompanying time markers are subject to two important uncertainties, undermining the precision of synchronization. One source of uncertainty is the short-term amplitude fading (Bhat *et al.* 1981a) which leads to a large second-to-second time jitter in the arrival of the time markers themselves. The second type of uncertainty is in the determination of propagation delay of the transmission between the transmitter and the receiver. This relatively long-term effect is a function of the user location, season, time of the day and the mode of propagation and sets the ultimate limit on the accuracy of the derived absolute time information.

In the present communication, we show that, notwithstanding these uncertainties, it is feasible to adapt the HF time synchronization technique to adequately correct for the frequency drift and aging rate of a crystal oscillator over indefinitely long periods of time and also to derive absolute time information accurate to within 200 μs. Using simulated periodic data, we further demonstrate the viability of this simple and economical synchronization technique in permitting period searches down to the millisecond time-scale and thus allow to carry out γ–ray astronomy of a majority of short period sources from such good astronomical sites as may not fall within the range of timing satellites or the TV synchronization method.

2. Experimental details

High frequency timing transmissions broadcast at 10 and 15 MHz from ATA (New Delhi) and RWM (Moscow) have been regularly used over the years at Gulmarg, India, for a variety of scientific purposes (Bhat *et al.* 1980; Bhat 1982). The latest experiment to incorporate this synchronization facility is the Gulmarg γ-ray telescope (Koul *et al.* 1989) which has been recently commissioned to study point γ-ray sources

at TeV energies (1 TeV = 10^{12} eV) through the atmospheric Cerenkov technique. The atmospheric Cerenkc events result from the optical Cerenkov light released in the terrestrial atmosphere. This generally follows the incidence at the top of atmosphere of a very high energy cosmic-ray particle but in < 1–2 per cent cases that of a γ–ray photon from a cosmic source (Kaul 1987). The telescope is provided with a temperature-controlled crystal clock to time the onset of each registered event with a resolution of 1 μs. The time synchronization circuit used at Gulmarg has been discussed in detail earlier (Bhat, Kaul & Yadav 1981b) and we only outline here the essential features. The reference time-markers are tapped from the audio-frequency section of a communication receiver and, after amplitude discrimination against extraneous noise, are suitably shaped to yield a TTL-compatible rectangular pulse with a rise-time of $\leqslant$ l00 μs and a frequency of 1 Hz. The markers derived thus, over periods of upto 10 minutes on a given day, are used to repeatedly interrogate the latches of the Gulmarg clock and the resulting timing data are stored on a personal computer to infer the clock error $\varepsilon(t)$ at the time of the synchronization.

Fig. 1 shows a typical frequency distribution of $\varepsilon(t)$ plotted as deviations from the sample mean error $\langle\varepsilon\rangle$ in units of the corresponding standard deviation σ. A total of 15 samples, each only ~ 10 minutes long and having typically ~ 100 events, are superposed to obtain a correct perspective of the nature of distribution. The appreciable dispersion of $\varepsilon(t)$, seen in Fig. 1, cannot be due to the frequency drift and aging of the local clock oscillator because of the limited duration of individual data samples (~ 10 minutes). On the contrary, its main cause is the short-term jitter in the arrival of reference time-markers themselves. As the distribution of the error is in reasonable accord with a Gaussian distribution, it presumably arises from random modulations, like fading, suffered by the HF transmission while propagating through

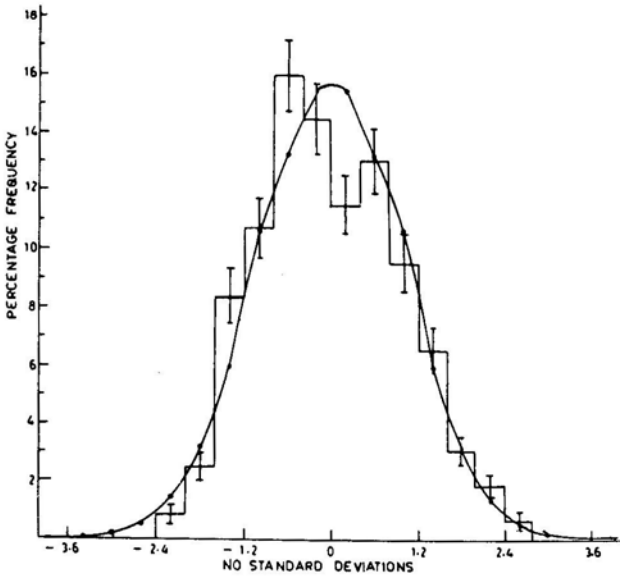

Figure 1. A typical frequency distribution of clock error plotted as deviations from the sample mean error. The histogram represents the observed distribution while the continuous curve shows the expected Gaussian fit to the observed distribution.

the ionosphere (Bhat *et al.* 1981a). The sample mean value is essentially free of this short-term jitter because of the symmetrical nature of the distribution and therefore represents the most probable value of the clock error at the time of synchronization.

During the period of monitoring of the clock error, the timing data are recorded in the above discussed manner on various days at around the same local time so as to keep to a minimum the effects on $\varepsilon(t)$ of possible longterm variations in the ionospheric conditions. Finally the sample mean error $\langle\varepsilon(t)\rangle$ is determined for each individual day alongwith the corresponding standard deviation.

3.1 *Correction for Oscillator Drift and Aging*

Fig. 2 displays the long-term behaviour of $\langle\varepsilon(t)\rangle$ during 2 different observation spells, viz., 1987 July-August and 1988 October-December, for a minimum of ~ 20 days during each period. The error bars attached to each data point represent the above-mentioned $\pm\ 1\sigma$ standard deviation values for the daily sample of $\varepsilon(t)$. We can represent $\varepsilon(t)$, the clock error at a given time t, by the following expression,

$$\varepsilon(t) = \varepsilon_0 + a\,t + 1/2\,bt^2. \tag{2}$$

Here e_0 is the initial clock time offset (but does not include correction for the propagation delay suffered by the reference time markers); $a = \Delta f/f$ *is* the frequency offset and *b,* the aging rate of the oscillator. The broken lines in Fig. 2 represent the best parabolic fits to the experimental data of the form given by Equation (2) and are obtained by the method of least squares. The excellent agreement observed with the expectation is reassuring and the resulting values of ε_0, a and b are listed in Table 1 for the two observation epochs alongwith the 1σ uncertainty limits in predicting $\varepsilon(t)$. Using these values of ε_0, a and b, the clock error due to oscillator frequency drift and

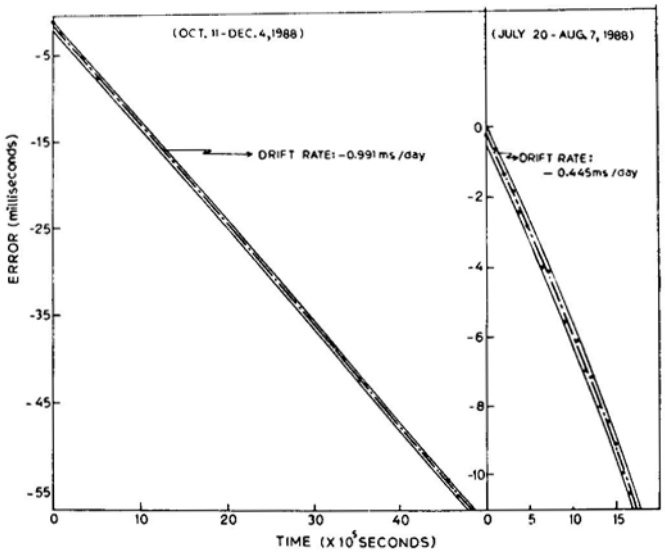

Figure 2. Long term behaviour of the clock error for the two different observation epochs. The $\pm\ 1\sigma$ error bands are also shown for both the fits.

Table 1. Initial offset, drift rate and aging rate.

Observation period	ε_0 μs	Drift rate a $\mu s\, s^{-1}$	Aging rate b $\mu s\, s^{-2}$
1987 July/Aug	−235.09	-0.5153×10^{-2}	-0.1153×10^{-8}
Standard deviation in $\varepsilon(t) = 167\,\mu$s			
1988 Oct/Nov	−1373.37	-0.1147×10^{-1}	-0.1099×10^{-10}
Standard deviation in $\varepsilon(t) = 215\,\mu$s			

aging rate can be computed and the time of registration of a Cerenkov event can be determined with a relative accuracy of ± 150 μs at any time during a given observation spell. It may be mentioned here that a study of the long-term behaviour of the clock-oscillator for six different epochs during the period extending from 1987 July to 1989 February, has shown a systematic variation in the drift rate with time. This is clearly seen in Fig. 3 in which we have plotted the drift rate as a function of the measurement epoch. It is observed that this variation in the drift rate, which essentially arises from the aging of the crystal oscillator, varies linearly with time as expected.

3.2 *Correction for Propagation Delay*

We note that, although using a portable atomic clock provides a more accurate and straightforward option for determining the propagation delay, it could not be done for the Gulmarg clock because of the non-availability of such a time standard. For this purpose we monitored the error of the Gulmarg clock on 4 consecutive days (1988 January 10–13), with respect to time-markers from ATA (New Delhi), RCH (Tashkent), RID (Irkutsk), BPM (China) and RWM (Moscow). These stations are situated at crow-flight distances of 650 km, 924 km, 3115 km, 3212 km and 3663 km respectively from Gulmarg. As in the normal course, the clock error with respect to each station was monitored ~ 100 times in quick succession (5–10 minutes each) and the sample mean errors with respect to individual stations determined. The time signals from BPM (China) could be monitored only on two days due to poor reception conditions.

As already explained, the errors contain contributions from initial offset, frequency drift and aging rate of oscillator as well as propagation delay. In order to separate the contribution to the clock error due to the local frequency standard, we find the difference between $\varepsilon(t)$ recorded on the last 3 days with respect to the corresponding error for January 10. These differences lead to a drift rate of $-\ 0.7722 \times 10^{-2}$ μs s^{-1}, which is in excellent agreement with its value derived independently for RWM (Section 3.1) and is shown by the encircled point in Fig. 3. Using this value of the drift rate, the errors recorded on the different days from all the five stations have been corrected for frequency drift and contain contributions from initial offset and propagation delay alone. We now proceed to account for these two contributions in the following manner.

Assuming a mirror-type reflection of the HF time signals from a thin, single-layer ionosphere at an effective reflection height $h/2$, the propagation delay suffered by the

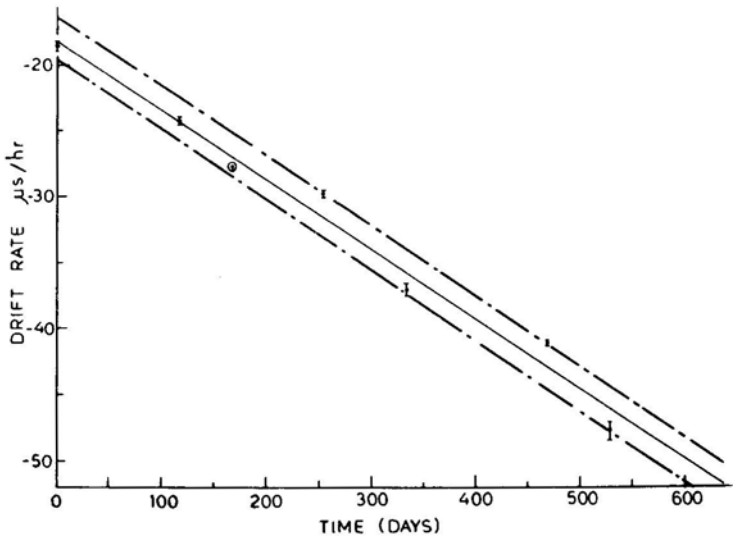

Figure 3. Variation of drift rate with time during the period 1987 July–1989 February. Note the ± 1σ error band for the straight line fitted to the data.

time-markers in reaching the Gulmarg clock from a transmitter separated by a crow-flight distance x_i is given by,

$$(T_i - t_0) = 1/c(x_i^2 + h^2)^{0.5} \tag{3}$$

where T_i is the total clock error expected and t_0, the initial clock offset. The term on the right-hand side represents the propagation delay expected on the basis of the above model and a one-hop propagation mode. If t_i is the experimentally observed error for the station at the distance x_i, we expect

$$\Sigma(T_i - t_i)^2 = \Sigma[t_0 + 1/c(x_i^2 + h^2)^{0.5}]^2 - t_i^2 \tag{4}$$

to be minimum if the experimental data conform to the hyperbolic fit represented by Equation (3).

Using a base value of $h/2$ = 200 km for the effective reflection height, we have altered it progressively in small steps and used a successive approximation method to minimize the above expression for each of the five stations for which we have data. This leads to the most probable value of 228 km for the effective height of the reflection layer and – 5694.5 μs for the initial clock offset for the period 1988 January 10–13. Using this value for t_0, the propagation delay (T_i – t_0) for the five stations can be determined. The resulting values of the propagation delay (Table 2) are plotted as a function of receiver-transmitter distance x_i in Fig. 4 alongwith the best hyperbolic fit to the data. The scatter in the plotted values on a day-to-day basis sets the ultimate limit on predicting accurately the propagation delay for a given transmission. In our case, it is found to vary between 64.3 μs and 451.5 μs. The scatter observed for RWM (Moscow) has a low value of only 96.7 μs which is due to the distinctly better quality of reception of these time signals at Gulmarg.

We note that the propagation delay values obtained here closely match with earlier predictions (Morgan 1959) for a one-hop propagation mode. This means that other

Table 2. Propagation delay as a function of transmitter distance.

Date	Observed propagation delay $(T_i - t_0)$ μs				
1988 January	ATA 651 km	RCH 924 km	RID 3115 km	BPM 3212 km	RWM 3663 km
10	2631.1	3098.3	11032.5	—	12123.8
11	2853.4	3011.6	10840.0	10958.6	12185.5
12	2898.1	3127.7	10488.3	—	12365.2
13	3264.9	2968.5	10507.6	10935.5	12135.7
Mean	2911.9	3051.3	10717.1	10947.1	12202.5
σ	±227.6	±64.3	±229.6	±16.8	±96.7
Expected propagation delay (μs)	2649.7	3436.5	10493.5	10814.9	12303.1

Value for t_0 is –5694.484 μs.

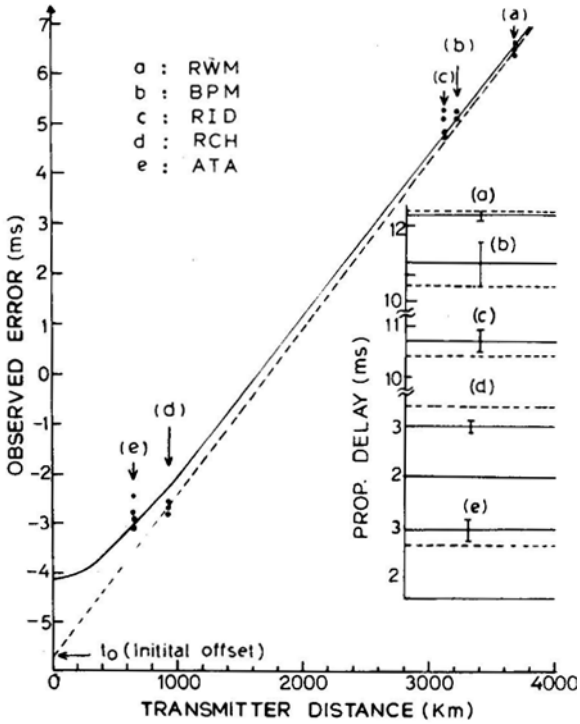

Figure 4. The observed clock error as a function of distance; the solid curve represents the best hyperbolic fit to the errors and the dotted line is the asymptote to the hyperbola meeting the ordinate at the value of initial time off-set in the clock. Inset shows the observed (full line) and the expected (broken line) propagation delays for each station.

users may directly refer to Morgan's charts for estimating propagation delay for their transmitter-receiver distances. The maximum uncertainty in this estimate can be upto 500 μs on account of the need to guess a proper value for the reflection height. However, the corresponding uncertainty in the case of Gulmarg clock, with appropriate corrections for frequency drift, aging rate and propagation delay as described above, turns out to be only ~ 180 μs.

4. Application to short-period source searches

In a search for periodic signals from potential γ-ray sources, several different statistical techniques, including phasogram analysis, Rayleigh power analysis, Z_n^2 test and Protheroe statistic have been employed. Among all these methods the phase histogram technique, involving binning of timing data into various phase bins associated with a source of given period, is more popular. This method is, therefore, used here to illustrate that for an absolute time accuracy of ~ 180 ps possible by slaving the Gulmarg clock to RWM (Moscow) it should be feasible to limit phase uncertainty to within 10 per cent of period or, equivalently, to within 1 bin in the customary 10-bin phasogram, even while dealing with sources with periods down to a few ms. We carried out a simple simulation study to verify this inference. A selection of ~ 1057 RWM timing pulses, out of a total of 4000 markers received between 1988 March 24–April 29, were randomly picked to mimic events from a cosmic source whose period remains essentially unchanged over indefinitely long periods. In view of the known large

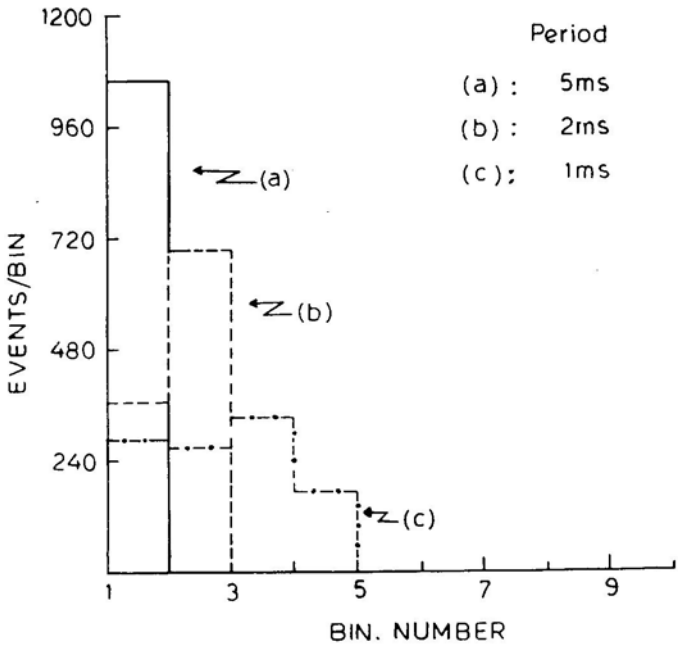

Figure 5. Phasograms derived from the simulated data. The three phase-histograms refer to representative trial periods of 5 ms (a), 2 ms (b) and 1 ms (c) respectively. For trial periods > 5 ms, the phase-histogram is expected to be identical to that shown in (a).

Second-to-second jitter that these markers can suffer in the ionosphere (unlike periodic events of cosmic origin), the selection was made randomly out of those markers for which the predicted clock error ε was within ± 150 μs of the corresponding sample mean value ⟨ε⟩. This is comparable with the error in predicting the absolute event time using RWM and will thus enable to give a realistic measure of phase smearing in our case. The times of registration of these selected events were duly corrected for. the clock error by using appropriate values for ε_0, a and b for the period 1988 March 24–April 29, and also for the propagation delay by referring to Table 2. The resulting time series was subjected to a phasogram analysis by using the relation

$$\phi(t) \sim (t - t_0)/p \tag{5}$$

where $\phi(t)$ is the phase of the event registered at the absolute time t as obtained above, t_0 is the time of arrival of the first event used in the analysis and p is the desired trial period. As the time-markers involve a basic period of 1 s, submultiple values of this period were assigned to p and 10-bin phasograms derived every time. Fig. 5 shows a selection of the resulting phasograms. For all periods down to 5 ms, all the events are found to line up in the same phase bin and, as expected, no phase-wandering is noticed. On the contrary, for trial periods p = 2 ms and l ms, the events are found to be distributed in two and four adjacent bins of a 10-bin phasogram respectively, which is indeed due to a residual error of ~ 200 μs in predicting absolute time. This simulation study thus clearly demonstrates that period searches down to 5 ms can be reliably made using the HF technique without running the risk of any phase smearing.

5. Conclusions

HF time synchronization technique offers a simple and economical way of predicting absolute time to an accuracy of ~ 200 μs over data-collection 'seasons' of at least a few months duration. This makes the method viable for conducting period searches in γ-ray and other astronomies for most species of candidate sources, including a majority of millisecond pulsars.

References

Bhat, C. L., Yadav, R. C., Kaul, S. K., Bemalkhedkar, M. M., Kaul, R. K. 1981a, *J. Inst. Elec. & Telecom. Engs.,* **27,** 553.

Bhat, C. L., Kaul, I. K., Yadav, R. C. 1981b, *J. Inst. Elec. & Telecom. Engs.* (*India*)*,* **27**, 559.

Bhat, C. L., Sapru, M. L., Razdan, H. 1980, *Astrophys. Sp. Sci.,* **73**, 513.

Bhat, C. L. 1982, *PhD Thesis,* Kashmir University.

Chadwick, P. M., Dipper, N. A., Dowthwaite, J. C., Gibson, A. I., Harrison, A. B., Kirkman, I. W., Lotts, A. P., Macrae, J. H., McCornb, T. L. J., Orford, K. J., Turver, K. E., Walmsley, M. 1985, *Nature,* **318**, 642.

De Jager, O. C., Raubenheimer, B. C, North, A. R., Nel, H. I., Van Urk, G. 1988, *Astrophys. J.,* **329**, 831.

Jain, C. L., Kumar, K., Andharia, H. I., Singh, M., D'Souza, V., Goel, V. K., Sisodia, A. K. 1981, *J. Inst. Elec. & Telecom. Eng.* (*India*)*,* **27**, 473.

Jelly, J. V. 1967, in *Progress in Elementary Particle and Cosmic Ray Physics,* North Holland, Amsterdam, **9,** 39.

Kaul; R. K. 1987, *PhD Thesis,* Kashmir University.

Koul, R., Bhat, C. L., Tickoo, A. K., Kaul, 1. K., Kaul, S. K., Qazi, R. A., Kaul, R. K., Rawat, H. S., Senecha, V. K., Rannot, R. C., Sapru, M. L., Razdan, H. 1989, *J. Phy. E. Sci. Instrum.*, **22**, 47.

Kovacevic, B., Dimitrijevic, B., Arsic, M., Golubobic, Lj. 1981, *J. Inst. Elec. & Telecom. Eng.* (*India*), **27**, 450.

Lake, R. 1981, *J. Inst. Elec. & Telecom. Eng.* (*India*), **27**, 456

Morgan, A. H. 1959, National Bureau of Standards (USA) Technical Note No. 22.

Putkovich, K. 1981, *J. Inst. Elec. & Telecom. Eng.* (*India*), **27**, 460.

Ramana Murthy, P. V. 1981, *J. Inst. Elec. & Telecom. Eng.* (*India*), **27**, 549.

Weekes, T. C. 1988, *Phys. Rep.*, **160,** 1.

J. Astrophys. Astr. (1990) **11**, 151–166

CCD Photometry in *VRI* Bands of the Galactic Cluster NGC 2818*

R. Surendiranath, N. Kameswara Rao, Ram Sagar, J. S. Nathan & K. K. Ghosh *Indian Institute of Astrophysics, Bangalore 560034*

Received 1989 October 23; accepted 1990 February 22

Abstract. The open cluster NGC 2818 containing a planetary nebula has been observed in *VRI* bands using the CCD system at prime focus of the 2.3-metre Vainu Bappu Telescope. The study extending to stars $V \sim 21$ magnitude establishes the distance modulus as $(m - M)_0 = 12.9 \pm 0.1$ for the cluster. Based on the fitting of theoretical isochrones computed for solar metallicity, an age of $5(\pm 1) \times 10^8$ years has been assigned to the cluster. Association of the planetary nebula with the cluster indicates that the progenitor mass of the planetary nebula on the main sequence is $\geqslant 2.5 M_{\odot}$.

Key words: open clusters—*VRI* photometry—planetary nebulae—stellar evolution—open clusters, individual: NGC 2818

1. Introduction

NGC 2818 (C 0914-364) has the unique distinction of being one of the two galactic clusters associated with a planetary nebula (PN) also designated as NGC 2818 (= PK 261 + 8º1). An accurate estimate of the distance to the cluster gives us an opportunity to determine the size as well as the mass of the progenitor of the planetary nebula. Tifft, Connolly & Webb (1972; hereafter denoted as TCW) have presented *UBV* photographic photometry up to a limiting magnitude of $V \simeq 16.8$ and estimated the reddening and the distance to the cluster as $E(B - V) \simeq 0.22$ and 3.2 kpc respectively. According to TCW the cluster radial velocity of + 3 ± 20 km s^{-1} agrees with that of the PN + 8 ± 13 km s^{-1}. The reddening of the nebula estimated as $E(B - V) = 0.24$ is roughly the same as that of the cluster. However there seems to be a discrepancy in the estimated distance of the nebula and the cluster. Various statistical methods of estimating the distance of the PN range from 1.61 to 2.64 kpc (Kohoutek, Roth-Hopper & Lausten 1986) whereas estimates of the cluster distance range from 3.5 to 3.8 kpc (Dufour 1984). The estimate of the cluster distance modulus by TCW was based on main-sequence stars located in a narrow range of magnitude between the limit of their photometry (V ~ 16.8) and the turnoff point ($V \sim 16$) which gave little scope for a good zero age main sequence fitting for estimating the distance modulus. Thus to have a better estimate of the distance modulus it is necessary to extend the photometry deeper at least to $V \sim 19$ to 20 magnitude, and as such we have observed

* Based on observations obtained with the Vainu Bappu Telescope.

this cluster with the 2.3-metre Vainu Bappu Telescope (VBT) with the main aim of estimating a better distance modulus.

2. Data

2.1 *Observations*

The observations in *VRI* filters (*R* and *I* in Cousins system) have been obtained with the CCD system described by Ananth *et al.* (1989) operating at the prime focus of the 2.3-m VBT. In brief, the CCD camera consists of a GEC P8603 chip with 512 × 320 pixels with a pixel size of 22 μm and operated through a PC/AT system. At the prime focus of the telescope a pixel of the CCD camera corresponds to ~ 0.6 arcsec on the sky and the entire camera covers a field of 5 × 3 arcmin^2. Observations of three fields of the cluster shown in Fig. 1 (primarily the zone 1 of TCW) have been obtained during 1989 April 3–5 in the three filters *V, R* and *I.* The evening and morning twilight sky was used for the flat field corrections. The details of the exposures are given in Table 1. Along

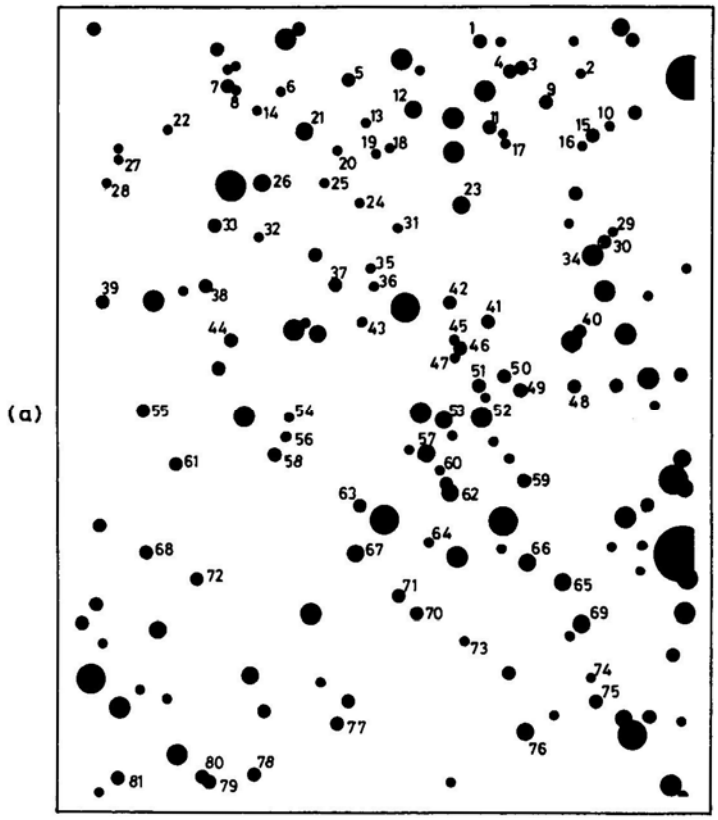

Figure 1. The observed CCD fields of the cluster NGC 2818; the numbers beside the stars correspond to Table 2. (a) Centred around star # 2–65 of TCW. α, δ(1950): $9^h\ 13^m\ 48^s4$, – 36°24'37.0" (b) Centred around star # 1–89 of TCW. The star shown by an open circle may be a variable. (c) Right: centred around star # 1–167 of TCW.

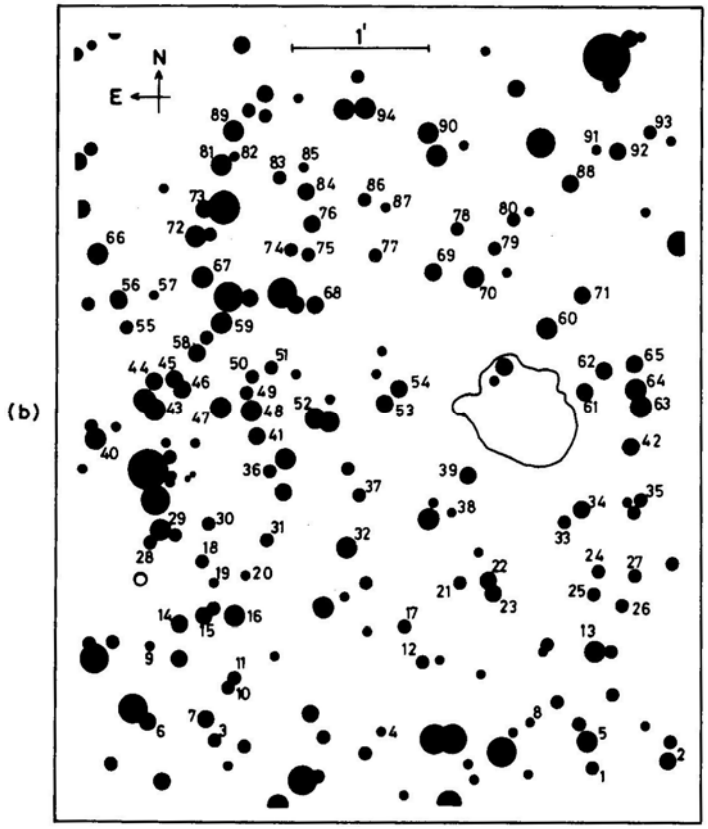

Figure 1. Continued.

with the cluster fields, standards located in clusters NGC 4147 and M 92 (Christian *et al.* 1985) have also been observed on these nights for calibration.

2.2 *Reductions*

The reductions of the CCD images were done using the STARLINK and STARMAN programs devised for stellar photometry (Penny 1987), using the VAX 11/780 system at Vainu Bappu Observatory. The magnitude estimation of stars on each of the data frames has been done by an iterative least squares fitting using the modified Lorentzian profile introduced by Penny & Dickens (1986) to account for the wide halo around stars. It is a rotated-elliptical Lorentzian with a wide low circular modified Gaussian base. The profile parameters were estimated for each frame using several bright (good S/N ratio) and isolated stars in the frame. Display and interaction with the image frames were done outside the STARLINK package, using the software developed locally for the COMTAL vision/1 image display station. About 400 stellar images have been measured in each filter. The pixel to pixel variation of the flat field frames was less than ~ 10 per cent. The mean atmospheric extinction coefficients for the site have been used to correct the instrumental magnitudes for atmospheric extinction. The colour

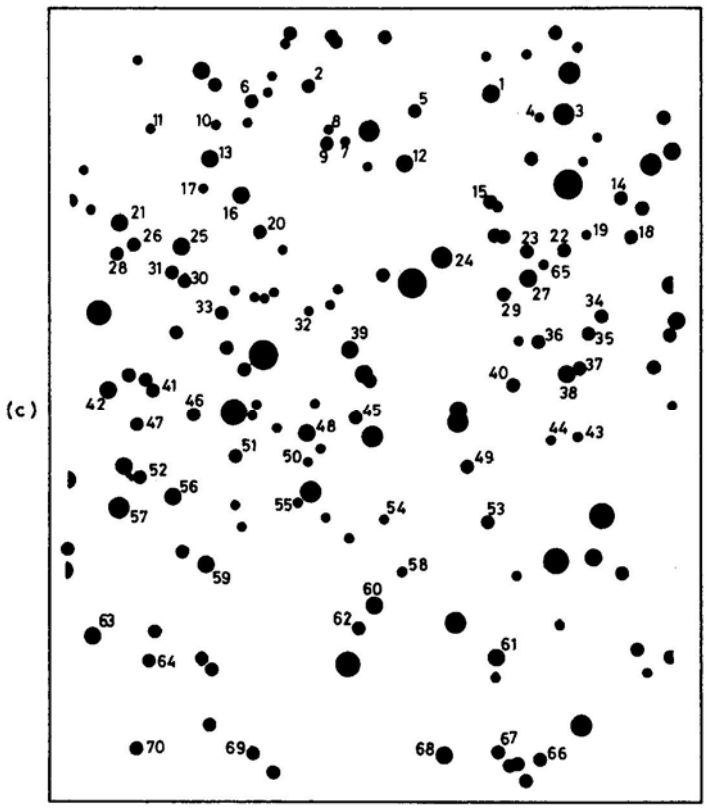

Figure 1. Continued.

and magnitudes were transformed using linear equations which were found to be adequate.

The equations used were

$$V = C_5 + C_6(V - I) + v_i,$$

$$(V - I) = C_1(v - i)_i + C_2,$$

$$(V - R) = C_3(v - r)_i + C_4.$$

The rms error in each of these fits was 0.06 mag. The magnitude and colour range covered by the standards are V = 15.9 to 18.3, $V - I$ = – 0.09 to 1.44, and $V - R$= – 0.09 to 0.71. The standards used (Christian a al. 1985) for transformation themselves have residuals of this order: 0.05 in ($V - I$) and 0.025 in ($V - R$). Since we do not have local standards for R and I magnitudes, we checked these transformations using the standards in the following way: for stars which occur on the cluster main-sequence in the V/($B - V$) diagram of TCW (*i.e.* Fig. 2 of TCW, V = 14.8 to 15.7 and $B - V$= 0.22 to 0.40) we applied the cluster reddening corrections (see Section 3.1 for the relations used) to estimate the expected $V - R$ and $V - I$ colours using the intrinsic colours for dwarfs as given by Bessell (1979). These values agree with direct transformations within ±0.05 and ±0.04 magnitudes in $V - I$ and $V - R$ colours respectively. The zero points of the colours have been checked thus and the V magnitude zero point was

Table 1. Log of observations.

Date (1989)	Filter	Exp. time (s)	Field covered
April 3	*V*	720	Fig. 1(b)
	R	120	"
	I	60	"
	V	600	M 92
	R	420	"
	I	300	"
	V	600	N 4147
	R	300	"
	I	480	"
April 5	*V*	1200	Fig. 1(a)
	R	240	"
	I	360	"
	V	1200	Fig. 1(c)
	R	240	"
	I	360	"
	V	1200	N 4147
	R	240	"
	I	360	"

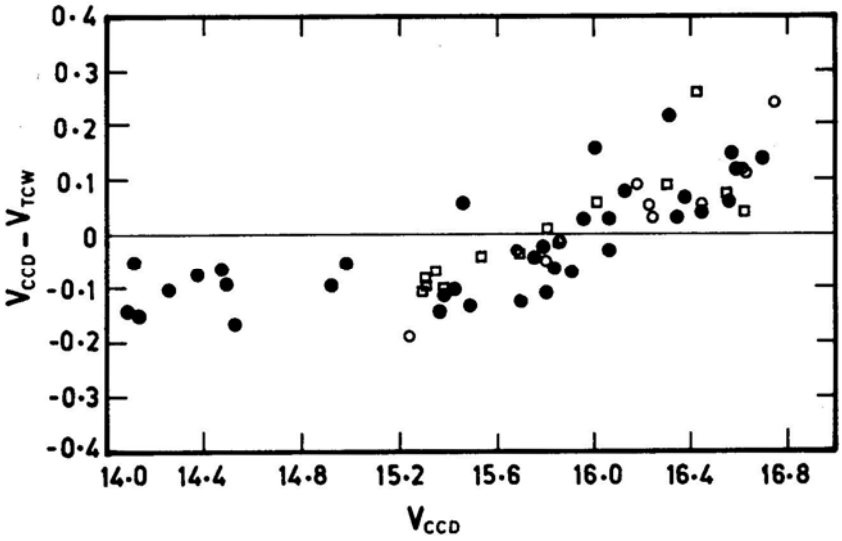

Figure 2. The difference of *V* magnitudes of this study and of TCW ($V_{CCD} - V_{TCW}$) plotted with respect to the *V* magnitudes of this study (V_{CCD}).

checked with that of TCW stars. The internal errors in *V, V–R* and *V–I* (*i.e.* for the same stars from different frames) are ± 0.035, ± 0.02 respectively. The *V*, *V–I* and *V–R* values are tabulated in Table 2, along with cross identification with TCW. These star numbers correspond to the numbers given in Fig. 1.

The comparison with TCW's *V* magnitudes is shown in Fig. 2. The TCW magnitudes are based on photographic photometry and are claimed to be accurate to

Table 2. Photometric results on NGC 2818.

Fig. 1(a) No.	TCW No.	V	$V-R$	$V-I$
1		20.62	3.87	4.75
2		19.46	0.97	1.64
3		16.99	0.62	1.31
4		17.49	0.53	0.62
5		18.07	0.81	1.51
6		19.62	1.75	3.12
7		16.95	0.45	0.82
8		18.63	0.26	0.74
9		17.69	0.78	1.42
10		18.98	0.67	1.12
11		17.52	0.34	0.62
12		16.99	0.42	0.76
13		18.22	0.43	0.77
14		18.65	0.67	1.27
15		17.81	0.60	1.06
16		18.77	0.64	1.03
17		18.44	0.67	1.15
18		18.65	0.71	1.37
19		18.70	0.46	0.85
20		18.36	0.48	0.93
21		16.51	0.44	0.83
22		18.03	0.90	1.63
23	1–13	15.29	0.21	0.45
24		19.77	1.02	1.92
25		19.21	0.15	0.50
26	2–134	15.69	0.31	0.58
27		18.18	0.50	1.05
28		18.98	0.28	0.23
29		19.09	0.91	1.56
30		17.59	1.14	2.04
31		18.34	0.43	0.82
32		18.66	−0.07	0.15
33	2–136	16.30	0.35	0.65
34	1–17	15.38	0.24	0.50
35		18.00	0.43	0.85
36		18.45	0.29	0.32
37	1–14	16.62	0.41	0.76
38		17.51	0.50	0.85
39		18.02	0.66	1.27
40		19.12	0.38	0.97
41		18.33	0.91	1.57
42		17.14	0.60	1.03
43		18.29	0.40	0.76
44		18.44	0.60	1.31
45		19.32	1.29	2.35
46		17.04	0.64	1.16
47		18.72	0.64	1.12
48		17.18	0.47	0.87
49		17.95	0.51	0.88
50		18.63	0.72	1.23
51		17.44	0.58	1.04
52	1–169	15.31	0.19	0.41

Table 2. Continued.

Fig. 1(a) No.	TCW No.	V	$V-R$	$V-I$
53	1–168	16.58	0.50	0.91
54		19.37	0.95	1.66
55		18.39	0.65	1.34
56		17.81	0.70	1.27
57	1–163	15.81	0.33	0.63
58	1–164	16.55	0.36	0.69
59	1–162	16.42	0.68	1.19
60		19.34	0.74	1.13
61		18.12	0.82	1.50
62	1–160	16.44	0.48	0.85
63		17.50	0.47	0.87
64		18.68	0.00	−0.01
65	1–149	15.35	0.25	0.52
66	1–150	15.53	0.31	0.60
67	1–157	16.01	0.46	0.86
68		17.13	0.62	1.22
69	1–148	15.31	0.19	0.41
70		16.74	0.42	0.78
71		17.90	0.50	0.94
72		17.42	0.45	0.87
73		18.52	0.43	0.70
74		19.63	0.65	1.36
75		17.83	0.54	1.00
76	1–152	15.16	0.12	0.30
77		18.13	0.71	1.29
78		16.85	0.42	0.89
79		18.08	1.13	1.56
80		16.91	−0.12	1.16
81		17.02	0.37	1.10
Fig. 1(b) No.				
1		17.79	0.40	0.64
2		16.14	0.23	0.53
3		17.57	0.39	0.80
4		18.99	0.43	0.88
5	2–48	14.09	—	0.24
6	1–134	16.31	0.22	0.70
7	1–136	15.84	0.28	0.58
8		18.25	0.41	0.93
9		18.56	0.03	0.41
10		17.40	0.30	0.48
11		19.36	0.60	1.74
12	1–123	16.78	0.30	0.59
13	1–100	14.13	—	0.29
14		17.37	0.56	1.09
15	1–140	15.48	0.19	0.46
16	1–138	14.37	—	0.50
17		19.16	0.88	1.94
18		18.06	0.43	0.77
19		19.42	0.70	1.46
20		18.56	0.11	0.10

Table 2. Continued.

Fig. 1(b) No.	TCW No.	V	$V-R$	$V-I$
21		18.73	0.57	0.77
22	1–103	16.34	0.29	0.56
23	1–102	15.70	0.16	0.41
24		16.96	0.40	0.77
25	1–97	15.76	0.43	0.85
26	1–98	16.32	0.13	0.46
27		18.63	0.77	1.05
28		18.34	0.40	0.73
29		16.33	0.48	0.99
30		17.05	0.39	0.75
31		20.74	1.65	2.99
32	1–121	14.52	—	0.14
33	1–95	16.57	0.29	0.86
34	1–94	15.24	0.10	0.28
35		16.78	0.46	0.97
36		17.51	0.55	0.83
37		17.53	0.51	0.92
38		18.78	0.49	0.70
39		17.23	0.50	0.95
40	1–144	14.25	—	0.32
41	1–117	16.13	0.37	0.71
42	1–81	16.44	0.29	0.59
43	1–114	15.15	0.21	0.48
44	1–112	16.06	0.30	0.69
45	1–111	16.55	0.29	0.56
46	1–115	16.61	0.33	0.66
47		15.20	0.24	0.58
48	1–116	14.49	—	0.39
49		17.78	0.40	0.76
50		17.36	0.54	0.97
51		16.91	0.38	0.81
52	1–106	15.93	0.37	0.69
53	1–90	16.70	0.35	0.68
54	1–89	15.42	0.20	0.38
55		19.20	0.69	1.65
56	1–25	15.38	0.21	0.44
57		18.61	0.38	0.92
58	1–109	15.79	0.31	0.68
59		15.32	0.24	0.52
60	1–77	15.80	0.21	0.50
61		16.91	0.30	0.76
62		16.31	0.63	1.15
63	1–82	16.06	0.20	0.47
64	1–83	16.01	0.62	1.21
65	1–84	16.38	0.33	0.68
66		14.62	—	0.58
67	1–26	14.44	—	1.05
68	1–70	16.01	0.25	0.52
69	1–74	14.98	0.16	0.34
70	1–75	15.46	—	1.12
71		17.24	0.14	0.23
72	1–27	14.38	—	0.27

Table 2. Continued.

Fig. 1(b) No.	TCW No.	V	$V-R$	$V-I$
73	1–29	16.10	0.30	0.60
74		17.64	0.44	0.87
75		17.50	0.33	0.81
76	1–67	14.92	0.11	0.28
77		18.42	0.49	1.03
78		17.01	0.47	0.98
79		18.79	0.59	1.16
80		17.39	0.40	0.81
81	1–32	14.47	—	0.27
82		18.70	0.79	1.48
83		18.21	0.44	1.22
84	1–66	15.95	0.30	0.56
85		18.57	0.31	0.94
86	1–65	15.85	0.24	0.46
87		19.95	1.04	2.05
88	1–62	15.91	0.24	0.64
89	1–33	14.12	—	0.48
90	1–64	15.23	—	1.13
91		17.78	0.66	0.97
92		16.84	0.62	1.30
93		17.50	0.48	1.07
94	1–50	14.57	—	0.48
Fig. 1(c) No.				
1	2–76	16.75	0.41	1.13
2	3–24	17.25	0.40	2.03
3		15.67	0.39	0.79
4		18.88	0.77	1.15
5		18.62	0.45	0.61
6		17.57	0.47	1.00
7		18.75	0.61	−0.50
8		18.90	0.74	1.41
9	2–79	16.63	0.59	1.14
10		19.33	1.18	2.00
11		19.01	0.71	1.39
12		17.06	0.42	0.84
13		16.97	0.32	0.75
14		17.10	0.34	0.67
15		18.40	0.64	1.50
16	2–80	16.18	0.51	1.00
17		18.98	0.88	1.59
18		17.96	0.49	0.70
19		19.21	0.81	1.39
20		18.67	0.36	0.97
21	1–57	16.45	0.40	0.69
22		18.37	0.66	1.32
23		18.35	0.48	0.73
24	2–74	15.80	0.23	0.50
25		16.73	0.28	0.76
26		17.73	0.23	0.66
27	2–73	16.60	0.68	1.26

Table 2. Continued.

Fig. 1(c) No.	TCW No.	V	$V-R$	$V-I$
28		16.68	0.36	0.69
29		18.43	0.65	1.23
30		17.89	0.34	−0.19
31		18.27	0.23	0.70
32		20.31	1.73	3.11
33		18.68	0.66	−0.03
34		18.59	0.57	1.29
35		17.90	0.47	0.92
36		18.12	0.47	0.88
37		16.84	0.31	0.22
38		16.74	0.39	0.98
39		17.13	0.44	0.91
40		17.58	0.90	1.72
41		17.66	0.50	1.23
42		17.44	0.47	1.07
43		18.48	0.47	0.78
44		18.88	0.98	1.80
45		17.89	0.47	0.85
46		18.81	0.63	1.67
47		17.74	0.42	0.72
48	2–66	16.23	0.32	0.66
49		18.18	0.43	0.64
50		18.97	0.38	1.20
51		18.08	0.49	0.85
52		19.00	1.06	2.15
53		18.33	0.61	1.27
54		18.35	0.43	0.68
55		18.57	0.62	1.34
56		17.17	0.20	0.56
57	1–80	15.37	0.17	0.37
58		18.07	0.42	0.67
59		16.70	0.26	0.75
60	2–60	16.24	0.34	0.73
61		17.34	0.73	1.39
62		18.57	0.41	0.93
63		16.91	0.13	1.03
64		18.10	0.51	1.25
65		18.36	0.64	1.17
66		17.54	1.53	0.75
67		18.90	1.31	1.08
68		15.69	0.26	0.50
69		17.99	0.47	0.67
70		18.55	0.27	1.07

± 0.02 magnitude in V and $B–V$. As can be seen from Fig. 2, there seems to be a systematic difference in the values of V_{CCD} and V_{TCW} In the magnitude range 14 to 15.8 a constant difference of – 0.08 (*i.e.* V_{CCD} is brighter) exists and between 15.8 and 16.8 the difference continuously increases from –0.08 to +0.19 magnitude. We compared the V magnitude of four common photoelectric standards measured by TCW which lie

in the V range of 15.4 to 16.86. The mean difference of V_{CCD} and V_{TCW} is − 0.01. (Moreover our CCD standards are from V = 15.9 to 18.3.) Further, (a) CCD, unlike the photographic plate, is an intrinsically linear detector, and (b) in the present analysis magnitude estimation is based on the complex type profile which tackles not only crowding but also matches the star profile very closely. Therefore, we believe that magnitude estimation has been done in a relatively better way than TCW. So we conclude that the photographic V of TCW is affected by a systematic error which increases with magnitude for $V \geqslant 15.8$. Consequences of this systematic difference is mentioned in Section 4. One source of error in our photometry was employing the mean atmospheric extinction values. We expect the total error in $V - I$ to be $\simeq$ 0.06 and in $V - R$ to be $\simeq$ 0.05 mag.

3. **The colour-magnitude diagram (CMD)**

Fig. 3 shows the $V/(V - I)$ diagram for NGC 2818 for the central frame (centred on star 1–89 of TCW) in which field star contamination is expected to be minimal. Fig. 4 shows the same for all three fields (frames) combined. Since we were concentrating on the fainter stars, we did not have enough short exposures to include stars brighter than $V \sim 14$. So the sampling is rather restricted towards the brighter end. The spread in the colour around the cluster main-sequence seems to be little more than expected from

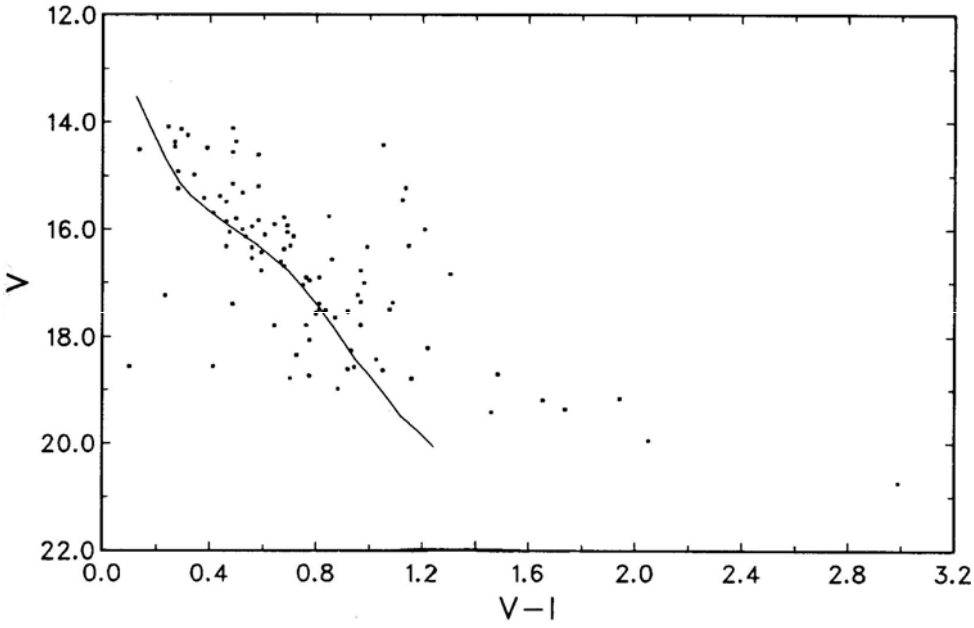

Figure 3. $V/V - I$ colour-magnitude diagram for the central frame covering 5 × 3 arcmin^2 around the cluster centre. The solid line corresponds to the ZAMS (Walker 1985) after applying reddening and interstellar extinction (A_V) corrections corresponding to $E(B - V)$ = 0.22 for a distance modulus of $(m - M)_0$ = 12.9.

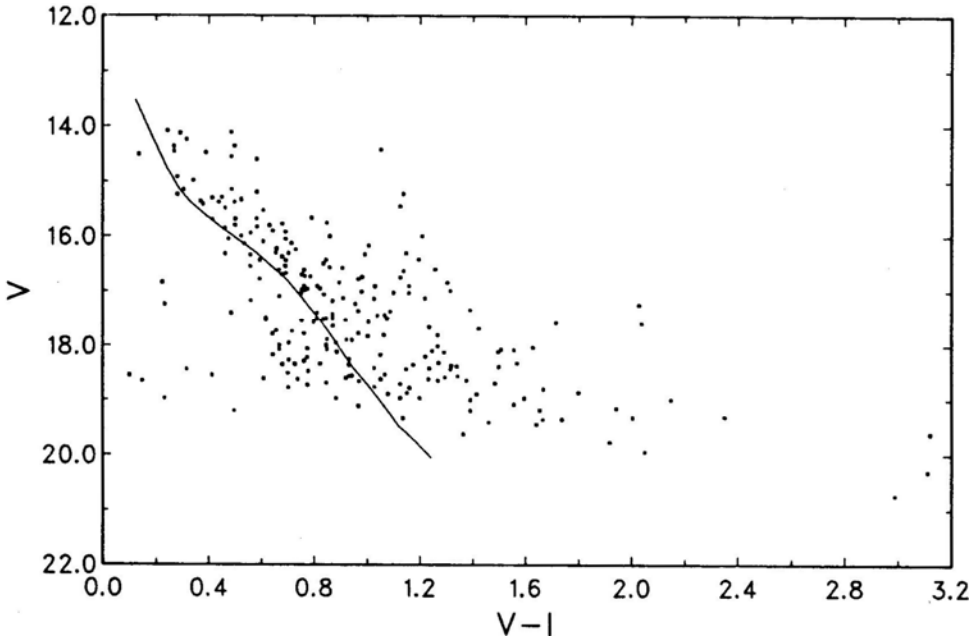

Figure 4. *V/V – I* colour–magnitude diagram of all the three fields observed. See caption to Fig. 3 for details.

the photometric errors alone. The *V/B – V* diagram of TCW also shows corresponding spread in the colour. Generally the spread in $V - I$ colour is more than in $V - R$ colour. As can be seen from Figs 3 and 4 the field star contamination increases for $V > 17$ and $V - I > 0.7$. However discrimination of the members and nonmembers based on $V - I$ and $V - R$ colours is not easy in practice.

3.1 *Reddening and ZAMS Fitting*

The mean cluster reddening was found by TCW from a $(U - B)$, $(B - V)$ plot as $E(B - V) = 0.22$. We adopt this value for the cluster reddening. Although $V - I$ colour is more sensitive to reddening (*i.e.* $E(V - I) \simeq 1.25\ E(B - V)$], as pointed out by Walker (1985) and Romeo et al. (1989) due to slope of the reddening lines, $V - I$ and $V - R$ colours are not best suited for reddening determination. We adopt the reddening relation given by Dean, Warren & Cousins (1978) for estimating $E(V - I)$ from $E(B - V)$:

$$E(V - I) = 1.25\ E(B - V)\ [1 + 0.06(B - V)_0 + 0.014\ E(B - V)],$$

and by Taylor (1986) for E(V - R):

$$E(V - R) = 0.59\ E(B - V).$$

The ratio of total to selective absorption R is expressed as a function of $(B - V)_0$ and $E(B - V)$ by Walker (1985) and Romeo *et al.* (1989). We adopt the following expression

given by Romeo *et al.* (1989):

$$R = 3.06 + 0.25(B - V)_0 + 0.05\, E(B-V)$$

which is seen to be consistent with $R = 3.06$ for $(B - V) = 0.0$ and $E(B–V) = 0.0$, the galactic mean as determined by Turner (1976) from his extensive work on open clusters.

The zero age main sequence fitted to the cluster CMD is that given by Walker (1985) based on the Pleiades CMD. Fitting CM diagrams of young clusters to the Pleiades CMD also avoids the problem of applying controversial metallicity corrections. The examination of CM diagram of NGC 2818 (see further) indicates that the colour at which main sequence 'evolutionary' deviation from ZAMS occurs is at a spectral type of ~ A0–Al which makes the cluster of comparable age to that of the Pleiades.

The location of the observed ZAMS in the CMD to an extent is a matter of taste, given the difficulty of discrimination between cluster members and nonmembers and the possible incidence of binaries. Thus, while fitting the ZAMS to the cluster we follow the theoretical definition which places it at the blue edge of the stellar distribution, once the photometric errors have been taken into account (*e.g.* Romeo *et al.* 1989).

We applied the reddening corrections to the ZAMS corresponding to $E(B - V)$ of 0.22 and using the above relation for $E(V - I)$ matched the ZAMS with the observed $V/(V—I)$ diagram as shown in Figs 3 and 4. The ZAMS can be fairly matched with $(m - M)_0$ of 12.9 ± 0.1. A similar value of the distance modulus is obtained from $V/(V - R)$ diagram; however, $V - R$ is less sensitive to the changes in the ZAMS fitting procedures. Based on the fit to the $V/(V - I)$ diagram we adopt $(m - M)_0 = 12.9$ which gives a distance of 3.8 kpc (or 3.66 kpc if $(m - M)_0 = 12.8$). This value is quite consistent with the estimate made by Dufour (1984) from an independent evaluation of the TCW data.

The above ZAMS fitting procedure assumes that the metal abundance is similar to the Pleiades (*i.e.* solar) and any deviation from this introduces uncertainty. The spread in the $V - I$ colour of the main sequence in the CMD is ~ 0.275 to 0.30 at $V = 16$ to $V = 17$ which in most part is intrinsic; as a comparison the Pleiades CMD also has a spread of 0.4 mag in $V - I$ at $V = 16$ (Stauffer 1984). This might be a result of several effects like the presence of binaries, spotted stars, rotation *etc.*; it could also have been a result of some variable extinction in the cluster stars but evaluation of this aspect would need colour excess estimates of individual stars across the cluster, which is not attempted here.

4. Discussion

Although the cluster sequence is well defined in our CM diagrams (Figs 3 and 4) the TCW CM diagrams indicate substantial foreground and background field star contamination. TCW mention a sequence of *F* to *K* dwarfs which show reddening less than the cluster. The group left of ZAMS and fainter than $V \sim 17$ present in Fig. 4 might correspond to this group.

TCW mention a break in the cluster main sequence at $V \sim 16.2$ (Fig. 2 of TCW) and also that the main sequence abruptly terminates at $V \sim 15.9$. They felt that the bend or break in the main sequence at $V \sim 15.9$ is probably real. But no such break can be seen in our CM diagram, and the similarity invoked with the break in the main sequence of

NGC 752 by TCW does not apply. TCW also mention that at this magnitude a redder group of stars appears and continues downward to the limit of photometry ($V \sim 16.8$). A similar 'displaced' configuration of stars appears in their intermediate and outer zones. This appears to be the result of the systematic error in V magnitude present in TCW's photographic photometry mentioned in Section 2.2. We have tried to study this further by supposing that only the V magnitudes of TCW had errors but not their B magnitudes. So for the common stars between these two studies we applied a correction to the $(B - V)$ of TCW by a value equal to the difference between V_{CCD} and V_{TCW} and plotted a colour-magnitude diagram for these stars with V_{CCD} versus corrected $B - V$ of TCW. No break in the sequence is found at $V \sim 16.2$; and moreover this is consistent with $(m - M)_0$ of 12.9 when the ZAMS (Walker 1985) was superposed on this CMD (Fig. 5) confirming that the photometric errors are responsible for the break in TCW's CMD at $V \sim 162$.

The turnoff spectral type from the ZAMS is estimated by TCW based on their $B - V$ colour as A5. ($(B - V)_0 = 0.15 \pm 0.04$). This is not consistent with the observations presented here. The zero age main sequence turnoff seems to occur at $V \sim 15.3$ and $(V - I)_0 = 0.04 \pm 0.03$ corresponding to a spectral type of ~ A1.5 (Bessell 1979) which would make the cluster younger than estimated by TCW.

4.1 *Association with the* PN

The association of the PN and the cluster has been discussed by Dufour (1984). The PN is a prototype of Type I nebulae with helium and nitrogen being abundant. It also

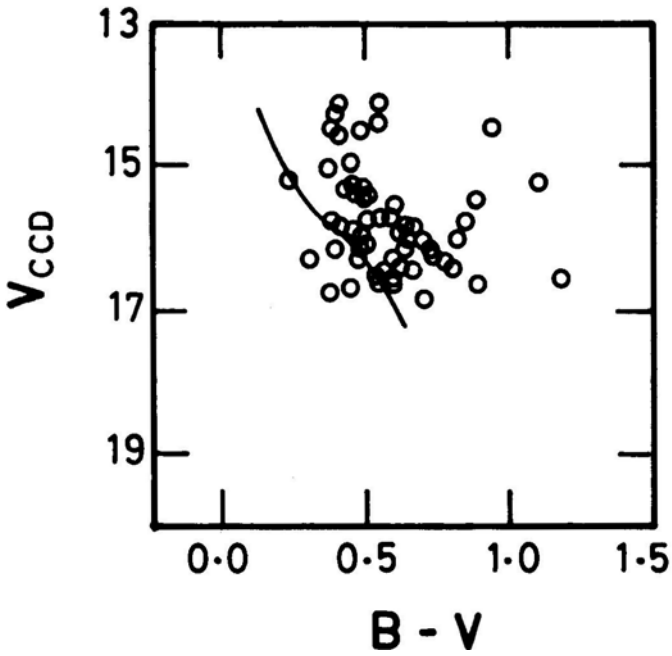

Figure 5. $V_{CCD}/(B–V)_{TCW}$ diagram for stars in common with TCW. A systematic correction to $B - V$ equal to the difference between V_{CCD} and V_{TCW} (Fig. 2) has been applied. The continuous line is the ZAMS as in fig. 3.

seems to be a bipolar nebula (Louise *et al.* 1987). Since the present investigation gives the same distance as that estimated by Dufour, there are no major changes to his derived parameters of the PN. However, the change of the turnoff spectral type of Al would increase the estimated PN progenitor mass. A comparison of our $V/(V-I)$ CMD with the isochrones computed by van den Berg (1985) (*i.e.* his tabulated M_v, $V-I$) for stars in the mass range of 1 to $3M_\odot$ and the solar metallicity indicates an age of $5 \pm 1 \times 10^8$ years to the cluster. And the progenitor mass of the PN would be greater than $\geqslant 2.58\ M_\odot$ if the cluster age is 5×10^8 years ($>2.45\ M_\odot$ if $\sim 6 \times 10^8$ years). Good agreement of the radial velocity as well as $E(B-V)$ value of the PN with those of the cluster strongly support the association of the cluster and the PN. Since the independent estimates of PN distances are statistical in nature, the larger values of distance obtained for the cluster need not be looked upon as a discrepancy. If the estimated distance of 3.8 kpc for the cluster is taken as the distance of the PN also (this value is also consistent with a kinematical distance estimated from the galactic rotation: Dufour 1984), then, the central star parameters as given by case B of Kohoutek, Roth-Hopper, Laustsen (1986) apply *i.e.* $L_*/L_\odot \sim 103$, $R_* \simeq 0.04\ R_\odot$, the nebular hydrogen mass $\sim 0.25\ M_\odot$ and $M_v \simeq 5$.

5. Conclusions

The CCD photometry of the cluster in *VRI* bands down to $V \sim 20$ mag, presents a well-defined ZAMS of the cluster. The fitting of the ZAMS applicable to the Pleiades (Walker 1985) with the $V/(V-I)$ CMD of NGC 2818 gives a distance modulus $(m - M)_0 = 12.9$ and a distance of 3.8 kpc for the cluster. Applying van der Berg's (1985) theoretical isochrones computed with solar metallicity indicates an age $\sim 5 \times 10^8$ years. If the PN is taken to be belonging to the cluster (which is likely) then the progenitor star mass must be $\geqslant 2.5 M_\odot$. Further observations of this cluster are planned in order to study the brighter members and the nebula.

Acknowledgements

We would like to express our thanks to M. J. Rozario and F. Gabriel for their help during the observations. We would also like to express our thanks to Dr R. Srinivasan, Messrs A. V. Ananth, V. Chinnappan and Ravi for the installation and maintenance of the CCD camera and data acquisition system at VBT and also for help in using it. Finally we would like to express our thanks to Prof. J. C. Bhattacharyya for encouragement.

References

Ananth, A. V., Srinivasan, R., Srinivasulu, G., Chandramouli, S. S., Chinnappan, V. 1989, *VBT News,* No. 1.

Bessell, M. S. 1979, *Publ. astr. Soc. Pacific,* **91**, 589.

Christian, C. A., Adams, M., Barnes, J. V., Butcher, H., Hayes, D. S., Mould, J. R., Spiegel, M. 1985, *Publ. astr. Soc. Pacific,* **97**, 363.

Dean, J. F., Warren, P. R., Cousins, A. W. J. 1978, *Mon. Not. R. astr. Soc*., **183**, 569.

Dufour, R. J. 1984, *Astrophys. J.,* **287,** 341.
Kohoutek, L., Roth-Hopper, M. L., Laustsen, S. 1986, *Astr. Astrophys.,* **162**, 232.
Louise, R., Macron, A., Pascoli, G., Maurice, E. 1987, *Astr. Astrophys. Suppl.,* **70**, 201.
Penny, A. J., Dickens, R. J. 1986, *Mon. Not. R. astr. Soc.,* **220**, 845.
Penny, A. J. 1987, *Space Teles. Sci. Inst. Rep.*
Romeo, G., Bonifazi, A., Fusi Pecci, F., Tosi, M. 1989, *Mon. Not. R. astr. Soc.,* **240**, 459.
Stauffer, J. R. 1984, *Astrophys. J.,* **280**, 189.
Taylor, B. J. 1986, *Astrophys. J. Suppl. Ser.,* **60**, 577.
Tifft, W. G., Connolly, L. P., Webb, D. F. 1972, *Mon. Not. R. astr. Soc,* **158**, 47 (TCW).
Turner, D. G. 1976, *Astr. J.,* **81**, 1125.
van den Berg, D. A. 1985, *Astrophys. J. Suppl.,* **58**, 711.
Walker, A. R. 1985, *Mon. Not. R. astr. Soc.,* **213**, 889.

Note added in proof

After this paper went to press we became aware of the work of Pedreros (*Astr. J.* 1989 **98,** 2146.) on this cluster. He derives a distance modulus which is smaller by a magnitude. Pedreros' photometry is on TCW system which according to us, has a systematic error for stars fainter than $V = 15.8$. He adapts [Fe/H] value of – 0.34 and compares his CM diagram with theoretical isochrones of van den Berg. We assumed solar metallicity based on the work of Dufour on the metallicity of PN (particularly sulphur) and we used the observational ZAMS of Walker to fit the cluster main sequence. Independent determination of the metallicity of the cluster is needed.

J. Astrophys. Astr. (1990) **11**, 167–191

Effects of Rotation on the Colours and Line Indices of Stars
2. The Effect on *uvby* and H*β* Indices

Annamma Mathew* and R. Rajamohan *Indian Institute of Astrophysics, Bangalore 560034*

Received 1989 August 17; revised 1990 March 13; accepted 1990 April 4

Abstract. The intrinsic *uvby* and Hβ indices of member stars of α-Persei, Pleiades and Scorpio-Centaurus association have been analysed in detail for rotation effects. These stars range in spectral type from B0 to F0 and the observed effects of rotation are found to be in agreement with photometric effects calculated by Collins & Sonneborn (1977) for rigidly rotating B0 to F0 stars.

Key words: stars, rotation—stars, colours—star clusters, individual.

1. Introduction

The need for determining the effects of rotation on the colours and line indices of stars, and the methodology adopted together with references to the earlier work in this field has been discussed in Paper 1 of this series in some detail (Rajamohan & Mathew 1988) Theoretical computations of rotation effects on the colours and spectral lines were carried out by a number of investigators (Collins & Sonneborn 1977; Slettebak, Kuzma & Collins 1980; Collins &. Smith 1985 and references therein) while Guthrie (1963) Petrie (1965), Kraft & Wrubel (1965), Dickens, Kraft & Krzeminski (1968), Warren (1976) attempted to relate the hydrogen line equivalent widths and colour indices with $V \sin i$ with varying degrees of success. The works of Crawford & Barnes (1974) and Rajamohan (1978) indicated that the c_1 index is definitely affected but no systematic work in this field had been taken up until recently to resolve the varying results obtained by different authors. The present authors undertook such a study and showed that in α-Persei the rotation effects in various colour indices can be firmly established for B and A stars (Paper 1). The works of Gray (1988) and Gray & Garrison (1987,1989) shows that rotation effects on colours are no more a subject of controversy. They refined the MK spectral classification system for A and F type field stars and considered the effect of rotation on the intermediate band indices c_1 and β. In this paper we extend our analysis to Pleiades cluster and the Scorpic Centaurus association and make a detailed comparison between observed effects and theoretical photometric effects due to rigid rotation predicted by Collins & Sonneborn (1977).

*On leave of absence from Assumption College, Changanacherry, Kerala.

2.1 *The Data*

References to the cluster data used in this study are given in Table 1. As discussed in Paper 1 before analysing these data for rotation effects, the factors that affect their colours other than rotation were first taken into account. They are differential reddening across the cluster, binary nature, peculiarity, evolutionary effects and systematic errors in photometry. Also the use of observed indices is likely to magnify the reddening due to rotation especially for clusters with large variable extinction. Hence we have dereddened the colour indices before analysing for rotation effects. The analysis of each cluster was carried out independently so that the evolutionary effects and any systematic error in photometry are kept to a minimum. Double-lined spectroscopic binaries and close visual doubles with a magnitude difference less than 2 were excluded. Emission-lined objects and known peculiar stars were in general excluded and only luminosity class IV and V stars were included for data analysis. The final group of stars left for analysis should therefore represent a sample of normal single stars and single-lined spectroscopic binaries at the same stage of evolution. Hence the reddening effect found should be due to rotation alone.

2.2 *The Analysis*

The methodology adopted is similar to that given in Paper 1. Assume that all stars in a cluster are formed at the same time with zero rotation. A colour-colour plot then would define, for example, the zero-age, zero-rotation, main sequence. If all the members are single, we expect this observed sequence to have a scatter of ±0.01 magnitudes about the mean relationship purely due to observational uncertainties alone. If some of the objects happen to be binaries, this scatter would increase depending on the mass ratio distribution of the binary components. Further contribution to the scatter would come from the existence of circumstellar envelopes around some stars, differences in line blanketing effects at a given mass *etc.* Differential interstellar reddening across the cluster would further increase the scatter in their observed position. We have to add the effect of rotation to all these uncertainties to understand the observed cosmic scatter in the zero-age main sequence of a cluster.

Now a group of coeval main sequence single stars will move across the HR diagram as they age and the rate of this shift would depend only on their masses. This of course

Table 1. References to four colour, H_β, $V \sin i$ data for clusters.

Cluster	Data	Reference
α-Persei	$uvbyH_\beta$	Crawford & Barnes (1974)
	$V \sin i$	Kraft (1967)
Pleiades	$uvbyH_\beta$	Crawford & Perry (1976)
	$V \sin i$	Anderson, Stoeckly & Kraft (1966)
Sco-Cen	$uvbyH_\beta$	Glaspey (1971)
	$V \sin i$	Rajamohan (1976)
		Slettebak (1968)
		Uesugi & Fukuda (1982)

assumes that the rate of energy production and transport is independent of rotation which is a reasonable assumption for early type stars.

Hence our approach to this problem was to choose stars of a given mass and age, that are single and whose colours can be expected to be different from the mean just because they have different rotational velocities. There is an implicit assumption that two groups of stars of the same mass close to the main sequence but differing ages will be affected to the same extent by rotation. If many groups are indiscriminately combined, the mean colour for each group would be different due to the difference in age which in effect is likely to mask the effect of rotation by making the data noisy.

The problem is that of finding a statistically significant sample of single stars of a given mass on the main sequence at the same stage of evolution with observed colours that are not affected due to causes other than rotation. The problem gets further complicated by the fact that we can derive only the projected rotational velocity and *i,* the inclination of the line of sight to rotation axis, is unknown. However, theory predicts (Collins & Sonneborn 1977) that the effect of differences in true rotational velocity v is much larger than that due to differences in i.

Our approach, therefore, towards this problem is the following. A colour-colour plot of chosen main sequence, presumably single, stars of a cluster will define a sequence which depends only on the masses of the individual members. A single intrinsic line that defines the mean relationship, also defines their position for the mean rotational velocity of the cluster members. The advantage of this approach is that while we use all stars to get a statistically significant sample, the intrinsic differences in the angular momentum distribution at any given mass will not affect the results significantly. Also we have no reason to believe for example that in a cluster the B stars will all be fast rotators and late A stars will all be born as slow rotators. If there are differences between cluster to cluster, then it is taken care of automatically by analysing the clusters independently.

We have used the data for each cluster to define its own relationship between different colour indices. To calculate the colour excess for example in c_0 a plot of β versus c_0 was made. A second order polynomial was fitted to the data for each star, a calculated c_0 value was derived using the polynomial coefficients for its observed β, we define Δc_0, the colour excess in c_0 as the observed minus computed value of c_0 for its observed value of β.

3. Results

3.1 *The Effect of Rotation on the Colours of* α*-Persei Stars*

There is a possibility that the use of observed colour indices may serve to increase the magnitude of rotation effects found in Paper 1. Since any calibration of colour indices must be finally done using intrinsic indices, we have reanalysed the α-Persei cluster data in order to check whether we have overestimated the rotation effects in Paper 1. α-Persei cluster is highly suited to check rotation effects since it has the least frequency of binary and peculiar stars.

A procedure similar to that in Paper 1 was followed and stars in Tables 1 and 2 of Paper 1 were reanalysed using the dereddened indices rather than the observed indices.

Table 2. Effect of rotation for Pleiades B stars.

Hz	HD	Sp.	$V \sin i$	from β, c_0		from $(u-b)_0, \beta$		from $\beta, (b-y)_0$	
				Δc_0	$\Delta\beta$	$\Delta(u-b)_0$	$\Delta\beta$	$\Delta(b-y)_0$	$\Delta\beta$
255	23432	B8V	220	−0.041	0.021	−0.052	0.018	−0.004	0.021
436	23568	B9.5V	260	0.012	−0.006	−0.004	0.002	0.001	−0.006
722	23753	B8V	270	0.001	−0.008	0.006	−0.007	0.000	−0.008
910	23873	B9.5V	120	0.003	0.000	0.001	0.000	0.000	0.000
977	23923	B9V	310	0.037	−0.023	0.036	−0.014	0.004	−0.023
1129	24076	A2V	155	−0.016	0.011	0.023	−0.006	−0.002	0.011
508	23629	A0V	160	−0.019	0.014	−0.037	0.013	−0.002	0.014
510	23632	A1V	235	0.023	−0.009	0.025	−0.005	0.002	−0.009

3.1.1 *B Stars*

Δc_0, the colour excess in co derived from the mean relationship between β and c_0, is plotted against $V \sin i$ in Fig. 1. The B stars of α-Persei cluster are represented by open circles. For the α-Persei members alone, a least square solution for the residuals give

$$\Delta c_0 = 0.442(\pm 0.033) \times 10^{-3} V \sin i - 0.032(\pm 0.007),$$
$$\Delta\beta = -0.150(\pm 0.013) \times 10^{-3} V \sin i + 0.028(\pm 0.003).$$

Similarly from the $\beta\,(u-b)_0$ relation, we derive

$$\Delta(u-b)_0 = 0.528(\pm 0.045) \times 10^{-3} V \sin i - 0.097(\pm 0.009),$$
$$\Delta\beta = -0.125(\pm 0.011) \times 10^{-3} V \sin i + 0.023(\pm 0.002).$$

The residuals $\Delta(u-b)_0$ are plotted against $V \sin i$, in Fig. 2. From the β, $(b-y)_0$ relation, we derive

$$\Delta(b-y)_0 = 0.043(\pm 0.003) \times 10^{-3} V \sin i - 0.008(\pm 0.001),$$
$$\Delta\beta = -0.162(\pm 0.014) \times 10^{-3} V \sin i + 0.029(\pm 0.003).$$

The residuals, $\Delta(b-y)_0$ are plotted against $V \sin i$ in Fig. 3(a) as open circles.

The $\Delta\beta$ values derived from β, co and β, $(u-b)_0$ relationships are shown as open circles in Figs 4(a) and 5(a) respectively. For comparison, the predicted theoretical effects (see Section 3.4) are also shown for a representative value of $i = 45°$ and $60°$.

From c_0,$(b-y)_0$, plane for the B stars in the α-Persei cluster, we find that $\Delta(b-y)_0$ is not related to the rotational velocity of the stars in conformity with the expectations from theory (see Section 3.4).

3.1.2 *A Stars*

From β, c_0 for A stars in α-Persei we derive

$$\Delta c_0 = 0.305(\pm 0.040) \times 10^{-3} V \sin i - 0.040(\pm 0.006),$$
$$\Delta\beta = -0.156(\pm 0.029) \times 10^{-3} V \sin i + 0.021(\pm 0.005).$$

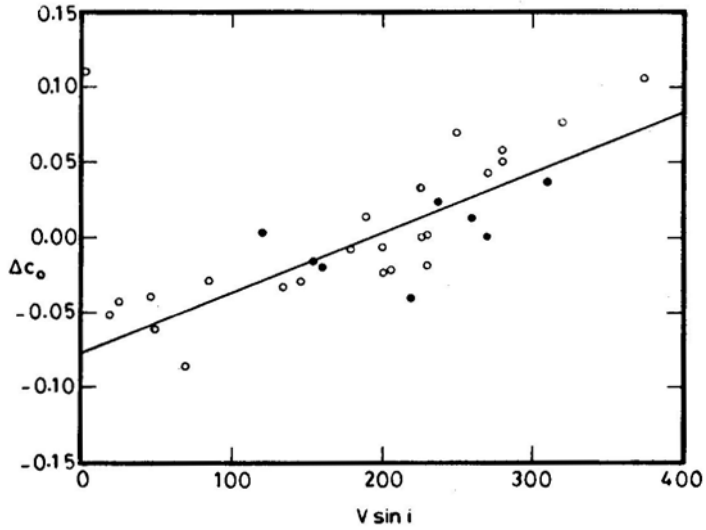

Figure 1. The deviations in c_0 from the observed mean relation between β and c_0 of Alpha Persei (open circles) and Pleiades B-stars (filled circles) are plotted against V sin i.

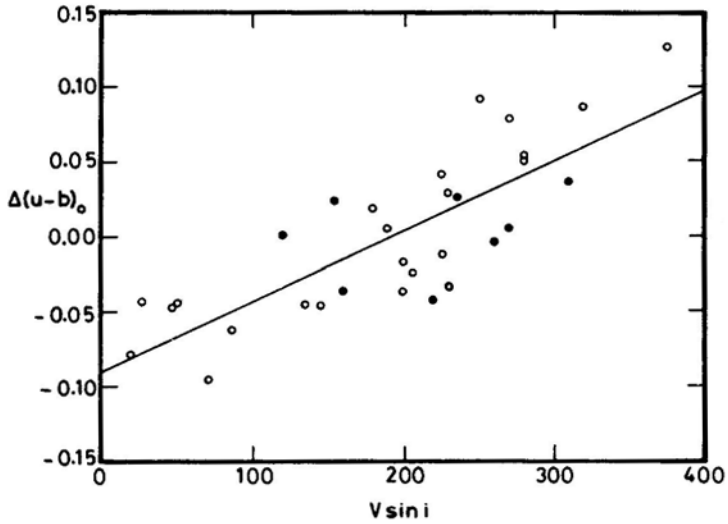

Figure 2. The deviations in $(u—b)_0$ for α Persei (open circles) and Pleiades B-stars (filled circles) are plotted against V sin i.

Δc_0 and $\Delta\beta$ are plotted against V sin i in Figs 6(a) and 7(a) respectively. The predicted theoretical effects (Section 3.4) are shown for comparison. From c_0, $(b - y)_0$ relation for A stars in α-Persei we derive

$$\Delta(b-y)_0 = 0.118\,(\pm 0.048) \times 10^{-3} V \sin i - 0.016\,(\pm 0.007),$$

$$\Delta c_0 = 0.198\,(\pm 0.041) \times 10^{-3} V \sin i - 0.026\,(\pm 0.006).$$

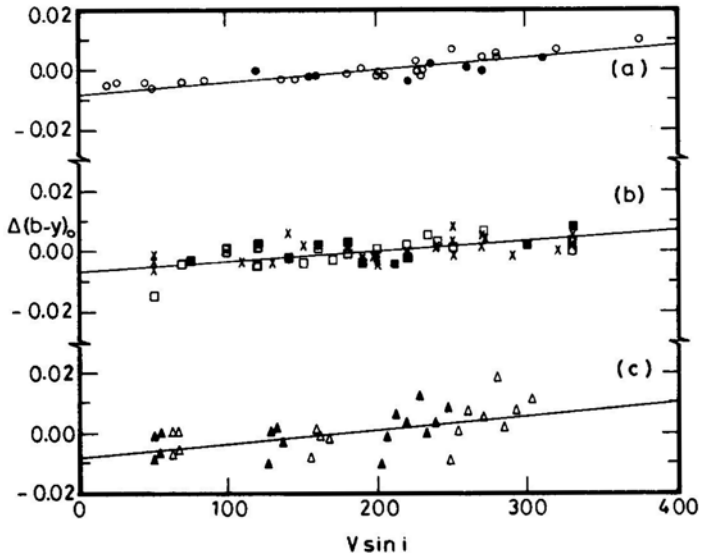

Figure 3. The deviations in $(b - y)_0$ derived from $\beta\,(b - y)_0$ for (a) Alpha Persei and Pleiades and (b) Scorpio-Centaurus association are plotted against V sin i for B-stars. The three subgroups in Sco-Cen are denoted by different symbols. (c) Theoretical effects predicted by Collins and Sonneborn's (1977) work for rigidly rotating B5 to B9 stars for i = 45° (filled triangles) and i = 60° (open triangles) are shown for comparison.

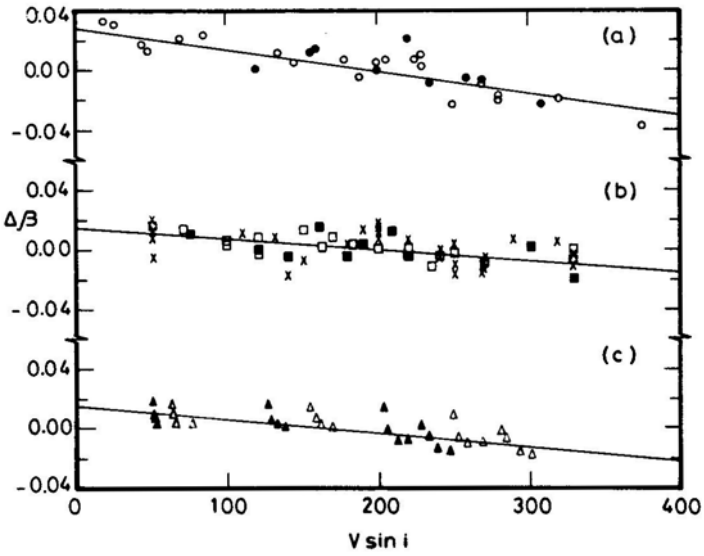

Figure 4. The deviations in β derived from observed β, c_0 for B-stars of (a) Alpha Persei and Pleiades, (b) Sco-Cen association, and (c) Theoretical model predictions for i = 45° and 60° are plotted against V sin i. Theoretical values are shown for B5 to B9 stars. Symbols are as in Fig. 3.

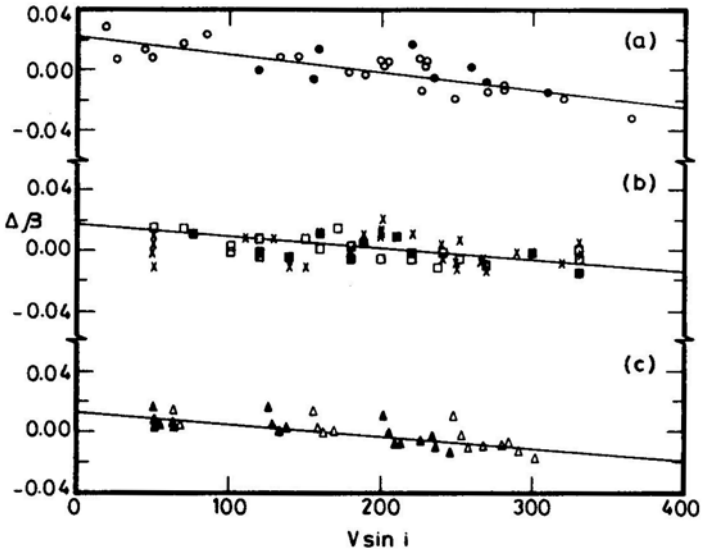

Figure 5. $\Delta\beta$ derived from β, $(u—b)_0$ relation is plotted against V sin i. Other details are similar to Fig. 4.

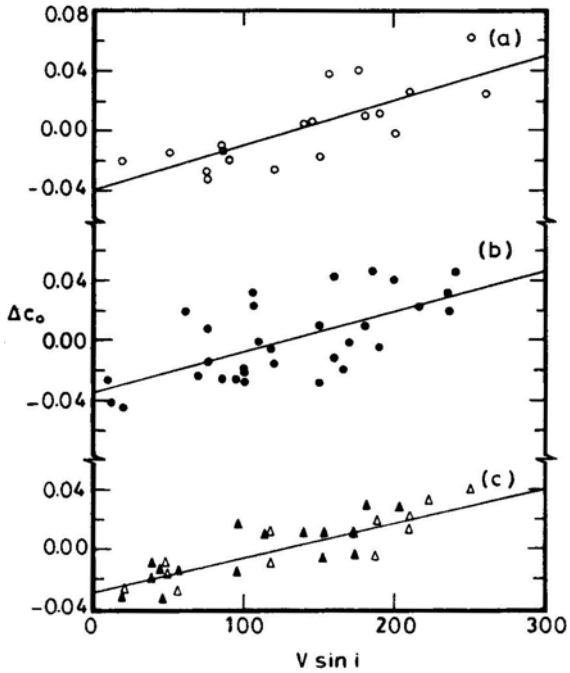

Figure 6. The deviations in c_0 derived from (observed) β, c_0 of A stars of (a) Alpha Persei, (b) Pleiades, (c) theoretical predictions for i = 45° and 60° are plotted against V sin i.

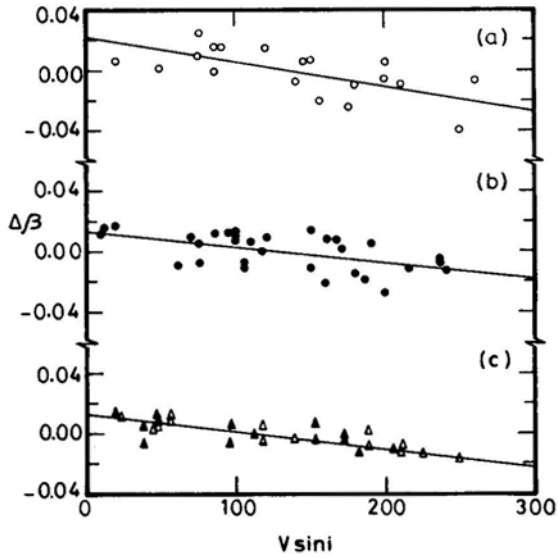

Figure 7. The deviations in β derived from (observed) β, c_o of A-stars in (a) Alpha Persei, (b) Pleiades, and (c) theoretical predictions for $i = 45°$ and $60°$ are plotted against V sin i.

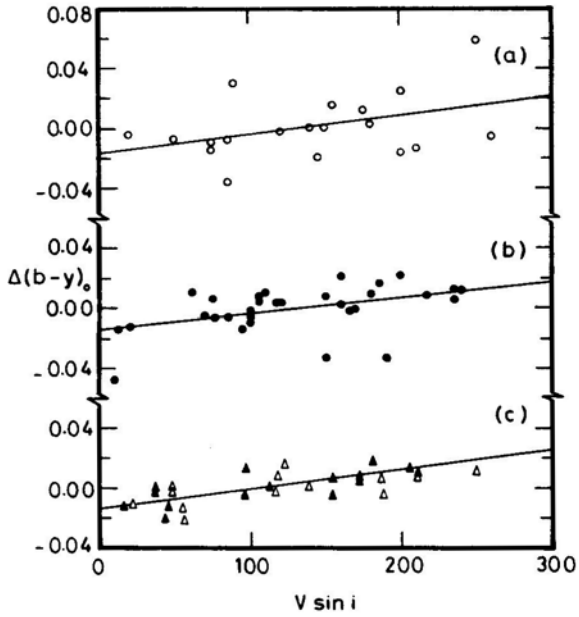

Figure 8. The deviations in $(b - y)_0$ derived from (observed) c_o, $(b - y)_0$ of A stars in (a) Alpha Persei, (b) Pleiades, and (c) theoretical predictions for $i = 45°$ and $60°$ are plotted against V sin i

The colour excess $\Delta(b - y)_0$ derived from this is plotted against V sin i and is shown in Fig. 8 along with predicted theoretical effects (Section 3.4).

$\Delta(b - y)_0$ derived from β versus $(b - y)_0$ relation is found to be extremely small and is not related to the rotational velocity in good agreement with theoretical predictions.

These results are not much different from the conclusions arrived at in Paper 1. However, the derived magnitude of the rotation effect in $(u - b)$ for B stars is found to be larger with the use of observed indices compared to the derived results from dereddened indices. The results for c_1 index for both the B and A stars are similar whether we use dereddened or observed indices. This is as expected since the $(u - b)$ index is affected more by reddening than is c_1.

Gray & Garrison (1989) point out that the system calibration and dereddening procedures for A stars are themselves affected by rotation which would cast some doubt on the use of dereddened indices. This problem of the use of the observed indices as opposed to the use of the dereddened indices must be looked into in greater depth. While the dereddening procedure itself may be affected to some extent by rotation for A stars, the use of observed colour indices for cluster members strongly affected by variable extinction will lead to misleading results for B stars. Probably the variable reddening across the α-Persei cluster is not large enough to have affected our earlier results. However, such variable reddening may be serious for very young clusters embedded in nebulosities. We have therefore decided to use the dereddened indices in the present paper. We will address the question of the role of reddening by extinction and rotation finally when an attempt to calibrate these indices are made.

3.2 *The Effect of Rotation on the Colours of Pleiades Stars*

3.2.1 *B Stars*

Amongst B stars in Pleiades the majority belong to the category of variable radial velocity and emission-lined objects. There are 23 stars of type B in table 4 of Crawford & Perry (1976). If we drop the giants, double-lined binaries, and close visual pairs with $\Delta m < 2.0$ magnitudes, we are left with only 8 stars which can be considered as normal main sequence objects whose colours are free from effects other than that due to rotation. These objects are listed in Table 2. Notwithstanding the fact that this sample is too small to warrant a separate analysis, we derived the residuals in β, c_0, $(u - b)_0$ and $(b - y)_0$ and have listed them in Table 2. The identification numbers for the stars are from Hertzsprung (1947).

From a second-order polynomial fit to β, c_0 values, the residuals Δc_0 and $\Delta\beta$ were derived. The residuals in c_0 for Pleiades B stars are superposed (in Fig. 1) over those derived for the members of the α-Persei cluster. Similarly $\Delta\beta$ for B stars in Pleiades are superposed (in Fig. 4(a)) over those derived for the members of the α-Persei cluster. From the combined data points, we derive

$$\Delta c_0 = 0.402\,(\pm 0.032) \times 10^{-3} V \sin i - 0.077\,(\pm 0.007),$$
$$\Delta\beta = -0.145\,(\pm 0.013) \times 10^{-3} V \sin i + 0.028\,(\pm 0.003).$$

Similarly from the combined data for Pleiades and α-Persei B stars (Fig. 2) we derive from the β, $(u - b)_0$ relation

$$\Delta(u-b)_0 = 0.468\,(\pm 0.045) \times 10^{-3} V \sin i - 0.090\,(\pm 0.009),$$
$$\Delta\beta = -0.114\,(\pm 0.012) \times 10^{-3} V \sin i + 0.022\,(\pm 0.002).$$

The $\Delta(b-y)_0$ derived for β, $(b-y)_0$ *are* superposed over the data for α-Persei in Fig. 3(a). The combined data points yield

$$\Delta(b-y)_0 = 0.039\,(\pm 0.003) \times 10^{-3} V \sin i - 0.008\,(\pm 0.001).$$

For comparison in Figs 3, 4 and 5 the predicted values from Collins & Sonneborn (1977) are also shown (see Section 3.4).

3.2.2 *A Stars* .

The frequency of double-lined binaries, peculiar stars, emission-lined objects and visual binaries of small separation and small magnitude difference are very small amongst the 32 A type stars listed by Crawford & Perry (1976) in the Pleiades cluster. Following similar procedures we derive from β, c_0 and c_0, $(b-y)_0$ relations

$$\Delta c_0 = 0.273\,(\pm 0.039) \times 10^{-3} V \sin i - 0.035\,(\pm 0.006),$$

$$\Delta\beta = -0.108\,(\pm 0.014) \times 10^{-3} V \sin i + 0.014\,(\pm 0.003),$$

$$\Delta(b-y)_0 = 0.110\,(\pm 0.029) \times 10^{-3} V \sin i - 0.014\,(\pm 0.004),$$

$$\Delta c_0 = 0.345\,(\pm 0.051) \times 10^{-3} V \sin i - 0.044\,(\pm 0.007).$$

These results for A stars are displayed in Figs 6(b), 7(b) and 8(b). For comparison we also show in each of these figures the expected theoretical relationship (see Section 3.4) from Collins & Sonneborn (1977). The residuals in c_0, β and $(b-y)_0$ for the Pleiades A stars are listed in Table 3.

3.3 *The Effect of Rotation on Colours of Scorpio-Centaurus Association Stars*

The existence of different subgroups in this association and the fact that the upper Scorpius subgroup is younger than the other two subgroups was pointed out by Blaauw (1959, 1964). If the sample does not confirm to a homogeneous coeval group this would introduce a spread in the observed colour–magnitude diagrams. This is illustrated in Figs 9 and 10. A second-order common polynomial fit was determined for the β versus co relation for the stars in the upper Centaurus and upper Scorpius regions and the colour excess Δc_0 was determined. Fig. 9 is a plot of Δc_0 versus $V \sin i$. Only the two subgroups—upper Centaurus and upper Scorpius—are plotted. Upper Centaurus stars are represented by open squares and upper Scorpius stars by crosses. Similarly in Fig. 10 $\Delta(u-b)_0$ is plotted against $V \sin i$. It is clear from Figs 9 and 10 that the upper Scorpius stars which are younger, lie below the upper Centaurus stars. This would appear as a scatter in the diagram if all the points are plotted with the same symbol. In order to take into account such evolutionary effects even on the main sequence, the data analysis was carried out independently for the lower Centaurus, upper Centaurus and upper Scorpius subgroups. Removing the binaries, peculiar and emission-lined stars, whose colours may be affected due to reasons other than rotation, we are left with 10 stars out of the 13 possible stars of luminosity class IV and V in the lower Centaurus subgroup and 27 stars out of the possible 42 in the upper Centaurus subgroup listed in table 3 of Glaspey (1971). We have analysed them

Table 3. Effects of rotation for Pleiades A stars.

Hz	HD	Sp.	$V \sin i$	from β, c_0		from $c_0, (b-y)_0$		from $\beta, (b-y)_0$	
				Δc_0	$\Delta\beta$	Δc_0	$\Delta(b-y)_0$	$\Delta(b-y)_0$	$\Delta\beta$
27	23157	A9V	100	−0.021	0.010	−0.023	−0.007	0.003	0.001
28	23156	A7V	70	−0.024	0.010	−0.036	−0.005	0.002	−0.003
43	23194	A5V	20	−0.044	0.017	−0.034	−0.012	0.006	0.004
92	23246	A8V	200	0.040	−0.027	0.031	0.022	−0.004	−0.005
146	23325	Am?	75	0.008	−0.007	−0.006	0.006	−0.002	−0.005
187	23361	A3V	235	0.019	−0.007	0.009	0.005	−0.003	−0.004
206	23375	A9V	75	−0.014	0.005	−0.007	−0.006	0.000	0.002
248	23410	A0V	190	−0.005	0.005	−0.029	−0.033	−0.027	−0.011
251	23409	A2V	170	−0.001	0.002	0.008	−0.002	0.001	0.003
313	23479	A7	150	0.010	−0.011	0.021	0.007	−0.001	0.002
341	23489	A2V	110	−0.001	0.006	0.048	0.010	0.018	0.018
371	23512	A0V	150	−0.029	0.014	−0.027	−0.033	−0.015	−0.001
447	23567	A9	95	−0.026	0.013	−0.036	−0.014	−0.001	−0.004
457	23585	A9V	100	−0.027	0.013	−0.023	−0.010	0.004	0.003
501	23607	A7V	12	−0.040	0.017	−0.053	−0.014	0.002	−0.004
508	23629	A0V	160	−0.012	0.008	0.020	0.002	0.011	0.012
510	23632	A1V	235	0.032	−0.005	0.059	0.013	0.009	0.010
513	23628	A4V	215	0.023	−0.011	0.003	0.009	−0.004	−0.007
520	23631	A2V	10	−0.026	0.011	−0.071	−0.048	−0.036	−0.019
534	23643	A3V	185	0.046	−0.019	0.026	0.016	−0.005	−0.008
693	23733	A9V	180	0.010	−0.015	0.043	0.010	0.001	0.008
742	23763	A1V	105	0.031	−0.011	0.054	0.028	0.016	0.011
792	23791	A8V	85	−0.025	0.012	−0.034	−0.007	0.003	−0.001
885	23863	A7V	160	0.043	−0.022	0.018	0.021	−0.004	−0.009
891	23872	A2V	240	0.045	−0.011	0.059	0.013	0.003	0.005
924	23886	A3V	165	−0.020	0.008	−0.014	−0.003	0.005	0.003
975	23924	A7V	100	−0.019	0.007	−0.028	−0.002	0.003	−0.002
996	23948	A2V	120	−0.016	0.009	0.027	0.004	0.016	0.016
Tr47	23155		106	0.023	−0.007	0.019	0.005	−0.002	−0.002
S84	23430		118	−0.005	0.001	−0.014	0.003	0.002	−0.002
S108	23610			0.006	−0.005	−0.009	0.009	0.001	−0.004
S115	23664		61	0.017	−0.010	−0.002	0.011	−0.002	−0.006

separately and the colour excesses were calculated in c_0, $(u-b)_0$, β and $(b-y)_0$. $\Delta\beta$ was calculated from both β, c_0 and β, $(u-b)_0$ relations.

One has to be careful in the choice of the stars for determining rotation effects on colours. We illustrate this for the members of upper Scorpius subgroup. The notes given in various papers listed in Table 1 and the work of Garrison (1967) and Rajamohan & Pati (1980) were used for the selection of stars. Out of the 61 stars listed by Glaspey (1971) in the upper Scorpius region 4 have no β value. 8 stars deviate considerably in the β, c_0 plot. Among these 8, HD 142983 is classified as B5III Pe and HD 147196 as B8V nnP (Bright Star Catalogue: Hoffleit & Jaschek 1982) and therefore are emission-lined objects. HD 142301 and HD 147890 are spectroscopically peculiar. HD 148594 is classified as B8Vnn with a $V \sin i$ value of 300 km s^{-1}. It was probably an emission-lined object at the time of Glaspey's observation. HD 146332 is not a main-sequence star (B5II). That leaves HD 146029 and HD 147889 without any specific explanation. Their $V \sin i$ values are 250 and

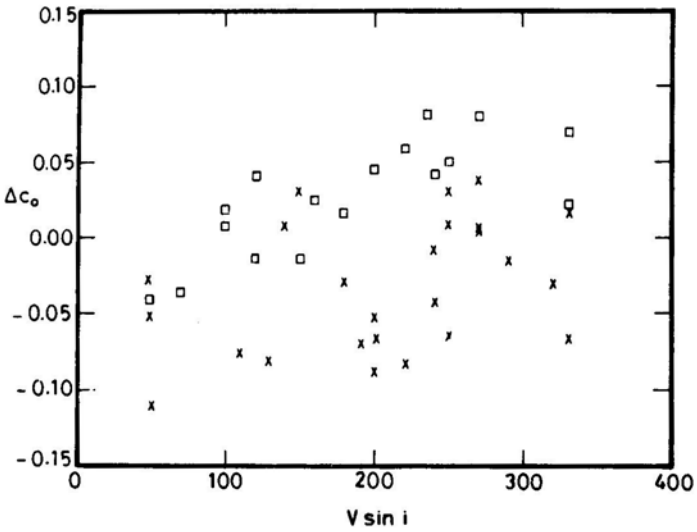

Figure 9. The deviations in c_0 derived from the observed β, c_0 of the two large subgroups of Scorpio-Centaurus association members are plotted against V sin i. Note the different distribution of upper Centaurus (open squares) and upper Scorpius (crosses) members due to evolutionary effects.

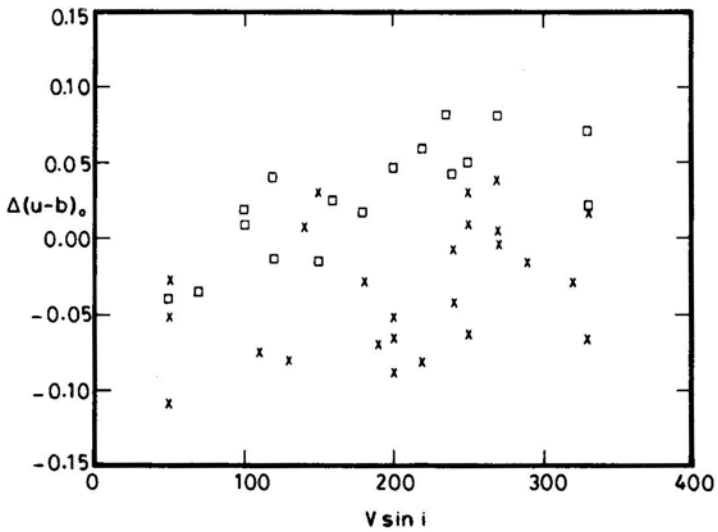

Figure 10. The deviations in $(u - b)_0$ derived from the observed β, $(u - b)_0$ of the two large subgroups of Scorpio-Centaurus association members are plotted against V sin i. Notice the different distributions of upper Centaurus (open squares) and upper Scorpius (crosses) members due to evolutionary effects.

100 km s^{-1}. Among the rest of the 49 stars 3 are giants. This leaves a sample of only 46 stars, of which 28 are apparently normal single main-sequence stars, 7 peculiar, 3 probably peculiar, 3 emission-lined objects, 3 double-lined spectroscopic binaries and 2 very close binaries with Δm less than 2 magnitudes.

We used this sample of 28 apparently normal stars to derive the relationship between β and c_0. Seven of the objects deviate considerably while we found that six out of the 10 peculiar stars seem to fit the Δc_0 versus $V \sin i$ relationship defined by normal single stars. Probably the line blanketing effects for these six stars are not large enough to have affected their colours. These 27 were used to derive the relationship between β and c_0.

The deviation Δc_0 for these 27 stars together with Δc_0 for 27 upper Centaurus and 10 lower Centaurus members are given in Table 4 and are plotted in Fig. 11. Fig. 11 may be compared with Fig. 9 to see the effect produced by small evolutionary differences between the subgroups even on the main sequence. Rotation effects cannot be noticed for such groups unless this evolutionary effect is taken into account. It must be emphasized once again that in the methodology adopted, only differences in age of stars within a cluster will produce a scatter. Differences in age of main sequence stars from cluster to cluster is taken care of by analysing them independently. On an average, we still find that the upper Scorpius subgroup objects lie slightly below the upper Centaurus subgroup. One possible cause could be the highly variable reddening across the upper Scorpius subgroup. A least square fit excluding HD 145792 and 142669 gives

$$\Delta c_0 = 0.280\,(\pm 0.033) \times 10^{-3} V \sin i - 0.059\,(\pm 0.007).$$

Similarly $\Delta\beta$ for these 27 stars together with $\Delta\beta$ for 27 upper Centaurus and 10 lower Centaurus members derived from β, c_0 relation are plotted in Fig. 4(b). A least square fit gives

$$\Delta\beta = -0.070\,(\pm 0.009) \times 10^{-3} V \sin i + 0.015\,(\pm 0.002).$$

The same 27 stars of upper Scorpius are used to derive the relationship between β and $(u - b)_0$. The deviations $\Delta(u - b)_0$ for these 27 stars together with $\Delta(u - b)_0$ for 10 lower Centaurus and 27 upper Centaurus members are plotted in Fig. 12. In the $\Delta(u - b)_0$ versus $V \sin i$ diagram HD 129116, 144294, 142114, 144334, 145792, and 146285 are found to deviate considerably. Excluding them, we derive

$$\Delta(u-b)_0 = 0.327\,(\pm 0.044) \times 10^{-3} V \sin i - 0.064\,(\pm 0.009).$$

$\Delta\beta$ for the 27 stars in upper Scorpius together with $\Delta\beta$ for 10 lower Centaurus and 27 upper Centaurus stars derived from β, $(u - b)_0$ relation are plotted in Fig. 5(b). A least square fit excluding the 6 stars listed above gives

$$\Delta\beta = -0.078\,(\pm 0.010) \times 10^{-3} V \sin i + 0.018\,(\pm 0.002).$$

The colour excess in $(b - y)_0$ is calculated from β, $(b - y)_0$ relation for the 27 stars in the upper Scorpius and is plotted in Fig. 3(b) together with $\Delta(b - y)_0$ for 10 lower Centaurus and 27 upper Centaurus stars. From this (excluding 145792 and 142669) we derive

$$\Delta(b-y)_0 = 0.030\,(\pm 0.004) \times 10^{-3} V \sin i - 0.006\,(\pm 0.008).$$

The various colour excesses due to rotation derived for the Scorpio-Centaurus association members are given in Table 4.

Table 4. Effect of rotation for Sco-Cen association B stars.

HD	Sp.	$V \sin i$	from β, c_0		from $(u-b)_0, \beta$		from $\beta, (b-y)_0$	
			Δc_0	$\Delta\beta$	$\Delta(u-b)_0$	$\Delta\beta$	$\Delta(b-y)_0$	$\Delta\beta$
				Lower-Cen				
105937	B3V	210	−0.026	0.010	−0.022	0.008	−0.005	0.014
106490	B2IV	120	0.022	−0.001	0.028	−0.002	0.002	0.001
106983	B2.5V	140	−0.014	−0.005	−0.009	−0.004	−0.002	−0.005
108483	B2V	220	−0.023	−0.005	−0.028	−0.003	−0.002	−0.006
109026	B5V	180	0.026	−0.005	0.046	−0.007	0.003	−0.005
109668	B2IV–V	190	−0.046	0.004	−0.056	0.004	−0.004	0.001
110956	B3V	75	−0.038	0.009	−0.057	0.011	−0.003	0.008
112078	B4V	330	0.084	−0.021	0.079	−0.018	0.008	−0.020
113703	B5V	160	0.002	0.013	−0.008	0.011	0.001	0.013
116087	B3V	300	0.014	0.000	0.027	−0.002	0.002	0.000
				Upper-Cen				
120307	B2IV	100	−0.008	0.004	−0.010	0.003	−0.001	0.000
121743	B2IV	120	−0.027	0.007	−0.040	0.007	−0.005	0.012
121790	B2V	200	0.006	−0.001	0.022	−0.005	0.000	−0.002
123291	B9	—	0.088	−0.022	0.115	−0.022	0.008	−0.021
125238	B2.5IV	235	0.044	−0.013	0.053	−0.012	0.005	−0.015
125823	B3P	100	−0.003	0.000	−0.009	0.001	0.000	−0.002
126110	B9	—	0.031	−0.004	0.032	−0.003	0.002	−0.002
126135	B9V	—	0.024	−0.009	0.038	−0.009	0.002	−0.005
128819	B7	—	0.017	−0.006	0.028	−0.007	0.001	−0.002
129116	B2.5V	170	−0.039	0.008	−0.089	0.016	−0.003	0.006
132094	B8	—	−0.002	0.006	−0.008	0.006	−0.001	0.006
132955	B3V	50	−0.065	0.014	−0.081	0.014	−0.015	0.039
133937	B7V	330	0.021	−0.010	0.025	−0.008	0.003	−0.009
136298	B2IV	240	0.033	−0.006	0.028	−0.004	0.003	−0.010
136482	B8	—	0.070	−0.021	0.079	−0.017	0.008	−0.020
136504	B2IV–V	120	0.003	−0.002	0.013	−0.004	0.001	−0.004
136664	B3V	220	0.003	−0.004	0.022	−0.006	0.002	−0.006
137432	B3V	160	−0.017	0.001	−0.016	0.001	0.000	0.000
138564	B9V	—	−0.109	0.043	−0.124	0.035	−0.010	0.034
138690	B2V	250	0.017	−0.004	0.029	−0.006	0.002	−0.008
138769	B3IVP	150	−0.050	0.011	−0.052	0.008	−0.004	0.010
138940	B8	—	0.032	−0.005	0.033	−0.004	0.003	−0.006
139233	B7V	—	−0.020	0.009	−0.034	0.010	−0.002	0.010
140008	B6V	70	−0.065	0.013	−0.080	0.014	−0.005	0.013
143118	B2V	270	0.051	−0.011	0.065	−0.012	0.005	−0.015
143699	B6V	180	−0.021	0.002	−0.024	0.002	0.000	−0.002
144294	B2.5	330	−0.011	0.001	−0.013	0.001	0.000	0.000
				Upper-Sco				
139160	B7IV	200	−0.040	0.011	−0.037	0.008	−0.003	0.009
141637	B2V	270	0.017	−0.007	0.046	−0.010	0.001	−0.006
142096	B2.5Vn	200	−0.043	0.012	−0.056	0.011	−0.004	0.011
142114	B2.5Vn	330	0.013	−0.005	−0.030	0.005	0.001	−0.005
142165	B6IVn	250	0.038	−0.011	0.038	−0.008	0.003	−0.010
142315	B8V	250	0.069	−0.017	0.059	−0.012	0.007	−0.018
142378	B3V	240	0.020	−0.007	0.025	−0.006	0.002	−0.007
142669	B2IV–V	140	0.059	−0.019	0.049	−0.011	0.006	−0.020
142883	B3V	110	−0.042	0.011	−0.045	0.009	−0.004	0.010
142884	B9P Si	220	−0.017	0.004	−0.051	0.010	−0.001	0.004

Table 4. Continued.

HD	Sp.	$V \sin i$	from β, c_0		from $(u-b)_0, \beta$		from $\beta, (b-y)_0$	
			Δc_0	$\Delta\beta$	$\Delta(u-b)_0$	$\Delta\beta$	$\Delta(b-y)_0$	$\Delta\beta$
142990	B5IV	150	0.024	−0.008	0.065	−0.014	0.002	−0.008
143567	B9V	290	−0.017	0.006	0.016	−0.002	−0.002	0.006
143600	B9V	320	−0.001	0.003	0.005	0.001	0.000	0.002
144334	B8P	50	−0.020	0.005	0.003	−0.001	−0.001	0.004
144470	B1V	130	−0.034	0.008	−0.034	0.005	−0.004	0.009
144844	B9IVP?	190	−0.044	0.012	−0.040	0.009	−0.004	0.012
145554	B9V	180	0.001	0.002	0.003	0.001	0.000	0.002
145631	B9.5Vn	200	−0.029	0.009	−0.018	0.006	−0.003	0.010
145792	B5V	50	0.022	−0.007	0.059	−0.012	—	—
146001	B7IV	240	0.008	−0.002	−0.014	0.003	0.001	−0.003
146285	B8IV	200	−0.039	0.011	−0.090	0.020	−0.002	0.007
146416	B9V	330	0.058	−0.013	0.047	−0.009	0.005	−0.012
146706	B9V	270	0.061	−0.014	0.069	−0.014	0.005	−0.013
147010	B9P	50	−0.061	0.017	−0.022	0.005	−0.006	0.016
148579	B9V	250	−0.008	0.004	−0.032	0.008	−0.001	0.004
148605	B2V	270	0.050	−0.016	0.043	−0.010	0.004	−0.015
149438	B0V	50	−0.044	0.011	−0.058	0.009	−0.004	0.009

3.4 *Theoretical Predictions*

3.4.1 *The B-Stars*

Collins & Sonneborn (1977) have calculated theoretical values of $(b - y)$, c_1, m, and β for rigidly rotating model stars. Plots are made with β and the different predicted colour indices at each value of i, the inclination between the line of sight and the rotation axis for various values of fractional angular velocity ω. Fig. 13 is a plot shown as an example between β and c_1 for $i = 60^0$ and ω = 0.2, 0.5, 0.8 and 0.9 for B0 to B9 stars. The points corresponding to different ω values are marked with different symbols and joined by dotted lines for each spectral class. The shift Δc along the x-axis for each value of ω for a given spectral type was determined from Fig. 12. Similarly the shift $\Delta\beta$ along the y-axis was determined for each value of ω. This was repeated for each value of i and the deviation in c_1 and β from the relation for ω = 0.2 is given in Table 5. We chose to derive the reddening due to rotation relative to ω = 0.2 for the following reason. Observationally one derives only the projected rotational velocity and the value of i is unknown. We do not know whether a really nonrotating, single, normal, main-sequence star exists (Rajamohan 1978). Also for comparison of observations with theory, it is sufficient if we derive the slope of the reddening effect due to rotation.

In $(u - b)$ also a similar analysis was done for various values of i and different values of ω and for different spectral types of the stars. These deviations are given in Table 6.

As an example we have plotted in Figs 14 and 15 the deviations in Δc_1 and $\Delta(u—b)$ in Tables 5 and 6 against $V \sin i$ for a representative value of i = 60° and ω = 0.2 to 0.9 for B0 to B9 stars. It is evident that the slope of the predicted effect is a function of the spectral type: low for B0 stars and high for B9 stars.

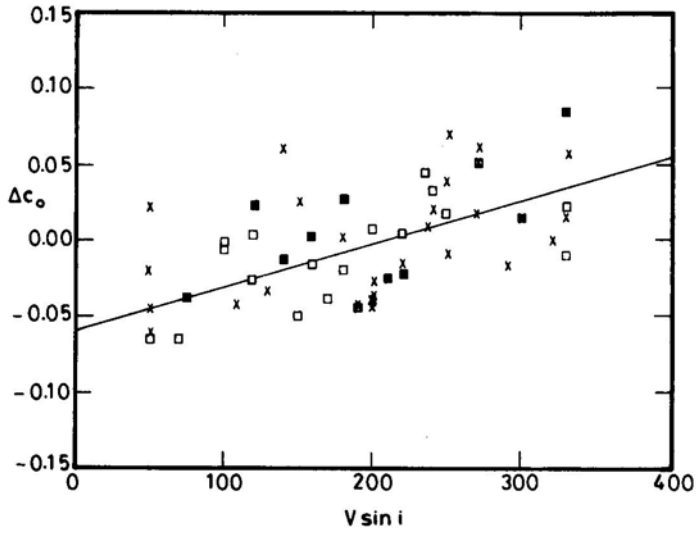

Figure 11. The deviations in c_0 derived from β, c_0 are plotted against V sin i for Scorpio-Centaurus members. Each subgroup was analysed independently and then superposed in this figure. Lower Centaurus (filled squares), upper Centaurus (open squares) and upper Scorpius (crosses).

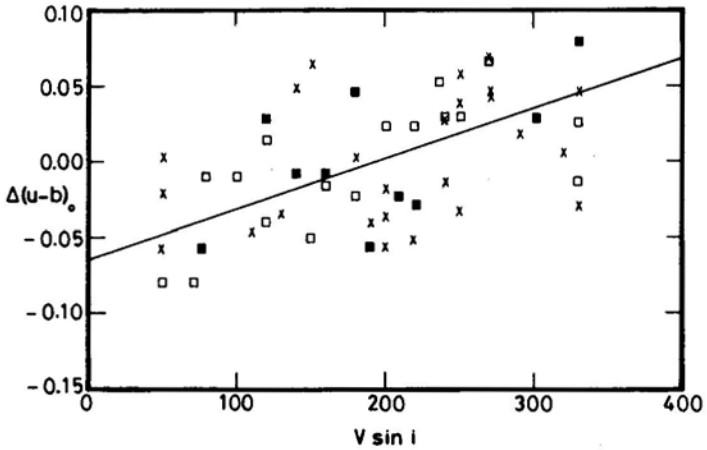

Figure 12. The deviations in $(u - b)_0$ are plotted against V sin i for Scorpio-Centaurus members. Symbols have the same meaning as in Fig. 10.

In order to compare these predictions from theoretical models of Collins and Sonneborn (1977) we have analysed the theoretical u, *v*, *b*, *y* and Hp indices in a similar way as we did for the cluster data. For this we have arranged the B stars into two groups B0 to B3 and B5 to B9. For each group at a given value of i and different values of ω, a second order polynomial fit was determined for the β versus c_1, β versus $(u - b)$ and β versus $(b - y)$ relation and the deviations $\Delta\beta$, Δc, $\Delta(u - b)$ and $\Delta(b - y)$ were determined. This was done for i = 30, 45, 60 and 90°. The slopes of the relation between V sin i and the colour excess derived for different values of i for B5 to B9 stars are given

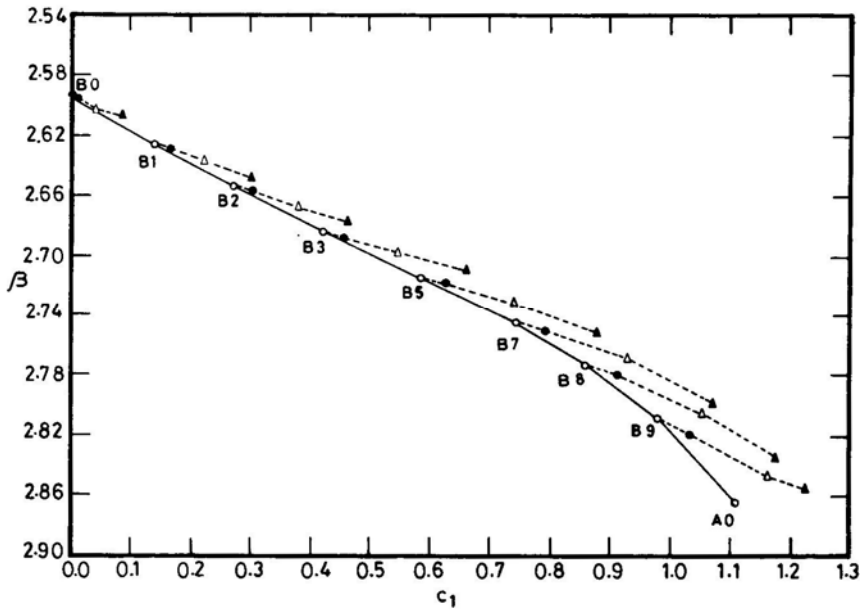

Figure 13. β versus c_1 plot from Collins & Sonneborn (1977) for $i = 60°$ and $\omega = 0.2$ (open circles), $\omega = 0.5$ (filled circles), $\omega = 0.8$ (open triangles) and $\omega = 0.9$ (filled triangles).

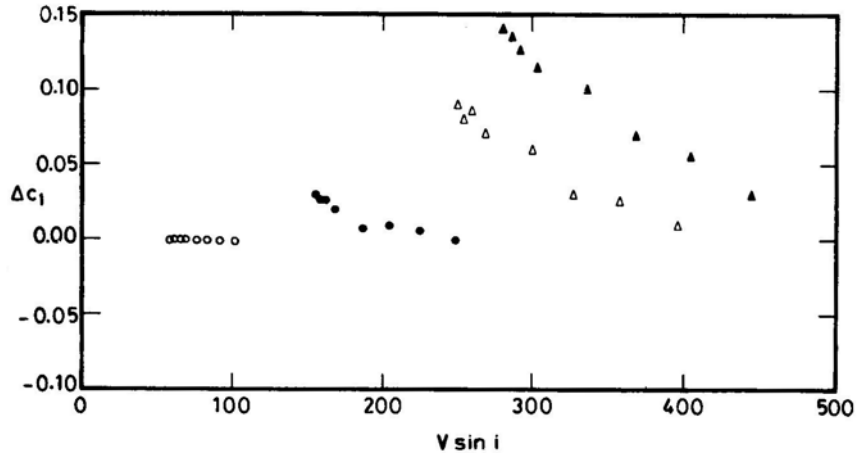

Figure 14. The deviations in c_1 derived from Fig. 12 are plotted against V sin i for $\omega = 0.2$ (open circles), $\omega = 0.5$ (filled circles), $\omega = 0.8$ (open circles) and $\omega = 0.9$ (filled triangles). The deviation at any given w increases from B0 to B9.

in Table 7 and for B0 to B3 stars are given in Table 8. These were derived in the following manner. Four values of ω were assigned to each spectral type. There are four spectral subclasses between B0 to B3 and B5 to B9 for which predicted values of β and various colour indices are available. Hence for each group at a given value of i we have sixteen values of various colour indices. These sixteen values were analysed the same way as we did the cluster stars. This was repeated for the next value of i.

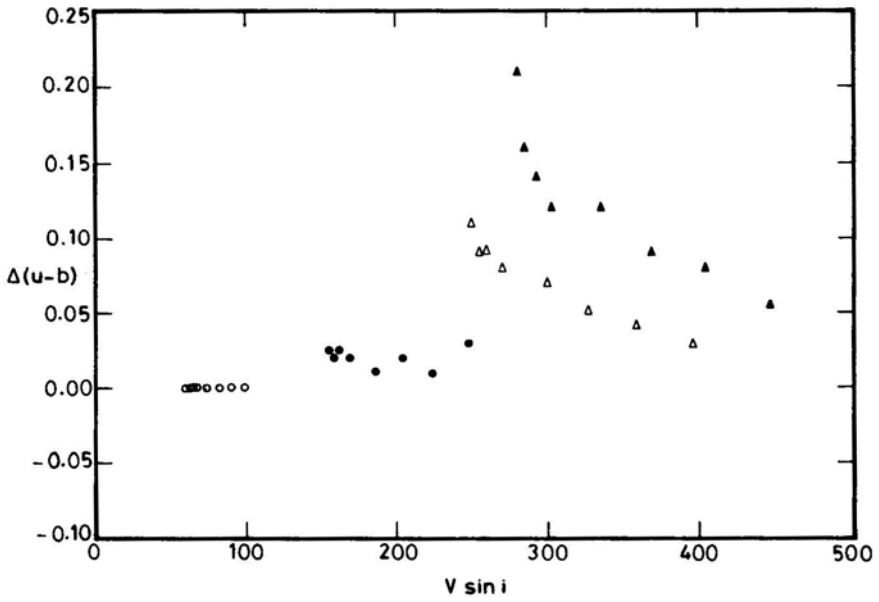

Figure 15. Deviations in $(u - b)$ derived from theoretical predictions for β, $(u - b)$ are plotted against V sin i. Symbols have the same meaning as in Fig. 13. Note that the slope of the rotation effect is a function of spectral type in Figs 14 and 15.

Typical examples for $i = 45°$ and $i = 60°$ (32 values each set) are plotted in Figs 3c, 4c and 5c.

3.4.2 *A Stars*

For A type stars, we followed a similar procedure and analysed the theoretical data the same way as we did for cluster data. We chose the theoretical indices for A3 to F0 type stars since the α-Persei and Pleiades cluster A type groups that we analysed contain mainly A3 to F0 type stars. For each value of i and different values of ω a second order polynomial fit was determined for β, c_1; c_1, $(b - y)$; and β, $(b - y)$ and the deviations $\Delta\beta$, Δc and $\Delta(b - y)$ were determined. This was done for $i = 30$, 45, 60 and 90°. The slopes of the relation between V sin i and the colour excess derived for different values of i are given in Table 9.

4. Discussion

4.1 *The B Stars*

Before analysing the available observational data for determining rotation effects, we first had to choose a homogeneous group of stars, at a common stage of evolution, with colours unaffected due to reasons other than rotation. However, the sample of such a group available is small in each cluster and further division by spectral type is

Table 5. Theoretical effects of rotation.

Sp..	ω	$i=30$		$i=60$		$i=90$	
		$\Delta\beta$	Δc_1	$\Delta\beta$	Δc_1	$\Delta\beta$	Δc_1
BO	0.2	0.000	0.000	0.000	0.000	0.000	0.000
	0.5	0.010	0.070	0.000	0.000	0.010	0.070
	0.8	0.010	0.070	0.002	0.010	0.010	0.070
	0.9	0.010	0.070	0.008	0.030	0.012	0.090
B1	0.2	0.000	0.000	0.000	0.000	0.000	0.000
	0.5	0.003	0.015	0.002	0.005	0.001	0.005
	0.8	0.008	0.035	0.006	0.025	0.006	0.035
	0.9	0.009	0.050	0.012	0.055	0.014	0.080
B2	0.2	0.000	0.000	0.000	0.000	0.000	0.000
	0.5	0.003	0.015	0.007	0.010	0.002	0.015
	0.8	0.005	0.025	0.017	0.030	0.007	0.040
	0.9	0.010	0.050	0.014	0.070	0.016	0.080
B3	0.2	0.000	0.000	0.000	0.000	0.000	0.000
	0.5	0.003	0.015	0.005	0.007	0.002	0.015
	0.8	0.005	0.025	0.010	0.060	0.013	0.060
	0.9	0.010	0.050	0.020	0.100	0.020	0.100
B5	0.2	0.000	0.000	0.000	0.000	0.000	0.000
	0.5	0.003	0.025	0.004	0.020	0.004	0.020
	0.8	0.012	0.060	0.014	0.070	0.016	0.080
	0.9	0.018	0.090	0.030	0.115	0.030	0.120
B7	0.2	0.000	0.000	0.000	0.000	0.000	0.000
	0.5	0.003	0.015	0.006	0.025	0.005	0.030
	0.8	0.020	0.060	0.026	0.085	0.023	0.080
	0.9	0.040	0.110	0.040	0.125	0.047	0.130
B8	0.2	0.000	0.000	0.000	0.000	0.000	0.000
	0.5	0.005	0.020	0.008	0.025	0.006	0.025
	0.8	0.027	0.070	0.031	0.080	0.038	0.090
	0.9	—	0.130	—	0.135	—	0.150
B9	0.2	0.000	0.000	0.000	0.000	0.000	0.000
	0.5	0.010	0.030	0.012	0.030	—	0.030
	0.8	—	0.085	—	0.090	—	0.100
	0.9	—	0.130	—	0.140	—	0.160

not possible at this stage. Therefore a comparison with theoretical predictions at each spectral type is impossible except for B2 and B3 stars in upper Centaurus: Further, only projected rotational velocities can be derived from observations and i remains unknown. Therefore, the α-Persei and Pleiades B and A stars were analysed separately. The Scorpio-Centaurus association members are all of type B. However, we found that the predicted slope of the rotation effect for various colour indices is strongly dependent on the spectral type. The slope increases as we go from B0 to B9. Therefore, we decided to subdivide the B-stars into two subgroups; namely B0 to B3 and B5 to B9. The choice of this subdivision was based on the spectral type distribution in these three clusters.

In α-Persei and Pleiades, out of the total 31 apparently normal main sequence stars 19 are in the spectral type range B5 to B9, 2 stars in the range B0 to B3 and 10 in the range A0 to A2. In Scorpio-Centaurus association, out of the 64 apparently normal

Table 6. Theoretical effects of rotation

Sp.	ω	$i=30$		$i=60$		$i=90$	
		$\Delta\beta$	$\Delta(u-b)$	$\Delta\beta$	$\Delta(u-b)$	$\Delta\beta$	$\Delta(u-b)$
B0	0.2	0.000	0.000	0.000	0.000	0.000	0.000
	0.5	0.001	0.004	0.003	0.030	0.001	0.010
	0.8	0.003	0.020	0.004	0.030	0.002	0.020
	0.9	0.006	0.040	0.008	0.055	0.009	0.070
B1	0.2	0.000	0.000	0.000	0.000	0.000	0.000
	0.5	0.001	0.010	0.002	0.010	0.001	0.010
	0.8	0.005	0.035	0.006	0.040	0.006	0.040
	0.9	0.008	0.050	0.012	0.080	0.013	0.090
B2	0.2	0.000	0.000	0.000	0.000	0.000	0.000
	0.5	0.001	0.010	0.003	0.020	0.002	0.010
	0.8	0.004	0.030	0.008	0.050	0.007	0.050
	0.9	0.008	0.060	0.012	0.090	0.015	0.100
B3	0.2	0.000	0.000	0.000	0.000	0.000	0.000
	0.5	0.002	0.010	0.002	0.010	0.002	0.020
	0.8	0.006	0.045	0.009	0.070	0.010	0.080
	0.9	0.012	0.080	0.017	0.120	0.020	0.120
B5	0.2	0.000	0.000	0.000	0.000	0.000	0.000
	0.5	0.002	0.015	0.003	0.020	0.002	0.020
	0.8	0.009	0.060	0.010	0.080	0.014	0.090
	0.9	0.016	0.100	0.020	0.120	0.020	0.140
B7	0.2	0.000	0.000	0.000	0.000	0.000	0.000
	0.5	0.002	0.020	0.005	0.025	0.006	0.025
	0.8	0.015	0.070	0.018	0.090	0.025	0.110
	0.9	0.030	0.120	0.033	0.140	0.024	0.160
B8	0.2	0.000	0.000	0.000	0.000	0.000	0.000
	0.5	0.004	0.020	0.005	0.020	0.006	0.030
	0.8	0.020	0.080	0.022	0.090	0.024	0.100
	0.9	—	0.140	—	0.160	—	0.180
B9	0.2	0.000	0.000	0.000	0.000	0.000	0.000
	0.5	0.005	0.020	0.006	0.025	0.010	0.030
	0.8	—	0.090	—	0.110	—	0.120
	0.9	—	0.180	—	0.210	—	0.250

Table 7. Theoretical reddening due to rotation for 100 km s^{-1} of $V \sin i$ for B5 to B9 stars.

i	from β, c_1		from β, $(u-b)$		from β, $(b-y)$		from c_1, $(b-y)$	
	c_1	β	β	$(u-b)$	β	$(b-y)$	c_1	$(b-y)$
30	0.058	−0.014	−0.012	0.066	−0.010	0.006	0.006	0.000
	±0.007	±0.002	±0.002	±0.009	±0.003	±0.002	±0.005	±0.002
45	0.046	−0.011	−0.010	0.054	−0.009	0.005	0.000	0.000
	±0.005	±0.001	±0.002	±0.007	±0.002	±0.001	±0.004	±0.001
60	0.041	−0.010	−0.009	0.049	−0.008	0.005	0.001	0.000
	±0.004	±0.001	±0.001	±0.006	±0.002	±0.001	±0.003	±0.001
90	0.038	−0.009	−0.008	0.047	−0.007	0.005	0.000	0.000
	±0.004	±0.001	±0.001	±0.005	±0.002	±0.001	±0.003	±0.001
mean	0.046	−0.011	−0.010	0.054	−0.009	0.005	0.002	0.000

Table 8. Theoretical reddening due to rotation for 100 km s^{-1} of V sin *i* for B0 to B3 stars.

i	from β, c_1		from β, $(u-b)$		from β, $(b-y)$		from c_1, $(b-y)$	
	c_1	β	β	$(u-b)$	β	$(b-y)$	c_1	$(b-y)$
30	0.021	−0.004	−0.004	0.027	−0.004	0.004	−0.001	0.001
	±0.002	±0.000	±0.000	±0.003	±0.000	±0.000	±0.001	±0.000
45	0.016	−0.003	−0.003	0.022	−0.004	0.003	−0.004	0.001
	±0.002	±0.000	±0.000	±0.003	±0.000	±0.000	±0.001	±0.000
60	0.016	−0.003	−0.003	0.021	−0.004	0.003	−0.003	0.001
	±0.002	±0.000	±0.000	±0.002	±0.000	±0.000	±0.001	±0.000
90	0.015	−0.003	−0.003	0.021	−0.003	0.003	−0.002	0.001
	±0.002	±0.000	±0.000	±0.002	±0.000	±0.000	±0.000	±0.000
mean	0.017	−0.003	−0.003	0.023	−0.004	0.003	−0.003	0.001

main-sequence stars, 32 are of type B5 to B9 and 32 are of spectral type B0 to B3. Among them the *V* sin *i* values of 9 stars of type B5 to B9 are not known.

In order to compare the results of analysis of the data for these clusters with predictions of Collins & Sonneborn (1977), the theoretical line indices were divided into B0 to B3 and B5 to B9 groups (see Section 3.4). In Table 10, the slopes of the observed relation between colour excess and *V* sin *i* are tabulated.

For Δc_0, the observed slope for α-Persei and Pleiades members is 0.040 ± 0.003 magnitudes per 100 km s^{-1} of *V* sin *i*. This can be compared with the expected theoretical value for B5 to B9 stars in Table 7. The value of the slope for Δc_0 ranges from 0.038 ± 0.004 for $i = 90°$ to 0.058 ± 0.007 for $i = 30°$. We have no specific reason to believe that the rotation axes in clusters are randomly distributed (Rajamohan 1978). Therefore, the observed value of 0.04 for the slope of Δc_0, *V* sin *i* relation for α-Persei and Pleiades members can be deemed to be in excellent agreement with theoretical predictions of Collins & Sonneborn (1977).

Similarly in $(u - b)_0$, the observed effect of 0.044 ± 0.005 per 100 km s^{-1} of *V* sin *i* is in excellent agreement with the average predicted value of about 0.05 for B5 to B9 stars. From β, $(b - y)$ we derive that the effect in $(b - y)$ is 0.004 per 100 km s^{-1} of *V* sin *i* for α-Persei and Pleiades in agreement with the value of 0.003 predicted by theory. In a colour-colour plot of. c_1 , $(b - y)$ no effect is found, again in excellent agreement with theoretical predictions. Comparison of the various observed slopes given in Table 9 for α-Persei and Pleiades are found, in general, to be in excellent agreement with predictions made from theory for B5 to B9 stars.

The Scorpio-Centaurus association consists of B0 to B9 stars and the average slope derived for various colour indices are in good agreement with the average value predicted for B0 to B9 stars. We tested this, in particular, by deriving the reddening in c_0 independently for upper Centaurus stars which are mostly B2 and B3 stars. The derived value of 0.017 ± 0.005 for this subgroup is in excellent agreement with that predicted by theory for B2 and B3 stars (see Fig. 16). The value derived from Collins & Sonneborn (1977) predicted colour indices lead to a value for Δc_1 of 0.018 ± 0.002 for B2 and B3 stars.

Rotation also affects the observed spectral types at a given mass. However, this effect is considerable only when the stars rotate close to their breakup speeds. Such objects have already been eliminated as most of them would appear as emission-lined

Table 9. Observed reddening due to rotation for 100 km s^{-1} of $V \sin i$ in B stars.

Sp.	No. of stars	from β, c_0		from β, $(u-b)_0$		from β, $(b-y)_0$		from c_0, $(b-y)_0$	
		c_0	β	β	$(u-b)_0$	β	$(b-y)_0$	c_0	$(b-y)_0$
α-Persei									
B0–B3	2	0.044	−0.015	−0.013	0.053	−0.016	0.004	0.000	0.000
B5–B9	14	±0.003	±0.001	±0.001	±0.005	±0.001	±0.000	±0.000	±0.000
A0–A2	7								
α-Persei + Pleiades									
B0–B3	2	0.040	−0.015	−0.011	0.047	−0.016	0.004	0.000	0.000
B5–B9	19	±0.003	±0.001	±0.001	±0.005	±0.001	±0.000	±0.000	±0.000
A0–A2	10								
Sco-Cen									
B0–B3	31	0.028	−0.007	−0.006	0.033	−0.008	0.003	0.000	0.000
B5–B9	22	±0.003	±0.001	±0.001	±0.004	±0.001	±0.000	±0.000	±0.000
				Theoretical means					
B5–B9		0.046	−0.011	−0.010	0.054	−0.009	0.005	0.002	0.000
B0–B3		0.017	−0.003	−0.003	0.023	−0.004	0.003	−0.003	0.001
B0–B9		0.032	−0.007	−0.007	0.039	−0.007	0.004	0.000	0.000

Table 10. Theoretical reddening due to rotation for 100 km s $^{-1}$ of V sin i in A stars.

i	from β, c_1		from c, $(b-y)$		from β, $(b-y)$	
	c_1	β	$(b-y)$	c_1	$(b-y)$	β
30	0.035	−0.016	0.020	0.041	0.003	0.003
	±0.004	±0.002	±0.003	±0.006	±0.002	±0.002
45	0.027	−0.012	0.013	0.026	0.000	0.000
	±0.003	±0.001	±0.002	±0.005	±0.001	±0.001
60	0.022	−0.011	0.009	0.019	−0.001	−0.002
	±0.003	±0.001	±0.002	±0.004	±0.001	±0.001
90	0.016	−0.008	0.006	0.012	−0.002	−0.002
	±0.003	±0.001	±0.002	±0.003	±0.001	±0.001
mean	0.025	−0.012	0.012	0.025	0.000	0.000

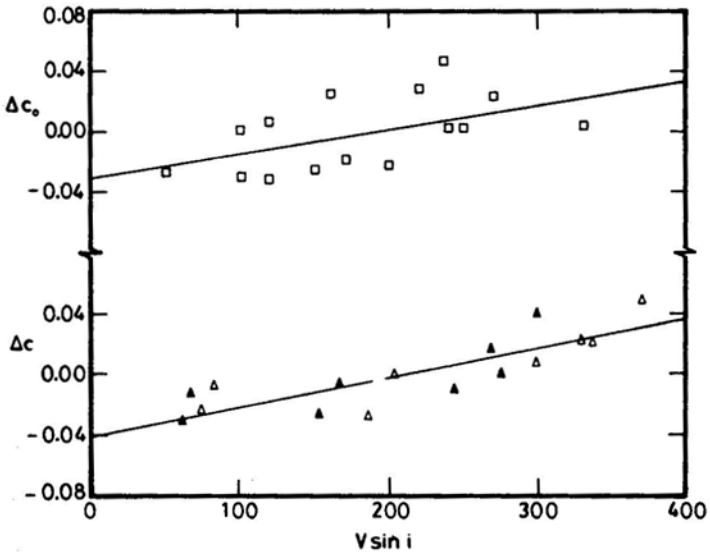

Figure 16. The deviations in c0 derived from β, c_0 of B2, B3 stars in (a) Upper-Centaurus, (b) theoretical predictions for i = 45° and 60° are plotted against V sin i.

objects. Only few stars rotate near breakup limits (see also Collins & Sonneborn 1977). For the large majority of the stars in Table 2–4 this effect would not be more than one or two spectral subdivisions. The results in Tables 8 and 10 should be highly representative for the observed spectral type groups given.

These results suggest that the main-sequence stars of type B are probably rigid rotators and that differential rotation for these objects can be ruled out. Gray & Garrison (1987) suggested that the A stars in the field are probably rotating differentially. We discuss this in the next subsection on A-stars.

Table 11. Observed reddening due to rotation for 100 km s^{-1} of $V \sin i$ in A stars.

Cluster	from β, c_0		from c_0, $(b-y)_0$		from β, $(b-y)_0$	
	c_0	β	$(b-y)_0$	c_0	$(b-y)_0$	β
α-Persei	0.031	−0.016	0.012	0.020	−0.005	−0.004
	±0.004	±0.003	±0.005	±0.004	±0.003	±0.001
Pleiades	0.027	−0.011	0.011	0.035	0.001	0.002
	±0.004	±0.002	±0.002	±0.005	±0.002	±0.002

4.2 *A Stars*

The reddening for various colour indices derived for α-Persei and Pleiades A stars together with that derived from colour indices predicted by Collins & Sonneborn (1977) are given in Table 11. The majority of the stars analysed for the A-group in α-Persei and Pleiades are in the spectral type range A3 to FO. The theoretical predictions for this spectral type range for i = 45° and 60° are in excellent agreement with the observed values.

In fact it is a bit surprising that in spite of the various uncertainties the agreement is excellent between observations and predictions of Collins & Sonneborn (1977) for rigidly rotating stars. We believe that this became possible because we eliminated all that scatter in the diagrams that would have been introduced by including double-lined binaries, emission-lined objects and highly peculiar objects. Further, by analysing each cluster separately, and each subgroup in Scorpio-Centaurus separately we were able to eliminate most of the uncertainties that would have otherwise been introduced.

Gray & Garrison (1989) derived a higher slope for the effect in c_0 for field F-type stars. They suggested that field F stars may be rotating differentially but that no firm conclusion can be drawn and that the different slopes derived may also be due to evolutionary effects. We find that differences in the evolutionary stage of the stars even on the main sequence will introduce a large scatter in the observed effect. This is amply demonstrated by the Scorpio-Centaurus association where we find that the two subgroups, if analysed together, produces a large scatter in the Δc_0, $V \sin i$ and $\Delta (u - b)_0$, $V \sin i$ diagrams. Even though F stars have much longer main sequence lifetime than B-stars, evolutionary effects may be important for field F-stars.

5. Conclusion

The reddening effect due to rotation on various colour indices and H_β is firmly established. These effects as observed in α-Persei, Pleiades and Scorpio-Centaurus association members, having a range in spectral type in B0 to F0, are in excellent agreement with theoretical calculations of photometric effect due to rigid rotation by Collins & Sonneborn (1977).

We emphasize that evolutionary effects even on the main sequence can lead to scatter in the reddening effects if not properly taken into account. This is amply

demonstrated by our analysis of different subgroups in the Scorpio-Centaurus association.

Acknowledgements

We are thankful to the referees of paper 1 of this series for pointing out the problem of using observed indices instead of dereddened indices especially for B-stars to evaluate the rotation effects. We are also thankful to Drs R. O. Gray and R. F. Garrison for pointing out to us the problem of using dereddened indices, especially for A-stars, instead of the observed colour indices. The suggestion of Prof. G. W. Collins II that a detailed theoretical comparison be made helped in improving this paper considerably. We are thankful to Messrs Arvind Paranjpye, S. Rajasekaran and S. Muthukrishnan for the help rendered by them in the preparation of this paper.

References

Anderson, C. M., Stoeckly, R., Kraft, R. P. 1966*, Astrophys. J.,* **143**, 299.
Blaauw, A. 1959 *IAU Symp.* 10: *The Hertzsprung Russell Diagram,* J. Greenstein, Ed. p. 105.
Blaauw, A. 1964, *A. Rev. Astr. Astrophys.* **2**, 213.
Collins, G. W. II, Sonneborn, G. H., 1977, *Astrophys. J. Suppl.,* **34**, 41.
Collins, G. W. II., Smith, R. C. 1985, *Mon. Not. R. astr. Soc,* **213**, 519.
Crawford, D. L., Perry, C. L. 1976, *Astr. J.,* **81**, 419.
Crawford, D. L, Barnes, J. V. 1974, *Astr. J.,* **79**, 687.
Dickens, R. J., Kraft, R. P., Krzeminski, W. 1968, *Astr. J.,* **73**, 6.
Garrison, R. F.1967, *Astrophys. J.,* **147**, 1003.
Glaspey, J. W. 1971, *Astr. J.,* **76**, 1041.
Gray, R. O., 1988, *J. R. astr. Soc. Can.,* **82**, 336.
Gray, R. O., Garrison, R. F.1987, *Astrophys. J. Suppl.,* **65**, 581.
Gray, R. O., Garrison, R. F.1989, *Astrophys. J. Suppl.,* **69**, 301.
Gray, R. O., Garrison, R. F. 1989, *Astrophys. J. Suppl.,* **70**, 623.
Guthrie, B. N. G., 1963, *Edinburgh Obs. Bull, III* No. **4**, 82.
Hertzsprung, E. 1947, *Ann. Sterrew. Leiden* **19**, pt. 1.
Hoffleit, D., Jaschek, C,1982, *The Bright Star Catalogue,* Yale Univ. Obs., New Haven (BSC).
Kraft, R. P. 1967, *Astrophys. J.,* **148**, 129.
Kraft, R. P., Wrubel, M. 1965, *Astrophys. J.,* **142**, 703.
Petrie, R. M. 1965, *Publ. Dom. Astrophys. Obs.,* **12**, 317.
Rajamohan, R. 1978, *Mon. Not. R. astr. Soc.,* **184**, 743.
Rajamohan, R. 1976, *Pramana,* **7**, 160.
Rajamohan, R., Mathew, A.1988, *J. Astrophys. Astr.,* **9**, 107.
Rajamohan, R., Pati, A. K. 1980, *J. Astrophys. Astr.,* **1**, 155.
Slettebak, A.1968, *Astrophys. J.,* **151**, 1043.
Slettebak, A., Kuzma, T. J., Collins, G. W. 1980, *Astrophys. J.,* **242**, 171.
Uesugi, A., Fukuda, I. 1982, *Revised Catalogue of Stellar Rotational Velocities.* Kyoto Univ., Japan.
Warren, W. H. 1976, *Mon. Not. R. astr. Soc.,* **174**, 111

J. Astrophys. Astr. (1990) **11**, 193–208

Radiative Transfer With Compton Scattering in Plane Parallel Geometry

A. Peraiah *Indian Institute of Astrophysics, Bangalore 560034*

Received 1989 July 27; revised 1990 March 23; accepted 1990 April 5

Abstract. We have solved the equation of radiative transfer with Compton scattering. The specific intensity has been expanded by Taylor series with respect to wavelength and the first three terms have been retained in solving the transfer equation. It is noted that in a medium stratified in plane parallel layers, the multiple Compton scattering redistributes the initial energy over a range of 3 to 5 Compton wavelengths. A good fraction of the incident radiation is transferred across the layer with redistribution in wavelength, the actual value depending on the optical thickness of the medium.

Key words: radiative transfer—Compton scattering

1. Introduction

One of the many reasons for broadening and asymmetry of the spectral lines formed in the outer layers of stars is the scattering of radiation by free electrons which also contributes to the continuous opacity in hot stars. The electrons produce a change in wavelength of photons due to this effect. It is necessary to investigate how the energy is redistributed in wavelengths and what fraction of incident energy is emerging out of a plane parallel slab with consequent redistribution.

Pomraning & Froehlich (1969), considered the equation of transfer with Compton and inverse Compton scattering which admits an eigen-function expansion. Viik (1968a, b) attempted to solve the equation of transfer in an analytical way following Chandrasekhar's approach. However, no physical effects are shown. Missana & Piana (1976) have shown that Compton scattering can cause a reduction in the central intensity in the absorption and emission lines. Pozdnyakov, Sobol & Sunyaev (1976) have studied multiple Compton scattering of low frequency photons by relativistic electrons. Langer (1979) studied the problem of Comptonization of X-rays by cold-electrons by using Monte Carlo method. Nagel (1981) studied the problem of Comptonization in hot and strongly magnetized plasma using a two-stream transfer equation with redistribution of photons in a cyclotron line. Barbosa (1982) gives useful expressions for Compton scattering coefficients by evaluating the full Klein-Nishina cross-section. Missana (1982) suggested the possibility of a large Compton redshift in the spectra of β Orionis. Ipser & Price (1983) have shown that dissipative heating due to magnetic reconnection, and dissipation of turbulence leads to high accretion rates in a spherical accretion of gas onto a black hole, to densities and temperatures at

which Comptonization becomes important. Pozdynakov, Sobol & Sunyaev (1983) have described different aspects of Compton scattering. Czerny & Sztajno (1983) studied the effects of Compton scattering on the spectrum of X-ray bursts. You *et al.* (1982) studied the synchrotron self-Compton effect. Keiner & Shikhovtseva (1983) have obtained analytical solutions for the transfer equation for the photon density matrix in the case of inverse Compton reflection. Ochelkov & Usov (1983) analysed the spontaneous Compton scattering of electromagnetic radiation by ultra-elativistic particles in magnetic fields. Nagirner (1984) studied multiple Compton scattering by gas in which the photon energy is much less than the electron rest-energy. Gould (1984) has given the cross-section of double Compton scattering for $\gamma + r \gg e + \gamma + \gamma'$ for the energies in the spectrum of outgoing photons.

Sunyaev and Titarchuk (1985) considered Comptonization of low-frequency radiation in accretion discs. They have employed the method of successive approximations over the number of scatterings. However, they did not consider the frequency dependence of the scattering cross-section and indicatrix. They have shown that in the accretion discs the angular distribution and polarization of hard radiation forming via Comptonization, that is, multiple scatterings in the discs depend only on the optical thickness of the disc and are independent of either the photon frequency or the geometric distribution of low-frequency photons. They have presented calculations of polarization and angular distribution for several values of optical thickness. Bloemen (1985) studied the production of diffuse galactic gamma radiation above 1 MeV from the interaction of cosmic-ray electrons with the interstellar photon field. The source function for the inverse Compton scattering is described. Fukue, Kato & Matsumoto (1985) examined the radiative transfer in a hot moving plasma which interacts with photons through the Compton process. Xia *et al.* (1985) obtained the total cross-sections for the inverse Compton scattering in strong magnetic fields (10^{12}–10^{13} G). They found that these are large when the frequencies of the incoming photons are near the resonance frequencies. Guilbert (1986) obtained exact results for calculating Compton heating and cooling in optically thin gases. Kirk (1986) suggested that the flat spectrum of X-ray pulsars is due to the optically thin emission from resonant double Compton scattering. Bhat, Kifune & Wolfendale (1986) have used different data to determine the number of Cygnus X3 like X-ray sources in the Galaxy. They have developed a method of studying the number of sources which have existed in the past by way of high latitude inverse Compton photons. Lovelace (1987) developed a model for a possible early phase of extragalactic jets. Mezaros & Bussard (1986) calculated the angle-dependent Compton redistribution function which can be applied in studying X-ray sources. Daugherty & Harding (1986) calculated the angle-dependent Compton redistribution function which can be applied in studying X-ray sources. They also derived relativistic cross-sections for Compton scattering by electrons in strong magnetic fields. Zdziarski & Lamb (1986) presented a model of γ-ray burst sources based on repeated Compton scatterings of soft photons by relativistic nonthermal electrons. Nishimura, Mitsuda & Itoh (1986) studied analytically the Comptonization of soft X-ay photons in a plane parallel infinite plasma cloud. Kirk, Nagel & Storey (1986) solved the equation of transfer using Feautrier's method in calculating the phase dependent spectra of X-ray pulsars in a slab geometry,

Different methods of solution to the hard X-ray transfer problem are required. Particularly we need a method that works for soft and hard X-ray transfer problems

with Compton and inverse Compton scattering included. Peraiah (1986) has derived transmission and reflection functions with Compton scattering.

We start with the assumption that the medium is divided into plane parallel layers and each is of equal optical thickness. The scattered radiation is a function of the wavelength and therefore we have to consider the specific intensities in different wavelengths. For this purpose the specific intensity is expanded in Taylor series as was done in Chandrasekhar (1960) and Code (1967). However, these authors have considered only the first derivative $\partial I/\partial\lambda$ and we shall include the second derivative $\partial^2 I/\partial\lambda^2$ also so that the solution represents a fairly good approximation to the reality.

2. Calculations

Following Chandrasekhar (1960) and Code (1967), the equation of transfer can be written as,

$$\mu\frac{\partial I(z,\mu,\lambda)}{\partial z}=-KI(z,\mu,\lambda)+K\Bigg[(1-\omega)B+\frac{\omega}{4\pi}\int_{-1}^{+1}\int_{0}^{2\pi}I(z,\mu',\lambda-\delta\lambda)d\mu'd\varphi'\Bigg], \tag{1}$$

where

$$\delta\lambda=\gamma(1-\cos\theta), \tag{2}$$

$$\gamma=\frac{h}{mc}=0.024\ \text{Å}, \tag{3}$$

B = Planck function,

$$\cos\theta=\mu\mu'+(1-\mu^2)^{1/2}(1-\mu'^2)^{1/2}, \tag{4}$$

ω = albedo for single scattering.

We have to consider the contribution of $I(z,\ \mu',\lambda\ \delta\lambda\ )$ to the radiation field after scattering. We shall expand $I(z,\ \mu',\ \lambda-\delta\lambda)$ by Taylor series as,

$$I(z,\mu',\lambda-\delta\lambda)=I(z,\mu',\lambda)-\frac{\delta\lambda}{1!}\frac{\partial I(z,\mu',\lambda)}{\partial\lambda}+\frac{(\delta\lambda)^2}{2!}\frac{\partial^2 I(z,\mu',\lambda)}{\partial\lambda^2}. \tag{5}$$

After substituting equation (5), in (1) and performing the integration over φ' we obtain,

$$\mu\frac{\partial I(z,\mu,\lambda)}{\partial z}=-KI(z,\mu,\lambda)+K\Bigg[(1-\omega)B+\frac{\omega}{2}\int\Bigg\{I(z,\mu',\lambda)-\gamma(1-\mu\mu')\times\frac{\partial I(z,\mu',\lambda)}{\partial\lambda}+\Bigg[\frac{1}{2}\gamma^2\Bigg((1-\mu\mu')^2+\frac{1}{2}(1-\mu^2)(1-\mu'^2)\Bigg)\times\frac{\partial^2 I(z,\mu',\lambda)}{\partial^2\lambda}\Bigg]\Bigg\}d\mu'\Bigg]. \tag{6}$$

We shall retain the two terms containing $\partial I/\partial\lambda$ and $\partial^2 I/\partial\lambda^2$ and choose the points for wavelengths in steps of the Compton wavelength. If we choose n discrete points of λ,

then we have η equations each similar to that given in (6). Therefore we have *n* terms of $\partial I_i/\partial\lambda i$, and $\partial^2 I_i/\partial^2\lambda_i$ in *n* equations. The term $\partial Ii/\partial\lambda i$, is replaced by its difference as given below.

$$\frac{\partial I_i}{\partial\lambda_i}=\frac{I_i-I_{i-1}}{\lambda_i-\lambda_{i-1}}.$$

When all the *n* equations are considered, the quantities $\partial I_i/\partial\lambda_i$, $\partial I_{i+1}/\partial\lambda_{i+1}$, $\partial I_{i+2}/\partial\lambda_{i+2}$ *etc.* will form into a vector. Consequently the terms $\partial I/\partial\lambda$ in *n* equations when combined will form into $\mathbf{D_1I}$ where

$$\mathbf{D}_1=\begin{bmatrix} -\frac{1}{\lambda_2-\lambda_1} & \frac{1}{\lambda_2-\lambda_1} & & \\ -\frac{1}{\lambda_2-\lambda_1} & 0 & \frac{1}{\lambda_3-\lambda_1} & \\ & -\frac{1}{\lambda_4-\lambda_2} & 0 & \frac{1}{\lambda_4-\lambda_2} \\ & \ddots & \ddots & -\frac{1}{\lambda_n-\lambda_{n-1}} \end{bmatrix} \tag{7}$$

and

$$\mathbf{I}=[I_1, I_2, \ldots, I_n]^{\mathrm{T}}, \tag{8}$$

where λ's are the quadrature points (trapezoidal points here) and I_1, I_2 *etc.* are the corresponding intensities. Similarly the $\partial^2 I/\partial\lambda^2$ term can be written as $\mathbf{D_2I}$, where

$$\mathbf{D}_2=\begin{bmatrix} \frac{1}{(\Delta\lambda)^2} & -\frac{2}{(\Delta\lambda)^2} & \frac{1}{(\Delta\lambda)^2} & & \\ 0 & \frac{1}{(\Delta\lambda)^{2-}} & \frac{2}{(\Delta\lambda)^2} & \frac{1}{(\Delta\lambda)^2} & \\ & & \ddots & \ddots & \frac{1}{(\Delta\lambda)^2} \\ & & & & -\frac{1}{(\Delta\lambda)^2} \end{bmatrix} \tag{9}$$

and **I** is the corresponding intensity vector. We choose m angle points on Gauss-Legendre quadrature.

The transfer equation in (6) is integrated on the angle-wavelength mesh as described in Peraiah & Grant (1973; hereafter referred to as PG). After integration, we have

$$\begin{aligned}\mathbf{M}[\mathbf{I}^+_{n+1}-\mathbf{I}^+_n]+\tau_{n+1/2}\mathbf{I}^+_{n+1/2}=\tau_{n+1/2}(1-\omega)\mathbf{B}^+_{n+1/2}+(\tfrac{1}{2}\omega\mathbf{P}^{++}_{n+1/2}\mathbf{C}\\ -\gamma\mathbf{P}^{++}_{1,n+1/2}\mathbf{Cd}_{1,n+1/2}\\ +\tfrac{1}{2}\gamma^2\mathbf{P}^{++}_{2,n+1/2}\mathbf{Cd}_{2,n+1/2})\mathbf{I}^+_{n+1/2}\\ +(\tfrac{1}{2}\omega\mathbf{P}^{+-}_{n+1/2}\mathbf{C}-\gamma\mathbf{P}^{+-}_{1,n+1/2}\mathbf{Cd}_{1,n+1/2}\\ +\tfrac{1}{2}\gamma^2\mathbf{P}^{+-}_{2,n+1/2}\mathbf{Cd}_{2,n+1/2})\mathbf{I}^-_{n+1/2}.\end{aligned} \tag{10}$$

For the oppositely directed beam,

$$\begin{aligned}\mathbf{M}[\mathbf{I}_n^- - \mathbf{I}_{n+1}^-] + \tau_{n+1/2}\mathbf{I}_{n+1/2}^- = \tau_{n+1/2}(1-\omega)\mathbf{B}_{n+1/2}^- + (\tfrac{1}{2}\omega\mathbf{P}_{n+1/2}^{-+}\mathbf{C} \\ -\gamma\mathbf{P}_{1,n+1/2}^{-+}\mathbf{Cd}_{1,n+1/2} + \tfrac{1}{2}\gamma^2\mathbf{P}_{2,n+1/2}^{-+}\mathbf{Cd}_{2,n+1/2})\mathbf{I}_{n+1/2}^+ \\ +(\tfrac{1}{2}\omega\mathbf{P}_{n+1/2}^{--}\mathbf{C} - \gamma\mathbf{P}_{1,n+1/2}^{--}\mathbf{Cd}_{1,n+1/2} \\ +\tfrac{1}{2}\gamma^2\mathbf{P}_{2,n+1/2}^{--}\mathbf{Cd}_{2,n+1/2})\mathbf{I}_{n+1/2}^- . \end{aligned} \tag{11}$$

The quantities Q^{++}, Q^{--} *etc.* in PG will become

$$\mathbf{Q}_{n+1/2}^{++} = \tfrac{1}{2}\omega_{n+1/2}\mathbf{P}_{n+1/2}^{++}\mathbf{C} - \gamma\mathbf{P}_{1,n+1/2}^{++}\mathbf{Cd}_1 + \tfrac{1}{2}\gamma^2\mathbf{P}_{2,n+1/2}^{++}\mathbf{Cd}_{2,n+1/2}, \tag{12}$$

$$\mathbf{Q}_{n+1/2}^{--} = \tfrac{1}{2}\omega_{n+1/2}\mathbf{P}_{n+1/2}^{--}\mathbf{C} - \gamma\mathbf{P}_{1,n+1/2}^{--}\mathbf{Cd}_1 + \tfrac{1}{2}\gamma^2\mathbf{P}_{2,n+1/2}^{--}\mathbf{Cd}_{2,n+1/2}, \tag{13}$$

$$\mathbf{Q}_{n+1/2}^{-+} = \tfrac{1}{2}\omega_{n+1/2}\mathbf{P}_{n+1/2}^{-+}\mathbf{C} - \gamma\mathbf{P}_{1,n+1/2}^{-+}\mathbf{Cd}_1 + \tfrac{1}{2}\gamma^2\mathbf{P}_{2,n+1/2}^{-+}\mathbf{Cd}_{2,n+1/2}, \tag{14}$$

$$\mathbf{Q}_{n+1/2}^{+-} = \tfrac{1}{2}\omega_{n+1/2}\mathbf{P}_{n+1/2}^{+-}\mathbf{C} - \gamma\mathbf{P}_{1,n+1/2}^{+-}\mathbf{Cd}_1 + \tfrac{1}{2}\gamma^2\mathbf{P}_{2,n+1/2}^{+-}\mathbf{Cd}_{2,n+1/2}, \tag{15}$$

where

$$\mathbf{P}^{++} = \begin{bmatrix} \mathbf{p}^{++} & & \\ & \mathbf{p}^{++} & \\ & & \ddots \end{bmatrix} = \mathbf{P}^{+-} = \mathbf{P}^{-+} = \mathbf{P}^{--}, \tag{16}$$

$$P^{++}(\mu_j, \mu_k) = 1, \tag{17}$$

$$P_1^{++} = \begin{bmatrix} P_1^{++} & & \\ & P_1^{++} & \\ & & \ddots \end{bmatrix}, \tag{18}$$

$$P_1^{++}(j,k) = \{1 - (+\mu_j)(+\mu_k)\}, \tag{19}$$

$$P_1^{++} = \begin{bmatrix} P_1^{+-} & & \\ & P_1^{+-} & \\ & & \ddots \end{bmatrix}, \tag{20}$$

with

$$P_1^{+-}(j,k) = \{1 - (+\mu_j)(-\mu_k)\}. \tag{21}$$

Similarly P_1^{-+}, P_1^{--} and P_1^{-+} and P_1^{--} are defined.

$$\mathbf{M} = \begin{bmatrix} \mathbf{m} & & \\ & \mathbf{m} & \\ & & \ddots \end{bmatrix}, \mathbf{m} = [\mu_{jk}, \delta_{jk}], \tag{22}$$

$$\mathbf{C} = \begin{bmatrix} \mathbf{C} & & \\ & \mathbf{C} & \\ & & \ddots \end{bmatrix}, \mathbf{C} = [C_{jk}, \delta_{jk}]. \tag{23}$$

The quantities s^{++}, s^{--}, s^{+-}, s^{-+} in Peraiah & Grant (1973) become

$$\mathbf{S}^{++}_{n+1/2} = \mathbf{M} - \tfrac{1}{2}\tau_{n+1/2}\mathbf{E} + \tfrac{1}{4}\tau_{n+1/2}\omega_{n+1/2}\mathbf{P}_{n+1/2}\mathbf{C} - \tfrac{1}{2}\tau_{n+1/2}\gamma\mathbf{P}^{++}_{1,n+1/2}\mathbf{Cd}_{1,n+1/2} + \tfrac{1}{4}\tau_{n+1/2}\gamma^2\mathbf{P}^{++}_{2,n+1/2}\mathbf{Cd}_{2,n+1/2}, \tag{24}$$

$$\mathbf{S}^{--}_{n+1/2} = \mathbf{M} - \tfrac{1}{2}\tau_{n+1/2}\mathbf{E} + \tfrac{1}{4}\tau_{n+1/2}\gamma^2\omega_{n+1/2}\mathbf{P}^{--}_{n+1/2}\mathbf{C} - \tfrac{1}{2}\tau_{n+1/2}\gamma\mathbf{P}^{--}_{1,n+1/2}\mathbf{Cd}_{1,n+1/2} + \tfrac{1}{4}\tau_{n+1/2}\gamma^2\mathbf{P}^{--}_{2,n+1/2}\gamma^2\mathbf{Cd}_{2,n+1/2}, \tag{25}$$

$$\mathbf{S}^{-+}_{n+1/2} = \tfrac{1}{4}\tau_{n+1/2}\omega_{n+1/2}\mathbf{P}^{-+}_{n+1/2}\mathbf{C} - \tfrac{1}{2}\tau_{n+1/2}\gamma\mathbf{P}^{-+}_{1,n+1/2}\mathbf{Cd}_1 + \tfrac{1}{4}\tau_{n+1/2}\gamma^2\mathbf{P}^{-+}_{2,n+1/2}\mathbf{C}_2\mathbf{d}_{2,n+1/2}, \tag{26}$$

$$\mathbf{S}^{+-}_{n+1/2} = \tfrac{1}{4}\tau_{n+1/2}\omega_{n+1/2}\mathbf{P}^{+-}_{n+1/2}\mathbf{C} - \tfrac{1}{2}\tau_{n+1/2}\gamma\mathbf{P}^{+-}_{1,n+1/2}\mathbf{Cd}_{1,n+1/2} + \tfrac{1}{4}\tau_{n+1/2}\gamma^2\mathbf{P}^{-+}_{1,n+1/2}\mathbf{Cd}_{2,n+1/2}, \tag{27}$$

and

$$(\Delta^{+})^{-1}_{n+1/2} = \mathbf{M} + \tfrac{1}{2}\tau_{n+1/2}\mathbf{E} - \tfrac{1}{4}\tau_{n+1/2}\omega_{n+1/2}\mathbf{P}^{++}_{n+1/2}\mathbf{C} + \tfrac{1}{2}\tau_{n+1/2}\gamma\mathbf{P}^{++}_{1,n+1/2}\mathbf{Cd}_{1,n+1/2} - \tfrac{1}{4}\tau_{n+1/2}\gamma^2\mathbf{P}^{++}_{2,n+1/2}\mathbf{Cd}_{2,n+1/2}, \tag{28}$$

$$(\Delta^{-})^{-1}_{n+1/2} = \mathbf{M} + \tfrac{1}{2}\tau_{n+1/2}\mathbf{E} - \tfrac{1}{4}\tau_{n+1/2}\omega_{n+1/2}\mathbf{P}^{--}_{n+1/2}\mathbf{C} + \tfrac{1}{2}\tau_{n+1/2}\gamma\mathbf{P}^{--}_{1,n+1/2}\mathbf{Cd}_{1,n+1/2} - \tfrac{1}{4}\tau_{n+1/2}\gamma^2\mathbf{P}^{--}_{2,n+1/2}\mathbf{Cd}_{2,n+1/2}, \tag{29}$$

where $\tau_{n+1/2}$ is the mean optical depth of the nth layer and E is the unit matrix. The transmission and reflection operators follow those given in PG.

3. Results and discussion

The radiation field is calculated according to the procedure described in PG. We have considered 3 different cases of total optical depths: T = 1.0, 2.0 and 5.0. The medium is

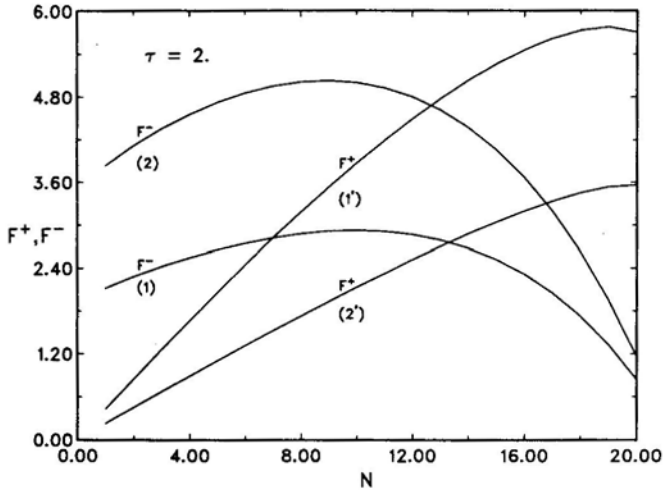

Figure 1. The inward (F^+) and outward (F^-) fluxes are plotted against the shell numbers. Curves 1 and 1′ represents the fluxes without the $\partial^2 I/\partial\lambda^2$ term and curves 2 and 2′ represent the curves calculated by including the $\partial^2 I/\partial\lambda^2$ term.

divided into 20 plane parallel layers each of equal optical thickness. We have considered 4 angle points and 10 frequency points. The wavelength points are chosen in units of Compton wavelength γ. Trapezoidal points are choosen for frequency mesh and are taken as $\gamma, 2\gamma, \ldots, 10\gamma$, so that the step length is one Compton wavelength. The roots and weights of Gauss-Legendre quadrature on $\mu \in (0, 1)$ are chosen as the angle points. We have chosen 4 angle points μ_1, μ_2, μ_3 and μ_4 on $\mu \in (0,1)$ with the corresponding weights C_1, C_2, C_3 and C_4 (Abramowicz & Stegun 1965) given by

$$\mu_1 = 0.06943, \qquad C_1 = 0.17393,$$
$$\mu_2 = 0.33001, \qquad C_2 = 0.32607,$$
$$\mu_3 = 0.66999, \qquad C_3 = 0.32607,$$
$$\mu_4 = 0.93057, \qquad C_4 = 0.17393.$$

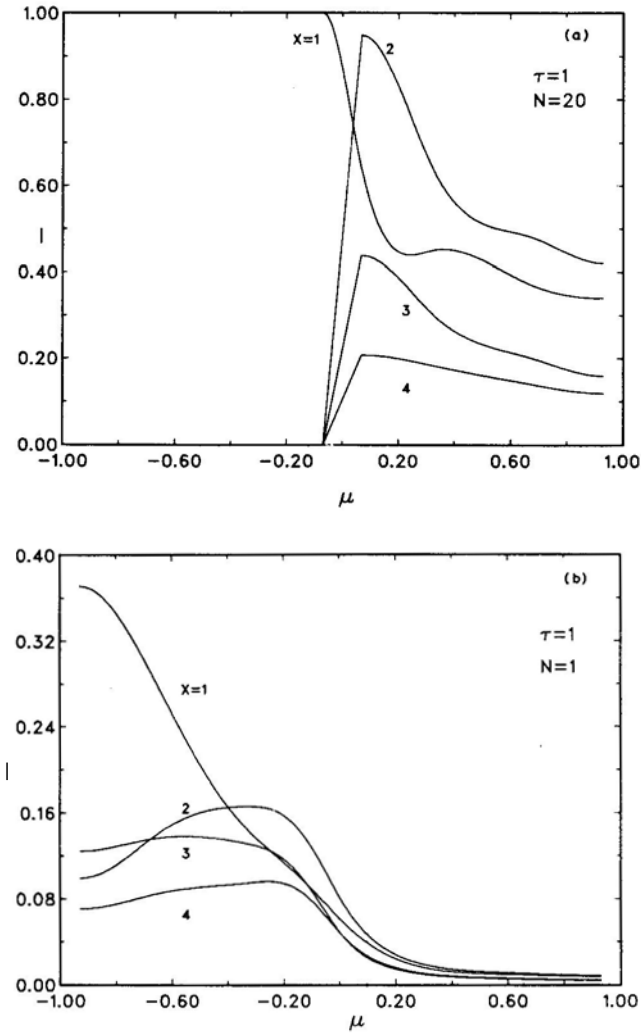

Figure 2. (a) Angular distribution of specific intensities at $\tau = T = 1 (N = 20)$, and (b) the emergent intensities at $\tau = 0$.

We have given incident radiation at $\tau = T$ and no radiation is incident at $\tau = 0$:

$$I^-(\mu_j, x(1), \tau = T) = 1.0,$$
$$I^-(\mu_j, x(2, \ldots 10), \tau = T) = 0,$$
$$I^+(\mu_j, x_i, \tau = 0) = 0.$$

In Fig. 1, we presented a comparison of the calculations performed with and without the term $\partial^2 I/\partial\lambda^2$. Here N represents the number of layers. $N = 20$ represents the layer where $\tau = \tau_{\max} = T$ and $N = 1$ represents the layer where $\tau = 0$, the emergent side of the medium. We calculated the inward and outward fluxes F^+ and F^- for a total optical depth of 2.0. The inward fluxes (F^+) in both the cases (for 1′ and 2′ in Fig.

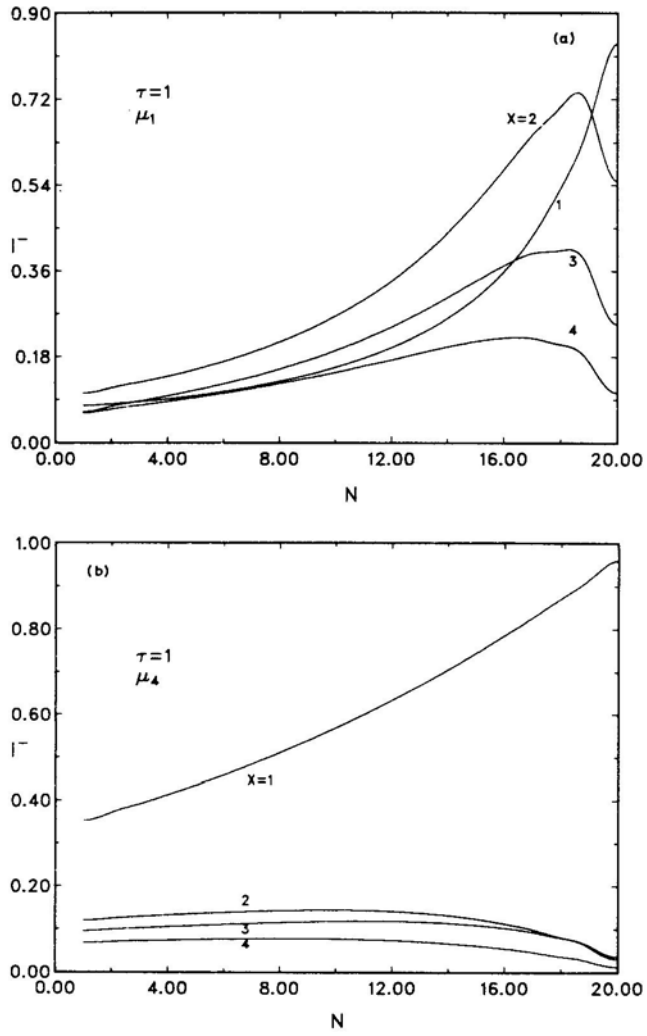

Figure 3. The emergent intensities across the medium corresponds to different Compton wavelengths (x) and for the angular (a) μ_1 and (b) μ_4. Here $N = 1$ corresponds to the emergent intensities and at $N = 20$ corresponds to $\tau = T$.

1) are larger at $N = 20$ or $\tau = T$ because of the back scattering at the innermost surface. The contribution to this comes from the diffuse radiation field from the layer bounded by $\tau = 0$ and $\tau = T$. However the effect of back scattering is reduced considerably towards the emergent side of the layer and only a small fraction of the flux is directed towards the surface $\tau = T$. The emergent fluxes (F^-) in both cases behave in a different way. Although these fluxes are considerably smaller than those of (F^+) they reach maxima at about $N = 10$ exactly halfway of the layer and then fall slowly towards the emergent side of the shell ($\tau = 0$). We can see that the introduction of the term $\partial^2 I/\partial\lambda^2$ into the calculations produces considerable changes in the radiation field. It also shows that we cannot compare these results with those of Chandrasekhar (1960).

In Figs 2(a) and (b) we show the angular distribution of specific intensities for a total optical depth $T = 1$. Unit intensity at $x = \gamma$ is incident at $\tau = T$. We see in Fig. 2(a), that

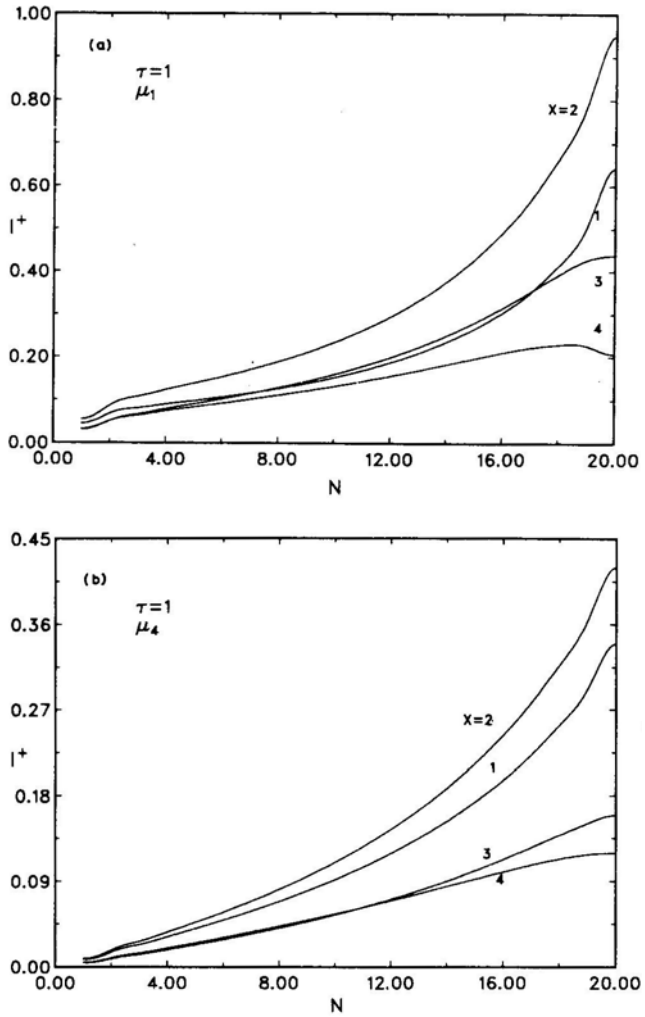

Figure 4. The redistribution of intensities across the medium for the inward scattered specific intensities corresponding to (a) μ_1 and (b) μ_4.

the outward intensities are all equal to 1 unit at $x = \gamma$ for all μ_j and no radiation is directed outwards $[-1 < \mu < 0]$ at wavelength $x = 2\gamma, 3\gamma, 4\gamma$. We also notice that a small amount of radiation is directed into the medium $[0 < \mu < 1]$ at wavelengths $x = \gamma, 2\gamma, 3\gamma$ and 4γ. It is interesting that more radiation is scattered at $x = 2\gamma$ instead of at $x = \gamma$. The radiation at $x = 3\gamma$ and 4γ is a small fraction of that at $x = \gamma$ in the range of $-1 \leqslant \mu < 0$. This is expected because of the diffuse radiation field contributed by the medium between $\tau = 0$ and $\tau = T$.

In Fig. 2(b), the angular distribution of radiation field is presented at the shell $N = 1$ or $\tau = 0$ which is the emerging side of the medium. Most of the radiation is directed outwards while in Fig. 2(a) in which the radiation is shown at $N = 20$ ($\tau = T$) we see

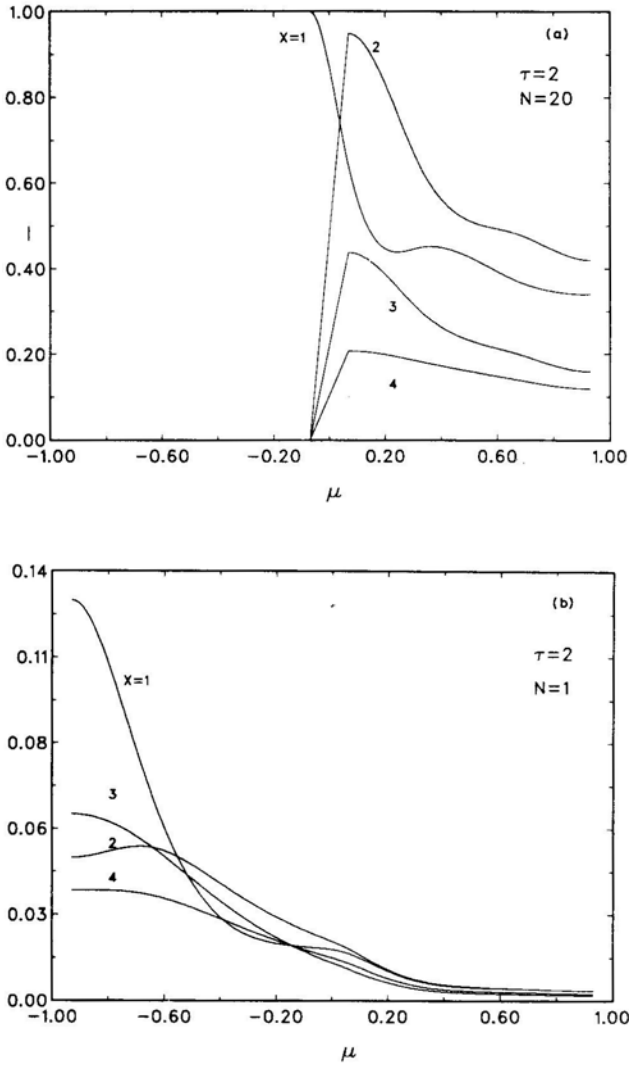

Figure 5. (a) Angular distribution of specific intensities at $\tau = T = 2$, and (b) the emergent intensities at $\tau = 0$.

that the trend is opposite to what is seen in Fig. 2(b). Largest fraction of radiation is transferred through the specific intensity at $x = 1$. The radiation in the range $0 < \mu \leqslant 1$ (backward directed radiation) is considerably small.

It would be interesting to see how the radiation is redistributed across the medium corresponding to different directions and wavelengths after several Compton scatterings. In Figs 3(a) and (b) we plot the distribution of radiation directed towards the emergent side across the medium for the directions μ_1 and μ_4 respectively for different values of x (we have not plotted values for $x > 4\gamma$ because these values are small). In the direction μ_1, we see that a substantial part of radiation is emergent for $x = \gamma$ and the radiation corresponding to $x = \gamma$, 3γ and 4γ is slightly less than that at x

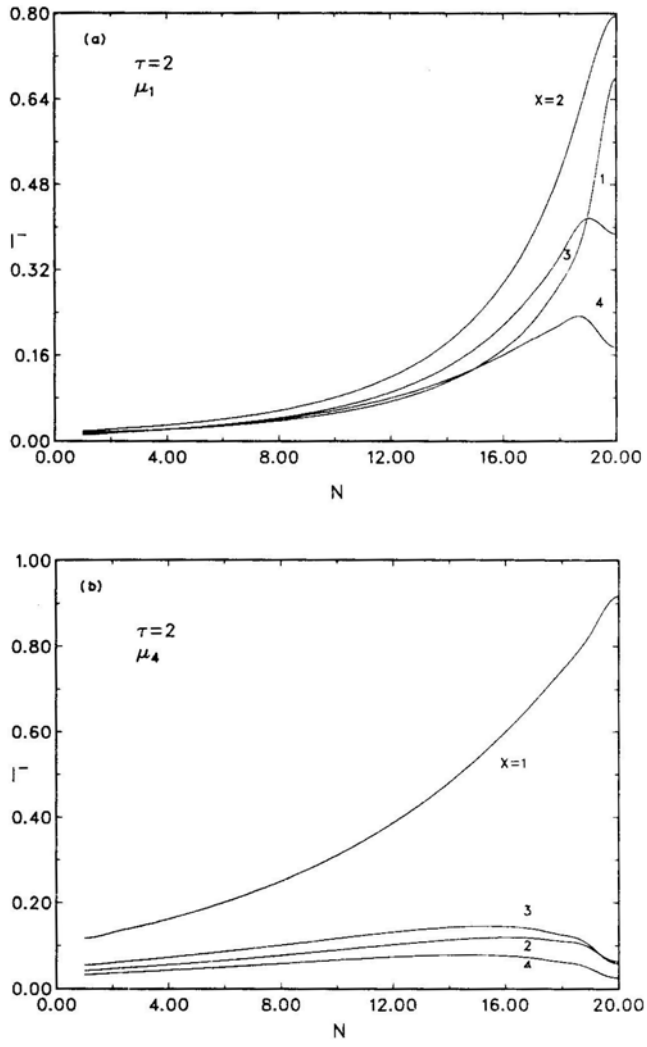

Figure 6. The emergent intensities across the medium corresponding to different Compton wavelengths and for the direction (a) μ_1 and (b) μ_4. Here $N = 1$ corresponds to the emergent intensities and $N = 20$ corresponds to $\tau = T$.

$= 2\gamma$. In the direction μ_4 most of the radiation is emerging in the wavelength $x = \gamma$ while the emergent radiation at $x = 2\gamma$, 3γ and 4γ is about 25 per cent of that at $x = \gamma$. The rays corresponding to μ_4 and μ_1 carry more energies at $x = \gamma$ and $x = 2\gamma$. In Fig. 4(a) and (b), we plot the inward directed intensities across the medium for the directions μ_1 and μ_4 respectively. It appears that the maximum intensities occur at $N = 20$ and at $N = 1$ ($\tau = 0$). Very little radiation is directed into the medium. More radiation is redistributed in the wavelength $x = 2\gamma$ than in other wavelengths, *i.e.,* $x = \gamma$, 3γ and 4γ in both the directions μ_1 and μ_4. This is slightly different from the radiation directed outwards (see Figs 3(a) and (b)).

In Fig. 5(a), we present the angular distribution of the intensities for $\tau = 2$ at $N = 20$. The variation of I is similar to that shown in Fig. 2(a). In Fig. 5(b), we plot the angular

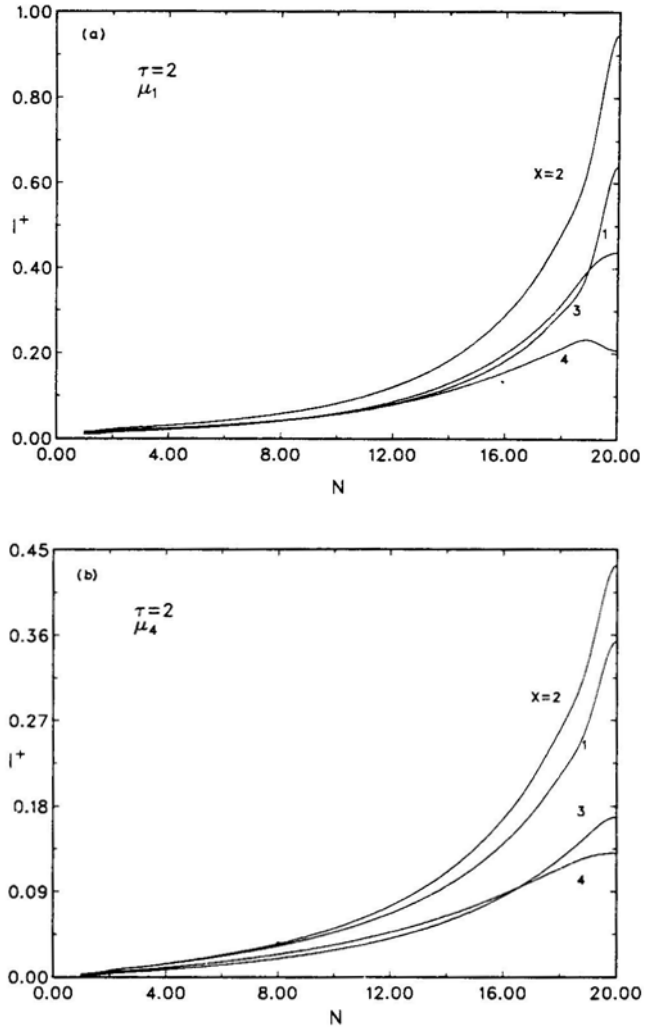

Figure 7. The redistribution of radiation across the medium for the inward scattered specific intensities corresponding to (a) μ_1 and (b) μ_4.

distribution of I at $N = 1$ or $\tau = 0$. Major fraction of radiation is distributed at $x = \gamma$, and the intensities at $x = 2\gamma$, 3γ and 4γ are quite small. If we compare these results with those presented in Fig. 2(b), we notice that the magnitudes of the intensities given in Fig. 5(b) are reduced considerably. This is due to higher optical depth used in the latter calculations. The backward directed radiation ($0 < \mu \leqslant 1$) is negligibly small.

In Figs 6(a) and (b) we plot the redistribution of the radiation across the medium. Larger fraction of radiation is redistributed at the wavelength $x = 2\gamma$ which is similar to the distribution shown in Figs 3 and 2(b). Figs 7(a) and (b) describe the distribution of intensities across the medium for $\tau = 2$ in the directions μ_1 and μ_4 respectively. They show the same behaviour as in Figs 4(a) and (b).

Fig. 8(a) gives the angular distribution at $N = 20$ or $\tau = 5$. Although the optical depth is higher than what is used to calculate the results given in Figs 2(a) and 5(a), we

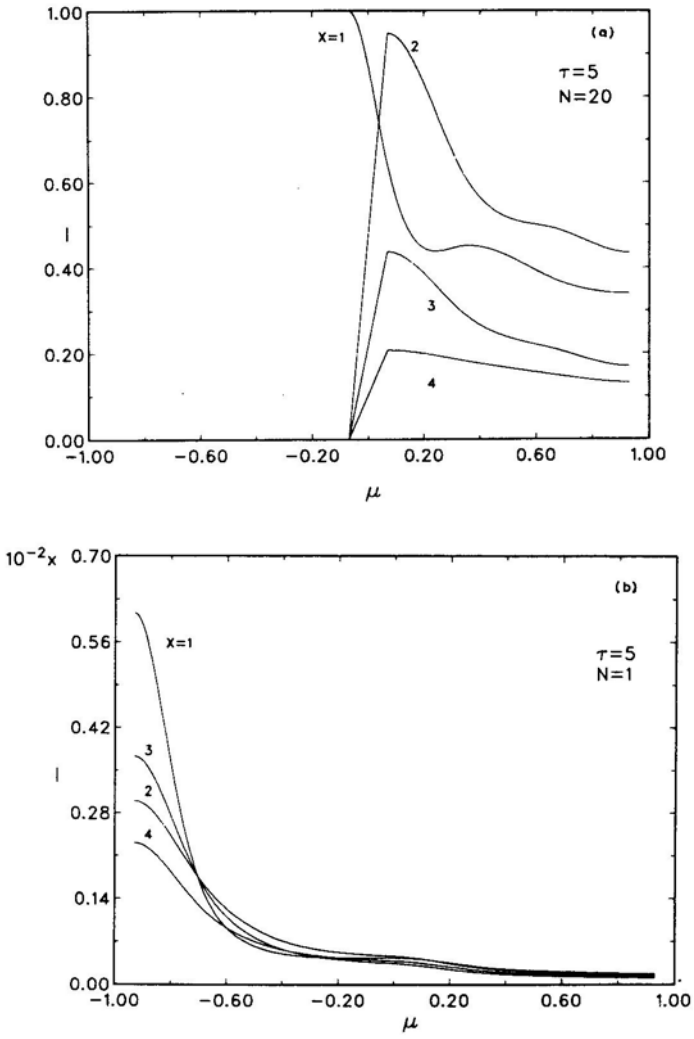

Figure 8. (a) Angular distribution of specific intensities at $\tau = T = 5$, and (b) the emergent intensities at $\tau = 0$.

find the behaviour at $\tau = 5$. In Fig. 8(b), the angular distribution of the emergent intensities is described. The magnitudes of intensities is considerably reduced due to the larger optical depth. Moreover, we see that radiation is spread to $x = 3\gamma$ more than at $x = 2\gamma$ near $\mu \approx -1$. Figs 9(a) and (b) describe the distribution of outward directed radiation across the medium at $x = \gamma$, 2γ, 3γ and 4γ in the direction μ_1. However the radiation in the direction μ_4 is emerging mostly at wavelengths $x = \gamma$ and 3γ.

The backward directed intensities in the direction μ_1 and μ_2 are plotted in Figs 10(a) and (b). The trend is the same as that shown in Figs 7(a) and (b); that is, more back-scattered radiation is in wavelength $x = 2\gamma$.

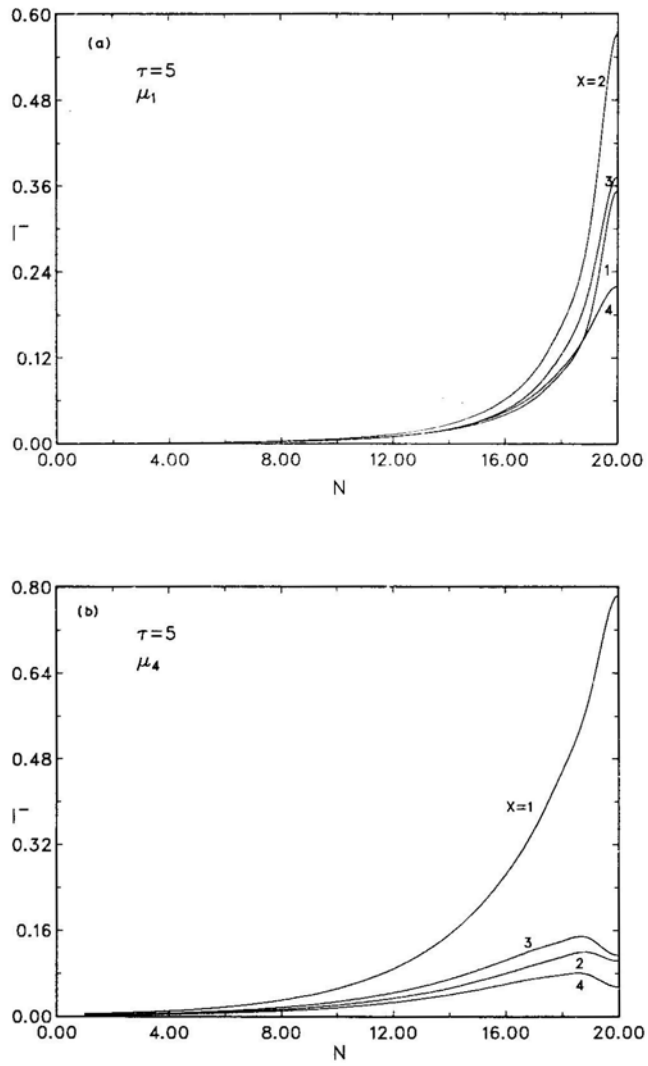

Figure 9. The emergent intensities across the medium corresponding to different Compton wavelengths and for the angular (a) μ_1 and (b) μ_2. Here $N = 1$ corresponds to the emergent intensities and $N = 20$ corresponds to $\tau = \tau_{max}$.

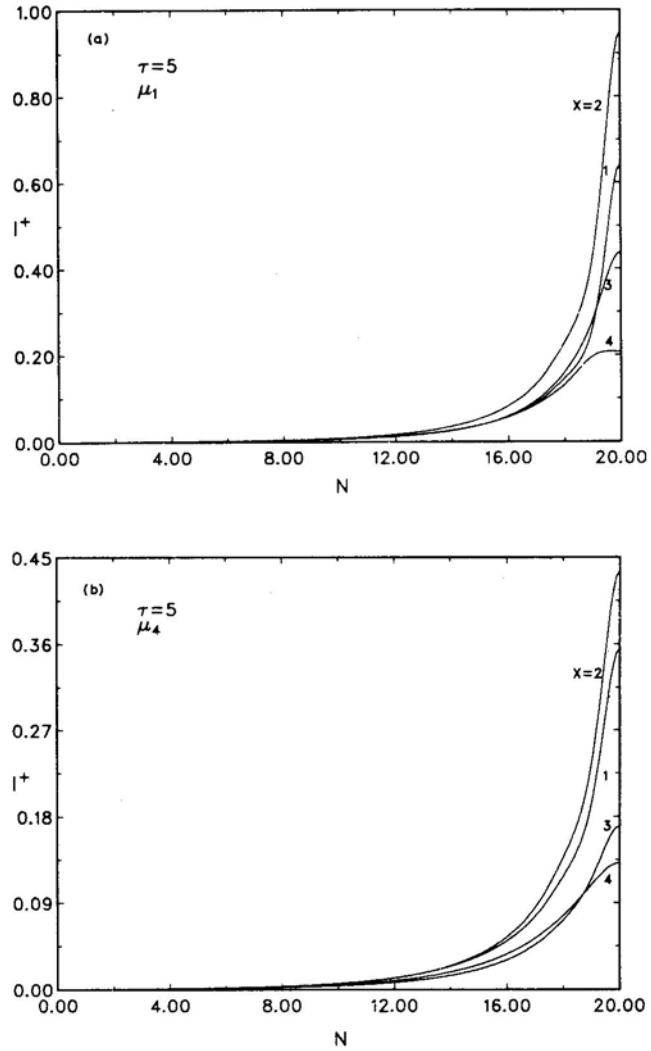

Figure 10. The redistribution of radiation across the medium for the involved scattered specific intensities corresponding to (a) μ_1 and (b) μ_4.

References

Abramowicz, M., Stegun, I. A. 1972, *Hand book of Mathematical Functions,* Dover, New York.
Barbosa, D. D. 1982, *Astrophys. J.,* **254**, 301.
Bhat, C. L, Kifune, T., Wolfendale, A. W. 1986, *Astr. Astrophys.,* **159**, 299.
Bloemen, J. B. G. M.1985, *Astr. Astrophys.,* **145***,* 391.
Chandrasekhar, S. 1960, *Radiative Transfer,* Dover, New York.
Code, A. D. 1967, *Astrophys. J.,* **149**, 253.
Czerny, M., Sztajno, M. 1983, *Acta Astronomica,* **33**, 213.
Daugherty, J. K. Harding, A. K. 1986, *Astrophys. J.* **309**, 362.
Fukue, J., Kato S., Matsumoto R. 1985, *Publ. astr. Soc. Japan,* **37**, 383.
Gould, R. J. 1984, *Astrophys. J.,* **285**, 275.
Guilbert, P. W. 1986, *Mon. Not. R. astr. Soc,* **218**, 171.

Ipser, J. R., Price, R. H. 1983, *Astrophys. J.,* **267**, 371.
Keiner, S. R., Shikhovtseva, E. S. 1983, *Astrophysics,* **19**, No. 4.
Kirk, J. G. 1986, *Astr. Astrophys.,* **158**, 305.
Kirk, J. G., Nagel, W., Storey, M. C. 1986, *Astr. Astrophys.,* **169**, 259.
Langer, S. H. 1979, Astrophys. J, **232**, 891.
Lovelace, R. V. E. 1987, *Astr. Astrophys.,* **173**, 237.
Meszaros, P., Bussard R. W. 1986, *Astrophys. J.,* **306**, 238.
Missana, M. 1982, *Astrophys. Sp. Sci.,* **85**, 137.
Missana, M., Piana A. 1976, *Astrophys. Sp. Sci.,* **43**, 129.
Nagel, W. 1981, *Astrophys. J.,* **251**, 288.
Nagirner, D. I. 1984, *Astrophysics,* **20**, 95.
Nishimura, J., Mitsuda, K., Itoh, M. 1986, *Publ. astr. Soc. Japan,* **38**, 819.
Ochelkov, Yu. P., Usov, V. V. 1983, *Astrophy. Sp. Sci.,* **96**, 55.
Peraiah, A. 1986, *Kodaikanal. Obs. Bull,* **5**, 113.
Peraiah, A., Grant, I. P. 1973, *J. Inst. Maths, Appl,* **12**, 75 (PG).
Pomraning, G. C, Froehlich, R. 1969, *Astr. Astrophys.,* **1**, 286.
Pozdnyakov, L. A., Sobol, I. M., Sunyaev, R. A. 1976, *Sov. Astr.,* **2**, L55.
Pozdnyakov, L. A., Sobol, I. M., Sunyaev, R. A. 1983, *Astrophys. Sp. Phys. Rev.,* **2**, 189.
Strong, A. W. 1985, *Astr. Astrophys.,* **145**, 81.
Sunyaev, R. A., Titarchuk, L. G. 1985, *Astr. Astrophys.,* **143**, 374.
Viik, T. 1968a, *Tartu Astr. Obs. Teated,* No. 19, p. 71.
Viik, T. 1968b, *Tartu Astr. Obs. Teated,* No. 19, p. 91.
Xia, X. Y., Qiao, G. J., Wu, X. J., Hou Y. Q. 1985, *Astr. Astrophys.,* **152**, 93.
You, J. -h., Xie, G.-z., Bao, M.-x., Li K.-h. 1982, *Acta Astr. Sinica,* **23**, 353.
Zdziarski, A. A., Lamb, D. Q. 1986, *Astrophys. J.,* **309**, L362.

J. Astrophys. Astr. (1990) **11**, 209–219

Equivalent Widths of Hydrogen Lyman Alpha Line in an Expanding Spherical Atmosphere

A. Peraiah & M. F. Ingalgi *Indian Institute of Astrophysics, Bangalore 560034*

Received 1989 October 20; accepted 1990 April 5

Abstract. We have calculated the profiles of hydrogen Lyman α line in an expanding spherical atmosphere containing dust and gas. We have investigated the variation of equivalent widths with velocities of expansion of the atmosphere, together with the amount of dust present in the medium. We have drawn curves of growth for different velocities and dust optical depths.

Key words: radiative transfer—Lyman α line—expanding atmospheres —circumstellar dust

1. Introduction

Infrared observations have shown that many stars with extended outer layers as well as planetary nebulae contain dust mixed with the ionized gas (Miller 1974; Osterbrock 1974). Moreover, these objects have complicated internal motions. Dust can influence the structure and dynamics of the planetary nebulae. It may cause reduction in the size of the Strömgren sphere (Mathis 1971; Petrosian, Silk & Field 1972). Calculations of the profiles of lines formed in such media are necessary to investigate the dynamical and structural changes that may be brought out by the presence of dust. Earlier, Peraiah & Wehrse (1978) and Wehrse & Peraiah (1979) have investigated the effects of dust and expansion velocities on the formation of hydrogen Lyman α line. They considered small velocities as the transfer equation was solved in the rest frame. Large velocities can be incorporated only in comoving frame of the fluid (Peraiah, Varghese & Rao 1987). We study here the effects of large velocities on equivalent widths of H Lyman α line.

Curves of growth are generally plotted for a medium which is stationary. However, we find that atmospheres of stars are normally in motion, mostly radial. Therefore it would be difficult to plot the curves of growth for such atmospheres as the optical depth (which contains the absorption coefficient or scattering coefficient) changes with the velocity of expansion, depending upon the thermal velocities of gases. For example, in an electron scattering atmosphere, we have (Mihalas 1978)

$$\tau = \sigma v_{\rm th} \left(\frac{{\rm d}v}{{\rm d}r} \right)^{-1}, \tag{1}$$

where τ is the optical depth, σ is the electron scattering coefficient, $v_{\rm th}$ is the thermal velocity of the medium in motion and (dv/dr) is the velocity gradient. One should remember that this relation would become invalid in stellar photospheres. In such

situations it is difficult to obtain the information about the number density that is influencing line formation. We shall investigate here the effects of expansion velocities and dust on the equivalent widths of resonance lines. For this purpose we choose hydrogen Lyman α line whose parameters are well known. We assume a spherical atmosphere with dust.

2. Calculations

We require the number of neutral hydrogen atoms to calculate the strength of the Lyman a line. For this purpose we need to solve either the statistical equilibrium equation or obtain the number density by using Saha equation of ionization in a simple way. The latter is easy to solve provided we know the temperature structure and electron density. We can specify the electron density distribution in advance while the temperature distribution is calculated by assuming that the Planck function dilutes at the rate of $(r_0/r)^2$ where r_0 and r are the inner and outer radii of the spherical shell. This gives us,

$$B_\nu(T_r)=\left(\frac{r_0}{r}\right)^2 B_\nu(T_{r_0}), \tag{2}$$

where B_ν is the Planck function at frequency ν, T_r is the temperature at the radial point r in the spherical shell and T_{r_0} is the temperature at the inner radius r_0 of the spherical shell. Equation (1) will give us a temperature distribution

$$T(r)=\frac{h\nu}{k}\frac{1}{\ln\left[1+\left(\frac{r}{r_0}\right)^2(e^{h\nu/kTr_0}-1)\right]}, \tag{3}$$

where h and k are the Planck's constant and Boltzmann's constant respectively.

We have assumed a temperature of 15000 K at $r = r_0$ and the distribution is plotted in Fig. l(a). The assumed electron density is shown in Fig. l(b).

If we have pure hydrogen gas, then the electron density is given by (Mihalas 1978)

$$n_e(H)=\Phi_H^{-1}[(N\Phi_H+1)^{1/2}-1] \tag{4}$$

where

$$\Phi_H=\frac{U_1(T)}{U_2(T)}c_I T^{-3/2}e^{\chi_I/kT} \tag{5}$$

and χ_I is the ionization potential, $c_I = 2.07 \times 10^{-16}$ cgs units, $U1$ and $U2$ are the partition functions, $N = N_0 + 2n_e$, the total number of particles. We derive

$$N_0=\Phi n_e^2 \tag{6}$$

The distribution of neutral atoms is plotted in Fig. l(c).

We require to calculate the number of hydrogen atoms in the level 1 or N_1 for obtaining the absorption coefficient This is done by using Boltzmann equation (Aller 1963)

$$\log\frac{N_2}{N_1}=-\theta e+\log\frac{g_2}{g_1} \tag{7}$$

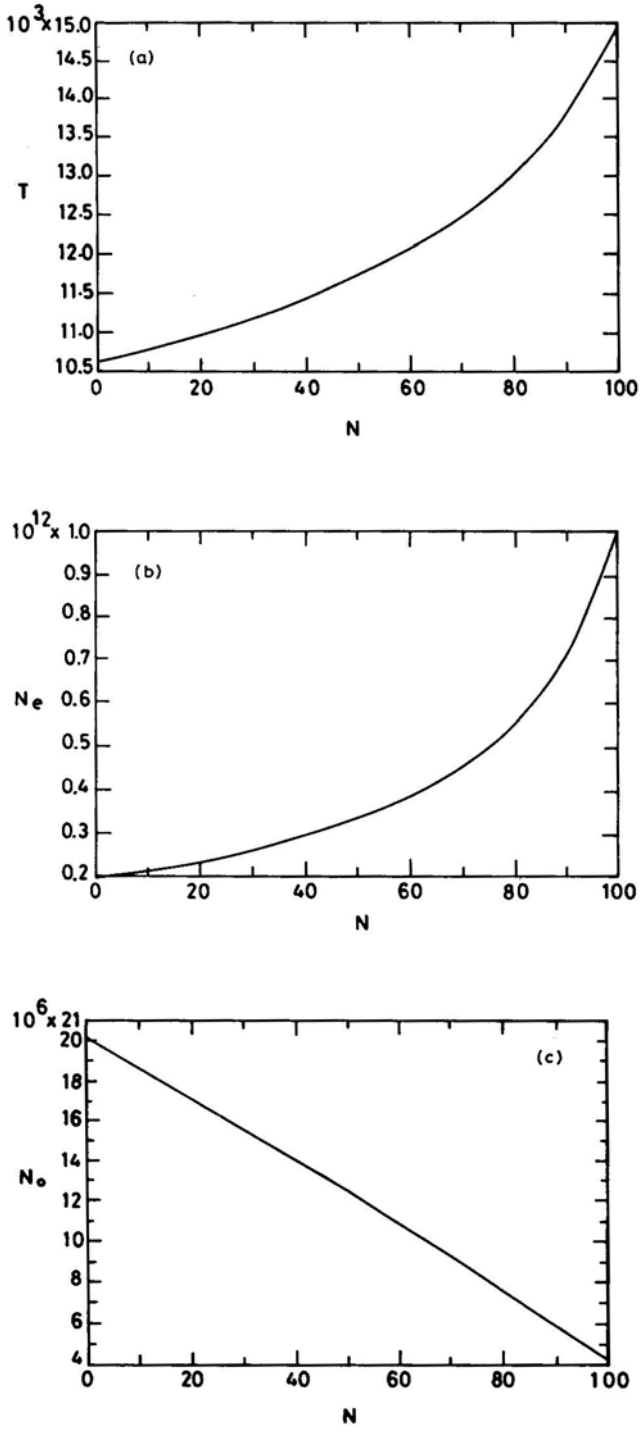

Figure 1. (a) Temperature, (b) electron density, and (c) number of neutral atoms at various points in the spherical shell in which hydrogen Lyman α line is forming. Here $T(r_0)$= 15000 K. Shell no. 1 is at $r = r_{max}$ and shell no. 100 is at $r = r_0$.

where $\theta = 5040/T$, e is the excitation potential in eV, and g_1, g_2 are statistical weights of and N_1, N_2 the number of atoms in levels 1 and 2 respectively. With $N_0 = N_1 + N_2$ and $N_2/N_1 = p$, we obtain,

$$N_1 = \frac{N_0}{1+p}. \tag{8}$$

We calculate the absorption coefficient for hydrogen Lyman α line using the formula,

$$\chi_1(\nu) = N_1 A_{21} \frac{g_2}{g_1} \frac{c^2}{2h\nu^3} \frac{h\nu}{4\pi} \phi_\nu \left(1 - \frac{N_2}{N_1} \frac{g_2}{g_1}\right) \tag{9}$$

where A_{21} is the Einstein coefficient for spontaneous emission, c is the velocity of light, ν is the central frequency of H Lyman a line and ϕ_ν is the profile function of the line such that

$$\int_{-\infty}^{+\infty} \phi_\nu d\nu = 1.$$

We have employed a Doppler profile.

The optical depth in each shell of the medium is plotted in Fig. 2(a) and the total optical depth up to every shell is plotted in Fig. 2(b). We assumed that the medium contains dust in addition to hydrogen gas. The amount of dust and its distribution is represented by the dust optical depth. The spherical medium is expanding radially outwards and the line transfer is solved in a comoving frame (see Peraiah, Varghese & Rao 1987):

$$\mu \frac{\partial I(r,\mu,x)}{\partial r} + \frac{1-\mu^2}{r} \frac{\partial I(r,\mu,x)}{\partial \mu} = \chi_L[\beta + \phi(x)]\,[S(r,x,\mu) - I(r,\mu,x)] + \left[(1-\mu^2)\frac{V(r)}{r} + \mu^2 \frac{dV(r)}{dr}\right] \frac{\partial I(r,\mu,x)}{\partial x} + \chi_{dust}(r)\{S_{dust}(r,\mu,x) - I(r,\mu,x)\}, \tag{10}$$

and for the oppositely directed beam,

$$-\mu \frac{\partial I(r,-\mu,x)}{\partial r} - \frac{1-\mu^2}{r} \frac{\partial I(r,-\mu,x)}{\partial \mu} = \chi_L[\beta + \phi(x)]\,[S(r,x,-\mu) - I(r,-\mu,x)] + \left[(1-\mu^2)\frac{V(r)}{r} + \mu^2 \frac{dV(r)}{dr}\right] \frac{\partial I(r,-\mu,x)}{\partial x} + \chi_{dust}(r)\{S_{dust}(r,-\mu,x) - I(r,-\mu,x)\}, \tag{11}$$

where $\mu \in (0, 1)$, and β is the ratio of absorption coefficients in the continuum and line centre. The quantity x is the normalized frequency given by

$$x = \frac{\nu - \nu_0}{\Delta}$$

where Δ is the standard width such as Doppler width and $V(r)$ is the velocity of expansion in units of Doppler width. The source function is given by

$$S(r, \pm\mu, x) = \frac{\phi(x)}{\beta + \phi(x)} S_L(r) + \frac{\beta}{\beta + \phi(x)} S_c(r,x), \tag{12}$$

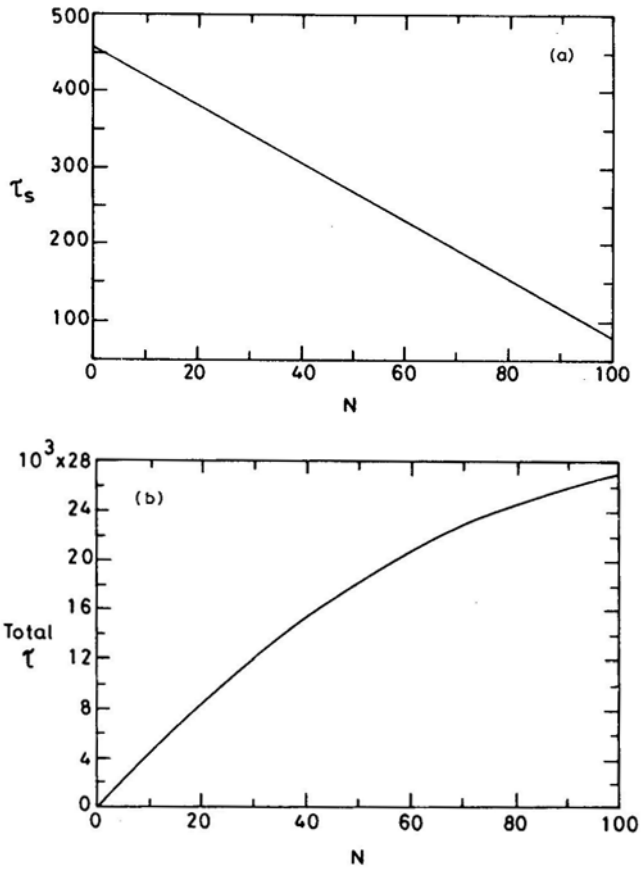

Figure 2. (a) Optical depth in each shell and (b) total optical depth at various layers of the medium.

with

$$S_L(r)=\frac{1-\varepsilon}{2}\int_{-\infty}^{+\infty}\phi(x)\int_{-\infty}^{+\infty}I(r,\mu',x)\,dx\,d\mu'+\varepsilon B(T(r),x), \tag{13}$$

and

$$S_c(r)=\rho(r)B(T(r),x). \tag{14}$$

Here, ε is the probability per scattering that a photon is thermalized by collisional de-excitation. S_L and S_c are the line and continuum source functions respectively. $B(T(r), x)$ is the Planck function and $\rho(r)$ is an arbitrary factor specified in advance. χ_{dust} is the dust absorption coefficient and S_{dust} the source function for the dust given by,

$$S_{dust}(r,\pm\mu,x)=(1-\omega)B_{dust}+\frac{1}{2}\omega\int_{-1}^{+1}P(\mu,\mu',r)I(r,\mu',x)\,d\mu', \tag{15}$$

where B_{dust} is the dust source function, ω is the albedo for single scattering and $P(\mu, \mu', r)$ is the phase function of dust scattering which is assumed to be isotropic.

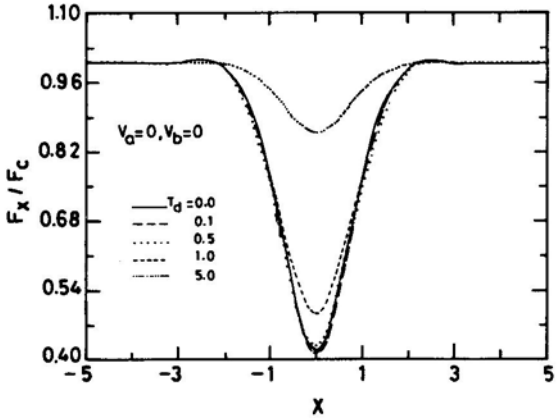

Figure 3. Hydrogen Lyman a line profiles formed in a static medium with different amounts of dust (τ_D). Distribution of dust is constant throughout the atmosphere.

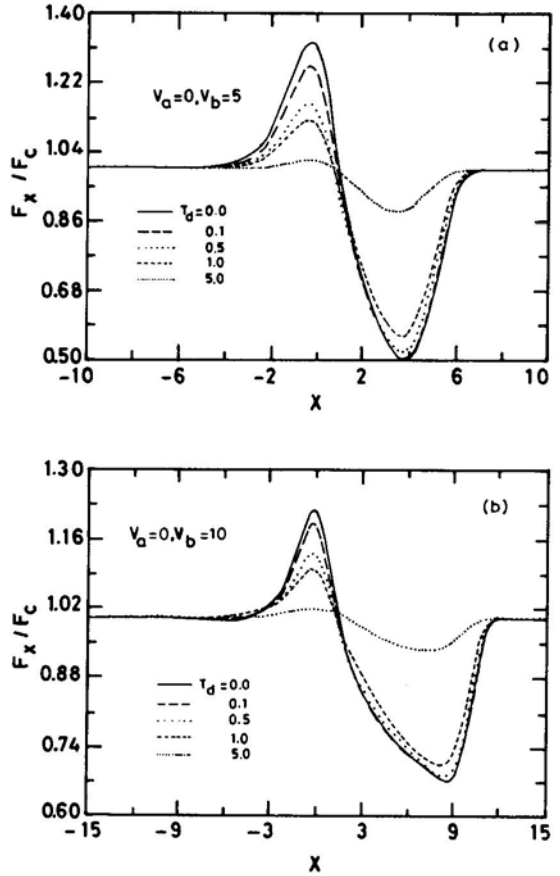

Figure 4. Line profiles of hydrogen Lyman α formed in a medium moving with velocity of expansion (a) V_b = 5 mtu and (b) V_b = 10 mtu (with velocity gradient).

Equations (10) and (11) are solved according to the procedure given in Peraiah, Varghese & Rao (1987).

3. Results

We have assumed a non-LTE line with a two-level atom approximation. We have set $\varepsilon = 0$ and therefore no internal source is assumed. The boundary conditions are given as follows:

$$U^{-}(\tau = \tau_{\max}, \mu_j, X_i) = 1,$$

and

$$\text{for } \varepsilon = 0,\ \beta = 0 \text{ and } B(T(r), x) = 0. \qquad (16)$$

$$U^{+}(\tau = 0,\ \mu_j,\ x_i) = 0,$$

If a is the inner radius and b is the outer radius of the spherical medium then V_a and V_b represent the velocities in Doppler units at a and b respectively. We consider here two

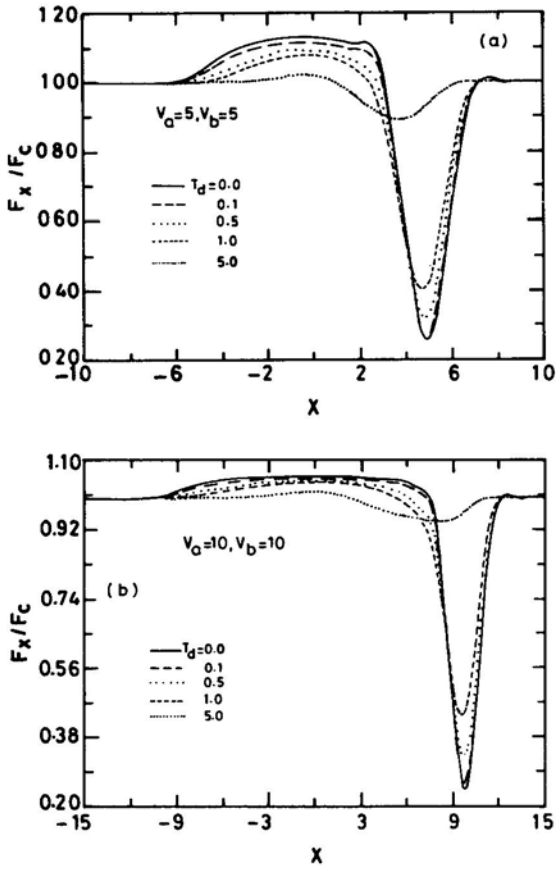

Figure 5. Hydrogen Lyman α line profiles formed in a medium expanding with a velocity of (a) 5 mtu and (b) 10 mtu without velocity gradients.

cases:

and

$$(1)\ V_a = V_b$$

$$(2)\ V_a = 0; \quad V_b > 0.$$

In case (1) we have a uniformly expanding spherical shell and in case (2), we have an expanding spherical shell with velocity gradients. The profiles of hydrogen Lyman α line are given in Figs 35. The dust optical depth τ_D is specified in advance and this is shown in the corresponding figures.

In Fig. 3 we plot the ratio of F_x/F_c where

$$F_x = 2\pi \int I_x \mu d\mu,$$

$$F_c = 2\pi \int I_c \mu d\mu,$$

I_x and I_c being the intensities in the line and continuum respectively, versus x for a static medium and with various dust optical depths. We obtain symmetric profiles in a static medium and as the dust optical depth is increased more photons are scattered into the centre of the line. In Fig. 4(a) we have introduced the velocity of expansion in which V_b = 5 mtu (mean thermal units) while keeping V_a = 0. We notice that *P*-Cygni type profiles have developed. The absorption is being shifted towards violet side while the emission peak remains at the centre of gravity of the line. When the dust optical thickness increases the emission reduces considerably while dust scatters more photons into the centre of the absorption core. Therefore it is clear that dust has opposite effects in the emission wings and in the absorption core. In Fig. 4(b) we plot the profiles with the increased expansion velocity of V_b = 10 mtu. The effects are similar to those for V_b = 5 mtu. Fig. 5 shows profiles from a spherical shell moving with constant velocities of 5 and 10 mtu. Here we note that the wing has become broader while the absorption has become narrow. However, the effects of dust remain the same. The shifts of the absorption core from the centre of the line are almost the

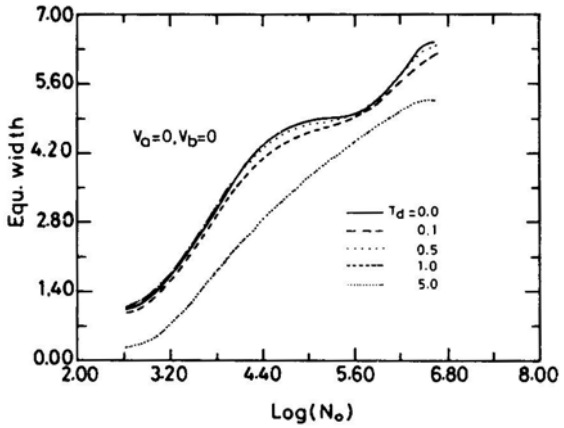

Figure 6. Variation of equivalent widths of hydrogen Lyman α line with the increasing number of neutral atoms (log N_0) for a static medium and for various dust optical depths (τ_D).

same as the expansion velocity used and the emission wing is nearly symmetrically broadened.

In Figs 6 to 8 we plot the equivalent widths versus the number of neutral hydrogen atoms. The equivalent width is defined by

$$\text{Eq.w.} = \int_{-\infty}^{+\infty} \left(1 - \frac{F_x}{F_c}\right) dx,$$

In Fig. 6 we plot equivalent widths in units of mtu against log (N_0) for a static medium. It resembles the curve of growth. First we have linearly increasing portion and then a flat portion and again a linearly increasing portion. In Fig. 7 we have plotted the curves of growth for expanding spherical medium with velocity gradient for V_b = 5 and 10 mtu. Here we notice a slight change in the flat portion. For a given equivalent width the presence of dust implies larger number of neutral atoms. In Fig. 8 we have considered a spherical shell moving with constant velocity of 5 and 10 mtu. The behaviour is similar to a static case for low values of N_0. However, after

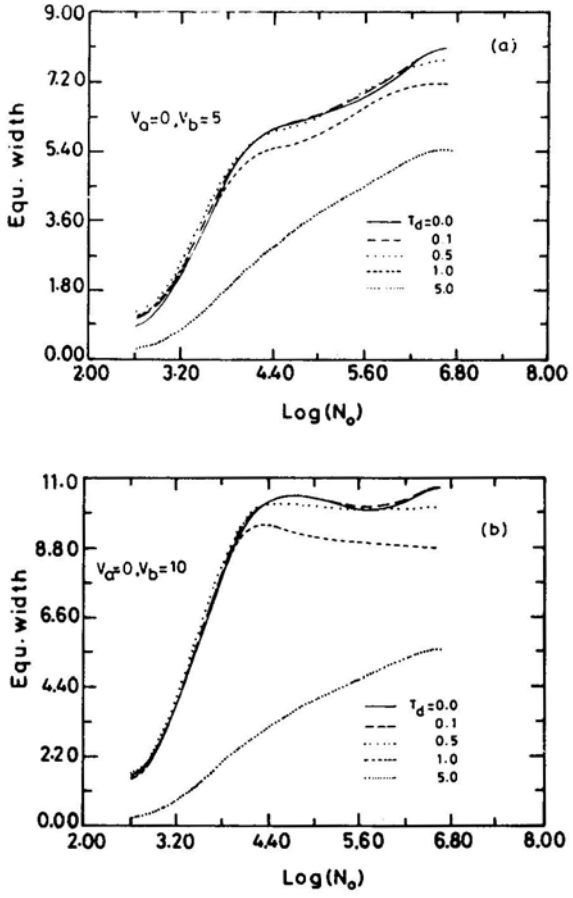

Figure 7. Variation of equivalent widths of hydrogen Lyman α line with increasing number of atoms when the atmosphere is expanding with velocity gradient, and (a) V_b = 5 mtu, and (b) V_b = 10 mtu.

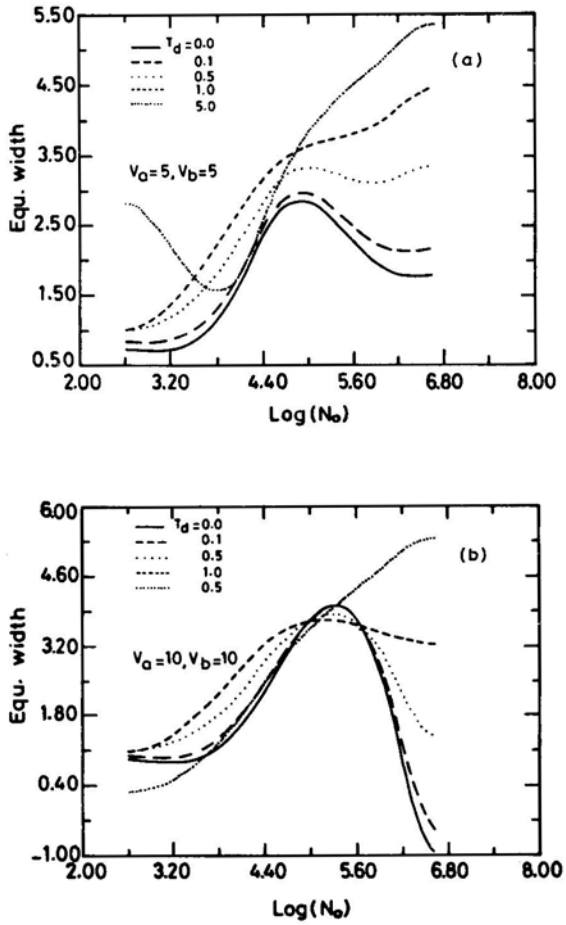

Figure 8. Variation of equivalent widths of hydrogen Lyman α line with increasing number of atoms in a uniformly expanding atmosphere with (a) $V_a = V_b = 5$ mtu and (b) $V_a = V_b = 10$ mtu.

equivalent widths reach a maximum, the width falls and the line appears more in emission. This means that the emission component of the *P*-Cygni profile is larger than the absorption component. The presence of dust increases the equivalent width.

4. Conclusion

In this paper we have calculated the effects of both velocity and dust on the equivalent widths of lines formed in spherically expanding atmospheres. It is found that substantial changes in the equivalent width are caused by the presence of dust in an expanding medium. It is also noticed that dust may increase the equivalent widths and one would overestimate the number of neutral atoms when the effect of dust is ignored.

References

Aller, L. H. 1963, *The Atmospheres of the Sun and Stars,* Ronald Press, New York.
Miller, J. S. 1974, *A. Rev. Astr. Astrophys.,* **12**, 331.
Osterbrock, D. E. 1974, *Astrophysics of Gaseous Nebulae,* Freeman, San Francisco.
Mathis, J. S. 1971, Astrophys. J., **167**, 261.
Mihalas, D. 1978, *Stellar Atmospheres. II,* Ed. Freeman, San Francisco.
Petrosian, V., Silk, J., Field, G. B. 1972, *Astrophys. J.,* **177**, L69.
Peraiah, A., Wehrse, R. 1978, *Astr. Astrophys.,* **70**, 213.
Peraiah, A., Varghese, B. A., Rao, M. S. 1987, *Astr. Astrophys. Suppl. Ser.,* **69**, 345.
Wehrse, R., Peraiah, A. 1979, *Astr. Astrophys.,* **71**, 289.

J. Astrophys. Astr. (1990) **11**, 221–235

A Search for Protocliisters at z = 3.3

Ravi Subrahmanyan *Radio Astronomy Centre, Tata Institute of Fundamental Research, Post Box 8, Ootacamund 643001*

K. R. Anantharamaiah *Raman Research Institute, Bangalore 560080*

Received 1989 December 13; accepted 1990 April 17

Abstract. We have used the Very Large Array to image a single field in a set of adjacent frequency bands around 333.0 MHz in an attempt to detect 21 cm emission from large scale H I inhomogeneities at a redshift of $z = 3.3$. Following the subtraction of continuum radio sources, the absence of any spectral signals apart from that expected due to the system thermal noise has been used to derive constraints on the evolutionary scenario leading to the formation of the present day clusters of galaxies. The observations rule out the existence of H I protoclusters at $z = 3.3$ with masses $\simeq 3.5 \times 10^{14}\ M_{\odot}$ in H I gas and space density exceeding $(74\ \mathrm{Mpc})^{-3}$. This indicates that the present day rich clusters of galaxies either formed as gaseous protocluster condensates prior to $z = 3.3$ or else they formed through the clustering of their constituent galaxies.

Key words.: Clusters of galaxies, formation—HI observations—HI regions, cosmological—protoclusters

1. Introduction

Structure in the Universe on large scales is believed to have formed by the growth of seed density perturbations through gravitational instabilities (Peebles 1980). In theoretical scenarios where short wavelength fluctuations are damped as a consequence of astrophysical processes like the Silk (Silk 1968; Peebles & Yu 1970) or Landau (Bond & Szalay 1983) damping mechanisms, the first objects that condense out of the Hubble flow are expected to have scales exceeding clusters of galaxies. During the epoch corresponding to a redshift of z when these protoclusters are predominantly neutral gaseous condensates, the 21 cm emission from neutral hydrogen atoms in the matter inhomogeneities is expected to be observable around a frequency of $1420.4/(1 + z)$ MHz. The observational consequences have been discussed by Sunyaev & Zel'dovich (1974), Hogan & Rees (1979) and more recently by Subrahmanyan (1990) for a variety of plausible evolutionary scenarios.

Several observational attempts have been made to detect this 21 cm emission from cosmological redshifts. Each such experiment has searched an area of the sky over an observing bandwidth. The noise levels, in units of .flux density, vary in the different searches and also take on a range of values depending on the spatial and spectral resolution in the observational data. The relationship between these search parameters and physical quantities in the emitter's frame is determined by the Cosmology.

The search volume, located at a redshift determined by the observing frequency, has a line-of-sight depth determined by the bandwidth, and a face area determined by the sky area covered. Condensates having a specific line-of-sight velocity dispersion are optimally detected by data having the corresponding frequency resolution, with upper limits on the observed flux density yielding upper limits on the H I masses of these condensates.

Constraints on the existence of supercluster mass condensates require searches covering large volumes since these objects have small space densities. But these searches can be performed with relatively low sensitivity because the superclusters have large masses. Useful observational constraints on the existence of proto-superclusters have been placed at both z = 3.3 (Subrahmanyan & Swarup 1990) and at z = 8.4 (Bebbington 1986). In this paper we are concerned with observations that constrain the existence of lower mass protoclusters, the progenitors of the present day clusters of galaxies, whose detection requires searches with relatively higher sensitivity, but where smaller search volumes suffice. A preliminary search for protoclusters using the Very Large Array was reported by Hardy & Noreau (1987). A protocluster search using the Westerbork Synthesis Radio Telescope (WSRT) was conducted by de Bruyn *et al.* (1988).

As a complementary experiment to the Ooty search for proto-superclusters (Subrahmanyan & Swarup 1990), we have conducted sensitive observations using the NRAO Very Large Array (VLA; Thompson *et al.* 1980; Napier *et al.* 1983) in an attempt to detect protoclusters or any signatures of inhomogeneous H I at z = 3.3. In contrast with the Ooty observations, the VLA search had better resolution and sensitivity in order to detect the lower mass protoclusters. Since these objects of smaller mass are expected to be more abundant, the volume surveyed was also correspondingly reduced. Although our sensitivity is not an improvement on the WSRT effort (de Bruyn *et al* 1988), the volumes surveyed are independent and our interpretations of the observational data differ in methodology and viewpoint. The Hubble constant H_0 = 75 km s^{-1} Mpc^{-1}, and a density parameter Ω_0 = 1 corresponding to an Einstein-de Sitter universe, are used in this paper. Regions of Universe situated at the redshift of z = 3.3, possessing comoving dimensions d_p Mpc along the line-of-sight and d_t Mpc perpendicular to the line-of-sight, and having zero peculiar motions, will have their emission confined to an angular size

$$\Delta\theta = 0.81\, d_t \text{ arcmin} \tag{1}$$

and a frequency range

$$\Delta\nu_0^{\mathrm{H}} = 0.17 d_p \text{ MHz}. \tag{2}$$

Structures that have a characteristic mass scale M will possess a characteristic angular scale

$$\Delta\theta = 7.07(M/10^{14}\, M_\odot)^{1/3} \text{ arcmin}, \tag{3}$$

and a characteristic frequency scale

$$\Delta\nu_0^{\mathrm{H}} = 1.46(M/10^{14}\, M_\odot)^{1/3} \text{ MHz}. \tag{4}$$

These equations relate comoving volumes and closure density masses in physical space at z = 3.3 with parameters in the observed spectral-line cube and follow from the equations presented in Subrahmanyan (1990). An optically thin gas cloud at z

= 3.3, having an H I mass $M_{H\,I}$, will be observed in its redshifted 21 cm emission with a peak flux density

$$S_p = 6.4\,(M_{H\,I}/10^{14}\,M_\odot)\,(\Delta\nu_0/1\ \mathrm{MHz})^{-1}\ \mathrm{mJy}. \quad (5)$$

2. The observations and data reduction

The observed field lies within the 5C7-survey region (Pearson & Kus 1978) and is centred at a right ascension of $08^h\ 13^m$ and a declination of + 25°00′ (coordinates are referred to 1950.0 epoch). The half-power area of the antenna primary beam contains two sources that have a flux density ~ 600–700 mJy at 333 MHz. All the other sources are ⩽300 mJy. On the average, extrapolation of the 408 MHz source counts of Pearson (1975) with an assumed spectral index of $\alpha = 0.7$ (defining $S_\nu \sim \nu^{-\alpha}$) indicates that a field of this size is expected to have ~ 2 sources with flux density > 1 Jy and ~ 9 sources with flux density > 300 mJy. The total continuum flux density of all the discrete sources in the field is ~ 6 Jy, whereas the expected value is 17.1 Jy. The relative paucity of strong background continuum sources favoured the choice of this field.

The observations with the VLA were made during the night of 1986 December 22/23, from 2130 to 0730 Mountain Time (local time at the telescope site). A total of 14 antennas were used in the C configuration. The antenna primary beam has a half power beam width (HPBW) of 156 arcmin at the observing frequency, the synthesized beam has a HPBW of ~ 1 arcmin with naturally weighted visibilities, and structures of up to ~ 18 arcmin are 'visible' to the telescope in this configuration. A total bandwidth of 3.076 MHz was covered by 63 frequency channels, each of 48.828 kHz width. Channel 32 was centred at 333.00 MHz. Owing to interference being generated at multiples of 100 kHz by the electronics at the antennas, half the spectral channel data were affected by interference and consequently considerable amount of careful data rejection had to be performed by examining the visibility amplitudes as a function of time and baseline. The data were calibrated in amplitude and phase using the source 3C 196 whose flux density was calibrated using 3C 286; the flux density of this primary calibrator (3C 286) was adopted to be 26.77 Jy. Bandpass calibration was performed using the spectral response on 3C 196.

The continuum source flux density was substracted in two stages. The data in Channel 0 (an average of the data in frequency channels lying in the central three quarters of the band) were used to obtain a deconvolved image covering the half power area of the telescope primary beam. The deconvolution, using the algorithm of Clark (1980), yielded 1000 clean components containing a total of 6.255 Jy which accounts for most of the continuum flux density of the discrete sources in the image. The visibilities corresponding to these clean components were subtracted from the ungridded visibility data of all the channels. This stage of subtraction ensured that the stronger sources along with their sidelobe structure (which is frequency dependent) would be absent in later images. Each of the 63 frequency channels were then processed separately—the channel visibilities were gridded with natural weighting and without the application of any taper in order to maximize sensitivity, and the gridded data were Fourier transformed to produce images over a field of 2°.84 × 2°.84. The synthesised beam had half-power dimensions of 70 × 57 arcsec^2 and an orientation at a position angle of 75°.4. A subset of 30 channels that had relatively low

interference levels was chosen and an average image of these 'good' channel-images was subtracted from all the 63 channel-images. This second stage of subtraction removed the weaker continuum emission.

Eight channel-images suffered from the effects of severe interference and roughly half of the remaining 55 channel-images showed the effects of weaker levels of interference. The interference manifested itself as prominent east-west oriented bands over the entire image. The 55 channel-images had an average rms noise of 9.3 mJy/beam. The expected thermal noise is ~ 6 mJy/beam based on the best operational parameters of the VLA. An increase in the noise towards the edges of the passband was observed which is indicative of a decrease in the signal-to-noise ratio in the peripheral channels. This probably arises as a consequence of delay errors in the channels close to the passband edges where the antenna receiver electronics is expected to have large phase gradients.

In order to detect the interference present in the visibility data, the Fourier transform of all the channel-images were examined. The Fourier transform of an image having moderate interference essentially showed noisy data that were confined to specific tracks on the (u, v)–plane corresponding to the locations at which visibility measurements were made. A few abnormally high amplitude values were present on these tracks with a distribution over the entire range of v but mostly confined to $u \leqslant 60\lambda$ corresponding to cells in the (u, v)plane containing measurements strongly affected by interference (Thompson 1982). We rejected the effects of interference in this Fourier transform domain by setting both the real and imaginary components in these cells to zero. The inverse Fourier transform of the resulting Hermitian-form gridded visibilities returned our real celestial image, but without the east-west interference stripes. Cells in the (u, v) –plane that are blanked lie within $u \leqslant 60\lambda$ and, in addition, only the abnormally high amplitude cells have been rejected leaving other neighbouring cells unaltered. This implies that the data rejection will have a marginal effect confined to structures with angular sizes $\geqslant 30$ arcmin. Our interests are on scales $\leqslant 10$ arcmin. We find that in the data rejection for channel 32, which is a typical case, the number of (u, v)-plane cells blanked constitutes ~ 1 % of the total number of cells in the (u, v)-plane that contain visibility measurements. In order to assess the change in the 'dirty' beam due to this blanking, we made a Fourier transform of the beam corresponding to channel 32, blanked out the very same (u, v)-plane cells that were blanked in the interference rejection for channel 32, and performed an inverse Fourier transform to obtain the new beam corresponding to the interference-free image. The beam maximum was found to have reduced by 2 per cent. Owing to the use of the natural weighting scheme, cells in the central region of the (u, v)-plane have relatively higher weights. Therefore a 1 % blanking of cells in this area has resulted in the 2 per cent reduction of the beam maximum. The half power contour of the new beam differs by < 1 per cent in comparison with the original beam, which implies that subsequent to interference rejection in this manner, we do not expect the variations in the beam sizes from channel-to-channel to exceed 1 per cent. These arguments suggest that this procedure for the removal of interference stripes from the images is acceptable and hence it was followed to eliminate the effects of interference from all the affected channels. Subsequently, the channel-images have a mean rms noise of 8.8 mJy/beam.

The two stages of continuum subtraction removes all of the continuum emission that is constant across the frequency channels. Consequently, the spectral-line cube

thereafter contains only channel-to-channel relative intensities and does not contain information regarding the mean intensity at any pixel. But continuum source emission that appears in a frequency dependent form will remain. Discrete sources having spectral indicies $\alpha \sim 2.0$ (defining $S_\nu \sim \nu^{-\alpha}$) and a flux density $S_{333} \approx$ 600 mJy could leave residuals of ~ 3 mJy in the spectral line cube even after the continuum subtraction. In addition, chance superpositions of residual sidelobe responses of sources in the field-of-view can result in low order baselines. These considerations have led us to subtract linear baselines from each image pixel position. The baselines were computed by fits to the 'good' set of central 40 channels consisting of channels 13 through 53, but subtraction of the baseline was performed from all the 63 channels. Subsequently, the channel images had a mean rms-noise of 8.1 mJy/beam. The contiguous set of 41 channel-images from channel number 13 to 53, spanning a frequency range of 2.0 MHz, is free of interference and had a mean rms noise of 6.5 mJy/beam. The individual channel-images displayed rms noise values ranging from 5.6 to 8.0 mJy/beam. The rms noise in the channel-images at this final stage are plotted in Fig. 1 as a function of channel number.

3. Data analysis

The spectral signature of redshifted 21 cm emission/absorption can have a great diversity in form depending on the nature of H I distribution at the search redshift (Subrahmanyan 1990). The observed spectral-line data cube is a three dimensional

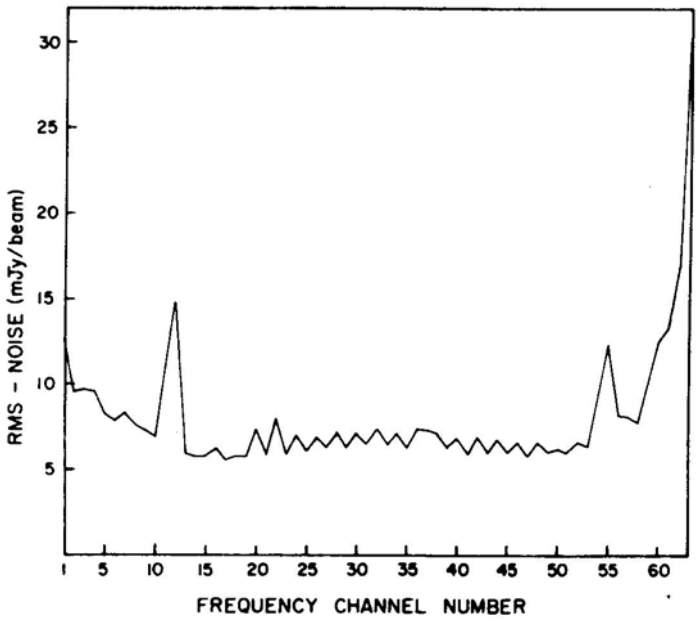

Figure 1. The rms noise in the channel-images plotted as a function of frequency channel number. These values were obtained subsequent to continuum subtraction, interference rejection and the removal of linear baselines.

array of intensities, two of the dimensions are sky coordinates (right ascension and declination) while the third dimension is the observing frequency (refer to Roelfsema 1988 for details). In the frame of the emitter at $z = 3.3$, the sky coordinate axes represent orthogonal distance coordinates perpendicular to the line-of-sight of the observer. The frequency axis denotes distance in redshift space and smearing of emission can occur along this axis if the emitting atoms have peculiar velocities with respect to the Hubble expansion. We first analyse the spectral-line cube in a model independent manner, seeking to detect signals that represent significant departures from the instrument thermal noise for different resolutions. We have smoothed the spectral-line cube to obtain four cubes, each of which have identical resolutions in all the three dimensions in comoving coordinates. We created the first smoothed cube, referred to as Cube A, by averaging channels 1 through 60 into 12 images of 5 channels each and then convolving the images to a final resolution of 70.6 × 70.6 arcsec^2. The resulting cube has a spatial resolution of 1.42 Mpc in all the three dimensions in comoving coordinates at $z = 3.3$. The mean matter density in the cube is expected to be $4.6 \times 10^{11}\ M_\odot$ per resolution element (assuming closure density). Using the images of channels 1 to 60, we constructed two more data cubes, referred to as Cubes B and C, having comoving resolutions of 2.84 Mpc and 4.25 Mpc. A fourth cube, D, was constructed from channels 13 through 52 by averaging 20 channels and smoothing to an angular resolution of 282.5 arcsec. A summary of the resolutions as well as the mean mass expected per resolution element for all the four smoothed cubes is contained in Table 1. The thermal rms fluctuations expected from beam-to-beam in the images of the four cubes is listed in the last column of Table 1. This noise has been estimated by considering the decrease in rms noise as a result of channel averaging and the increase due to smoothing. Channel averaging effectively increases the bandwidth and consequently the rms noise in the average image will be smaller than that in the individual images. Smoothing of the image in the celestial plane effectively tapers the visibility in the (u, v)plane and consequently the effective number of visibility measurements is reduced. This implies that the beam-to-beam thermal fluctuations in the image will increase as the image is smoothed to lower resolutions. The effects of smoothing were determined by noting the fractional change in the peak of the 'dirty' beam (the resultant change in the sum of the weights of the visibility points) when the beam is convolved to resolutions corresponding to those of the four cubes, A through D.

No primary-beam correction was applied. This simplifies searches for the presence of signals above the noise level since the thermal-noise statistics will be uniform over the images. Positive detections, if any, will have to be subjected to a correction in flux density prior to interpretation. Upper limits derived from the data will therefore be relevant for an ‘effective’ search volume that is lower than the volume obtained from the observing bandwidth and the half power area of the primary beam.

In order to explore the existence of signals above the noise in the data cube, we have compared histograms of the pixel intensities with the distribution of intensities expected from thermal noise itself. We have chosen to compare the peak intensities with the predicted peaks based simply on Gaussian statistics. In a sample N independent measurements of a random variable obeying Gaussian statistics with a standard deviation of σ, the deviation x_m above which only one measurement is expected is given by the equation

$$\mathrm{erf}(x_m/\sqrt{2}\sigma) = (N-1)/N. \tag{6}$$

Table 1. A summary of the parameters of the four-smoothed spectral-line cubes.

Cube	Number of channel images	Resolution $\Delta\nu$ MHz	Resolution Δv km s^{-1}	Resolution $\Delta\theta$ arcsec	Comoving length d Mpc	M $M_\odot$/resol. element	Number of resol. elements per channel	x_m/σ per channel	Thermal rms noise mJy
A	12	0.244	244	70.6	1.42	4.6×10^{11}	1.7×10^4	4.0	3.1
B	6	0.488	488	141.3	2.84	3.7×10^{12}	4.2×10^3	3.7	4.1
C	4	0.732	672	211.9	4.25	1.2×10^3	1.9×10^3	3.5	4.6
D	2	0.976	895	282.5	5.67	3.0×10^{13}	1.0×10^3	3.3	5.0

Some images of the smoothed cubes had high intensity pixels which were confined to stripes at the image edges and are residuals from the interference-removal procedures adopted earlier in the analysis. After excluding these image edges, the final number of independent resolution elements per channel-image in each of the four cubes, as well as the expected values of x_m/σ for each channel-images as computed from equation (6), are also listed in Table 1. The noise statistics for the channel-images of the four cubes are listed in Table 2. We have displayed the histograms of the individual image pixel intensities in Fig. 2 for sample images from each of the four cubes. For each image, a grid of pixels spaced so as to roughly provide two pixels per resolution element have been used in creating the histogram. Parabolic profiles corresponding to Gaussian noise distribution have also been plotted as a reference. All the smoothed data cubes show no significant departures from Gaussian noise. For each image, we have compared the number of pixels (N_x) exceeding the value of x_m, which was computed using the rms values listed in Table 2, with the number of pixels per beam (N_b) for that image. This normalised ratio, N_x/N_b, is also listed in Table 2 for each image. Except for a couple of images in cube A, the ratio is in the range 0.4–2.3 as compared to the expected value of N_x/N_b = 1.0. This confirms the absence of significant systematic departures from Gaussian form in the tails of the distribution function.

Table 2. Statistics of the pixel-intensities in the images of the smoothed spectral-line cubes.

Cube	Image number	Freq. MHz	Max mJy	Min mJy	rms mJy	(N_x/N_b)
A	1	331.584	33.9	−29.8	7.0	2.0
	2	331.828	27.8	−25.1	5.2	2.3
	3	332.073	28.1	−26.0	5.0	5.0
	4	332.317	13.7	−12.7	2.9	2.0
	5	332.561	15.8	−16.7	3.5	1.7
	6	332.805	20.1	−19.6	3.8	2.3
	7	333.049	18.2	−17.5	3.9	2.0
	8	333.293	17.1	−16.7	4.0	0.3
	9	333.537	14.4	−14.3	3.3	2.0
	10	333.782	14.1	−17.7	3.0	2.5
	11	334.026	20.3	−22.5	4.2	3.6
	12	334.270	27.9	−26.6	5.9	1.2
B	1	331.706	38.0	−33.9	8.5	0.7
	2	332.195	25.2	−23.7	5.7	2.3
	3	332.683	23.1	−19.6	4.8	1.8
	4	333.171	21.0	−18.6	4.9	1.0
	5	333.569	15.3	−15.6	3.8	0.6
	6	334.148	29.3	−27.7	7.3	0.8
C	1	331.828	40.7	−49.0	11.5	0.6
	2	332.561	21.7	−49.0	11.5	1.0
	3	333.293	26.7	−22.8	6.1	0.9
	4	334.026	32.2	−32.8	8.1	0.4
D	1	332.536	22.1	−20.8	5.4	1.2
	2	333.513	22.5	−23.3	5.4	1.3

4. Interpretation of the data

The search covers a field 170.7 × 170.7 arcmin^2 which corresponds to an area of 206 × 206 h_{75}^{-2} Mpc^2 in comoving coordinates at z = 3.3. The survey bandwidth of 3.076 MHz corresponds to a depth of comoving length 17.9 h_{75}^{-1} Mpc. The resulting search volume is a rectangular parallelepiped having a comoving volume of 7.6 $\times 10^5$ h_{75}^{-3} Mpc^3. The angular resolution of 70 × 57 arcsec^2, corresponding to the HPBW of the synthesised beam, implies a comoving linear resolution of 1.27 h_{75}^{-1} Mpc. The frequency resolution of 48.828 kHz implies a comoving linear resolution of 0.28 h_{75}^{-1} Mpc along the line-of-sight for matter having zero peculiar velocity with respect to the Hubble flow. The survey volume is expected to contain a total mass of 10^{17} $h_{75}^{-1} M_\odot$ assuming a mean matter density of closure value.

4.1 *Upper Limits on H I Density Fluctuations*

Considering the central channels in the four smoothed cubes, that are relatively interference free, there is no significant rms noise above that expected from the

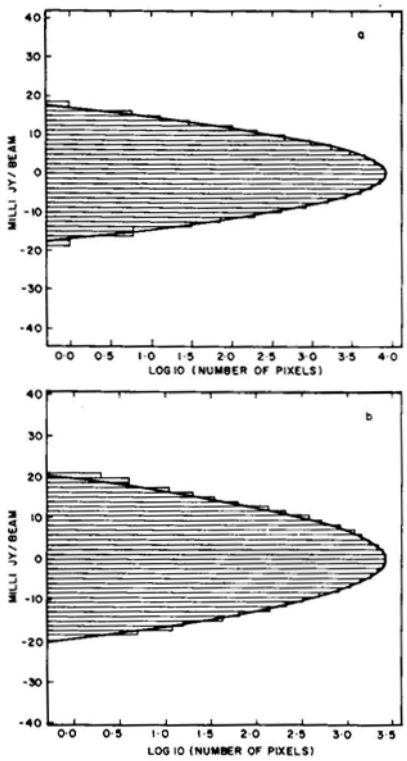

Figure 2. Histogram displays of the pixel intensities in selected images of the four smoothed cubes: 'a' pertains to channel 6 of Cube A; 'b' is for channel 4 of Cube B; 'c' is for channel 2 of Cube C; 'd' and 'e' are for channels 1 and 2 respectively of Cube D. In all the displays, continuous curves corresponding to Gaussian probability distribution functions are also plotted as a reference.

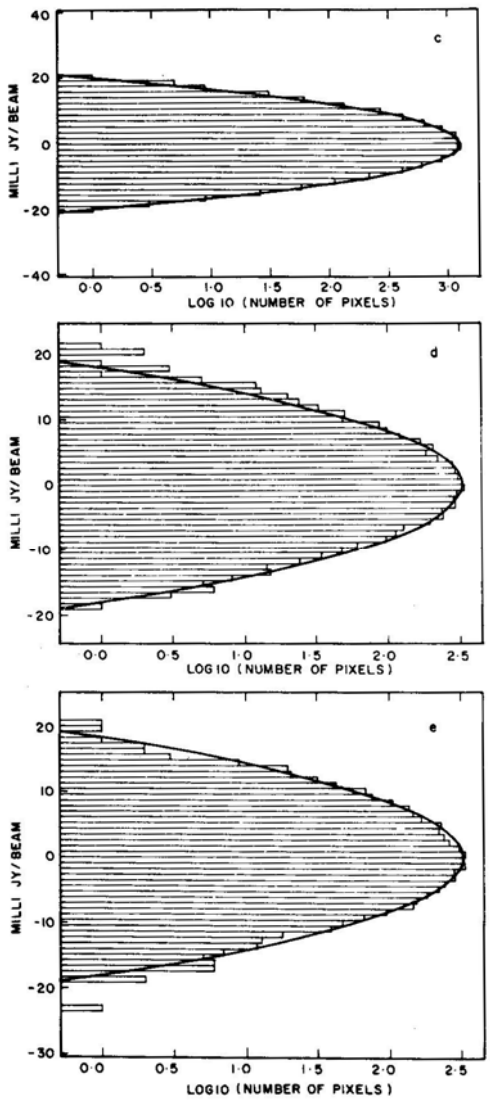

Figure 2. Continued.

instrument thermal noise. Hence we conclude that out experiment has not detected H I density fluctuations at redshift $z = 3.3$. Our results can nevertheless place upper limits on the rms H I density fluctuations at this redshift. Considering Cube D as an example, we note that the rms flux density is 5.4 mJy/beam, whereas the theoretically expected thermal noise is 5.0 mJy/beam. This implies a nominal excess fluctuation of 2.0 mJy/beam ($\approx \sqrt{(5.4)^2 - (5.0)^2}$). From the variations of the rms noise among the central 'good' channels within the four cubes, we judge that the error in our estimate of the mean observed rms is about 10 %. We also assume a 10 per cent error in our estimate of the standard deviation expected from thermal noise. Allowing for these errors, we obtain a 1σ limit of 4mJy/beam for the excess fluctuations in the flux density. Using Equation (5), this corresponds to a 1σ upper limit of $6 \times 10^{13}\, h_{75}^{-2}\, M_{\odot}$

for the H I density fluctuations. Assuming that baryonic matter, comprising of hydrogen and helium atoms in the number ratio 10:1, consitutes a fraction Ω_B of the mean matter density of the Einstein de Sitter Universe, these limits translate to a 1σ upper limit of $\Delta\rho/\rho$ of $3\Omega_B^{-1}$. We have summarised the results obtained using the central 'good' channels of all the four cubes in Table 3.

In order to comprehend the significance of these limits, we compare these with the $\Delta\rho/\rho$ of known astronomical objects. From the data in Lang (1980), we note that objects ranging from small groups of spirals to large groups of ellipticals possess a small spread in density around $6 \times 10^{13}\ M_\odot$ Mpc^{-3}. Assuming, as we have done above, that this represents the baryonic density which is a fraction Ω_B of the total closure density ($1.6 \times 10^{11}\ M_\odot$ Mpc^{-3}), these structures represent density enhancements of $\Delta\rho/\rho \approx 4000\Omega_B^{-1}$. If we adopt a value for Ω_B of 0.05, consistent with the constraints imposed by conventional theories of primordial nucleosynthesis (Yang *et al.* 1984), we find that groups of galaxies have a present day $\Delta\rho/\rho \approx 8000$. If the evolution of the parent perturbations are independent of the evolution on other scales, as is expected in a hierarchically developing universe, we infer from the discussions in Subrahmanyan (1990) that the parent perturbations of structures having the $\Delta\rho/\rho \approx 8000$ virialize at $z_v \approx 2.5$ and turn around at the redshift $z_m \approx 4.6$. Hence, at the redshift $z = 3.3$ their density contrast is expected to be ≈ 50. The low resolution cubes, C and D, that place constraints on H I density fluctuations on a proper length scale of $\sim 1 - 1.5$ Mpc at $z = 3.3$, are relevant for the derivation of constraints on the perturbations that are approaching the virialized state at $z = 3.3$ and which would lead to the formation of groups of galaxies having sizes ≈ 1 Mpc. From Table 3, we infer an upper limit of $\Delta\rho/\rho \approx 5/\Omega_B \approx 100$ (for $\Omega_B = 0.05$) on the H I mass fluctuations having the above scale at $z = 3.3$. The rms fluctuations permitted by the observational data are a factor of two larger than the intensity peaks expected if the progenitors of the present day groups of galaxies were neutral and gaseous at $z = 3.3$ It is interesting to note that by improving the sensitivity of the observations by a factor 4–6, which should be within the capabilities of future instruments like the Giant Metrewave Radio Telescope, it may be possible to directly observe the inhomogeneous matter distribution at high redshifts as fluctuations in intensity above the instrument thermal noise.

4.2 *Upper Limits on H I Masses of Condensates in the Search Volume*

We next turn our attention to the peak intensities observed at the various resolutions and derive firm upper limits on the H I masses of condensates within the search

Table 3. Upper limits on $\Delta\rho/\rho$ from limits on H I mass fluctuations.

Cube	Proper length scale Mpc	Expected thermal rms-noise mJy	Observed mean rms-noise mJy	Upper limit (1σ) on fluctuations due to H I inhomogeneities mJy	($h_{75}^{-2}\ M_\odot$)	1σ limits on $\Delta\rho/\rho$ (Ω_B^{-1})
A	0.33	3.1	3.5	2.7	1×10^{13}	< 30
B	0.66	4.1	4.5	3.3	2.5×10^{13}	< 9
C	1.00	4.6	5.6	4.6	5.3×10^{13}	< 6
D	1.32	5.0	5.4	3.9	6×10^{13}	< 3

Table 4. Upper limits on H I masses of condensates in the search volume.

Cube	Comoving search volume h_{75}^{-3} Mpc^3	Resolution element linear scale km s^{-1}	Mpc proper	$S_p\Delta v$ mJy MHz	M_{HI} h_{75}^{-2} $M_\odot$
A	85^3	224	0.33	4.9	0.77×10^{14}
B	84^3	448	0.66	11.3	1.8×10^{14}
C	83^3	672	1.00	19.5	3.0×10^{14}
D	74^3	895	1.32	22.7	3.5×10^{14}

volume. In cube D, over the entire comoving volume of (74 Mpc)^3, resolution elements having (5.7 Mpc)^3 volumes have an upper limit for $S_p\,\Delta v$ of 22.7 mJy MHz. Using Equation (5), this limit translates to an upper limit of $3.5 \times 10^{14}\ M_\odot$ for the mass of H I gas in any protocluster resident in the search volume. The corresponding limits derived from all the four smoothed spectral-line cubes are listed in Table 4. Structures in the present-day Universe ranging from small clusters of galaxies to rich clusters of galaxies possess virial velocities of several hundred km s^{-1} and H I masses in the range $10^{13} - 10^{15}\ M_\odot$, Their linear sizes range from a few hundred kpc to ≈ 1 Mpc. As seen from Table 4, our search covers the relevant range if we assume that the evolution of the virialised gaseous protoclusters to the present day rich clusters entailed only astrophysical processes with no dynamical evolution. The limits obtained in Table 4 do not place strong constraints on the lower mass clusters, but indicate that the richer clusters do not exist as gaseous condensates within our search volume at redshift $z = 3.3$.

4.3 *Implications for Abell Clusters*

The cores of rich clusters of galaxies represent the most massive virialized entities in the Universe today. We now examine our data seeking to detect the counterparts of these objects at the redshift $z = 3.3$. The cores have present day sizes ≈ 0.3 Mpc and masses of $\sim 10^{15}\ M_\odot$. The galaxies have a velocity dispersion $\approx 10^3$ km s^{-1}. These rich Abell clusters with richness class $R \geqslant 1$ have a comoving number density of $6 \times 1.0^{-6}\ h^3$ Mpc $^{-3}$ (Bahcall & Soniera 1983). For our adopted value of $h = 0.75$, we expect to find the counterpart of one such object in our (74 Mpc)^3 search volume. If these cluster cores have a constant proper dimension out to the redshift of $z = 3.3$, they should appear as emission features with a line width of ≈ 1 MHz and an angular size of ~ 1 arcmin. The central 40 channels of our spectral-line cube, at an angular resolution of ~ 1 arcmin and a frequency resolution of 1 MHz, display a peak intensity of 15 mJy/beam. The corresponding H I mass limit is $2.3 \times 10^{14}\ M_\odot$. Hence, neutral gaseous condensates corresponding to the present day rich Abell clusters are absent in our search volume although the counterpart of one rich Abell cluster is expected to be present. It is therefore possible that the rich Abell clusters did not exist as neutral gaseous condensates at $z = 3.3$.

4.4 *Implications for Protoclusters*

In this sub-section, all the matter at the search redshift is assumed to exist in the form of condensates (protoclusters) having a single arbitrary mass. These are not identified with known objects. The observational data is used to constrain their masses. In an Einstein-de Sitter universe, ~ 10 potentially observable condensates could exist in our search volume of 6×10^5 Mpc^3 if the individual condensate has a total mass of $\sim 10^{16}\ M_\odot$ For $\Omega_B = 0.05$, the H I mass within each condensate would be $\sim 4 \times 10^{14}\ M_\odot$ More than one of these objects are expected to be 'visible' if the lifetime of the condensate exceeds one tenth the dispersion in the epoch of their formation (which includes $z = 3.3$). The peak flux density detected within the survey region (Table 4) rules out the existence of condensates having the above H I mass within the search volume. Considering lower masses for the condensates, the assumptions stated above predict that greater than 10 'visible' condensates having H I masses of $\sim 4 \times 10^{13} M_\odot$ exist within the search volume. Considering the sensitivity achieved in our VLA observations, the existence of these condensates are ruled out only if their line-of-sight velocity dispersions do not exceed ~ 400 km s^{-1} . Hence, for the above assumptions in Ω_B and lifetimes, the VLA observations indicate that protoclusters with total masses $\sim 10^{16}\ M_\odot$ do not exist at $z = 3.3$ unless their velocity dispersions exceed $\sim 10^3$ kms $^{-1}$, with masses as low as $\sim 10^{15}\ M_\odot$ are unlikely unless their velocity dispersion exceeds ≈ 400 km s $^{-1}$ .The upper limit to the range of masses that are constrained is determined by the limited search volume and the lower limit is set by the search sensitivity. Increasing the assumed value for Ω_B or increasing the assumed lifetime would enable constraints on a greater range of masses. These VLA observations complement the observations in Subrahmanyan & Swarup (1990), where constraints were derived on larger mass condensates. As discussed in Subrahmanyan (1990), the velocity dispersion expected in a $10^{15}\ M_\odot$ scale over density at turn around is expected to be $\approx 10^3$ km s^{-1} for a smoothly peaked perturbation. Hence, the constraints derived here are valid even if the perturbations are yet to virialize.

5. **Comparison with earlier observations**

The observations of Hardy & Noreau (1987), that were also made using the VLA, covered a search volume that was a factor of 2.7 larger than the volume covered in our experiment. They adopted a channel-differencing technique for reducing the 'noise' level, with the consequence that only sources with velocity dispersions $\leqslant 350$ km s^{-1} would survive and a 2σ (2 standard deviation) upper limit of $3.6 \times 10^{14}\ h_{75}^{-2}\ M_\odot$ was inferred on the H I masses of protoclusters having this velocity dispersion Their comoving search volume of $1.5 \times 10^6\ h_{75}^{-3}$ Mpc^3 was located at a redshift $z = 3.3$. The observed rms-noise levels were a factor $\geqslant 5$ higher than the expected thermal noise and this was attributed to interference. The limits placed by their search were an order of magnitude poorer than our limits.

de Bruyn *et al.* (1988) used the WSRT to image a pair of fields at 327 MHz in spectral-line mode with a useful bandwidth of 2.0 MHz. The spectral-line cube was smoothed to various spatial and velocity resolutions in a matched-filter approach to

detect signatures of protoclusters. Since the flux density peaks in the smoothed cubes were as expected from thermal noise alone, upper limits in the range 3–13 $\times 10^{13}\ h_{75}^{-2}\ M_{\odot}$ were inferred on the H I masses of protoclusters that could exist in their search volume with a line-of-sight velocity dispersion in the range 150 to 1200 km s^{-1}. Their comoving search volume, encompassing $7 \times 10^5\ h_{75}^{-3}$ Mpc^3, was located at a redshift of $z = 3.3$. Our search volume was 85 % of the volume searched by de Bruyn *et al.* (1988) and our search sensitivity was a factor of two poorer.

The earlier workers derived upper limits to the masses of protoclusters that could exist in their search volume from the peak flux densities observed in their smoothed spectral-line cubes and this approach yields poorer limits if larger volumes were searched. Apart from computing limits in this manner, we have interpreted our data in certain novel ways. We have modelled the protoclusters as a population of condensates having an arbitrary but single mass, with reasonable assumptions for the H I content and lifetimes. The data have been interpreted as constraining the existence of protoclusters in dispersion velocity-mass space. The limits obtained would improve with increasing search volume. We have smoothed our independently observed data cube maintaining identical resolutions in all the three dimensions in comoving coordinates and hence derived upper limits on rms H I density fluctuations on a range of length scales. We have also specifically searched for counterparts of the present day Abell clusters at $z = 3.3$.

6. Conclusions

1. If the comoving space density of the protoclusters exceeds $(74\ Mpc)^{-3}$, condensates having $\geqslant 3.5 \times 10^{14}\ M_{\odot}$ in H I gas do not exist at the redshift of $z = 3.3$ in an Einstein-de Sitter universe. This result is valid provided that the line-of-sight velocity dispersion within the condensate is 1000 km s^{-1} Condensates having $\geqslant 5 \times 10^{13}\ M_{\odot}$ in H I gas are ruled out if their line-of-sight velocity dispersions are $\leqslant$ 400 km s^{-1} and their comoving space densities exceed $(35\ Mpc)^{-3}$.

2. Virialized neutral gaseous condensates, corresponding to the present day rich ($R \geqslant 1$) Abell clusters, are not present at the redshift of $z = 3.3$ if their comoving space densities exceed $(74\ Mpc)^{-3}$.

3. The VLA observations indicate an upper limit of $\approx 5\Omega_B^{-1}$ on the rms fractional density fluctuations at $z = 3.3$ on smoothing the matter distribution to a comoving linear scale of $\sim$ 5 Mpc. This result is valid in an Einstein-de Sitter universe with Ω_B representing the mass fraction of the closure density that is in the form of neutral baryons.

The observations presented in Subrahmanyan & Swarup (1990) indicated that supercluster mass ($\geqslant 10^{15}\ M_{\odot}$ in H I gas) condensates do not exist at the redshift of $z = 3.3$. The observations discussed in this paper do not place strong constraints on supercluster scale structures, since less than 10 objects having H I masses $> 5 \times 10^{14}\ M_{\odot}$ are expected in the search volume for an adopted $\Omega_B \approx 0.05$. On the other hand, the VLA observations discussed in this paper indicate that protoclusters having H I masses in the range $4 \times 10^{13} - 4 \times 10^{14}\ M_{\odot}$ and having velocity dispersions $\sim$ 400-1000 km s^{-1} may not exist in the neutral gaseous phase at the redshift of $z = 3.3$. This result suggests that counterparts of the groups and clusters of galaxies that we see in the present day Universe may not exist in the neutral gaseous phase at the

redshift z = 3.3. This implies that if condensates corresponding to the present day groups and clusters do form in the galaxy formation scenario, they are likely to have completed their gaseous phase prior to the redshift of z = 3.3. Since some of these structures that have low densities are expected to be still approaching the virialised state at that epoch, it appears that the groups and clusters do not form through a collapse of the parent gaseous perturbations followed by fragmentation into galaxies. The observations are suggestive of a scenario where galaxies form first followed by their clustering into groups and clusters as perturbations on larger scales turn around and undergo dissipationless collapse. Such a sequence of events is expected in a cold dark matter dominated universe. However, a neutrino dominated universe where the initial supercluster mass condensates fragment into galaxies at redshifts $z > 3.3$, followed by their undergoing hierarchical clustering, is not ruled out.

Acknowledgements

We thank Prof. Govind Swarup for his encouragement and helpful discussions. The NRAO is operated by Associated Universities, Inc., under cooperative agreement with the National Science Foundation. The data were reduced at the National Image Processing Facility for Astronomy (NIPFA) at the Radio Astronomy Centre, Ooty. This facility is financed by the Department of Science and Technology, Government of India. We also thank Juan Uson and Durga Bagri for useful discussions.

References

Bahcall, N. A., Soneira, R. M.1983, *Astrophys. J.,* **270**, 20.
Bebbington, D. H. O. 1986, *Mon. Not R. astr. Soc,* **218**, 577.
Bond, J. R., Szalay, A. S. 1983, *Astrophys. J.,* **274**, 443.
Clark, B. G. 1980, *Astr. Astrophys.,* **89**, 377.
De Bruyn, A. G., Wieringa, M. H., Katgert, P., Sancisi, R. 1988, in *IAU Symp. 132: Large Scale Structure of the Universe,* Eds Audouze, J., Pelletan M. C. & Szalay, A., D. Reidel, Dordrecht, p. 211.
Hogan, C. J., Rees, M. J. 1979, *Mon. Not. R. astr. Soc,* **188**, 791.
Hardy, E., Noreau, L.1987, *Astr. J.,* **94**, 1469.
Lang, K. R., 1980, *Astrophysical Formulae,* Springer-Verlag, Berlin, Heidelberg.
Napier, P. J., Thompson, A. R., Ekers, R. D. 1983, *Proc IEEE,* **71**, 1295.
Pearson, T. J. 1975, *Mon. Not. R. astr. Soc,* **171**, 475.
Pearson, T. J., Kus, A. J. 1978, *Mon. Not. R. astr. Soc,* **182**, 273.
Peebles, P. J. E., 1980, *Large Scale Structure of the Universe,* Princeton University Press, New Jersey.
Peebles, P. J. E., Yu, J. T. 1970, *Astrophys. J.,* **162**, 815.
Roelfsema, P. R. 1980, in *Proc Third NRAO Synthesis Imaging Summer School,* Eds Bridle, A., Schwab F. & Perley, R. A., *Astr. Soc. Of the Pacific Conference Series,* Vol. **6**.
Silk, J. 1968, *Astrophys. J.,* **151**, 459.
Subrahmanyan, R. 1990, *Mon. Not. R. astr. Soc,* Submitted.
Subrahmanyan, R., Swarup, G. 1990, J. Astrophys. Astr., submitted.
Sunyaev, R. A., Zel'dovich, Ya. B. 1974, *Mon. Not. R. astr. Soc,* **171**, 375.
Thompson, A. R.1982, *IEEE Trans. Antennas Propagat.,* **AP-30**, 450.
Thompson, A. R., Clark, B. G., Wade, C. M., Napier, P. J. 1980, *Astrophys. J. Suppl.,* **44**, 151.
Yang, J., Turner, M. S., Steigman, G, Schramm, D. N., Olive, K. A. 1984, *Astrophys. J.,* **281**, 493.

J. Astrophys. Astr. (1990) **11**, 237–253

An Observational Constraint on the Existence of Proto-Superclusters at z =3.3

Ravi Subrahmanyan & G. Swarup *Radio Astronomy Centre, Tata Institute of Fundamental Research, Post Box 8, Ootacamund 643001, India*

Abstract. Observations have been conducted using the Ooty Radio Telescope in order to place constraints on the evolutionary scenario leading to the formation of the present day superclusters. The experiment attempted to detect 21 cm emission from massive neutral hydrogen condensates at a redshift of $z = 3.3$. In an Einstein de-Sitter universe with baryon density $\Omega = 0.05$, about ten condensates were expected in the volume surveyed if superclusters, having H I masses $\simeq 5 \times 10^{15}\ M_{\odot}$, were the first objects to separate out of the Hubble expansion. The sensitivity of our experiment rules out the existence of these condensates at $z = 3.3$ unless their lifetimes are less than one-tenth the dispersion in their epoch of formation or the proto-superclusters subtend angles greater than 6 arcmin. The result indicates that superclusters form at $z > 3.3$ if indeed they were the first objects to condense out of the Hubble flow.

Key words: Clusters of galaxies, formation—HI observations—HI regions, cosmological—protoclusters—superclusters, formation

1. Introduction

If hot dark matter dominates the mean matter density in the Universe, adiabatic density perturbations are expected to have resulted in the formation of massive gaseous condensates which subsequently fragmented and formed the clusters and galaxies. At redshifts when these predicted progenitors of the present-day galaxy clusters and superclusters are expected to be predominantly neutral gas condensates of primordial composition, they should be 'visible' to us in their 21 cm emission. Following the theoretical predictions of Sunyaev & Zel'dovich (1972), Novokreshchenova & Rudnitskii (1973) and Sunyaev & Zel'dovich (1974), the first observing programme attempting to detect redshifted 21 cm emission from protoclusters at $z = 3.33$ and 4.92 was conducted by Davies, Pedlar & Mirabel (1978) using the Jodrell Bank Mk 1A telescope. Hogan & Rees (1979) computed the observable properties of H I gas having an inhomogeneous distribution with a clustering scale at high redshifts estimated using the present day galaxy two-point correlation length and an adopted growth rate for the fluctuations. Bebbington (1986) used the Cambridge 6C telescope and searched the entire sky north of 82° declination in an attempt to detect primordial pancakes at a redshift of $z = 8.4$. Motivated by the possibility of discovering primordial H I condensates, de Bruyn *et al.* (1988) as also Hardy & Noreau (1987) conducted sensitive observations with the Westerbork and Very Large Array Telescopes respectively adopting spectral-line Fourier-synthesis techniques in fields

devoid of strong continuum radio sources. More recently, the spectral appearance of this emission from H I at high redshifts has been theoretically discussed by Subrahmanyan (1990) for a variety of plausible matter distributions.

All observational efforts towards the detection of redshifted 21 cm emission/absorption from inhomogeneities in the primordial neutral gas at epochs prior to the 'first light'—emission of optical radiation from the first 'stars'—have so far been unsuccessful. They have been useful in deriving constraints on the nature of the Universe at high redshifts and consequently on the possible scenarios that lead to the formation of the galaxies and the observed large scale structure of the present-day Universe. The importance of knowledge regarding the state of the Universe during the 'dark ages' led us to attempt an experiment that has resulted in improved constraints on the scenario leading to the formation of clusters and superclusters. Our interpretations of the observational results have stronger implications as compared to those of previous workers. We have conducted complementary observations using the Ooty radio telescope and the Very Large Array (VLA). The Ooty experiment encompassed a greater search area with a larger velocity depth and was designed to seek evidence for the most massive structures theoretically expected, in which the velocity dispersions are the highest. The VLA experiment had higher spatial and velocity resolutions and attempted to detect smaller-mass isolated structures and also signatures of a patchy H I distribution. The observational results obtained with the Ooty Radio Telescope form the subject matter of this paper. The observations with the VLA are discussed in an accompanying paper (Subrahmanyan & Anantharamaiah 1990).

Our searches were conducted at a frequency of 326.5 MHz corresponding to the receipt of 21 cm emission from a redshift of $z = 3.35$. This choice of search redshift was primarily constrained by the operating frequency of the ORT. Discoveries of examples of ongoing galaxy formation at low redshifts (Bothun *et al.* 1987; Bergvall & Jorsater 1988) and primeval galaxy candidates at redshifts $z \sim 2$–3 (Djorgovski *et al.* 1987; McCarthy *et al.* 1987; Chambers, Miley & van Breugel 1988) suggest that galaxy formation is an extended process which may begin at high redshifts but continues to the present day. The existence of forming galaxies at low redshifts suggests that our search-redshift of $z = 3.3$ could contain H I condensates where star formation is yet to commence. We adopt the Hubble constant $H_0 = 75$ km s^{-1} Mpc^{-1} and the density parameter $\Omega_0 = 1$ throughout this paper while relating the observables to physical quantities in the emitter frame. A line-of-sight velocity dispersion of Δv (km s^{-1}) in an H I region at a redshift of $z = 3.35$ causes the observed line profile to have a width

$$\Delta\nu_0^{\nu} = 1.09\ (\Delta v/1000\ \mathrm{km\,s^{-1}})\ \mathrm{MHz}. \tag{1}$$

Line emission from an optically-thin cloud at $z = 3.35$ having an H I mass $M_{\mathrm{H\,I}}$ will be observed with a peak flux density (Subrahmanyan 1990)

$$S_{\mathrm{p}} = 6.4\ (M_{\mathrm{H\,I}}/10^{14}\,M_{\odot})(\Delta v_0/1\ \mathrm{MHz})^{-1}\ \mathrm{mJy}. \tag{2}$$

2. The observations with the Ooty Radio Telescope

All the observations discussed here were conducted over the period June 6 to August 16, 1988 using the Ooty Radio Telescope (ORT; Swarup *et al.* 1971; Joshi *et al.* 1988). The observations were made during the period between 1800 and 0800 hrs local time,

with the bulk of data acquired during the night in order to avoid spurious spectral responses as a result of the Sun appearing through distant sidelobes of the telescope beam. In addition, interference due to activities in the neighbourhood of the telescope site was less at night. The ORT antenna consists of a parabolic cylindrical reflector with its axis in the north-south direction and with a dipole array feed along the focal line. The beam is steered in hour-angle by mechanical rotation with pointing in declination being achieved by electrical phasing of the array. Multiple beams are simultaneously formed on the sky by separately combining the signals from the feed elements with suitable delays and phase shifts. The telescope, along with the associated receiver system, was configured to simultaneously provide a 64-point spectrum over a 9.216 MHz bandwidth centred at 326.5 MHz towards each of four regions of the sky, which are defined by four beams of the telescope.

The spectra were obtained as the discrete Fourier transforms of the cross-correlation between the signals from the northern and southern halves of the north-south ORT aperture; the cross-correlation measurements being computed at discrete delay values. Hence the spectra are complex with the real and imaginary components having point source responses of the form

$$V_R(\sigma) \sim \frac{\sin^2(\pi\sigma \cdot \mathbf{U}_\lambda)}{(\pi\sigma \cdot \mathbf{U}_\lambda)^2} \cos(2\pi\sigma \cdot \mathbf{U}_\lambda)$$

and

$$V_I(\sigma) \sim \frac{\sin^2(\pi\sigma \cdot \mathbf{U}_\lambda)}{(\pi\sigma \cdot \mathbf{U}_\lambda)^2} \sin(2\pi\sigma \cdot \mathbf{U}_\lambda) \tag{3}$$

respectively in the north-south direction. In these expressions U_λ is the baseline vector (with a length, in units of wavelengths at the observing frequency, corresponding to the distance between the phase centres of the two halves of the north-south continuous aperture of ORT) and σ (radians) is a celestial position vector with origin on the celestial sphere at the celestial position towards which the beam is pointed. The quantity $1/U_\lambda$ corresponds to 12.5 sec δ arcmin. The real and imaginary component spectra pertain to orthogonal beam patterns that together cover a primary beam having half power beam widths (HPBW) of 2°.2 in east-west and 11.1 sec δ arcmin in north-south directions. The adjacent beams are separated in declination by 9 secδ arcmin. Response to sources having angular scales exceeding ≈ 6 arcmin would be severely attenuated in the correlation beams.

The H I condensates are expected to manifest themselves as position dependent spectral features. When one of the antenna beams is pointed towards an arbitrary celestial position, the telescope provides a complex spectrum that contains flux contributions from the sources lying in the field, sources lying outside the field that are seen through the beam sidelobes and grating lobes, and spurious responses arising from the coupling of signals into the two halves of the telescope that constitute the interferometer pair. Each of these contributions are modified by the bandpass characteristics of the receiver electronics that they traverse. In order to cancel all the spurious additive signals that are generated within the telescope receiver system, we have chosen to take a difference of the spectra obtained for each beam from a pair of fields on the sky. This beam-switching was performed by slewing the telescope antenna in hour angle between two fields keeping the declination setting (phasing of

the array) unchanged because changing the telescope declination setting entails a change in the signal pathway and consequently the spurious responses will be altered. Correction for the bandpass characteristics was performed by calibrating the observed spectrum using the spectral response obtained on a strong continuum source, the bandpass calibrator. The pair of fields have been selected so that their declinations are identical to the declination of the calibrator at the observing epoch. Since four beams of ORT which are separated in declination are simultaneously used, only one of these beams will have a declination identical to that of the calibrator. Hence only one of the beams will be perfectly calibrated without any change of declination setting. Calibration of the remaining three beams requires a small (< 18 sec δ arcmin) declination change and consequently these beams will suffer a small calibration error. The spurious spectral features arising as a result of this calibration error are negligible in comparison with the spurious spectral features arising due to distant background continuum sources appearing through the ORT antenna grating lobes.

Every field-pair was observed for 4 to 6 sessions (nights) of ~ 6 hours each so as to accumulate a minimum of ~ 20 hours of interference-free data on each field-pair. The bandpass calibrator was observed once for every session; data being acquired with each of the four beams being pointed sequentially on the source for 5–10 min. The calibrator flux density and observing duration were chosen sufficiently large so as to obtain a higher signal-to-noise ratio on the calibrator as compared to that on the difference spectra obtained for each session. The field-pair was observed, with data being acquired for 10 min on each of the fields alternately, by slewing the antenna in hour angle. The data acquired in an observing session was calibrated using the observations of the calibrator made during the same session. The normalized complex bandpass frequency response in each of the four beams displayed < 5 per cent peak variations over the few days period encompassing the 4–6 sessions that were devoted to observations on a single field-pair. On a few occasions when the calibrator data for a particular session could not be obtained—owing to the telescope becoming inoperative prior to the completion of the calibration scan—the data were calibrated using the bandpass response obtained on an adjacent night's observation, with an overall multiplicative correction factor applied based on the relative telescope sensitivity.

Careful off-line data rejection was required in order to eliminate interference. Since the fields are chosen to be devoid of sources $\geqslant$1 Jy, no signal is expected at the 2σ level in the 20-s integrated spectra that are obtained during observations on the field-pair. Hence, these data records were scanned and those containing spectra with peaks exceeding the expected rms thermal noise by a factor ~ 4 were rejected. Since the beams are formed by offset-phasing of the array, interference does not appear with equal prominence in all the beams. Therefore, whenever peaks exceeding the 4σ limit were detected in any one beam, the data on all the four beams were rejected during that integration period. On the average, data for ~ 15 per cent of the observing duration was lost due to interference. Prior to the averaging of all the thirty 20-s integrated complex spectra within a 10-min scan duration, an rms-amplitude (σ_a) was computed for all the 64 × 30 = 1920 spectral measurements and values exceeding a $2.5\sigma_a$. limit were excluded from the averaging. Typically $\geqslant$1 per cent of the points were eliminated by this procedure.

The correlation coefficient measured between the signals from the two halves of the telescope antenna, when observing the unresolved continuum calibrator, varied between 0.17 per cent to 0.21 per cent per Jansky flux density. Adopting a value of

240 K for the system temperature, the implied sensitivity for each half of ORT is between 0.4 and 0.5 K Jy^{-1}.

A total of 12 pairs of regions were surveyed in the beam-switching mode. Since four beams of the ORT were used, the total search area corresponding to 96 beam areas is 33.2 square degrees. The useful bandwidth is 8.5 MHz centred at the operating frequency of 326.5 MHz. For each field-pair, each beam yields a complex difference-spectrum whose real and imaginary components pertain to orthogonal beam patterns. Hence, we have obtained a total of 96 independent real difference-spectra.

Within the right ascension and declination range visible to the telescope at night during the observing months, and lying off the galactic plane, a list of candidate calibrator sources was prepared by including all the sources that have a flux density $\geqslant$ 10 Jy at 327 MHz and, in addition, were unresolved by the ORT correlation beam. The fields were now constrained to lie on declination strips having precessed declination coordinates identical to that of the candidate calibrators. The major cause for spurious spectral features in ORT are continuum sources lying at the positions of the antenna grating lobes. These spectral features arise because the grating lobe positions are themselves frequency dependent. The quality of a field was hence determined by the relative paucity of sources at the grating-lobe positions. Fields having strong sources in the main lobe were also avoided. The radio source catalogue which was scanned for confusing sources was constructed by merging non-overlapping sections of the 408 MHz Molonglo survey (Large *et al.* 1981), the 365 MHz Texas catalogue (Douglas *et al.* 1979) and the 408 MHz galactic plane survey by Clark & Crawford (1974). The telescope beam was arrived at by actual observations of a strong source through the grating lobes. With the pair of fields constrained to have a separation in hour-angle between 3°.75 and 7°.5 in order to minimize the time that is lost during the slew between successive scans, a final list of 12 pairs of fields was arrived at by an assessment of the relative confusion levels at positions along the allowed declination strips.

In order to obtain a rough estimate of the nature of spectra expected to be observed as a consequence of sources lying in the grating lobes, we computed theoretical spectra for the two positions corresponding to the field-pair number 12. These spectra are essentially a sum of the contributions made at each frequency channel by sources, in the catalogue described above, that lie in the main or grating lobe positions. Peak-to-peak variations of about 100–150 mJy are seen, and the channel-to-channel fluctuations in the flux density have an rms value of ~ 30 mJy. This figure represents a pessimistic estimate of the telescope confusion limit for broadband spectral-line work. Due to our lack of precise knowledge regarding the amplitude and phase responses in the individual grating lobes, we cannot overcome this limitation arising from continuum sources by attempting to eliminate their effects by a subtraction of the theoretical spectra from the observed spectra.

In Table 1 we have listed the 1950.0 epoch coordinates of the twelve field-pairs observed. Both right ascension and declination as well as Galactic coordinates are listed along with the total useful interference-free observing duration on each field-pair. These coordinates pertain to the positions of the third beam used. The first two and the fourth beams occupy adjacent positions to the south and north respectively. The amount of data rejected was roughly equal for both the fields in any field-pair and hence half the listed time constitutes the useful observing duration on each field. For each of the twelve pairs of regions, a calibrated complex difference spectrum was

Table 1. The field pairs observed with the ORT.

Field pair	RA (1950)	DEC (1950)	l	b	T (hrs)
1	14 26 55.0	−10 55 44	−21.93	44.92	20.9
	14 44 54.2	−10 56 22	−16.85	42.47	
2	14 27 04.8	07 14 10	−3.40	59.24	19.9
	14 45 05.1	07 13 32	2.14	55.90	
3	14 40 13.8	21 37 31	26.26	64.11	17.9
	15 00 15.0	21 36 46	29.30	59.68	
4	15 32 05.3	06 39 30	12.45	46.15	22.4
	15 52 05.5	06 38 34	16.11	41.94	
5	21 38 57.4	−05 11 15	50.34	−39.70	19.2
	21 58 57.8	−05 11 52	53.93	−43.91	
6	20 41 11.3	15 56 44	61.04	−15.96	21.9
	20 58 10.6	15 56 01	63.57	−19.25	
7	20 49 56.5	−05 09 25	42.95	−29.12	24.5
	21 06 56.8	−05 10 06	45.34	−32.83	
8	20 39 02.7	03 53 07	50.10	−22.21	21.6
	20 58 02.5	03 52 19	52.88	−26.21	
9	22 37 53.2	−20 58 02	37.93	−59.51	20.8
	22 57 54.9	−20 58 24	41.17	−63.93	
10	20 39 06.9	09 51 14	55.48	−19.00	22.4
	20 58 06.4	09 50 27	58.31	−22.86	
11	20 39 48.9	−15 32 16	30.87	−31.40	20.0
	21 06 50.1	−15 33 23	33.92	−37.40	
12	22 41 55.4	−15 36 13	48.23	−58.30	25.1
	23 00 56.6	−15 36 32	52.62	−62.33	

computed corresponding to each of the four beams used. The real and imaginary components of these spectra obtained on the four beams for the twelfth pair of fields is displayed as an example in Fig. 1.

3. Data analysis and results

The search with the Ooty radio telescope has been-an attempt to detect signatures of massive H I condensates in the search volume located at the redshift of z = 3.35. The condensates are expected to manifest themselves as redshifted emission lines which would appear as either emission or absorption features in the difference spectra depending on their location in the pair of fields observed in the beam-switching mode. If condensates are present in both the fields, with the same Hubble velocity as well as position with respect to the field centres, their responses will cancel in the difference spectrum. However, the probability of such an occurrence is expected to be small. The procedure described below was adopted for detecting features in the spectra as it gives the most likely value for the amplitude of a feature of a specified width that is present at each location in the difference spectra.

We first decompose the 'difference spectrum' into a 'smooth spectrum' and a 'residue component'. We have represented the smooth spectrum by a cubic-spline function (Schwab 1983). Our procedure consists of firstly computing a spline fit using the method of cross validation. In the presence of spiky spurious signals in the

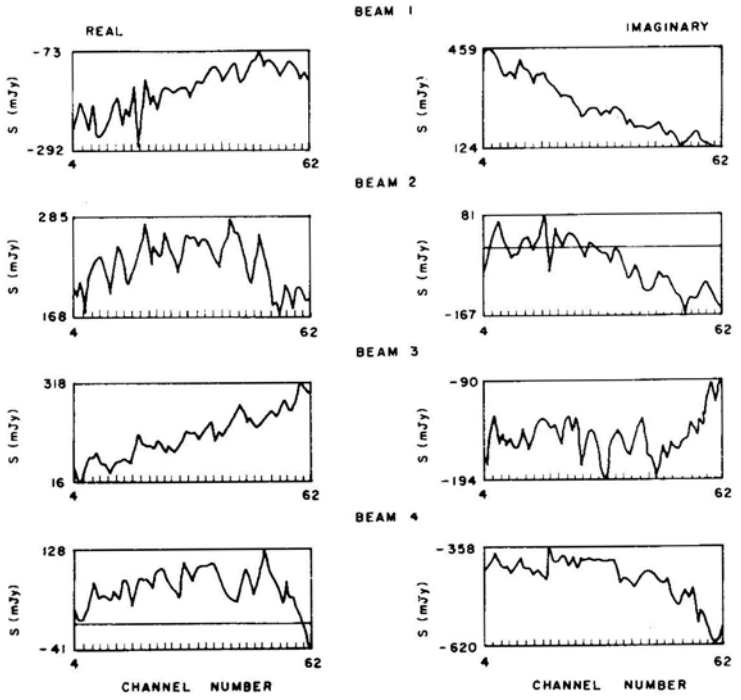

Figure 1. The real and imaginary components of the complex difference spectra obtained on differencing the observations on each of the four beams for the field-pair 12. The spectra are plotted in units of mJy flux density as a function of channel number.

spectrum, which could have arisen from interference, this fit would recognize the narrow features as untrue and the resulting smooth spectrum would not be influenced by interference present in the difference spectrum. If the cross-validation method for the determination of the smoothing parameter fails, as evidenced in the rms noise of the residue component having a value lower than the expected thermal noise, we repeat the spline smoothing with the smoothing parameter fixed so that the rms value of the residue component is equal to the specified thermal noise. The decomposition is illustrated in Fig. 2. The continuous curve is the difference spectrum and the smooth spectrum is shown as a dashed line.

We next performed a search for features having Gaussian profiles with widths corresponding to velocity dispersions of 600, 900, 1200, 1800 and 2400 km s^{-1}. At every point in the spline-smoothed spectrum for each such search, we demarcate, as a 'signal domain', a neighbourhood centred at the point of current interest and having an extent that is twice the full width at half maximum (FWHM) of the features that we seek to detect. Considering the point corresponding to channel number 36 in Fig. 2, the signal domain is the region marked S. The 'interpolated baseline' in this signal domain is determined by performing a second-order polynomial-interpolation from a pair of segments of the smooth spectrum, which adjoin the signal domain on either side, and each of which have a length that is at most equal to the extent of the signal domain. In Fig. 2, interpolation from regions R_1 and R_2 that adjoin the region S have yielded the baseline shown as a dot-dashed curve within the signal domain. This

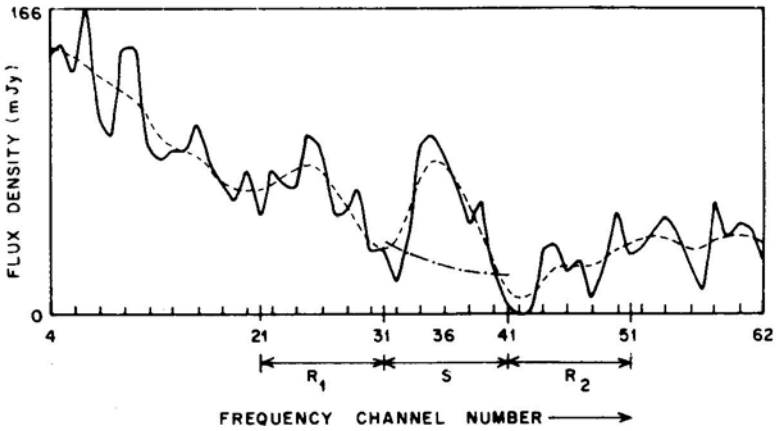

Figure 2. An illustration of the spectral segments involved in the search for signals. The continuous curve shows the difference spectrum and the dotted curve shows the smooth spectrum; both being plotted as a function of channel number. For the point of interest (channel 36), the range of channels marked S is the signal domain while the segments marked R_1 and R_2 are the remainder regions; the demarcation is valid for a search for a feature having a velocity dispersion of 600 km s^{-1}. The dot-dashed curve is the interpolated baseline.

baseline is subtracted from the difference spectrum in the signal domain to obtain a 'residue' version of this spectral segment. The best-fit amplitude of a template Gaussian, that has the required FWHM and whose truncated tail-end points are placed on the smooth-spectrum at the two boundaries of the signal domain, is computed by a weighted least squares fit to the residue difference-spectrum within the signal domain. Spikes in the difference spectrum, that deviate significantly from the smooth spectrum and occur in those frequency channels where interference was noticed during data rejection, are given a weight of zero. The Gaussian fit smoothes over sharp fluctuations in the difference spectrum, which arise from the thermal noise and from interference, that have characteristic widths which are much smaller than the Gaussian width. The subtraction of the interpolated baseline ensures that high-amplitude low-order baselines, which could arise due to continuum sources being present in low order sidelobes, make a very diminished contribution to the amplitude estimate.

For each complex difference spectrum, the procedure detailed above was repeated at all the frequency channel locations separately for the components of the complex spectrum. Those points located within a FWHM of the ends of these spectra were excluded. The maximum of the absolute values of the best-fit amplitudes obtained at each frequency channel location on the component spectra was deemed to be the amplitude estimate at that location in the complex difference spectrum. A few fields that showed obvious effects of confusion arising from antenna grating lobe responses were trimmed in spectral extent to reject the affected frequency channels. Hence, a set of amplitude estimates were separately obtained at all the frequency channel locations in each of the 48 complex difference spectra observed. Histograms of the amplitude estimates were computed by binning all the amplitudes into 10 mJy-wide flux density bins. The number of amplitudes obtained in each bin was normalized by the number of amplitude estimates computed within a FWHM of the template Gaussian. The

histograms are displayed in Fig. 3. A continuous curve having a Rayleigh distribution is superimposed on each histogram as a reference. The flux density corresponding to the peaks of the Rayleigh forms are approximately the 1σ (1 standard-deviation) values of the amplitudes. The 1σ values are larger at larger velocity dispersions because of the presence of low-order baselines in the difference spectra as seen in Fig. 1. Although the detected amplitudes have an rms value that are mostly a factor of $\sim$ 3–7 higher than the expected rms thermal noise, we do not consider the search as having successfully detected proto-superclusters. These large deviations from the expected thermal noise arise as a consequence of the telescope grating responses. Hence, the spectra are basically confusion limited, and the 1σ amplitudes only reflect the confusion limit of the observations. The histograms roughly follow the Rayleigh form with no significant high-amplitude tails. Hence, we only infer upper limits on the existence of proto-superclusters in the search volume. The results are summarized in Table 2. For each velocity dispersion, the total comoving survey volume and the mean mass enclosed in a resolution element (volume defined by the HPBWs of the telescope beam and the FWHM of the template Gaussian) assuming closure density are listed in the table. The flux densities corresponding to the peaks of the Rayleigh forms and the corresponding H I masses are also listed. The 1σ of the amplitudes roughly correspond to H I masses that are a factor of 10 smaller than the closure-density mass expected in the resolution volume elements. These H I masses represent 1σ limits on the existence of proto-superclusters within the search volume at the redshift z = 3.3

4. Interpretation of the observational results

The search covers an area of the celestial sphere corresponding to 1.734×10^5 Mpc^2 at z = 3.35 and the useful bandwidth corresponds to a depth of 49.45 Mpc in comoving coordinates. The total comoving search volume is 8.6×10^6 Mpc^3. A 2.6 per cent redshift range has been covered around the redshift z = 3.35. Spherical condensates whose parent perturbations turn around at $z_t \approx 7$ and virialize at $z_v \approx$ A.3 would possess virialized radii $r_v \geqslant 2\ (\mathrm{M}/10_{16}\ M_\odot)^{1/3}$ Mpc resulting in their observed line profiles having widths $\Delta v_0^v \geqslant 0.6\ (\mathrm{M}/10^{14}\ M_\odot)^{1/3}$ MHz (Subrahmanyan 1990). For masses in the range 10^{14}–$10^{16}\ M_\odot$, the observed line-width is expected to have values ranging from several hundred kHz to a few MHz. Although objects having the virialised radii estimated above would subtend angular sizes of $\Delta\theta \geqslant 16\ (M/10^{16}\ M_\odot)^{1/3}$ arcmin, subsequent to collapse and virialization only the central

Table 2. 1σ upper limits on the H I masses of condensates at z = 3.3.

Δv km s^{-1}	Comoving survey volume h_{75}^{-3} Mpc^3	Closure mass in a resolution element $h_{75}^{-1}\ M_\odot$	1σ amplitude mJy	1σ upper limits on $M_{\mathrm{H\,I}}$ $h_{75}^{-2}\ M_\odot$
600	7.2×10^6	2.1×10^{15}	20	2.0×10^{14}
900	7.0×10^6	3.1×10^{15}	22	3.4×10^{14}
1200	6.8×10^6	4.2×10^{15}	23	4.7×10^{14}
1800	6.0×10^6	6.2×10^{15}	30	9.2×10^{14}
2400	5.4×10^6	8.3×10^{15}	42	1.7×10^{15}

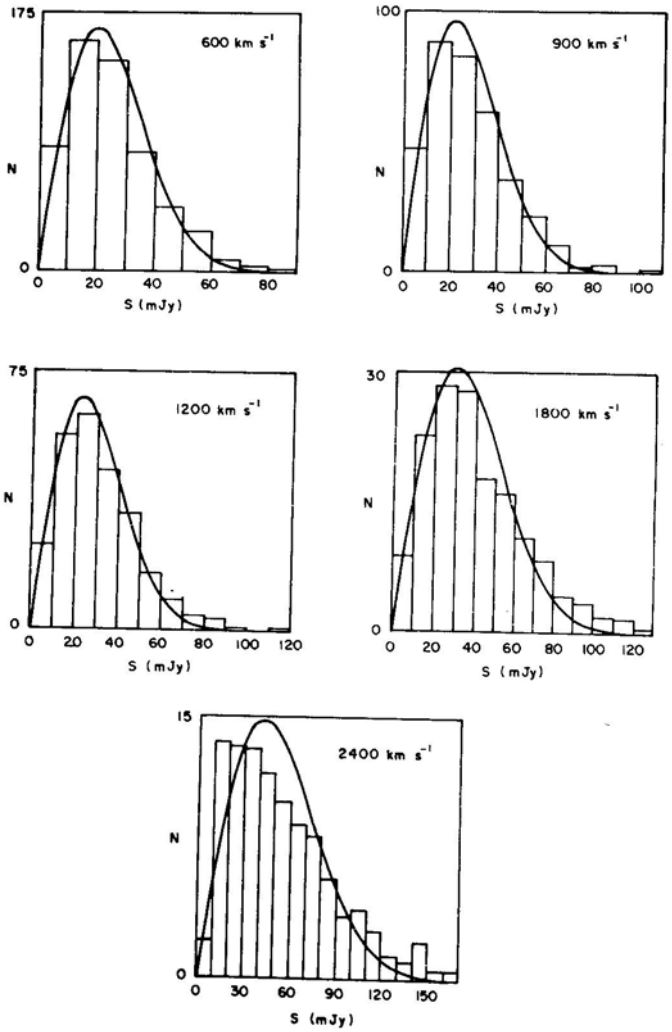

Figure 3. Histogram display of the amplitudes detected in the difference spectra. Each histogram pertains to features having a specific velocity dispersion as indicated in the plots. The continuous curves are Rayleigh distribution functions that have been plotted as a reference.

dense regions that cool rapidly are expected to abound in H I. Hence, the 21 cm line-emitting region would subtend an angle of a few arcmin. The ORT, when operated as a two-element interferometer as in this search experiment, is sensitive to structures $\leqslant$ 6 arcmin. If the condensates have the form of oblate pancakes, with the dense H I being in a sheet having a size as large as the longest dimension of the pancake, our search would fail to detect the pancakes if they were observed face-on. When observed edge-on, the velocity dispersion along the line-of-sight would approximately equal the differential Hubble velocity across the length of the pancake. This leads to an observed line width of $\Delta\nu_o^H \approx 1.5\ (M/10^{14}\ M_\odot)^{1/3}$ MHz and this could be as large as several MHz for supercluster mass pancakes. Hence, although proto-superclusters

having spherical or prolate structures can be detected in our search, highly flattened pancakes may well escape detection.

4.1 *Interpretation of the Cumulative Histograms*

In order to facilitate a comparison with the predictions from the theoretical scenarios of galaxy formation, the data have been presented in the form of cumulative histograms in Fig. 4. The bins along the *x*-axis are in units of solar masses of H I gas. Each plot corresponds to structures of a specific velocity dispersion, and the height of each histogram-bar is an upper limit to the mass fraction contained in proto-superclusters

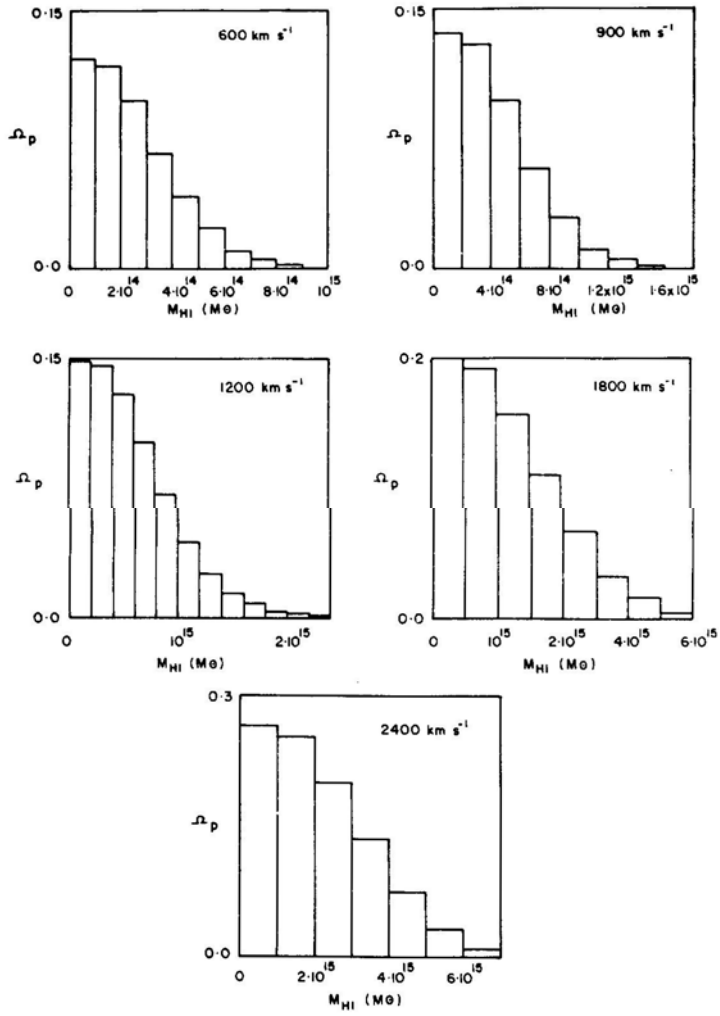

Figure 4. Cumulative histogram display of the amplitudes detected in the difference spectra. The heights of the histogram-bar denote upper limits on the fraction of the closure-density mass that can reside in H I condensates having masses exceeding the bar ordinate.

of mass exceeding the bar abscissa. This cumulative H I mass is expressed as a fraction, Ω_p, of the total closure-density mass expected within the search volume. From the maximum of the heights of histogram bars of Ω_p, we can rule out scenarios where $\geqslant 0.2$ of the closure density of the Universe exists as 'visible' proto-superclusters at the redshift $z = 3.3$. The observational limits on the Gunn-Peterson test have been used to infer upper limits on the baryon fraction Ω_B that are significantly smaller than our limit (Steidel & Sargent 1987). Nevertheless, our limit is based on a direct attempt to detect clumpy H I at $z = 3.3$ in its 21 cm emission and is important in the light of recent work suggesting that the observed abundances of light elements could imply primordial nucleosynthesis with $\Omega_B = 1.0$ (Maloney & Fowler 1988).

The maximum number of structures (N_m) of any arbitrary mass M that are expected to be present in the entire search volume is given by the ratio of the total closure-density mass expected to be present in the volume to the mass M. An upper limit to the number actually present (N_0) is obtained by computing the cumulative number of flux density peaks corresponding to H I masses exceeding the mass M. A peak corresponding to any arbitrary mass M^*, with $M^* > M$, is counted as M^*/M number of masses. We assume that the baryon density parameter $\Omega_B \approx 0.1$ and that proto-supercluster lifetimes exceed one-tenth the dispersion in their epoch of formation (which includes z = 3.3). Then we would expect the observed number, No, to be larger than a fraction, 1/100, of the number N_m. For each velocity dispersion, we can now set an upper limit to the individual proto-supercluster mass as that value of M above which the number N_m exceeds the number that is allowed by the data by at least a factor of 100. From Fig. 4, we hence obtain upper limits that range from $6 \times 10^{14}\ M_\odot$ at a dispersion velocity of 600 km s^{-1} to a value of $6 \times 10^{15}\ M_\odot$ at the dispersion velocity of 2400 km s^{-1} on the H I masses of proto-superclusters. These limits are very nearly three times the 1σ limits obtained in Table 2. If we make a further assumption that 50 per cent of the gas in a proto-supercluster is neutral and that the gas has a composition which is 70 per cent hydrogen and 30 per cent helium by mass, we obtain corresponding upper limits on the total baryonic masses of individual proto-superclusters that are $1.7 \times 10^{15}\ M_\odot$ and $1.7 \times 10^{16}\ M_\odot$ at the dispersion velocities of 600 and 2400 km s^{-1} respectively. The limits at intermediate velocity dispersions lie within the range defined by these two values. If we relax the above assumption and accept as a limit the value of mass M at which the expected number is a factor of 10 larger than the number allowed by the data (in contrast to the factor 100 adopted previously), we obtain limits ranging from 2.3×10^{14} to $3.6 \times 10^{15}\ M_\odot$ of H I over the range of velocity dispersions 600 to 2400 km s^{-1}. These limits correspond to standard deviations between 1.1σ and 2.1σ of the detected peaks. These limits are relevant if the Universe contains baryonic matter of ≈ 10 per cent density and the proto-supercluster lifetimes are comparable to the dispersion in the epoch of their formation (which again includes $z = 3.3$).

4.2 *Implications of the Search Sensitivity and Volume*

In Fig. 5, we have compared the search volumes of all the experiments conducted at the redshift of $z = 3.3$. The figure provides the fiducial number of proto-superclusters of any fixed mass that could be present in each of the comoving search volumes by assuming that all the closure-density mass resident in the search volume is present as

proto-superclusters of the adopted mass. The horizontal lines denote the commoving search volumes of the Ooty, Westerbork (de Bruyn *et al.* 1988), VLA (Hardy & Noreau 1987), and Jodrell (Davies *et al.* 1978) observations. In Fig. 6, we have compared the 2a upper limits set by these different observations. Consistent with the constraints of primordial nucleosynthesis (Yang *et al.* 1984), we now assume that 5 per cent of the closure-density matter in the Universe is baryonic. We note from Fig. 5 that the Ooty observations cover a search volume that could have greater than 10 condensates if the individual condensate H I masses are less than $\approx 5 \times 10^{15} M_{\odot}$ Of these 10 condensates, only a fraction would be actually observable to us in their 21 cm emission depending on the dispersion in the epoch of formation of the condensates and their lifetimes in the neutral gaseous phase. For example, if the lifetimes are one-tenth of the dispersion in the formation epoch, and our search redshift is situated within the epochs of formation, we would expect to observe one-tenth of the total number of condensates resident in the search volume. Hence, in the case of condensates with $\approx 5 \times 10^{15} M_{\odot}$ in H I gas, we would expect to observe one proto-supercluster within the search volume. Comparing this expectation with the 2σ limits plotted in Fig. 6 and the histograms of the amplitudes in Fig. 3, we infer that not a single amplitude peak corresponding to a proto-supercluster having an H I mass exceeding $\approx 5 \times 10^{15} M_{\odot}$ has been detected within the search volume for dispersion velocities < 2000 km s^{-1}. Hence, under the assumptions stated above, the Ooty observations have the necessary sensitivity and search volume in order to place meaningful constraints on condensates at the redshift of $z = 3.3$ that have total masses $\approx 10^{17} M_{\odot}$. Larger mass condensates could be ruled out only if the assumed lifetimes exceed one-tenth the dispersion in the epoch of formation. Considering condensates of lower masses, we infer from Fig. 5 that the maximum number of condensates that could be expected within the search volume exceeds 10^2 for total masses $< 10^{16} M_{\odot}$. Adopting the same assumptions as discussed above, $\approx$ 10 proto-superclusters each having $\approx 5 \times 10^{14} M_{\odot}$ in H I gas are expected to be detected within the search volume. The sensitivity of the search indicates that condensates with H I masses $> 5 \times 10^{14} M_{\odot}$ do not exist at $z = 3.3$ with their expected space densities, but the sensitivity does not constrain the existence of condensates having H I masses $\leqslant 5 \times 10^{14} M_{\odot}$ for the assumptions adopted. Useful constraints can be inferred for lower mass condensates only if Ω_B exceeds 0.05. The search volume determines the value of the largest condensate mass on which meaningful constraints can be derived, while the search sensitivity determines the lowest condensate masses.

4.3 *Abell Clusters*

Abell clusters of richness class $R \geqslant 1$ have a local space density of $2.5 \times 10^{-6} h_{75}^3$ Mpc^{-3} (Bahcall & Soniera 1983). Assuming that this also represents the comoving space density of the counterparts of these rich clusters at the redshift $z = 3.3$, we expect a total of ~ 20 such objects within the comoving search volume of $8.6 \times 10^6 h_{75}^{-3}$ Mpc^3 encompassed by the Ooty observations. We now examine the 20 highest amplitude estimates obtained in the histograms in Fig. 3. At the velocity dispersion of ~ 900 km s^{-1}, similar to the observed velocity dispersions in the galaxy clusters today, all these 20 peaks have flux densities that correspond to H I masses exceeding $10^{15} M_{\odot}$ by at most a factor of 2, with all the other peaks being below this

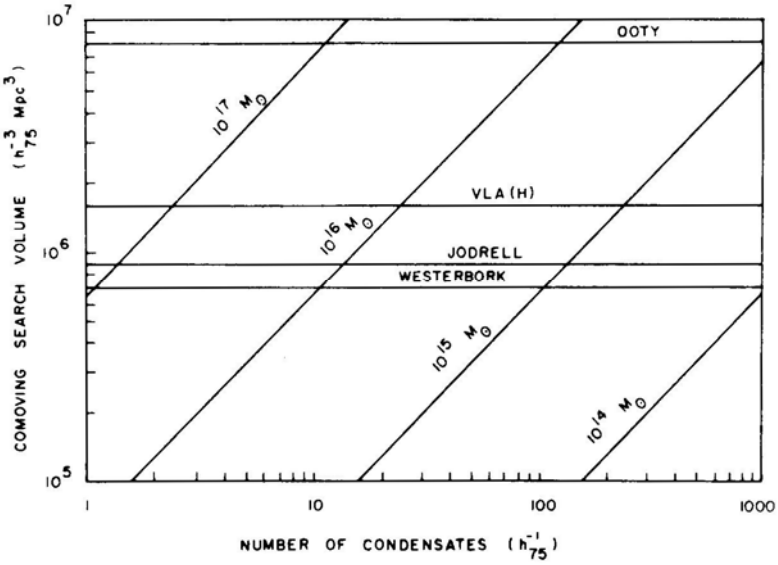

Figure 5. The relationship between the search volume and the expected number of proto-superclusters for various possible proto-supercluster masses. The assumption has been made that all the closure-density mass within the search volume is resident in proto-superclusters of a single mass. The horizontal lines represent the search volumes covered in various experiments.

mass limit. The rich clusters have total masses $\sim 7 \times 10^{14 \pm 1}\ h_{75}^{-1}\ M_{\odot}$ (Bahcall 1977). We infer that the richest Abell clusters, having $\geqslant 2 \times 10_{15}\ M_{\odot}$ in H I, do not seem to be present as neutral gaseous condensates at the redshift of $z = 3.3$.

4.4 *General Considerations*

The peak fluctuation expected, due to the system noise alone, depends on the number of independent measurements in the volume searched. Since the peak fluctuation expected is larger in searches covering larger volumes, the limits placed by an experiment that searches greater volumes will be poorer if the peak deviation is used to derive the upper limits. Hence, we have adopted the approach outlined in the preceeding paragraphs, where the limits would be better if larger volumes are surveyed. In our method of deriving limits, the expected number of structures exceeding an arbitrary mass M would be directly proportional to the volume surveyed. But the number allowed by the data, assuming that the data contains only Gaussian noise, would increase slowly with increasing number of measurements. This is because in a sample of N independent measurements of a Gaussian random variable (with standard deviation σ) the deviation x_m above which only one measurement is expected is given by the relationship: $\mathrm{erf}\,(x_m/\sqrt{2}\sigma) = (N - 1)/N$.

5. A comparison with earlier searches

The theoretical predictions of Sunyaev & Zeldovich (1974) suggest that our search volume should contain ~ 4 proto-superclusters and that the upper limit set by our

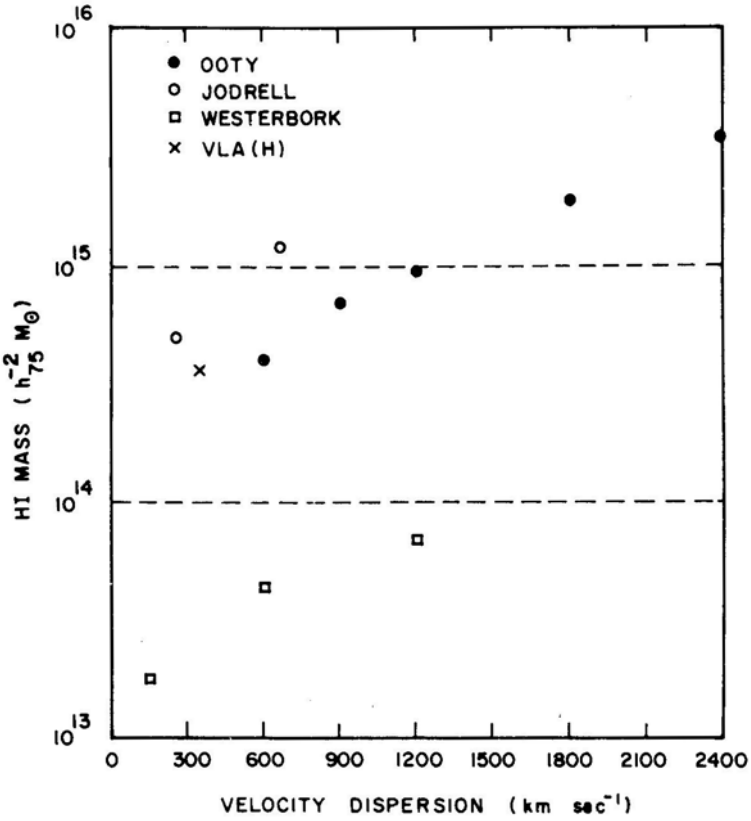

Figure 6. The 2σ limits on H I masses of protoclusters at the redshift of $z = 3.3$. The limits placed by various experiments are plotted as a function of the line-of-sight velocity dispersion. The implications of these limits for the formation of various large scale structures strongly depend on the comoving volume searched.

observations on the total mass of each proto-supercluster, derived using the same assumptions as used by Davies et al. (1978), is $2 \times 10^{15}\ M_\odot$. The observational upper limits presented in Fig. 2 of Davies et al. (1987) imply an upper limit of ≈180 mJy on the peak flux density from proto-superclusters having a velocity dispersion of 660 km s^{-1}. We infer the corresponding upper limit on the total mass of a proto-supercluster to be $6 \times 10^{15}\ M_\odot$ at $z = 3.3$. These observations conducted by Davies et *al.*, at the frequency corresponding to a search at the redshift of $z = 3.3$, cover a total comoving search volume, as defined by the half-power areas of their telescope beam, in which only 0.4 proto-superclusters are expected. Hence their upper limit does not seem significant and is, in addition, a factor of three above our limit. The search for protoclusters that was conducted by Hardy & Noreau (1987) encompassed a volume that is a factor of 5 smaller than the Ooty observations and, in addition, had a relatively poorer sensitivity because their data were strongly affected by interference. Observations conducted using the Westerbork Telescope (de Bruyn et al. 1988) attained rms noise levels that were an order of magnitude better than the Ooty observations. But the comoving search volume, encompassing ≈ 6–7 × $10^5\ h_{57}^{-3}$ Mpc^3, is an order of magnitude smaller than that covered by us at Ooty. In addition, the

restricted bandwidth used in the observations prevented searches for proto-superclusters that have line-of-sight velocity dispersions exceeding ≈ 1000 km s^{-1}. Their observations constrain the evolution of smaller mass entities whose dispersion velocities are less than ≈ 1000 km s^{-1} We interpret the 2σ flux density limits set by Bebbington (1986) as implying 2σ upper limits of 2×10^{15} $h_7^{-\frac{2}{5}}$ $M_\odot$ on the H I inhomogeneities at the redshift of $z = 8.4$ that have line-of-sight velocity dispersions ≈ 1600 km s^{-1}. These observations encompassed a search volume of 1.8×10^7 $h^{-\frac{3}{5}}_{7}$Mpc^3, which is by far the largest volume searched in any such experiment. The sensitivity of the search allows strong constraints to be placed on only the most massive supercluster scale condensates and the observations indicate that supercluster mass condensates (of ≈ 10^{17} $M_\odot$ total mass) do not exist at the redshift of z= 8.4 as well.

6. Conclusions

1. Less than a fraction 0.2 of the closure density of the Universe exists as condensates which are 'visible' in 21 cm emission at the redshift $z = 3.3$.

2. The observations place 2σ limits in the range $4 \times 10^{14} - 3.5 \times 10^{15}$ h_7^{-2} $M_\odot$ on the H I content of individual primeval condensates that have line-of-sight velocity dispersions in the range 600-2400 km This limit pertains to a comoving search volume of 8×10^6 h_7^{-3} Mpc^3 situated at the redshift of $z = 3.3$. In an $\Omega_B = 0.05$ Einstein-de Sitter universe, the observations indicate that proto-superclusters having total masses in the range 10^{16}–10^{17} $M_\odot$, with their baryonic content in the neutral gaseous phase, may not exist at the redshift $z = 3.3$.

The Ooty observations have the sensitivity and the survey volume required in order to place constraints on the evolution of superclusters. The results indicate that superclusters, if indeed they are the first objects that condense out of the Hubble flow (as would be expected in a hot dark matter dominated universe), probably form at redshifts $z > 3.3$.

Acknowledgements

We thank the staff of the Radio Astronomy Centre, Ooty, for their cooperation during the conduct of these observations and Dr K. R. Anantharamaiah for a critical reading of the manuscript.

References

Bahcall, N. A. 1977, *Ann. Rev. Astr. Astrophys.,* **15**, 505.
Bahcall, N. A., Soneira, R. M. 1983, *Astrophys. J.,* **270**, 20.
Bebbington, D. H. 0. 1986, *Mon. Not. R. astr. Soc.,* **218,** 577.
Bergvall, N., Jorsater, S. 1988, *Nature,* **331**, 589.
Bothun, G. D., Impey, C. D., Malin, D. F., Mould, J. R. 1987, *Astr. J.,* **94,** 23.
Chambers, K. C., Miley, G. K., van Breugel, W. J. M. 1988, *Astrophys. J.,* **327,** L47.
Clark, D. H., Crawford, D. F. 1974, *Aust. J. Phys.,* **27**, 713.
Davies, R. D., Pedlar, A., Mirabel, I. F. 1978, *Mon. Not. R. astr. Soc.,* **182,** 727.

de Bruyn, A. G., Wieringa, M. H., Katgert, P., Sancisi, R. 1988, in *IAU Symp. 132: Large Scale Structures of the Universe,* Eds J. Audouze, M. C. Pelletan & A. Szalay, D. Reidel, Dordrecht, p. 211.

Djorgovski, S., Strauss, M. A., Perley, R. A., Spinrad, H**.,** McCarthy, P. 1987, *Astr. J.,* **93,** 1318.

Douglas, J. N., Bash, F. N., Torrence, G. W., Wolfe, C. 1979, Univ. Texas Publ. Astr. No. 17.

Hardy, E., Noreau, L. 1987, *Astr. J.,* **94,** 1469.

Hogan, C. **J.,** Rees, M. J. 1979, *Mon. Not. R. astr. Soc.,* **188,** 791.

Joshi, M. N., Swarup, G., Bagri, D. S., Kher, R. K. 1988, *Bull. Astr. Soc. India,* **16,** 111.

Large, M. I., Mills, B. Y., Little, A. G., Crawford, D. F., Sutton, J. M**.** 1981, *Mon. Not. R. astr. Soc.,* **194,** 693.

Maloney, R. A., Fowler, W. A. 1988, *Astrophys. J.,* **333,** 14.

McCarthy, P. J., Spinrad, H**.,** Djorgovski, S., Strauss, M. A., van Breugel, W., Liebert, J. 1987, *Astrophys. J.,* **319,** L39.

Novokreshchenova, S. I**.,** Rudnitskii, G. M. 1973, *Astr. Zh.,* **50,** 877.

Schwab, F. R. 1983, VLA Scientific Memorandum No. 147.

Steidel, C. C., Sargent, W. L. W. 1987, *Astrophys. J.,* **318,** L11.

Subrahmanyan, R. 1990, *Mon. Not. R. astr. Soc.,* submitted.

Subrahmanyan, R., Anantharamaiah, K. R. 1990, *J. Astrophys. Astr.*, submitted.

Sunyaev, R. A., Zel'dovich, Ya. B. 1972, *Astr. Astrophys.,* **20,** 189.

Sunyaev, R. A., Zel'dovich, Ya. B. 1974, *Mon. Not. R. astr. Soc.,* **171,** 375.

Swarup, G., Sarma, N. V. G., Joshi, M. N., Kapahi, V. K., Bagri, D. S., Damle, S. H**.,** Ananthakrishnan, S., Balasubramanian, V., Bhave, S. S., Sinha, R. P**.** 1971, *Nature Phys. Sci.,* **230,** 185.

Yang, J**.,** Turner, M. S., Steigman, G., Schramm, D. N., Olive, K. A. 1984, *Astrophys. J.,* **281,** 493.

J. Astrophys. Astr. (1990) **11**, 255–263

The Spectroscopic Orbit of 6 Draconis*

R. F. Griffin *The Observatories, Madingley Road, Cambridge CB3 OHA, England*

J. J. Eitter *Erwin W. Fick Observatory, Iowa State University, Ames, Iowa 50011, U.S.A.*

D. Reimers *Hamburger Sternwarte, Gojenbergsweg 112, D–2050 Hamburg 80, Federal Republic of Germany*

Received 1989 July 7; revised 1990 March 21; accepted 1990 April 10

Abstract. 6 Dra has long been known to show small variations in radial velocity, and there is photometric and spectroscopic evidence that its spectrum is composite. We show, largely on the basis of a generous number of photoelectric radial velocities mainly obtained at Cambridge and Fick observatories, that the orbit is of mild eccentricity and has a period of 562 days and a semi-amplitude of 7 km s^{-1}. *IUE* observations show that the spectrum between 1600 and 1800 Å is consistent with its arising from a late-A main-sequence companion.

Key words: radial velocities—spectroscopic binaries—orbits—stars, individual—6 Dra

1. Introduction

6 Draconis (HR 4795, HD 109551; $12^h34^m44^s$, + 70°1'18" (2000)) is a fifth-magnitude star and is therefore clearly identifiable by the naked eye that is sufficiently well backed up by a knowledge of the heavens: it is to be found only 15′ north-following the brighter star *k* Dra, with which it forms a pair reminiscent of Mizar and Alcor—from which system, indeed, it may be located, being nearly halfway from there to Polaris.

2. Spectral type, photometry, and duplicity

In the earliest days of spectral classification, 6 Dra was assigned by Miss Maury (1897) to Group XlVa, corresponding to what has subsequently become known as class G. The *Henry Draper Catalogue* (Cannon & Pickering 1920) calls its type K0. When spectroscopic criteria of stellar luminosity were developed (Adams 1916), 6 Dra was recognized as a giant star: Rimmer (1925) found its absolute magnitude to be + 1.1, and subsequently Adams *et al.* (1935) gave a value of + 0.3 and also revised the

* Based in part on observations made with the Cambridge radial-velocity spectrometer, in part on those made with the Erwin W. Fick Observatory spectrometer, and in part on those made by the International Ultraviolet Explorer and collected at the Villafranca Satellite Tracking Station of the European Space Agency.

spectral type to K2. Wilson (1976) obtained M_V = – 1.1 from the K-line width criterion (Wilson & Bappu 1957); in a footnote he remarked "Moderate rotational broadening. Measured M_V(K) too bright". A referee, Dr D. M. Popper, has kindly explained that remark to us (we are ashamed of not having understood it ourselves when this paper was first submitted for publication): if the star shows significant rotation, the K line is broadened by it, and since the inferred luminosity increases with the width measured for that line the luminosity comes out too high. However, the comment on rotational broadening is actually inaccurate, since radial-velocity traces show line-widths in 6 Dra to be in the range typical of giant stars.

Photometry by Haggkvist & Oja (1966) yielded for 6 Dra the magnitude and colour $V = 4^m.94$, $(B - V) = 1^m.313$; Eggen (1966) gave $V = 4^m.89$, $(B - V) = 1^m.31$, $(U - B) = 1^m.13$:. Such a combination of colours immediately arouses curiosity: all normal K giants with $(B - V)$ as great as $1^m.3$ have $(U - B) > (B - V)$. The obvious explanation for the discrepancy in the colours is that the ultraviolet end of the spectrum is held up by a hot companion. Such a possibility is strongly supported by the very large value, $0^m.25$, of the quantity res(k) derived from Copenhagen photometry (Hansen & Kjaergaard 1971): the value is several times larger than the threshold at which res(k) definitely indicates abnormality in the distribution of light in the spectrum. Still further evidence pointing in the same direction is the detailed spectral classification given by Keenan (1983) and Keenan & Yorka (1985) for 6 Dra: K3 **III** CN – 1 CH – 1 H,K – 1 Fe – 1 Hδ 1. The classification shows that all the principal features in the violet part of the spectrum are weakened apart from Hδ which is strengthened—exactly what would be expected if the spectrum of a normal K giant were compounded with that of an A- or F-type main-sequence companion which is not quite bright enough for the composite nature of the spectrum to be explicitly apparent. That a companion of some sort does exist is rendered certain by the orbital motion documented in this paper; the best estimate that we can make of its type, on the basis of the evidence presented above, is late A. We view the still more recent classifications of 6 Dra by Keenan & Yorka (1988: K2.5 **III** Fe – 2 Hδ I) and Keenan & McNeil (1989: K2.5 III CN – 2 Hδ 1 Fe – 1) as indicating the continuing efforts of the classifiers to come to terms with a spectrum that is incipiently composite.

3. *IUE* spectroscopy

A low-resolution, short-wavelength *IUE* spectrum clarifies the nature of the companion. As displayed in Fig. 1, the composite ultraviolet spectrum has a sharp decline in the energy distribution between 1750 and 1700 Å. Since a fifth-magnitude K giant like 6 Dra would be expected to show barely any continuum flux between 1700 and 1900 Å in such a 120-minute exposure, we conclude that the observed flux in that range is due to the companion. We compared the spectrum with other *IUE* spectra of late-A to early-F main-sequence stars from the *IUE Ultraviolet Spectral Atlas* (Wu *et al.* 1983). According to the 1730-Å flux of about 1.4×10^{-13} erg cm^{-2} s^{-1} Å^{-1} and a distance modulus of $6^m.0$ (see below), and according to the shape of the spectrum between 1650 and 1750 Å, the companion of 6 Dra is an A8 to A9 main-sequence star. Since the flux at 1730 Å varies strongly with spectral type, the accuracy of our classification relies mainly on the closest comparison stars in the spectral atlas, namely 51 Tau (A8 V) and 44 Oph (A9 V).

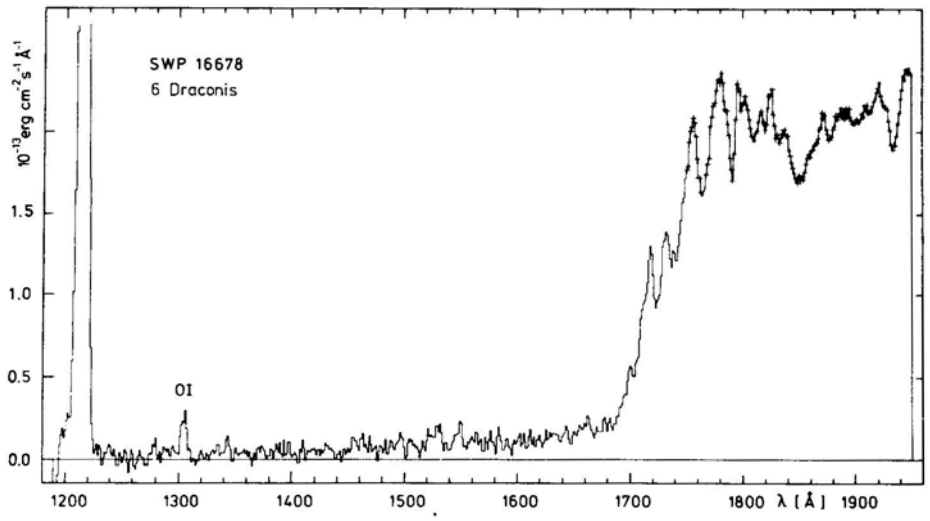

Figure 1. IUE spectrum of 6 Draconis (large aperture, 120 minutes' exposure). The flux at Earth is given. The spectrum is saturated at wavelengths above about 1750 Å, where it is denoted by crosses. Lyman-α emission is geocoronal.

The comparison with late-A main-sequence stars also shows that the O I 1300-Å emission blend is from the K giant. Its flux at Earth is about 8×10^{-14} erg cm^{-2} s^{-1}. With a distance modulus of 6^{m} and a K-giant radius of about 35 $R_{\odot}$ according to its spectral type and luminosity, 6 Dra is found to have an O I surface flux of about 3×10^{3} erg cm^{-2} s^{-1}, normal for a K giant with a relatively low activity level (*cf.* Ayres *et al.* 1981).

6 Dra has been observed to have circumstellar Ca II H and K lines (Reimers 1977), although the star is supposedly located in a region of the HR diagram where stars do not generally show circumstellar lines. A high-resolution long-wavelength *IUE* spectrum confirms that finding: 6 Dra has broad circumstellar Mg II absorption lines with a shortward edge at about – 60 km s^{-1}. Mg II emission is highly asymmetrical and apparently red-shifted owing to circumstellar absorption on the shortward side. It is difficult to see why the duplicity of 6 Dra should be the cause of the broad circumstellar absorption, since the companion star is not close in the sense in which that term is understood in connection with binary stars, and since rotation seems to be normal. One might suspect that, if circumstellar absorption were anything like as pronounced in the Ca II lines as it is in Mg II, it could so cut into the H and K profiles as to cause the Wilson–Bappu effect to underestimate the luminosity of 6 Dra. However, we do not think that that is really so. For one thing, even if 6 Dra were of absolute magnitude –2 or – 2.5, at which circumstellar Ca II and Mg II lines would be expected, the actual profiles of Mg II h and k would still be extremely peculiar. In a normal, single bright K giant the circumstellar line is far shifted shortwards, and the absorption never extends redwards to zero velocity, whereas in 6 Dra deep circumstellar absorption is found from – 60 all the way to 0 km s^{-1}. Furthermore, a high-resolution tracing of the violet spectrum of 6 Dra, kindly obtained for us on 1989 December 14 with the Lick 120-inch telescope and the Hamilton echelle spectrometer (Vogt 1987) by Mr. A. Misch, shows no unusual structure in the Ca II lines. Although

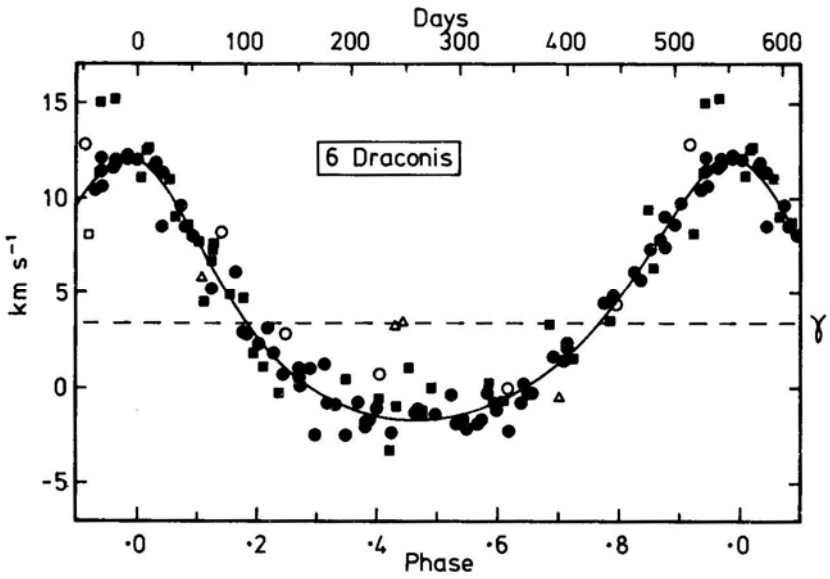

Figure 2. The computed radial-velocity curve of 6 Draconis, with the measured radial velocities plotted. Photoelectric observations from Cambridge, Coravel and the DAO are shown as filled circles, while those made at the Erwin W. Fick Observatory of Iowa State University are represented by filled squares. Open symbols are used for the published photographic data from Mount Wilson (triangles; not used in the solution of the orbit) and Lick (circles).

circumstellar absorption has been seen in the 6 Dra Ca II profiles, and such absorption has proved to be variable in other stars (Reimers 1977), it is doubtful whether it would ever be of such strength and extent to vitiate the K-line absolute magnitude determined for 6 Dra by the Wilson-Bappu method. In conclusion, we must admit that we have no good explanation for the peculiar circumstellar Mg II lines of 6 Dra, and no reason to dispute the absolute magnitude of $-1^{m}.1$ given by Wilson (1976). Such a luminosity would also be consistent with the fact that the A8 V companion appears to be detectable but not obtrusive in the violet part of the integrated spectrum of the system.

4. Radial velocities and orbit

The radial velocity of 6 Dra was first measured with the Mills Spectrograph on the 36-inch refractor of Lick Observatory, where its variability soon came to attention and was announced by Campbell (1922) but appears not to have been followed up. The mean velocity given by four low-dispersion Mount Wilson plates was published by Christie & Wilson (1938); the individual data have since been published by Abt (1973).

The present authors placed 6 Dra independently upon the observing programmes of the photoelectric radial-velocity spectrometers at Cambridge (Griffin 1967) and Fick (Beavers & Eitter 1977) observatories; they subsequently learnt of their shared interest in the object and agreed to join forces in this paper. Altogether there are 74 ‘‘Cambridge’’observations (included in that number are a few obtained by R.F.G.

Table 1. Radial-velocity measurements of 6 Draconics.

Date	MJD	Velocity km s^{-1}	Phase	(O−C) km s^{-1}	Source*
1919 Apr 27.46	22075.46	+2.8	$\overline{38}$.249	+1.8	Lick
July 24.45	163.45	+0.7	.406	+2.3	Lick
1920 May 6.32	22450.32	+12.8	$\overline{38}$.916	+2.5	Lick
1921 June 3.21	22843.21	0.0	$\overline{37}$.616	+0.5	Lick
1922 Mar 25.50	23138.50	+8.2	$\overline{36}$.142	+2.8	Lick
1923 Mar 27.50	23505.50	+4.4	$\overline{36}$.795	−0.1	Lick
1930 May 13.23	26109.23	+3.2	$\overline{31}$.431	+4.9	Mt. Wilson
20.18	116.18	+3.4	.443	+5.1	Mt. Wilson
1931 May 29.18	26490.18	+5.8	$\overline{30}$.109	−1.4	Mt. Wilson
1935 May 24.17	27946.17	−0.5	$\overline{28}$.702	−1.8	Mt. Wilson
1978 Mar 29.99	43596.99	−1.9	0.567	−0.7	Cambridge
Apr 14.97	612.97	−0.8	.595	0.0	Cambridge
Nov 20.22	832.22	+12.2	.986	+0.1	Cambridge
1979 Jan 13.13	43886.13	+8.5	1.082	−0.3	Cambridge
Mar 8.01	940.01	+2.9	.178	−0.8	Cambridge
Apr 29.07	992.07	+0.5	.270	+0.1	Cambridge
May 14.87	44007.87	−2.5	.299	−2.3	Cambridge
June 11.91	035.91	−2.5	.348	−1.5	Cambridge
Nov 28.22	205.22	−0.3	.650	−0.4	Cambridge
Dec 31.14	238.14	+1.4	.708	−0.1	Cambridge
1980 Mar 10.02	44308.02	+5.7	1.833	−0.5	Cambridge
Apr 29.19	358.19	+8.1	.922	−2.5	Fick C
May 5.99	364.99	+10.4	.934	−0.6	Cambridge
8.17	367.17	+11.3	.938	+0.1	Fick A
9.17	368.17	+15.0	.940	+3.8	Fick B
10.91	369.91	+12.1	.943	+0.8	Cambridge
23.15	382.15	+15.2	.965	+3.3	Fick B
July 22.88	442.88	+9.6	2.073	+0.3	Cambridge
1981 Jan 16.11	44620.11	−1.7	2.389	−0.2	Cambridge
Feb 5.05	640.05	−2.4	.424	−0.7	Cambridge
20.32	655.32	+1.0	.451	+2.7	Fick A
Mar 6.29	669.29	−1.3	.476	+0.4	Fick A
May 4.92	728.92	−0.3	.582	+0.7	Cambridge
6.19	730.19	+0.2	.585	+1.2	Fick A
20.13	744.13	−0.7	.609	−0.1	Fick A
24.94	748.94	−2.3	.618	−1.8	Cambridge
July 4.93	789.93	+1.6	.691	+0.6	Cambridge
1982 Mar 5.96	45033.96	+5.2	3.125	−1.1	Cambridge
6.27	034.27	+7.3	.126	+1.0	Fick B
Apr 7.89	066.89	+2.8	.184	−0.6	Cambridge
14.23	073.23	+1.8	.195	−1.1	Fick B
23.16	082.16	+1.1	.211	−1.2	Fick B
May 7.15	096.15	−0.3	.236	−1.7	Fick A
11.96	100.96	+0.7	.245	−0.4	Cambridge
25.93	114.93	+1.0	.270	+0.6	Cambridge
June 29.94	149.94	−0.9	.332	−0.1	Cambridge
July 27.87	177.87	−1.8	.382	−0.4	Cambridge

Table 1. Continued.

Date			MJD	Velocity km s^{-1}	Phase	(O−C) km s^{-1}	Source*
1983	Feb	4.44	45369.44	+1.6	3.723	−0.3	DAO
	Apr	20.24	444.24	+6.3	.856	−1.1	Fick A
		24.05	448.05	+6.3	.863	−1.4	Cambridge
	May	10.04	464.04	+8.6	.891	−0.5	Cambridge
	June	8.93	493.93	+10.6	.944	−0.8	Cambridge
		21.90	506.90	+11.8	.967	−0.1	Cambridge
	July	2.93	517.93	+12.1	.987	0.0	Cambridge
	Aug	3.87	549.87	+8.5	4.044	−2.2	Cambridge
1984	Jan	2.15	45701.15	+1.2	4.313	+1.7	Cambridge
	Feb	9.05	739.05	−2.1	.381	−0.7	Cambridge
		21.35	751.35	−0.6	.403	+1.0	Fick A
	Apr	13.95	803.95	−1.4	.496	+0.3	Cambridge
		29.06	819.06	−0.4	.523	+1.1	Cambridge
	May	13.01	833.01	−2.2	.548	−0.8	Cambridge
	June	8.93	859.93	−1.2	.596	−0.4	Cambridge
	July	11.91	892.91	−0.3	.655	−0.5	Cambridge
	Nov	8.57	46012.57	+7.8	.868	−0.1	DAO
	Dec	21.18	055.18	+11.4	.944	+0.1	Cambridge
1985	Jan	1.14	46066.14	+11.6	4.963	−0.2	Cambridge
		23.06	088.06	+12.0	5.002	0.0	Cambridge
		26.45	091.45	+11.1	.008	−0.8	Fick A
	Feb	8.46	104.46	+11.7	.031	+0.5	Cambridge
		27.38	123.38	+9.0	.065	−0.7	Fick A
	Mar	26.31	150.31	+4.5	.113	−2.5	Fick A
	May	2.20	187.20	+4.7	.179	+1.1	Fick A
		29.97	214.97	+1.8	.228	+0.1	Cambridge
	July	2.94	248.94	+1.0	.289	+1.0	Cambridge
1986	Jan	17.13	46447.13	+0.2	5.641	+0.3	Cambridge
	Feb	10.40	471.40	+3.3	.685	+2.4	Fick A
		14.01	475.01	+1.6	.691	+0.6	Cambridge
		26.99	487.99	+2.1	.714	+0.4	Cambridge
	Apr	7.25	527.25	+3.5	.784	−0.6	Fick A
		10.01	530.01	+4.8	.789	+0.5	Coravel
	May	12.13	562.13	+9.4	.846	+2.5	Fick A
		13.95	563.95	+7.3	.849	+0.3	Cambridge
		27.94	577.94	+7.4	.874	−0.9	Cambridge
	June	11.93	592.93	+9.7	.901	+0.1	Cambridge
	Aug	24.81	666.81	+11.8	6.033	+0.6	Coravel
	Dec	7.19	771.19	+3.1	.218	+1.1	Cambridge
1987	Jan	6.11	46801.11	+0.1	6.272	−0.3	Cambridge
	Feb	1.07	827.07	−0.8	.318	−0.2	Cambridge
		18.41	844.41	+0.4	.349	+1.5	Fick A
	Mar	1.23	855.23	−0.8	.368	+0.5	Coravel
		18.97	872.97	−1.1	.400	+0.4	Cambridge
		31.34	885.34	−3.3	.422	−1.6	Fick A
	Apr	6.25	891.25	−1.0	.432	+0.7	Fick A
		27.87	912.87	−1.2	.471	+0.5	Cambridge
	May	1.17	916.17	−1.4	.477	+0.3	Fick A
		8.16	923.16	0.0	.489	+1.7	Fick A
		31.98	946.98	−1.9	.531	−0.4	Cambridge

Table 1. Continued.

Date	MJD	Velocity km s^{-1}	Phase	(O−C) km s^{-1}	Source*
June 24.90	970.90	−1.7	.574	−0.6	Cambridge
Dec 10.21	47139.21	+9.0	.874	+0.8	Cambridge
1988 Jan 31.44	47191.44	+12.0	6.967	+0.1	DAO
Feb 28.35	219.35	+12.5	7.016	+0.8	Fick A
Mar 1.34	221.34	+12.6	.020	+1.0	Fick A
14.95	234.95	+11.3	.044	+0.6	Coravel
21.30	241.30	+11.0	.055	+0.8	Fick A
Apr 7.27	258.27	+8.6	.086	0.0	Fick A
12.88	263.88	+8.0	.096	0.0	Cambridge
17.21	268.21	+7.7	.103	+0.1	Fick A
30.17	281.17	+6.7	.126	+0.4	Fick A
May 1.17	282.17	+7.6	.128	+1.4	Fick A
16.13	297.13	+4.9	.155	+0.1	Fick A
21.91	302.91	+6.1	.165	+1.9	Cambridge
June 12.90	324.90	+2.3	.204	−0.2	Cambridge
Nov 5.23	470.23	−1.3	.463	+0.4	Coravel
Dec 20.13	515.13	−1.7	.543	−0.3	Cambridge
1989 Feb 11.03	47568.03	−0.8	7.637	−0.6	Cambridge
Mar 26.87	611.87	+2.3	.715	+0.6	Coravel
Apr 29.13	645.13	+4.4	.774	+0.7	Coravel
May 26.98	672.98	+6.1	.824	+0.3	Cambridge

* Sources of radial velocities or descriptions of the equipment with which they were obtained, with the weights attributed in the 6 Dra orbit:

Lick: Campbell & Moore (1928); weight 0.15
Mt. Wilson: Christie & Wilson (1938); weight 0
Cambridge: Griffin (1967); weight 1
Fick: Beavers & Eitter (1977, 1986); weight 0.3 (A), 0.15 (B), 0.05 (C)
DAO: Fletcher et al. (1982); weight 1
Coravel: Baranne, Mayor & Poncet (1979); weight 1

with other spectrometers) and 34 Fick measurements, the first 14 of which have already been published by Beavers & Eitter (1986). The Fick data were already as nearly as possible on the IAU scale (Beavers & Eitter 1986); an effort has been made to place the Cambridge velocities on the same scale by the subtraction of 0.8 km s^{-1} from the raw values (*cf.* Griffin & Herbig 1981).

A preliminary orbit solution utilizing the photoelectric measurements alone yielded a period quite accurate enough to enable the six early Lick velocities to be phased to the correct cycle without ambiguity. The Lick data showed r m.s. residuals of 2.0 km s^{-1} , which were in part systematic: their scatter was 1.3 km s^{-1} about a mean value of + 1.6 ± 0.6 km s^{-1}. We do not attach great significance to the systematic offset, which is in any case only just significant statistically. Not only is 6 Dra, whose declination is + 70°, in an unusual part of the sky, but most of the observations were made at unusual hour angles (10 hours west in one instance!), so atmospheric dispersion and possibly mechanical flexure may have had unusual effects. We have thought it safe to use the Lick velocities, as they stand, in the solution of the orbit and to attribute to them the weight to which their raw residuals entitle them: in that way

some benefit to the period determination is gained from the greatly increased time base that they offer, but, since their combined weight only represents about one hundredth of that of the total data set, any systematic zero-point difference that they may show has negligible effect on the derived γ-velocity. The Mount Wilson velocities are not expected to be of high accuracy and have not been utilized in the solution.

All the velocities are listed in Table 1, with their respective sources noted. The Fick measurements are routinely graded A, B, or C at the time of reduction; typical Standard deviations for the three grades have been determined (Beavers & Eitter 1986). The corresponding relative weights have been attributed to them, and then they have been globally weighted to bring their weighted variance into equality with that of the Cambridge data. The final orbital solution has the following elements:

$P = 561.7 \pm 0.3$ days
$\gamma = +3.38 \pm 0.09$ km s^{-1}
$K = 6.90 \pm 0.12$ km s^{-1}
$e = 0.262 \pm 0.017$
$\omega = 9 \pm 4$ degrees
$T = \text{MJD } 45525 \pm 5$
$a \sin i = 51.4 \pm 0.9$ Gm
$f(m) = 0.0172 \pm 0.0009\ M_\odot$
R.m.s. residual (unit weight) $= 0.8$ km s^{-1}

Acknowledgements

We are very grateful to Mr A. Misch for obtaining a spectrum of 6 Dra. The Fick Observatory contribution to this paper owes a great deal to the work of Dr W. I. Beavers, and has been supported in part by the NSF and the Department of the Air Force. R.F.G. is grateful to the Geneva and Dominion Astrophysical observatories for the use of their radial-velocity instruments, and to SERC for travel grants. D. R. is pleased to acknowledge the use of the *IUE* satellite; his travelling to make the *IUE* observations has been supported by the Deutsche Forschungsgemeinschaft.

References

Abt, H. A. 1973, *Astrophys. J. Suppl.,* **26**, 365.
Adams, W. S. 1916, *Commun. Mt. Wilson Obs. to the Nat. Acad. Sci.,* nos. **24** & 25.
Adams, W. S., Joy, A. H., Humason, M. L, Brayton, A. M. 1935, *Astrophys. J.,* **81**, 187.
Ayres, T. R., Marstad, N.C., Linsky, J. L.1981, *Astrophys. J.,* **247**, 545.
Baranne, A., Mayor, M., Poncet, J. L. 1979, *Vistas Astr.,* **23**, 279.
Beavers, W. I., Eitter, J. J. 1977, *Publ. astr. Soc. Pacific,* **89**, 733.
Beavers, W. I., Eitter, J. J. 1986, *Astrophys. J. Suppl.,* **62**, 147.
Campbell, W. W. 1922, *Publ. astr. Soc. Pacific,* **34**, 167.
Campbell, W. W., Moore, J. H. 1928, *Publ. Lick Obs.,* **16**, 186.
Cannon, A. J., Pickering, E. C. 1920, *Ann. Harv. Coll. Obs.,* **95**, 62.
Christie, W. H., Wilson, O. C. 1938, *Astrophys. J.,***88**, 34.
Eggen, O. J. 1966, *R. Obs. Bull,* no. **125**, 151.
Fletcher, J. M., Harris, H. C, McClure, R. D., Scarfe, C. D.1982, *Publ. astr. Soc. Pacific,* **94**, 1017.
Griffin, R. F. 1967, *Astrophys. J.,* **148**, 465.
Griffin, R. F., Herbig, G. H. 1981, *Mon. Not. R. astr. Soc,* **196**, 33.
Häggkvist, L., Oja, T. 1966, *Ark. Astr.,* **4**, 137.
Hansen, L., Kjaergaard, P. 1971, *Astr. Astrophys.,* **15**, 123.

Keenan, P. C. 1983, *Bull. Inf. Centre de Donnees Stellaires,* no. 24, 19.
Keenan, P. C, McNeil, R. C. 1989, *Astrophys. J. Suppl.,* **71**, 245.
Keenan, P. C., Yorka, S. B. 1985, *Bull. Inf. Centre de Donnees Stellaires,* no. 29, 25.
Keenan, P. C, Yorka, S. B. 1988, *Bull. Inf. Centre de Donnees Stellaires,* no. 35, 37.
Maury, A. C. 1897, *Ann. Harv. Coll. Obs.,* **28**, part 1.
Reimers, D. 1977, *Astr. Astrophys.,* **57**, 395.
Rimmer, W. B. 1925, *Mem. R. astr. Soc,* **64**, 1.
Vogt, S. S. 1987, *Publ. astr. Soc. Pacific,* **99**, 1214.
Wilson, O. C. 1976, *Astrophys. J.,* **205**, 823.
Wilson, O. C, Bappu, M. K. V. 1957, *Astrophys. J.,* **125**, 661.
Wu, C.-C. *et al.* 1983, *The IUE Ultraviolet Spectral Atlas, IUE NASA Newsletter,* no. 22.

J. Astrophys. Astr. (1990) **11**, 265–270

1965 Light Curves of BV Dra and BW Dra

Robert H. Hardie *Dyer Observatory, Vanderbilt University, Nashville, Tennessee 37235 USA*

Douglas S. Hall* *Center of Excellence in Information Systems, Tennessee State University, Nashville, Tennessee 37201, USA*

Received 1990 March 9; accepted 1990 May 9

Abstract Differential *B*-band photometry of BV Dra and BW Dra, obtained in 1965, is presented. Times of primary and secondary minima are derived and combined with published times for a period study. Period variations are found in both binaries and magnetic cycles are proposed as an explanation. The cycle length is 19 years in BV Dra and 8 years in BW Dra.

Key words: eclipsing binaries, period variations—magnetic fields, cycles—stars, individual—W UMa binaries

1. Introduction

Shortly after the first author's death on December 19, 1989, a search of his files uncovered some photoelectric photometry which seemed valuable enough to publish. It comprised a complete light curve of both BV Dra and BW Dra, two W UMa-type eclipsing binaries which make up the visual binary ADS 9537AB, with A corresponding to the former and B to the latter. These are the original observations which led to the discovery that the two stars were variable. They were referred to in an abstract by Batten & Hardie (1965), although at that time the two variable star designations had not been assigned.

In the intervening years, this physical pair of(presumably coeval) W UMa binaries has attracted considerable attention and has been the subject of numerous papers. Two recent comprehensive treatments are those of Kaluzny & Rucinski (1986) and Batten & Lu (1986). Although good multi-bandpass light curves of both variables have now been published, and solved with physically realistic models, the Hardie light curves should be useful for times of minimum which extend the $O - C$ curve's baseline in time back towards earlier epochs.

According to Batten, Fletcher & McCarthy (1989) BV Dra has a spectral type of F9V+F8V and varies in V between 7.88 and 8.48 mag, while BW Dra has a spectral type of G3V + G0V and varies in V between 8.61 and 9.80 mag.

* On leave from Dyer Observatory, Vanderbilt University, Nashville, Tennessee.

2. Observations

The individual differential magnitudes have been sent to the I.A.U. Commission 27 Archive of Unpublished Observations of Variable Stars (Breger 1988) where they are available as file no. 159. Each value is a differential magnitude in the sense variable minus 121 Draconis, was corrected for differential atmospheric extinction, and was transformed to *B* of the standard *UBV* photometric system. The 24-inch Seyfert telescope at Dyer Observatory was used with a 1P21 photomultiplier, a DC amplifier, and a strip-chart recorder. A diaphragm 10 arcsec in diameter was used, small enough to handle the small angular separation between BV Dra and BW Dra, which is about 16 arcsec.

The data, 214 for BV Dra and 197 for BW Dra, are plotted as light curves in Fig. 1. Phases have been computed with the ephemerides given by Kaluzny & Rucinski (1986), namely, their Equation (1) for the former and their Equation (2) for the latter.

3. Times of minimum

Times of mid-eclipse were derived from the data using the method of bisected chords. These are presented in Table 1. The two entries marked with a colon are relatively uncertain; for them there was not very good overlap between the rising and falling eclipse branches. It turns out that four were times of primary minimum and seven were times of secondary; primary and secondary eclipses are comparably deep in both systems.

4. The *O – C* curves and improved ephemerides

In addition to the times of minimum presented here for the first time, other, more recent times have been published since Kaluzny and Rucinski prepared their *O – C* curves of BV Dra and BW Dra.

Fig. 2(a) is the *0 — C* curve of BV Dra including the times in Table 1, those used by Kaluzny and Rucinski (1986, Table 1), those of Gorda (1986), those of Dapergolas, Kontizas & Kontizas (1989a), and the time of conjuction of Batten & Lu (1986), which should correspond to a time of mid-eclipse. *O – C* residuals in Fig. 2(a) are computed with respect to the ephemeris

$$JD(\text{hel.})\ \text{pri. min.} = \underset{\pm 4}{2{,}440{,}362.7927} + \underset{\pm 4}{0.35006660}\, n, \qquad (1)$$

which is the result of a linear fit by least squares giving each time equal weight. Both the epoch and the period differ somewhat from the corresponding values of Kaluzny & Rucinski (1986, Equation 1).

Fig. 2(b) is the *O – C* curve of BW Dra including the times in Table 1, those used by Kaluzny & Rucinski (1986, Table 2), those of Gorda (1986), those of Dapergolas, Kontizas & Kontizas (1989b), and the time of conjuction of Batten & Lu (1986). The first three times of Rovithis & Rovithis-Livaniou (1982, Table 1), which Kaluzny & Rucinski (1986) had concluded were systematically in error, were not included. The five new times presented by Rovithis & Rovithis-Livaniou (1987, Table 3) seem to be

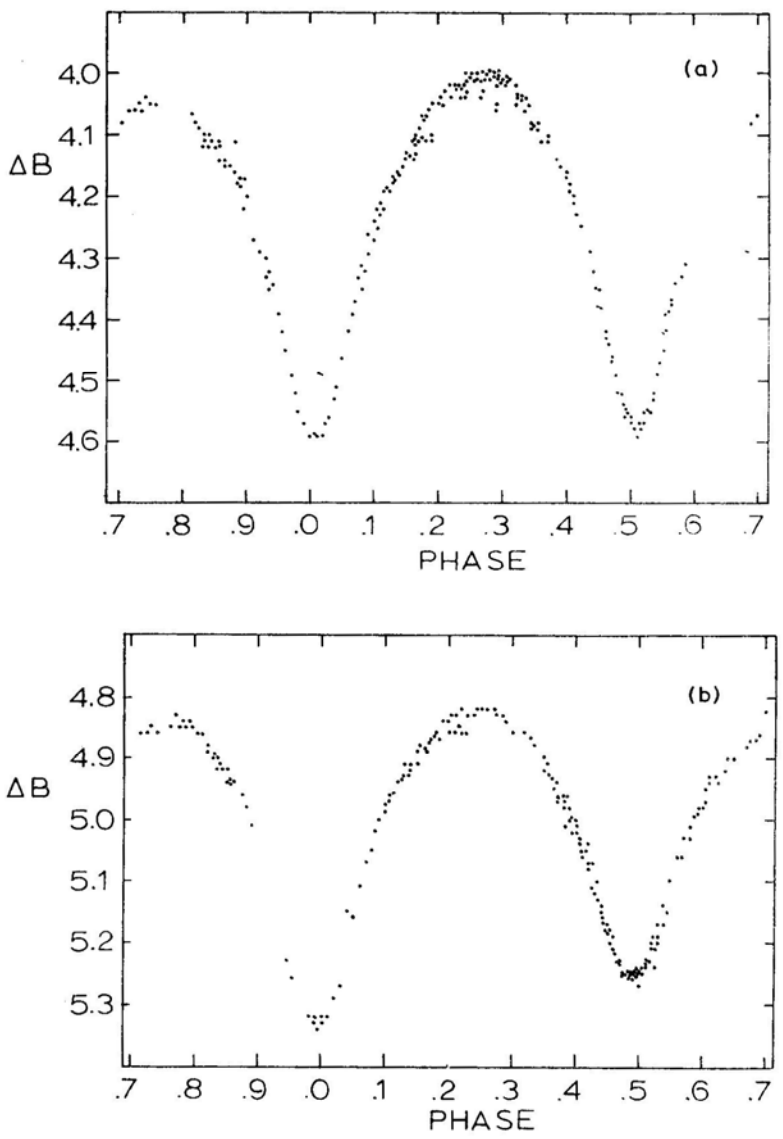

Figure 1. Light curve of (a) BV Dra and (b) BW Dra in 1965. Ordinate is differential *B* magnitude in the sense variable minus comparison. Abscissa is phase computed with the ephemerides in Kaluzny & Rucinski (1986).

affected by perhaps the same systematic error and, for the same reason, were not included. $O - C$ residuals in Fig. 2(b) are computed with respect to the ephemeris

$$JD(\text{hel.})\ \text{pri. min.} = \underset{\pm 3}{2{,}442{,}572.5405} + \underset{\pm 3}{0.29216707}\, n, \tag{2}$$

which is the result of a linear fit by least squares giving each time equal weight. Neither the epoch nor the period differs very much from the corresponding values of Kaluzny & Rucinski (1986, Equation 2).

Table 1. Times of Minimum.

Star	*JD* (hel.) 2438000+	Type
BV Dra	882.8857	sec
	883.7604	pri
	884.8104	pri
	941.6969	sec
BW Dra	881.7370	sec
	882.907:	sec
	883.7825	sec
	886.8523	pri
	888.753:	sec
	939.7343	pri
	941.6328	sec

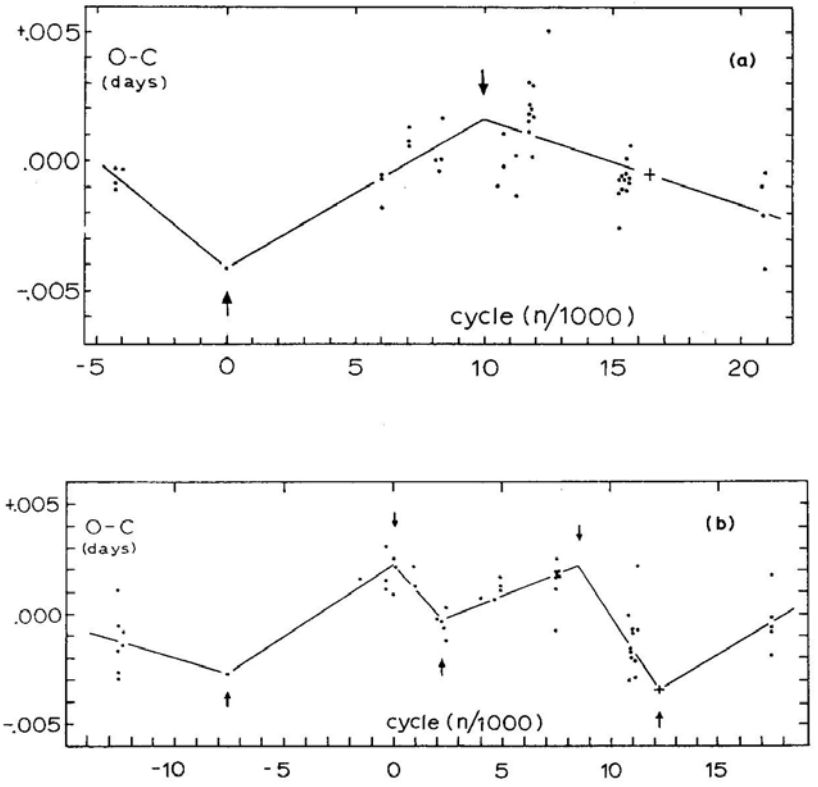

Figure 2. *O – C* curve for (a) BV Dra, with residuals and cycle numbers computed using Equation (1), and (b) BW Dra, with residuals and cycle numbers computed using Equation (2). The filled circles are photoelectrically determined times of primary or secondary minimum and the plus sign is a spectroscopically determined time of conjuction. Note the period increases and decreases marked with arrows, and also given in Table 2.

5. Possible magnetic cycles

The $O - C$ curves for both BV Dra and BW Dra show systematic deviations which are larger than can be reasonably accounted for by uncertainties in the observed times of minimum. That means the orbital period is variable in some way, although Kaluzny and Rucinski did not come to that conclusion, probably because their $O - C$ curves had shorter baselines in time.

The straight-line segments in each *0-C* curve (Figs 2(a) and (b)) are given as approximate representations of the period variation. In both cases the one time of Wood (1971) plays a critical role in the interpretation but the uncertainty of each one is probably quite small, because each represents a mean epoch for a series of observations including several different cycles. Note that the spectroscopically determined times of conjunction are not discordant in either star's $O - C$ diagram. Batten & Lu had estimated an uncertainty of ±0.0007 day in the case of BV Dra and one can presume that it is similar in the case of BW Dra.

In the O — C curves times of both primary and secondary minima are included. Consideration of residuals from'the straight-line fits shows that there is no significant systematic difference between the two. For BV Dra the primary minima were systematically early by only $0^{d}.000\ 1 \pm 0^{d}.0003$ and the secondaries were systematically late by only $0^{d}.0003 + 0^{d}.0003$. For BW Dra primary was late by an insignificant amount ($+ 0^{d}.0001 \pm 0^{d}.0002$) and secondary was on time ($0^{d}.0000 \pm 0^{d}.0002$). The rms deviation of the scatter is $0^{d}.0013$ in Fig. 2(a) and $0^{d}.0011$ in Fig. 2(b) and neither would have been lessened in the last decimal place by shifting times of secondary relative to primary.

In proposing a physical explanation for the observed period changes in these two W UMa binaries, it is not reasonable to consider apsidal motion nor orbital motion around a third body. The former mechanism requires an orbital eccentricity, which does not exist in contact binaries. The second mechanism would, in the case of ADS 9537AB, produce apparent period variations with a cycle approximately 20000 years long (Batten & Lu 1986).

The likelihood of magnetic cycles in late-type stars of various types has been reviewed by Hall (1990). One manifestation of such cycles is a cyclic (but not strictly periodic) variation in the orbital period of a binary. These cyclic variations are observed in several types of (eclipsing) binaries: Algol-type (Hall 1989), RS CVn-type (Hall & Kreiner 1980), and W UMa-type (Kreiner 1977). The physical mechanism for the period changes has been explored by Matese & Whitmire (1983), Applegate & Patterson (1987), Bolton (1989), and Hall (1990).

Both stars in a typical W-type W UMa system are of late spectral type and hence might be expected to have magnetic cycles, which probably would be different from each other. Rucinski (1985) points out, however, that dark spot activity occurs predominantly on the more massive component. This fact, though not necessarily understood theoretically, suggests that other magnetic phenomena (such as the cycles we are suggesting here) are similarly confined to the more massive component.

The time between one period decrease and the next decrease would be one full magnetic cycle. This suggests cycle lengths of about 19 years in BV Dra and 8 years in BW Dra, one longer and the other shorter than the sun's 11-year cycle. Hall (1990) had found similar cycles in 18 other W UMa binaries. The sizes of the period changes, indicated by arrows in Fig. 2, are listed in Table 2.

Table 2. Period Changes.

Star	Epoch	$\Delta P/P$
BV Dra	1969.4	$+4.0\times10^{-6}$
	1978.9	-2.6×10^{-6}
BW Dra	1969.4	$+3.2\times10^{-6}$
	1975.4	-6.0×10^{-6}
	1977.2	$+5.1\times10^{-6}$
	1982.2	-4.6×10^{-6}
	1985.2	$+7.2\times10^{-6}$

Acknowledgements

This work was supported in part by N.A.S.A. research grant N.A.G. 8111. The bibliographical search was aided by the SIMBAD data retrieval system of the Astronomical Data Center in Strasbourg, France.

References

Applegate, J. H., Patterson, J. 1987, *Astrophys. J.,* **322**, L99.
Batten, A. H., Fletcher, J. M., MacCarthy, D. G. 1989, *Publ. Dominion Astrophys. Obs.,* **17**, 76
Batten, A. H., Hardie, R. H. 1965, *Astr. J.,* **70**, 666.
Batten, A, H., Lu, W. 1986, *Publ Astr. Soc. Pacific,* **98**,92.
Bolton, C. T. 1989, in *IAU Coll. 107: Algols,* Kluwer, Dordrecht, 311.
Breger, M. 1988, *Publ. astr. Soc. Pacific,* **100**, 751.
Dapergolas, A., Kontizas, E., Kontizas, M. 1989a, *IBVS* No. 3377.
Dapergolas, A., Kontizas, E., and Kontizas, M. 1989b, *IBVS* No. 3382.
Gorda, S. Yu. 1986, *IBVS* No. 2906.
Hall, D. S. 1989, *IAU Coll.* No. 107, *Algols,* Kluwer, Dordrecht, 287.
Hall, D.S. 1990, in *Active Close Binaries,* Eds C. Ibanoglu & I. Yavuz, Kluwer, Dordrecht, in press.
Hall, D. S., Kreiner, J. M. 1980, *Acta Astr.,* **30**, 387.
Kaluzny, J. and Rucinski, S. M. 1986, *Astr. J.,* **92**,666.
Kreiner, J. M. 1977, *IAU Coll.* No. 42, 373.
Matese, J. J., Whitmire, D. P. 1983, *Astr. Astrophys.,* **117**,L7.
Rovithis, P., Rovithis-Livaniou, H. 1982, *IBVS* No. 2137.
Rovithis, P., Rovithis-Livaniou, H.1987, *Astr. Astrophys. Suppl,* **70**,63.
Rucinski, S. M. 1985, in *Interacting Binaries,* Eds P. P. Eggleton & J. E. Pringle, D. Reidel, Dordrecht, p. 13.
Wood, D. B. 1971, *Bull. Am astr. Soc,* **2**,357.

J. Astrophys. Astr. (1990) **11**, 271–275

New Times of Minimum and a Period Study for GO Cygni

Douglas S. Hall* *Center of Excellence in Information Systems, Tennessee State University, Nashville, Tennessee 37201 USA*

Howard Louth *2199 Hathaway Road, Sedro Woolley, Washington 98284, USA*

Received 1990 March 16; accepted 1990 May 10

Abstract. Times of minimum derived from photometry obtained in 1963, 1967, 1978, and 1979 are presented. With these and previously published times, the period is studied. A constant period increase (quadratic ephemeris) represents most of the times but there was a period decrease in 1934 and possibly in 1984. A 50-year magnetic cycle is discussed.

Key words: eclipsing binaries—magnetic cycles—period variations—times of minimum—stars , individual

1. Introduction

GO Cygni is an eclipsing binary with a spectral type of B9*n* +A0*n*, a β Lyrae-type light curve, and a short $0^{d}.72$ period. There have been numerous studies of its period, several of them indicating that the period is increasing. The two most recent ones (Cester *et al.* 1979 and Sezer, Gülmen & Güdür 1985) contain references to the earlier studies.

In this paper we present times of minima obtained in 1963,1967,1978, and 1979 and not published before now. These are useful in filling gaps in the $O - C$ curve.

We also take this opportunity to study the period of GO Cygni using all available times of minima, including new ones of Rovithis-Livaniou and Rovithis (1985), which appeared subsequent to the papers mentioned above, as well as our own.

2. Times of minimum

Differential *UBV* photometry was obtained during the summer of 1963 at the Agassiz Station of the Harvard College Observatory with the 24-inch telescope described by Hall (1986). The comparison star was HD 196490=BD + 35°4188. Analysis yielded the first three times of primary minimum listed in Table 1. The uncertainty of each is estimated to be about $\pm 0^{d}.002$.

Differential photometry in the *U* band on the night of September 23-24, 1967 yielded the one time of secondary minimum given in Table 1. The 24-inch Seyfert telescope at Dyer Observatory was used and the comparison star was HD 196589 = BD+36°4150.

*On leave from Dyer Observatory, Vanderbilt University, Nashville, Tennessee.

Table 1. Times of minimum.

JD (hel.)	Type	Observatory
2438242.7313	pri.	Agassiz
2438260.6772	pri.	Agassiz
2438268.5673	pri.	Agassiz
2439757.5743	sec.	Dyer
2443677.6492:	pri.	Louth
2443702.7706:	pri.	Louth
2443785.6794:	sec.	Louth
2443790.6938:	sec.	Louth
2443795.7225	sec.	Louth
2443807.5702:	pri.	Louth
2443822.6396	pri.	Louth
2443833.7577:	sec.	Louth
2444075.2925:	pri.	Louth

Differential photometry in the *V* band was obtained during 1978 and 1979 with the 10- inch telescope which has been described by Hall & Genet (1988). The comparison star was HR 7807= HD 194335. These data have been sent to the I.A.U. Commission 27 Archive for Unpublished Observations of Variable Stars(Breger 1988), where they are available as file no. 158. The light curve is shown in Fig. 1, where phases have been computed with the ephemeris in Equation (1). The 9 times of minimum derived from these data are given in Table 1. Only two are considered relatively good. The others, marked with a colon, were based on measurements which were relatively few in number and/or did not give good overlap between the falling and rising eclipse branches.

3. The *O* –*C* curve

Fig. 2 is the *O* – *C* curve showing times of minimum from Cester *et al.* (1979, Table 1), Sezer, Gülmen & Güdür (Table 1), Rovithis-Livaniou & Rovithis (1985, Table 1), and our Table 1. In cases where the same eclipse was observed in more than one bandpass, we have plotted the mean. The four times given by Pohl *et al.* (1985) appear to be identical to times given by Sezer, Gülmen & Güdür (1985) and are not repeated. The two times of secondary minimum from Rovithis-Livaniou & Rovithis (1985) appeared discordant and are not plotted. We located a few photographic and visual timings in the iterate but these were not used. And the times marked with a colon in our Table 1 are not plotted. In this figure the *O* –C residuals are computed with the linear ephemeris

$$JD(\text{hel.}) = 2433930.40561 + 0^{d}.71776382\, n \qquad (1)$$

of Sezer, Gülmen & Güdür (1985, Equation 2).

4. Fitting the *O* – *C* curve

For most of the time since its discovery in 1928, GO Cygni seems to have been increasing its period. The quadratic fit of Sezer Gülmen & Güdür (1985, Equation 4) is

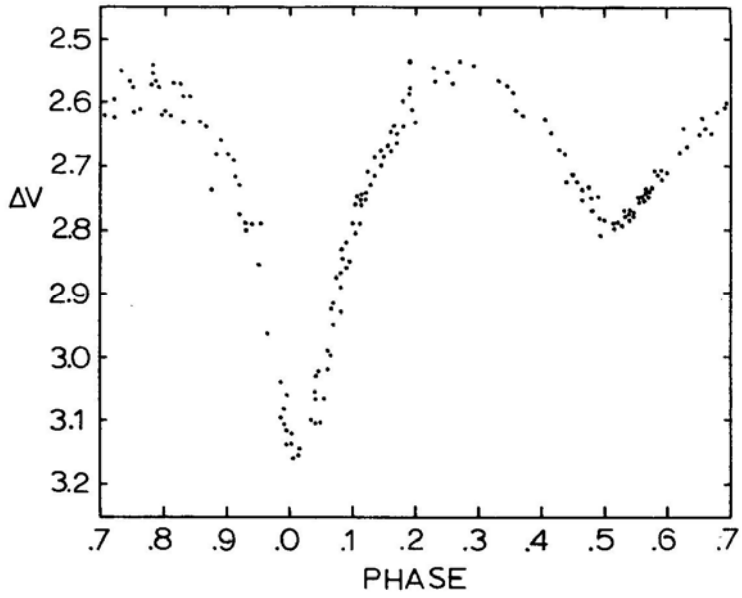

Figure 1. Light curve of GO Cygni based on 1978 and 1979 *V* band photometry. This yields the last 9 times of minimum given in Table 1. Phases are computed with the ephemeris in Equation (1).

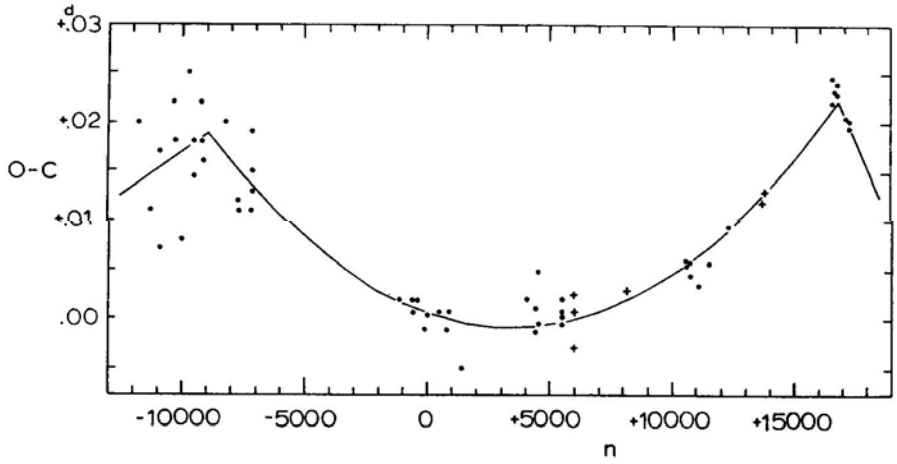

Figure 2. *O* – *C* curve for GO Cygni. The times before $n = -4000$ are either photographic or visual; all others are photoelectric. Times marked with a + are the new ones, from Table 1. The parabola represents the quadratic fit to all times in the range $-8500 < n < 17000$ and is the ephemeris in Equation (2). The two period decreases are discussed in the text.

quite convincing. We notice, however, that the more recent photoelectric times of Rovithis-Livaniou & Rovithis (1985) fall earlier than the prediction of that quadratic ephemeris, by about $0^d.005$. This indicates a possible decrease in period occurred recently. We also notice that the overall fit of the *O* – *C* curve would be improved if

another period decrease occurred around 1934, in the midst of the timings determined visually and photographically.

The solid curve in Fig. 2 represents fits, by least squares, based on the assumption that those two period decreases occurred. All of the times plotted in Fig. 2 have been included, with equal weight. The first portion is a linear fit of all times before $n = -8500$ and corresponds to a period of $0^d.7177655$: The second is a quadratic fit over the range $-8500 < n < +17000$. It corresponds to the ephemeris

$$JD(\text{hel.}) = 2433930.4064 + 0^d.71776294\, n + 1^d.28 \times 10^{-10}\, n^2 \qquad (2)$$
$$\pm.0005 \quad \pm.00000008 \quad \pm.07$$

and compares favourably with the quadratic fit of Sezer *et al.* (1985, Equation 4). The third portion is a linear fit of all times after $n = +16000$ and corresponds to a period of $0^d.7177576$. Allowing for the first period decrease has the effect of decreasing the sum of the squares of the residuals for the early visual and photographic times by almost a factor two, compared to the quadratic fit of Sezer, Gülmen & Güdür (1985, Equation 4), which had included all of them.

The magnitudes of the two period decreases are $\Delta P/P = -0.7 \times 10^{-5}$ and $\Delta P/P = -1.4 \times 10^{-5}$, respectively. The magnitude of the net period increase, which occurs during the parabolic portion, is $\Delta P/P = +0.9 \times 10^{-5}$.

5. Discussion

If a binary exhibits period changes in both directions, *i.e.*, both decreases and increases, and if neither apsidal motion nor Keplerian motion around a third star is reasonable, then the most promising physical explanation is that one of the two stars has a magnetic cycle (Hall 1990). Such a cycle would cause its radius to increase and decrease on a time scale of decades, modulate the quadrapole term of the gravitational potential, and alter the orbital period (Matese & Whitmire 1983). Alternating period changes of this sort are found in many types of binaries containing at least one convective star (Hall 1990) but not in binaries with both stars radiative (Hall 1989). Thus the B9*n*+A0*n* spectral type of GO Cygni would seem to argue against a magnetic cycle. On this point we can remark that the spectral type assigned to the secondary star by Pearce (1933) might be seriously affected by the strong reflection effect (Ovenden 1954) and the secondary's spectrum actually might not be visible at all (Popper 1957). Since there is no modern light curve solution of this complicated eclipsing binary, it may be possible that the secondary is small enough in mass and low enough in surface brightness to be convective after all.

Alternating period changes in principle can be produced by other physical mechanisms. (1) Apsidal motion is not likely in this case because binaries of very short period have circular orbits and, moreover, the shape of the observed $O - C$ curve is not sinusoidal as required by apsidal motion. (2)A starspot wave can distort the light curve and produce spurious shifts in the $O - C$ curve which might mimic a real period change. If this were happening in GO Cygni, the maximum proceeding primary eclipse must have been consistently brighter during the early and late epochs (when the $O - C$ was large) and consistently fainter during the intermediate epochs (when the $O - C$ was small). This was not observed. Moreover, the B9 component, which contributes virtually all of the system's light, is too early to have starspots. (3) Mass transfer or

mass loss can produce a period increase or a period decrease, depending on the source and nature of the mass flow, but all reasonable mechanisms produce a monotonic increase *or* a monotonic decrease, *not both* in the same binary system. (4) If GO Cygni is revolving around a third star with a period of 50 years and a highly eccentric orbit, the light travel time effect could account for the observed O — C curve. Although there is no evidence yet (visual, astrometric, photometric, or spectroscopic) for the existence of a third body, this interpretation cannot be excluded.

The length of the magnetic cycle in GO Cygni would be the time between one period decrease and the next, which is very nearly 50 years. This is quite typical of magnetic cycle lengths found in other types of stars (Hall 1990). The magnitude of the decreases and increases in $\Delta P/P$, which have an average of 1.0×10^{-5}, also compare favourably.

We caution that our interpretation of the second period decrease depends critically on two groups of eclipse timings, those of Sezer *et al.* and those of Rovithis-Livaniou and Rovithis. We stress, however, that it will be very easy to test whether or not that period decrease has occurred. A linear ephemeris based on our $0^d.7177576$ period predicts $O - C$ residuals *decreasing* rapidly with time, whereas a continuation of our quadratic ephemeris in Equation (2) predicts $O - C$ residuals *increasing* rapidly with time. By 1990.5 the difference between the two predictions will amount to $0^d.030$, which is the entire vertical range of the $O - C$ diagram in Fig. 2. Therefore, needless to say, we urge photometrists to obtain more times of minimum of this interesting eclipsing binary.

Acknowledgements

This work was supported in part by N.A.S.A. research grant N.A.G. 8111.

References

Breger, M. 1988, *Publ. astr. Soc. Pacific,* **100**, 751.
Cester, B., Giuricin, G., Mardirossian, F., Mezzetti, M. 1979, *Acta Astr.,* **29**, 433.
Hall, D. S. 1986, in *The Study of Variable Stars Using Small Telescopes,* Ed. J. R. Percy, Cambridge University, Cambridge, p. 63.
Hall, D. S. 1989, in *IAU coll. 107: Algols,* Kluwer, Dordrecht, 219.
Hall, D. S. 1990, in *Active Close Binaries,* Eds C. Ibanoglu & I. Yavuz, Kluwer, Dordrecht, in press.
Hall, D. S., Genet, R. M. 1988, *Photoelectric Photometry of Variable Stars,* Willmann-Bell, Richmond, p. 146.
Matese, J. J., Whitmire, D. P. 1983, *Astr. Astrophys.,* **117,** L7.
Ovenden, M. W. 1954, *Mon. Not. R. astr. Soc,* **114**, 569.
Pearce, J. A. 1933, *J. R. astr. Soc. Canada,* **27**,62.
Pohl, E., Tunca, Z., Gülmen, Ö., Evren, S. 1985, *IBVS* No. 2793.
Popper, D. M. 1957, *Astrophys. J. Suppl.,* **3**, 107.
Rovithis-Livaniou, H., Rovithis, P. 1985, *IBVS* No. 2842.
Sezer, C, Gülmen, Ö., Güdür, N. 1985, *IBVS* No. 2743.

J. Astrophys. Astr.(1990) **11**, 277–280

UBV Photometry of the Ap Variable UZ Psc = HD 10783

Robert H, Hardie & Edwin J. Reichmann[a] *Dyer observatory, Vanderbilt University, Nashville, Tennessee 37235 USA*

Edward W. Burke, Jr.[b] *Department of Physics, King College, Bristol, Tennessee 37620 USA*

Douglas S. Hall[c] *Center of Excellence in Information Systems, Tennessee State University, Nashville, Tennessee 37201 USA*

Received 1990 March 16; accepted 1990 May 10

Abstract. New *UBV* photometry, obtained between late 1965 and early 1969, is presented and combined with existing published photometry to derive an improved ephemeris for times of maximum brightness: $2439758.00+4^{d}.1328\ n$.

Key words: photometry stars—individual stars—peculiar A

1. Introduction

According to the Second Supplement to the Second Edition of the General Catalogue of Variable Stars (GCVS) the photometric variability of the Ap star HD 10783 = UZ Psc was discovered by Abt & Golson (1962). Their *V* magnitudes determined on six nights show a full range of 0.22 mag, however, far more than the 0.02 range indicated by subsequent differential photometry.

The variability was actually established by 1964 differential photometry presented graphically by Van Genderen (1964) and in tabular form by Van Genderen (1965). He preferred a photometric period of $4^{d}.1565$ over the $4^{d}.134$ period derived by Steinitz (1964) from magnetic measures of Babcock (1957).

In the most complete discussion of HD 10783 to date, Preston & Stepien (1968) presented *UBV* photometry and measurements of the magnetic field, both obtained in 1967. Analysis of these data along with estimated times of magnetic maximum in 1950, 1954, and 1964 and the 1964 photometry of Van Genderen (1965) showed that the magnetic field and the brightness in *U*, *B,* and *V* vary in phase. Their revised ephemeris was

$$JD(\max) = 2439757.91 + 4^{d}.1327\ n, \tag{1}$$

for times of magnetic maxima.

---

[a]Present address: Space Sciences Laboratory, Marshall Space Flight Center, Huntsville, Alabama, U.S.A.
[b]Guest Observer at Kitt Peak National Observatory, which is operated by the Association of Universities for Research in Astronomy, under contract with the National Science Foundation.
[c]On leave from Dyer Observatory, Vanderbilt University, Nashville, Tennessee, U.S.A.

A little later Van Genderen (1967,1971) presented additional photometry, obtained in 1965 and 1966. In the first of these papers he suggested a period of $4^d.1334$ but in the second he found both his 1965 and 1966 photometry consistent with the $4^d.1327$ period of Preston and Stepien.

The Third Edition of the GCVS gave a period of $4^d.1683$, which does not appear in any of the references cited in that catalogue but was mentioned by Renson (1965)+. An earlier version (Second Supplement to the Second Edition) had given the $4^d.1565$ value of Van Genderen and a later version (First Supplement to the Third Edition) gave the $4^d.1327$ value of Preston and Stepien.

In this paper we present *UBV* photometry obtained at two observatories between late 1965 and early 1969, never before published. It is combined with existing published photometry to improve the photometric period and the time of maximum brightness.

To our knowledge, there is no published photometry in the literature more recent than that of Preston & Stepien (1968) in 1967.

2. New photometry

UZ Psc was observed photometrically on 31 nights between August 1965 and January 1969 with the 24-inch Seyfert telescope at Dyer Observatory and on 11 nights in December 1968 and January 1969 with one of the 16-inch telescopes at Kitt Peak National Observatory. In both cases the measurements were made differentially with respect to HD 10262, the same comparison star used by Preston and Stepien and by Van Genderen. Our differential magnitudes were corrected for differential atmospheric extinction and transformed differentially to the *UBV* system.

These new data have been sent to the I.A.U. Commission 27 Archive of Unpublished Observations of Variable Stars (Breger 1988), where they are available as file no. 155. Each value is a nightly mean of 3 to 15 individual intercomparisons. The standard error, based on the rms deviation from each mean, is included.

3. Ephemeris for maximum brightness

We combined all available photometry in order to derive the best photometric period and time of maximum brightness. We did this using the B bandpass only. Of the three bandpasses, the amplitude is smallest in *V* and the scatter is largest in *U*. As mentioned above, we had 31 nightly means from Dyer and 11 from Kitt Peak. The photometry of Preston and Stepien (Table 1) consisted of 22 nightly means. To get ΔB values from Van Genderen (1971, Table 2) we subtracted his Δ (V-B) from his ΔV and multiplied by –2.5, to convert his log intensity values into magnitudes. The 1964 and 1965 photometry of Van Genderen (1965, 1967) was potentially valuable for a period determination because it was the earliest and thus extended the baseline in time. The effective wavelength of its bandpass was 5960 Å, however, not that of the B bandpass; consequently its amplitude was smaller. To account for this we "stretched" these magnitudes and readjusted the zero point, thereby transforming them into *defacto* ΔB magnitudes. We omitted his first value, which had an especially large internal error and had not been measured by Van Genderen himself. Ironically, the time of that one

measurement had been chosen as the initial epoch for the puzzling ephemeris given in the Third Edition of the GCVS, which we discussed above.

Each of the data groups described above showed small systematic differences in brightness with respect to each other in the composite light curve, constructed provisionally using the ephemeris in Equation (1). We therefore added the following corrections: +0.001 mag to Dyer, 0.012 mag to Kitt Peak, 0.008 mag to Preston & Stepien, and +0.022 mag to Van Genderen (1971). Such shifts probably are the result of transformation errors and/or errors in the k_B'' extinction term. Because the variable and the comparison differ in colour by $\Delta(B-V) = 0.40$, an error of ± 0.01 in ε_B and ±0.01 in k_B'' each would produce a shift of about 0.005 mag. The shift for Van Genderen (1971) is relatively large probably because his blue bandpass was on the Walraven photometric system and was never transformed to *B* of the standard *UBV* photometric system at all.

To determine the best period and time of maximum brightness we used least squares to fit the corrected ΔB magnitudes to the equation

$$\Delta B = A + A_1 \cos\theta + A_2 \cos 2\theta, \tag{2}$$

where θ is phase. The best fit was obtained with the ephemeris

$$JD\ (\max) = \underset{\pm 23}{2439758.002} + \underset{\pm 14}{4^{d}13281}\ n, \tag{3}$$

where the uncertainties come from chi-squared analysis of the variance. These results are not very sensitive to the small shifts applied to the blue photometry. When the analysis was repeated with these shifts not applied, the corresponding elements were *JD* 2439757.995 and $4^{d}.13283$, with uncertainties approximately twice as large as before.

The resulting light curve, based on phases computed with Equation (3), is shown in Fig. 1. Different symbols indicate photometry from the different groups. The solid curve is the best fit by least squares. Although the light curve of an Ap variable does not necessarily obey the shape implied by our Equation (2), the representation is actually quite faithful. In this representation the principal maximum is 0.030 mag above the minimum and the secondary maximum is 0.005 mag above. The rms deviation of all the nightly means from this fit is ± 0.005 mag.

4. Discussion

It should be stressed that the period we have found in Equation (3) is a photometric period, derived entirely from analysis of the light curve. It should be the best one available, because earlier determinations were based on fewer data and a shorter baseline in time.

It is of interest to compare our ephemeris for times of maximum brightness with the ephemeris for times of magnetic maxima. Steinitz (1964) had found $4^{d}.134$ for the magnetic period; Preston & Stepien (1968) found $4^{d}.1327$ using more magnetic data with a longer baseline in time. Though Preston and Stepien did not provide uncertainties for the elements in their ephemeris, it is useful nevertheless to compare ours in Equation (3) with theirs in Equation (1). Our photometric period is consistent with their magnetic period within our uncertainty. Our time of maximum brightness

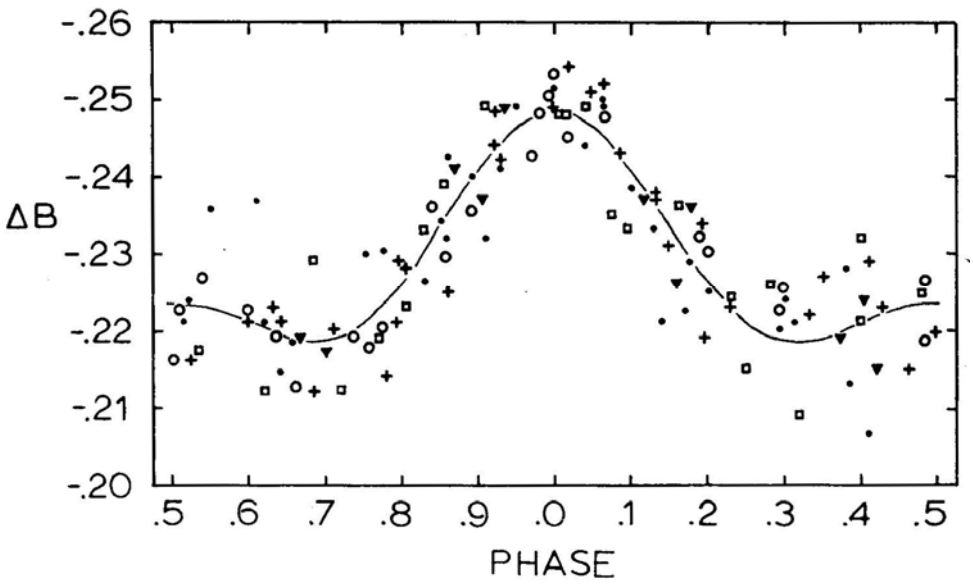

Figure 1. Light curve of the Ap variable UZ Psc =HD 10783 in *B*. Phases are from Equation (3). Plusses are Dyer. Triangles are Kitt Peak. Squares are Preston and Stepien. Open circles are Van Genderen (1971). Small filled circles are Van Genderen (1965,1967). The solid curve is the best fit with Equation (2). The rms deviation from the curve is ±0.005 mag.

differs from their time of magnetic maximum by 4 of our standard deviations, but the difference corresponds to only 0.02 phase.

Because more than two decades have passed since a light curve of UZ Psc has been determined, it would be relatively easy to increase the numerical precision of the photometric period by one more significant digit.

Acknowledgements

This work was supported in part by N.A.S.A. research grant N.A.G. 8111. The bibliographical search was aided by the SIMBAD data retrieval system of the Astronomical Data Center in Strasbourg, France.

References

Abt, H. A., Golson, J. C.1962, *Astrophys. J.,* **136**, 35.
Babcock, H. W. 1957, *Astrophys. J. Suppl.* ,**3**,141.
Breger, M. 1988, *Publ. astr. Soc. Pacific,***100**,751.
Preston, G. W., Stepien, K. 1968, *Astrophys. J.,* **154**, 971.
Renson, P.1965, *Bull Soc. R. Sci. Liege,* **34**, 118.
Steinitz, R. 1964, *Bull. astr. Inst. Netherlands,***17**, 504.
Van Genderen, A. M. 1964, *Inf. Bull. Var. Stars, No.* 76.
Van Genderen, A. M.1965, *Bull. astr. Inst. Netherlands,* **18**,67.
Van Genderen, A. M. 1967, *Bull astr. Inst. Netherlands,* **19**, 80.
Van Genderen, A. M. 1971, *Astr. Astrophys.,* **14**,48.

J. Astrophys. Astr. (1990) **11**, 281–290

Composite Spectra

Paper 4: HD 201270/1

R. & R. Griffin *The Observatories, Madingley Road, Cambridge, England CB3 OHA*

Received 1990 March 21; accepted 1990 May 17

Abstract. HD 201270/1 is a composite-spectrum binary whose components have spectral types close to G8 III and A2 V. They are in a circular orbit with a period of only 40 days. Photometric variability of RS CVn character is therefore not unlikely.

Key words: composite spectra—spectroscopic binaries—orbits—stars, individual—HD 201270/1

1. Introduction: existing knowledge concerning HD 201270/1

HD 201270/1 is a binary star in the constellation Cygnus, about 4° following Deneb. Its composite-spectrum nature was discovered by Miss Cannon in the course of her compilation of the *Henry Draper Catalogue* (Cannon & Pickering 1924), in which she gave the system the two numbers 201270 (type GO) and 201271 (type A0). In a remark in the back of the volume, she noted, "The spectrum is composite. The visual magnitudes may be nearly equal. In the photographic spectrum the lines of the component of class G are seen from Hβ to about 4250. The region of shorter wavelength is of class A." As a result of that entry in the *HD Catalogue* the system was listed in Hynek's (1938) catalogue of composite spectra, in which it is no. 526.

It is only quite recently that photoelectric photometry of the system has been undertaken: Oja (1986, who identified it by its alias BD + 45°3410) has given the magnitudes $V=7^{m}.25$, $(B-V)=0^{m}.56$, $(U-B)=0^{m}.34$. Two MK classifications of the system have been made. Fehrenbach & Rebeirot (1962) took five objective-prism spectrograms for radial-velocity purposes. Although their dispersion was much the same as that of the spectrograms from which Miss Cannon discovered the composite nature of the spectrum, the classification made from them was F4 V. Kuhi (1963) took spectrograms in red light in an effort to classify the late-type components in composite-spectrum binaries in a region where there is little interference by the hot components, and concluded that HD 201270 is of type G5 III.

The only radial velocities hitherto published are those of Fehrenbach & Rebeirot (1962), who gave a mean value of – 30 km s^{-1} , with quality C. Such a quality corresponds to an "écart probable" of 5–10 km s^{-1} , implying that the standard deviation of the five individual measurements was in the range 15–30 km s^{-1} . Thus those velocities would not be of much assistance in determining the orbit, even if they had been published individually, and will not be referred to again.

2. Radial velocities

HD 201270 was noticed as a potential spectroscopic binary from the work of Kuhi (1963), and in 1978 (before we undertook a systematic investigation of composite spectra) was placed on the Cambridge radial-velocity observing programme. In 1979 it was discovered to be a rapid binary, and in 1980 an intensive observing campaign

Table 1. Photoelectric radial-velocity measurements of HD 201270.

Date			MJD	Velocity km s^{-1}	Phase	$(O-C)$ km s^{-1}
1978	Oct	6.91	43787.91	+1.5	0.113	−2.0
1979	Aug	28.95	44113.95	−12.7	8.245	+1.1
	Sept	28.89	144.89	+9.3	9.016	+0.1
1980	May	10.08	44369.08	−33.2	14.608	0.0
		15.12	374.12	−16.5	.733	+0.6
		30.08	389.08	+5.1	15.106	+0.9
	June	27.49*	417.49	−5.8	.815	−0.7
	July	21.09	441.09	−35.2	16.403	−1.0
		22.05	442.05	−36.7	.427	−0.7
		23.05	443.05	−37.1	.452	+0.3
		24.09	444.09	−38.4	.478	−0.2
		24.94	444.94	−38.6	.499	−0.1
		25.93	445.93	−37.8	.524	+0.4
		27.11	447.11	−36.9	.554	+0.2
	Aug	16.96	467.96	+7.0	17.074	+0.2
		26.93	477.93	−25.0	.322	0.0
		31.98	482.98	−38.3	.448	−1.1
	Sept	3.04	485.04	−39.1	.500	−0.6
		5.96	487.96	−36.7	.572	−0.7
		7.95	489.95	−32.4	.622	−0.6
		21.90	503.90	+9.4	.970	+0.5
		24.90	506.90	+8.8	18.045	+0.4
	Oct	2.86	514.86	−13.9	.243	−0.3
		3.95	515.95	−18.0	.270	−0.4
		4.84	516.84	−21.2	.293	−0.3
		9.85	521.85	−35.8	.418	−0.5
		12.96	524.96	−38.0	.495	+0.4
		14.84	526.84	−38.7	.542	−1.1
	Nov	2.78	545.78	+7.7	19.014	−1.5
		12.77	555.77	−15.7	.264	+0.9
		18.77	561.77	−33.5	.413	+1.5
	Dec	15.70	588.70	+6.2	20.085	+0.2
		16.73	589.73	+2.9	.111	−0.9
1981	May	3.09	44727.09	−36.7	23.536	+1.1
	July	27.01	812.01	−27.3	25.654	+0.8
	Aug	26.93	842.93	−35.2	26.425	+0.7
	Sept	27.94	874.94	−8.8	27.224	+1.8
1982	July	20.06	45170.06	−34.7	34.584	+0.5

Table 1. Continued.

Date			MJD	Velocity km s^{-1}	Phase	$(O-C)$ km s^{-1}
1983	July	5.06	45520.06	−25.2	43.313	−1.4
		30.02	545.02	+5.8	.936	−1.6
	Aug	3.01	549.01	+8.9	44.035	+0.2
		4.01	550.01	+8.6	.060	+1.0
		7.01	553.01	+1.6	.135	+0.3
	Oct	16.14*	623.14	+3.5	45.884	+0.3
1984	Sept	4.96	45947.96	+9.4	53.985	+0.2
1985	Oct	5.87	46343.87	+0.2	63.859	−0.3
		29.79	367.79	−39.4	64.455	−1.9
1986	Aug	25.06†	46667.06	+7.8	71.919	+1.5
	Sept	18.95	691.95	−37.3	72.540	+0.4
		28.89	701.89	−7.6	.788	+1.3
1987	Oct	6.89	47074.89	+5.5	82.091	−0.1
		12.94†	080.94	−12.7	.242	+0.6
		18.88†	086.88	−32.9	.390	0.0
		21.80	089.80	−37.7	.462	+0.1
1988	June	22.98	47334.98	−34.3	88.577	+1.4
	July	19.03	361.03	−11.0	89.227	+0.1
		27.04	369.04	−35.3	.427	+0.7
	Sept	11.98	415.98	−34.5	90.597	−0.4
	Nov	2.86†	467.86	+2.2	91.891	−1.8
1989	Mar	29.20†	47614.20	−37.7	95.541	0.0
	May	3.12†	649.12	−35.2	96.412	−0.3

*Observed, in collaboration with Dr J. E. Gunn, with the 200 inch telescope (Griffin & Gunn 1974).
†Observed with 'Coravel' at Haute Provence (Baranne *et al.* 1979).

established its orbit. It has since been kept under occasional observation, and there are now 61 observations altogether. They are set out in Table 1 and lead to the orbit shown in Fig. 1 and having the following elements:

$P = 40.0961 \pm 0.0018$ days
$\gamma = -14.56 \pm 0.12$ km s^{-1}
$K = 23.89 \pm 0.15$ km s^{-1}
$e \equiv 0$
ω is undefined

$(T_0)_{38} =$ MJD 45307.03 ± 0.05
$a_1 \sin i = 13.17 \pm 0.08$ Gm
$f(m) = 0.0567 \pm 0.0011\ M_\odot$

R.m.s. residual $= 0.9$ km s^{-1}

In accordance with our usual practice, the subscript outside the brackets enclosing the epoch T_0 represents the cycle number of the epoch given there, corresponding to the cycle numbers given in Table 1 before the decimal point in the 'phase' column. That particular epoch is selected because it is the one nearest to the mean time of the whole ensemble of observations, and for that reason its standard deviation is smaller than that of any other choice of T_0.

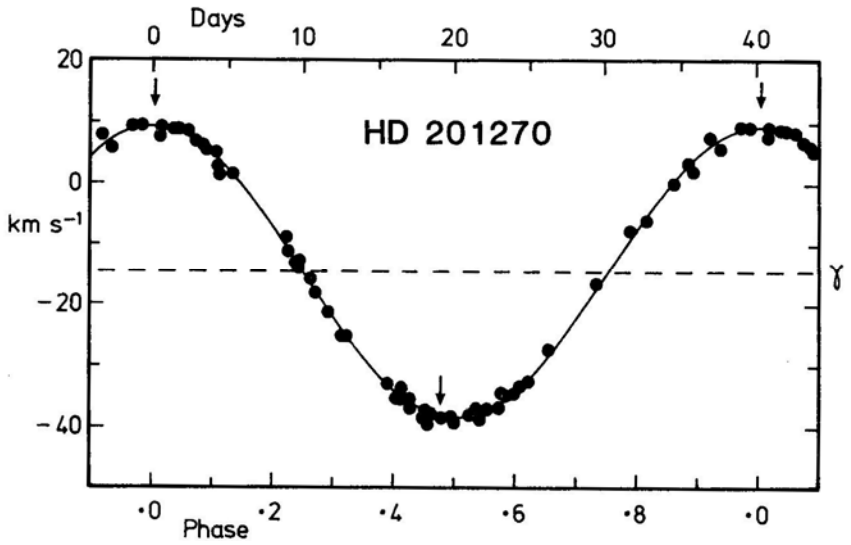

Figure 1. Radial-velocity orbit for HD 201270/1. The orbit is based on 61 photoelectric measurements of the radial velocity of the primary. Two measurements of the secondary, at the phases indicated by the arrows, were obtained differentially by analysis of Mount Wilson spectrograms to determine in the amplitude of the secondary's velocity curve.

3. Spectroscopy

3.1 *Spectral Types of the Components*

Two spectrograms were taken of HD 201270/1, one near each node of the orbit (1981 November 17 and 1985 April 13), with the 32-inch camera and coudé spectrograph of the Mount Wilson 100-inch telescope. Direct-intensity tracings were prepared from the plates in the manner described in Paper 1 (Griffin 1986). We endeavoured to unravel the composite spectrum by subtracting from it a surrogate primary spectrum. The most similar surrogates for HD 201270 among our library of standards were ε Vir and 15 Cyg, whose spectral types are given in the most recent Perkins catalogue (Keenan & McNeil 1989) as G8 IIIab and G8 III respectively. Those two standards have almost identical values of (B— V), namely 0.94 and 0.95 respectively (Hoffleit 1982). Subtraction of suitable (wavelength-dependent) fractions of one of the standard spectra revealed the spectrum of HD 201271, which was found to bear a striking resemblance to that of θ Leo (A2 V) in terms of line strength though not of line width, θ Leo having a notably low rotational velocity. Details of the technique are discussed in Paper 1. Fig. 2 contains reproductions of original spectrograms of HD 201270/1, ε Vir and 3 Crv. 3 Crv was substituted for *0* Leo in the figure because its spectrum *looks* more nearly like that of HD 201271: its rotational velocity is more comparable with that of the star involved in the binary system, even though the quantitative match of the absorption-line equivalent widths (which are of course unaffected by rotation) is not so good. Fig. 3 demonstrates the effectiveness of the subtraction technique in isolating the secondary spectrum of a composite system. In actual fact we subtracted the spectrum of ε Vir from one of the spectra of HD 201270/1 and that of 15 Cyg from

the other, in order to derive two totally independent versions of the spectrum of HD 201271. They have been averaged in Fig. 4, in which the spectrum of HD 201271 is compared with that of θ Leo throughout the whole region that we have investigated. The spectrum shown as that of θ Leo in Figs 3 and 4 is not the directly observed spectrum: we have blurred it digitally to mimic the spectrum that we would expect to observe if θ Leo had a projected rotational velocity of 65 km s^{-1}.

3.2 *Radial Velocities and Mass Ratio*

As explained in Paper 1, the secondary spectrum as uncovered by the subtraction technique has a wavelength scale that is in the rest frame of the primary star. The radial velocities of the primary on the dates of the two observations are known from the orbit, so measurement of the displacement of the secondary spectrum from the rest frame of the primary yields the radial velocity of the secondary and thereby also the mass ratio of the two components. However, since the two spectra of HD 201271 correspond nearly to times of maximum velocity separation in opposite senses, cross–correlating them with one another improves the accuracy of the result, partly because the two spectra necessarily match well and partly because the size of the quantity being measured is doubled (the orbit being circular). The value of that radial–velocity difference was found to be 107.7 km s^{-1}; the principal lines contributing to the determination were the Balmer lines, K line and Mg II λ4481 Å. Because the various lines were treated independently and their results subjectively weighted according to the symmetry or otherwise of the cross-correlation function, it is not possible to quote a meaningful standard deviation; however, we think that the value of 107.7 km s^{-1} found for the change in relative radial velocity of the secondary should be accurate within 5 km s^{-1}. We know from the orbit that the primary star contributed 47.5 km s^{-1} of that change, with negligible uncertainty, so the secondary must have contributed 60.2 ± 5 km s^{-1}. Those figures lead to a mass ratio of 1.27± 0.11, the G star being the more massive. From Popper (1980) we deduce that an A2 V star is expected to have a mass of about 2.0 $M_{\odot}$, in which case that of HD 201270 is about 2.5 $M_{\odot}$.

3.3 *Luminosity Ratio*

Our technique of spectral subtraction automatically apportions the flux in the composite spectrum between the two component spectra. The flux ratios (determined in 50-Å bands) may be compared directly with the normalized fluxes from suitable standard stars selected from the list of measurements by Willstrop (1965). In order to bring them into line with the observed flux ratios, the ratios derived from Willstrop's photometry have to be multiplied by a constant, which represents the difference in luminosity between HD 201270 and HD 201271 at λ5500 Å(the wavelength at which Willstrop's measurements are normalized). The observed flux ratios follow extremely faithfully those formed from Willstrop's photometry of ε Phe and ζ Aql and are given in Table 2; the derived magnitude difference in the V band is $0^{m}.56$, the G giant (HD 201270) being the brighter component at that wavelength.

Table 2. Relative fluxes of ε Phe (KO III) and ζ Aql (A0 V) in 50-Å bands, compared with the ratios between HD 201270 and HD 201271. The ε Phe/ζ Aql ratios have all been multiplied by the empirical factor 1.68, which represents the relative visual luminosity of HD 201270 in comparison with HD 201271

λ(Å)	From Willstrop (1965) ε Phe	ζ Aql	Ratio	HD 201270/1 (observed)
3650				.57
3700				.42
3750				.32
3800				.19
3850				.18
3900				.18
3950				.33
4000	196	850	.39	.39
4050	193	692	.47	.46
4100	193	661	.49	.50
4150	183	767	.40	.40
4200	205	736	.47	.47
4250	207	717	.49	.49
4300	226	526	.72	.74
4350	252	637	.67	.67
4400	271	667	.68	.68
4450	298	647	.77	.78
4500	317	626	.85	.85
4550	325	610	.90	.90
4600	340	595	.96	.95
4650				

The stars chosen from Willstrop's (1965) list as giving a run of flux ratios most closely mimicking those found for HD 201270/1 are both slightly cooler, according to their measured (*B*— *V*) colour indices, than the analogues selected by direct classification of the spectra. The difference in (*B*–*V*) of about $0^m.1$ between the best–matching Standard giant selected spectroscopically (ε Vir, (*B*–*V*)=0.94) and photometrically (ε Phe, (*B*–*V*)=1.03) is supported by the classification of ε Phe as K0 III, slightly later in type than ε Vir. The source of the slight disagreement is not clear and may not lie in a single cause, though it should be remarked that late type giants exhibit a natural scatter in the strengths of the violet CN and CH bands that constitute major sources of line absorption in that part of the spectrum, and Willstrop's list cannot be expected to

include all varieties, ζ Aql, which appears from its photometry to be just a little *cooler* than θ Leo, is classified as type A0. There has been a suggestion (Adelman 1988) that θ Leo is metal rich; if it is, it seems to us that it could easily be a star whose temperature corresponds to type A0, as the photometry might suggest, but whose metallic-line spectrum approximates to that of a more normal A2 star. In any case it is already obvious that there is no unique relationship between measured colours and assigned spectral types among A and Am-type stars. Of course, since we are seeking a ratio of fluxes between the two components of the binary system, an error in the classification of one component will perforce be compensated by an error in the same direction in the classification of the other, and minimal effect on the derived value of the magnitude difference, 0.56, is to be expected.

A photometric model of the binary can be constructed on the basis of the colours and magnitude difference of the stars. Since the stars chosen from Willstrop's list in Table 2 above seem to be excellent photometric analogues of the components in the binary system in the *V* bandwidth, we use the wideband (*UBV*) photometry given for those stars in the *Bright Star Catalogue* (Hoffleit 1982) in the model shown first in Table 3. Absolute magnitudes interpolated from the table on p. 18 of *Landolt–Börnstein* (Schaiffers & Voigt 1982) accord rather well with the magnitude difference we have determined. The colours derived from summing the luminosities of the components in the three photometric bands are not an exact match for the actual photometry of HD 201270/1; the (*B–V*) value is slightly, and the (*U-B)* value considerably, too blue. An effect of that sense is only to be expected, since HD 201270/1 is almost on the Galactic equator, and, at the apparent distance modulus of 7.1 implied by the model, is likely to be appreciably reddened. However, the reddening in (U–*B*) is expected (Allen 1973) to be only 0.8 times that in (*B–V*), so clearly not all the discrepancies in the colours can be attributed to reddening. It is perhaps significant that the principal discrepancy seems to lie in the *U* band, which is not covered by Willstrop's (1965) photometry, and there is no guarantee that the stars utilized in the model are indeed such good analogues of HD 201270 and 201271 in the *U* region as they are in *B*.

Table 3. Possible models for HD 201270/1.

		Absolute Magnitude			Colour Index	
		V	*B*	*U*	(*B*−*V*)	(*U*−*B*)
		m	m	m	m	m
Model 1	ε Phe	0.7	1.73	2.57	1.03	0.84
	ζ Aql	1.26	1.27	1.26	0.01	−0.01
	Combined	0.19	0.72	0.98	0.53	0.26
Model 2	ε Vir	0.9	1.84	2.57	0.94	0.73
	θ Leo	1.46	1.45	1.51	−0.01	0.06
	Combined	0.39	0.87	1.16	0.48	0.29
HD 201270/1	(observed)	7.26*			0.56	0.34

* *Apparent* magnitude

We therefore tried a second model based on the spectroscopic analogues ε Vir and θ Leo. An explicit absolute-magnitude determination of $+0^m.9$, based on the K-line width, is available (Wilson 1978) for ε Vir, and has been used to fix the zero-point of the absolute magnitudes in the second model. The model colours are both considerably bluer than the observed colours of the binary system, but the discrepancies are in the right proportion to arise from reddening.

We undertook an investigation of the colours of early-type stars in the direction of HD 201270/1 to see if the small amount of reddening suggested by the models was plausible in relation to the apparent distance of about 250 pc. Unfortunately the considerable spread in intrinsic colours at any given spectral type, as evidenced by nearby stars, is compounded with the patchy nature of Galactic obscuration and renders indeterminate the answer we seek. However, we point out that Deneb, which is said by Bonneau *et al.* (1981) to be at about twice the distance we find for HD 201270/1, has been credited by them with interstellar absorption of $A_v = 0^m.31$, corresponding to $E(B–V)=0^m.09$ and $E(U–B)=0^m.07$. Those colour excesses are not much larger than the quantities required to bring our second model into agreement with the observed colours of HD 201270/1; we are obliged to conclude either that Galactic obscuration is somewhat denser in the line of sight towards HD 201270/1 than that towards Deneb, or that interstellar reddening does not fully account for the discrepancy between the photometric model and the observed colours of the binary.

4. Inclination and size of the orbit

In Section 3.2 above we adopted a value of 2.0 $M_\odot$ for the mass of the A2 V star in the binary system, and derived from our own observations a mass ratio of 1.27 in the sense that the G giant is more massive by that factor. The mass function can be written in the form $m_2 \sin^3 i/(1 + q)^2$, which with $m_2 = 2.0$ and $q = 1.27$ equals $0.389 \sin^3 i$, and is known from the orbital elements (Section 2) to be 0.0567, whence $\sin^3 i=0.146$, with an uncertainty of the order of 30 per cent. Taking the cube root gives $\sin i=0.526$, with about 10 per cent uncertainty, so the orbital inclination is about 32 ± 3 degrees.

Another way of estimating the inclination is from the rotation of the G8 III component: the two Palomar radial–velocity traces give a mean value of 11 km s^{-1} for $v \sin i$. From an estimate of 13 $R_\odot$ (Schaiffers & Voigt 1982, p. 31) for the radius of the star, and making the probably correct assumption of synchronism between the axial rotation and orbital revolution of the star, we derive an equatorial velocity of 16.5 km s^{-1}, so $\sin i$ would be 11/16.5 or i=42°. The agreement is tolerable, but the uncertainties are probably greater than for the first method, so we adopt an inclination of 35°.

The orbital elements show that $a_1 \sin i$= 13.2 Gm, and we can now make use of the value estimated for the inclination to find that a_1 (the actual distance between the centre of mass of the giant star and the centre of mass of the binary system as a whole) is 23 Gm. Since the radius of the star is supposed to be about 13 $R_\odot$ or 9 Gm, we see that the star is a long way from filling its Roche lobe; and indeed we have seen no evidence for mass transfer either in the spectrum or in the mass ratio. The separation of the two stars is $a_1 (1+ q)$—about 52 Gm, or nearly the distance of Mercury from the Sun.

5. Photometric constancy?

Stars that are tidally distorted show photometric variations with half the rotational period as they rotate on their axes, owing to the variation in the area of the hemi-'sphere' presented to the observers' view. Furthermore, late-type stars which rotate at rates above a critical value tend to exhibit another form of rotationally modulated photometric variation which arises from large 'starspots' being carried into or out of view. In the cases of giant stars, it seems likely that axial rotation is synchronized (or nearly so) with orbital revolution for periods up to 100 days or so, at least in cases where there is a comparably massive secondary star to produce the necessary tidal effects. Such a secondary may be an upper-main-sequence star or another giant. Thus, among composite spectrum binaries that are somewhat analogous to HD 201270/1 (i.e. without obvious Roche-lobe overflow or other interaction), two systems with quite short periods are known to show photometric variability: they are 93 (DQ) Leo (Hall *et al.* 1980) and HR 7428 (V1817 Cyg) (Barksdale *et al.* 1985), whose periods are 71 and 109 days respectively. Two other systems which have comparably short periods but which are not known to show photometric variations are α Equ (99 days) and HR 5983 (108 days). However, on the basis that the shorter the period the more likely the giant component is to show variability, one might well expect HD 201270, with its period of only just over 40 days, to exhibit variations arising from the ellipticity effect and/or starspots. A photometric observing campaign certainly seems desirable; accordingly, we have recently drawn the attention of a number of photometric observers to the system, so if variability exists it ought quite soon to be discovered.

Acknowledgements

We are very grateful for the privilege of having worked at Mount Wilson Observatory and for the assistance of the staff there. We would also like to thank the Palomar and Geneva Observatories for allowing us to make radial-velocity observations, some of which appear in Table 1, with their equipment, and the Stellar Data Centre, Strasbourg, for the use of its data base via *Simbad.* Our expenses for the observing visits were defrayed by the SERC. One of us is pleased to acknowledge financial support successively from the SERC, St. John's College, Cambridge, and the Leverhulme Trust.

References

Adelman, S. J. 1988, *Mon. Not. R. astr. Soc,* **230**, 671.
Allen, C. W. 1973, *Astrophysical Quantities,* Athlone, London, p.206.
Barksdale, W. S., Boyd, L. J, Genet, R. M., Fried, R. E., Hall, D. S., Persinger, W. T., Hoff, D. B., Ingvarsson, S.I.,Nielsen, P., Stelzer, H. J., Wasson, N. F. 1985, *Inf. Bull. var. Stars,* no. 2737.
Baranae, A., Mayor, M., Poncet, J. L.1979, *Vistas Astr.,* **23**, 279.
Bonneau, D., Koechlin, L, Oneto, J. L, Vakili, F.1981, *Astr. Astrophys.,* **103**, 28.
Cannon, A. J., Pickering, E. C. 1924, *Ann. Harv. Coll. Obs.,* **99**, 21& 262.
Fehrenbach, G, Rebeirot, E. 1962, *J. Obs.,* **45**, 349.
Griffin, R. & R. 1986, J. *Astrophys. Astr.,* **7**, 195.(Paper 1).
Griffin, R. F., Gunn, J. E. 1974, *Astrophys.* J., **191,** 545.
Hall, D. S., Henry, G. W., Vaucher, C. A., Landis, H. J., Louth, H., Montle, R. E., Skillman, D. R. 1980, *Inf. Bull. var. Stars,* no. 1798.

Hoffleit, D. N. 1982, *Bright Star Catalogue,* Yale Univ. Obs., New Haven.
Hynek, J. A. 1938, *Contr. Perkins Obs.,* **1**, 185.
Keenan, P. C, McNeil, R. C. 1989, *Astrophys. J. SuppL,* **71**, 245.
Kuhi, L. V. 1963, *Publ. astr. Soc. Pacific,* **75**, 448.
Oja, T. 1986, *Astr. Astrophys. Suppl,* **65,** 409.
Popper, D. M. 1980, *Ann. Rev. Astr. Astrophys.,* **18**, 115.
Schaiffers, K., Voigt, H. H. (Eds) 1982, *Landolt-Börnstein,* New Series, Group 6, Vol. 2b, Springer–Verlag, Berlin.
Willstrop, R. V. 1965, *Mem. R. astr. Soc,* **69**, 83.
Wilson, O. C. 1976, *Astrophys. J.,* **205**, 823.

J. Astrophys. Astr.(1990) **11**, 291–295

A Note on the Self-Consistency of the EIH Equations of Motion

Rajat Roy *Sameer, IIT Campus, Hill Side, Bombay 400076*

N. C. Rana *Tata Institute of Fundamental Research, Homi Bhabha Road, Bombay 400005*

Received 1989 December 12; accepted 1990 May 31

Abstract. The self-consistency of the Einstein Infeld and Hoffman (EIH) equations of motion is critically examined in the limiting case of a three-body problem where two bodies are very close to each other and a third quite far removed from them.

Key words: self-consistency—post-Newtonian equations

1. Introduction

The field equations of General Theory of Relativity (GTR) as obtained by Einstien in 1915 do not yield exact analytical equations of motion for the many-body problem. Einstein, Infeld & Hoffmann (1938) obtained an approximate equation of motion for the many-body problem in GTR assuming the bodies to be point masses. Since the equations of motion thus obtained were one order higher with respect to a 'smallness parameter' ε^2 (Misner, Thorne & Wheeler 1970) than the Newtonian equations of motion they are called post-Newtonian equations. The equation of motion was first given explicitly by Eddington & Clark (1938). It was later reproduced in Misner, Thorne & Wheeler (1970) with minor modifications. In this paper we aim to examine the singularities of this EIH equation of motion when all bodies are assumed to be static, that is, the initial acceleration of a initially static body and its singularities are studied when other bodies are also assumed to be initially static. To do this we take an example of three bodies, two close to each other and a third slightly removed from them and we study the initial acceleration of the third body when the other two are put in various initial positions.

2. The EIH equations without velocity dependent terms

As given by Equation 39.64 of Misner, Thorne & Wheeler (1970, hereinafter MTW), the EIH equation of motion including the velocity dependent terms is given by (gravitational units, that is, G = l and c = 1 are always assumed in this work),

$$\frac{d^2\mathbf{x}_K}{dt^2} = \sum_{A\neq K} \mathbf{r}_{AK}\frac{M_A}{r_{AK}^3}\left[1-4\sum_{B\neq K}\frac{M_B}{r_{BK}}-\sum_{C\neq A}\frac{M_C}{r_{CA}}\left(1-\frac{\mathbf{r}_{AK}\cdot\mathbf{r}_{CA}}{2r_{CA}^2}\right)\right.$$
$$\left.+v_K^2+2v_A^2-4\mathbf{v}_A\cdot\mathbf{v}_K-\frac{3}{2}\left(\frac{\mathbf{v}_A\cdot\mathbf{r}_{AK}}{r_{AK}}\right)^2\right]$$

$$-\sum_{A\neq K}(\mathbf{v}_A-\mathbf{v}_K)\frac{M_A\mathbf{r}_{AK}\cdot(3\mathbf{v}_A-4\mathbf{v}_K)}{r_{AK}^3}+\frac{7}{2}\sum_{A\neq K}\sum_{C\neq A}\mathbf{r}_{CA}\frac{M_AM_C}{r_{AK}r_{CA}^3} \tag{1}$$

where all notations are exactly the same as given in MTW.

Since we are interested in the initial acceleration of a static body K when other bodies are also initially static we remove all velocity dependent terms from this equation which yields

$$\left.\frac{d^2\mathbf{x}_K}{dt^2}\right|_{t=0}=\sum_{A\neq K}\mathbf{r}_{AK}\frac{M_A}{r_{AK}^3}\left[1-4\sum_{B\neq K}\frac{M_B}{r_{BK}}-\sum_{C\neq A}\frac{M_C}{r_{CA}}\left(1-\frac{\mathbf{r}_{AK}\cdot\mathbf{r}_{CA}}{2r_{CA}^2}\right)\right]$$
$$+\frac{7}{2}\sum_{A\neq K}\sum_{C\neq A}\mathbf{r}_{CA}\frac{M_AM_C}{r_{AK}r_{CA}^3}. \tag{2}$$

Let us now have three bodies idealized as point masses and having the following initial rectangular Cartesian-like coordinates

$$(0,\ 0,\ 0)\rightarrow \text{body no. 1}$$
$$(\tilde{x}_1,\ \tilde{y},\ 0)\rightarrow \text{body no. 2}$$
$$(\tilde{x}_1,\ -\tilde{y},\ 0)\rightarrow \text{body no. 3}$$

We wish to study the initial acceleration of the first body due to the gravitational interaction with bodies no. 2 and 3.

Equation (2) reduces to

$$\left.\frac{d^2\mathbf{x}_1}{dt^2}\right|_{t=0}=\mathbf{r}_{21}\frac{M_2}{r_{21}^3}+\mathbf{r}_{31}\frac{M_3}{r_{31}^3}-4\mathbf{r}_{21}\frac{M_2}{r_{21}^3}\left(\frac{M_2}{r_{21}}+\frac{M_3}{r_{31}}\right)-4\mathbf{r}_{31}\frac{M_3}{r_{31}^3}\left(\frac{M_2}{r_{21}}+\frac{M_3}{r_{31}}\right)$$
$$-\mathbf{r}_{21}\frac{M_2}{r_{21}^3}\left(\frac{M_3}{r_{32}}-\frac{M_3}{r_{32}}\frac{\mathbf{r}_{21}\cdot\mathbf{r}_{32}}{2r_{32}^2}+\frac{M_1}{r_{12}}-\frac{M_1}{r_{12}}\frac{\mathbf{r}_{21}\cdot\mathbf{r}_{12}}{2r_{12}^2}\right)$$
$$-\mathbf{r}_{31}\frac{M_3}{r_{31}^3}\left(\frac{M_2}{r_{23}}-\frac{M_2}{r_{23}}\frac{\mathbf{r}_{31}\cdot\mathbf{r}_{23}}{2r_{23}^2}+\frac{M_1}{r_{13}}-\frac{M_1}{r_{13}}\frac{\mathbf{r}_{31}\cdot\mathbf{r}_{13}}{2r_{13}^2}\right)$$
$$+\frac{7}{2}\mathbf{r}_{32}\frac{M_2M_3}{r_{21}r_{32}^3}+\frac{7}{2}\mathbf{r}_{12}\frac{M_2M_1}{r_{21}r_{12}^3}+\frac{7}{2}\mathbf{r}_{23}\frac{M_3M_2}{r_{31}r_{23}^3}+\frac{7}{2}\mathbf{r}_{13}\frac{M_3M_1}{r_{31}r_{13}^3}, \tag{3}$$

where we have taken $K=1$, summation over A and B to include bodies nos 2 and 3 respectively since we have $A\neq K$ *and* $B\neq K$, and summation over C to exclude body no. 2 when $A=2$ or to exclude body no. 3 when $A=3$.

If we take $\hat{x}$ and $\hat{y}$ to be unit vectors along x- and y- axes respectively, we have

$$\mathbf{r}_{21}=-\mathbf{r}_{12}=\tilde{x}_1\hat{x}+\tilde{y}_1\hat{y},$$
$$\mathbf{r}_{31}=-\mathbf{r}_{13}=\tilde{x}_1\hat{x}-\tilde{y}_1\hat{y},$$
$$\mathbf{r}_{23}=-\mathbf{r}_{32}=2\tilde{y}_1\hat{y}.$$

Let us assume all masses to be unity $M_1=M_2=M_3=1$, and therefore, Equation (3) reduces to

$$\left.\frac{d^2\mathbf{x}_1}{dt^2}\right|_{t=0}=\frac{2\tilde{x}_1\hat{x}}{(\tilde{x}_1^2+\tilde{y}_1^2)^{1.5}}-\frac{26\tilde{x}_1\hat{x}}{(\tilde{x}_1^2+\tilde{y}_1^2)^2}-\frac{5}{4}\frac{\tilde{x}_1\hat{x}}{\tilde{y}_1(\tilde{x}_1^2+\tilde{y}_1^2)^{1.5}}. \tag{4}$$

3. Results and discussions

The acceleration of body no. 1 is broken up into three components corresponding directly to the RHS of Equation (4) as

$$\text{Accn (1)=Newtonian term—post Newtonian term no. 1} \\ \text{—post Newtonian term no. 2.} \tag{5}$$

The results are plotted in Fig. 1, where each of the above terms are plotted with $\tilde{x}_1$ = 100 gravitational units and $\tilde{y}_1$ varying from 5 to 0. At $\tilde{y}_1$=0 a singularity occurs in the post Newtonian term no. 2 which appears to be abnormal due to the following reason.

The problem of two bodies having masses M_1 = 1 and M_2 = 2 with initial co-ordinates (0,0,0) and ($\tilde{x}_1$,0,0) respectively gives the expression for the initial acceleration of the first body as (both bodies assumed to be initially static)

$$\left.\frac{d^2\mathbf{x}_1}{dt^2}\right|_{t=0} = \frac{2\hat{x}}{\tilde{x}_1^2} - \frac{26\hat{x}}{\tilde{x}_1^3}, \tag{6}$$

following Equation (2). However, in the problem of the three bodies situated at the points (0,0,0), ($\tilde{x}_1$, $\tilde{y}_1$, 0)and ($\tilde{x}_1$, –$\tilde{y}_1$, 0) each with unit mass we expect as $\tilde{y}_1$ tends to zero (the masses remaining static of course) the initial acceleration of the first body to tend to that in the limit of the two body problem given by Equation (6). Or in other words, the Equation (4) should tend to Equation (6) in the limit $\tilde{y}_1 \rightarrow 0$ This is because to the first body the presence of two different distant bodies which are close to each other should appear more and more as a single body when their mutual distance of separation that is the distance between second and third bodies is continually decreased. But the RHS of Equation (4) *does not* tend to that of Equation (6) when $\tilde{y}_1 \rightarrow 0$. The Newtonian term does as is expected. The post Newtonian term no. 1, that is, the second term on the RHS of (4) reduces to the only post Newtonian term of (6). But the post Newtonian term no. 2, that is, the third term on the RHS of (4) diverges as $\tilde{y}_1 \rightarrow 0$ whereas there is no such term present on the RHS of(6). So the two limits are not mathematically agreeing with each other.

It is desirable that no fundamental force of nature shows such an anomaly in the asymptotic limits. In reality $\tilde{y}_1$=0 is of course ruled out since no body can be collapsed to exactly a point mass with infinite density. But in the present case we have already assumed the particles to be point-like. However for the sake of argument one can say that the black hole radius of r = 2 gravitational units can be considered a practical limit which a body of mass = 1 can be contracted to. So in Fig. 1 we show it to be a limit of practical possibility to which the second and third bodies can be brought close to each other which is $\tilde{y}_1$=2. In this case, the post Newtonian term remains still finite and is not negligible even at $\tilde{y}_1$>6 or so which shows that the problem persists in the practical cases such as stably revolving close pair of neutron stars.

The post-Newtonian approximation as introduced by Damour (1989) introduces five parameters in his section 6.9. These are $\alpha=L/R$ the 'geometric coupling' parameter, β_e , β_i, γ_e and γ_i as defined therein. As noted by him in section 6.10 of the same article that the last four of these parameters have to be much smaller than unity for the post-Newtonian approximations to be valid, that is, in other words, the post-Newtonian approximations are made under these assumptions. But in a previous

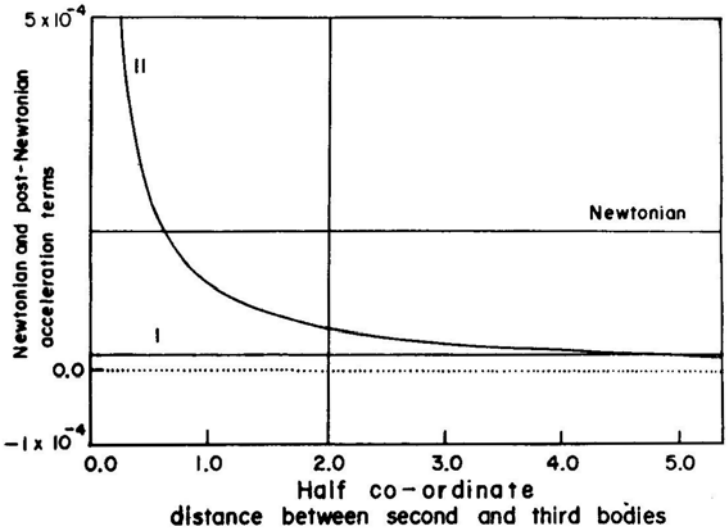

Figure 1. Relative strengths of the Newtonian and the post-Newtonian accelerations produced by a close pair of particles on another particle at far off distance as a function of separation between the pair. The Newtonian term remains fairly constant but one of the non-Newtonian terms coming from EIH equation is increasing indefinitely as the separation of the doublet is reduced. The non-Newtonian term exceeds the Newtonian value at a separation of about one unit of gravitational distance.

section (vide Equation (78) of the same reference) Damour makes a 'minimal assumption' $\alpha \ll 1$ which in our opinion is never an assumption under which post-Newtonian approximations (PNA) are valid. In fact in his chapter 9 Weinberg (1972) introduces $G\bar{M}/\bar{r}$ and $\bar{v}^2$ as the 'small parameters' of PNA (for $c = 1$), which is tantamount to stating that β_e, β_i, γ_e and γ_i are all $\ll 1$. Although it is true that in the real world all heavenly bodies are separated by much greater distances than their physical dimensions, it is possible to describe the mutual gravitational interaction of two hypothetically very close bodies and their combined interaction on a distant third body to a high degree of accuracy by Newtonian gravity and hence to a higher degree of accuracy by terms including upto PNA. This is to say that two earths or two suns or even two much denser and 'strongly' self-gravitating objects can be brought close enough so as to almost touch each other's surfaces and their gravitational interaction (mutual or otherwise) can be described perfectly well by Newtonian gravity and hence it must be possible to do it even better by including the terms of PNA. We have shown in this note the anomalous behaviour of one of the PNA terms in a special case where two close spherical bodies assumed to be point masses do not appear more and more as a single body to a distant observer unlike that in Newtonian gravity when the mutual distance between the two close bodies is reduced indefinitely. This in our opinion might cause problems with Weinberg's definition of quadrupole moment (Weinberg 1972). Damour (1989) further in his section 6.13 introduces an idea of 'effective' mass $m = m_0 + \gamma_i m_1 + \ldots$ (see page 168 of the article) for very strongly self-gravitating bodies to make PNA valid close to and inside the bodies. However by the phrase 'strongly self-gravitating' is meant bodies whose radii are very close to their black hole horizon which in the above discussion we have shown is not the only case where the second PNA term is anomalous in its behaviour. Thus the problem persists.

Another problem about such equations of motion is that an assumption has been made that all the bodies which are in actual cases nearly spherical can be represented as point masses with their entire mass concentrated at their centres. In Newtonian gravity such an assumption was later justified as a theorem by integration (summation of field due to infinitesimal mass points vectorially) over the whole body. To our knowledge such a theorem does not exist for the terms including up to the post-Newtonian approximation of GTR. This is still an open question. The last point to be noted is the fact that the velocity dependent terms in the PNA equations of motion can be neglected in studying the special case of our problem simply because velocities of all particles depend on the equations of motion and the initial conditions. Newtonian gravity describes the motion of bodies momentarily static in an inertial frame perfectly well and so should PNA since it does not invalidate any of the assumptions as stated earlier in deriving the PNA equations. Even in the case of all heavenly bodies having velocities such that $\bar{v}^2 \sim G\bar{M}/\bar{r}$ our conclusions remain valid.

However it should be noted that the basic assumptions behind the derivation of the EIH equation of motion is that the bodies should obey the post-Newtonian approximations, namely the mutual distances between any two bodies in gravitational units must be $\geqslant M$ where M can be considered as the mass of the heaviest object in the system. In that case, all the singularities are avoided. So the formulation remains althrough consistent, provided we never allow any two bodies to come very close to each other violating the basic assumption of the PPN which has been used in deriving the EIH equations of motion.

In conclusion, in this note we point out the fact that the Einstein, Infeld and Hoffman equations of motion contain some singularities that appear to violate the limiting nature of the gravitational forces, which can be avoided only if we strictly adhere to obeying the basic assumptions used to derive the EIH equations of motion during the course of dynamical evolution of a finite number of point-like particles.

References

Einstein, A., Infeld, L., Hoffman, B. 1938, *Ann. Math.,* **39**, 65.

Eddington, A., Clark, G. 1938, *Proc. Roy. Soc,* **A166**, 465.

Misner, C, Thorne, K., Wheeler, J. 1970, *Gravitation,* Freeman, San Francisco.

Damour, T.1989, *Three Hundred Years of Gravitation,* Eds S. Hawking & W. Israel, Cambridge Univ. Press.

Weinberg, S.1972, *Gravitation and Cosmology,* John Wiley, New York.

J. Astrophys. Astr. (1990) **11**, 297–310

A Digital Correlation Receiver for the GEETEE Radio Telescope

N. Udaya Shankar & T. S. Ravi Shankar *Raman Research institute, Bangalore 560080*

Received 1990 March 17; accepted 1990 May 29

Abstract. A 128-channel digital correlation receiver has been built for the GEETEE[1], the low-frequency radio telescope situated at Gauribidanur, South India, (latitude 13°36′12″ N). The receiver uses a modified double-sideband (DSB) technique. The quadrature samples required for a DSB system are obtained by sampling the digitized intermediate frequency (I.F.) signals by two clocks which are separated in time by one quarter of the period of the I.F. The visibilities required for one-dimensional synthesis are measured using one-bit correlators. A technique to measure amplitude information for the signal using a threshold detector and a one-bit correlator has been developed. The receiver has been successfully used for continuum, spectral-line and pulsar observations. The antenna system of GEETEE and its configuration for one dimensional synthesis are also described in this paper.

Key words: DSB system—one-bit correlator

1. Introduction

The GEETEE is a low-frequency radio telescope operating at 34.5 MHz. It is situated near Gauribidanur, about 80 km north of Bangalore, South India (longitude 77°26′07″E and latitude 13°36′12″N). The antenna system is a T-shaped array with 1000 dipoles, 640 in the 1.4-km long East-West array (EW) and 360 in the 0.45-km long South array (S). The basic dipole, its characteristics and the geometry of the array are shown in Figs la and b. This array can be phased in a Christmas-tree fashion to form a single beam with a resolution of 26′ ×42′ Sec $(\delta$–14°.1) (Dwarakanath, Shevgaonkar & Sastry 1982; Sastry 1989; Deshpande, Shevgaonkar & Sastry 1989).

To survey a wide field, a single-beam instrument needs a large amount of observing time thus reducing the surveying sensitivity compared with a multi-beam system. Also, at low frequencies, ionospheric effects can cause time-variable shifts in the apparent positions of radio sources. This makes it desirable to observe a large area of sky in a short time, which is not possible with a single-beam telescope. Another problem with low-frequency observing is man-made interference. This can be very destructive at decametre wavelengths and reduces the useable observing time. To obtain long periods of interference-free observing one should be able to change the frequency and the bandwidth of operation both quickly and easily.

[1] This telescope is jointly operated by the Indian Institute of Astrophysics, Bangalore and the Raman Research Institute, Bangalore.

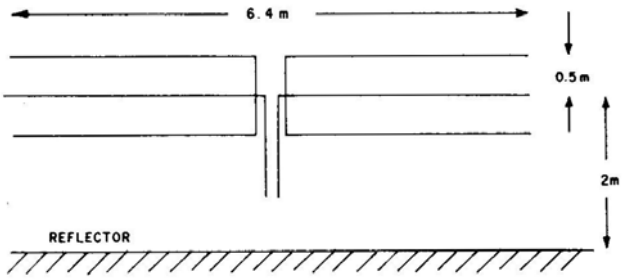

Figure 1a. Four fat dipoles (one of which is shown in this figure) are combined along the EW direction through open-wire transmission lines and appropriate impedance transformers to form a basic unit. Characteristic impedance of the dipole: 600Ω, Bandwidth: 25–35 MHz with a VSWR of 1.1–1.5, Polarization: linear, oriented along EW.

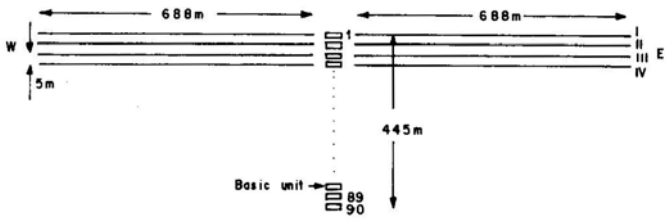

Figure 1b. The Gauribidanur radio telescope (GEETEE). Collecting area: EW array ≈ 12,000 m^2, S array ≈7,000 m^2, EW×S in correlation mode ≈ 18,000 m^2.

This paper describes a 128-channel digital correlation receiver (Fig. 2), the main design emphasis of which was to obtain long periods of interference-free observing over as large an area of sky as possible in a given time. The receiver system can be configured for both one-dimensional synthesis and spectral-line observations. A companion paper by Dwarakanath & Udaya Shankar (1990; DU) describes a large-scale continuum survey made at 34.5 MHz using this receiver system. Results of spectral-line observations made with the receiver are briefly described in Section 4.2 of the present paper. Results of pulsar observations using the receiver can be found in Deshpande (1987).

2. Array configuration for one-dimensional synthesis

For one-dimensional synthesis, a single row of the EW array (row III.of Fig. 1b) is used in the meridian transit mode (Fig. 3). The S array consists of 90 rows of dipoles placed 5 m apart (Fig. 4). Each row of dipoles in the EW array and each row in the S array have primary beams which cover essentially the whole range of elevations along the meridian, allowing synthesis of a very-large region of the sky in a single day. Since row III of the EW array was chosen for observations, only 88 visibilities along NS were measured. After amplification in the field, the outputs from the rows of the S array are earned to the observatory in 23 open-wire transmission lines using time-division

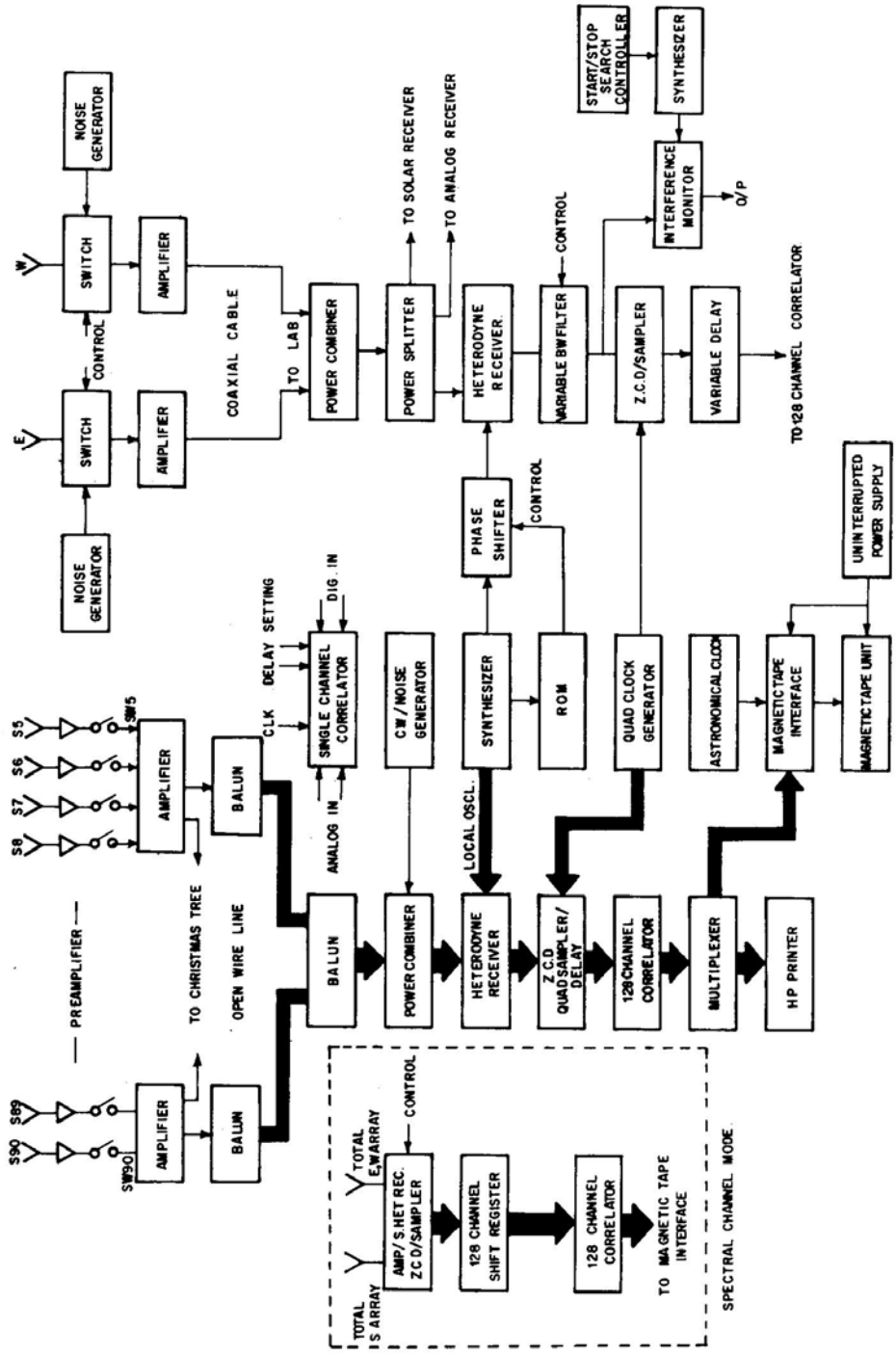

Figure 2. Block diagram of the 128-channel digital correlation receiver.

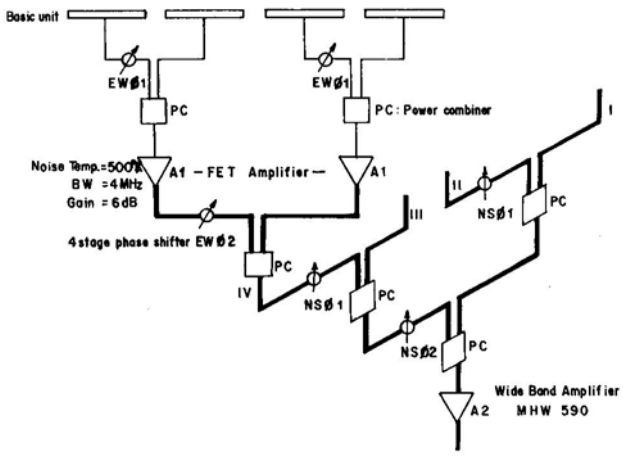

Figure 3. The Christmas-tree configuration of the EW array consisting of 4 basic units in each row is shown in detail.

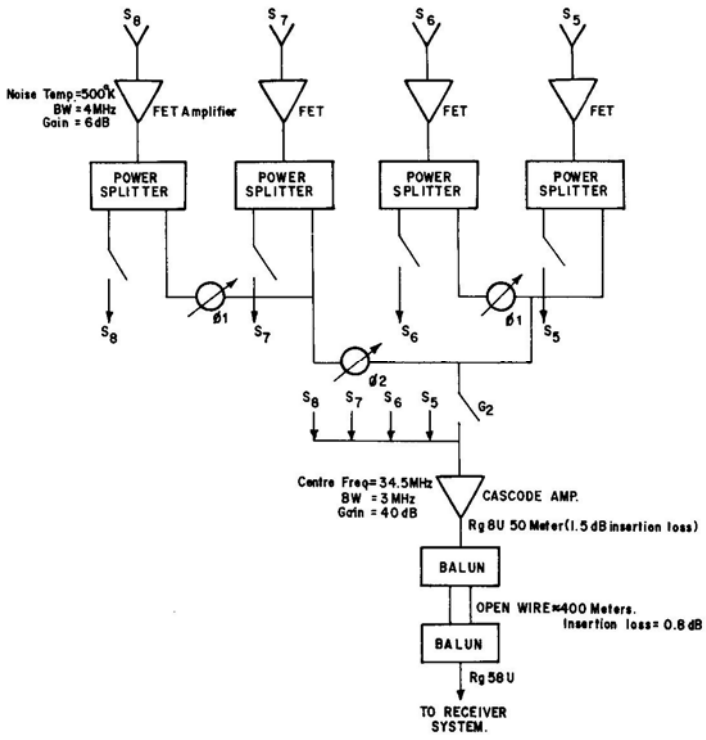

Figure 4. The configuration used in the S array for the sky survey. S_5, S_6, S_7, S_8 refer to rows of basic units in the S array.

multiplexing (Fig. 2). The dipoles at the centre of the array are included in both the EW and the S arrays (Fig. 5) so that the antenna responds to all spatial-frequencies up to those corresponding to its maximum extent. In particular, the zero spatial-frequency component of the brightness distribution is recorded.

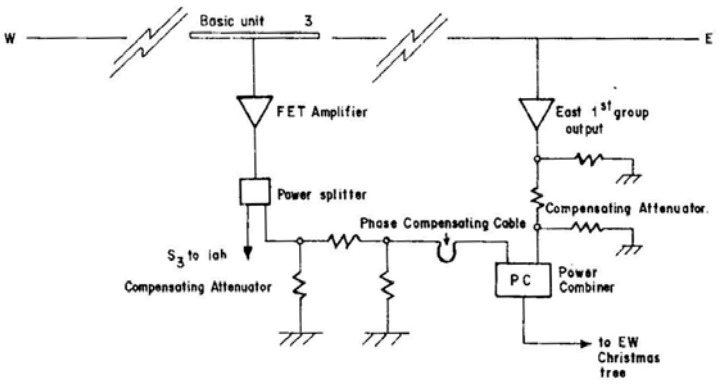

Figure 5. This figure illustrates the inclusion of the zero-spacing into the interferometer.

The above configuration uses only a quarter of the collecting area of the EW array. However, this is not a serious disadvantage since the telescope is essentially confusion limited (DU). The advantages of this configuration are that it

(1) reduces the hardware requirements,
(2) gives maximum sky coverage for a given observing time, and
(3) does not disturb the existing Christmas-tree configuration.

This last consideration permits utilization of the single-beam configuration which is preferred for both spectral-line and pulsar observations.

In the observatory building, the signals from the EW and S arrays are further amplified and then down-converted to an intermediate frequency of 4 MHz. At the front end, only 23 super-heterodyne receivers are used in a time-multiplexed mode to obtain 88 I.F. outputs from the S array. Each of these outputs is correlated with the EW-array I.F. output using one-bit correlators. This gives 88 visibilities sampled at 5 m intervals along the NS direction. The Fourier transform of these visibilities gives the one-dimensional brightness distribution of the sky along the meridian over a zenith angle range of ± 47°, without any grating response (DU).

3. Important design features of the receiver system

3.1 *Double-Sideband* (*DSB*) *System*

The receiver system uses a DSB technique (Read 1963; Radhakrishnan *et al.* 1972; Fomalont & Wright 1974; Udaya Shankar 1986; Thompson, Moran & Swenson 1986). A conventional DSB system for continuum observations is shown in Fig. 6a. In such a system, the sidebands are folded together before correlation. When observing in directions far from the zenith, a DSB system allows coarse delay steps to be used for delay compensation without introducing phase jumps and leaves the phase calibration unchanged. To obtain the same signal-to-noise ratio (S/N) for continuum observations as with a single-sideband (SSB) system, a DSB system requires twice the number of correlators since sidebands have to be unfolded. A conventional DSB system for spectral line observations is shown in Fig. 6b. In spectral line observations the extra

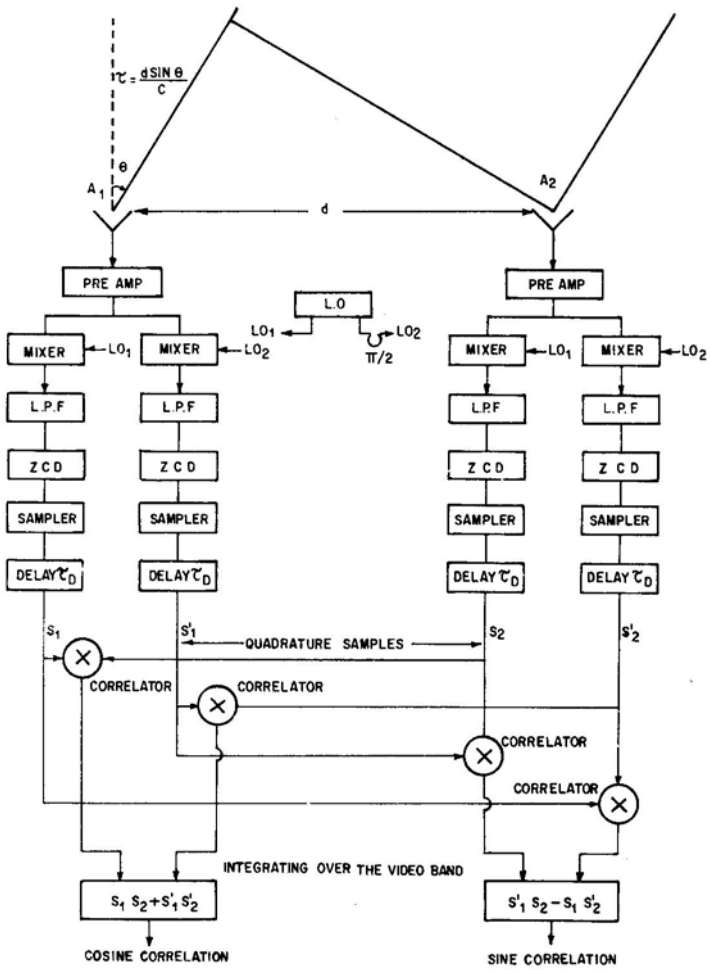

Figure 6a. The scheme for obtaining quadrature samples and correlation coefficients in a conventional DSB system for continuum observations.

correlators provide a reference spectrum without any conventional switching (such as frequency, beam or load switching). In these switching schemes observing time has to be split between on line and off line measurements thus reducing S/N.

A DSB system also requires the generation of quadrature samples of the signal without any significant deterioration of S/N. This is implemented in the present system by obtaining the quadrature samples after digitization. At our frequency, even a conventional DSB system does not suffer from a loss of S/N, as the system temperature is dominated by the contribution from the sky.

In a conventional DSB system, quadrature samples are obtained using two local oscillators shifted in phase by 90° (Fig. 6a). However, the present receiver system obtains the quadrature samples by sampling the digitized I.F. signal (Δf = 400 kHz, fc=4 MHz) by two clocks which are separated in time by a quarter of the I.F. period (62.5 ns) as shown in Fig. 7. The folding of the two sidebands is achieved by using a sampling frequency (2 MHz) which is a subharmonic of the I F . This scheme reduces

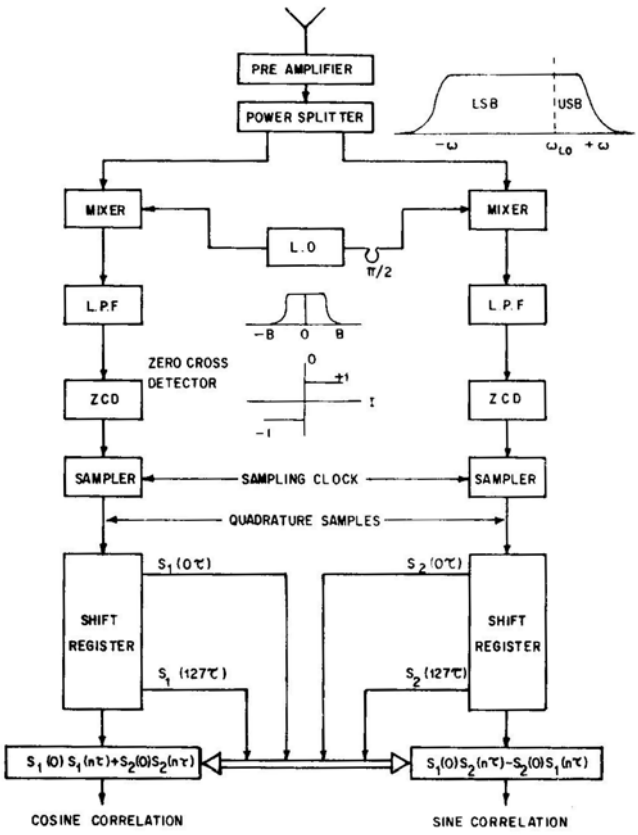

Figure 6b. The scheme for obtaining quadrature samples and correlation coefficients in the conventional DSB system, employed for spectral-line observations in the present receiver. Cosine transform of cos correlator output gives the sum of the two sidebands (USB +LSB). Sine transform of sine correlator output gives the difference between the two sidebands (USB — LSB).

the number of mixers, filters and digitizers required for a DSB system. Since matching the phase characteristics of these filters and equalizing reference voltages for digitizers are very difficult, the reduced hardware results in improved system performance. Correlation of the quadrature samples obtained at slightly different instants of time (62.5 ns) causes bandwidth decorrelation. This is less than 0.2 per cent as 62.5 ns is very small compared to the reciprocal of the I.F. bandwidth (2.5 μs). This method of obtaining the quadrature samples does not permit filtering after digitization. Thus the final observing bandwidth is equal to the I.F. bandwidth. For spectral-line observations it is preferable to retain the facility for altering the bandwidth after heterodyning. Thus, the conventional DSB scheme of Fig. 6b was employed for the spectral-line receiver.

Bandwidth decorrelation and the amount of hardware required for a DSB system could have been reduced further by digitizing directly at 34.5 MHz. However, in such a system, a jitter of even 1 ns in the sampling clock would have caused phase errors of ~ 15°. Hence such a scheme was not attempted.

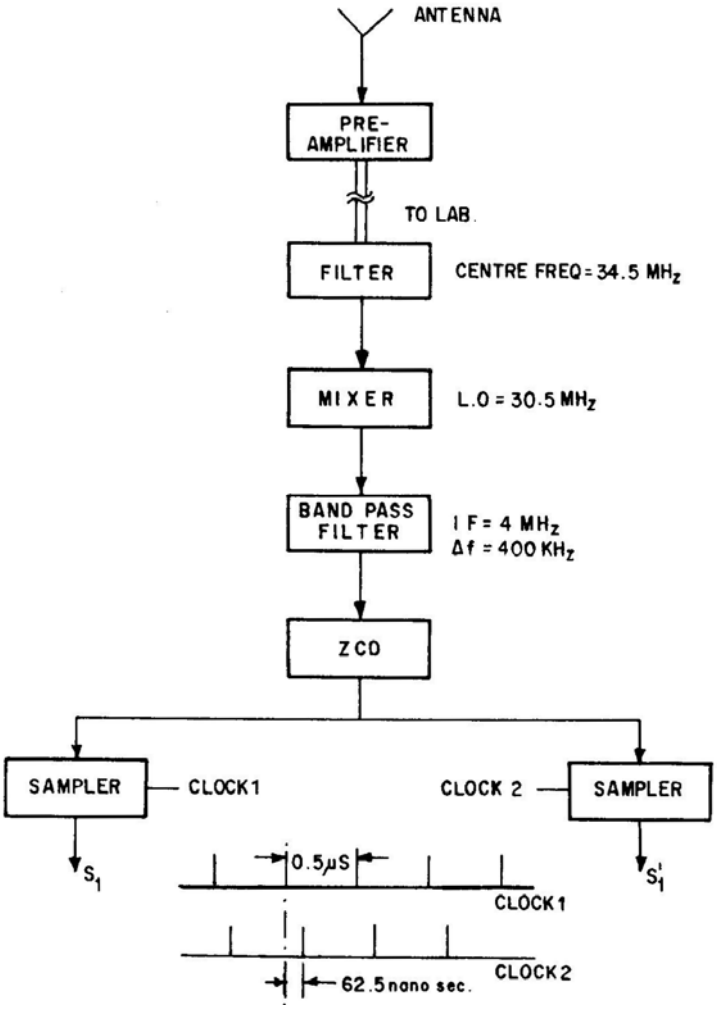

Figure 7. The technique employed in the present receiver system to obtain the quadrature samples of a bandpass signal.

3.2 *Variable Bandwidth Receiver*

Since the operating frequency of the telescope is very close to the broadcast and communication bands, manmade interference could be high. Two facilities are built into the system to increase the interference-free time for observations (Fig. 2).

Firstly, by tuning the L.O. the centre frequency of observation can be changed over a 2-MHz band. Since the EW array is ~ 1 km longer than the S array, a small change in the centre frequency alters the instrumental phase calibration and this could change by different amounts for different rows of the S array. To overcome this difficulty, a large delay in the form of a long chain of shift registers is included in the path of the S array signal A variable-delay shift register is incorporated in the EW signal path and adjusted to maximize the correlation. Further, the lengths of the cables bringing the

outputs from the various rows of the S array to the observatory building are equalized to within a wavelength. This makes the R.F.-phase change by the same amount in all channels when the centre frequency changes. To retain the advantages of DSB op–eration, a hardware scheme using a R.O.M. and a phase shifter is incorporated in the EW L.O. path to retain the phase calibration, independent of the centre frequency.

Interference-free observation can be increased by having variable-bandwidth filters in all channels. Interference monitoring indicated that the cost and complexity of the hardware required for such a system is not commensurate with the increase in observation time obtainable. However, to tackle low-level interference, a variable-bandwidth filter has been included in the EW array alone (Fig. 2). A variable-bandwidth filter in only one of the signal paths of a cross correlator changes the effective observing bandwidth. A filter present in the EW array introduces both a group delay and a phase which is a function of the frequency. Therefore, it is necessary to delay the S-array signals and also pass them through a phase-compensating network to retain the correlation value. However, this increases the complexity of the hardware. To simplify the hardware, the variable-bandwidth filters in the EW-array signal path are designed to have linear phase characteristics. The gross delay in the S-array signal path and the variable delay in the EW channels are then sufficient to maximize the correlation.

When two unequal bandwidth signals are correlated in a one-bit correlator, the correlation coefficient decreases. We note that if the scheme is implemented properly, the signal-to-noise ratio does not decrease below that expected for narrower band–width signals in both the signal paths of a cross correlator. The true correlation coefficient can be recovered by knowing the bandwidths of the signals correlated. A detailed description of the scheme used and the detailed S/N calculation may be found in Udaya Shankar (1986).

3.3 *The One-bit Correlator*

The correlator system uses one-bit quantization. A one-bit correlator using Nyquist sampling suffers a loss in sensitivity of 37 per cent (Van Vleck & Middleton 1966; Weinreb 1963). This system samples a 400-kHz I.F. band centred around 4 MHz at five times the Nyquist rate and thus reduces the loss of sensitivity to 20 per cent (Bowers & Klingler 1974). This is very close to the performance of a two-bit three-level correlator employing the Nyquist rate. The correlator is shown schematically in Fig. 8. The addition of correlations required for a DSB system is performed using two phased clocks and an up-counter. The input to the up-counter will be at a rate which is twice the sampling rate. At this rate, which is 4 MHz, a 20-bit counter gets filled in 256 ms. The system employs a variable-length counter (13 to 20 stages) enabling the pre-integration time to be varied from 2 ms to 256 ms. Independent of the integration time, only the eight most-significant bits of the counter are latched out and recorded on an incremental magnetic tape. To avoid loss of information, only these eight bits are reset following each integration and the lower-order bits are allowed to accumulate correlation for the next integration period (Ravindra 1983). It is for this reason that these correlators, unlike superheterodyne receivers, could not be time multiplexed. Thus 88 correlators are used to measure the 88 visibilities.

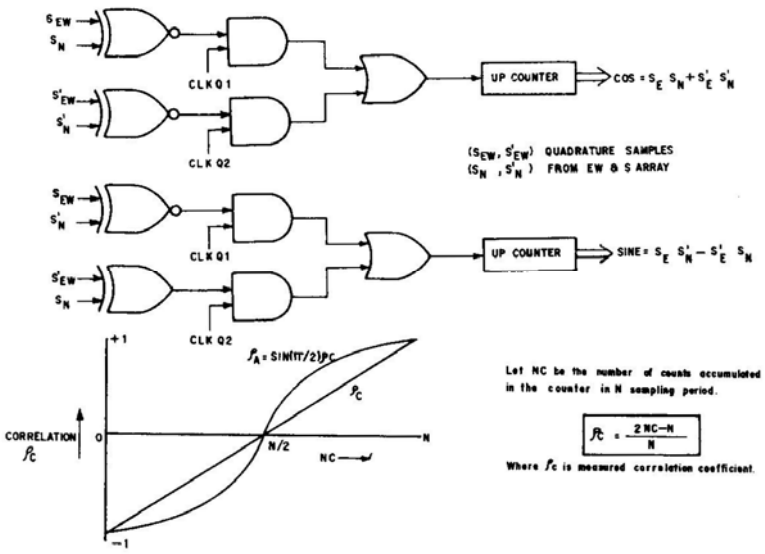

Figure 8. This figure illustrates a scheme for addition of correlations required for a DSB system. A DSB system needs four multipliers to obtain the desired correlation counts N_C The equation and the graph describe the relation between the desired correlation coefficient ρ_A and Nc.

3.4 *Amplitude Information of the Signal Using One-bit Correlators*

The amplitude information of the signal is lost in one-bit quantization. This results in identical correlations for a weak source in a weak background and a stronger source in a correspondingly-stronger background. The normalized correlation coefficient (ρ_C) measured in a one-bit correlator is related to the analog correlation (ρ_A) by the relation

$$\sin[(\pi/2)\rho_C] = \frac{\rho_A}{\sqrt{p_1 p_2}}, \tag{1}$$

where p_i and p_2 are the powers of the two signals correlated. Thus, in observations made using one-bit correlators to obtain the brightness distribution of the sky, it is necessary to measure the power output of each interferometer element being correlated. To measure the power, we have employed a scheme using a threshold detector and a one-bit correlator. This measures the probability that the signal amplitude is below a certain threshold V_{th} (Fig. 9). For a Gaussian signal with zero mean this is given by

$$P = \frac{NC}{N} = \frac{1}{2} + \frac{1}{\sqrt{\pi}} \int_0^{V_{th}/\sqrt{2}\sigma} \exp[-x^2]\,dx. \tag{2}$$

Knowing this, the RMS fluctuation σ of the signal can be obtained. The power then is simply equal to σ^2.

Even though 88 one-bit correlations are measured for one-dimensional synthesis, only the EW total power and the total power of one of the S array rows are required to reconstruct the brightness distribution of the sky. This is as all the S-array rows are

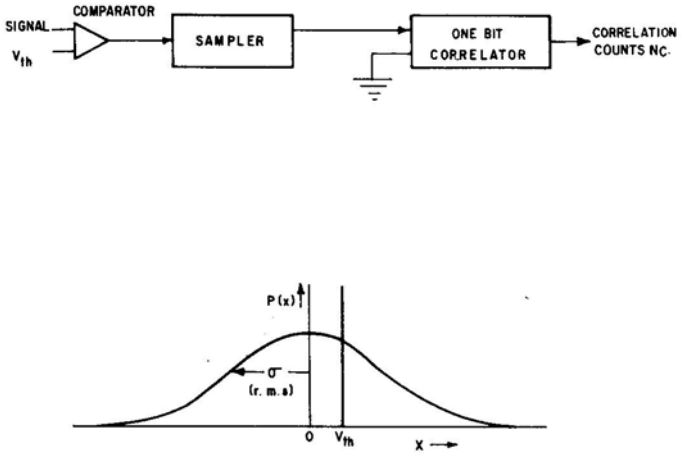

Figure 9. A schematic of the technique used to measure the power of a signal using a one-bit correlator and the threshold detector.

similar and the one-bit correlations are not affected by gain differences in the heterodyne receivers.

3.5 *Miscellaneous Circuits*

The philosophy adopted in the system design was to build circuits which could be used for testing the receiver and make it a stand-alone system. A single-channel one-bit correlator with a six-digit readout has been built which can accept both analog and digital inputs. Delays and phases can be measured accurately using this instrument. A noise generator and a crystal oscillator with a 32-channel power splitter is used to couple the correlated signals into the receiver system (Fig. 2). It is also possible to feed a sub-harmonic frequency of the sampling clock directly to the digital system. This helps ensure that the digital section of the receiver is functioning without adding sampling noise of its own. In the spectral-line mode, such a signal results in a triangular-shaped autocorrelation function. This helps to check the delay shift-register chain. A Hewlett-Packard printer interface in the receiver system helps to check the status of the system instantly. An interference monitor to locate an interference-free band has also been designed. This works on the principle that the autocorrelation function of band-limited noise which is free of narrow band inteference is very small at large delays. A general-purpose astronomical clock (Udaya Shankar & Selvamani 1981) providing solar and sidereal times and Julian date has been incorporated in the receiver system.

4. Observational results

4.1 *Continuum Observations*

The results of the continuum observations are discussed in DU. The receiver and antenna performances are also detailed in that paper.

4.2 *Recombination-line Observations*

With the installation of the digital correlation receiver, confirmation of the presence of recombination lines of carbon in the direction of Cas A (Konovalenko & Sodin 1981; Anantharamaiah, Erickson & Radhakrishnan 1985) and a search for low-frequency recombination lines in the direction of Cyg A, Tau A and the Galactic centre were attempted. The S array was used for these observations, phasing it to the source declination. The S array has a smaller collecting area than the EW array. The observing time obtainable per day using the tracking facility of the EW array and making transit observations with the S array are comparable. However, the measurements made using the S array do not require the beam-flipping logic that is used for tracking the beam of the EW array and hence simplify the observations. The L.O. and sampling frequencies were chosen to have a harmonic relation to avoid any harmonic of the sampling frequency giving rise to an in band product (except at D.C.).

Between the two possibilities of observing a single spectral line with higher resolution or two spectral lines with lower resolution, the latter was preferred because

1. it gives a higher S/N and thus enables more rapid detection, and
2. interference can be ruled out beyond doubt if two spectral lines, one in the upper sideband and the other in the lower sideband can be detected simultaneously.

We were successful in detecting the C574α and C575α lines in the direction of Cas A. The observed spectra for an integration time of 860 minutes are shown in Fig. 10. We obtained a ratio of line-to-continuum temperature, T_L / T_C = 0.002, confirming the

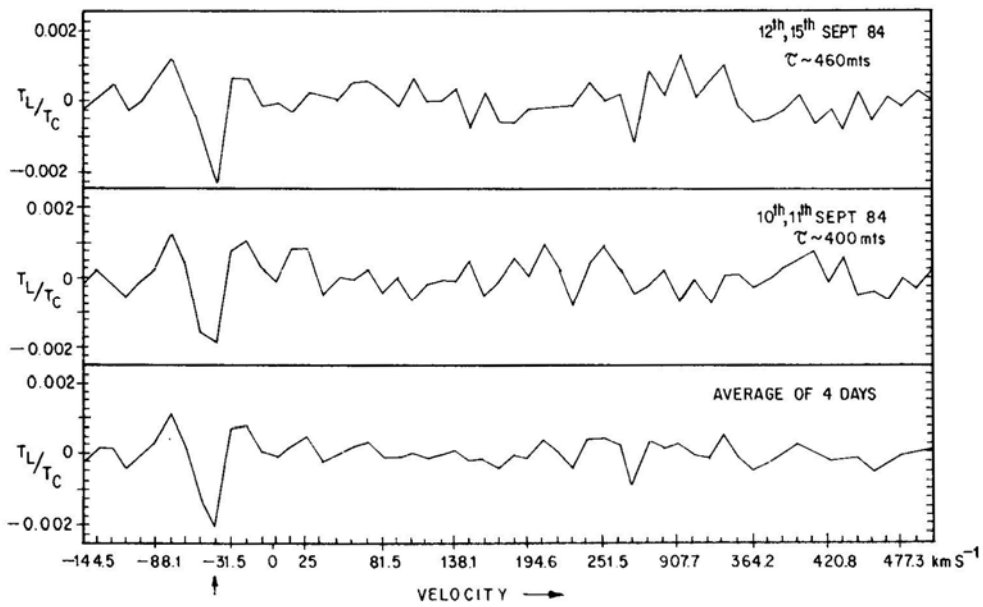

Figure 10. The summed profile of the carbon recombination lines C574α and C575α detected in the direction of Cas A at 44 km s^{-1}. Since the emission of Cas A dominates the system temperature, the optical depth (τ) is very close to the measured ratio of line-to-continuum temperature (T_L/ Tc).

results of the earlier observations. No line with $T_L / T_C \geqslant 0.002$ was detected in the direction of Cyg A for a similar integration time. The observations of Tau A and the Galactic centre were partly corrupted by interference and no lines were detectable.

5. Conclusions

The digital correlation receiver we describe has, made the Gauribidanur telescope a versatile instrument for decametre-wave observations. The receiver uses one-bit correlators for measuring visibilities. A new scheme for measuring the amplitude Information of the signal using one-bit correlators, plus the inclusion of the zero spacing in the synthesis, has enabled us to measure the total sky brightness. The receiver uses a DSB system. A new method of obtaining the quadrature samples of signals required for such a system has been developed. This technique requires less hardware than the conventional DSB technique and also achieves an improved system performance. The receiver offers the facility to correlate two unequal bandwidth signals in a one-bit correlator to maximize the interference-free observing time. On-board test equipment has made the instrument a standalone unit.

Using this system, a wide-field survey of the sky at 34.5 MHz has been completed. The system is capable of surveying the entire sky in a single day. It has opened up the possibility of detecting pulsar signals which are highly dispersed (even for DM ~ 35 cm^{-3} pc) at low radio frequencies.

The spectral-line receiver uses a conventional DSB technique. This measures spectral-line temperatures without any conventional switching. This receiver can serve as a prototype for a bigger system which can be used to survey low-frequency recombination lines.

Acknowledgements

We thank A. A. Deshpande, R. Nityananda, V. Radhakrishnan, D. K. Ravindra, and Ch. V. Sastry for their contributions throughout the project and for the many useful discussions we had with them. We thank G. Jayakumar who wired the entire system very neatly but for which the system would not have worked. K. S. Dwarakanath's inspiring presence and hard work was responsible for weeding out bugs in the system and making it astronomically productive. We also thank H. A. Ashwathappa, C. N. Nanje Gowda and G. N. Rajasekhar for all their help in setting up the antenna system. We also thank C. J. Salter for his valuable suggestions which have helped to improve the clarity and readability of this paper.

References

Anantharamiah, K. R., Erickson, W. C, Radhakrishnan, V. 1985, *Nature,* **315**, 647.

Bowers, F. K., Klingler, R. J. 1974, *Astr. Astrophys. SuppL,* **15**, 373.

Deshpande, A. A. 1987, *PhD Thesis,* Dept Electrical Eng., Indian Institute of Technology, Bombay, India.

Deshpande, A. A., Shevgaonkar, R. K, Sastry, Ch. V. 1989, *J. IETE,* **35**, 342.

Dwarakanath, K. S., Shevgaonkar, R. K., Sastry, Ch. V.1982, *J. Astrophys. Astr.,* **3**,207.

Dwarakanath, K. S., Udaya Shankar, N. 1990, *J. Astrophys. Astr.,* **11**, 323 (DU).
Fomalont, E. B., Wright, M. C. H. 1974, in *Galactic and Extragalactic Radio Astronomy,* Ed. G. L. Vrschuur & K. I. Kellermann, Springer-Verlag, New York.
Konovalenko, A. A., Sodin, L. G. 1981, *Nature,* **294**, 135.
Radhakrishnan, V., Brooks, J. W., Goss, W. M., Murray, J. D., Schwarz, U. J. 1972, *Astrophys. J. Suppl* 24, 1.
Ravindra, D. K. 1983, *PhD Thesis,* Dept. of Electrical Eng., Indian Institute of Science, Bangalore, India.
Read, R. B. 1963, *Astrophys. J.,* **138**, 1.
Sastry, Ch. V. 1989, *Indian J. Pure & Appl Phys.,* **27,** 331.
Thompson, R. A., Moran, J. M., Swenson Jr., G. W. 1986, *Interferometry and Synthesis in Radio Astronomy,* John Wiley, New York.
Udaya Shankar, N. 1986, PAD *Thesis,* Dept. of Physics, Bangalore Univ.
Udaya Shankar, N., Selvamani, M. 1981, *J. IETE,* **27**, 514.
van Vleck, J. H., Middleton, D. 1966, *Proc. IEEE,* **54**, 2.
Weinreb, S. 1963, *PhD Thesis,* Technical Report No. 412, MIT Research Lab. of Electronics, Boston, U.S.A.

J. Astrophys. Astr. (1990) **11**, 311–322

A Modified Algorithm for CLEANing Wide-Field Maps with Extended Structures

K. S. Dwarakanath, A. A. Deshpande & N. Udaya Shankar *Raman Research institute, Bangalore 560080*

Received 1990 April 5; accepted 1990 May 29

Abstract. A simple but effective modification to the conventional CLEAN algorithm is suggested. This modification ensures both stability and speed when CLEAN is applied to maps containing a mixture of point sources and extended structures. The method has been successfully applied to the recently-completed sky survey at 34.5 MHz (Dwarakanath & Udaya Shankar 1990). This survey was made using the Gauribidanur T array (GEETEE)[1] in 1-D aperture synthesis mode. Since in this case the 'dirty beam' (point spread function) cannot be directly computed, a method to obtain this is discussed in detail. The results of this deconvolution procedure have been encouraging in terms of reduced computing time and improved dynamic range in our maps. This algorithm should find wider application in deconvolving maps which have both extended structures and point sources.

Key words: CLEAN—wide-field map—extended structures—point spread function

1. Introduction

A wide-field synthesis map of the sky at 34.5 MHz has been completed recently by Dwarakanath & Udaya Shankar (1990; DU). In synthesis mapping, some form of deconvolution method is invariably employed to obtain high dynamic range. The conventional CLEAN algorithm (Högbom 1974; Schwarz 1978) is one of the most successful deconvolution methods when the angular extents of sources are not too large compared with the size of the synthesized beam. However, the conventional CLEAN is not particularly well-suited to applications at low radio frequencies, where large-angular-scale Galactic background emission dominates. A number of modified versions of CLEAN (Cornwell 1983; Steer, Dewdney & Ito 1984; Wakker & Schwarz 1988) have been suggested to treat situations where the performance of the conventional CLEAN is not satisfactory. However, in the present case, one is dealing for the first time with wide-field maps ($-50° \leqslant \delta \leqslant +70°$ and all the 24 hours of α) for which it is desired to compensate for the artefacts produced by the sharp cutoff in the aperture coverage without degrading the angular resolution ($26' \times 42'$ sec (δ—14°. 1)). Unfortunately, the existing procedures do not fulfil our requirements.

[1] This telescope is jointly operated by the Indian Institute of Astrophysics, Bangalore & the Raman Research Institute, Bangalore.

In this paper, we first describe the 34.5-MHz survey (Section 2) and then discuss the difficulties (Section 3) in using the existing deconvolution techniques when dealing with wide-field maps such as result from the survey. In Section 4, we present a modification to the conventional CLEAN algorithm which effectively applies the CLEAN process only to source structures comparable in size to the resolution of the dirty beam. This aspect makes our modified CLEAN a stable algorithm, even with large loop gains which increase considerably the speed of operation. In Section 5, we detail the procedure adopted to generate a point spread function (PSF or dirty beam). Its use in the modified algorithm to CLEAN the wide-field maps is discussed in Section 6.

2. The survey

The celestial brightness distribution, $B(l, m)$, is a function of the direction cosines(l, m) and is related to the visibility $V(u, v)$ through the Fourier transform relation:

$$B(l, m) = \iint V(u, v) e^{-j2\pi(ul+vm)} \mathrm{d}u\, \mathrm{d}v. \quad (1)$$

The dirty map, $B'(l_0, m_0)$, at any position in the sky is the convolution of the brightness distribution with the antenna response $P(l, m)$:

$$B'(l_0, m_0) = \iint P(l-l_0, m-m_0)\, B(l, m)\, \mathrm{d}\Omega \quad (2)$$

(Christiansen & Högbom 1985).

The procedure for obtaining the dirty map is discussed in detail by DU.

Using the Gauribidanur telescope (GEETEE) in the transit mode, the visibilities corresponding to the 88 baselines which the East-West (EW) array forms with the rows of the South (S) array are recorded continuously. Assuming Hermitian symmetry (see the discussion concerning 'Tee', and 'Cross' arrays in Christiansen & Högbom 1985) a 1024-point one-dimensional FFT is performed on each set of 88 complex visibilities (resulting from an integration of 24 s) to obtain a strip of dirty map that contains the entire observable sky in the NS direction along the meridian. Successive strips are obtained from successive integrations. The Fourier transform produces dirty maps in the m= sin(zenith angle) coordinate. The 1024 points are uniformly spaced in m and correspond to sufficiently fine sampling of the observed distribution in declination. Since the successive baselines are separated by 5 m and the wavelength is 8.69 m, the FFT produces maps in the range of –0.869 to +0.869 in m. The dirty maps are produced in sizes of 1 hr × full range of m for all 24 hours of Right Ascension.

We emphasize that the antenna response in the NS direction is shift-invariant when expressed in sin(zenith angle) coordinates (neglecting the effects of bandwidth decorrelation). Use of this property simplifies the CLEAN procedure.

3. Problems with existing deconvolution procedures

The dirty map is the convolution of the celestial brightness distribution with the antenna response (Equation 2). Unfortunately, the antenna response ('dirty beam' or

'point spread function (PSF)') has undesirable features, *viz.* sidelobes, if the corresponding aperture has any sharp cut-offs. It is desirable to obtain the brightness distribution of the sky corresponding to an antenna whose response is free of such sidelobes but has a similar resolution to that of the true response. Hence, to obtain the brightness distribution in the sky, the observed distribution (the 'dirty map') has to be deconvolved (CLEANed) for the dirty beam and the derived CLEAN components are convolved by a 'clean' (usually Gaussian) beam. To achieve this a two-dimensional CLEAN of the dirty maps can be made. However, we will first examine some simpler algorithms, as these are likely to be computationally more efficient. There are many methods of deconvolution/convolution that may be considered. We discuss some of them here and examine the problems in adopting them for the present survey.

3.1 *Two 1-D CLEAN or Convolution*

Given the dirty beams along hour angle and dec., it is possible to adopt CLEAN (Högbom 1974) or its variant (discussed in Section 4) to deconvolve the dirty maps. However, in our case this procedure cannot be used due to the complex nature of the beams along hour angle and dec, unless CLEAN is performed with complex dirty beams on the complex dirty map. This was not pursued further due to this 'complex' nature.

Methods of deconvolution exist to reduce the sidelobe levels of the dirty beam at the expense of resolution. Despite this loss of resolution, these methods are sometimes used due to their computational ease and efficiency. In our case, this advantage does not exist due to the complexities just mentioned.

3.2 *Difficulties with the Conventional 2-D CLEANs*

In the conventional method of CLEANing maps (Högbom 1974), successive maxima are located in the dirty map and at each stage a scaled version of the dirty beam placed at the location of the maximum is subtracted. The scale depends on the height of the maximum and the fraction of the dirty beam to be subtracted called the loop gain (typically 0.2). Each time a maximum is located, a delta function whose height equals the fraction of the maximum that has been subtracted is placed at the position of the maximum in a separate 'CLEAN map'. This procedure is repeated until a predetermined level is reached in the residual dirty map (usually 5 times the r m.s. value of noise). At this stage, the CLEAN components are convolved with a well-behaved (or CLEAN) beam, usually a Gaussian whose full-width-half-maximum equals that of the dirty beam. Finally, this distribution is added to the map of the residuals. The implicit assumption in this method is that the sky is empty except for point sources. In addition, the 'emptiness' is a function of the sidelobe level in the dirty beam (Schwarz 1978). In the present case, the dirty map contains both point sources and the Galactic background emission. In addition, the background level varies over the region being CLEANed. This poses problems if one uses CLEAN in its original form. Consider a case such as that shown in Fig. 1 where three sources A, B and C appear against a background. The source A has a height of $A_{\max}$ above zero while its height above the local background is only $A'_{\max}$ Conventional CLEAN will pick up $A_{\max}$ and proceed. It

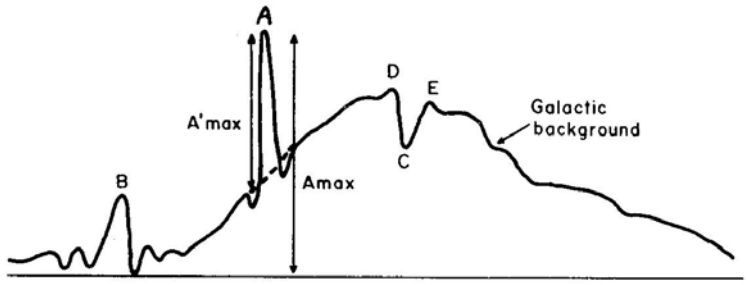

Figure 1. This illustrates the problems in CLEANing maps which contain both point sources and absorptions in the presence of a varying background. The sidelobe level in the map due to source A corresponds to a height A'_{max} and not to A_{max}. It will take considerable time before the dirty map can be deconvolved for responses from sources such as B since the background level is higher than the source height. In addition, discrete absorptions such as C will not be CLEANed—instead, the side lobes at D and E will be treated as sources. The present modification to the conventional CLEAN takes care of all of these problems.

may be seen, however, that the sidelobes due to A do not correspond to A_{max} but to $A'_{max.}$ In order not to oversubtract the source response, a very small loop gain could be used. However, this slows down the CLEAN process considerably. In addition, if the background were to vary over the region being CLEANed, it would take much longer before CLEAN can deconvolve the responses from sources like B or from absorptions like C (Fig. 1). Meanwhile, the algorithm would have selected maxima that represent the variations in the background and carried out the process of CLEAN on these. This is not a desirable situation.

There have been earlier attempts to take account of extended structures while CLEANing. For example, Wakker & Schwarz (1988) have proposed a Multi Resolution CLEAN (MRC). In this algorithm, the dirty map is smoothed to a lower resolution and subtracted from the original dirty map. Thus one produces a 'smooth map' and a 'difference map'. The dirty beams corresponding to these two maps are also generated and CLEAN applied to both maps separately. This makes the algorithm faster than the conventional CLEAN. However, in wide-field maps such as ours, where extended structures have varying angular scales, it is necessary to consider a 'Multi-Resolution' approach rather than a Double-Resolution' approach. This makes the MRC algorithm complicated. Further, if the extended structures in the map have widely different angular dimensions in a and b in different portions of the map *(e. g.* the Galactic plane emission), then it is not clear to us whether such an algorithm would be useful. It would have been possible to incorporate the Clark (1980) approach to CLEAN to enhance the speed of either MRC or conventional CLEAN (with very low loop gain) if we had a limited declination coverage. In the absence of such a situation, the speed enhancement due to Clark CLEAN is not obvious. For the same reason, the algorithm proposed by Steer, Dewdney & Ito (1984) may not be very helpful in our case.

4. Modified CLEAN

To make the basic CLEAN algorithm work satisfactorily in the presence of extended structures, we have introduced a simple modification. Instead of locating the maxima

in the dirty map (as with the conventional CLEAN and the MRC), we locate the maxima in the absolute value of the 'difference'. The 'difference' at any given point in the dirty map is obtained by subtracting from its value the average value in the map one resolution away. Using this procedure, the more slowly-varying background is essentially not deconvolved by the algorithm, but all sources with sizes of the order of the beam are CLEANed, including absorption features (*e.g.* feature *C* in Fig. 1) which are quite common at low frequencies. In addition, by not modifying the background, this procedure converges rapidly and a uniform level of CLEANing can be achieved over the region. However, for any deconvolution procedure, the PSF is an essential input (Section 5). Given the PSF, deconvolution can be achieved using the modified CLEAN. This procedure has been successfully applied in CLEANing our maps. Even with a loop gain of 0.5 (usually considered high) we had no difficulty with convergence. Compared to the conventional CLEAN, in regions where there is no significant variations in the background, this algorithm gave a reduction in processing time of at least a factor of three (due largely to the larger loop gain). We believe that the increase in speed using this algorithm is substantially larger than three for regions having significant contribution from extended structures.

5. Generation of the point spread function

The PSF required is the antenna response to a celestial point source. When visibilities at different spatial frequencies (u, v) have been measured, the PSF can be obtained directly from the u, v distribution (often graded by some weighting function) through a 2-D Fourier transform. However, in the present case where we use 1-D image synthesis, we can obtain only limited information about the PSF. To obtain the complete information, we need to know the complex weighting function over the EW array and therefore this needs to be measured accurately. In this connection, we note that the dirty map around a point source will be the PSF if the source is extremely strong and there exists a sufficiently wide field around the source which can be considered essentially empty. At low radio frequencies, due to the ubiquitious Galactic background, this situation does not occur. Though sources like Cas A and Cyg A are very strong compared to the noise in the map, the criterion of an empty field around them is not satisfied.

5.1 *The Complex Nature of the Antenna Response*

Since the telescope is used in the correlation mode (*i.e.* $EW \times S$) and the two arrays are expected to be uniformly illuminated, it is tempting to suggest that the PSF is simply the product of two $\sin(x)/x$ functions, one along hour angle and the other along declination. However, this does not give us the true PSF for two reasons. Firstly, the hour-angle beam departs from the $\sin(x)/x$ function significantly due to the fact that the actual illumination pattern of the *EW* array is not completely uniform. Secondly, the hour-angle beam is in general complex since the corresponding complex illumination pattern is unlikely be Hermitian symmetric.

Given these problems, one may generate the point spread function by measuring the antenna response to a strong source along hour angle (at the source δ) and along

declination (at the α of the source) and multiplying them. This should be a reasonable approach since in the correlation mode one produces the 2-D response by multiplying the response of the individual telescopes.

5.2 *Generating the PSF*

For a simple multiplying system, the antenna response, b, to a point source at (l_0, m_0) can be written as

$$b(l-l_0, m-m_0)=b_{EW}\,(l-l_0, m-m_0)\,b_{NS}(l-l_0, m-m_0), \tag{3}$$

where b_{EW} and b_{NS} refer to the far-field voltage radiation patterns of the *EW* and the *S* arrays respectively. Since the *EW* and the *S* arrays have slowly-varying patterns along *NS* and *EW* (*i.e* . along *m* and *l*) respectively, this can be approximated to

$$b(l-l_0, m-m_0)=b_{EW}\,(l-l_0, m_0)\,b_{NS}\,(l_0, m-m_0). \tag{4}$$

Both b_{EW} and b_{NS} are in general complex and

$$b_{NS}\,(l_0, m-m_0)=\frac{1}{2}C_1+\sum_{n=2}^{88}(C_n+jS_n)\,e^{j\phi n}, \tag{5}$$

where, C_n and S_n are the cosine and sine correlations obtained using the nth unit of the S array. (ϕ_n=2π(n— 1)d(sin(θ)— sin(θ_0,))/λ, m= sin (θ), and m_0 = sin(θ_0).

In the GEETEE synthesis system, the dirty map at any instant is a summation of Equation (4) and its complex conjugate. Here one assumes Hermitian symmetry to fill in the corresponding unmeasured visibilities. Hence the PSF is generated by obtaining the b_{EW} and b_{NS} from a point source response and obtaining the real part of the product.

5.3 *Producing the PSF in Practice*

There are several points to be borne in mind in constructing the PSF according to the above recipe:

1) Ideally one should use a strong source at the zenith on a flat background with no significant confusing sources. In such a case the response of the source will reflect any north-south asymmetries in the antenna behaviour. The closest approach to this requirement is Cygnus-A, with a flux density of ≈ 25000 Jy and a zenith angle of 26°. Using the calibrated visibilities around the Cygnus-A position, the complex responses in hour angle and declination (b_{EW}, $b_{NS)}$ were obtained.

2) The basic criterion in choosing the extent (in hour angle and declination) of the PSF is that the expected antenna response for Cygnus A should be well above noise on the map. Along declination this is true over the full extent of the map and the natural size for the PSF along *NS* is – 0.86 <m <0.86. In hour angle, the sidelobes of Cygnus A can be seen up to ± 3 hr from transit. However, for hour angles > ± 1 hr the curvature of the sidelobes (due to the apparent zenith angle change as a function of hour angle) becomes significant and there is no point in going beyond this extent (see Fig. 2 for a schematic illustration of this effect). In theory, this problem can be overcome by generating a PSF which takes into account the change in the apparent zenith angle of a

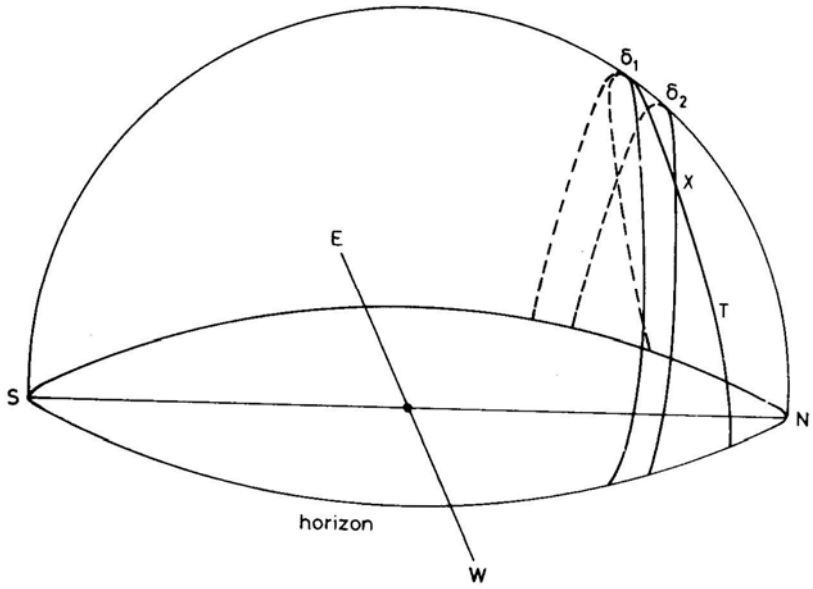

Figure 2. This illustrates the origin of the curved hour angle sidelobes. The response of the array will be in a plane perpendicular to the horizon corresponding to two declinations d1 and δ_2 at transit. A source at dec. δ_1 moves in a track (T) tilted at an angle to these. This angle is equal to the latitude of the array. Thus, at an hour angle corresponding to X, the response of the array to the source will be at δ_2

source as a function of its declination and hour angle. This was not done. Instead, the extent of the complex beam along hour angle was restricted to ± 1 hour to minimize this effect. Of course, the truncation of the PSF along hour angle may affect the dynamic range of the map outside the CLEANed region.

3) The Galactic background also contributes to the estimation of the PSF. One can investigate which baselines are sensitive to the background by looking at the visibility amplitudes as a function of baseline when there is no strong source in the *EW* beam. This exercise reveals a monotonic decrease in the visibility amplitude from the first to the seventh baseline. The contribution of the background drops well below noise for the longer baselines. To minimise the effects of the background in the generation of the PSF, the measured visibilities in the first *seven* baselines were replaced by suitably extrapolated values.

4) If our estimates of b_{EW} and b_{NS} are affected by ionospheric scintillations then these will affect the derived PSF. To minimise the effects of scintillation, the complex beam along hour angle has been convolved with a $\sin(x)/x$ function of resolution 100 s (the *E W* resolution of the antenna at $\delta = 0°$) in hour angle. This filters out most of the amplitude scintillations as their time scales are usually shorter than 100 s, but does not affect the resolution of the map.

5) When generating the PSF using Cygnus A, the measured visibilities were corrected for the bandwidth decorrelation at its zenith angle.

6) The implicit assumption in generating the PSF by the multiplication of the complex beams along hour angle and δ is that no other sources have contaminated this estimate. We believe this to be reasonable in the present case.

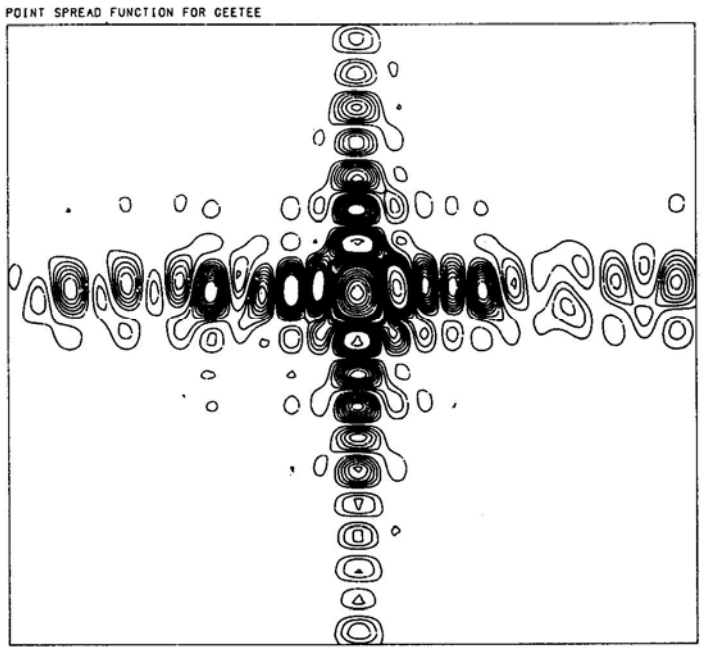

Figure 3. A small section (≈10 sq. deg.) of the Point Spread Function which was used for CLEANing. The PSF was derived from Cygnus A. Contours down to the 1% level of the peak have been plotted. The contour interval down to 30% of the peak is in steps of 10%. Between +30% and + 10% as also between –30% and – 10%, the interval is 5%. Upto ±10% of the peak value, the interval is 1%. Successive side-lobes have opposing signs. The four sidelobes surrounding the peak are each – 21% of the peak.

7) Interference could also affect the complex beams. An examination of the map around Cygnus A showed no noticeable effects from interference.

Fig. 3 shows a two-dimensional representation of the PSF derived from Cygnus A.

6. CLEANing in practice

Fig. 4 presents a flow chart for the algorithm used in CLEANing our maps. The individual dirty maps have a size of 1 hr × entire zenith-angle range. Since the PSF has an extent of $\pm$ 1 hr, we have to have the adjacent maps present to CLEAN the central hour. If the dirty map has non-astronomical features in it, CLEAN can oscillate. To prevent this, the raw data were prefiltered to remove all such features. To achieve this, the raw data were convolved along α with a $\sin(x)/x$ function of resolution ≈100s as described above. This filters out all features sharper than the beam at $\delta = 0°$, although it leaves some at higher declinations. This cannot be avoided without losing resolution. There is no need for smoothing in declination since it is the direction of synthesis.

The PSF covers the entire zenith angle range. The PSF resolution along *NS* does not change with its position in declination since both the PSF and the dirty maps are generated in the *m*. coordinate. However, the PSF will have to be expanded or contracted along hour angle depending on the declination of the source. In any run of

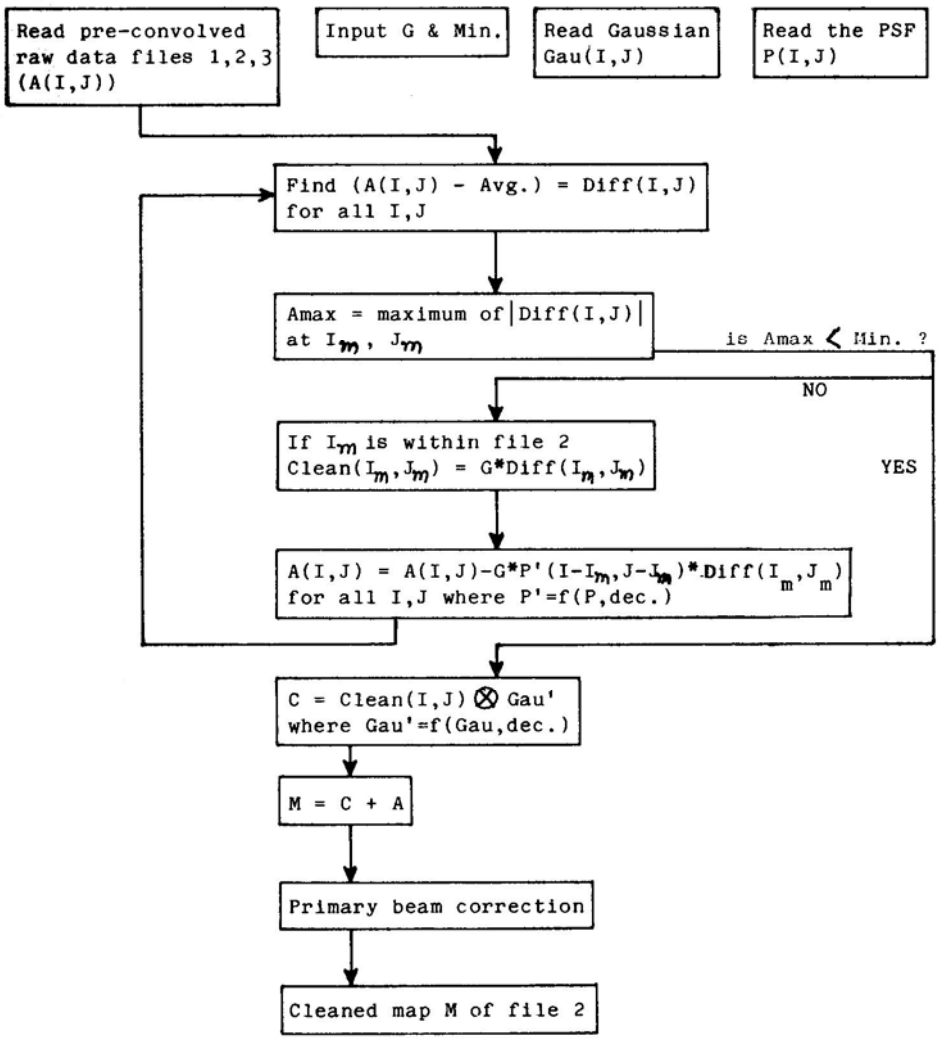

Figure 4. The modified CLEAN algorithm used to deconvolve the maps from the 34.5-MHz survey (DU) which contain both point sources and extended emission.

the program, only the central map of the three read in gets CLEANed and restored. The beam response due to any source in the three hour stretch (say, hours 1,2,3) is removed but CLEAN components are written only if the source is located within the central hour. This guarantees that the central hour is CLEANed of the sidelobes of all sources located within an hour of it. Along *NS*, the edges of the map in *N* and *S* are treated as though they are connected to each other. Thus, when the extent of the PSF overshoots any one edge, it continues on to the map from the other edge. In this sense CLEANing is performed as though the map was on a cylinder, with the *NS* extent equal to the circumference of the cylinder. At the end of the run, the middle hour (in this case, hour 2) will be CLEANed. The next run can take dirty maps 2,3,4 and so on. The CLEAN components are convolved with a Gaussian whose integral and full

widths at half maximum in the two perpendicular directions are equal to those of the PSF and then added to the map of residuals to obtain the final map.

It was possible to CLEAN the whole observed sky down to an almost uniform level of 5σ, where σ is the r.m.s. fluctuation in the dirty map.

The rows of dipoles in the South array are spaced 5 m apart while the wavelength of observation is 8.70 m. Hence, there is a grating response of beyond zenith angle θ, where,

$$\sin(\theta) = \frac{\lambda}{d} + \sin(\theta_0) \tag{6}$$

with d = 5 m, λ = 8.70 m and θ_0 = the zenith angle that is aliased with θ. Thus, a grating lobe appears at $\theta_0 = \mp 90°$ when the main beam is at $\theta = \pm 47°$, while at $\theta = \pm 60°$, the two responses are equal. However, for a very large fraction of the sky, we feel that the deconvolution procedure given here has brought out all the relevant features and removed the artefacts to a satisfactory extent.

Fig. 5 shows a dirty map of 1 hr × 15° in extent observed in this survey. We present in fig. 6 the CLEANed map of the same region. A weak source which is buried in the

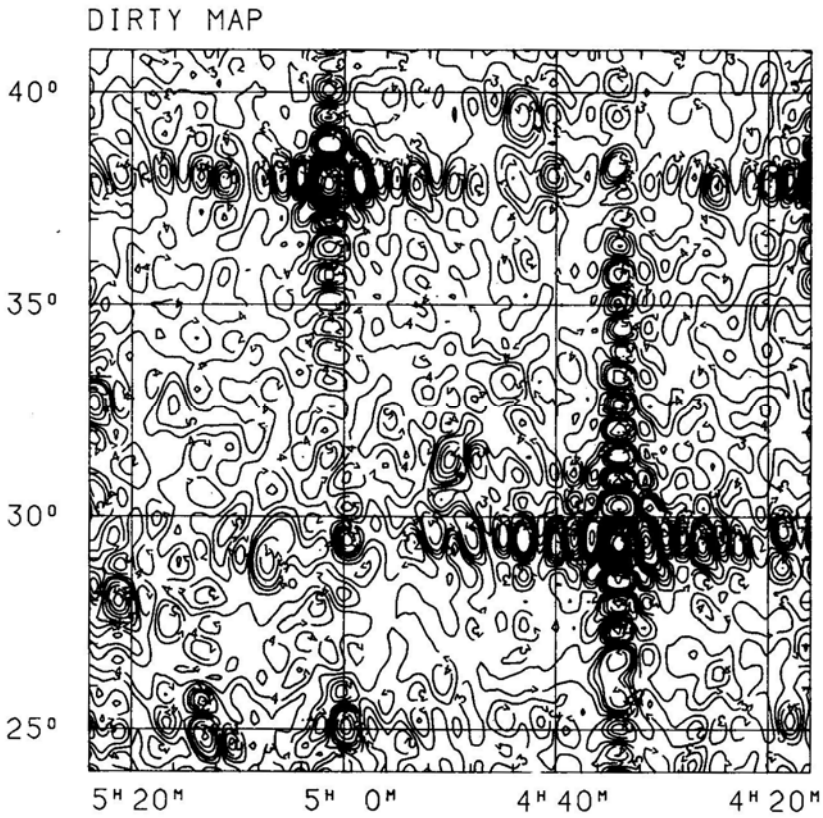

Figure 5. Dirty map of 1 hr × 15° in extent observed in the present survey. The two strong sources 3C 123 (α =04h34m; δ = 29°23′) and 3C 134 (α = 05h01m; δ = 37°51′) and their sidelobes are clearly seen.

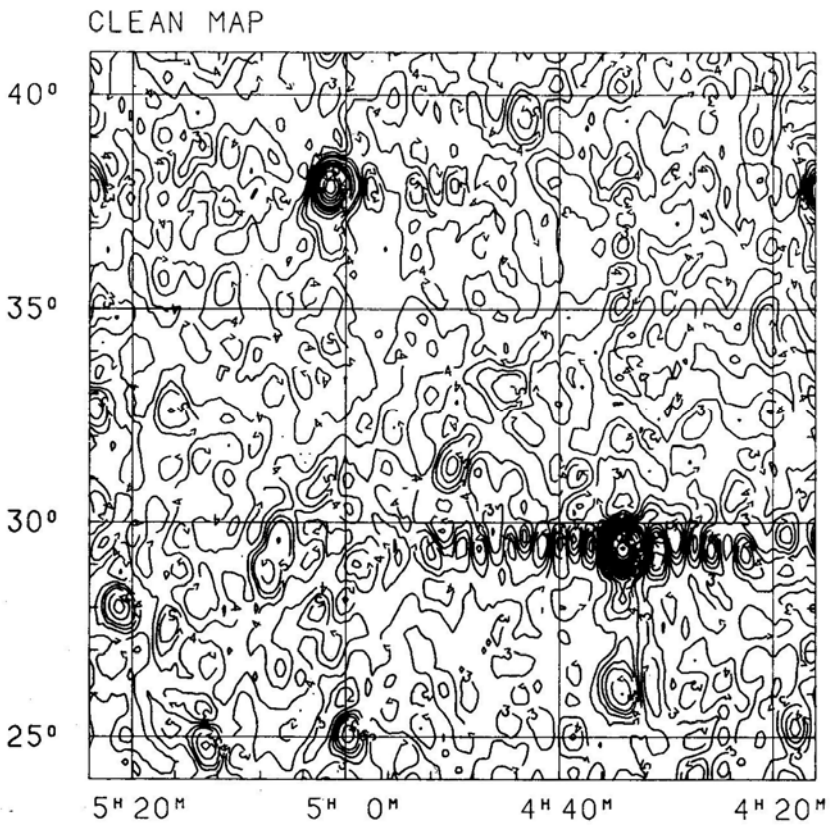

Figure 6. CLEANed map of the region shown in Fig. 5 obtained through the algorithm indicated in Fig. 4. Note that a weak source (α=04^h 34^m; δ = 26°04′) which was buried in the sidelobes of 3C 123 (Fig. 5) is clearly seen here.

sidelobes of 3C123 (α = 04^{h}34^m; δ = 29°23′) can be easily seen in the CLEANed map. However, there were some complications near strong sources like Tau A, Vir A, Cas A and Cyg A. Since the PSF extent was only ± 1 hr, sidelobes beyond ± 1 hr from a source cannot be CLEANed. So, when CLEANing any region, a strong source may not be in the field of analysis but the far off sidelobes from such a source could be. To avoid picking up such sidelobes as sources, these regions are flagged beforehand. While the sidelobes remain as they are in the final map, they will be restricted to a narrow range of declination around the source, albeit with a wider range in α.

7. Discussion

The simple modification to the conventional CLEAN proposed here makes the deconvolution algorithm both stable and faster. A method for estimating the PSF reliably from the observed visibilities has been described. These procedures have improved the dynamic range of the maps presented by DU to an estimated > 20 dB. It was not possible to achieve further improvement due to the limitations imposed by the ionosphere and other factors discussed below:

The residual sidelobes seen in the maps of DU are mainly due to the departure of the antenna response (at different α and zenith angles) from the PSF used for CLEANing These differences are due to changing ionospheric phase perturbations (and amplitude scintillations) as well as due to the changes in the antenna response at different times and zenith angles. Some of the residual sidelobes are due to the following systematic effects: uncompensated bandwidth decorrelation that is significant at large zenith angles, neglecting the curvature of the side lobes in hour angle and limiting the extent of the PSF in hour angle.

Since the final maps were obtained after correcting for the primary-beam gain in zenith angle, the level of the residual sidelobes will be exagerrated at large zenith angles.

All the above effects are easily noticeable for stronger sources, *e.g.* Cas A. Considerable improvements might be possible here if CLEANing were to be performed taking care of the curvature of the sidelobes in a and by correcting for the bandwidth decorrelation.

We believe that our modified CLEAN can be used (with a reliable estimate of the PSF) as a stable, rapid algorithm to deconvolve maps which contain both point sources and extended emission. We note that in our observations there were no 'holes' in the aperture and the purpose of CLEAN was only to remove the undesired sidelobe responses due to the uniform weighting of the aperture. It was not desirable to CLEAN the extended structures. If there are missing short spacings, the conventional CLEAN is expected to fill these in to some extent. It will be interesting to see how the modified CLEAN behaves under such circumstances.

Acknowledgements

We thank R. Nityananda for useful discussions during data analysis and for his many valuable suggestions which contributed significantly to the present work. We thank C. J. Salter for his valuable suggestions which have helped to improve the clarity and readability of this paper.

References

Christiansen, W. N., Högbom, J. A. 1985. *Radiotelescopes*, Cambridge Univ. Press.
Cornwell, T. J. 1983, *Astr. Astrophys*., **121,** 281.
Clark, **B.** G. 1980, *Astr. Astrophys*., **89,** 377.
Dwarakanath, K. S., Udaya Shankar, N. 1990, *J. Astrophys. Astr*., **11,** 323 (DU).
Högbom, J. A. 1974, *Astr. Astrophys. Suppl*., **15,** 417.
Schwarz, U. J. 1978, *Astr. Astrophys*., **65,** 345.
Steer, D. G., Dewdney, P. E., Ito, **M. R.** 1984, *Astr. Astrophys*., **137,** 159.
Wakker, B. P., Schwarz, U. J. 1988, *Astr. Astrophys*., **200,** 312.

J. Astrophys. Astr. (1990) **11,** 323–410

A Synthesis Map of the Sky at 34.5 MHz

K. S. Dwarakanath & N. Udaya Shankar *Raman Research Institute, Bangalore 560080*

Received 1990 March 17; accepted 1990 May 29

Abstract. This paper describes a wide-field survey made at 34.5 MHz using GEETEE,[1] the low frequency telescope at Gauribidanur (latitude 13°36′12″N). This telescope was used in the transit mode and by performing 1-D synthesis along the north-south direction the entire observable sky was mapped in a single day. This minimized the problems that hinder wide-field low-frequency mapping. This survey covers the declination range of – 50° to + 70° (– 33° to +61° without aliasing) and the complete 24 hours of right ascension. The synthesized beam has a resolution of 26′ × 42′ sec (δ – 14°.1). The sensitivity of the survey is 5 Jy/beam (1σ). Special care has been taken to ensure that the antenna responds to all angular scale structures and is suitable for studies of both point sources and extended objects.

Key words: radio continuum—synthesis mapping—wide-field—low-frequency.

1. Introduction

There have been many attempts to map large regions of the sky at decametric wavelengths. As early as 1960, Shain, Komesaroff & Higgins (1961) mapped a part of the Galactic plane at 19.7 MHz with 1°.4 resolution using a Mills Cross antenna. Soon afterwards, Williams, Kenderdine & Baldwin (1966) at Cambridge used the aperture synthesis technique to map the northern sky at 38 MHz with a resolution of 0°.7. In Table 1, we have summarized some of the mapping observations made at low frequencies. These surveys revealed several interesting phenomena, such as the turnovers in the spectra of supernova remnants due to absorption of the radiation in the intervening gas (Kassim 1989), and H it regions appearing in absorption against the more intense Galactic nonthermal background (Jones & Finlay 1974). Analyses of these observations have been rewarding and complement the studies made at metric and decimetric wavelengths. Such studies have thrown light on the distribution of thermal gas in the Galactic plane, the haloes around galaxies, *etc.* In addition, they played a vital role in the discovery of the first millisecond pulsar, which can be traced to the discovery of a very-steep-spectrum point source at low frequencies (Erickson 1983).

Notwithstanding these efforts, there is a need for a wide-field survey such as we present here. A low-frequency map of the Galactic background combined with a

[1] This telescope is jointly operated by the Indian Institute of Astrophysics, Bangalore and the Roman Research Institute, Bangalore.

Table 1. Some of the mapping observations made at low frequencies.

Freq. (MHz)	Size	Observatory	Resol. (deg.)	Coverage	Reference
19.7	'+' Array 1.6 km EW 1.6 km NS	C.S.I.R.O.	1.4	$224° < l < 16°$ $-6° < b < +6°$	Shain, Komesaroff & Higgins (1961)
38	Array 1 km EW Movable NS	Cambridge	0.75	$-10° < \delta < +90°$ 24 Hr in RA	Williams, Kenderdine & Baldwin (1966)
29.9	Array 1 km EW Movable NS	Fleurs, NSW	0.8	$225° < l < 30°$ $-10° < b < +10°$	Jones & Finlay (1974)
10	'T' Array 1.2 km EW 0.7 km NS	Penticton	2.0	$-5° < \delta < +71°$ 24 Hr in RA	Caswell (1976)
30.9	'T' Array 3 km EW 1.8 km NS	Clark Lake	0.2	$350° < l < 250°$ $-3° < b < +3°$	Kassim (1988)
30	Single dish 210 ft.	Parkes	11	$-90° < \delta < 0°$ 24 Hr in RA	Mathewson, Broten and Cole (1965)
38	Single dish 250 ft.	Jodrell	8	$-25° < \delta < +70°$ 24 Hr in RA	Milogradov-Turin and Smith (1973)

higher-frequency survey of comparable resolution, such as that at 408 MHz by Haslam *et al.* (1982), can yield useful spectral information. A detailed map of the sky can reveal not only the well-studied H II regions in the Galactic plane, but also those at higher latitudes. It is of interest to study these in the light of the results from the Infra-Red Astronomical Satellite (IRAS). The present low-frequency survey with its wide, uniform coverage is also a useful data base to investigate a number of problems pertaining to the distribution of extragalactic sources. In addition, it can be used to look for very-steep-spectrum sources which could represent millisecond pulsars.

Some of the problems that have plagued wide-field low-frequency mapping are those involved in the construction and maintenance of the large arrays needed to achieve even moderate resolutions, compounded with difficulties due to the ionosphere and terrestrial interference. In the present survey an attempt has been made to minimise these problems by choosing an appropriate time and mode for the observations.

In this paper, Section 2 describes the observations, along with the main features of the telescope. The methods of data analysis and calibration are described in Section 3, which also contains a discussion of the flux-density scale at 34.5 MHz. The final section contains the results of the survey in the form of contour maps covering almost the entire sky observable from Gauribidanur. This section also discusses the noise in these maps.

2. Observations

A detailed description of the telescope used for the observations is to be found in Udaya Shankar (1986) and Dwarakanath (1989), as well in Udaya Shankar &

Ravishankar (1990; UR). Below, we outline some of the salient features of the antenna, receiver system and observations.

The telescope (GEETEE) is situated near Gauribidanur (longitude 77°26′07″ E; latitude 13°36′12″ N), about 80 km north of Bangalore, India. The antenna system is in the shape of the letter T and consists of 1000 dipoles with a 1.4-km long East-West (EW) arm and a 0.45-km long South (S) arm. The dipoles are aligned East-West and spaced 8.6 m apart in this direction. They accept linear polarization. The East-West array consists of four rows of dipoles spaced 5 m apart in the north-south direction and has a collecting area of ≈ 12,000 m^2. The south array consists of 90 rows, each containing four dipoles, placed 5 m apart along the NS direction. It has a collecting area of ≈ 7000 m^2. Since the spacing between the rows of the S array is 5 m, while the wavelength of operation is 8.7 m, the array has a grating response for zenith angles greater than ±47°, which becomes equal to the main beam response at a zenith angle of ± 60°.

The receiver system consists of 32 front ends with a 128-channel one-bit digital correlator. One-bit correlators measure the normalized correlation coefficient. The advantage of this system is that the measured visibilities are not critically dependent on the gains of the S-array amplifiers but are only affected by their bandshapes and noise temperatures. While the amplifier gains can vary with time (*e.g.* diurnal effects), the bandshapes and noise temperatures are more stable.

A novel method has been employed to obtain the amplitude information (UR) using a hardware scheme similar to that used in the one-bit correlators. However, here a threshold detector is used instead of a zero-cross detector. A suitable threshold value is that which is sensitive to the change in the area of the probability density function of the input signal. If ρ_a and ρ_c are the analog correlation and the normalised one-bit correlation coefficient respectively, then,

$$\rho_a = \sigma_1 \sigma_2 \operatorname{Sin}\left(\frac{\pi}{2}\rho_c\right) \tag{1}$$

where, σ_1 and σ_2 are the r.m.s. values of the signals being multiplied. In our case, these signals correspond to those from the EW array and from any row of the S array. Their amplitudes were continuously recorded to obtain σ_1 and σ_2.

The continuum observations made with GEETEE were meridian transit observations. When making the sky survey, we used only one of the four dipole rows in the EW array. Rows I and IV (numbering from the north) were considered inappropriate since they see a more asymmetric environment (see UR for a schematic of the array) and either rows II or III were better suited for our observations. In fact, the observations were carried out using dipole-row III in the EW array and the 88 southernmost rows in the S-array. The 88 visibilities corresponding to the various baselines which row III of the EW array forms with the individual rows of the S-array were measured. Time-division multiplexing with a cycle time of 1 s was adopted and at any instant only one out of each adjacent four rows in the S array was active. This meant that the same transmission line and front end could be used for each set of four rows in the S-array. The 88 complex visibilities were recorded continuously, except for an interval of 1 min in each hour when the output from a noise diode in the field replaced the EW antenna. The recording from the noise diode monitored the gain variations of the last stage amplifiers in the front end and the subsequent sections of the antenna system in the EW array both of which affect the measurement of σ_1. These variations were found to

be <0.6 per cent. A similar recording was made to keep track of the factors affecting the measurement of σ_2. In addition, at the beginning of each 24-hour observation, the output from the noise diode in the EW array was recorded for about 15–30 min. Since the rows of the S-array were contributing the sky noise at this time, which is uncorrelated with the noise diode output, the measured correlation coefficient gives the receiver offsets caused by biases in the zero-cross detectors, etc.

An important objective of the present survey was to map the Galactic background radiation and give the brightness temperature unambiguously at each point in the sky. This is possible if the antenna system responds to all angular-scale structures (larger than its resolution) in the sky. With this in view, we have included all spacings in our observations and, in particular, the zero spacing (UR). The visibility resulting from the multiplication of the signals from row III of the EW array with the S-array row in line with it (S_3) corresponds to the zero spacing. The noise due to the F.E.T. amplifier in S_3, which is common to both the EW array and S_3, contributes ≈ 500 K to the signal from the sky in this spacing. Since the brightness temperature of the sky near 30 MHz is ≳10,000 K, this leads to a small, correctable offset in the estimated brightness temperatures of the sky.

Observing conditions at Gauribidanur depend critically on solar activity. Non-solar astronomy is best performed during a solar minimum. The present observations were made during a period (last 15 days of January 1987) when the ionospheric disturbances were at a minimum and the interference was remarkably low. In principle, any single day is sufficient to produce an all-sky map. By observing for 15 days, it was possible to make a detailed check of the repeatability of the measurements.

Observations of strong point sources are the most sensitive way of judging both telescope performance and observing conditions. We used the following five sources as routine checks of the system: 3C144 (Tau A), 3C218 (Hydra A), 3C274 (Virgo A), 3C405 (Cygnus A) and 3C461 (Cas A). All of these are unresolved by GEETEE and are sufficiently strong to measure the visibility for each baseline. They cover a wide range of R.A. and Dec. and give an overall picture of telescope performance. The results of the checks made on these point sources imply the following:

(a) the amplitudes of the illumination patterns of the S-array rows repeat with an r m.s. of 1 per cent as estimated from the same source on two different days and with an r m.s. of 6 per cent as estimated from two different sources on the same day.

(b) the instrumental phases repeat with an r m.s. of 1° from day to day as determined from the same source and with an r.m.s. of 6° from source to source.

(c) the amplitude and phase distributions over the EW aperture show r m.s. deviations of 0.6 dB and 8° respectively.

3. **Data analysis and calibration**

3.1 *Producing the CLEANed Map*

The brightness distribution $B(l, m)$ of the sky is related to the visibility $V(u, v)$ through the Fourier transform relation:

$$B(l, m) = \iint V(u, v)\, e^{-j2\pi(ul + vm)}\, du\, dv. \tag{2}$$

The raw or dirty map $B'(l_0, m_0)$ at any celestial position l_0, m_0 is the convolution of the brightness distribution with the antenna response $P(l, m)$:

$$B'(l_0, m_0) = \iint P(l - l_0, m - m_0) B(l, m)\, \mathrm{d}\Omega \tag{3}$$

(Christiansen & Högbom 1985). A single row of the EW array and each row of the S-array have primary beams which look at essentially the whole sky along the meridian—their far-field voltage pattern (E) in the plane perpendicular to the axis of the dipole is expected to be:

$$E(\theta) = \sin\left(\frac{2\pi}{\lambda} H \cos(\theta)\right) \tag{4}$$

where θ is the zenith angle, H is the height of the centre of the dipole above the reflecting screen and λ is the wavelength of observation. By Fourier transforming the visibilities along v, the instantaneous brightness distribution of the sky along NS can be obtained. Thus, in a single sidereal day, the entire observable sky was mapped. Hermitian symmetry was assumed for the visibilities (see the discussion about 'Tee' and 'Cross' arrays in Christiansen & Högbom 1985). The procedure for obtaining a raw or dirty map is outlined in Fig. 1.

Interference of short duration is easily detected by its appearance on the raw map. There were only about half a dozen occasions when such interference could be seen, each corrupting only 1 or 2 samples of data. An 8th-order polynomial was fitted to the adjacent data stretches and used to fill in these gaps.

To obtain the final brightness distribution, the dirty map has to be deconvolved. The conventional CLEAN algorithm (Högbom 1974) proceeds by locating successive maxima in the dirty map and subtracting the dirty beam from each such position. The height of the dirty beam subtracted is usually chosen to be a fraction of the maximum. This loop gain is often chosen to be 0.2. The implicit assumption here is that the sky is empty except for the discrete sources. This is not the case for our maps which contain both point sources and a varying Galactic background. A discussion of the unsuitability of CLEAN under such circumstances and of some possible solutions can be found in Thompson, Moran & Swenson (1986). The present method of deconvolution uses the two-dimensional point spread function (PSF) or the two-dimensional response of the antenna, and a modified version of the conventional CLEAN.

The PSF was generated from the dirty map around the strong source Cygnus A. The extent of the PSF was ± 1 hour in R.A. and the full extent in declination. The modified CLEAN algorithm adopts a 'local maximum' rather than a 'global maximum' criterion. Thus, the 'maxima' are heights above the local background and not absolute values in the dirty map. The details of generating the PSF and of the modified CLEAN are discussed in an accompanying paper (Dwarakanath, Deshpande & Udaya Shankar 1990; DDU). For the present purpose, we will just state the results—this method deconvolves only the sources of similar size to the beam, leaving the extended emission unaltered. In our case, this converges much faster than the conventional CLEAN. It was possible to CLEAN the whole map down to an almost uniform level of 5 σ, where σ is the r.m.s. fluctuation in the dirty map. To estimate the σ, the dirty map was divided into many 5° × 5° regions. The r.m.s. fluctuation in each region was estimated through an iterative scheme in which all values beyond 5σ were excluded. The σ in the dirty map was estimated by averaging these r m.s. fluctuations. The CLEAN components were convolved with a Gaussian beam of the same full-width-at-

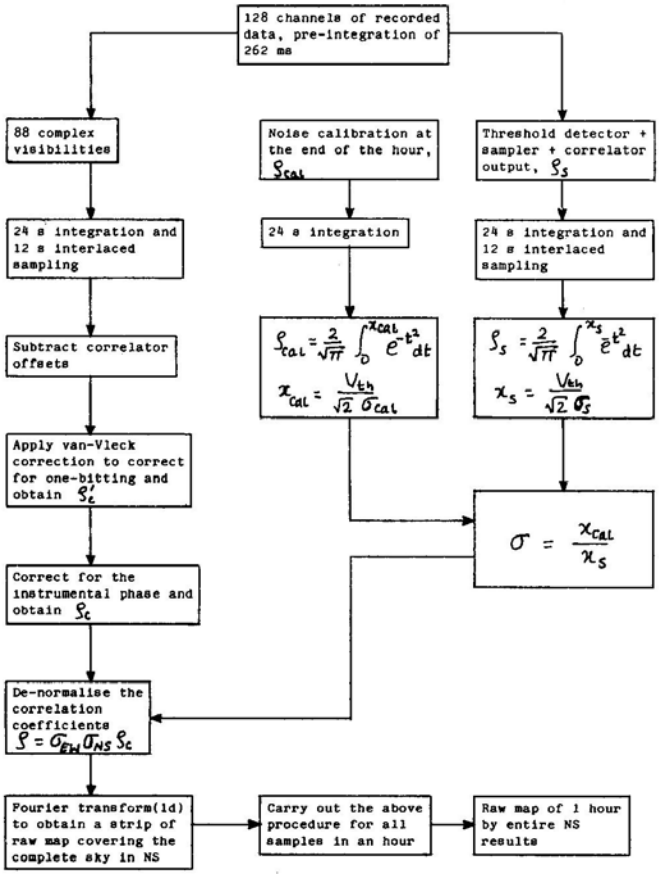

Figure 1. A flow chart of the procedure used to obtain the raw maps.

half-maximum and area (full-beam area) as the dirty beam and added to the map of the residuals to produce the final maps (Fig. 2).

The final maps showed several features which were suspected of being non-astronomical artefacts. These were of the size of the synthesized beam in NS but continued for hours in EW. With a view to understanding their origin and correcting for it, the following analysis was made. The residual map from the CLEANing of one hour by the full extent in declination was averaged along time and the resultant profile Fourier transformed to give the amplitude of correlations as a function of baseline. This showed values higher than expected from noise in the short spacings (< 50 m) due to the contribution from the celestial background. However, many of the longer baselines also showed unexpectedly high values. In addition, the pattern in the longer baselines repeated when this analysis was performed on the residuals at different sidereal times. This was a clear indication of an instrumental origin. These offsets were subtracted for the longer (> 50 m) baselines, although this could not be done for the shorter baselines due to the contribution from the sky background.

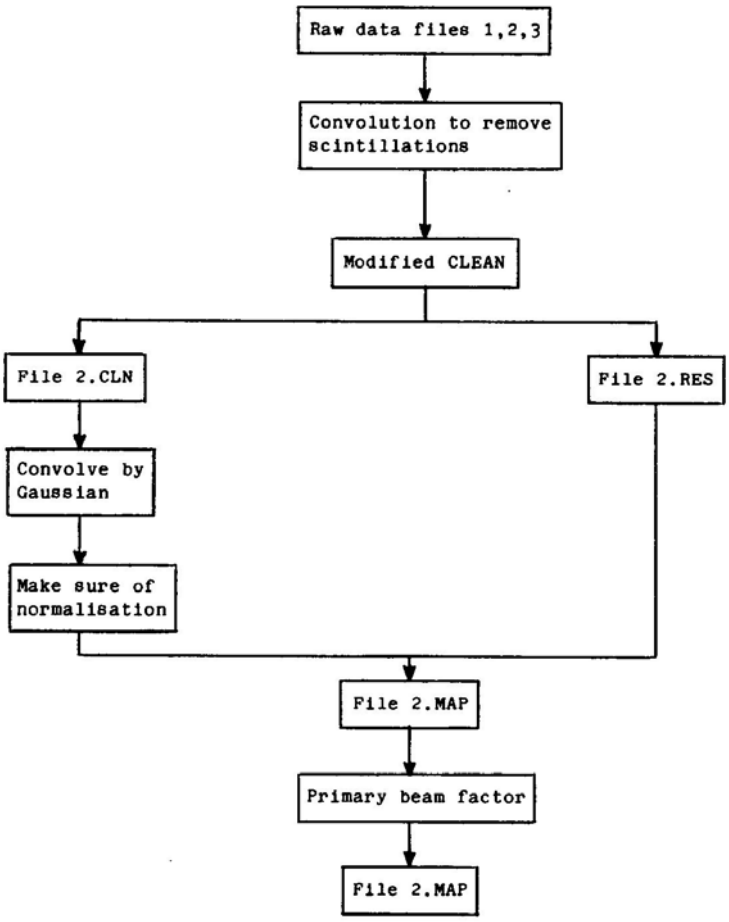

Figure 2. Overall scheme to produce the final maps from the raw maps.

3.2 *Calibration*

For further use, the CLEANed maps can be expressed in units of Jy/beam or, equivalently, in brightness temperature. Cygnus A was chosen as the calibrator for this purpose. Absolute flux density measurements of Cyg A are available from 10 MHz to 22 GHz (Baars *et al.* 1977). At frequencies around 30 MHz its absolute flux density is known to within 5 per cent, and has been calculated to be 25396 Jy at 34.5 MHz from the spectral fit given by Baars *et al.* To associate a brightness temperature with the Galactic background emission, we have to obtain the solid angle of the antenna response. This can be done by integrating the PSF that was used for CLEANing the maps.

It is important to check that the flux density scale so obtained is

(1) independent of the strength of the source
(2) does not have any systematic pattern as a function of R.A. or Dec. and,
(3) is repeatable with time.

For this purpose, the results from the survey at 38 MHz by Williams, Kenderdine & Baldwin (1966) were used. Kellermann, Pauliny-Toth & Williams (1969) list 38-MHz flux densities for most 3C sources. Their list contains 21 sources whose estimated standard error is 5 per cent (called 'A' sources) and 118 sources with estimated standard errors between 5 and 15 per cent (called 'B' sources). We have estimated the 34.5-MHz flux densities of these sources from our maps. A function of the form shown in Fig. 3 was convolved with the map in both the R.A. and Dec. directions. This essentially filters out all the background variations with angular scales larger than the separation between the negative delta functions. The resultant map can simply be summed within the size of the source to obtain the integrated flux density of the source. A percentage difference between the two flux densities was obtained as follows:

$$\% \text{ error} = \frac{\text{flux density at 38 MHz} - \text{flux density at 34.5 MHz}}{\text{flux density at 38 MHz}} \times 100. \qquad (5)$$

Fig. 4 shows this % error plotted against declination for the (B) sources. We omitted the (B) sources which are weak ($\lesssim$ 30 Jy) or at high declinations ($\gtrsim$70°), or which fall beyond 3σ of the distribution. A sloping trend is clearly seen. It is extremely unlikely that any of our antenna-based effects are monotonic in declination from –2° to + 60° when the instrumental zenith is at + 14°.1. A clue to understanding this pattern comes from the fact that the 38-MHz survey consists of two surveys—one centered at + 7° and the other centered at + 52°, with the FWHM of the NS antenna patterns being + 47°. Thus, the source list at 38 MHz is made up of two sets of sources with

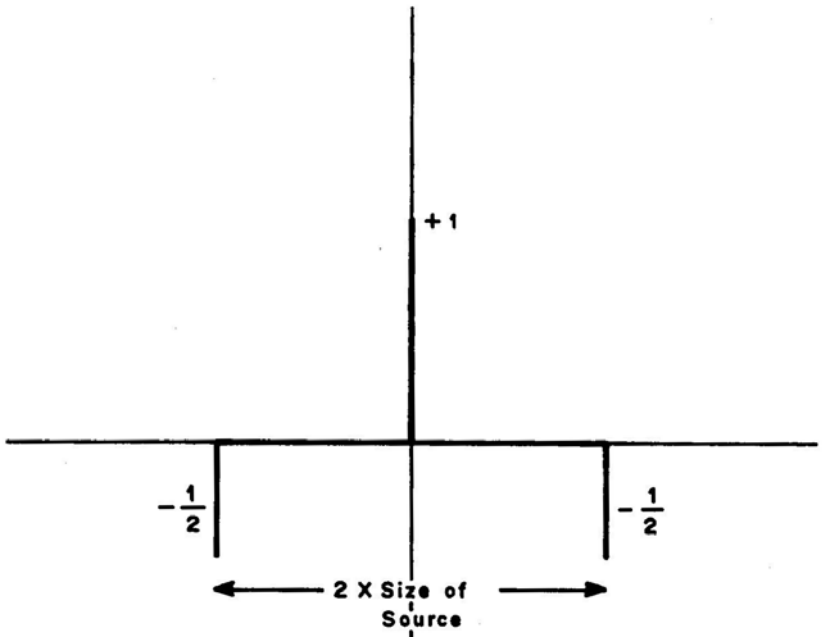

Figure 3. Convolving function used to filter the background. A special case of this has been used by Williams, Kenderdine & Baldwin (1966) to obtain flux densities of point sources in their survey.

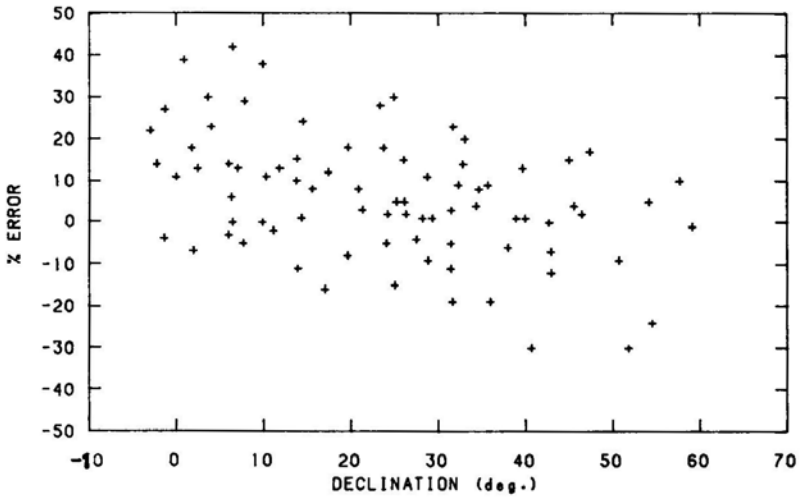

Figure 4. Percentage differences between the flux densities of some 3C sources at 34.5 and 38 MHz plotted *as a* function of the declination of the sources. The slope is probably due to the difference in the flux density calibration of the 3C sources at 38 MHz depending on whether they are above or below + 30° declination.

declinations greater or less than + 30°. We have calculated the average and r.m.s. value of the % error in the two zones – ⩽ + 30° and > + 30°. The results are as follows:

	avg.	r.m.s.	error on the mean	
If Dec. is $\leqslant +30°$, % error =	9.5	±18	2.5	(52)
$> +30°$, % error =	−0.5	±14	2.6	(30)

where the numbers in the brackets indicate the number of sources in the two zones. The averages are different at the 4σ level. Fig. 5 shows the same plot as Fig. 4 but with the offset subtracted for dec.⩽+ 30°. The slope is much less apparent. Similar plots of the % error *vs* R.A. and source flux density indicate that there are no systematic patterns against either parameter. Taking an average value for the r.m.s. of the % error between the flux densities at 38 and 34.5 MHz to be 16 per cent, and the r.m.s. value of the % error in the 38 MHz flux densities to be 10 per cent, an r.m.s. value of 12 per cent is implied to the flux densities of the (B) sources at 34.5 MHz.

For the (A) sources the results are as follows:

	avg.	r.m.s.	error on the mean	
If Dec. is $\leqslant +30°$, % error =	0.63	±4	1.4	(8)
$> +30°$, % error =	5.4	±8	2.5	(10)

Due to the small numbers involved, it is difficult to comment on the statistical significance of the difference in the averages. However, the average of the two r.m.s. values of 6 per cent implies an r.m.s. of < 5 per cent for the flux densities of the (A) sources at 34.5 MHz.

In obtaining the % error from Equation (5) we have not corrected the source flux densities for their spectra. However, this does not change the difference between the

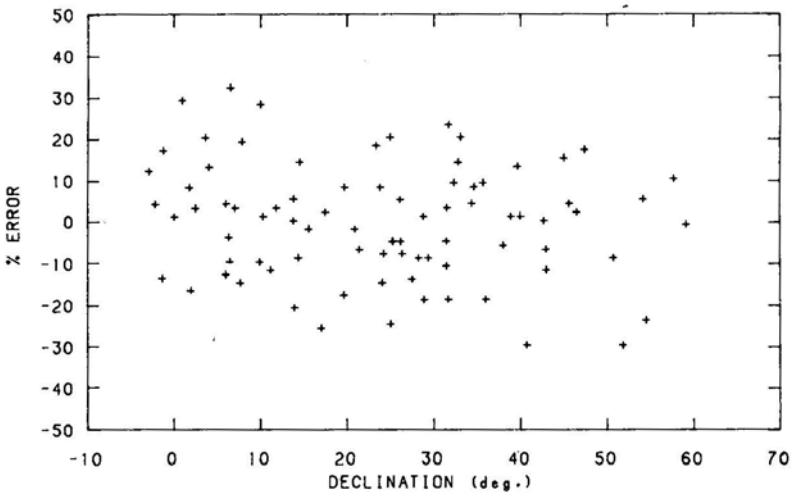

Figure 5. Percentage difference between the flux densities as in Fig. 4 but with the average calibration difference in the flux densities at 38 MHz between the sources above and below + 30° dec. subtracted. The systematic pattern seen in Fig. 4 is much less apparent here.

two averages (for declination greater or less than + 30°) significantly. With a view of comparing the flux density scales at 38 and 34.5 MHz we did the following—(a) the flux density scale at 38 MHz was brought to that Baars *et al.* (1977) by using a factor 1.1 as implied by the flux density measurements on Cygnus A at 38 MHz (Williams, Kenderdine & Baldwin 1966), and (b) the 38 MHz flux densities were then extrapolated to 34.5 MHz with a mean spectral index of – 0.75 (Kellermann, Pauliny-Toth & Williams 1969). These two corrections bring down the two averages for the (B) sources to + 7 and – 3 per cent respectively. Thus, the corrected flux density scale at 38 MHz and that at 34.5 MHz agree to within 5% as implied by the flux density estimates made on ≈ 100 (B) sources.

3.3 *Repeatability*

It was important to check the repeatability of the 34.5-MHz observations as interference, the ionosphere and system variations could have affected the data. With this in mind, the flux densities of all the (B) sources were estimated from another day's observation, and the flux density differences between the two days computed. They agreed to within 8 per cent (r m.s.).

3.4 *Bandwidth Decorrelation*

For a bandwidth of 400 kHz and a zenith angle of 50°, there is an average of 8 per cent decorrelation between the signals from the rows of the EW and S-arrays. Since this is a small percentage, it does not seriously degrade the signal-to-noise ratio. In addition, as we sum over the source size or the beam size (whichever is the larger) when estimating flux densities of the sources, these flux densities are unaffected by the bandwidth decorrelation.

4. The maps

The results of the survey are given in the form of contour maps in equatorial coordinates. We have used the NOD2 program library to prepare the contour maps. The maps have the same format as those of the 408 MHz all-sky survey (Haslam *et al.* 1982) and are precessed to 1950. Arrows on the contours which point clockwise enclose minima while those that point anti-clockwise enclose maxima. In Fig. 6 we present a low-resolution (2°) map from the present survey of the entire region of the sky that is not aliased (all 24 hr of R.A. for $-36° \leqslant \mathrm{Dec} \leqslant +64°$; Although the unaliased region should strictly be $-33° \leqslant \mathrm{Dec.} \leqslant +61°$, due to the effect of the primary beam, aliasing is <10 per cent at zenith angles of ± 50°, and we have set our declination limits by this). These low-resolution maps give an overall impression of the sky at 34.5 MHz. The numbers on the contours are in units of 5722 K (full-beam brightness temperature) above absolute zero. The absolute levels of the contours are accurate to within 5 per cent—the accuracy to which the flux density of Cygnus A, our calibrator, is known. The steps in the contour levels are as follows:

1 to 5 every 0.25 units, labelled every 1 unit,
5 to 10 every 0.5 units, labelled every 2 units,
10 to 20 every 1.0 units, labelled every 4 units,
20 to 32 every 1.5 units, labelled every 6 units.

For the purpose of comparison, we present the 408-MHz map of Haslam *et al.* (1982), also convolved to 2° (Fig. 7). In this figure, the labels on the contours are in units of 10 K. The steps in the contour level are as given above.

Some of the large-scale features that have been recognised earlier (Large, Quigley & Haslam 1962; Quigley & Haslam 1965; Berkhuijsen, Haslam & Salter 1971; Berkhuijsen 1971 and Milogradov-Turin & Smith 1973) and which can be seen clearly in the 408-MHz map are listed in Table 2. A comparison between Figs 6 and 7 shows

Table 2. Some large scale features that can be seen on both the 34.5 and 408 MHz maps and their temperature spectral indices (β) where temperature x frequency^{1}. The error in (β) is 0.03 (1σ).

	Position (α, δ) (hour, deg.)	Temperature spectral index between 34.5 MHz and 408 MHz
Loop II (Cetus Arc)	2.5, +30 to 21, −5	Varies from −2.6 to −2.8 as one moves from $2^h.5$, +30° to 21^h, −5°
Loop III	3, +45	−2.55
Spur 185−	5, +15	−2.55
Loop III	5, +60	−2.5; more pronounced at 5^h, +50°
	8, +15	not seen clearly
Loop I (North Polar Spur)	17, +10	Base of the spur is at more like 18^h, 0°. Spectral index varies from −2.7 at the base to −2.4 at the tip (13^h, +15°)
Loop III	19, +55	not seen clearly
Spur 80−	22, +20	−2.7
Loop III	22.5, +40	−2.7

that all but two of these are seen in the 34.5-MHz map. Some interesting features towards the Galactic centre can also be seen at 34.5 MHz. These are (a) the 1= 0° feature which is an arc of emission starting at $17^h\ 20^m$, – 25° and extending up to 16^h, – 22° (see Sofue *et al.* 1988 for a 408 MHz map), (b) the l=355° feature which is an arc starting at 16^h40^m, – 25° and going towards 16^h, – 30°, and (c) the l=345° feature between 15^h40^m, – 25° and 15^h, – 30°.

4.1 *Some Spurious Features*

The above inter-comparisons between the various maps give us some confidence in interpreting the large-scale features seen on our maps. However, there are some features which we believe to be spurious.

The areas of extended emission centred around $\alpha = 17^h40^m$, δ= + 42° and at $\alpha = 17^h$ δ= + 30°, as well as the adjacent minimum ($\alpha = 17^h40^m$, δ= + 60°) are unlikely to be of astronomical origin. For one thing they are not present in the 38-MHz map made with a single dish (Milogradov-Turin & Smith 1973). Further, they are aligned in R.A. with the brightest portion of the Galactic plane. These regions are 10° in extent and have an average brightness of ≈ 25 Jy/beam at full resolution.

Another feature we believe to be spurious is the ridge of emission at – 15° declination which extends from 20^h to 5^h.

From the geometry of these spurious features, and as they repeat at the same sidereal times we conclude that they are not due to interference, even from a satellite. Since they are also present in the raw maps, they could not be artefacts introduced in the CLEANing procedure. The common aspect of all these features is their large angular size. This immediately suggests an explanation in terms of the measured visibilities in the short baselines. As detailed in Section 3.1, we have not removed any offsets present in the short-spacing (< 50 m) visibilities since it was impossible to separate these from the contribution of the large-scale sky background in these baselines. The ridge of emission at declination – 15° running parallel to constant declination may be due to this. However, it is unlikely that this explains other features, which may be due to the peculiarities in the illumination pattern of the short-spacing S-array elements which may also be a function of the zenith angle. Interaction between the short spacing S-array elements and the EW antenna could lead to such effects, as noted previously by Jones and Finlay (1974) in their 29.9-MHz survey. If such peculiarities are indeed present, then given the intense broad emission region near the Galactic centre, one would expect to see its 'sidelobes'. An attempt was made to correct for this by using several strong point sources at different zenith angles (such as Cyg A, Cas A, Tau A, Vir A and Hyd A) but without success. Since there is no strong source at similar declination to the Galactic centre, we cannot test this hypothesis. Nevertheless, we believe this to be the most plausible explanation. It should be pointed out that the spurious features under discussion are at the level of 5 per cent of the intensity of the Galactic centre region. Hence, if the above explanation is correct we do not expect to see similar features elsewhere since there are no other extended regions comparable in brightness to the Galactic centre.

In addition, we wish to point out that the features seen in the maps between 20^h32^m < R.A. <20^h36^m and at almost all the declinations are due to interference which was not excised.

4.2 *The Full-Resolution Maps*

In this section, we present the full-resolution 34.5-MHz maps obtained from our survey. The numbers on the contours are in units of 5722 K (full-beam brightness temperature). The steps in the contour levels are as follows:

1 to 5 every 0.5 units, labelled every 1 unit,
5 to 10 every 1 unit, labelled every 2 units,
10 to 20 every 2 units, labelled every 4 units,
20 to 32 every 3 units, labelled every 6 units,
32 to Max. every 4 units, labelled every 8 units.

The convention for indicating maxima and minima are as described earlier in this section.

It is important to discuss the noise in the maps. There are two factors which are expected to contribute to the random fluctuations (over the size of the beam) in the map: *system noise* and *confusion.*

At decametric wavelengths, the system temperature is almost entirely determined by the sky noise. A typical antenna temperature encountered at 34.5 MHz is ≈10,000 K. In comparison, the first-stage amplifiers of the receiver have noise temperatures of only 500 K. Given a bandwidth of 400 kHz and an integration time of 24 s, the system noise is equivalent to a brightness of 3.5 Jy/beam (remembering that for this survey we have used only one EW row and adopted time multiplexing). However, the raw maps of the present survey were convolved along the EW direction with a sin (x)/x function. The half power width of this function was that of the EW antenna along the EW direction (≈ 100 s) so that astronomical spatial frequencies remained unaffected. This effectively increases the integration time by a factor of 4, bringing down the system noise to 1.8 Jy/beam.

It is possible to obtain a reasonable estimate of the system noise from the maps themselves. If the raw maps are convolved with a sin (x)/x function whose resolution corresponds that of the antenna, then all spatial variations smaller than the resolution will be smoothed out. A subtraction of the convolved map from the raw map leaves only the contribution of the system noise in the frequency range between $1/(2t_{\rm res})$ and $1/t_{\rm int}$ Hz. As discussed above, before CLEANing, the raw maps were smoothed in time with a sin (x)/x function of resolution (= $t_{\rm res}$) 84 s (corresponding to EW resolution of the EW antenna at 0° dec.). So, the system noise in the final maps is band-limited to 1/(2 x 84) Hz. This can be estimated by extrapolating the contribution obtained between $1/(2t_{\rm res})$ and $1/t_{\rm int}$ Hz. The value so obtained indeed agrees with our estimate made above.

The contribution from confusion is expected to be as important as the system noise in determining the sensitivity of the GEETEE for point source detection. One source per main beam of the GEETEE implies ≈ 4300 sources per steradian at the zenith. An estimate based on the log (N) *vs* log (S) plot at 408 MHz (Shaver & Pierre 1989), and assuming a spectral index of −0.8, gives the confusion limit at 34.5 MHz as 3.2 Jy/beam. Since this is almost twice the system noise, it follows that our maps are effectively confusion limited (at least in those regions where the antenna temperature is ≲10,000 K).

To estimate the confusion from the maps, we can find the difference between each point on the map and the average value of the map one resolution element away. The

r.m.s. value of this difference over the region of interest will then provide an estimate which includes both confusion and system noise. Since these two sources of noise are uncorrelated we can write $\sigma^2 = \sigma_s^2 + \sigma_c^2$ (where a is the r m.s. fluctuation on the map, σ_s the contribution from system noise and s, that due to confusion). Using the value of, σ_s obtained from the difference map (as described above), σ_c, can now be estimated. Such an analysis was made for regions of low and high intensity. The region of sky in the range $12^h\ 30^m$ R.A. $13^h\ 30^m$, and — 36° Dec. + 64° was divided into 5° x 5° areas and, for each, σ_s and σ were determined. The average values of σ_s 1.8 Jy/beam and σ = 4.9 Jy/beam gave σ_c = 4.6 Jy/beam. A similar analysis made for $17^h\ 30^m \leqslant$ R.A. 18" 30^m, — 36° Dec. + 64° gave values of σ, = 3.9 Jy/beam and σ = 6.0 Jy/beam implying σ_c = 4.6 Jy/beam. These numbers appear reasonable. The increase of system noise from 1.8 Jy/beam in the colder region to 3.9 Jy/beam in the hotter region is expected as the antenna temperatures of both the EW and the S array rows increase by a factor of 2 in going from the one to the other (the system noise will increase in proportion to the system temperature, T_{SYS}, all other parameters being equal. In a correlation telescope, $T_{SYS} = \sqrt{T_{SYS1} \times T_{SYS2}}$ where the subscripts 1 and 2 refer to the two telescopes whose outputs are multiplied in our case the EW antenna and a given row of the S-array). Thus, the variations of the total noise in the map are very small—varying from 4.9 Jy/beam in colder regions to 6.0 Jy/beam towards hotter regions.

4.3 *Dynamic Range of the Maps*

The dynamic range can be defined as the ratio of the flux densities of the strongest and the weakest sources detected in a given region. Clearly, this will depend upon how close or far away one is from a strong source. In addition, in the present case it also depends upon the 'direction'. In the R.A. and Dec. directions, for example, the residual sidelobe levels of a point source are 0.2 to 0.5 per cent of the peak value, implying a 5σ dynamic range of 20 to 16 dB. The 'diagonal' directions are much cleaner. Except around Cyg A and Cas A, the noise in the diagonal direction is essentially the noise inherent to the map and is not relevant to the discussion of the dynamic range of the map.

Since we have chosen Cygnus A to generate the PSF, the region around Cygnus A has the maximum apparent dynamic range. In the CLEANed map this is ≈ 27 dB.

Due to a variety of problems (*e.g.* curved R.A. sidelobes, sidelobes beyond ± 1 hr, differences between the true PSF and the Cygnus PSF used for CLEANing, strength of the source, etc.), CLEANing the region around Cas A posed more problems and this could not be cleaned down to the 5a noise level. Consequently, the dynamic range near Cas A is poorer than around Cyg A. The kind of dynamic range obtained around Cyg A is attainable only beyond 20° in declination and 30 min in R.A. from Cas A.

In general, one should be very cautious in identifying any sources at the same R.A. or Dec. as strong sources. We have deliberately left the residual sidelobes in the map to give the user a proper feeling for their strength, thus aiding their interpretation. In addition, beyond the declination ranges of –33° to + 61° care should be exercised as these regions are affected by the grating response of the antenna.

4.4 *Survey Parameters*

Summarizing the main parameters of the survey:

Telescope	GEETEE—Gauribidanur Radio Telescope located at 13°36′12″ N
Instrumental zenith	+14°.1
Coverage	$-50° < \text{Dec.} < +70°$ ($-33° < \text{Dec.} < +61°$ without aliasing), and the full R.A. range.
Operating frequency	34.5 MHz
FWHM	$26' \times 42'\text{sec}(\delta - 14°.1)$
Telescope Configuration	One row of EW array and 88 rows of S-array. 1-D synthesis along NS
Collecting area	EW array, 1 row: 3000 m^2 S-array: 7000 m^2
Bandwidth	400 kHz
Integration time	24 s; this is effectively decreased by a factor of 4 due to the switching but increased by a factor of 4 due to filtering of the raw data during analysis.
Systen noise	1.8 to 3.9 Jy/beam (1σ)
Confusion	5 Jy/beam (1σ)
Absolute accuracy	5 per cent

Acknowledgements

We thank A. A. Deshpande, R. Nityananda, V. Radhakrishnan, T. S. Ravishankar, Ch. V. Sastry and G. Srinivasan for their contributions at various stages of the survey and for the many useful discussions we had with them. We also thank H. A. Ashwathappa, G. Jayakumar, C. N. Nanje Gowda and G. N. Rajasekhar for their help and co-operation during the observations. We thank C. G. T. Haslam and C. J. Salter for providing us the NOD2 library and the 408 MHz all-sky survey data. We also thank C. J. Salter for his valuable suggestions which have helped to improve the clarity and readability of this paper.

References

Baars, J. W. M., Genzel, R., Pauliny-Toth, I. I. K., Witzel, A. 1977, *Astr. Astrophys.,* **61,** 99.
Berkhuijsen, E. M. 1971, *Astr. Astrophys.,* **14,** 359.
Berkhuijsen, E. M., Haslam, C. G. T., Salter, C. J. 1971, *Astr. Astrophys.,* **14,** 252.
Caswell, J. L. 1976, *Mon. Not. R. astr. Soc.,* **177,** 601.
Christiansen. W. N., Högbom, J. A. 1985, *Radiotelescopes,* Cambridge University Press.
Dwarakanath, K. S. 1989, *PhD Thesis,* Dept. of Physics, Indian Institute of Science, Bangalore.
Dwarakanath, K. S., Deshpande, A. A., Udaya Shankar, N. 1990, *J. Astrophys. Astr.,* **11**, 311 (DDU).
Erickson, W. C. 1983, *Astrophys. J.,* **264,** L13.
Haslam, C. G. T., Salter, C. J., Stoffel, **H.,** Wilson, W. E. 1982, *Astr. Astrophys. Suppl.,* **47,** 1.
Högbom, J. A. 1974, *Astr. Astrophys*. **15,** 417.

Jones, B. B., Finlay, E. A. 1974, *Aust. J. Phys.,* **27**, 687.
Kassim, N. E. 1988, *Astrophys. J. Suppl.,* **68**, 715.
Kassim, N. E. 1989, *Astrophys. J.,* **347**, 915.
Kellermann, K. I., Pauliny-Toth, I. I. K., Williams, P. J. S. 1969, *Astrophys. J.,* **157,** 1.
Large, M. I., Quigley, M. J. S., Haslam, C. G. T. 1962, *Mon. Not. R. astr. Soc.,* **124,** 405.
Mathewson, D. S., Broten, N. W., Cole, D. J. 1965, *Aust. J. Phys.,* **18,** 665.
Milogradov-Turin, J., Smith, F. G. 1973, *Mon. Not.* R. *astr. Soc.,* **161,** 269.
Quigley, M. J. S., Haslam, C. G. T. 1965, *Nature,* **208,** 741.
Shain, C. A., Komesaroff, M. M., Higgins, C. S. 1961, *Aust. J. Phys.,* **14,** 508.
Shaver, P. A., Pierre, M. 1989, *Astr. Astrophys.,* **220,** 35.
Sofue, Y., Reich, W., Reich, P. 1988, NRO Preprint no. 196.
Thompson, A. R., Moran, J. M., Swenson Jr., G. W. *1986, Interferometry and Synthesis in Radio Astronomy,* John Wiley & Sons.
Udaya Shankar, N. 1986, *PhD Thesis,* Dept. of Physics, Bangalore Univ.
Udaya Shankar, N., Ravi Shankar, T. S. 1990, *J. Astrophys. Astr.,* **11,** 297 (UR).
Williams, P. J. S., Kenderdine, S., Baldwin, J. E. 1966, *Mem. R. astr. Soc.,* **70,** 53.

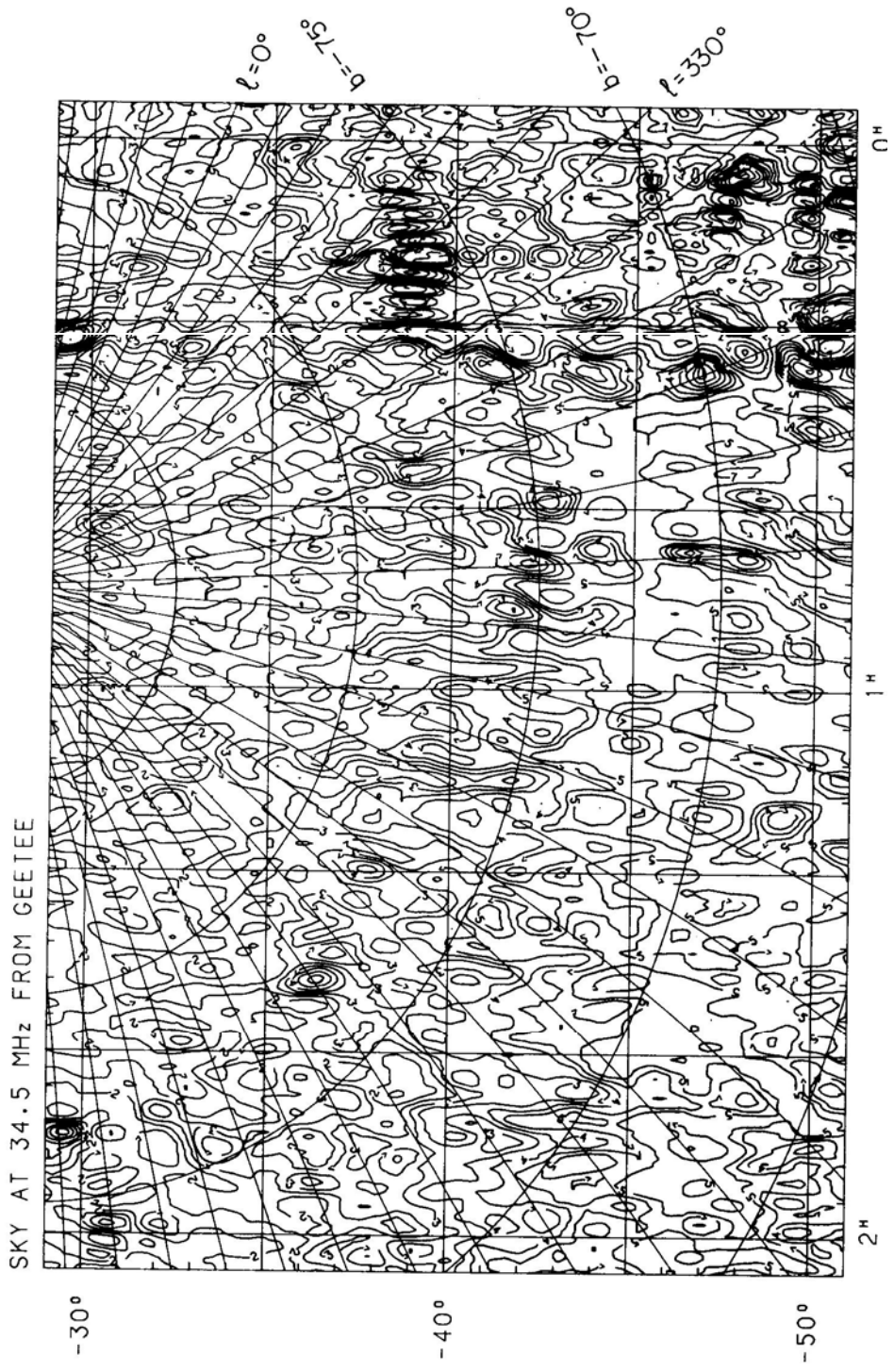
SKY AT 34.5 MHz FROM GEETEE
l=0°
b=-75°
b=-70°
l=330°
2H
1H
0H
-30°
-40°
-50°

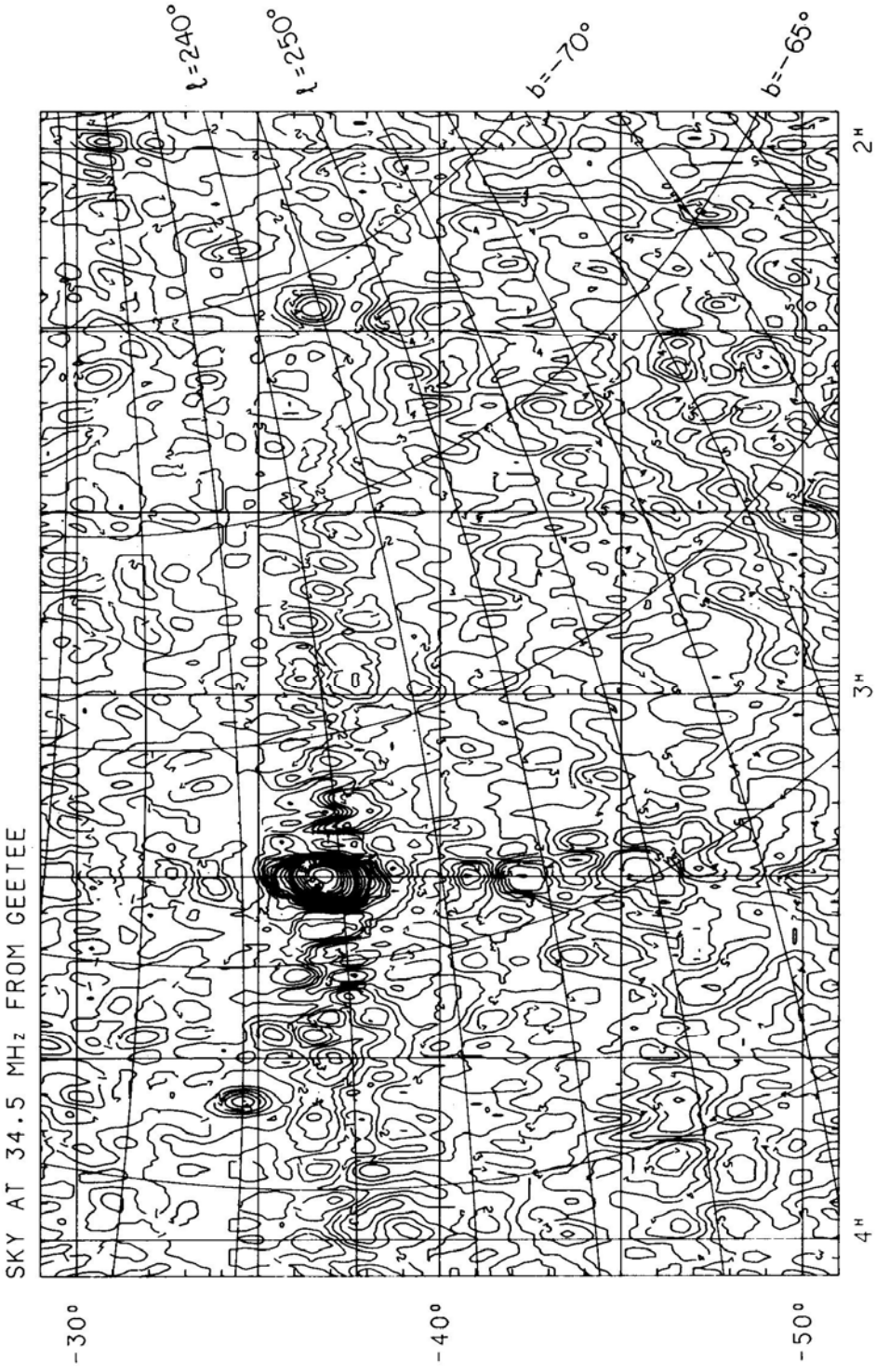
SKY AT 34.5 MHz FROM GEETEE
l=240°
l=250°
b=−70°
b=−65°
2H
3H
4H
−30°
−40°
−50°

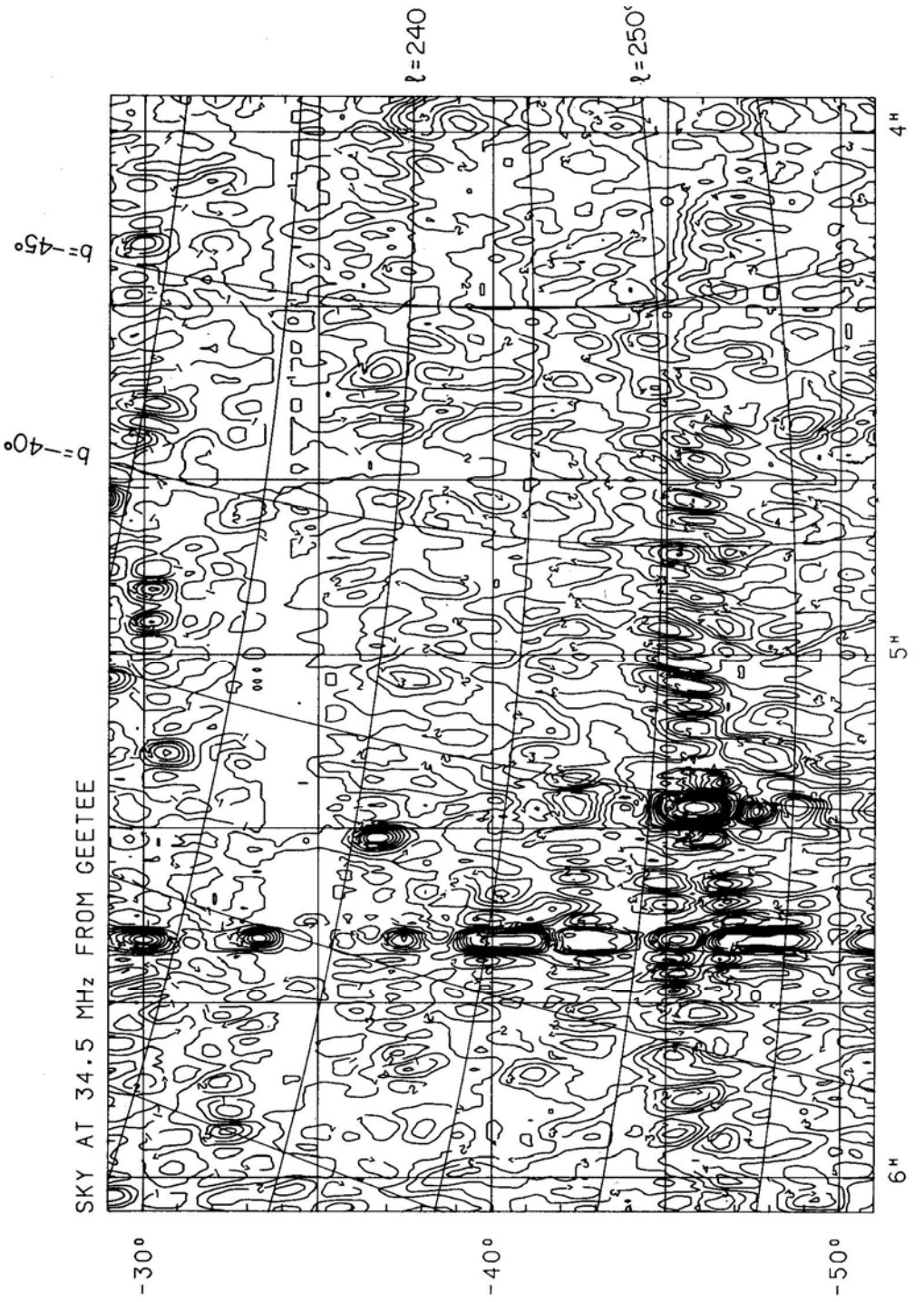
SKY AT 34.5 MHz FROM GEETEE
ℓ=240
ℓ=250
b=-40°
b=-45°
-30°
-40°
-50°
4ʰ
5ʰ
6ʰ

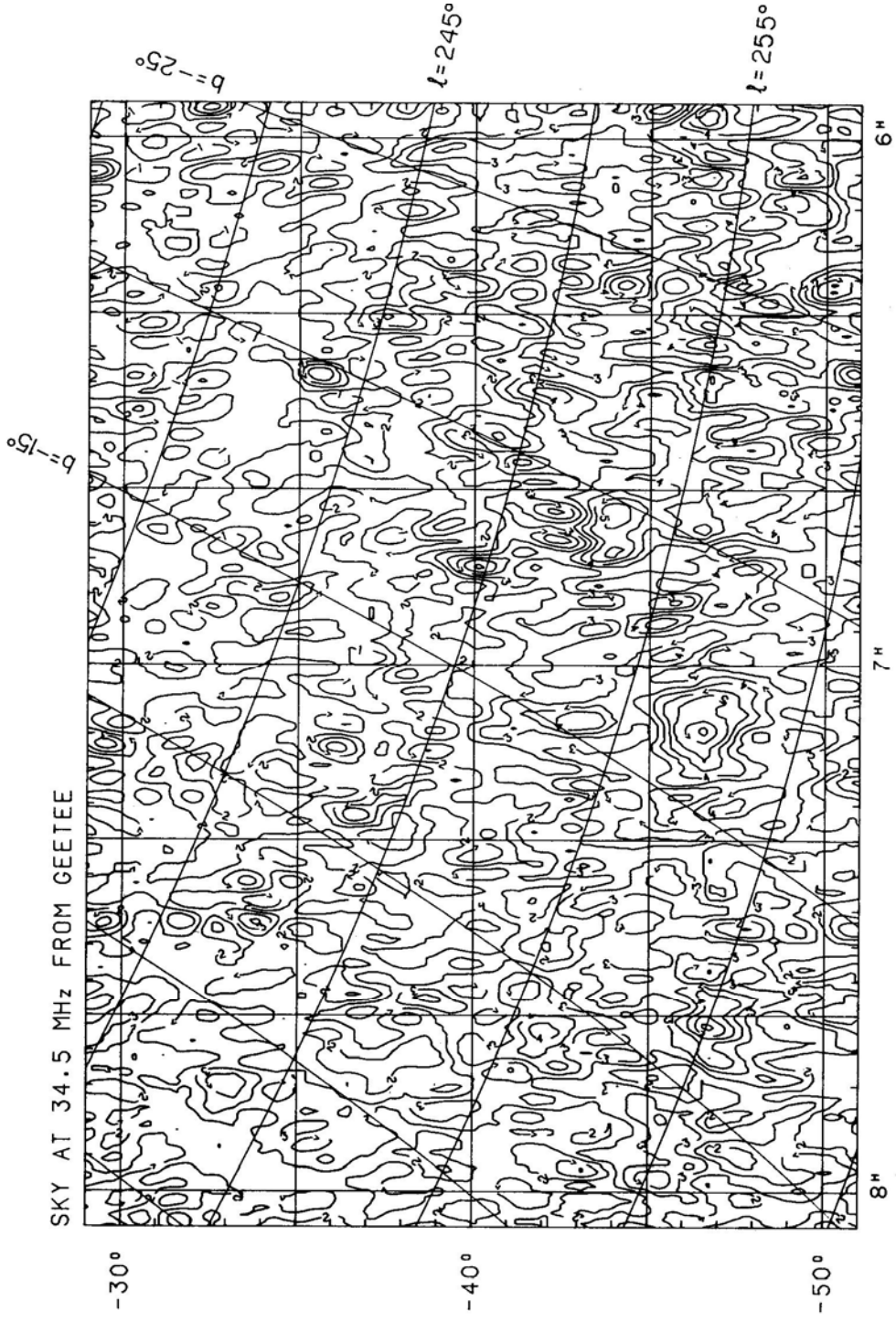
SKY AT 34.5 MHz FROM GEETEE
b=-15°
b=-25°
l=245°
l=255°
6H
7H
8H
-30°
-40°
-50°

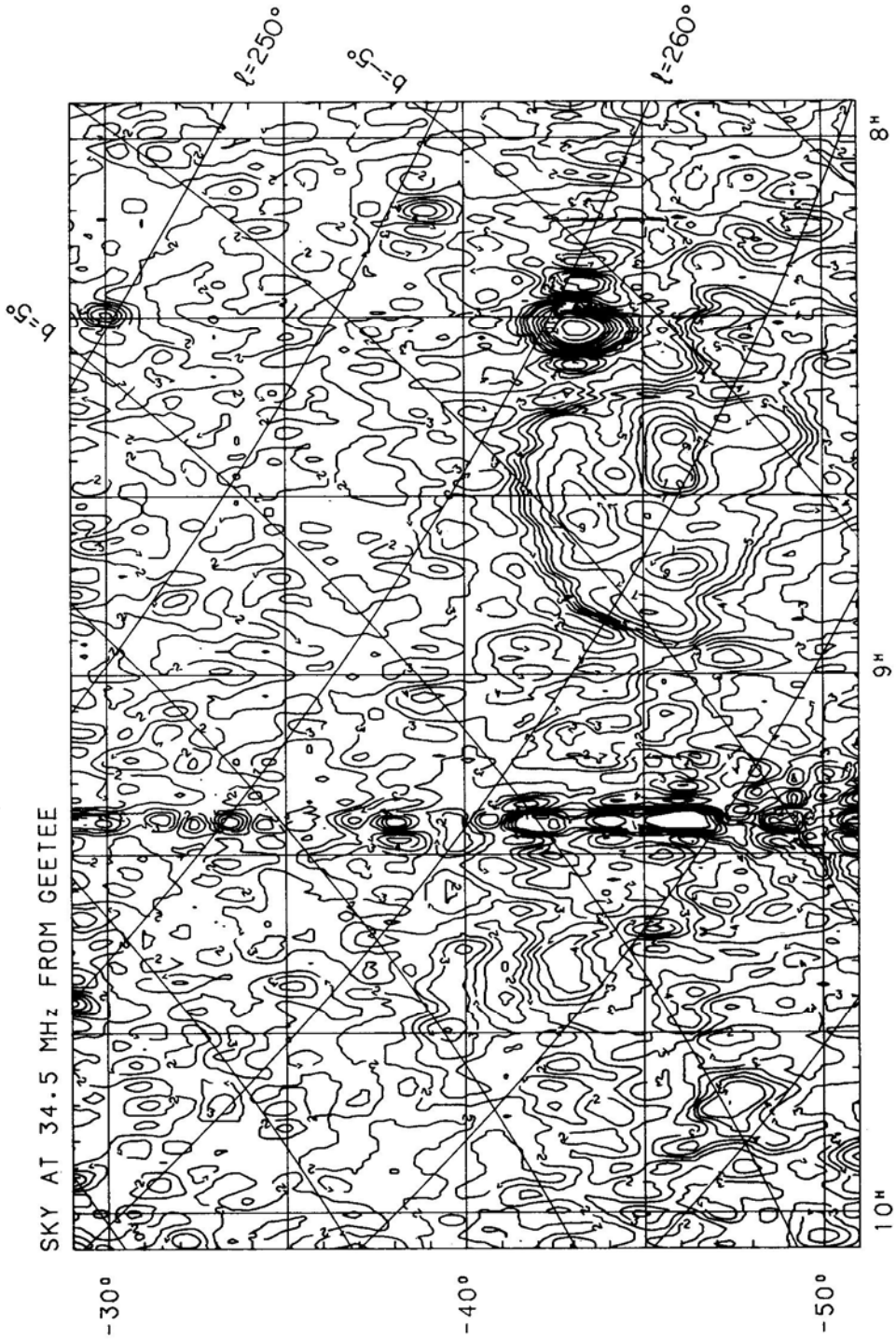
SKY AT 34.5 MHz FROM GEETEE
l=250°
l=260°
b=-5°
b=-5°
8H
9H
10H
-30°
-40°
-50°

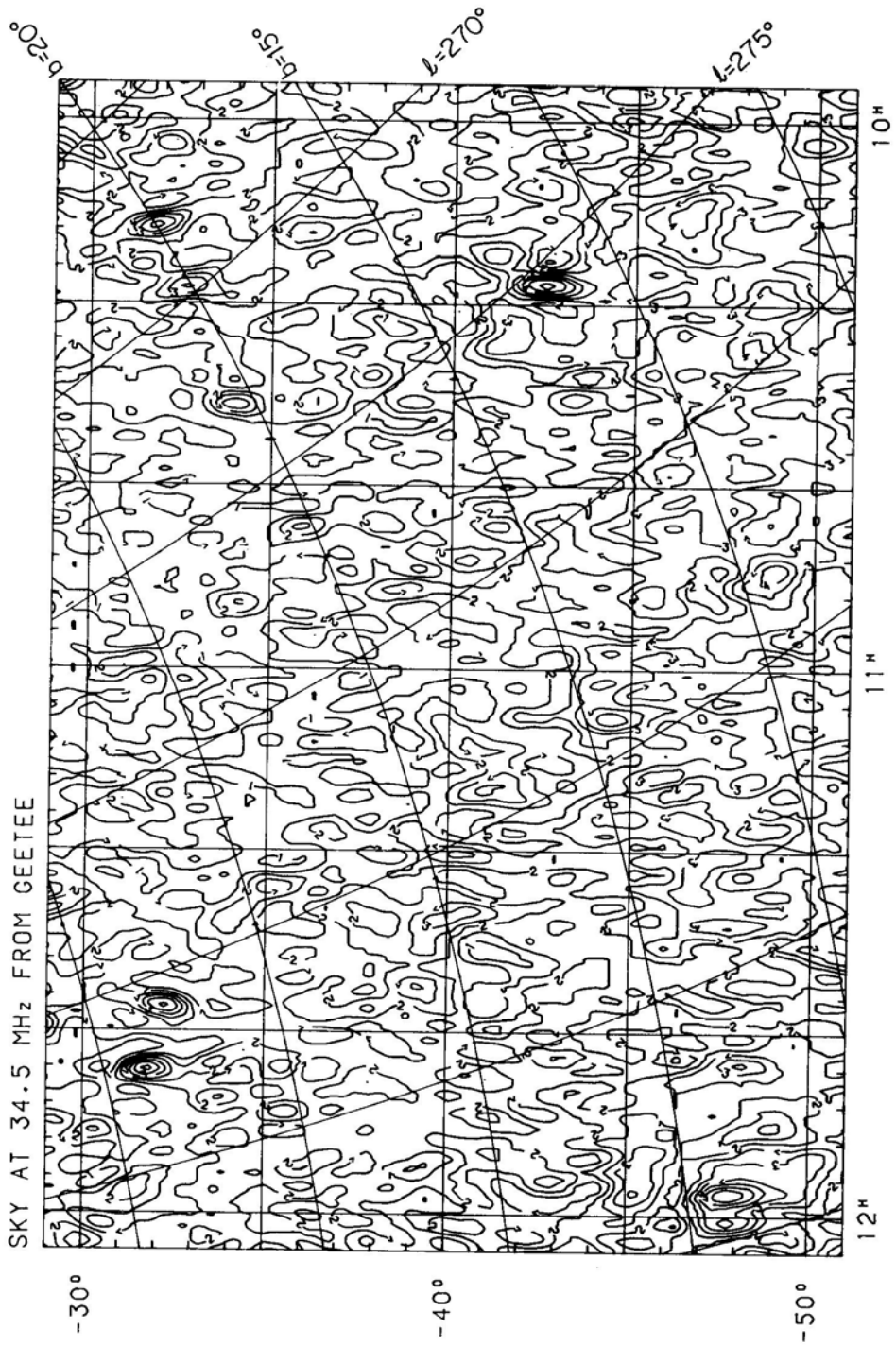
SKY AT 34.5 MHz FROM GEETEE
b=20°
b=15°
l=270°
l=275°
10ᴴ
11ᴴ
12ᴴ
-30°
-40°
-50°

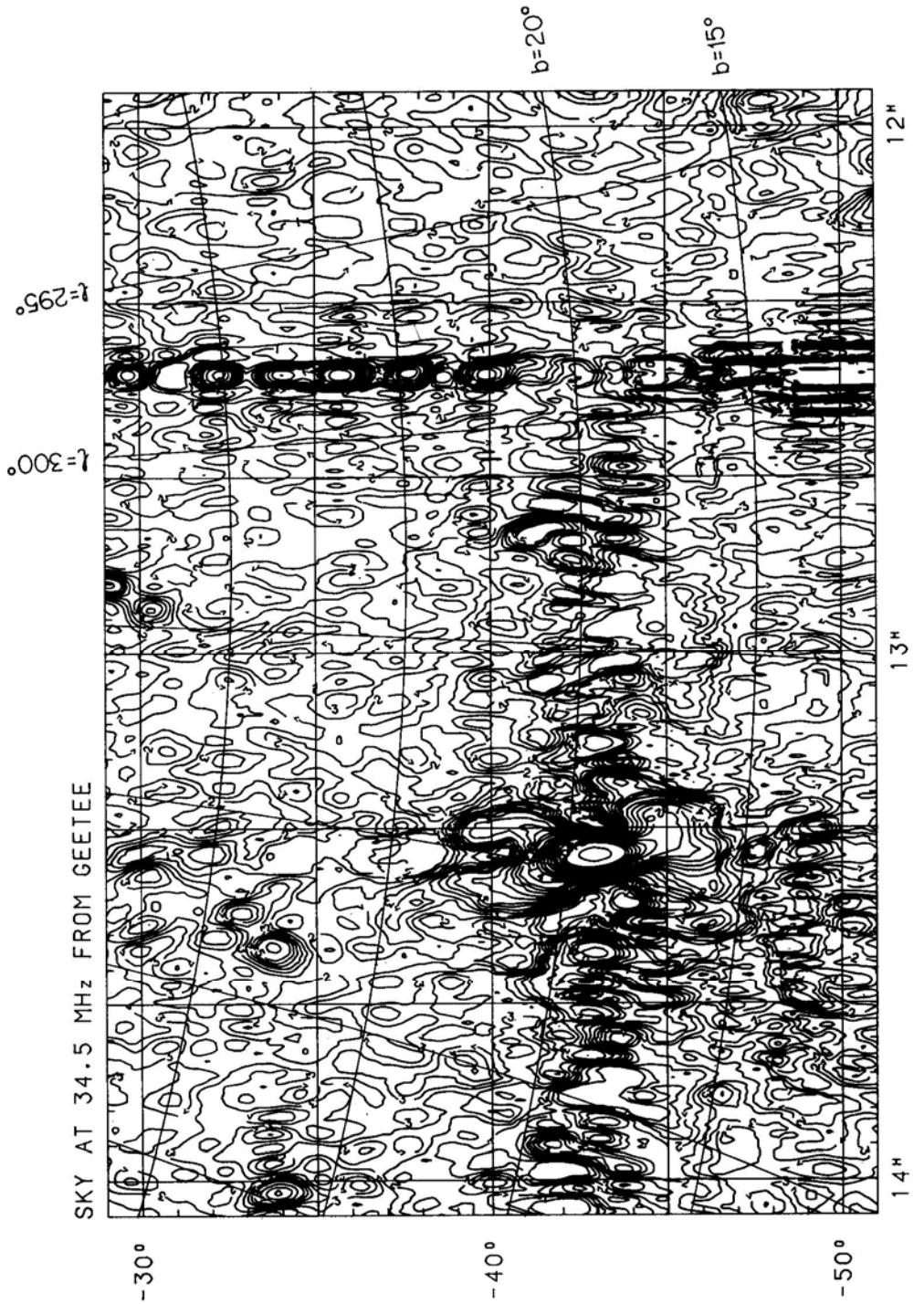
SKY AT 34.5 MHz FROM GEETEE
l=300°
l=295°
b=20°
b=15°
12ʰ
13ʰ
14ʰ
-30°
-40°
-50°

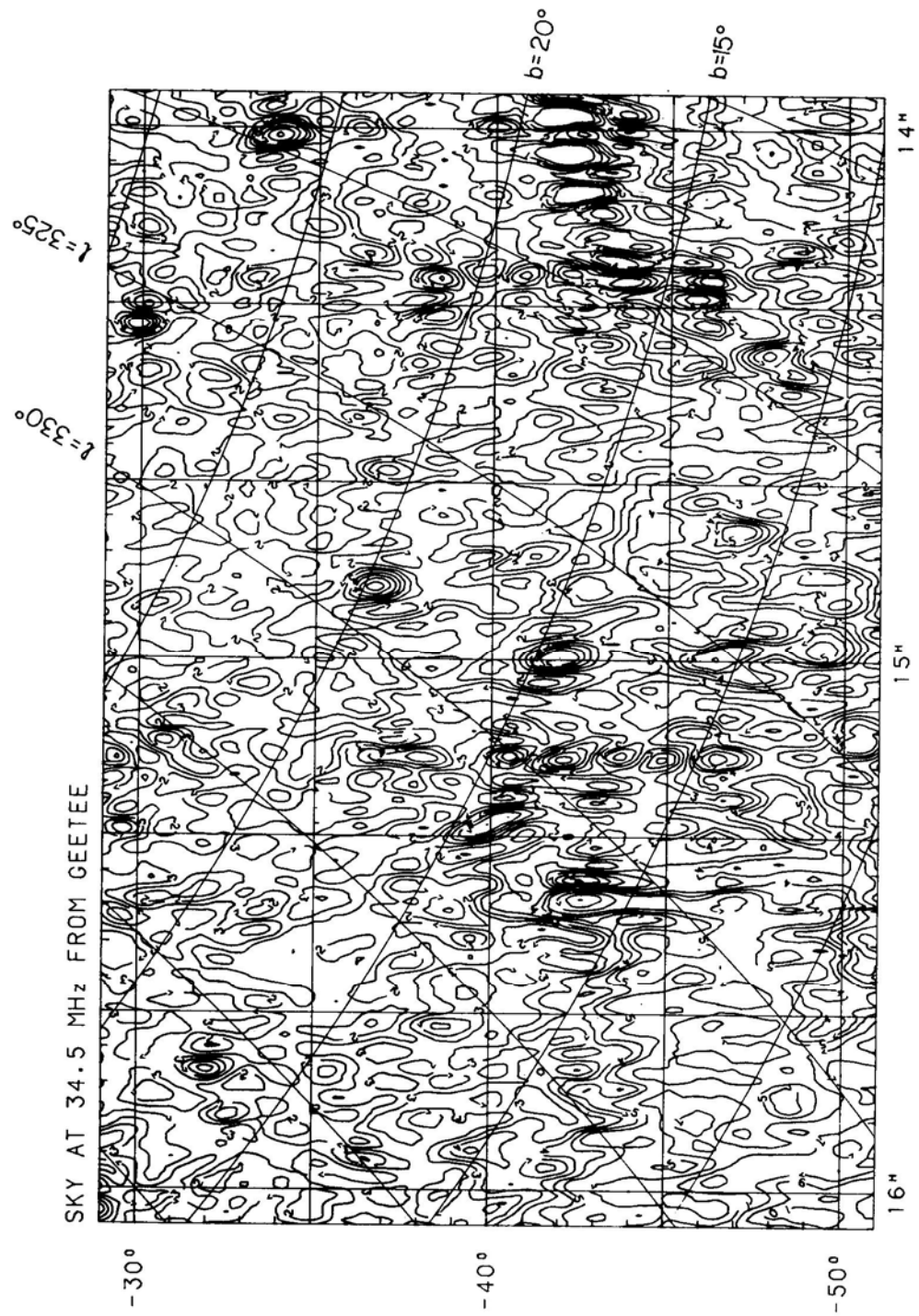
SKY AT 34.5 MHz FROM GEETEE
l=325°
l=330°
b=20°
b=15°
14ᴴ
15ᴴ
16ᴴ
-30°
-40°
-50°

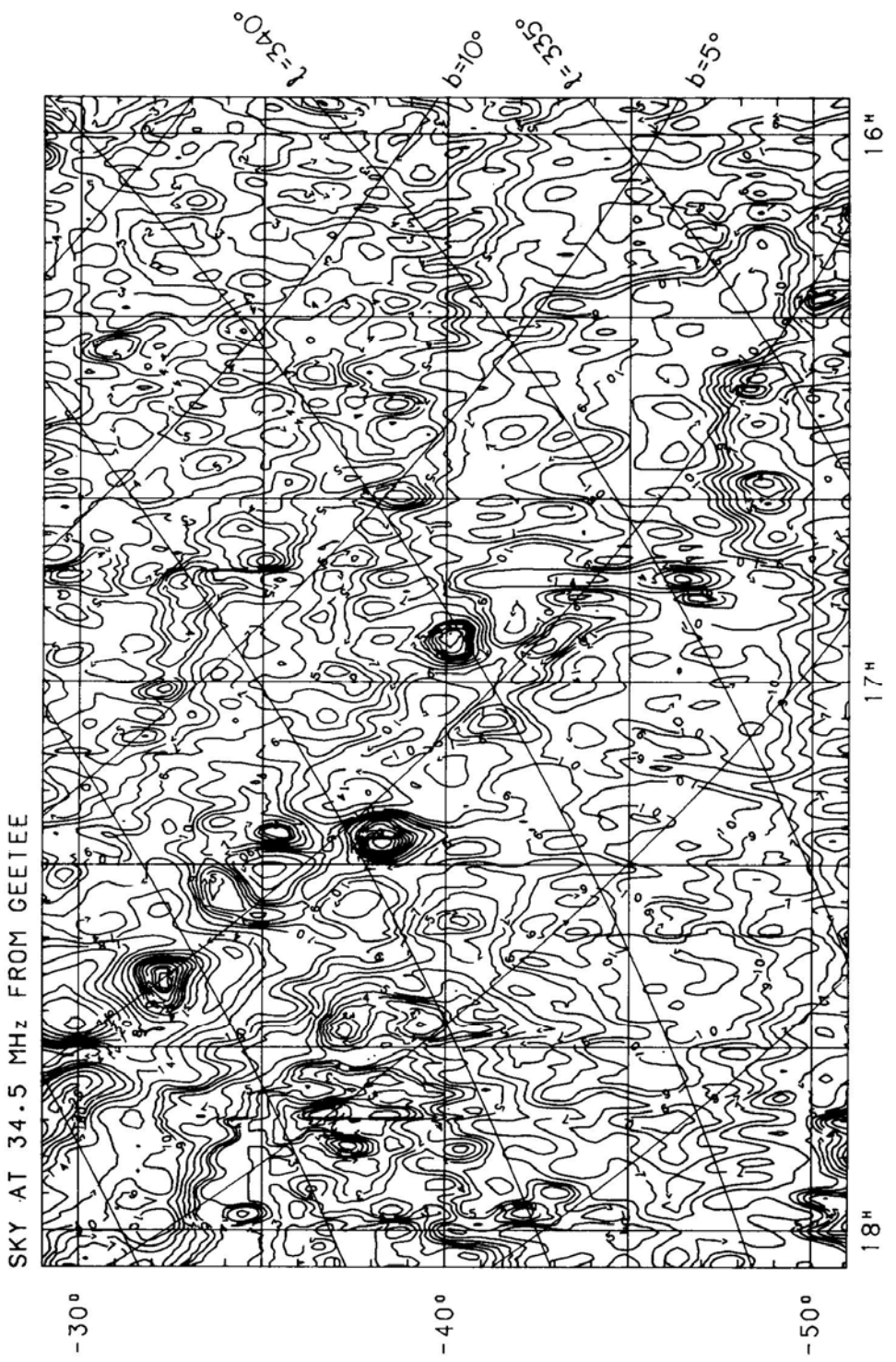
SKY AT 34.5 MHz FROM GEETEE
l=340°
b=10°
l=335°
b=5°
16ᴴ
17ᴴ
18ᴴ
-30°
-40°
-50°

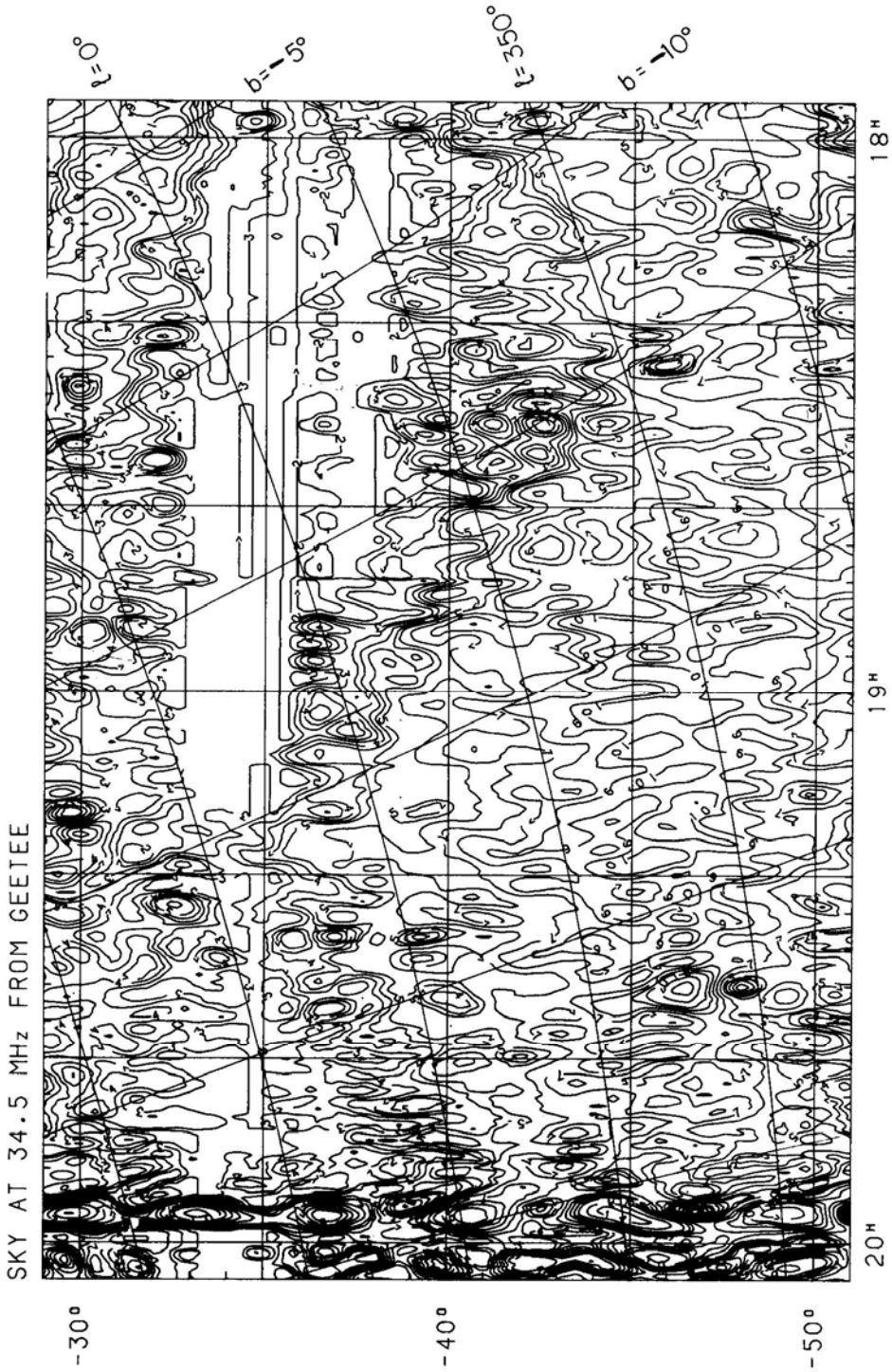
SKY AT 34.5 MHz FROM GEETEE
l=0°
b=-5°
l=350°
b=-10°
18ᴴ
19ᴴ
20ᴴ
-30°
-40°
-50°

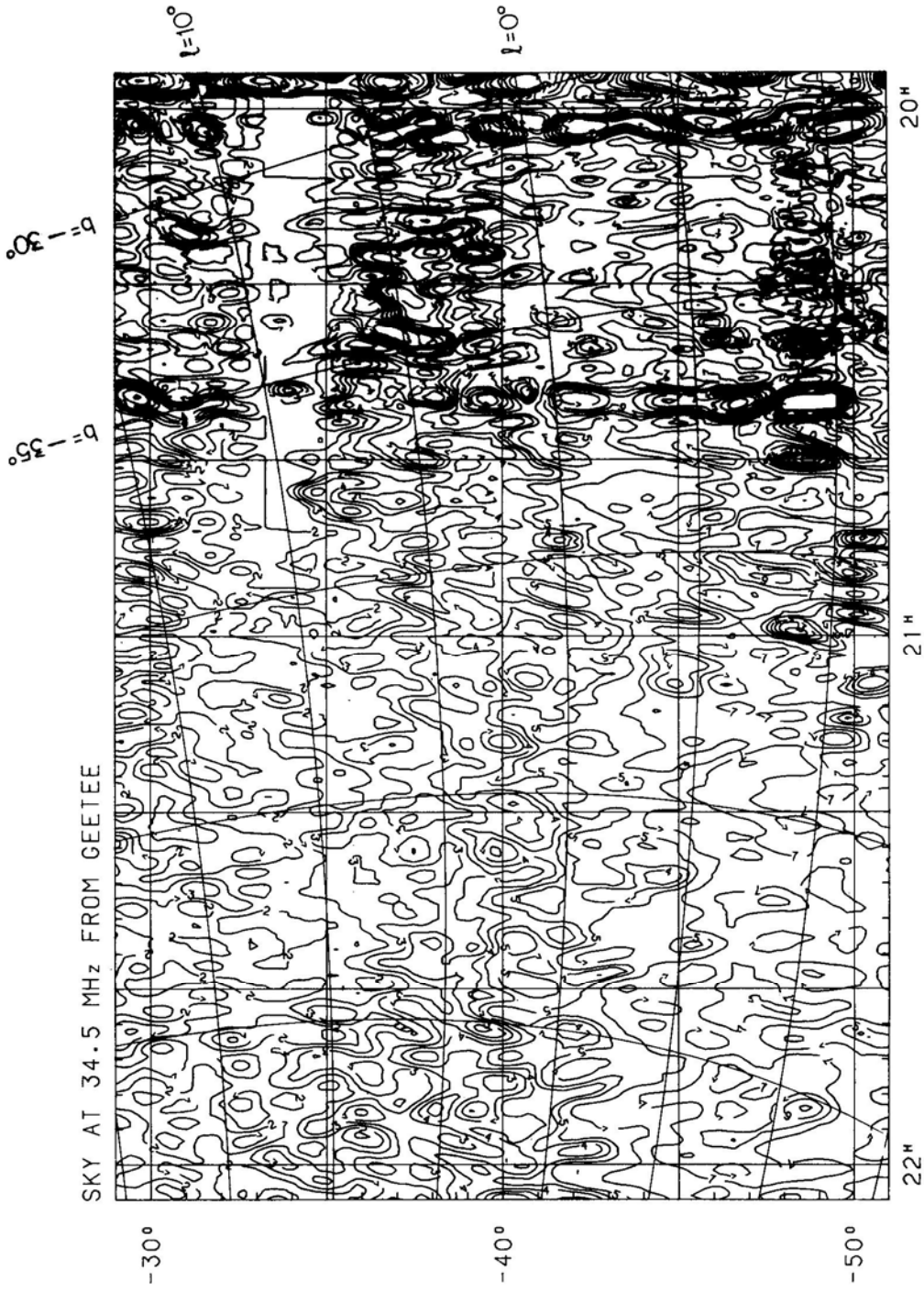
SKY AT 34.5 MHz FROM GEETEE
l=10°
l=0°
b=−30°
b=−35°
20ᴴ
21ᴴ
22ᴴ
-30°
-40°
-50°

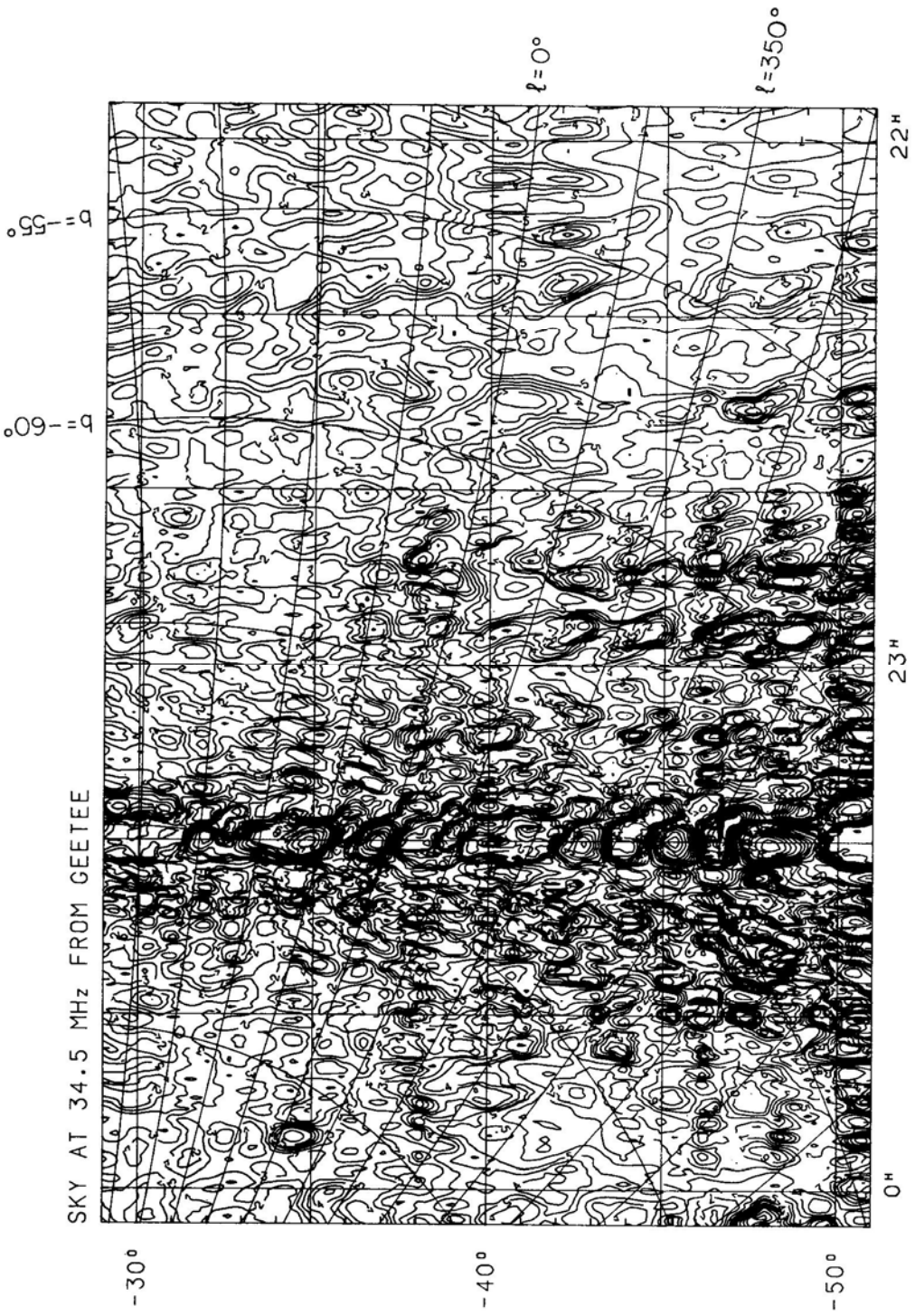
SKY AT 34.5 MHz FROM GEETEE
ℓ=0°
ℓ=350°
b=-55°
b=-60°
22ʰ
23ʰ
0ʰ
-30°
-40°
-50°

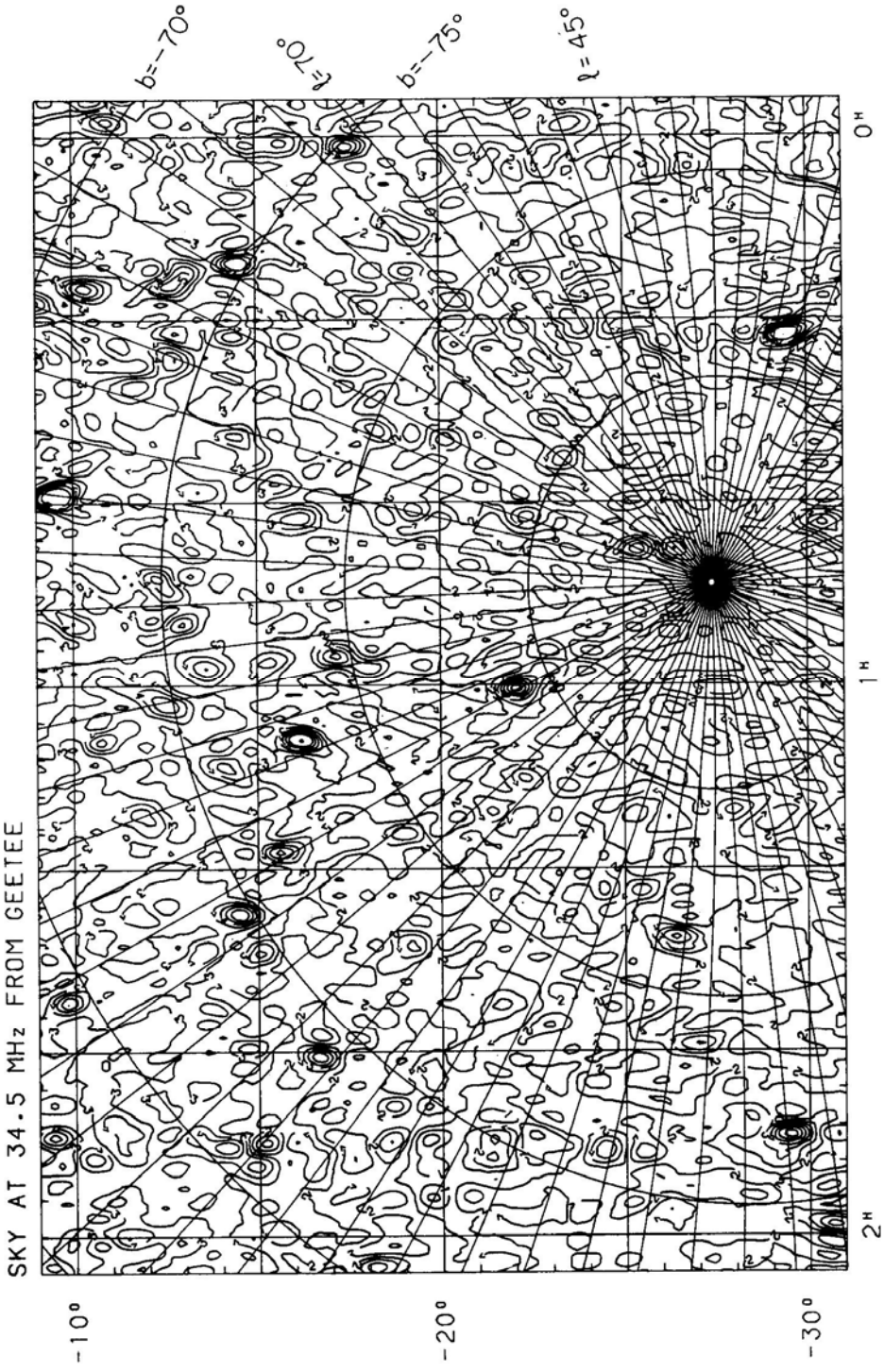
SKY AT 34.5 MHz FROM GEETEE
b=−70°
b=−75°
l=45°
0ʰ
1ʰ
2ʰ
−10°
−20°
−30°

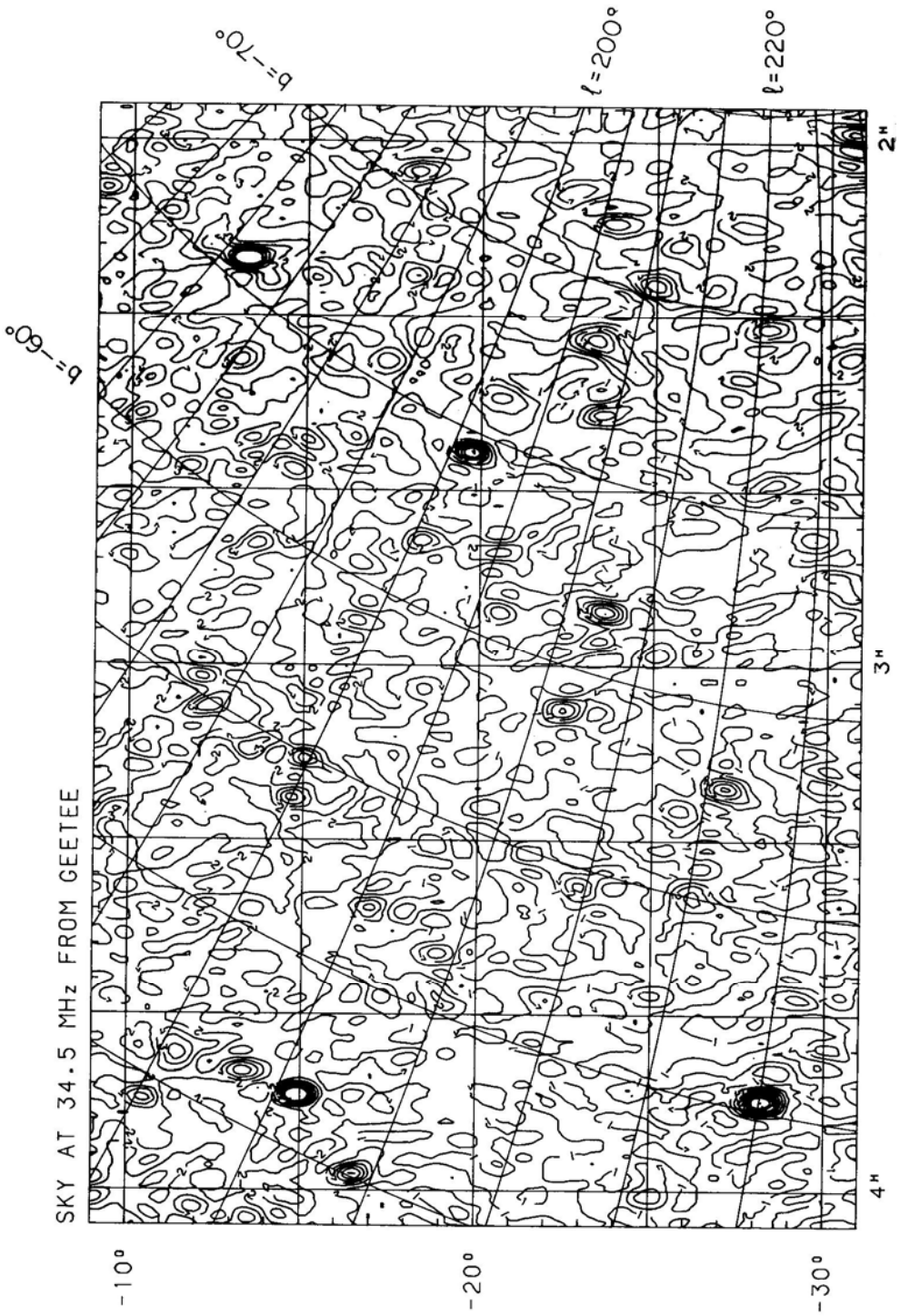
SKY AT 34.5 MHz FROM GEETEE
b=-60°
b=-70°
l=200°
l=220°
2H
3H
4H
-10°
-20°
-30°

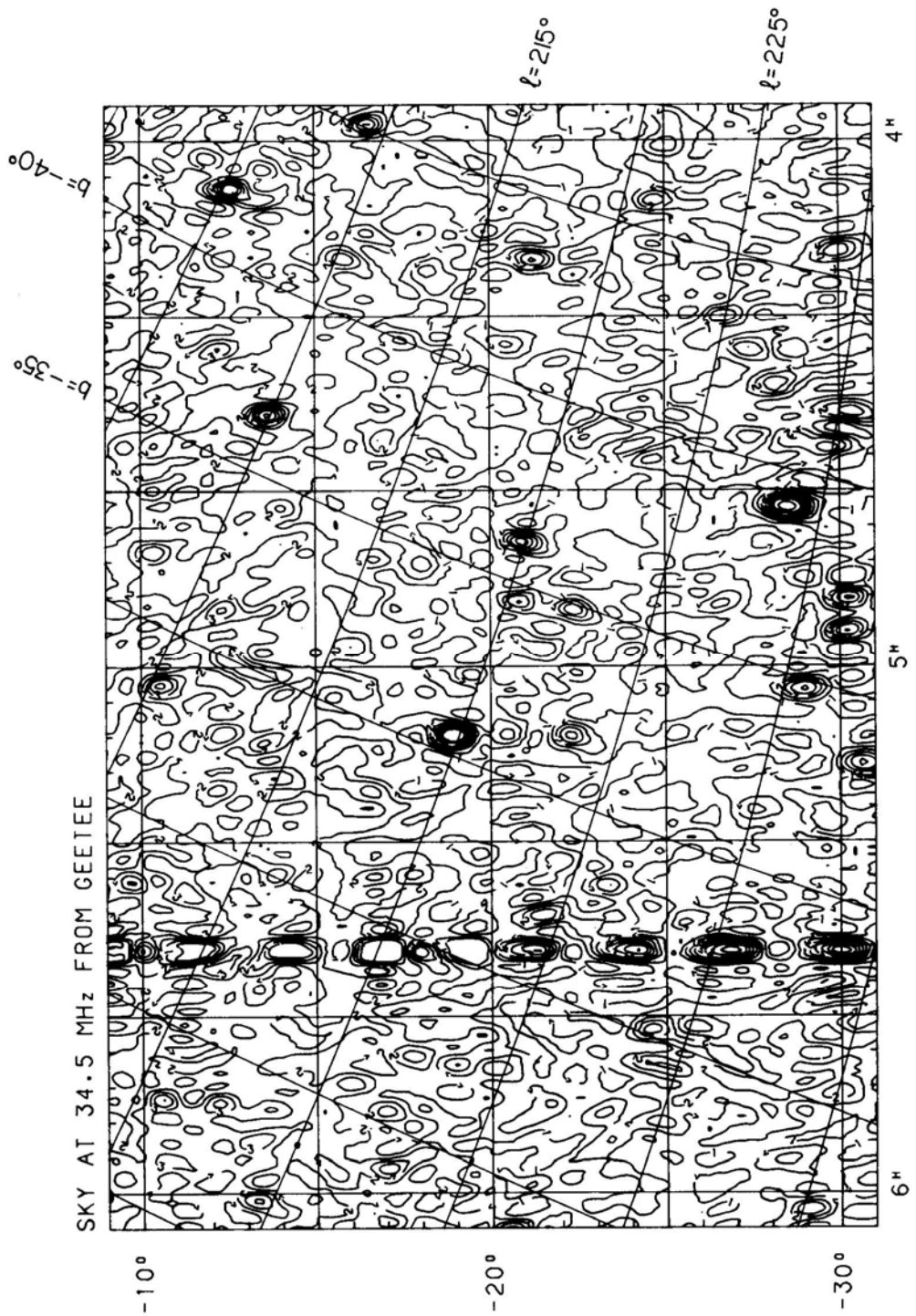
SKY AT 34.5 MHz FROM GEETEE
l=215°
l=225°
b=-40°
b=-35°
-10°
-20°
-30°
4H
5H
6H

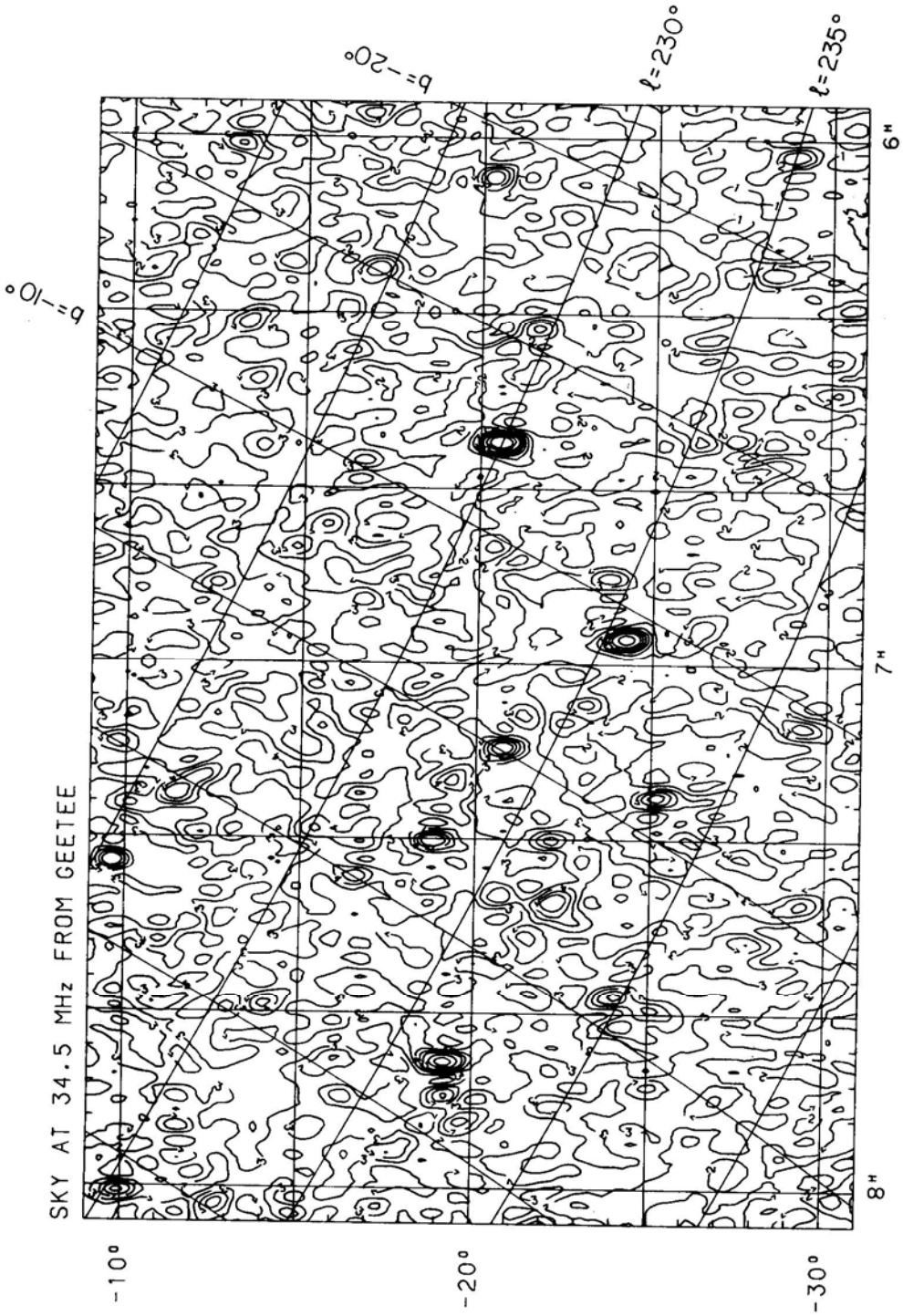
SKY AT 34.5 MHz FROM GEETEE
b=-10°
b=-20°
ℓ=230°
ℓ=235°
6H
7H
8H
-10°
-20°
-30°

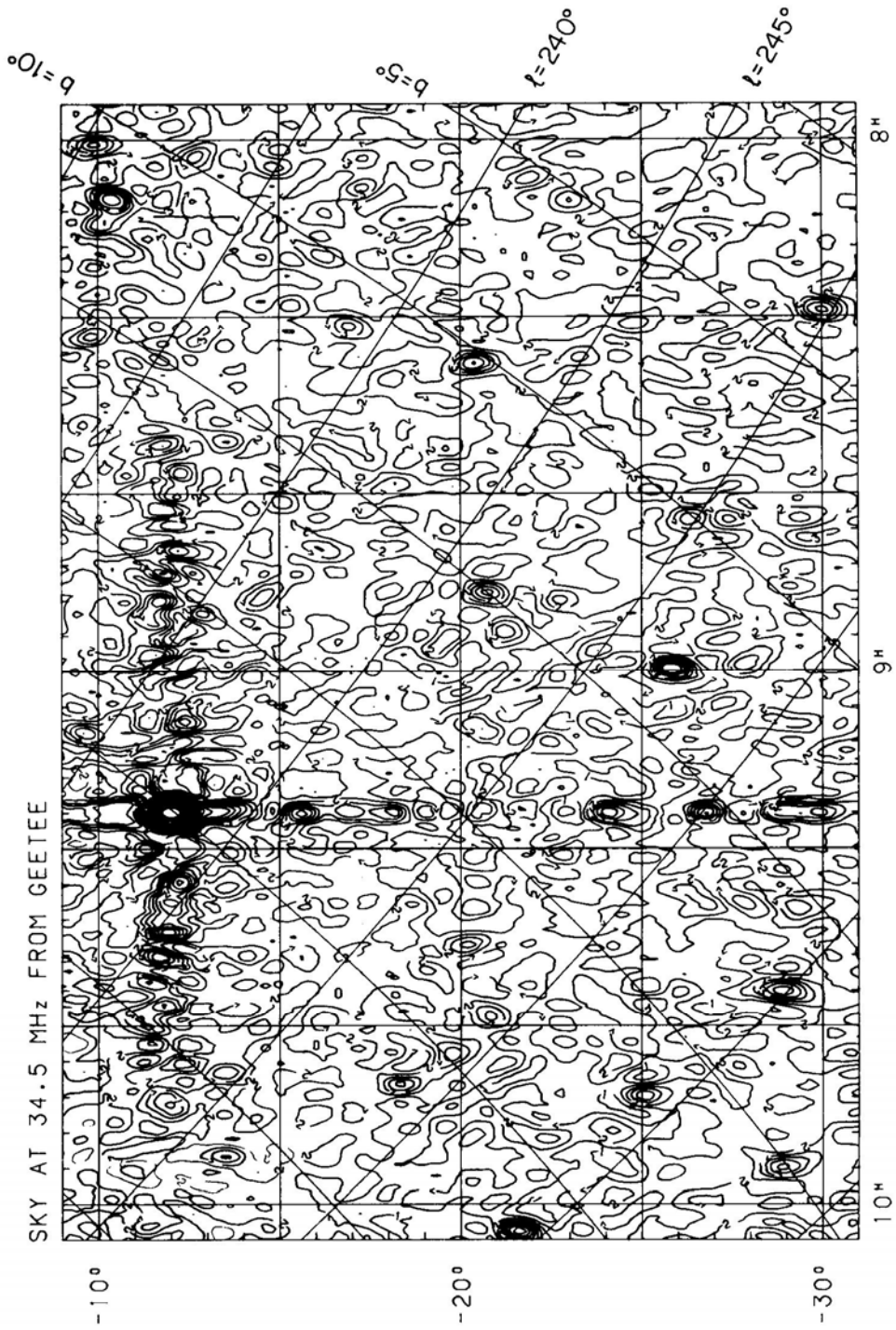
SKY AT 34.5 MHz FROM GEETEE
b=10°
b=5°
l=240°
l=245°
8ᴴ
9ᴴ
10ᴴ
-10°
-20°
-30°

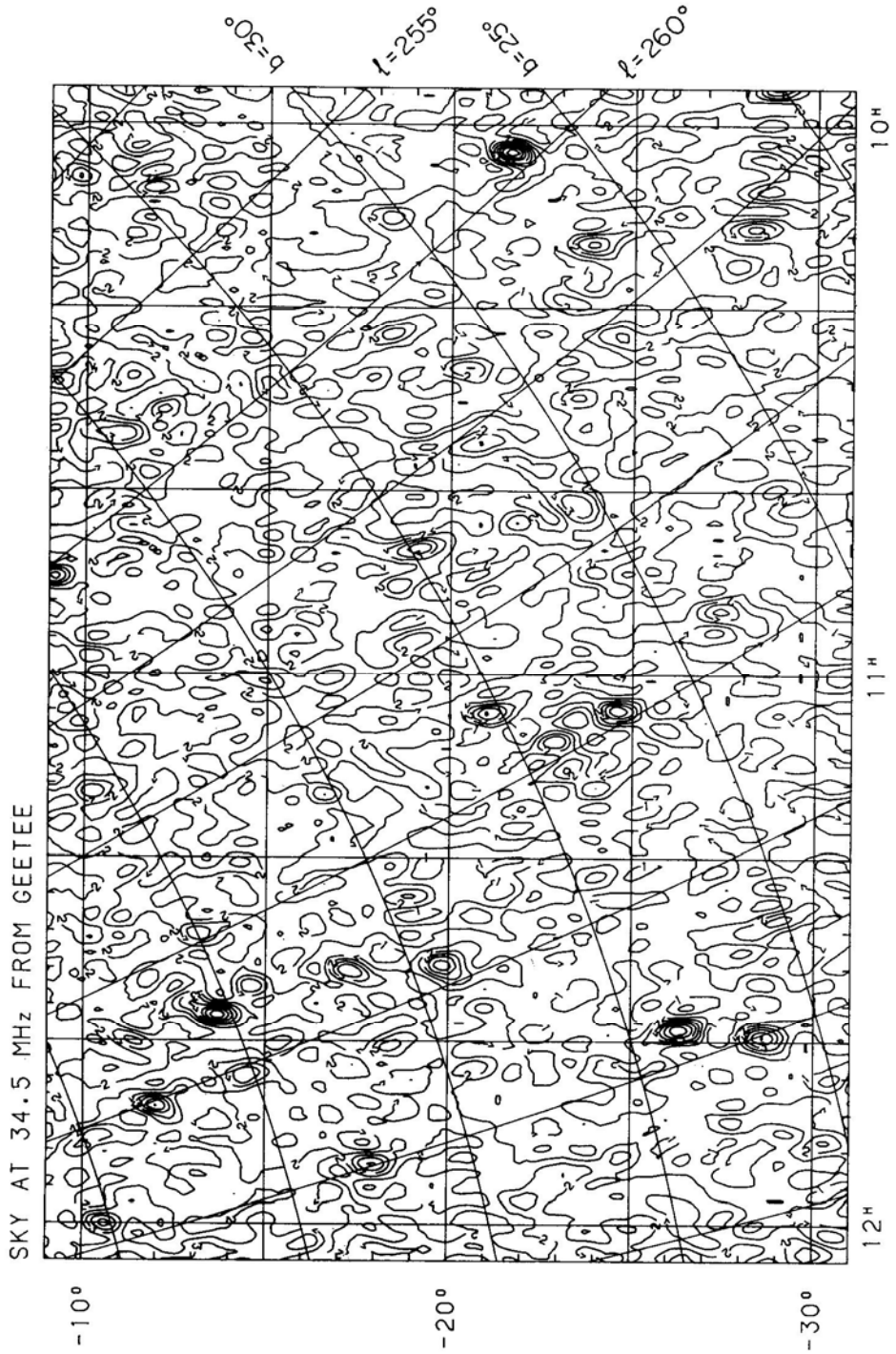
SKY AT 34.5 MHz FROM GEETEE
b=30°
l=255°
b=25°
l=260°
10H
11H
12H
-10°
-20°
-30°

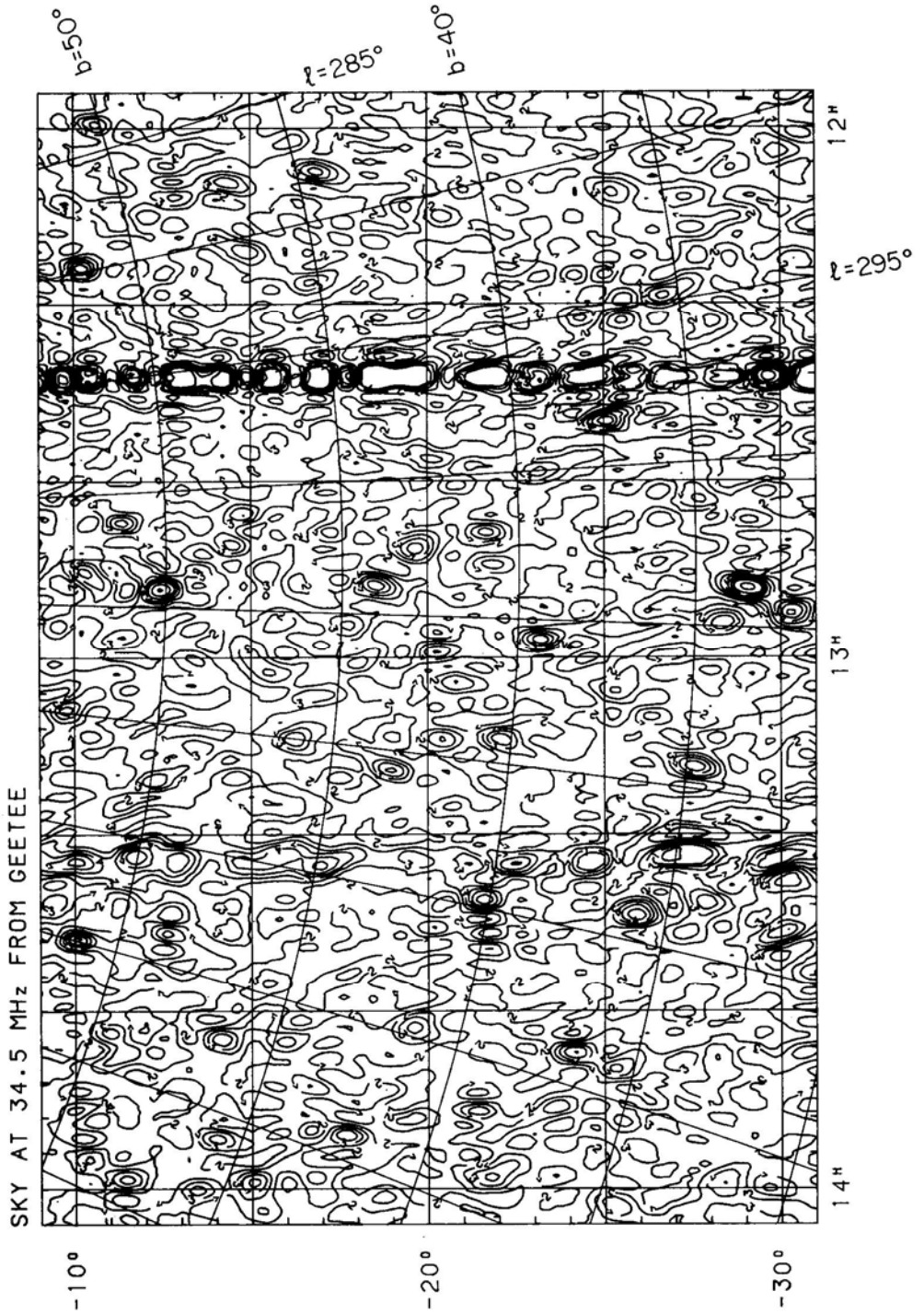
SKY AT 34.5 MHz FROM GEETEE
b=50°
ℓ=285°
b=40°
12ʰ
ℓ=295°
13ʰ
14ʰ
-10°
-20°
-30°

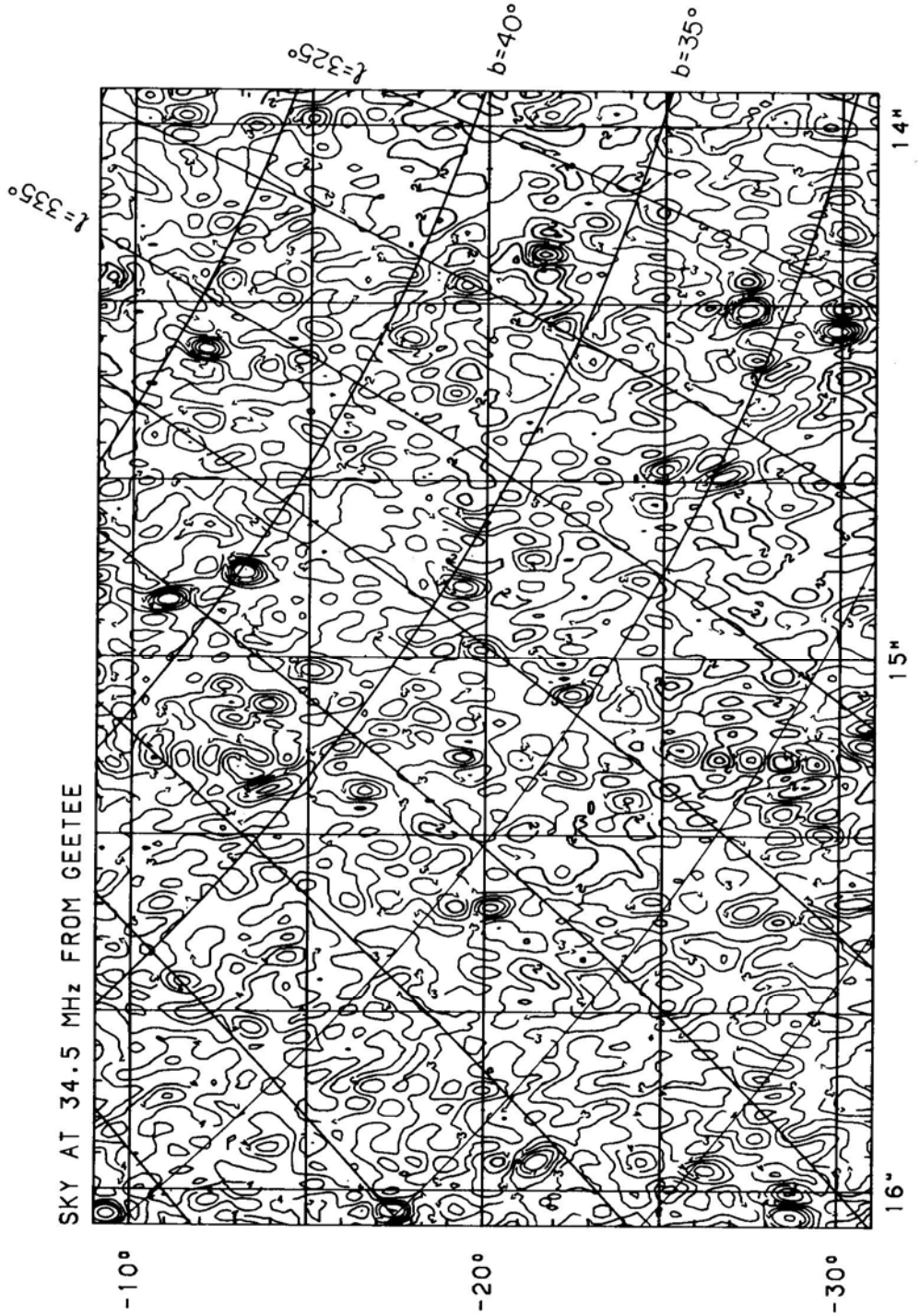
SKY AT 34.5 MHz FROM GEETEE
l=335°
l=325°
b=40°
b=35°
14ʰ
15ʰ
16ʰ
-10°
-20°
-30°

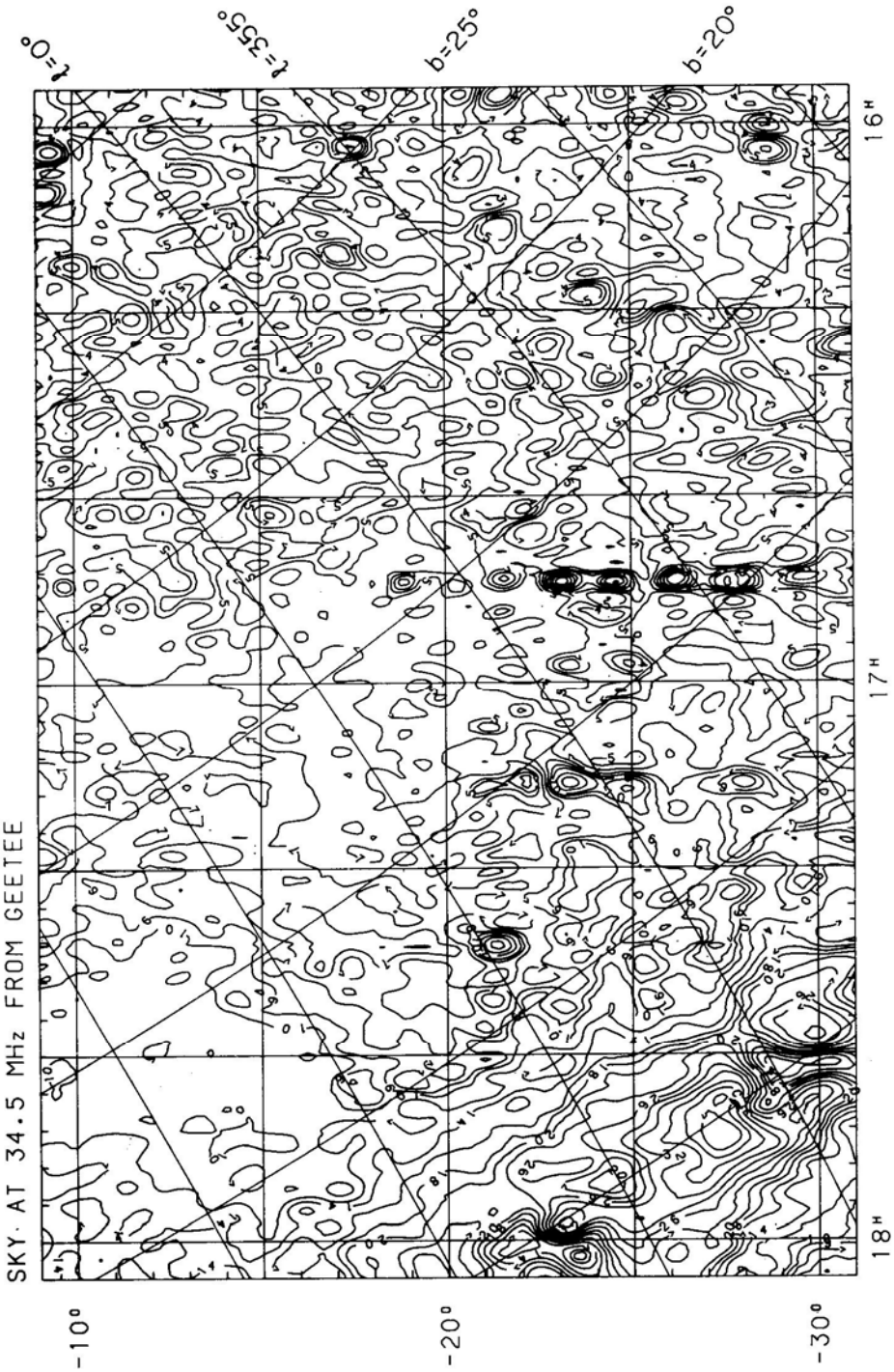
SKY AT 34.5 MHz FROM GEETEE
l=0°
l=355°
b=25°
b=20°
16ʰ
17ʰ
18ʰ
-10°
-20°
-30°

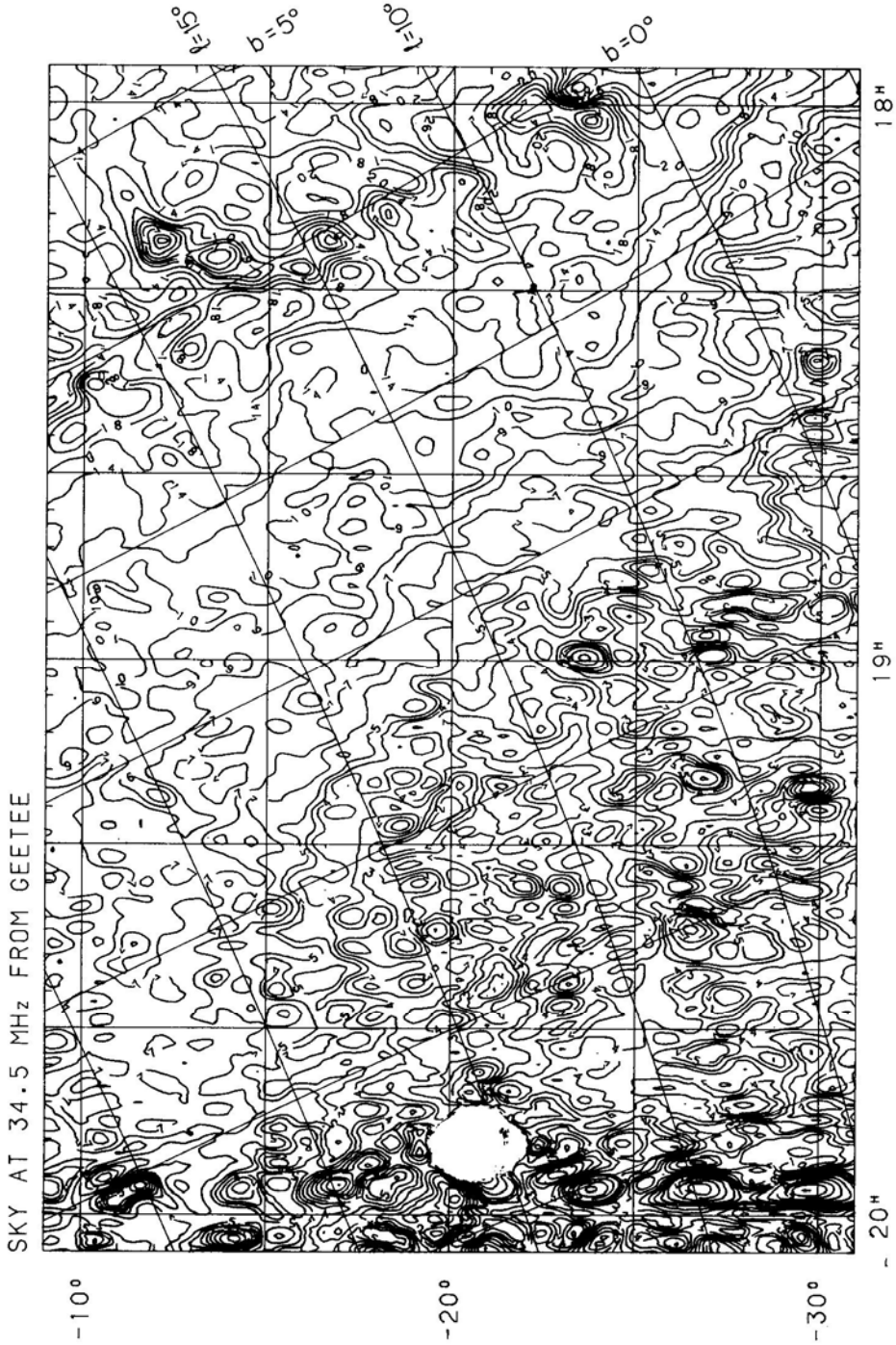
SKY AT 34.5 MHz FROM GEETEE
b=15°
b=5°
b=-5°
b=-10°
18H
19H
20H
-10°
-20°
-30°

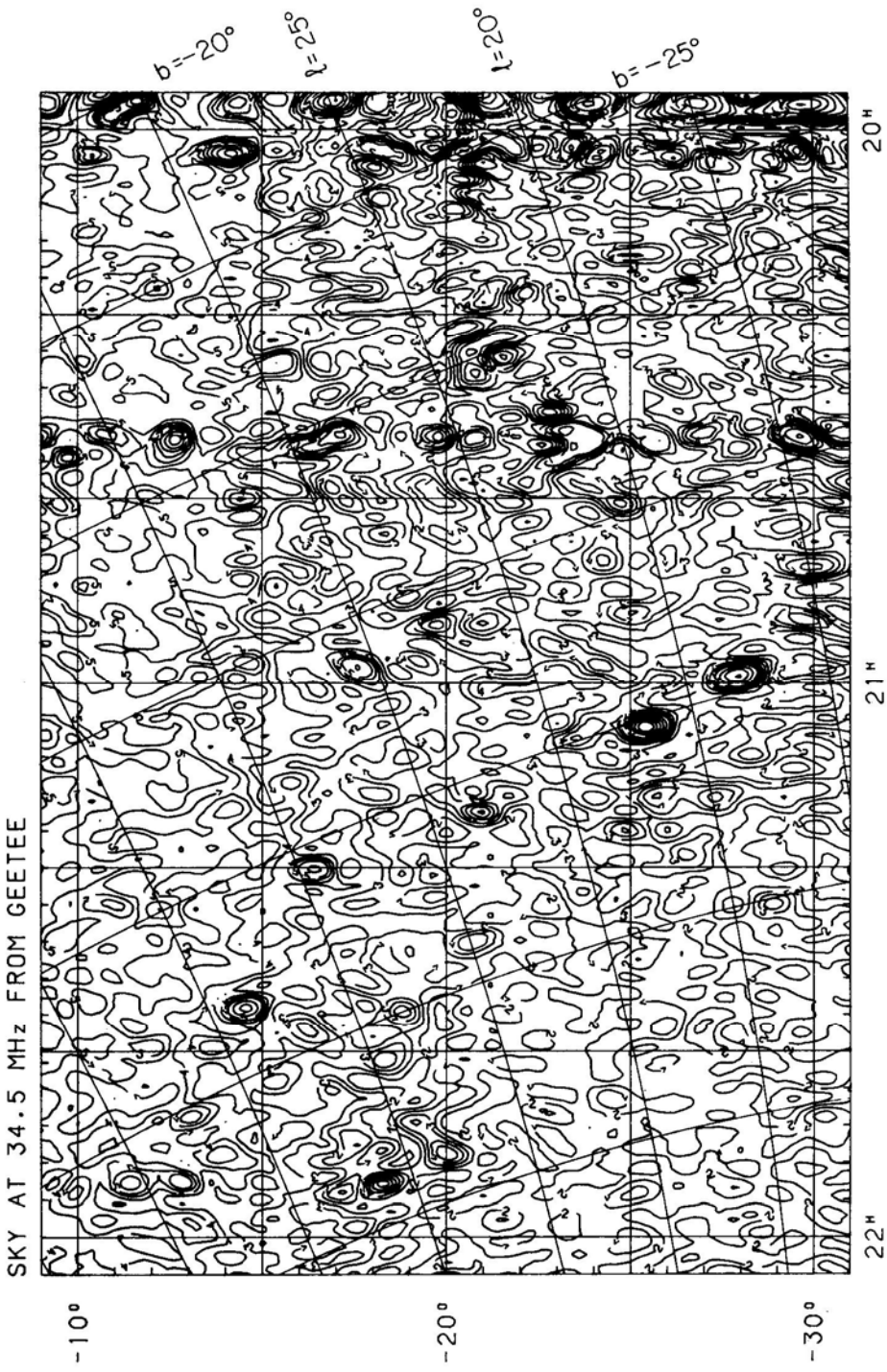
SKY AT 34.5 MHz FROM GEETEE
b=−20°
l=25°
l=20°
b=−25°
20ʰ
21ʰ
22ʰ
−10°
−20°
−30°

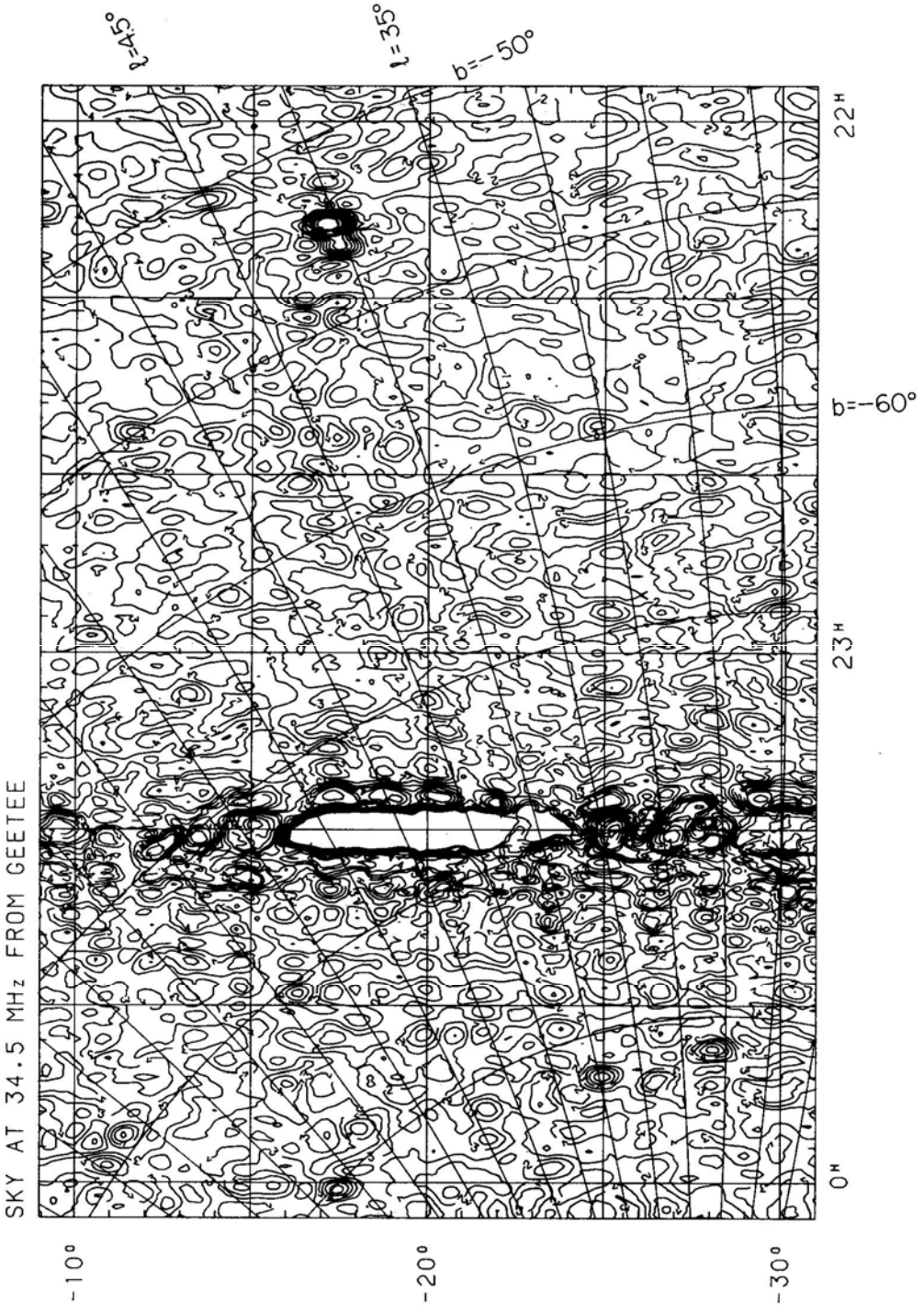
SKY AT 34.5 MHz FROM GEETEE
l=-45°
l=35°
b=-50°
b=-60°
22ʰ
23ʰ
0ʰ
-10°
-20°
-30°

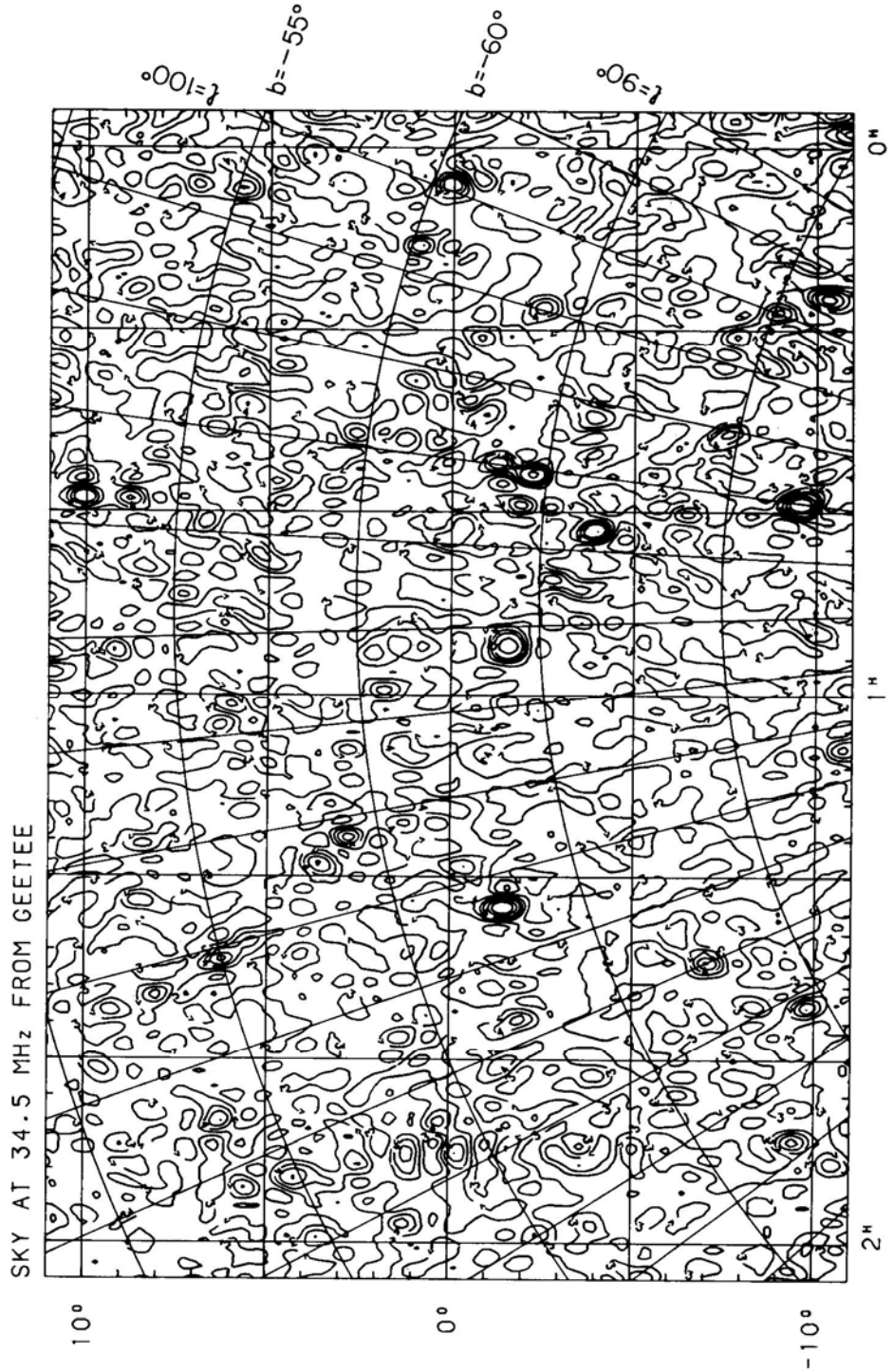
SKY AT 34.5 MHz FROM GEETEE
l=100°
b=−55°
b=−60°
l=90°
0ᴴ
1ᴴ
2ᴴ
10°
0°
−10°

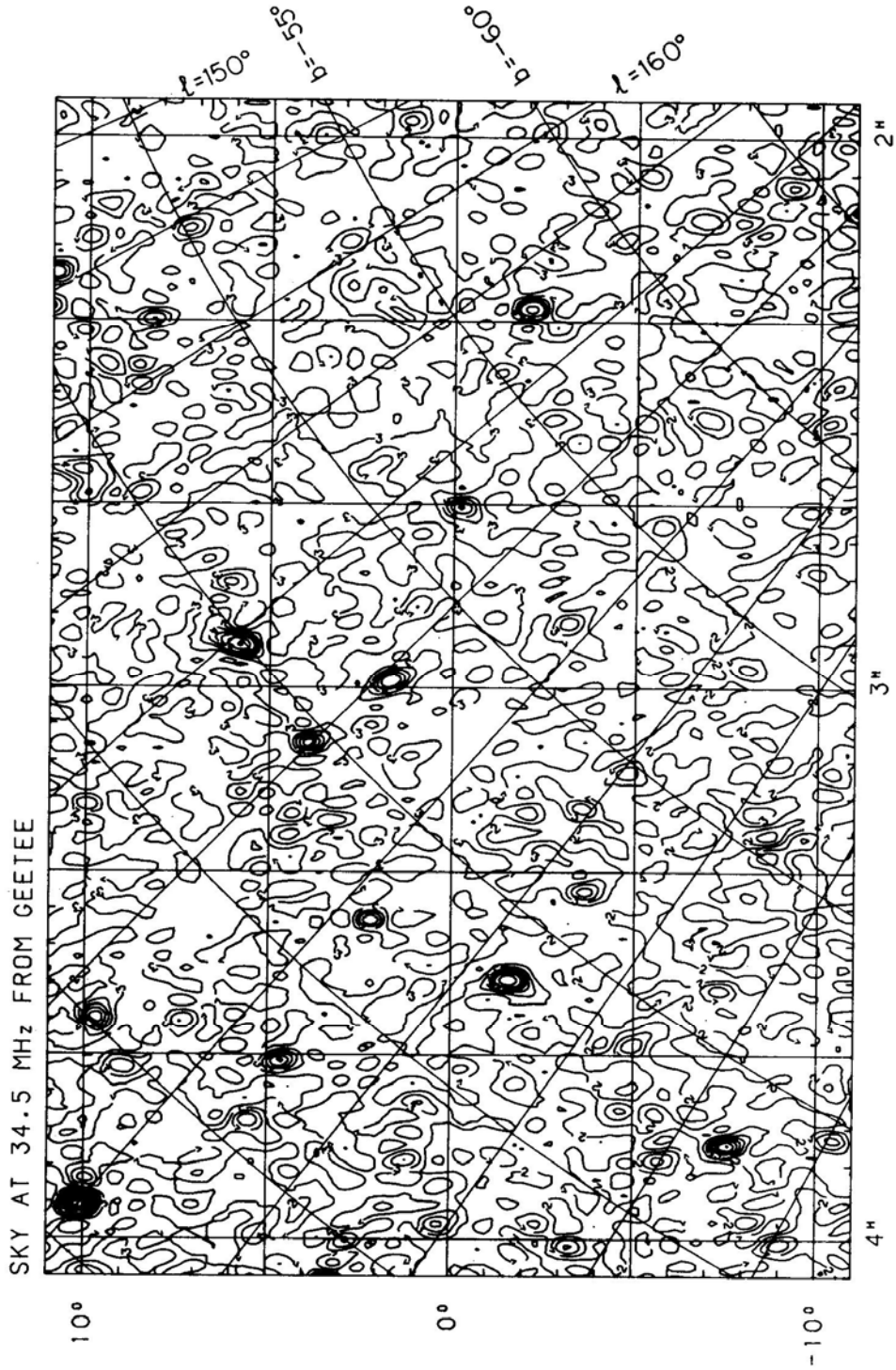
SKY AT 34.5 MHz FROM GEETEE
l=150°
b=-55°
b=-60°
l=160°
2H
3H
4H
10°
0°
-10°

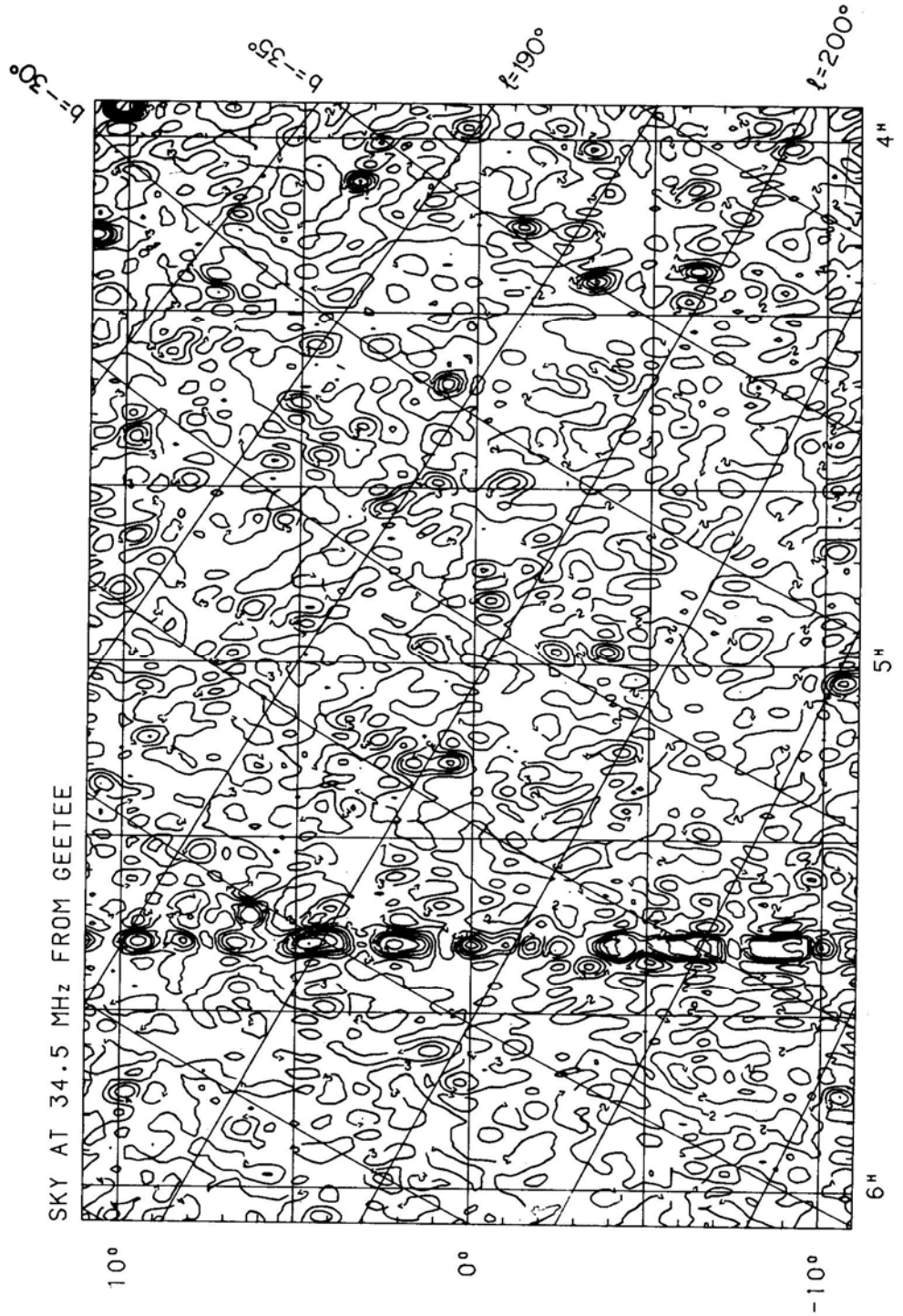
SKY AT 34.5 MHz FROM GEETEE
b=-30°
b=-35°
ℓ=190°
ℓ=200°
4ʰ
5ʰ
6ʰ
10°
0°
-10°

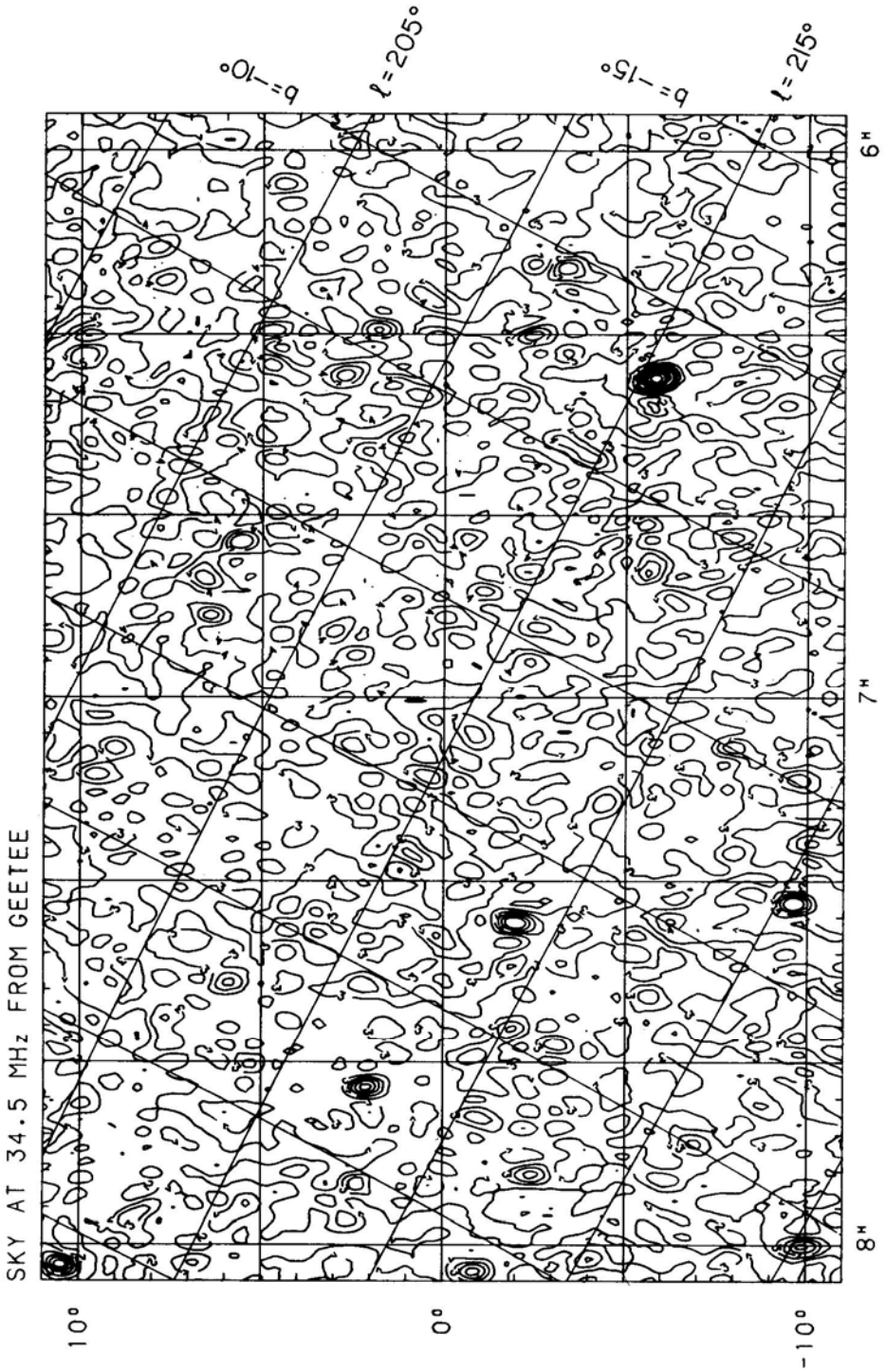
SKY AT 34.5 MHz FROM GEETEE
b=-10°
l=205°
b=-15°
l=215°
9H
7H
8H
10°
0°
-10°

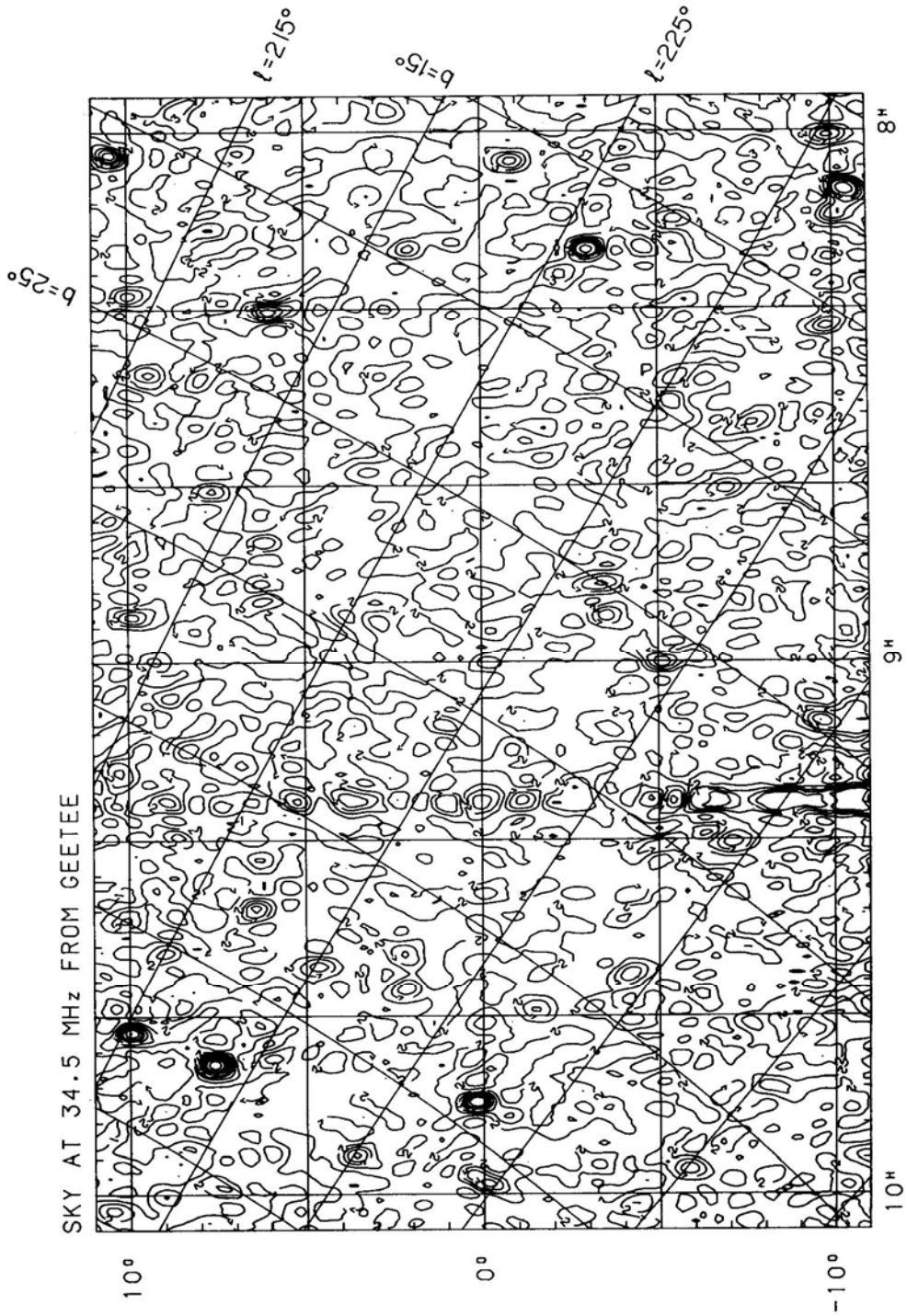
SKY AT 34.5 MHz FROM GEETEE
l=215°
b=15°
l=225°
b=25°
8ʰ
9ʰ
10ʰ
10°
0°
-10°

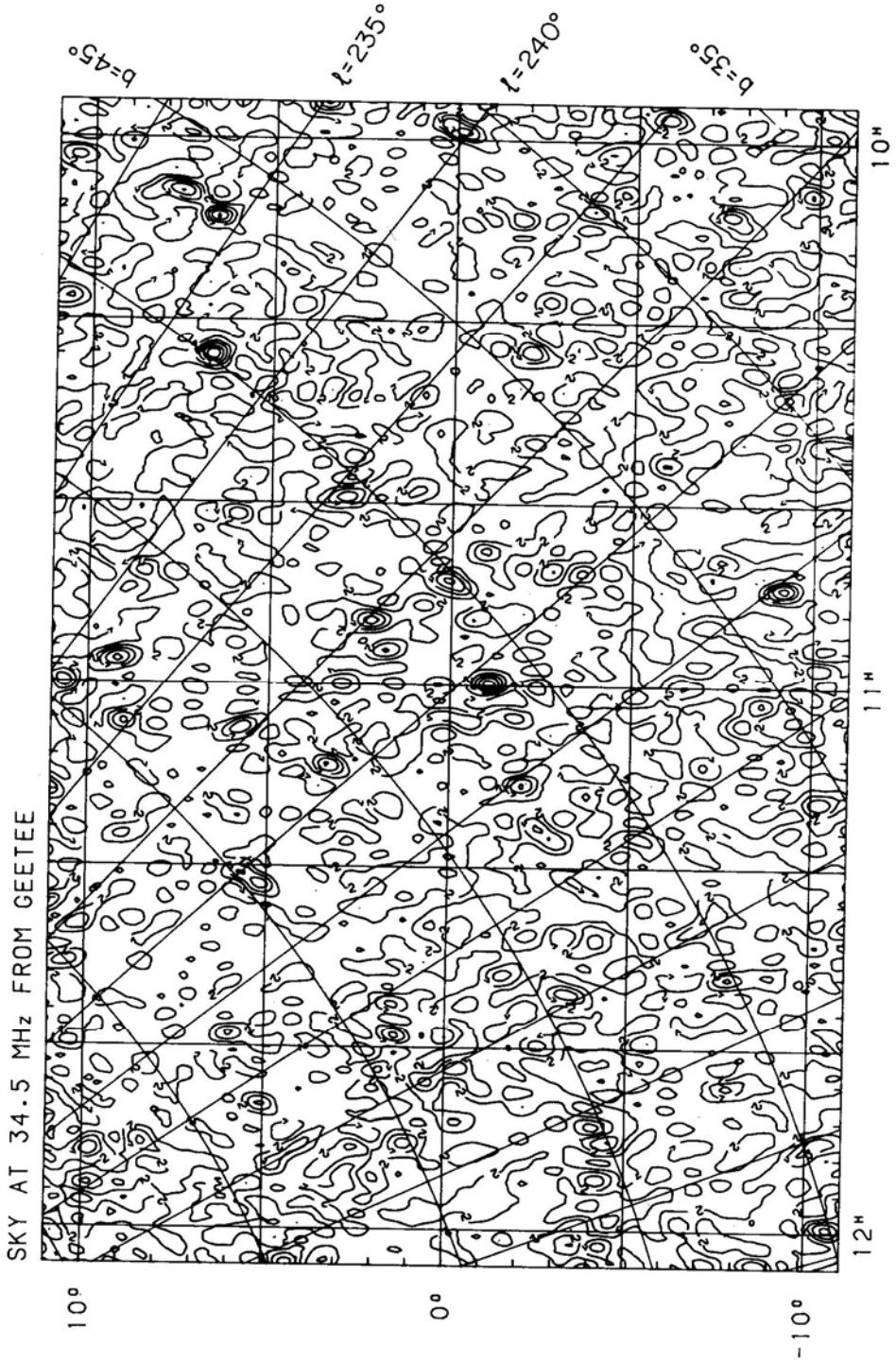
SKY AT 34.5 MHz FROM GEETEE
b=45°
l=235°
l=240°
b=35°
10°
0°
-10°
10ʰ
11ʰ
12ʰ

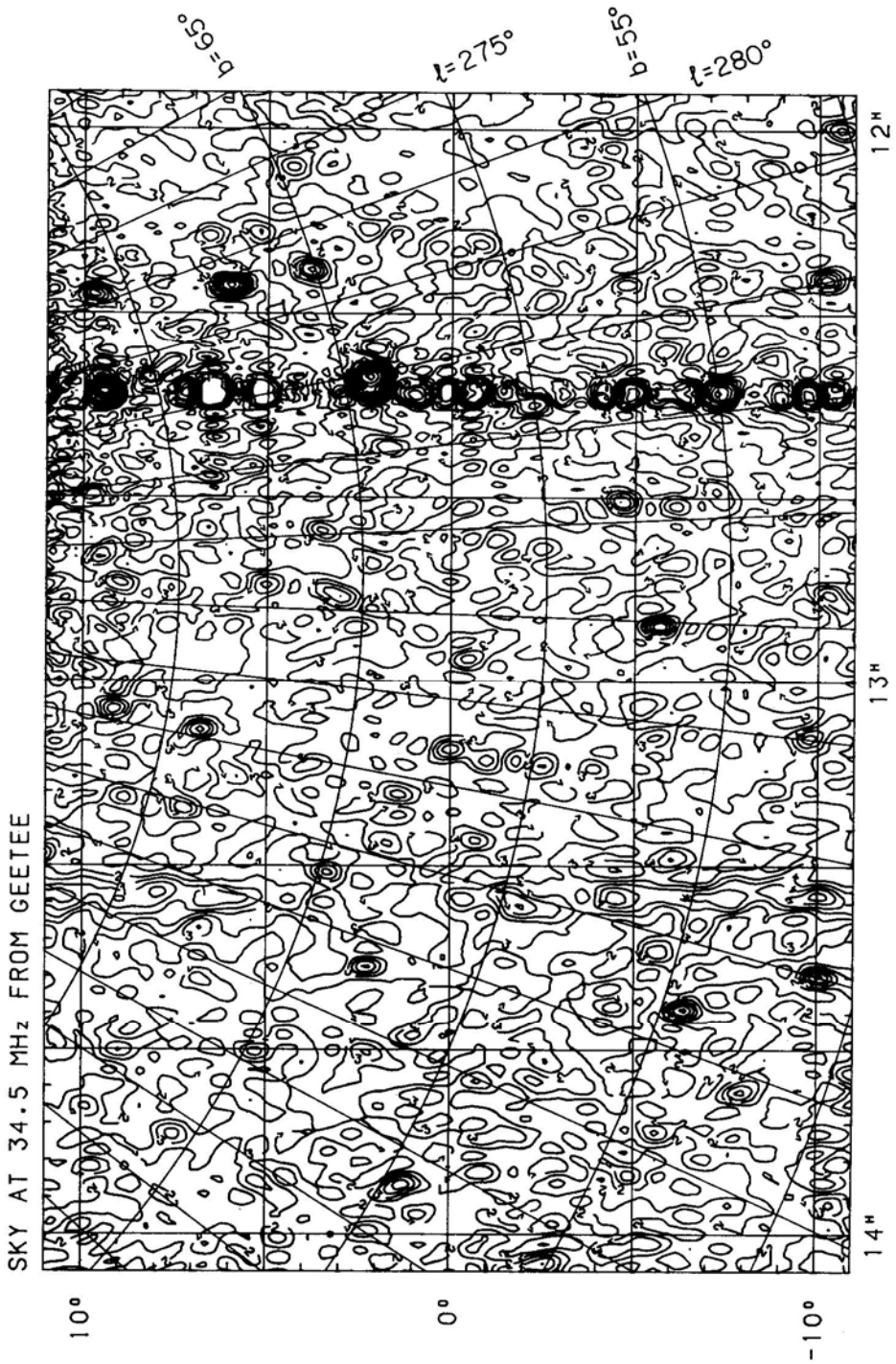
SKY AT 34.5 MHz FROM GEETEE
b=65°
l=275°
b=55°
l=280°
12H
13H
14H
10°
0°
-10°

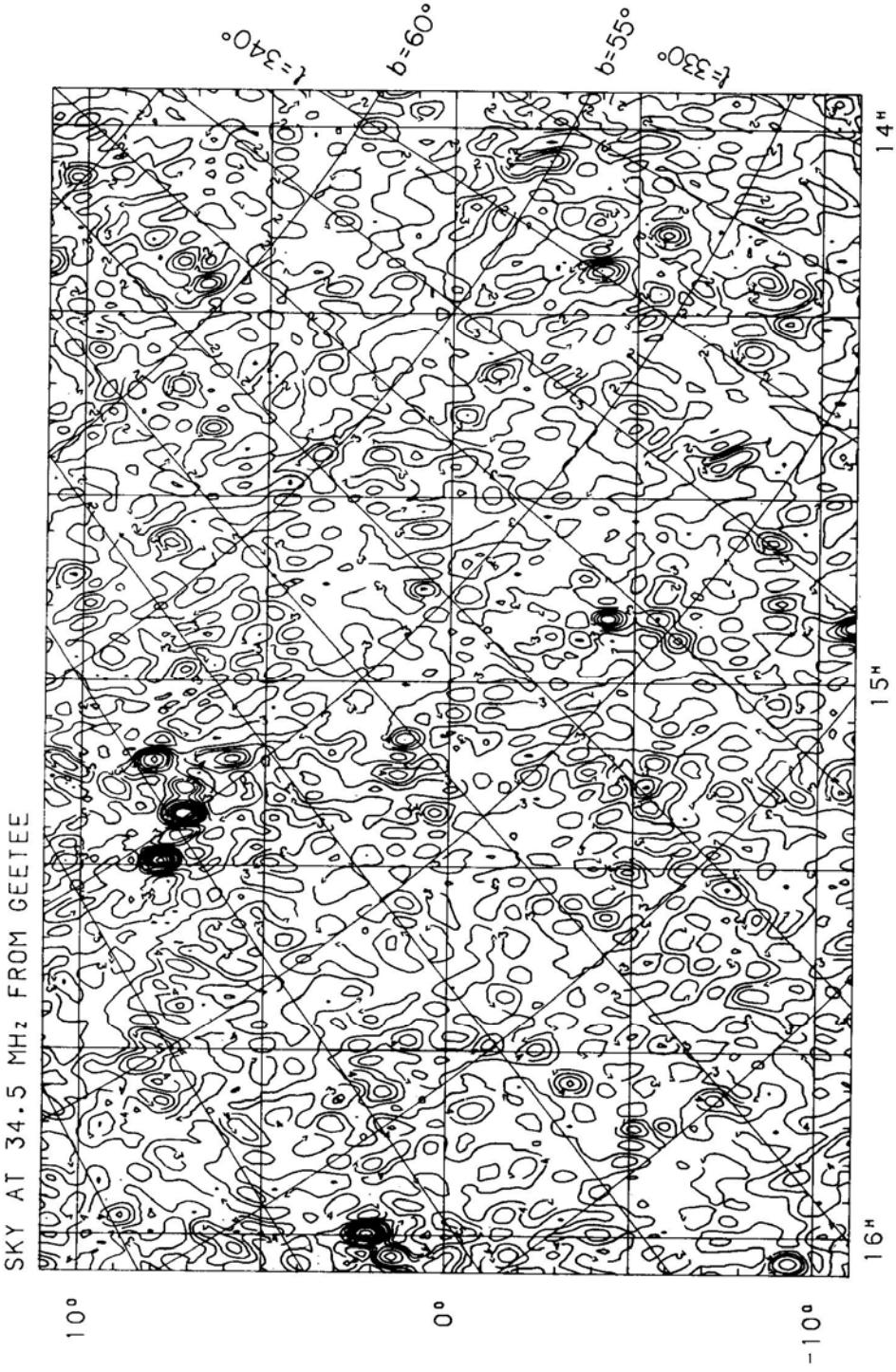
SKY AT 34.5 MHz FROM GEETEE
l=340°
b=60°
b=55°
l=330°
14ᴴ
15ᴴ
16ᴴ
10°
0°
-10°

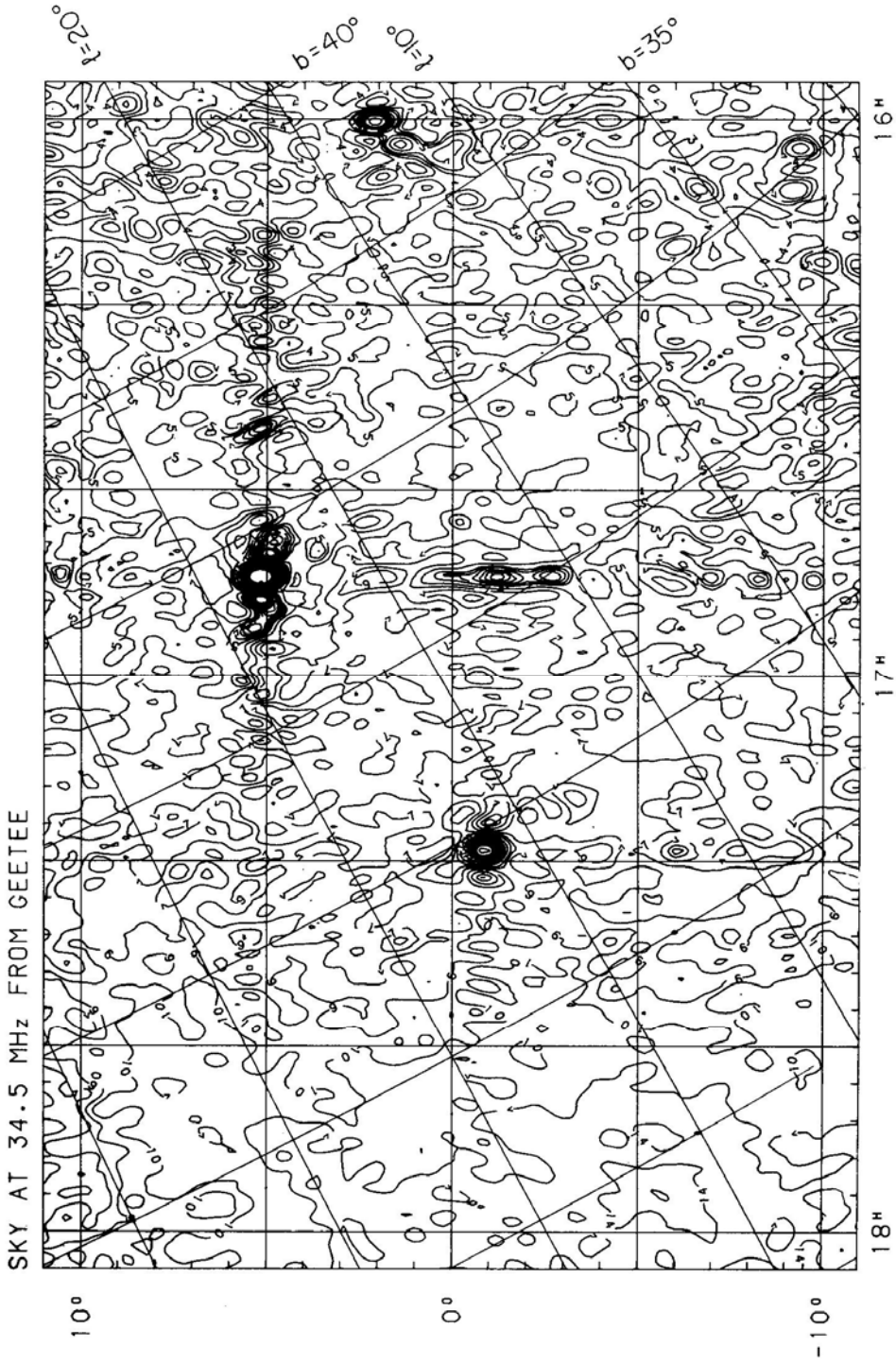
SKY AT 34.5 MHz FROM GEETEE
b=20°
b=40°
b=10°
b=35°
16ᴴ
17ᴴ
18ᴴ
10°
0°
-10°

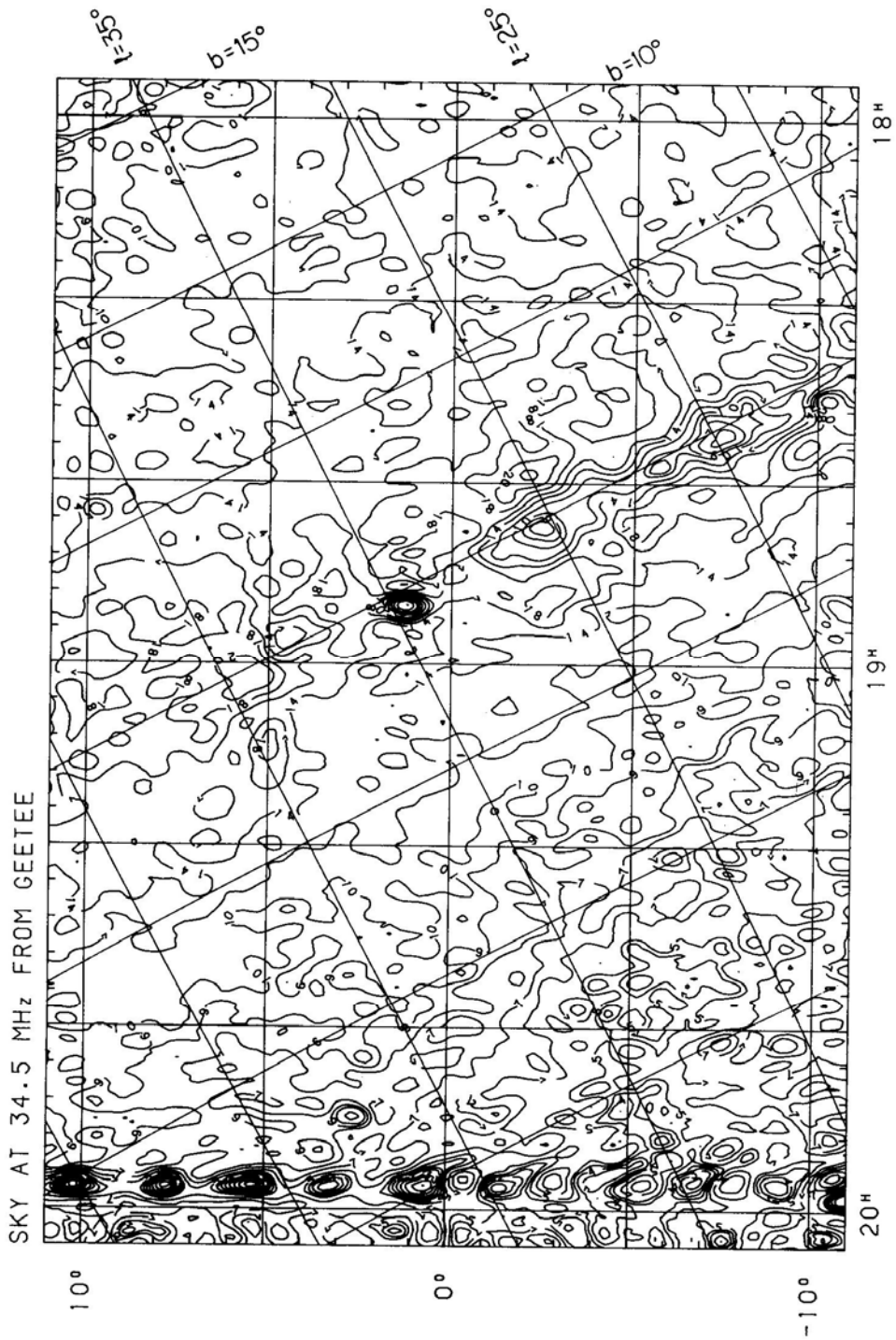
SKY AT 34.5 MHz FROM GEETEE
l=35°
b=15°
l=25°
b=10°
18H
19H
20H
10°
0°
-10°

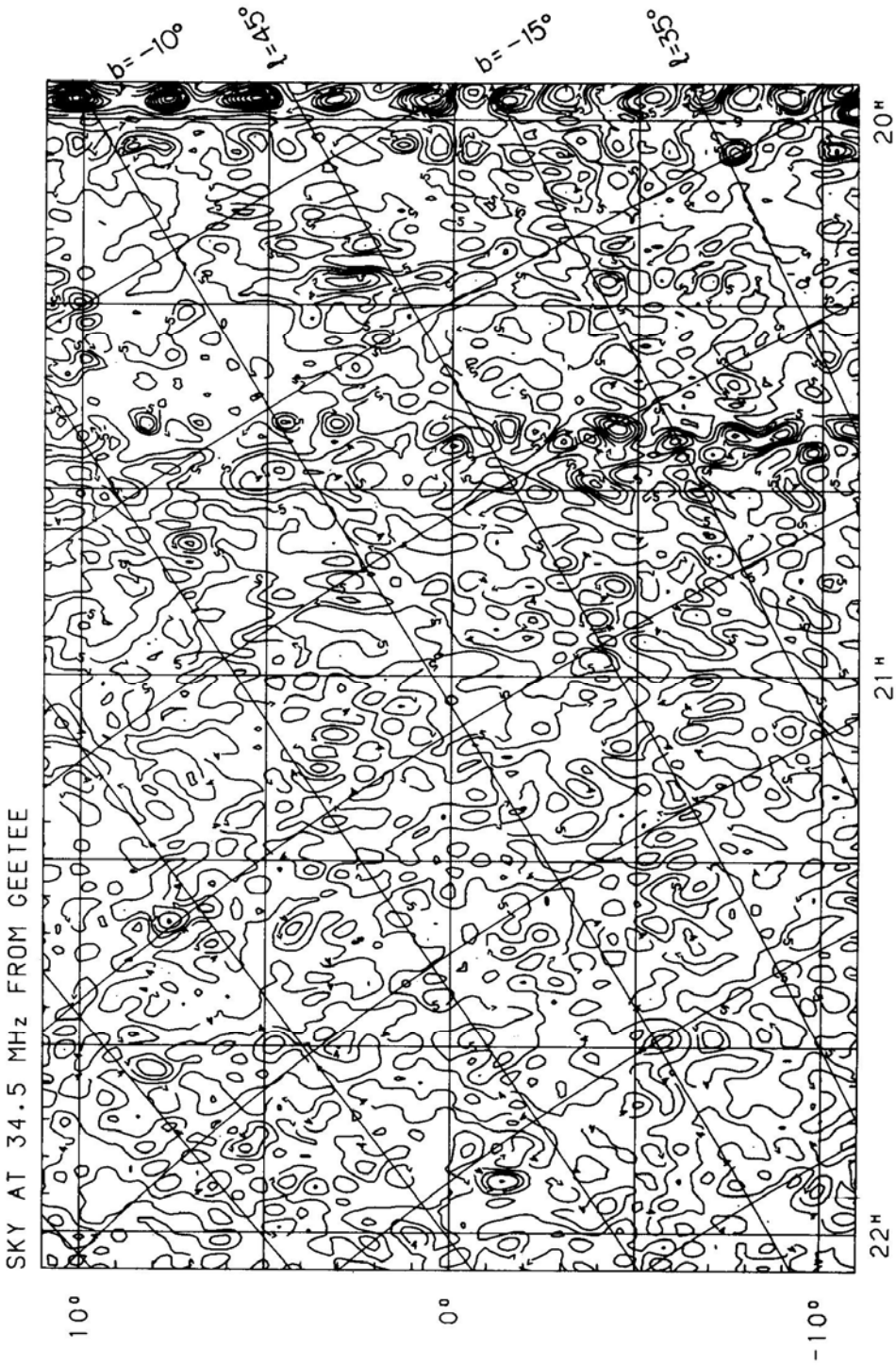
SKY AT 34.5 MHz FROM GEETEE
b= −10°
l=45°
b= −15°
l=35°
20ᴴ
21ᴴ
22ᴴ
10°
0°
−10°

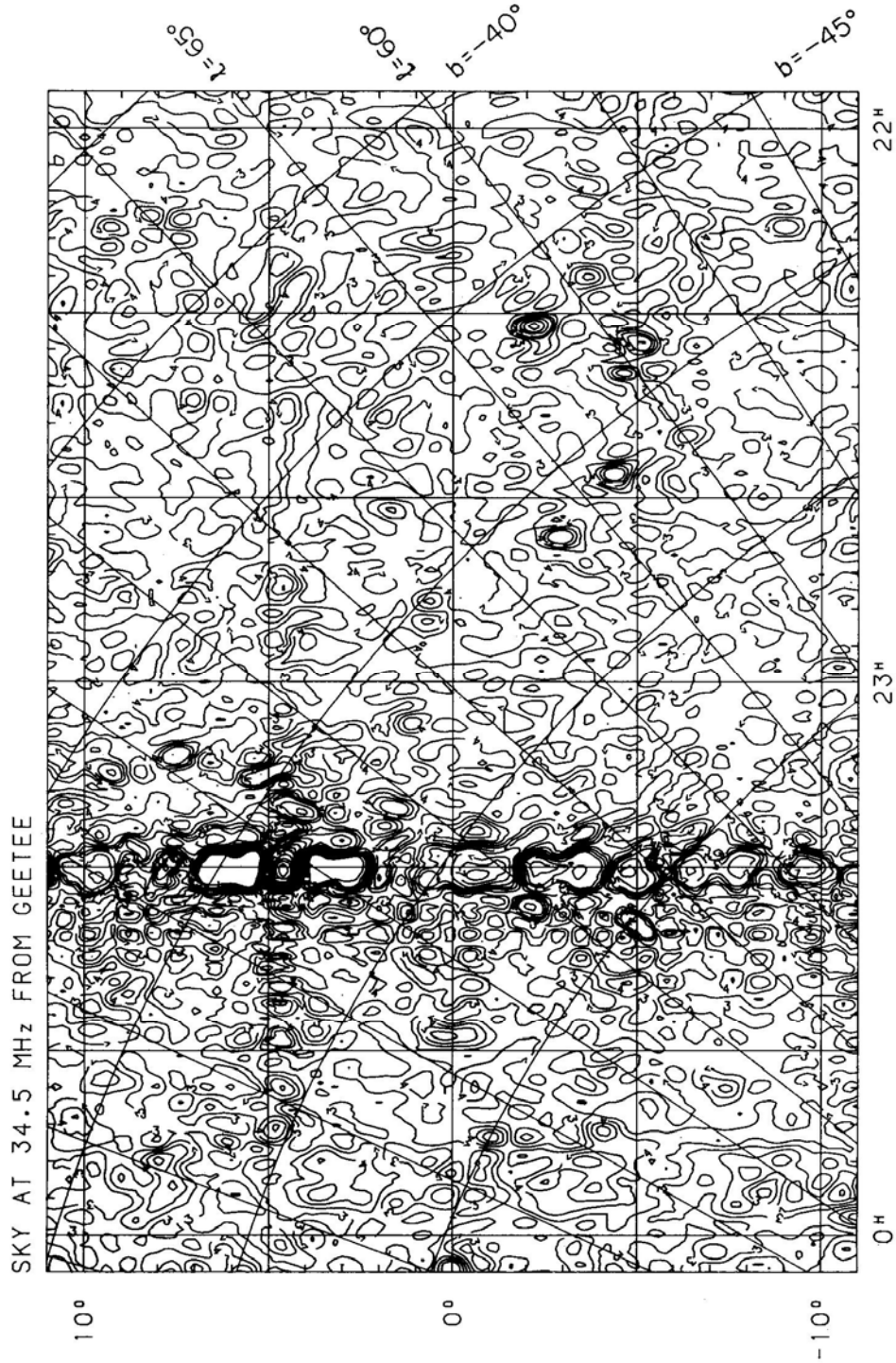
SKY AT 34.5 MHz FROM GEETEE
l=65°
l=60°
b=-40°
b=-45°
22ᴴ
23ᴴ
0ᴴ
10°
0°
-10°

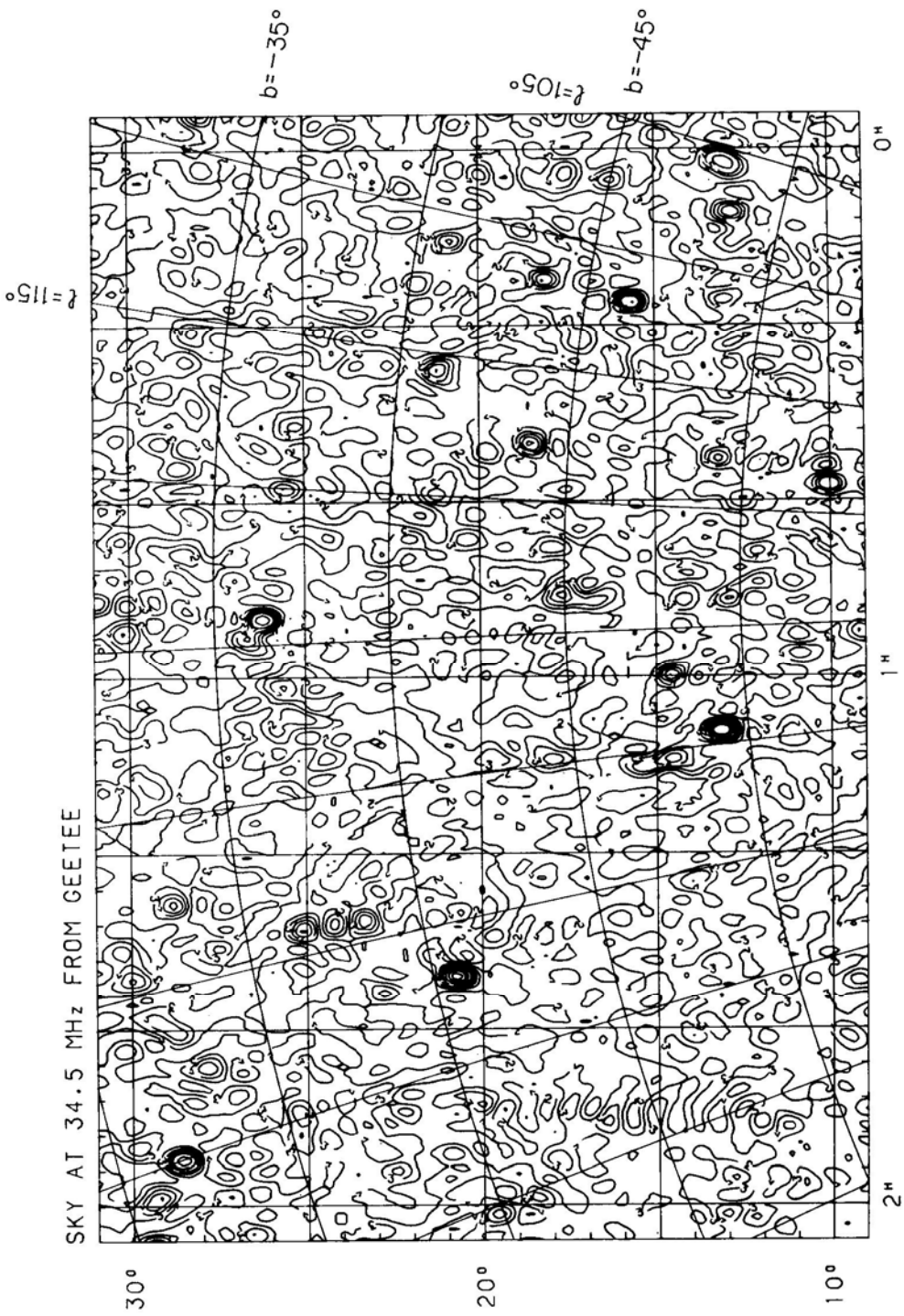
SKY AT 34.5 MHz FROM GEETEE
b=−35°
b=−45°
ℓ=105°
ℓ=115°
0ʰ
1ʰ
2ʰ
30°
20°
10°

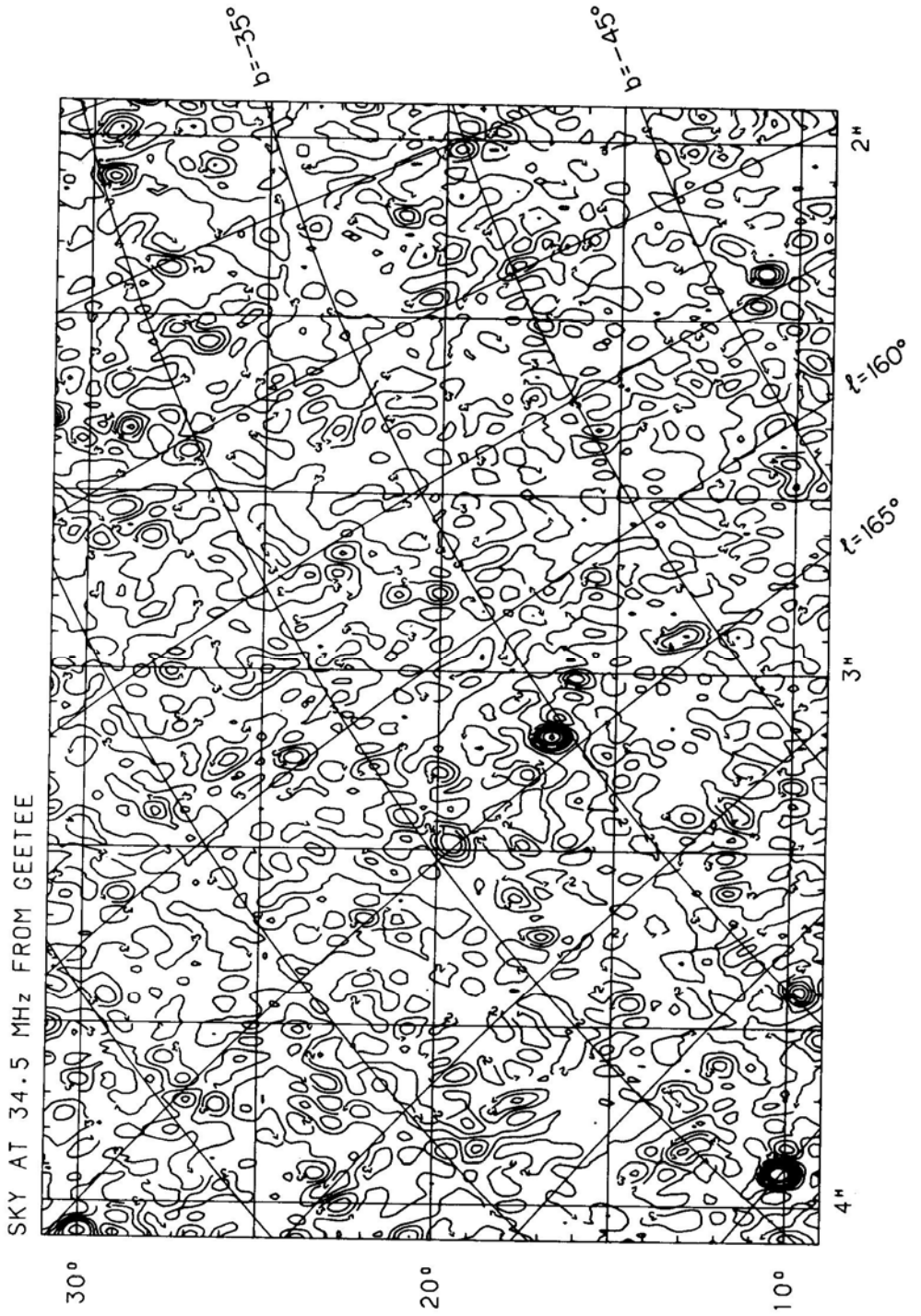
SKY AT 34.5 MHz FROM GEETEE
b=-35°
b=-45°
l=160°
l=165°
2H
3H
4H
30°
20°
10°

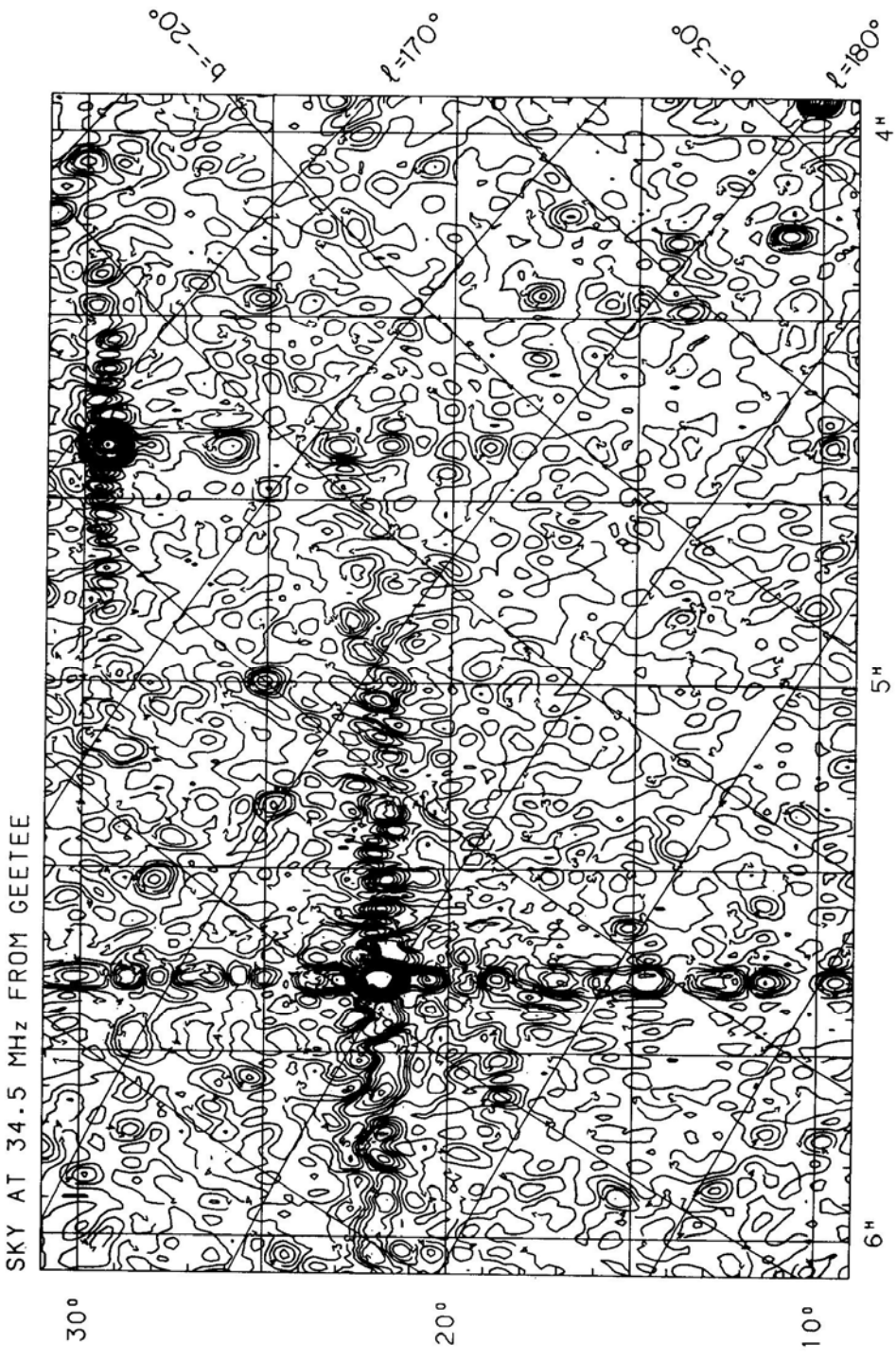
SKY AT 34.5 MHz FROM GEETEE
b=-20°
ℓ=170°
b=-30°
ℓ=180°
4ʰ
5ʰ
6ʰ
30°
20°
10°

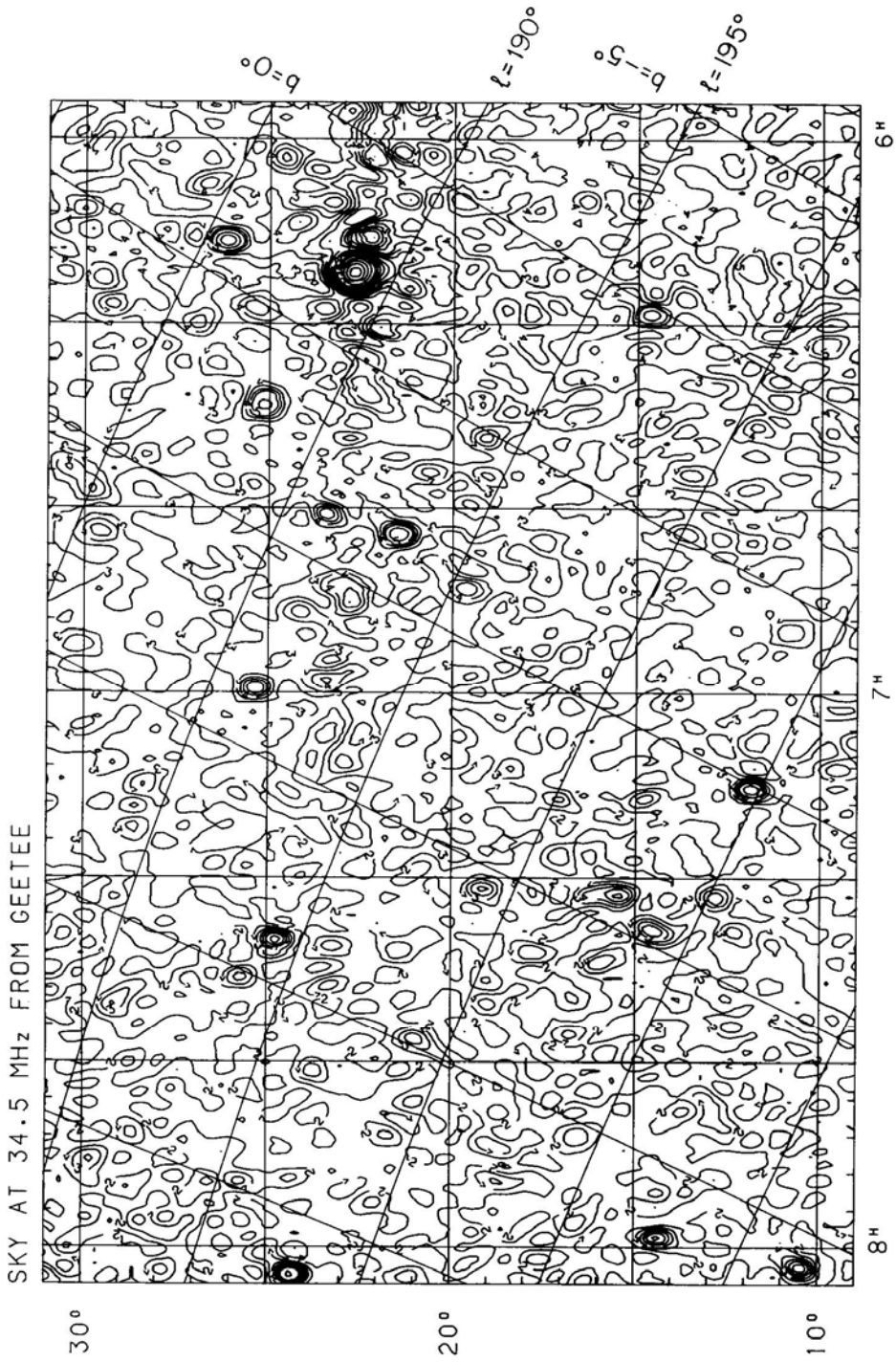
SKY AT 34.5 MHz FROM GEETEE
b=0°
ℓ=190°
b=−5°
ℓ=195°
6H
7H
8H
30°
20°
10°

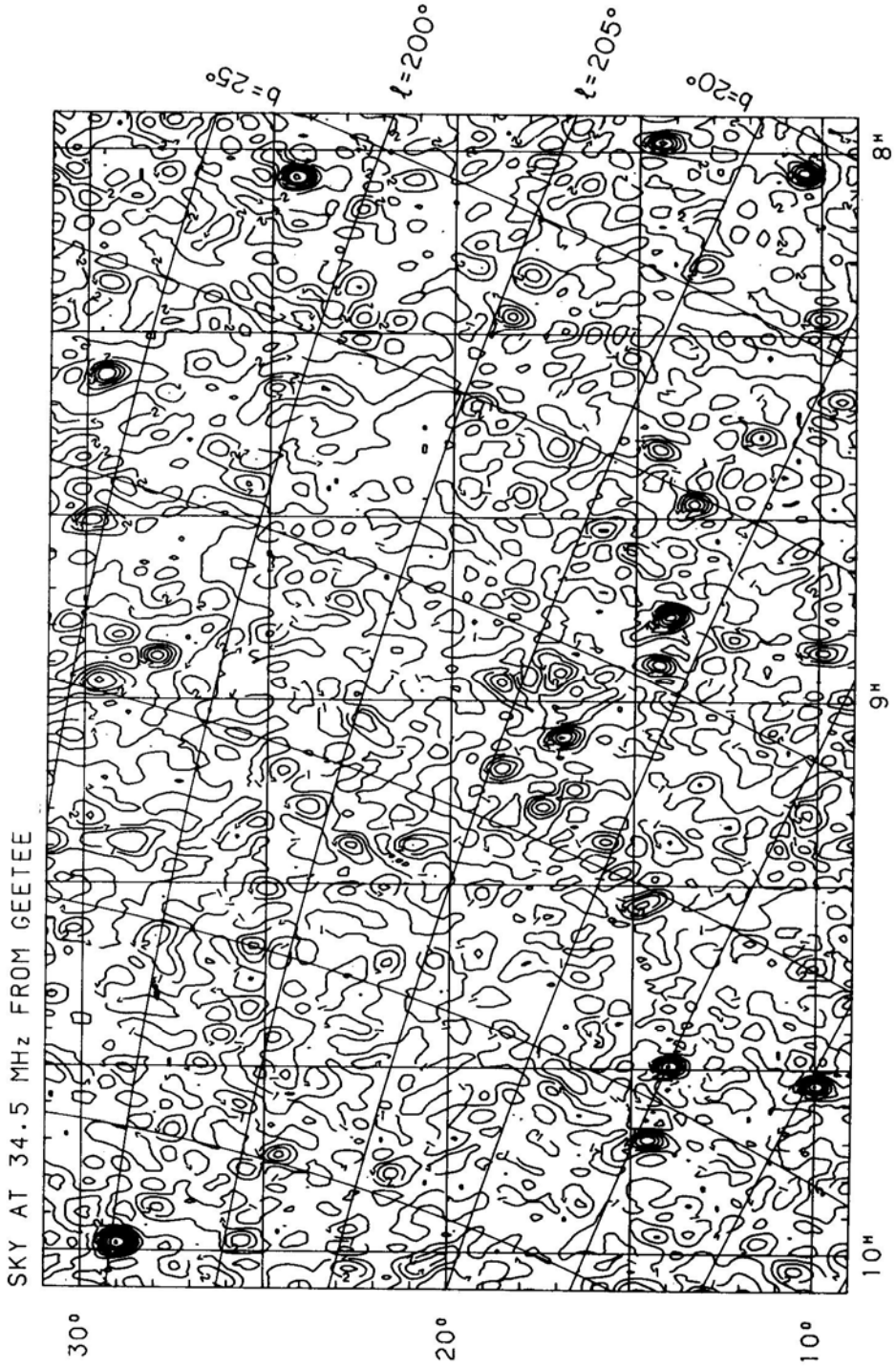
SKY AT 34.5 MHz FROM GEETEE
b=25°
ℓ=200°
ℓ=205°
b=20°
8ᴴ
9ᴴ
10ᴴ
30°
20°
10°

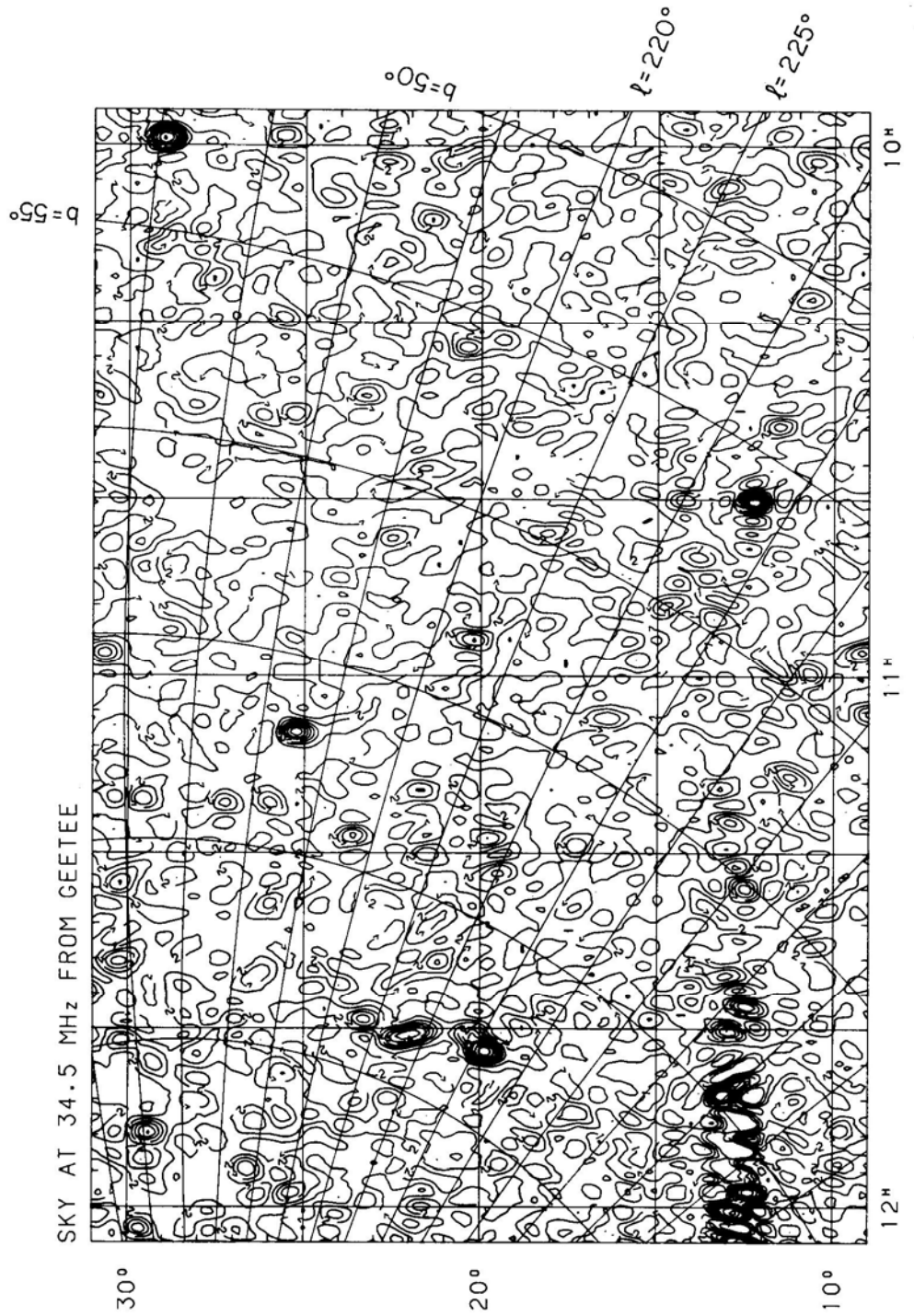
SKY AT 34.5 MHz FROM GEETEE
b=55°
b=50°
ℓ=220°
ℓ=225°
10H
11H
12H
30°
20°
10°

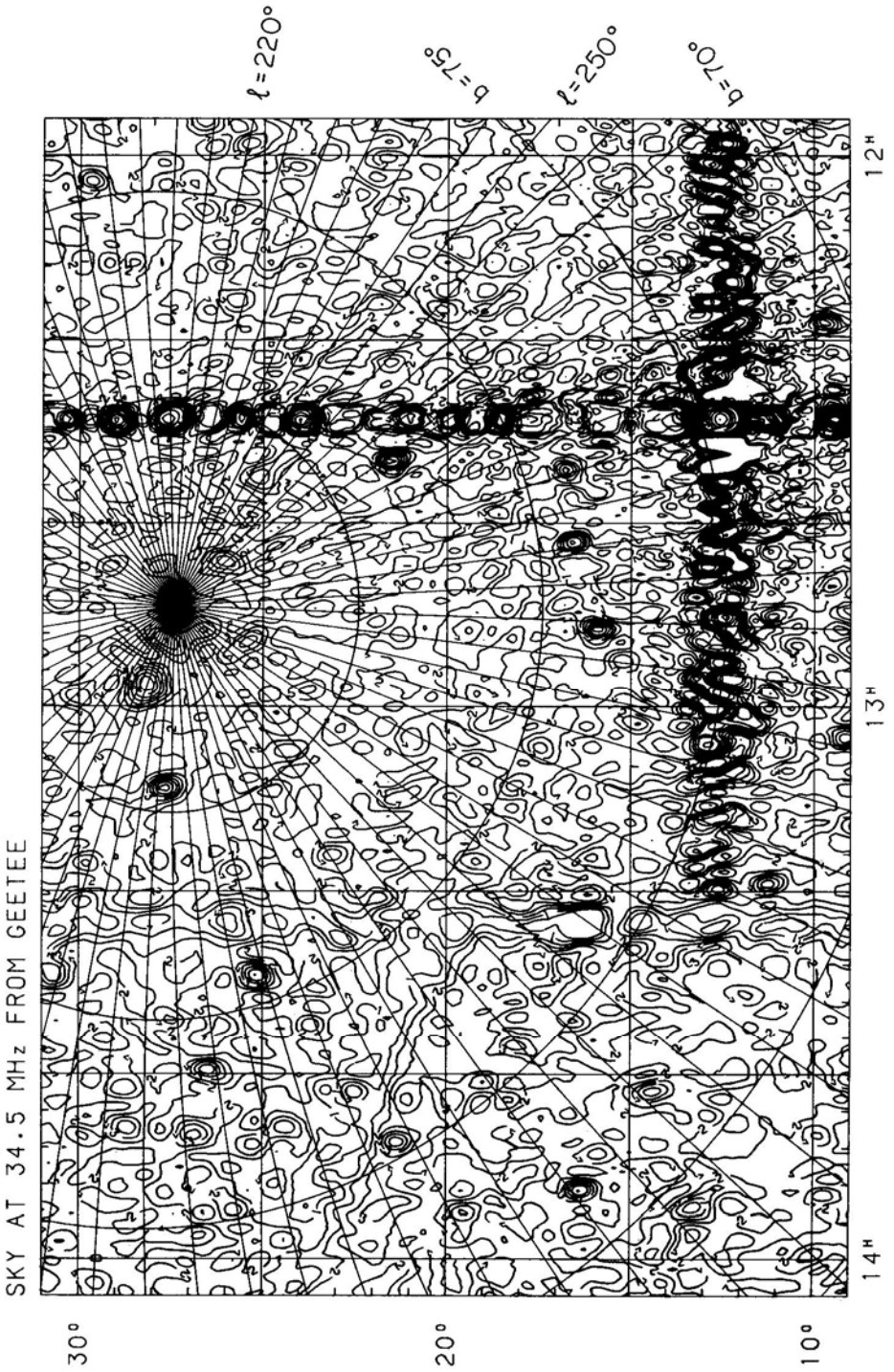
SKY AT 34.5 MHz FROM GEETEE
ℓ=220°
b=75°
ℓ=250°
b=70°
12ᴴ
13ᴴ
14ᴴ
30°
20°
10°

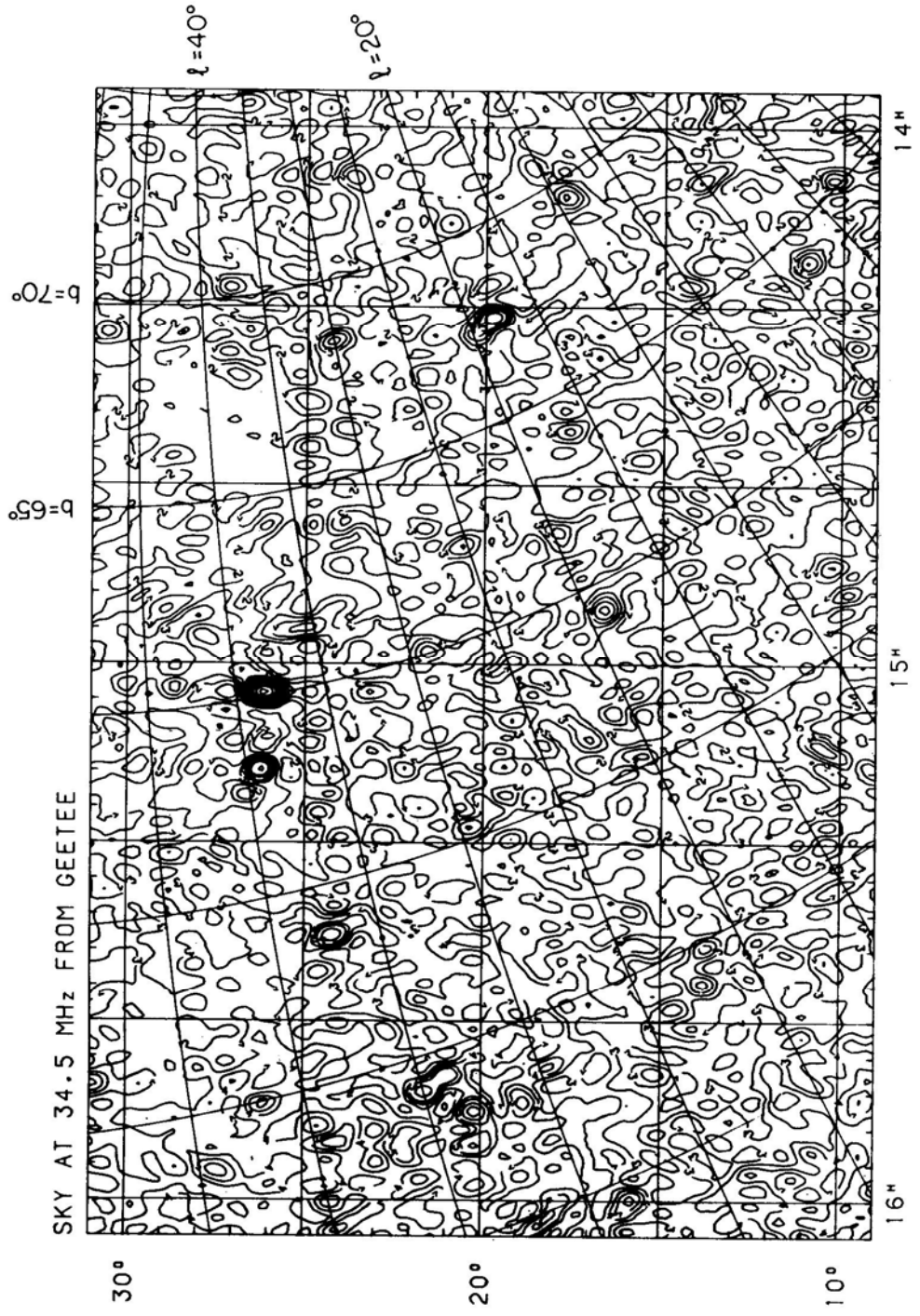
ℓ=40°
ℓ=20°
14ᴴ
b=70°
b=65°
15ᴴ
SKY AT 34.5 MHz FROM GEETEE
16ᴴ
30°
20°
10°

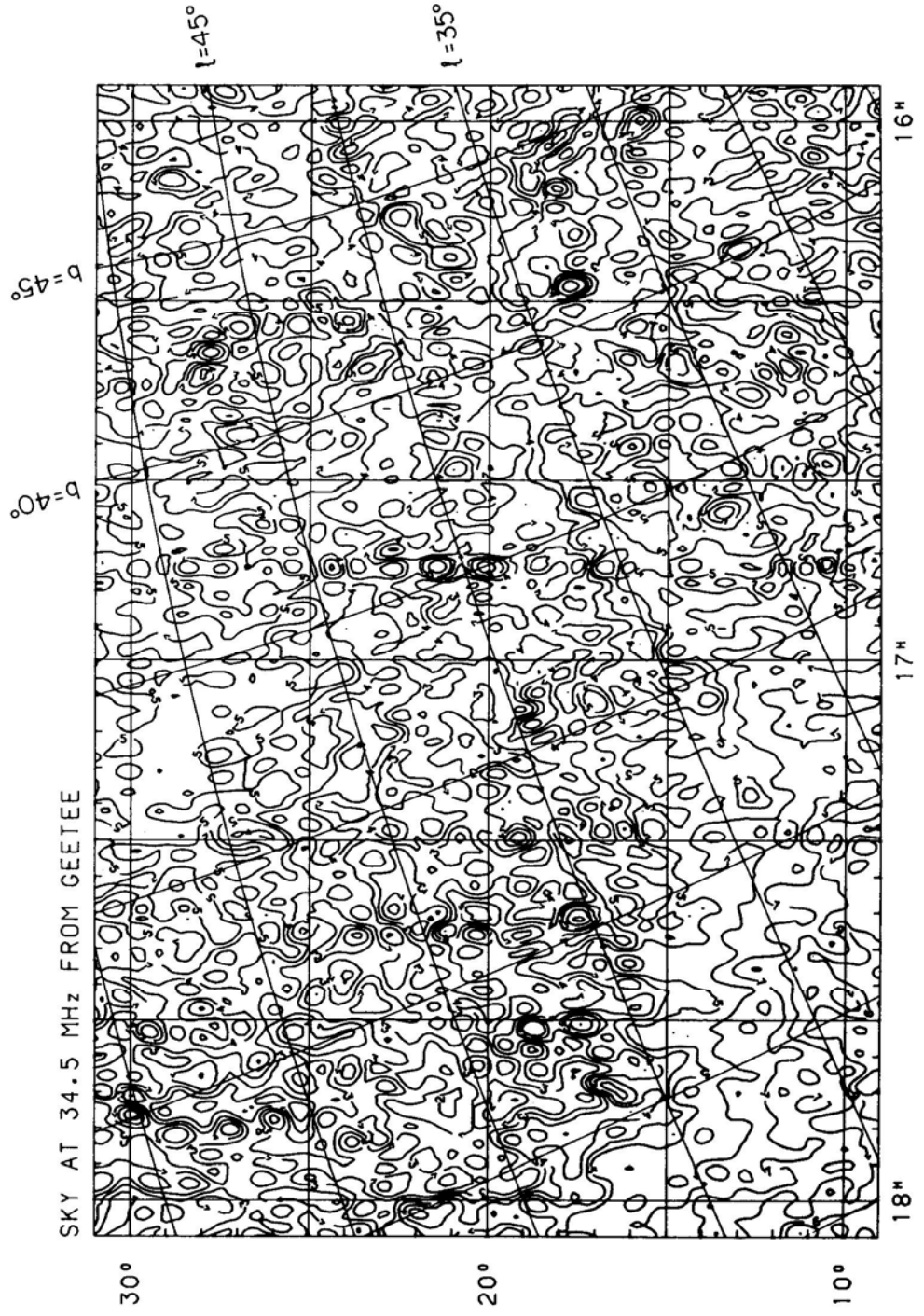
SKY AT 34.5 MHz FROM GEETEE
l=45°
l=35°
b=45°
b=40°
16ᴴ
17ᴴ
18ᴴ
30°
20°
10°

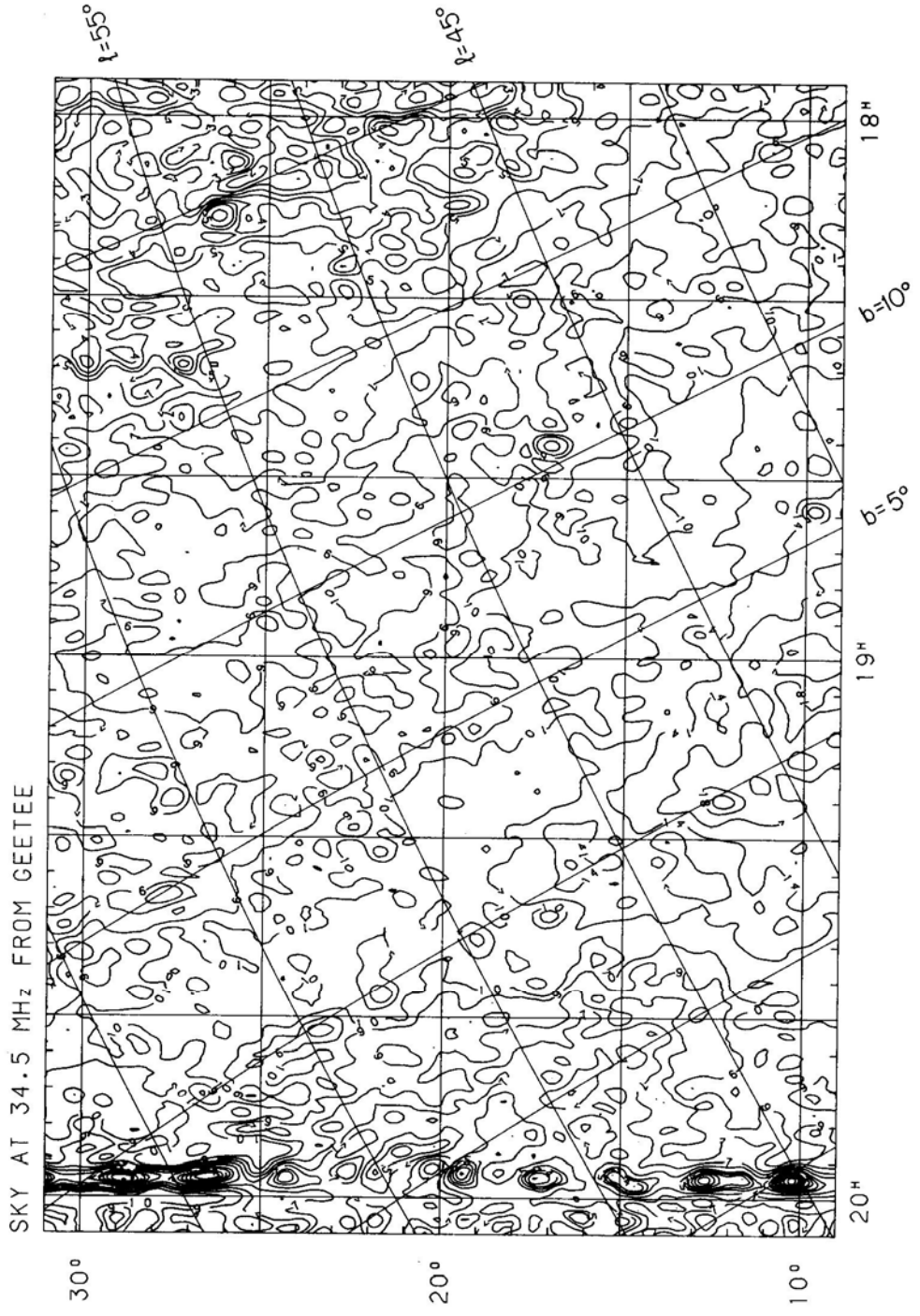
SKY AT 34.5 MHz FROM GEETEE
l=55°
l=45°
18ʰ
19ʰ
20ʰ
b=10°
b=5°
30°
20°
10°

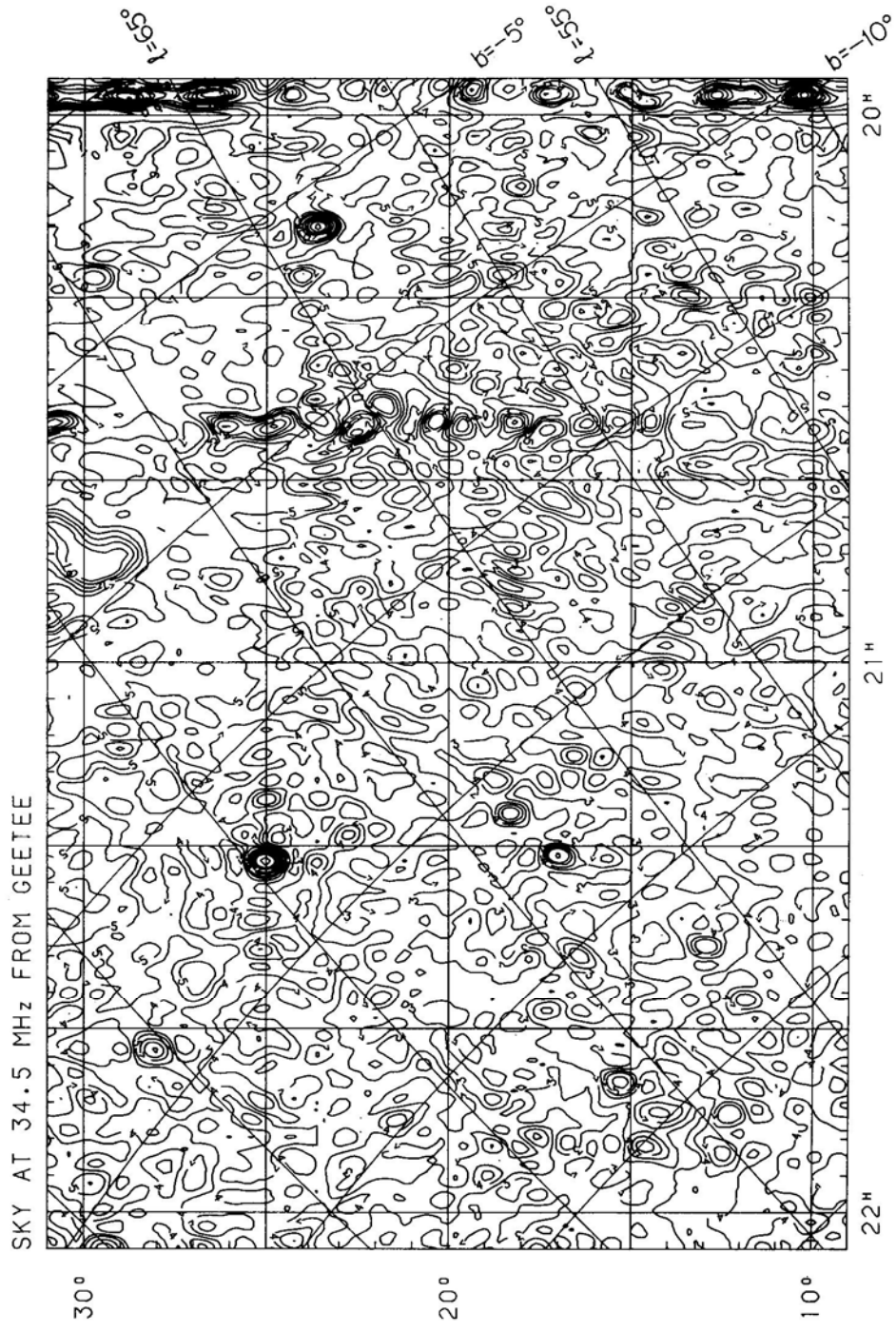
SKY AT 34.5 MHz FROM GEETEE
l=65°
b=-5°
l=55°
b=-10°
20ᴴ
21ᴴ
22ᴴ
30°
20°
10°

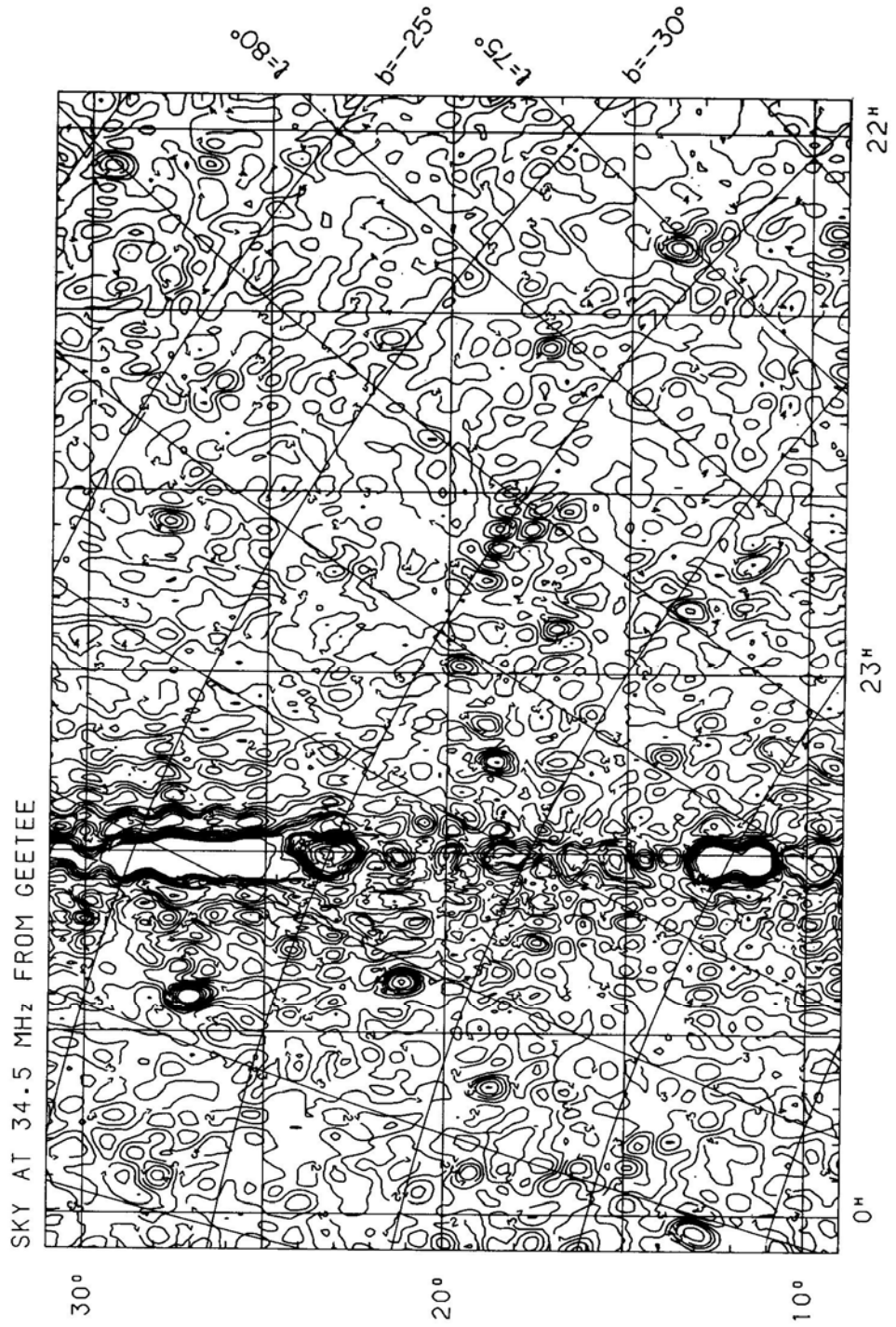
SKY AT 34.5 MHz FROM GEETEE
l=80°
b=−25°
l=75°
b=−30°
22ʰ
23ʰ
0ʰ
30°
20°
10°

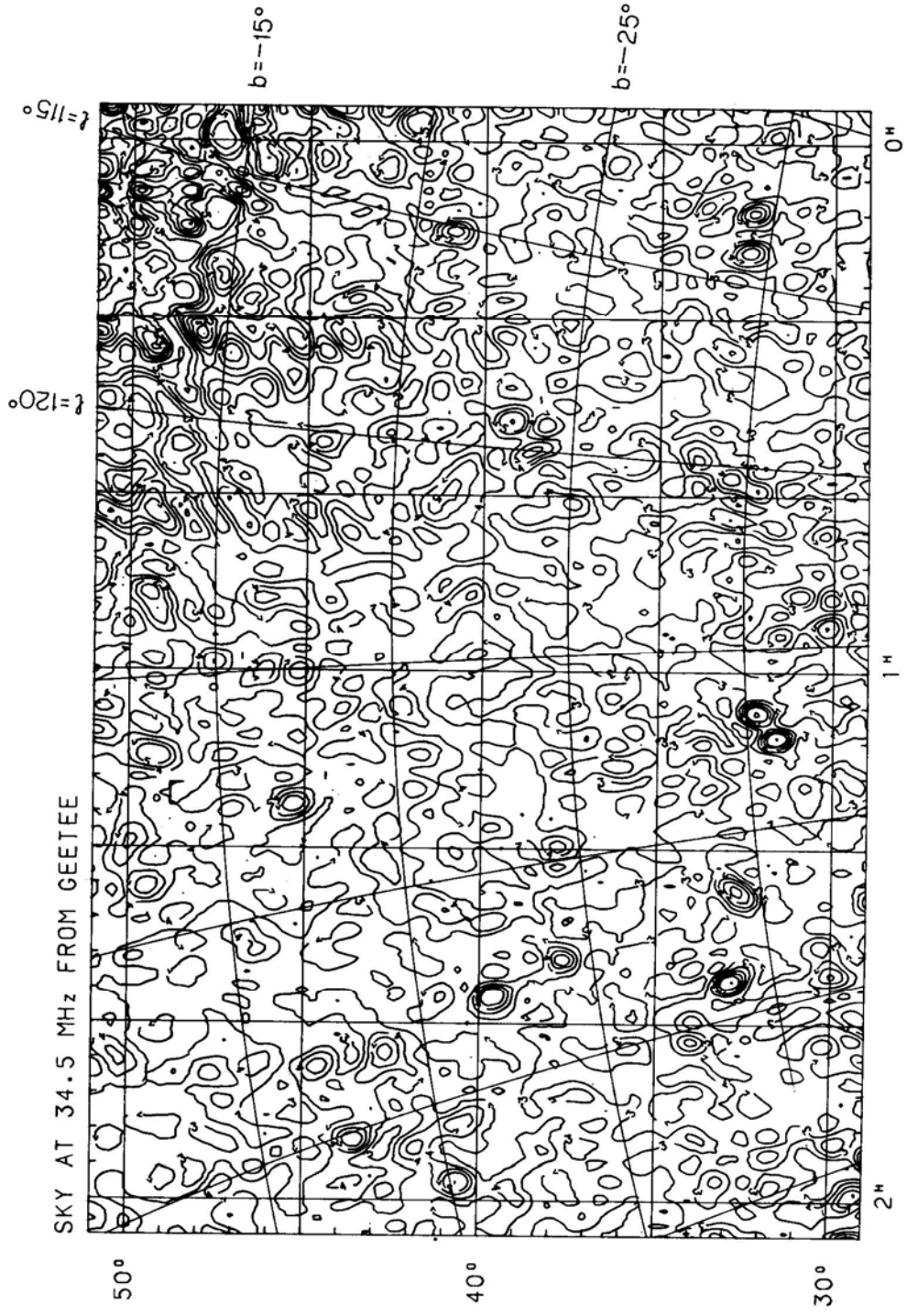
SKY AT 34.5 MHz FROM GEETEE
b=−15°
b=−25°
ℓ=115°
ℓ=120°
0ᴴ
1ᴴ
2ᴴ
50°
40°
30°

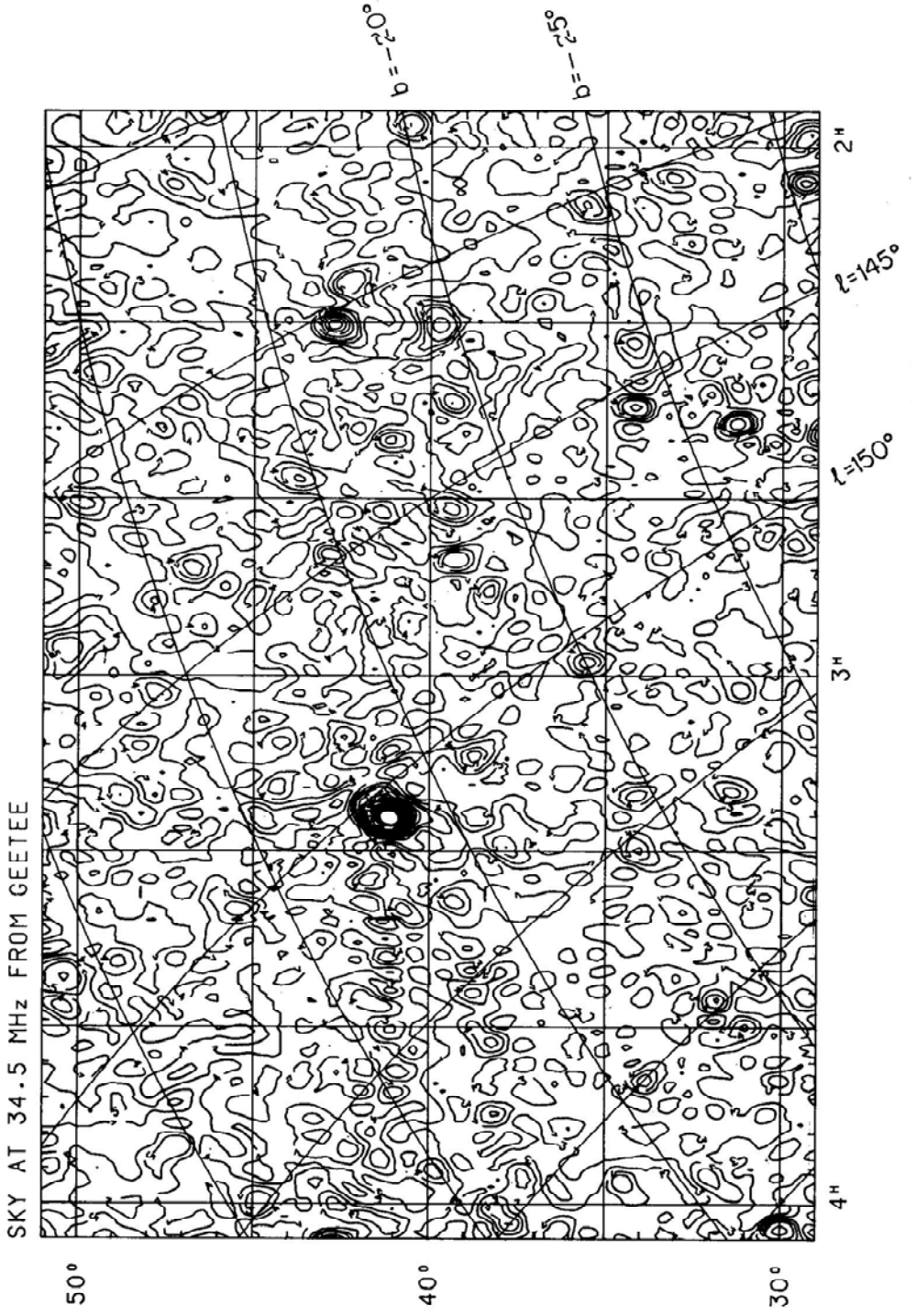
SKY AT 34.5 MHz FROM GEETEE
δ = −25°
δ = −20°
l=145°
l=150°
2ʰ
3ʰ
4ʰ
50°
40°
30°

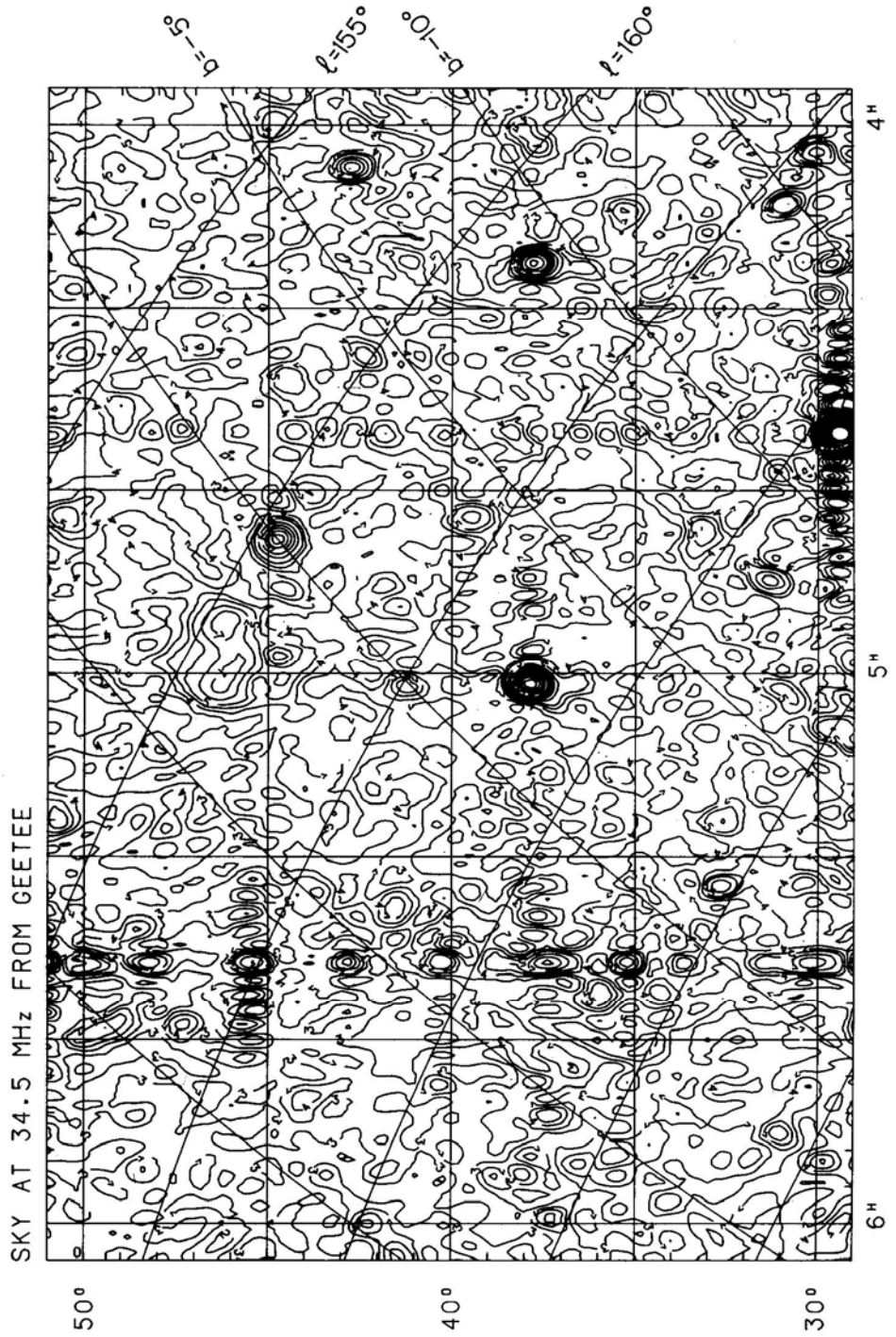
SKY AT 34.5 MHz FROM GEETEE
b=-5°
ℓ=155°
b=-10°
ℓ=160°
4H
5H
6H
50°
40°
30°

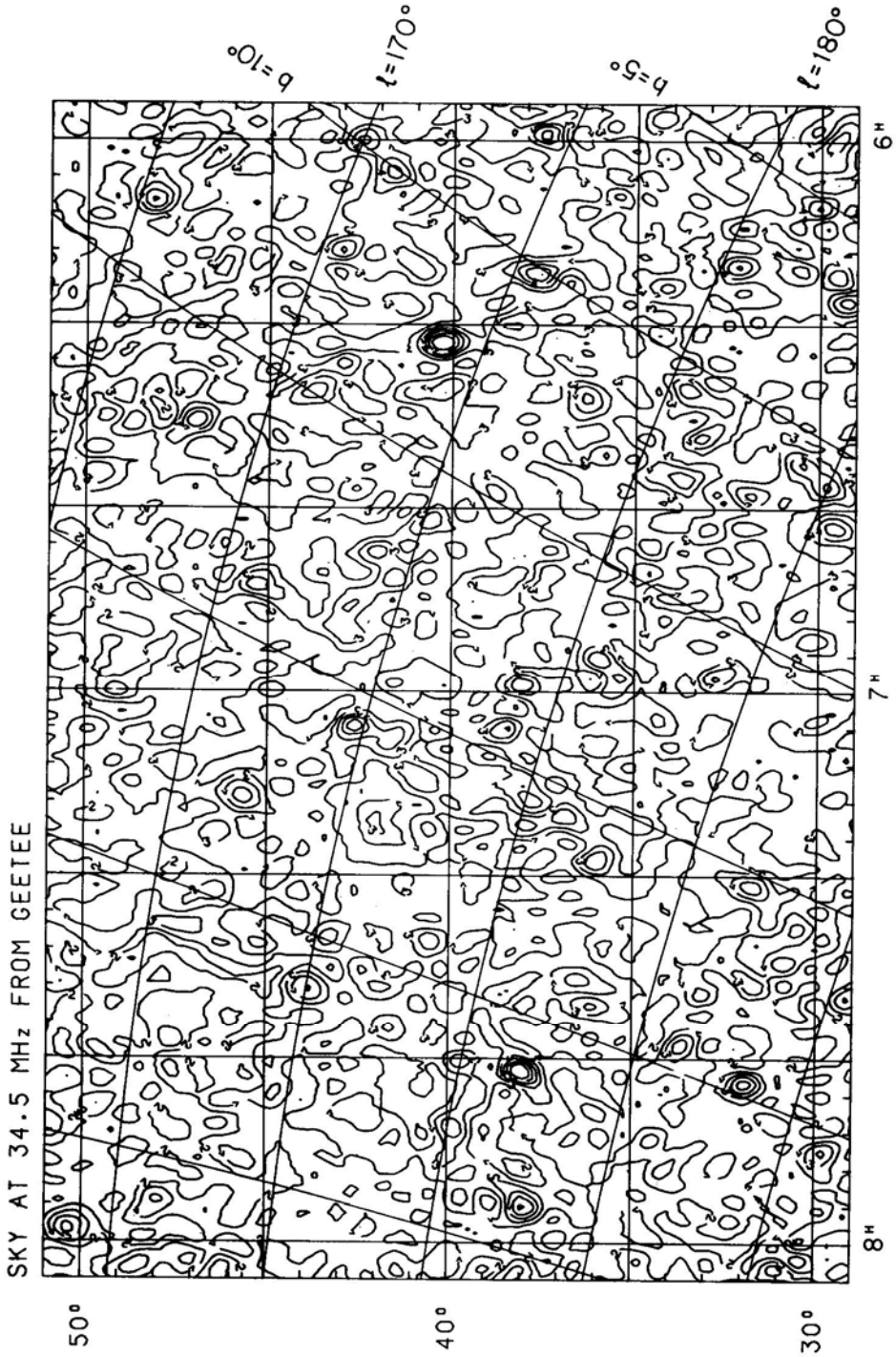
SKY AT 34.5 MHz FROM GEETEE
b=10°
l=170°
b=5°
l=180°
6H
7H
8H
50°
40°
30°

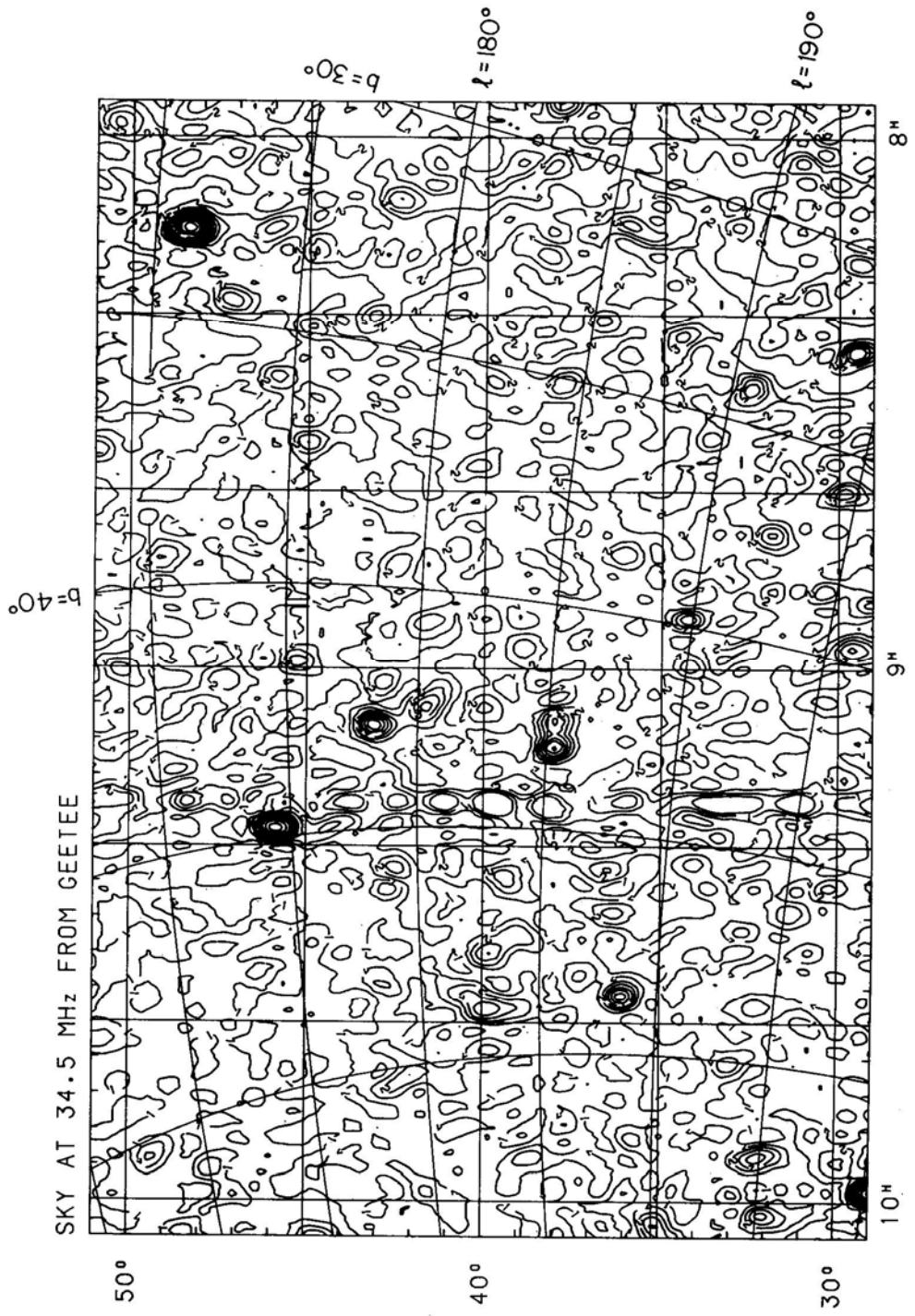
SKY AT 34.5 MHz FROM GEETEE
b=40°
b=30°
ℓ=180°
ℓ=190°
8ᴴ
9ᴴ
10ᴴ
50°
40°
30°

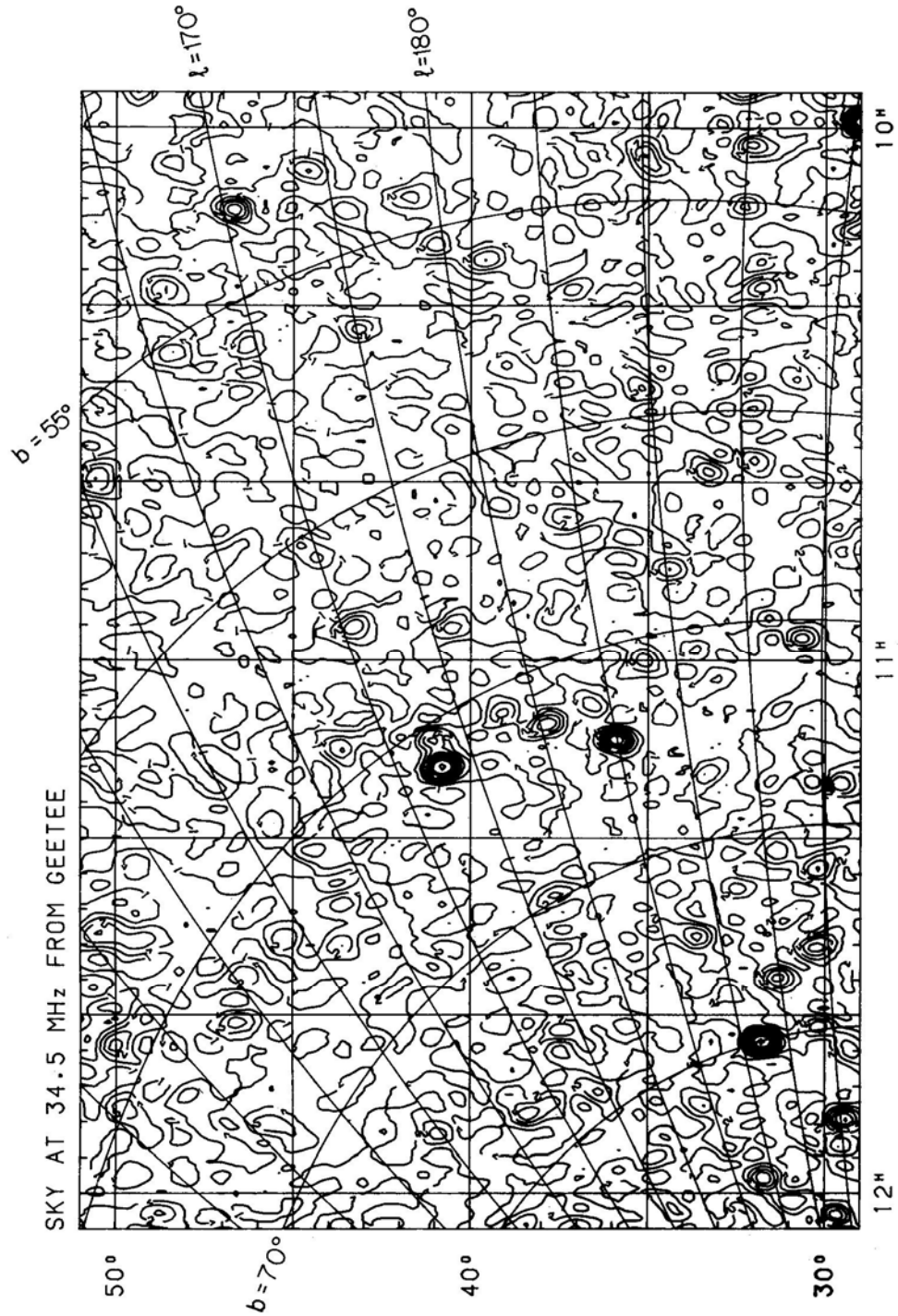
SKY AT 34.5 MHz FROM GEETEE
ℓ=170°
ℓ=180°
b=55°
b=70°
50°
40°
30°
10ᴴ
11ᴴ
12ᴴ

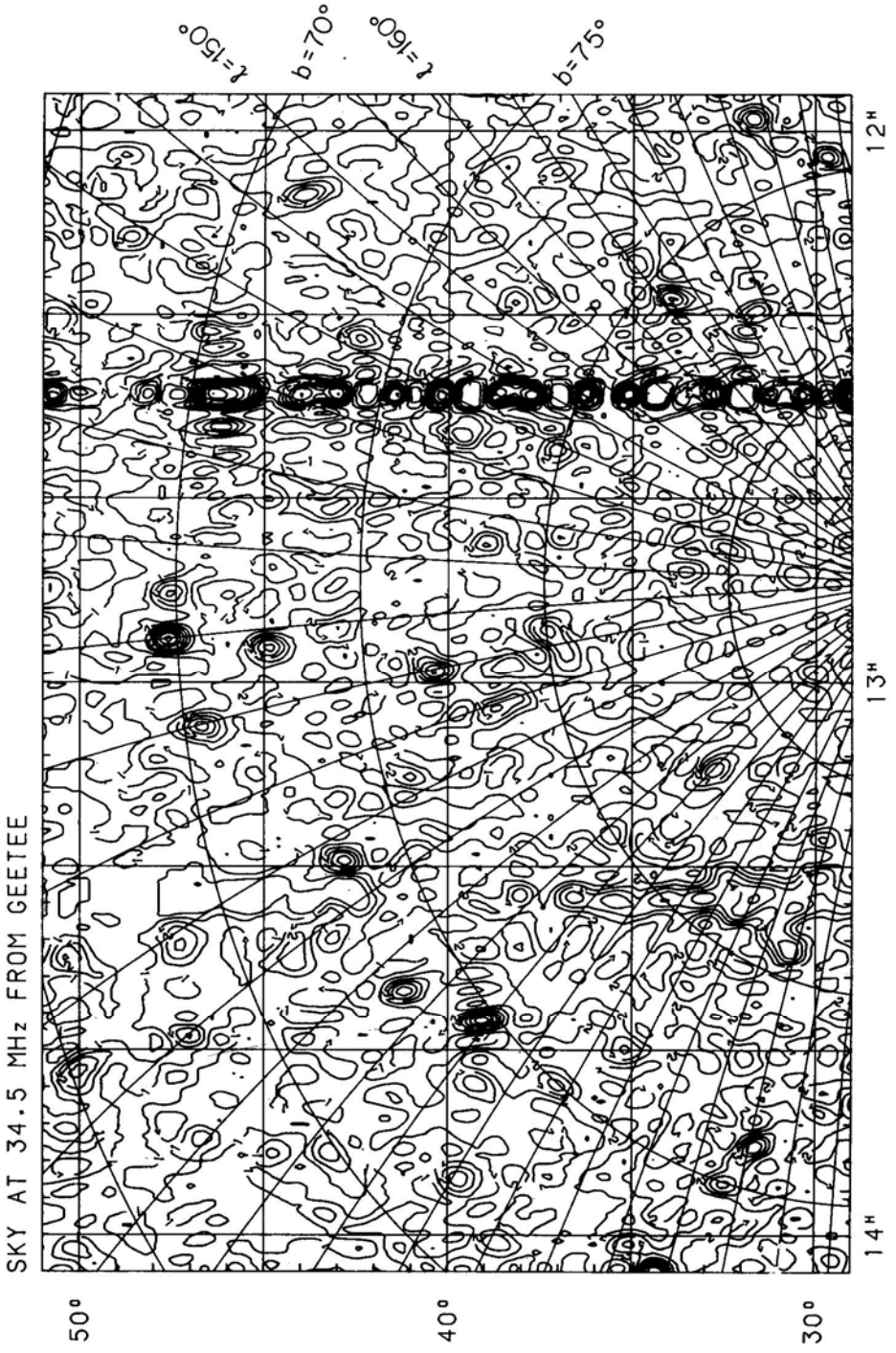
SKY AT 34.5 MHz FROM GEETEE
l=150°
b=70°
l=160°
b=75°
12ʰ
13ʰ
14ʰ
50°
40°
30°

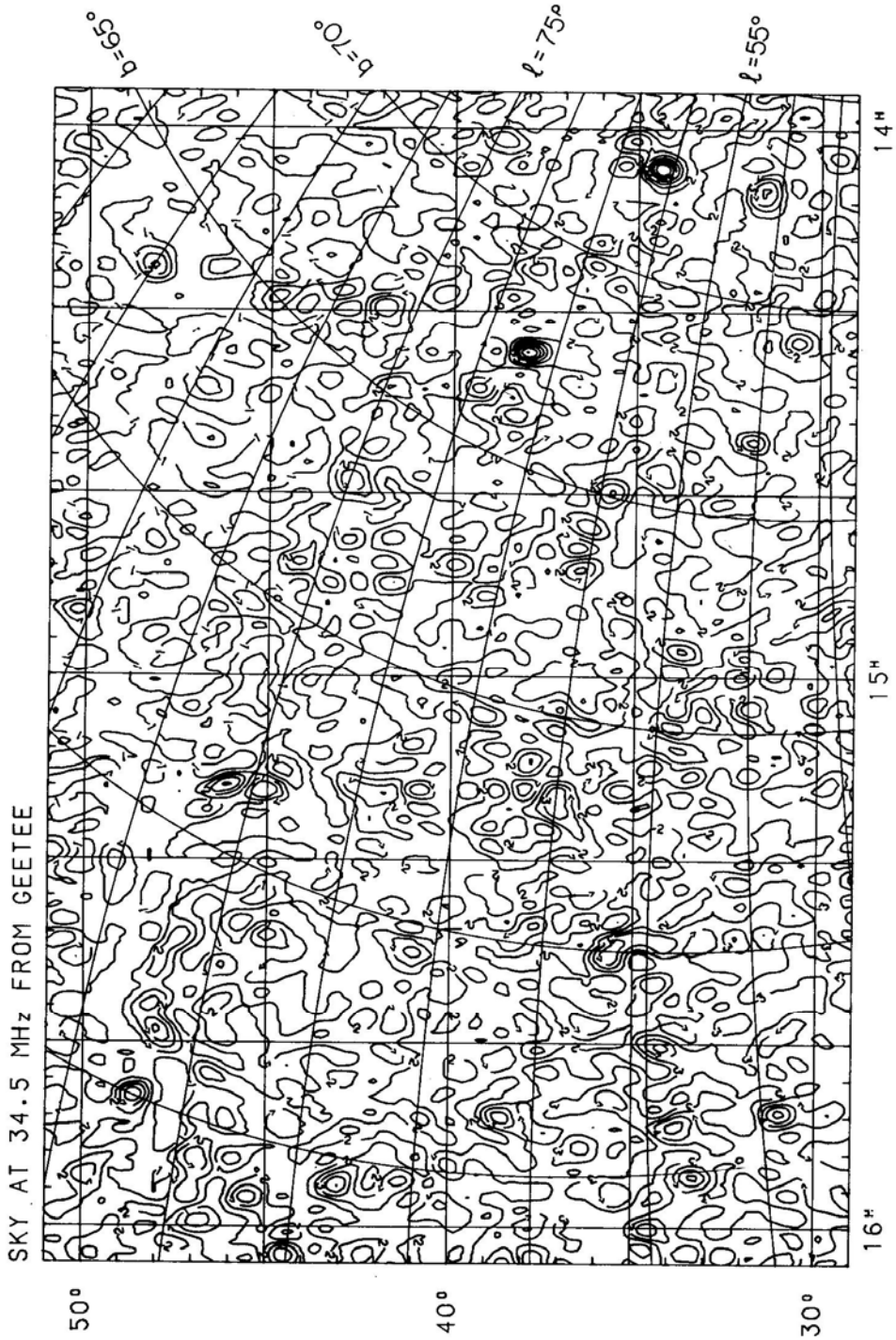
SKY AT 34.5 MHz FROM GEETEE
b=65°
b=70°
ℓ=75°
ℓ=55°
14ᴴ
15ᴴ
16ᴴ
50°
40°
30°

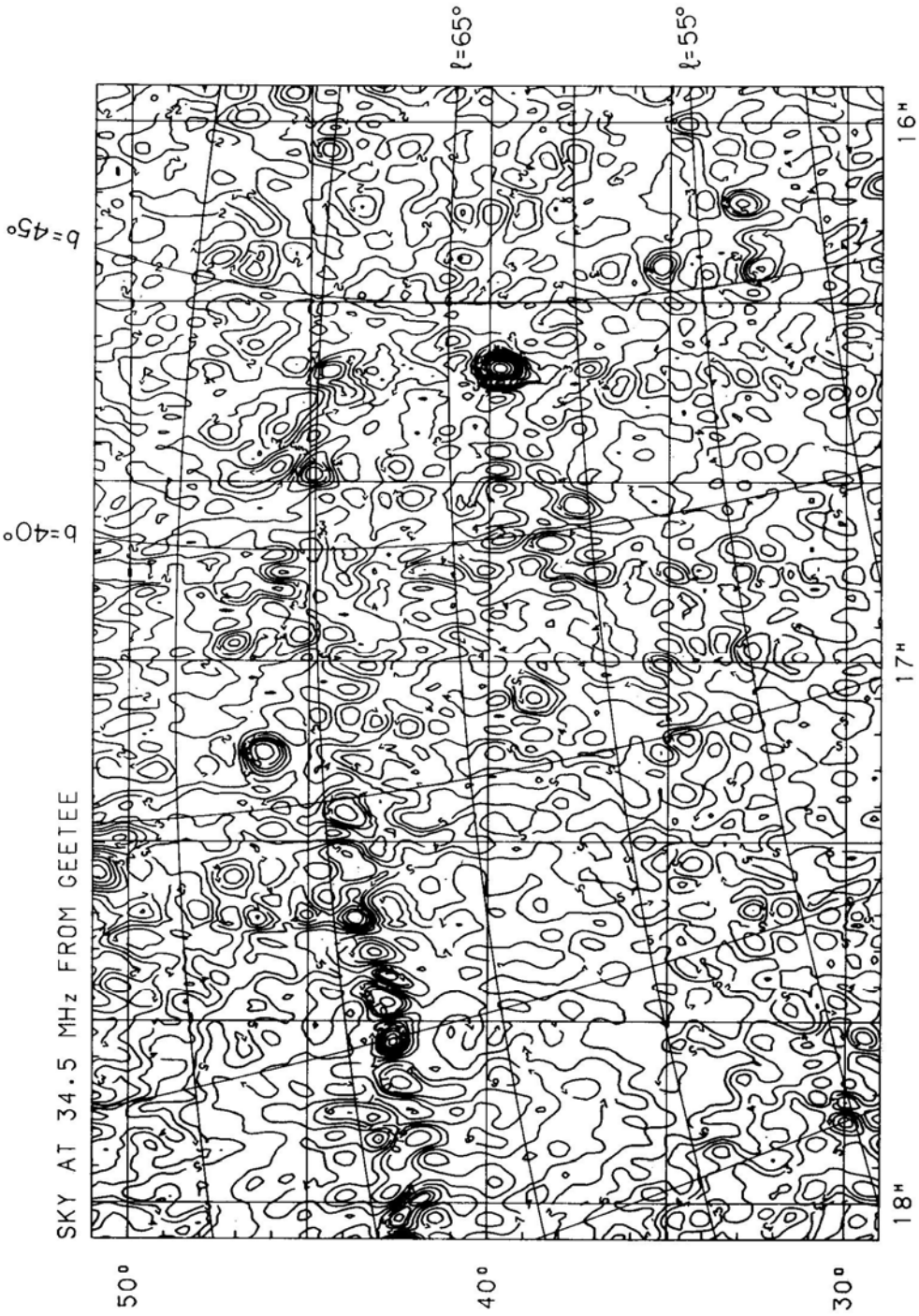
SKY AT 34.5 MHz FROM GEETEE
ℓ=65°
ℓ=55°
b=45°
b=40°
16ʰ
17ʰ
18ʰ
50°
40°
30°

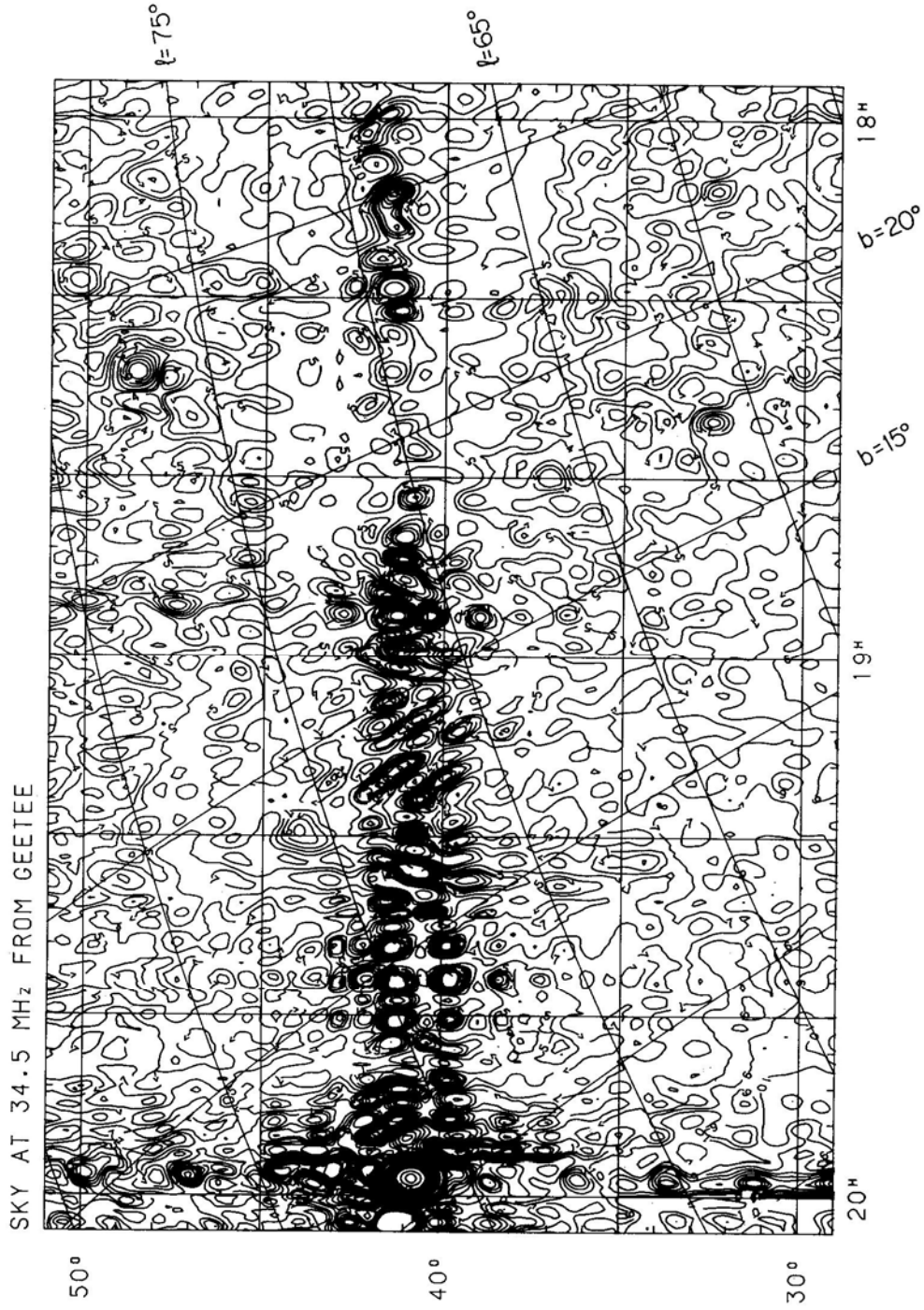
SKY AT 34.5 MHz FROM GEETEE
l=75°
l=65°
18ᴴ
19ᴴ
20ᴴ
b=20°
b=15°
50°
40°
30°

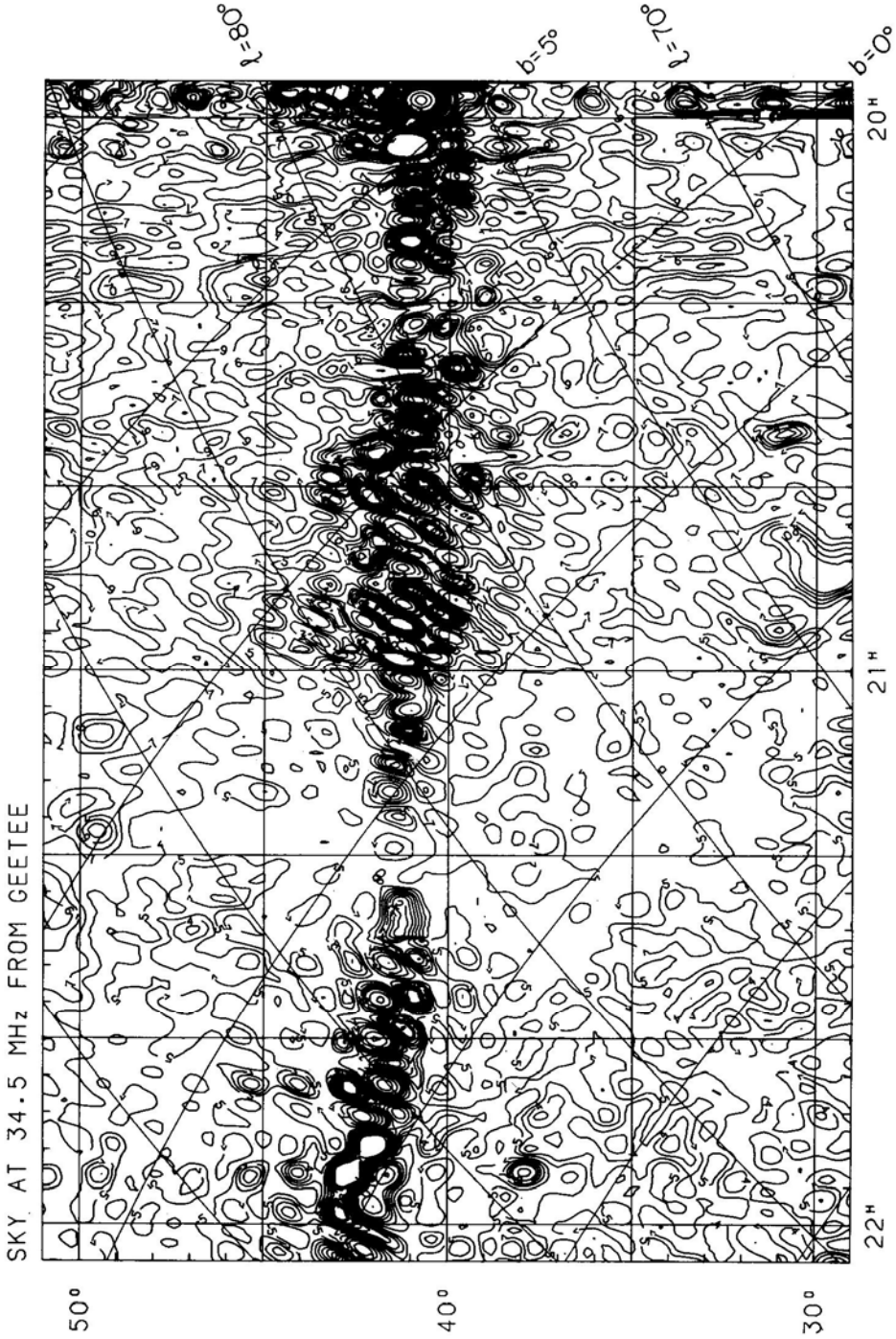
SKY AT 34.5 MHz FROM GEETEE
l=80°
b=5°
l=70°
b=0°
20ʰ
21ʰ
22ʰ
50°
40°
30°

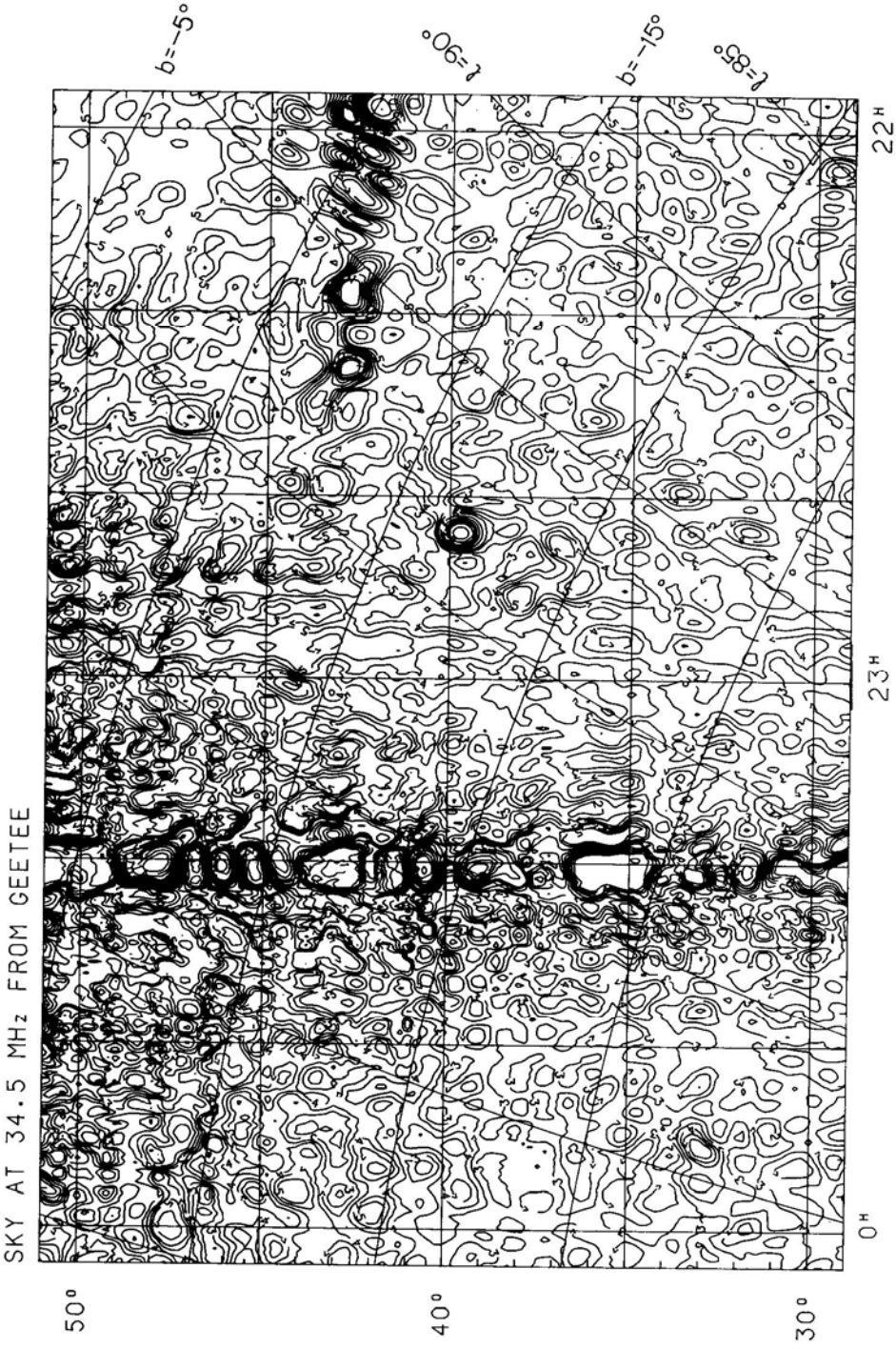
SKY AT 34.5 MHz FROM GEETEE
b=−5°
l=90°
b=−15°
l=85°
22ʰ
23ʰ
0ʰ
50°
40°
30°

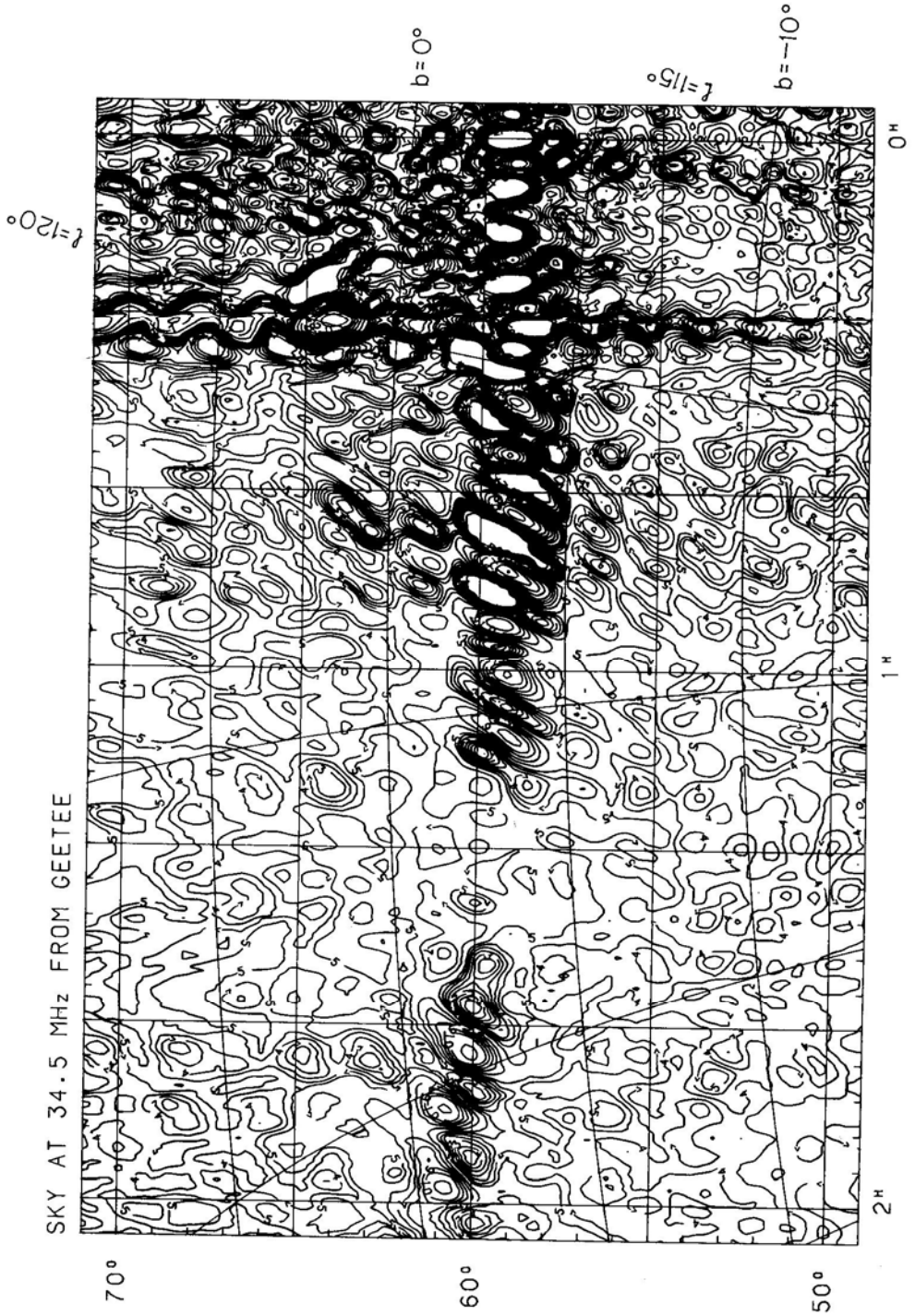
SKY AT 34.5 MHz FROM GEETEE
ℓ=120°
ℓ=115°
b=0°
b=−10°
0H
1H
2H
70°
60°
50°

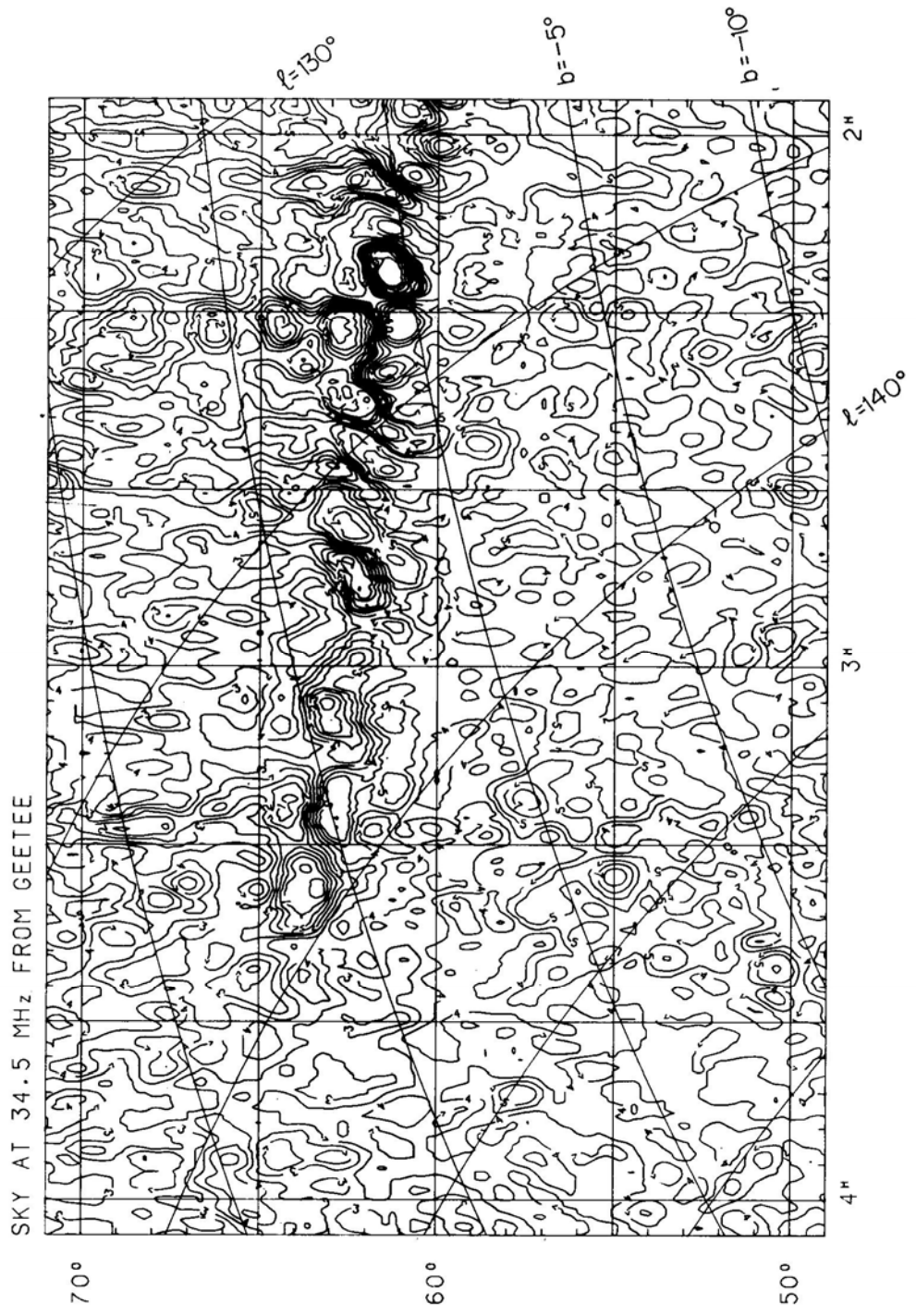
SKY AT 34.5 MHz FROM GEETEE
l=130°
b=-5°
b=-10°
l=140°
2H
3H
4H
70°
60°
50°

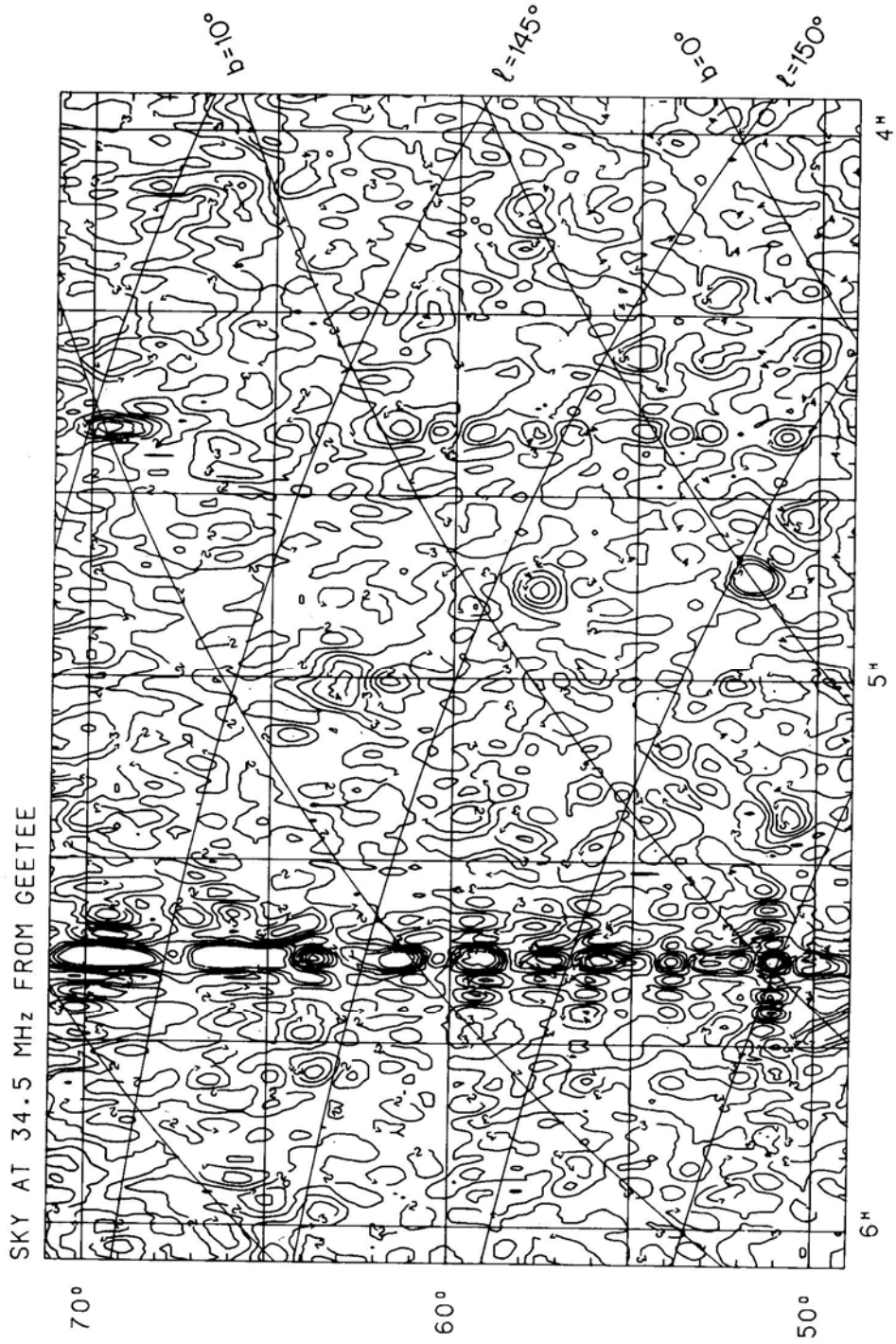
SKY AT 34.5 MHz FROM GEETEE
b=10°
ℓ=145°
b=0°
ℓ=150°
4ʰ
5ʰ
6ʰ
70°
60°
50°

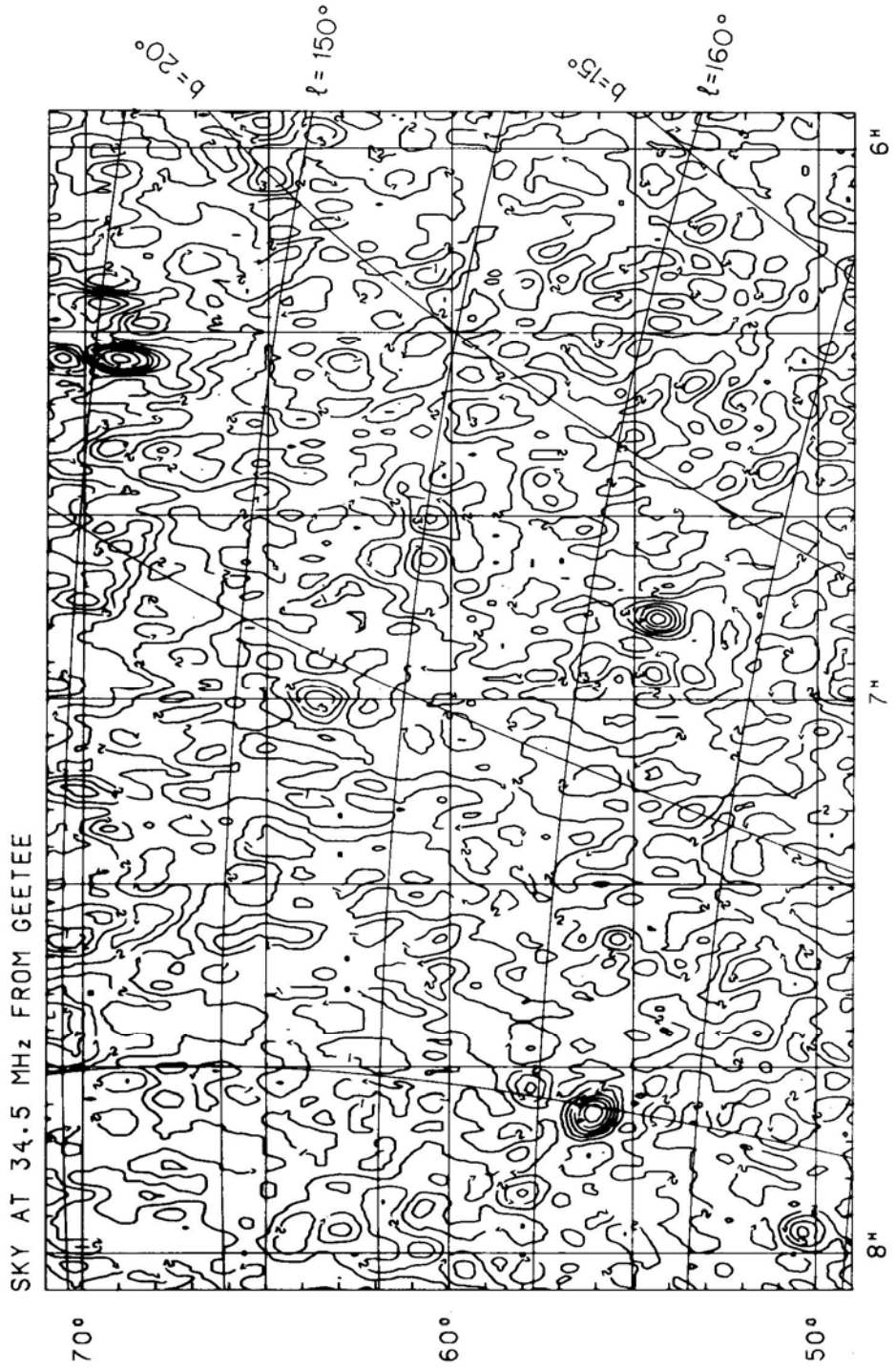
SKY AT 34.5 MHz FROM GEETEE
b=20°
ℓ = 150°
b=15°
ℓ=160°
6ᴴ
7ᴴ
8ᴴ
70°
60°
50°

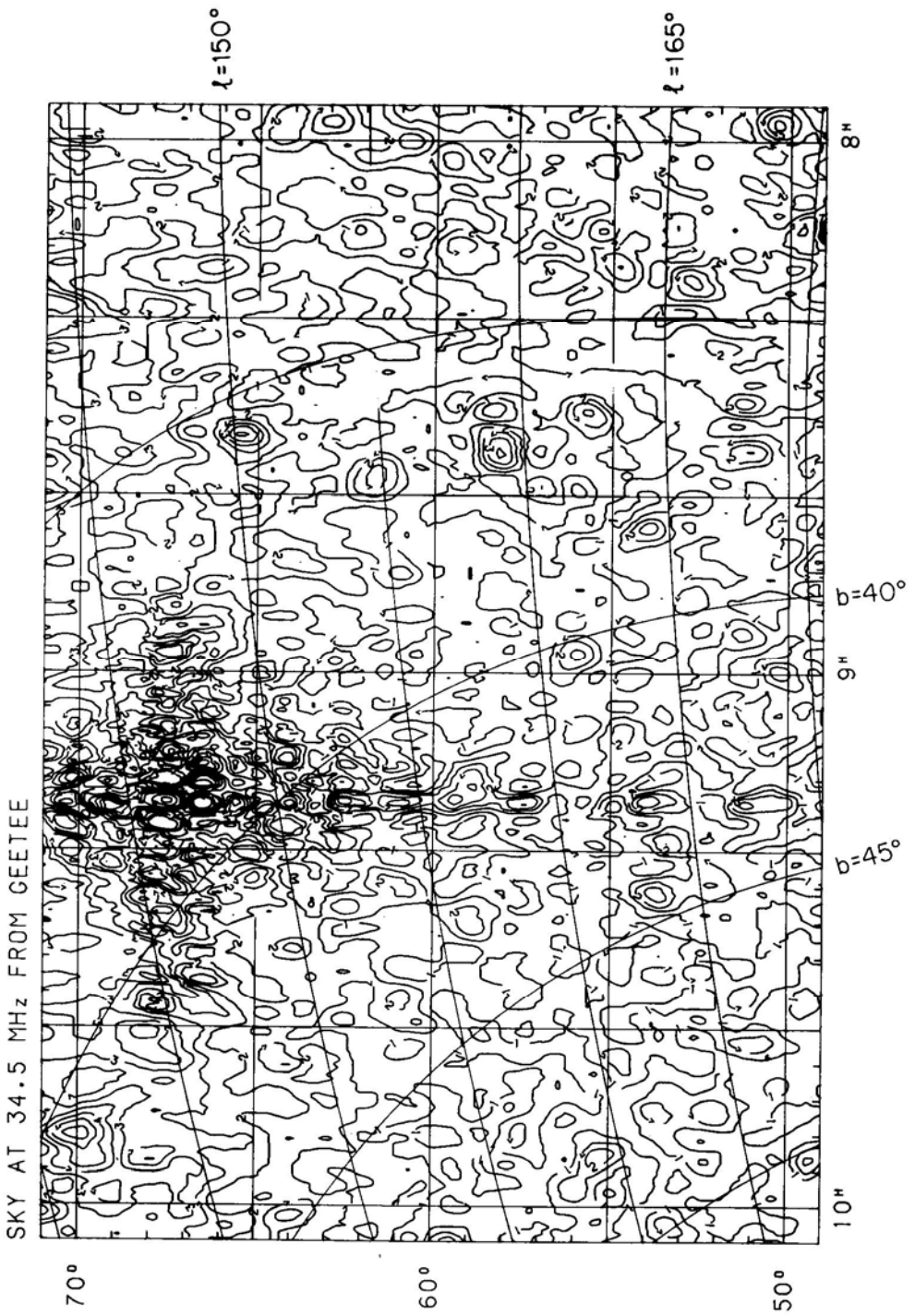
SKY AT 34.5 MHz FROM GEETEE
ℓ=150°
ℓ=165°
8ʰ
9ʰ
10ʰ
b=40°
b=45°
70°
60°
50°

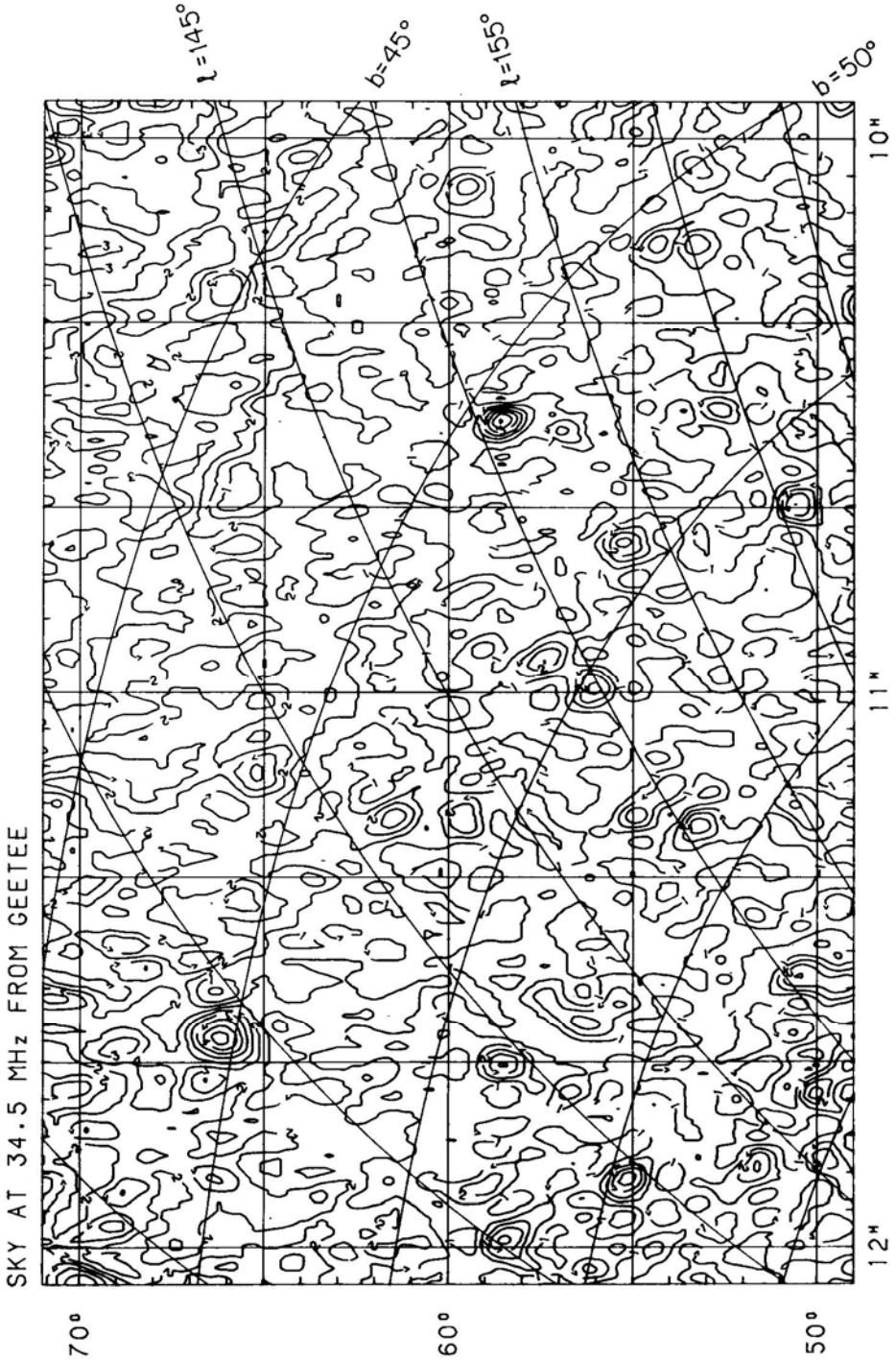
SKY AT 34.5 MHz FROM GEETEE
l=145°
b=45°
l=155°
b=50°
10ᴴ
11ᴴ
12ᴴ
70°
60°
50°

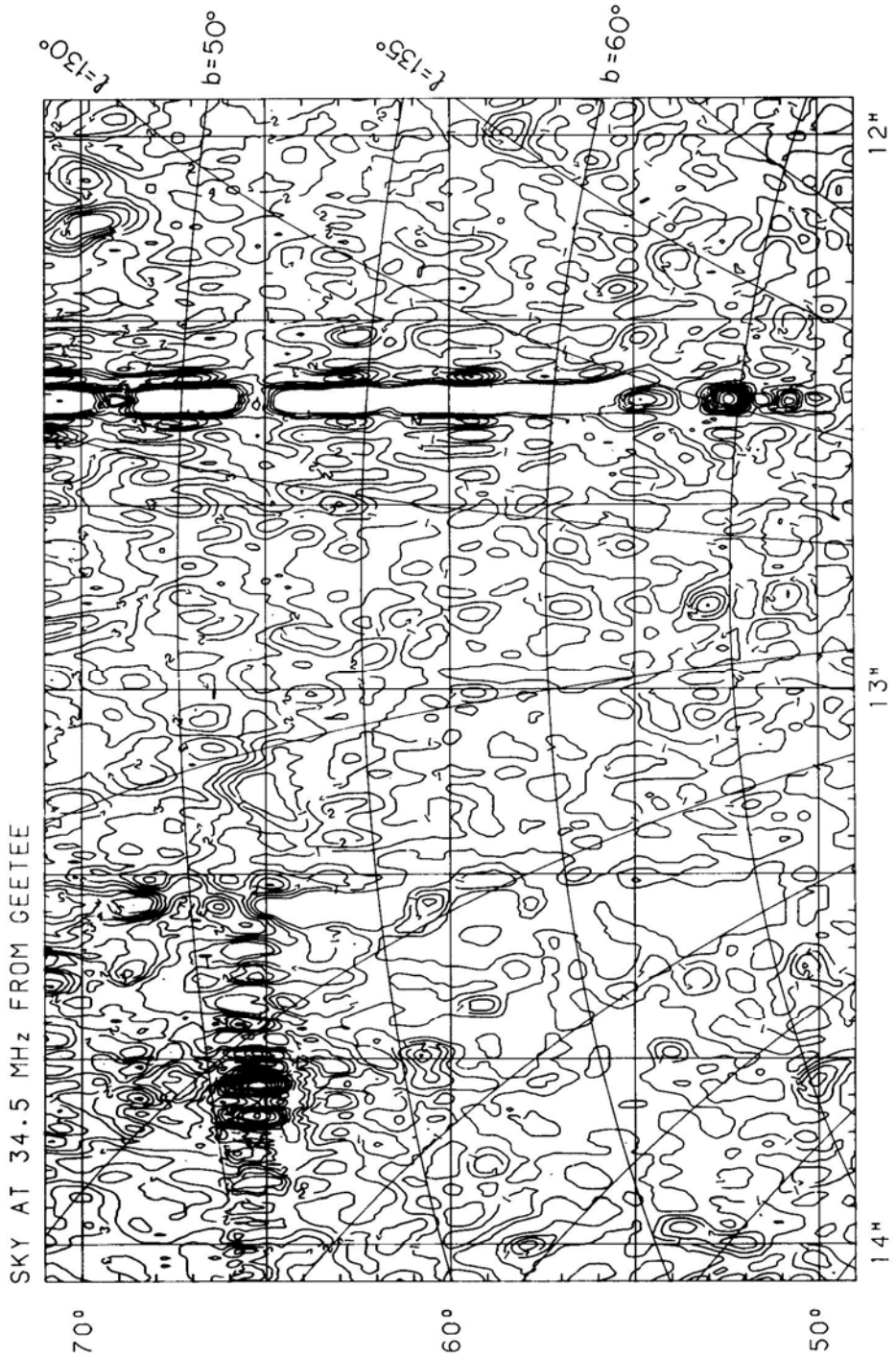
SKY AT 34.5 MHz FROM GEETEE
l=130°
b=50°
l=135°
b=60°
12ʰ
13ʰ
14ʰ
70°
60°
50°

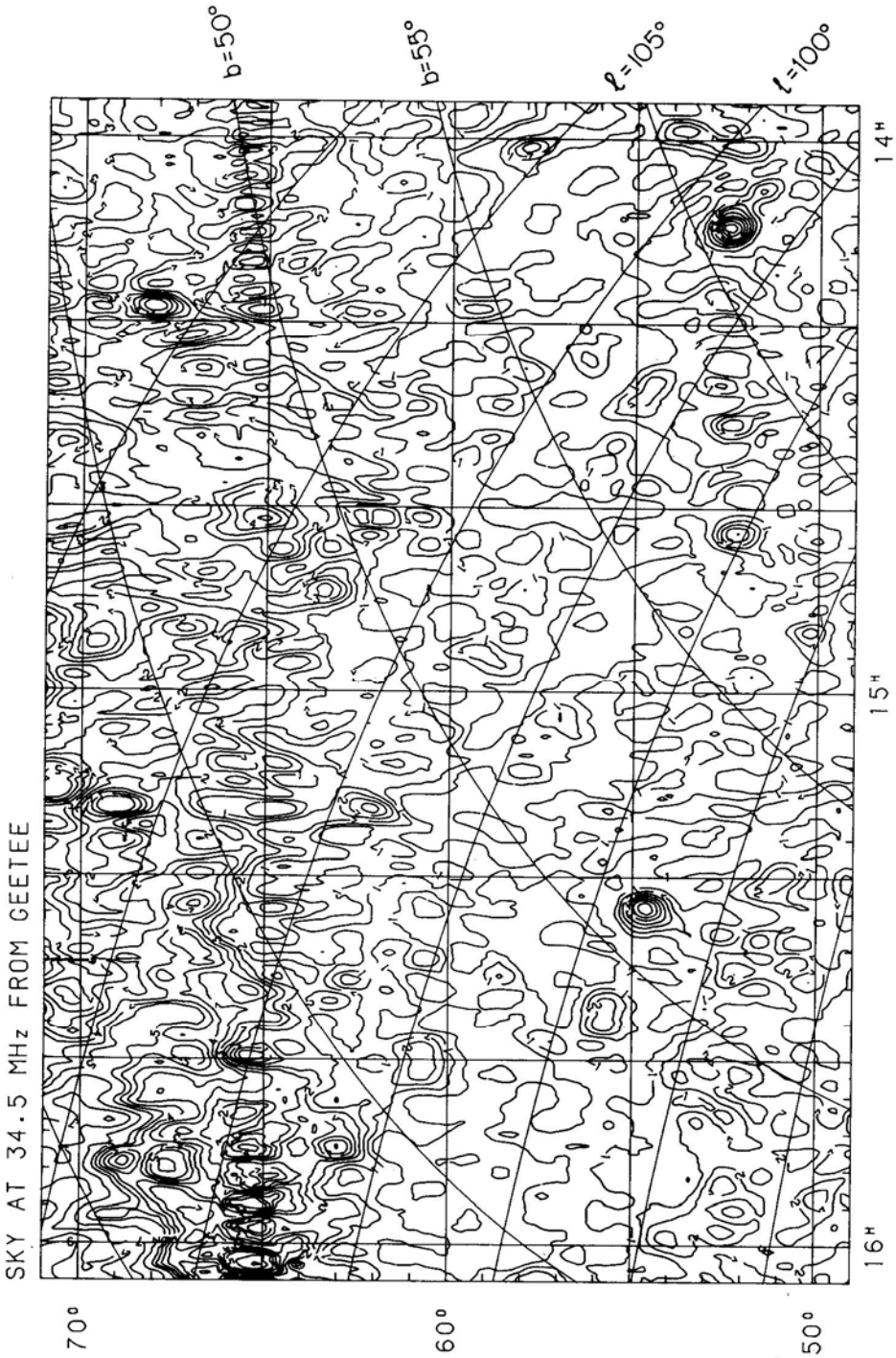
SKY AT 34.5 MHz FROM GEETEE
b=50°
b=55°
ℓ=105°
ℓ=100°
14ᴴ
15ᴴ
16ᴴ
70°
60°
50°

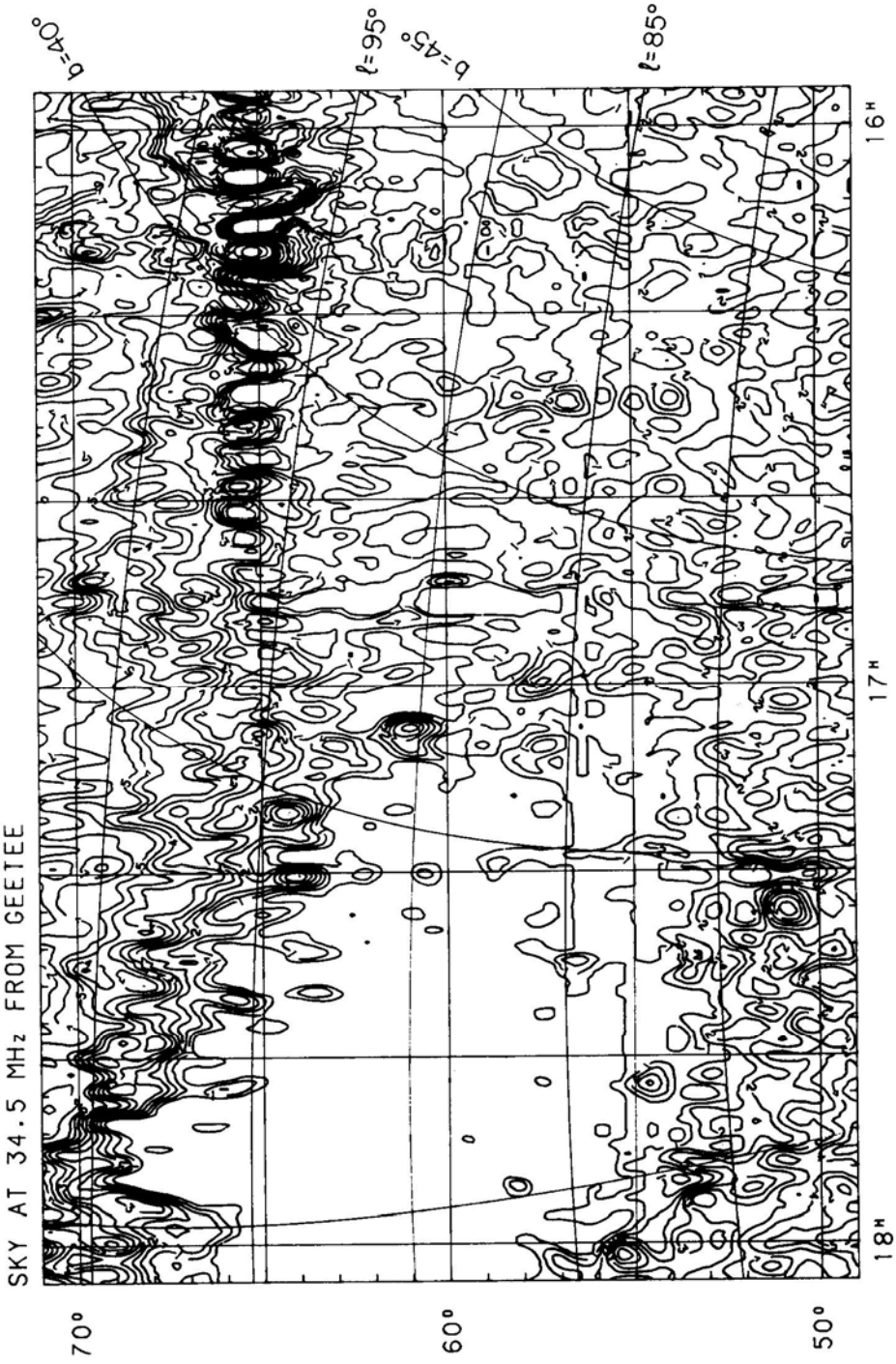
SKY AT 34.5 MHz FROM GEETEE
b=40°
l=95°
b=45°
l=85°
16ᴴ
17ᴴ
18ᴴ
70°
60°
50°

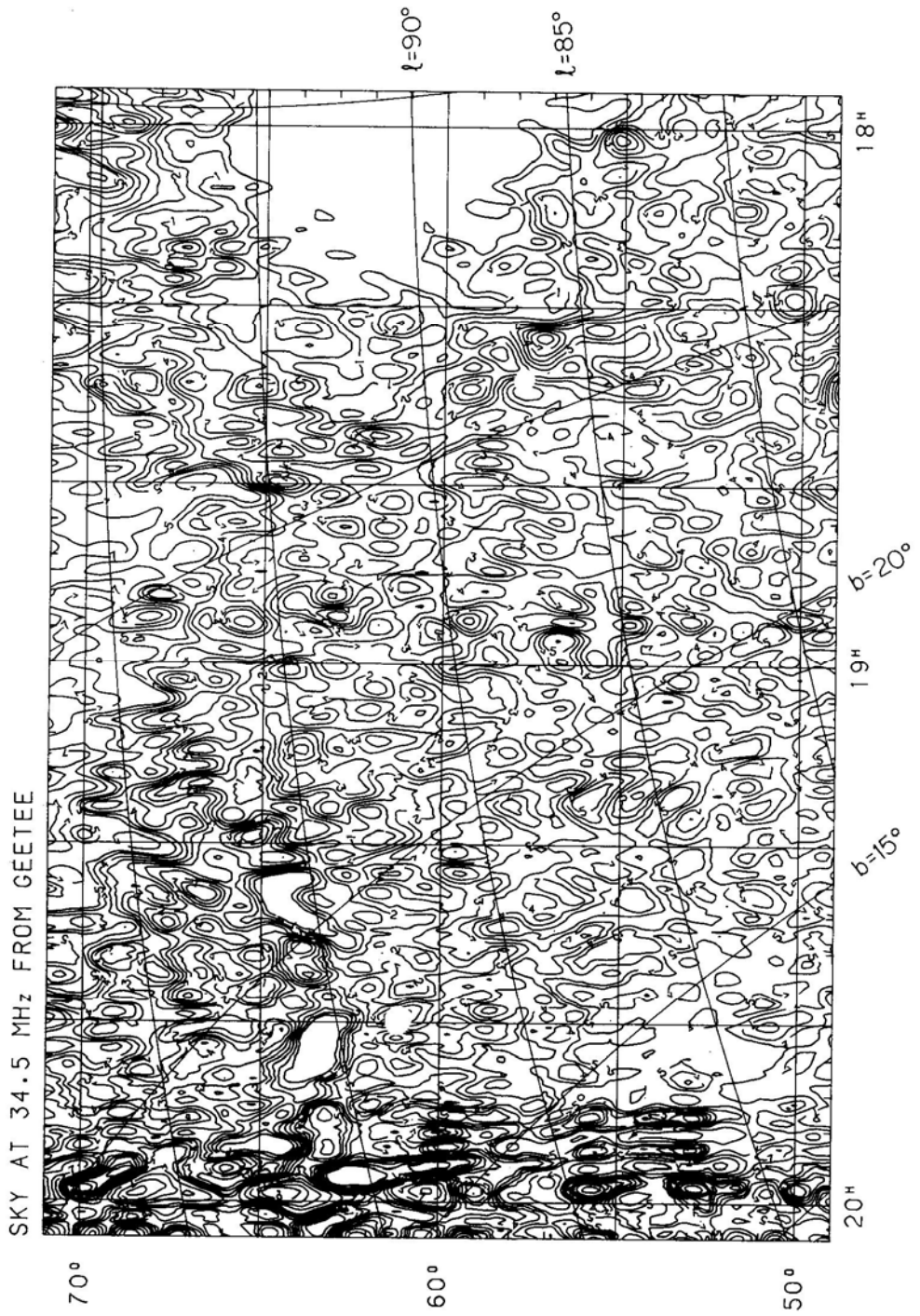
SKY AT 34.5 MHz FROM GEETEE
ℓ=90°
ℓ=85°
18ᴴ
19ᴴ
20ᴴ
b=20°
b=15°
70°
60°
50°

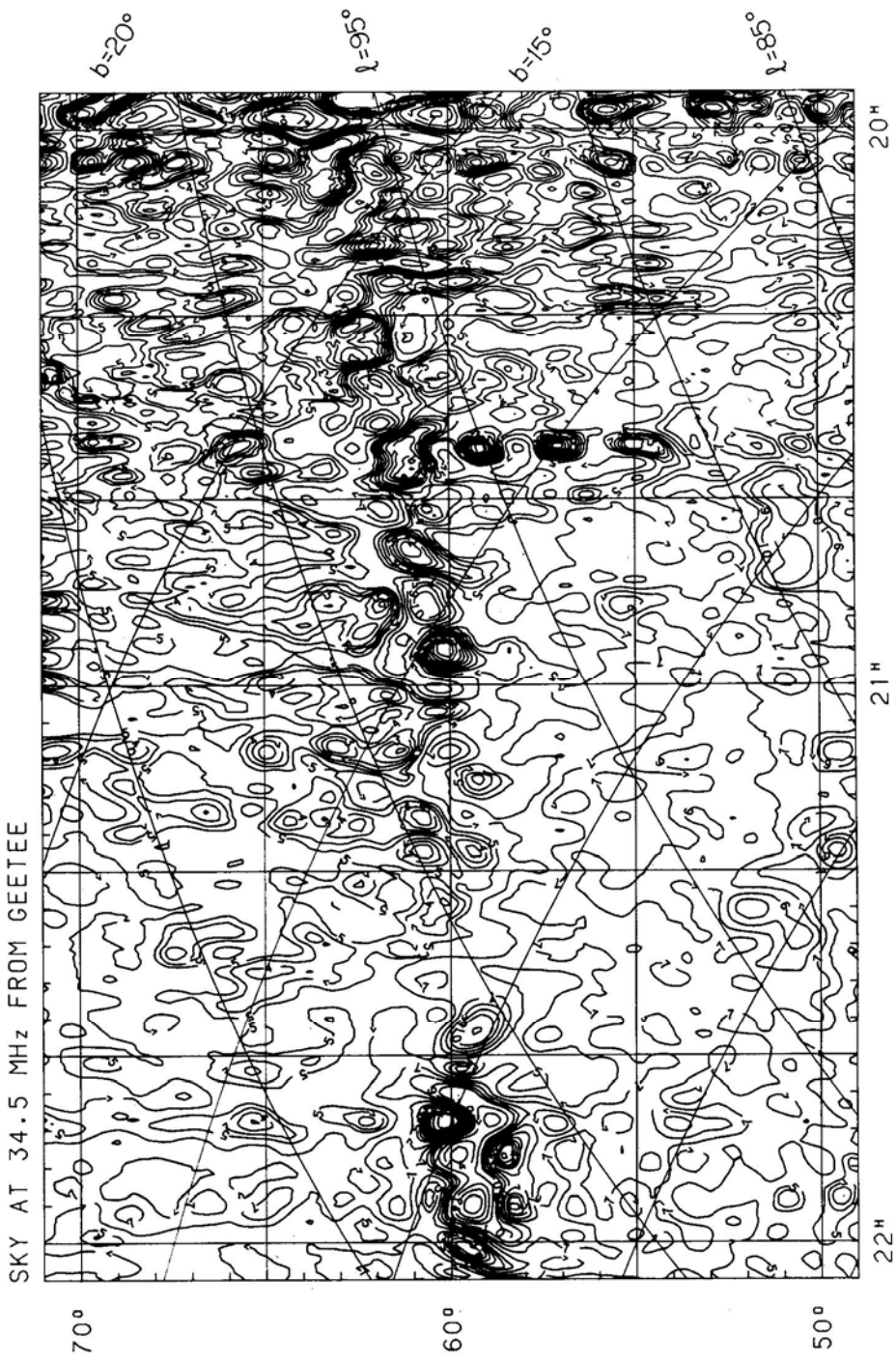
SKY AT 34.5 MHz FROM GEETEE
b=20°
l=95°
b=15°
l=85°
20ʰ
21ʰ
22ʰ
70°
60°
50°

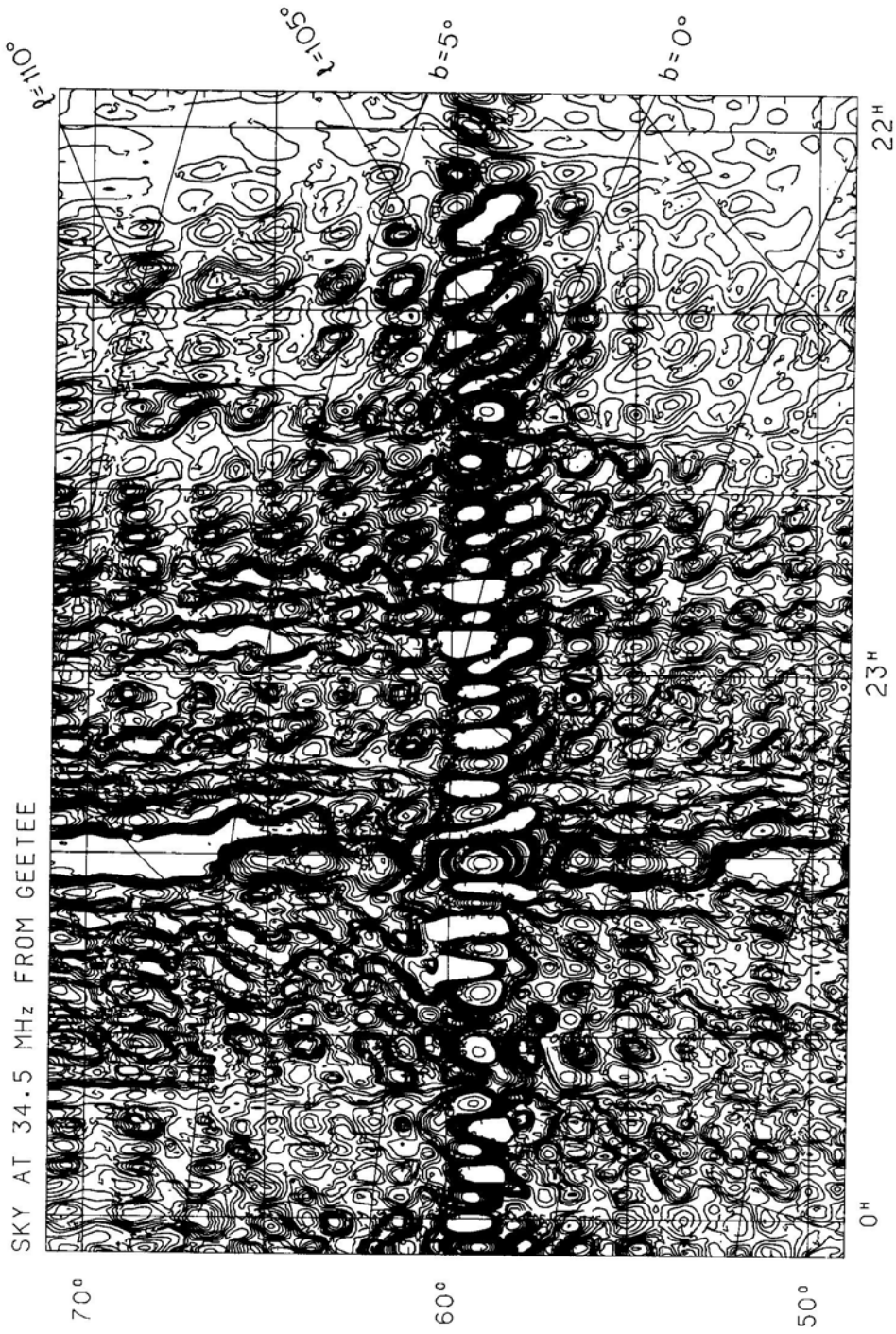
SKY AT 34.5 MHz FROM GEETEE
l=110°
l=105°
b=5°
b=0°
22ʰ
23ʰ
0ʰ
70°
60°
50°

J. Astrophys. Astr. (1990) **11,** 411– 443

Galaxy Alignments

Halton Arp *Max-Planck-Institut für Physik und Astrophysik, Institut für Astrophysik, Karl-Schwarzschild-Str. 1, 8046 Garching b. München, Germany*

Received 1989 November 15; revised 1990 July 16; accepted 1990 July 30

Abstract. It is well-known that galaxies tend to form elongated associations stretching many degrees across the sky. It is shown here that especially galaxies of about 3000 to 5000 km s^{-1} redshift define narrow filaments of from 10 to 50° in length. The surprising feature is that galaxies of very bright apparent magnitude tend to occur at the centre or ends of these alignments. The 20 brightest galaxies in apparent magnitude north of $\delta = 0°$ are investigated here and of the 14 which are uncrowded by nearby bright galaxies, a total of 13 have well marked lines and concentrations of fainter, higher redshift galaxies.

Key words: galaxies, alignments—galaxies, discordant redshifts

1. Introduction

The most conspicuous linear concentration of galaxies in the sky is the so-called Perseus-Pisces supercluster (Gregory, Thompson & Tifft 1981; Giovanelli & Haynes 1982, 1985; Chincarini, Giovanelli & Haynes 1983). Starting from the Perseus cluster of galaxies, one can trace galaxies about 15 degrees due west and then, discontinuously, for another 15 degrees to the southwest where their density diminishes and the feature becomes uncertain. All along this filament of galaxies the redshifts characteristically range between $cz \simeq 4000$ to 6000 km s^{-1}. Other, similar strings and elongated distributions of galaxies are rapidly being discovered.

There are already difficulties, however, with the standard interpretation of these filaments. The Perseus-Pisces galaxies form a filament of about two degrees in width over much of its more than 30 degrees in length. The observed dispersion in redshift shows a minimum range of from 4000 to 6000 km s^{-1}. In a time equal to the supposed age of the galaxies, random peculiar velocities of ± 1000 km s^{-1} would widen the filament to ~ 40 Mpc, or more than ten times the measured value of ~ 3 Mpc. To hold these galaxies on a line with gravitational forces would require an extremely large amount of mass distributed linearly down the core of the filament. It seems we already encounter an insoluble paradox if we make the standard interpretation of the redshifts of these galaxies as velocities.

In order to understand this alignment phenomenon better, galaxies in other regions of the sky are first investigated in the present paper. One listing of galaxies that can be used for this purpose is the Rood Catalogue. (Privately distributed in 1980, it lists all the galaxies with redshifts known to Rood at that time.) The galaxies in this catalogue are typically from such sources as Tully-Fisher and Bottinelli-Gougenheim (H I

redshifts) and Humason-Mayall-Sandage (predominantly absorption-line redshifts). Redshifts from many other sources are also listed. There is no claim to completeness of galaxies measured over any region of the sky but naturally bright galaxies are more completely surveyed than faint. For the purposes of the present analysis, however, incompleteness can only render the alignments and filaments less conspicuous than they really are. The reason for this is that if long lines of galaxies exist, it is implausible that observers would have unknowingly measured along them. Therefore any incompleteness in catalogues would only serve to degrade the lines. More complete surveys in the future would be expected to enhance these long linear concentrations.

Another catalogue which is very useful is the survey of low surface brightness (LSB) galaxies by Bothun, Beers & Mould (1985). That survey encompasses galaxies of fainter apparent magnitude than does, for example the CFA survey (Huchra *et al.* 1983). It turns out that galaxies in a narrow redshift range but over a wide range in apparent magnitude operationally define the lines better than galaxies of all redshifts to a bright apparent magnitude limit. The two catalogues designated here as Rood and LSB will form the bulk of the source material for the investigations in the following paper.

Investigations within these catalogues consisted of plotting large areas of the sky and examining whether galaxies of similar redshifts formed continuous chains or alignments.

2. The longest line of galaxies

Fig. 1 shows all the galaxies tested in the Rood Catalogue at northern declinations ($\delta \geqslant 50^0$) between $4^h40^m \leqslant \alpha \leqslant 13^h20^m$ Only galaxies with redshifts corrected to the centre of the Local Group which are between 3100 km $s^{-1} \leqslant cz_0 \leqslant 5100$ km s^{-1} are plotted (see Table 1). The filled circles represent the narrower redshift range $3100 \leqslant cz_0 \leqslant 3700$ and give the most unique definition of the filament. The higher redshift range $3700 \leqslant cz_0 \leqslant 5100$ also defines the major, long filament but in addition furnishes a short filament at about $\delta \simeq 65^0$ and and $\alpha \simeq 7^h30^m$ one just north of $\delta = 50°$ between $8^h < \alpha < 9^h$. These shorter alignments will be discussed in the following section.

The main concentration of galaxies in Fig. 1 is seen to run from $\alpha \simeq 6^h$, $\delta \simeq 73°$ to $\alpha \simeq 13^h$, $\delta \simeq 54^0$ This alignment of galaxies has about the same length ($\gtrsim 40^o$) as the Perseus-Pisces superfilament and is comprised of galaxies of roughly similar redshift. The reality of the Perseus-Pisces filament is widely accepted and the configuration in Fig. 1 represents another example of this large scale chaining or filamentary structure in the Universe. Such structures have recently been discussed extensively (see for recent review separate papers by G. Chincarini, M. Geller & J. Einasto in IAU Symposium 124, Beijing 1986). In order to explore further the nature of these galaxy alignments we examine other regions of the sky.

In Fig. 2 is shown the section of sky below the main filament in Fig. 1 (see Table 2).In this restricted range of redshift we see that the filament at the bottom edge of Fig. 1 is more conspicuous and angles to the southeast below $\delta = 50°$. This is the same linear alignment of galaxies that was identified as the Lynx-Ursa Major supercluster by Giovanelli & Haynes (1982). It was also noted by Focardi, Morano & Vettolani (1986). In addition Fig. 2 shows a sparser filament slightly south of $\delta \simeq 35^o$.

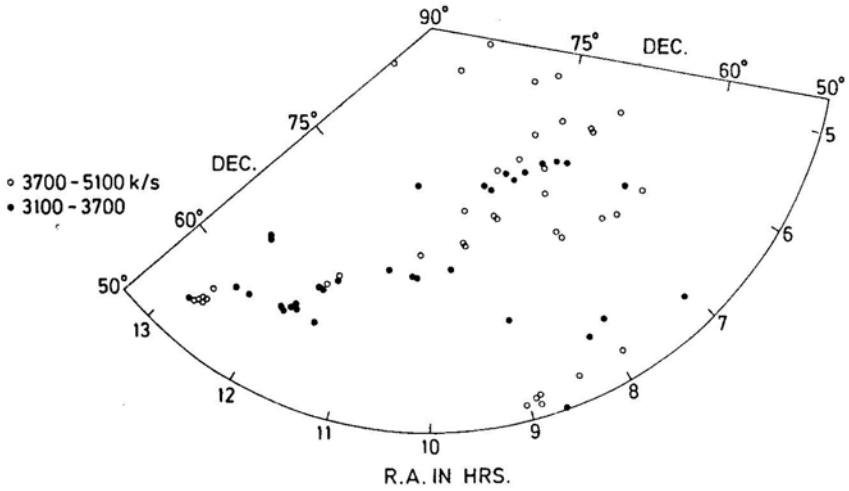

Figure 1. All galaxies listed in the Rood redshift catalogue are plotted in the pictured area. The filament is best defined by galaxies $3100 < v_0 < 3700$ km s^{-1} (filled circles).

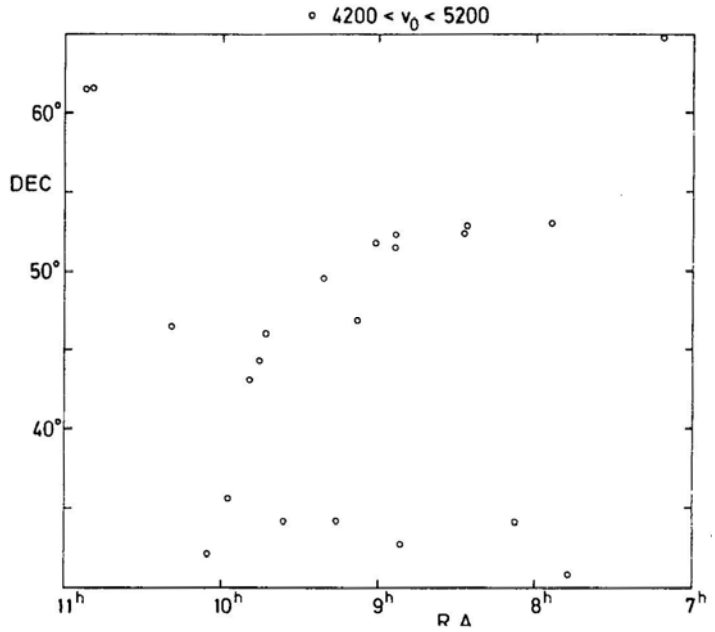

Figure 2. An extension of a region southward from Fig. 1. All Rood listings in the designated redshift range are plotted. Upper filament was designated as the Lynx-Ursa Major supercluster by Giovanelli & Haynes (1982).

Table 1. Rood galaxies: $4^h40^m \leqslant \alpha \leqslant 13^h20^m$, $\delta \geqslant 50^o$; $3100 < cz_0 < 5100$ km s^{-1}.

Galaxy	α h m	δ ° ′	m_p mag	Type	cz_0 km s^{-1}	Line*	Remarks
UGC 3253	5 07.0	84 00	13.1	SBb	4350		
3302	5 21.0	76 37	14.9	Sc	4365		
NGC 1961	5 36.6	69 21	12.2	Sb	4102	V	Sb II, Arp 184
UGC 3373	5 51.0	78 30	15.0	Sc	5014		
3422	6 09.3	71 09	14.5	Sb/SBb	4219	V	pw 3426
3426	6 09.8	71 03	13.8	SO:	3930	V	Mark 3, pw 3422
3460	6 21.5	74 18	15.0	SBb	4912	V	Mark 4
3478	6 28.0	63 43	13.3	Sb	3968	V	
3511	6 38.7	65 15	13.0	Sc	3689	V	pec
3642	6 59.6	64 06	13.5	So	4624	V	
3644	6 59.9	71 08	14.9	SBc	3399	V	
NGC 2314	7 03.7	75 25	13.1	E–So	4070	V	pw IC 2174, E3
UGC 3690	7 05.1	53 32	17	DwIrr	3223		Irr I
3697	7 05.6	71 55	13.1	. . .	3316	V	integral disturbed
NGC 2347	7 11.3	64 49	13.2	Sb	4552	V	Sb I–II, pw IC2179
UGC 3838	7 22.3	72 40	13.9	. . .	3250	V	pec, Mark 7
IC 2184	7 23.6	72 14	13.8	. . .	3728	V	DBL or TRIPLE, Mark 8
UGC 3984	7 39.9	70 10	14.2	SBb	4041	V	
3992	7 41.0	85 04	14.0	S0?	4572		compact Nuc
4028	7 44.8	74 28	12.7	S . . .	4108	V	Mark 12
NGC 2441	7 46.3	73 09	12.7	Sc/SBc	3630	V	Sc I–II
UGC 4095	7 52.1	66 44	14.4	. . .	4211	V	pec
4098	7 52.7	66 34	14.5	S . . .	5043	V	pec
NGC 2469	7 54.0	56 49	13.2	S. . .	3383	X	
NGC 2475	7 54.1	53 00	13.9	DBL	5084	X	DBL w N2474
UGC 4242	8 05.4	72 57	14.4	. . .	3307	V	Mark 14
NGC 2534	8 09.0	55 49	13.8	. . .	3593	X	pec, Mark 85
2523	8 09.3	73 44	12.4	SBb	3608	V	
UGC 4323	8 15.6	67 08	14.4	E?	4073	V	eruptive? KOA
4353	8 18.1	67 08	15.3	Sc	4433	V	KOS
DDO 51	8 19.3	74 36	14.9	SBc	3685	V	disturbed, pair
UGC 4376	8 20.2	67 00	15.1	. . .	4346	V	KOS
—	8 25.5	67 12	15.4	SO/a	4256	V	KOS
UGC 4438	8 26.2	52 52	13.9	S . . .	4290	X	pec, Mark 90
4516	8 36.7	67 02	15.2	Sc-Irr	3992	V	KOS
NGC 2614	8 37.4	73 09	14.0	Sc	3500	V	
UGC 4539	8 39.5	67 09	14.5	Sc	4030	V	pec, KOS
NGC 2639	8 40.0	50 22	12.4	Sa	3270		
UGC 4593	8 44.0	70 18	13.4	. . .	(3760)	V	pec, dbl Nuc
NGC 2650	8 45.0	70 30	14.3	SBb	(4000)	V	
2646	8 45.0	73 39	13.0	SB0	3731	V	SBO_2
UGC 4671	8 53.1	52 18	13.6	S . . .	4351	X	disturbed
NGC 2693	8 53.3	51 33	13.1	E	5041	X	E2
2692	8 53.3	52 16	14.1	SBa–b	3834	X	pw U 4671
UGC 4730	8 58.0	60 21	14.3	. . .	3345		pw U 4727
4749	9 01.0	51 50	13.6	S . . .	4802	X	Mark 101
4951	9 17.0	71 45	14.7	. . .	3719	V	Mark 20 = Mark 10
5028	9 23.6	68 39	13.9	. . .	3773	V	pec, Mark 111 pw 5029, Arp 308?
5029	9 23.8	68 40	14.3	Sc	3995	V	distorted, pw 5028
NGC 2909	9 40.0	66 13	14.1	. . .	3124	V	pec, Mark 119

Table 1. Continued.

Galaxy	α h m	δ ° ′	m_p mag	Type	cz_0 km s^{-1}	Line*	Remarks
UGC 5494	10 09.0	67 40	16.0:	pec	4633	V	or I/A pair
5520	10 11.3	65 24	14.4	Sc	3438	V	
5576	10 17.0	65 26	14.1	S?	3419	V	pec?
NGC 3183	10 17.5	74 26	12.5	SBb	3240		
NGC 3394	10 47.2	65 59	13.1	Sc	3564	V	one of pair
UGC 6429	11 22.4	64 01	14.1	Sc	3851	V	pw N3668
NGC 3668	11 22.5	63 43	13.1	Sb/Sc	3553	V	pw U6429
3690	11 25.7	58 50	12.6	DBL	3101	V	) Mark 171
IC 694	11 25.7	58 50	12.6	DBL	3216	V	∫ VV118, Arp 296
UGC 6520	11 29.6	62 48	14.1	S . . .	3772	V	Mark 175, in pair
6528	11 29.9	62 07	14.1	Sc	3372	V	pw N3725
NGC 3725	11 30.8	62 10	13.6	SBc	3449	V	Mark 179, pw U6528
UGC 6732	11 42.8	59 15	13.5	. . .	3201	V	
NGC 3894	11 46.1	59 42	12.9	SO	3370	V	pw N3895
3895	11 46.4	59 43	14.0	SBa	3340	V	pw N3894
3958	11 51.9	58 40	13.1	Sa	3492	V	pw N3963
3963	11 52.4	58 46	12.2	SBb	3297	V	pw N3958
4290	12 18.4	58 22	12.8	SBb	3155	V	SBb
4500	12 29.0	58 15	13.2	SBa	3122	V	Mark 213
4512	12 30.3	64 09	14.7	. . .	3124		pw N4521
4512	12 30.6	64 13	13.0	SO–a	3116		pw N4512
4644	12 40.4	55 25	(14.8)	SB: b	4953	V	disturbed, in pair
4646	12 40.6	55 07	13.8	. . .	4665	V	in N4686 group
UGC 7905	12 41.5	55 10	14.1	DBL	5018	V	Mark 220, disrupted
7922	12 42.3	56 25	15.3	SB? b–c	4919	V	
NGC 4675	12 43.3	55 00	15.4	SBb:	4920	V	N4686 grp.
4695	12 45.3	54 39	14.5	S . . .	5042	V	N4686 grp.
—	12 46.0	54 18	14.9		3496	V	no classification
UGC 8264	13 09.0	84 53	14.5	. . .	4854		pec

* V means line through M81 (including M81-N2403 line)
X denotes line through NGC 2841.
blank denotes galaxy not aligned.

There is an amazing property of these galaxy filaments, however, which bears not only on their reality but also on their origin. We proceed to the discussion of this.

3. Association with bright apparent magnitude galaxies

Fig. 3 is exactly the same as Fig. 1 except that we have now plotted the three brightest galaxies in the area as open squares. We see that M81, the brightest galaxy in the sky outside the Local Group, falls at the centre of the largest superfilament in the sky outside the Local Group. The two shorter filaments present in Fig. 1 contain the second and third brightest apparent magnitude galaxies in this sector of the sky, NGC 2403 and NGC 2841.

Further south than M81, Fig. 4 shows the same galaxy filaments as in Fig. 2 but the brightest galaxies in this region, NGC 2841 and NGC 2683, are now added as open

Table 2. Galaxies aligned through NGC 2841 and 2683

Galaxy	α h m	δ ° ′	m_p	Type	cz_0	Remarks
a) NGC 2841: $4200 < cz_0 < 5200$ km s^{-1}.						
NGC 2475	7 54.1	+53 00	13.9	DBL	5084	contact
UGC 4438	8 26.2	52 52	13.9	Spec:	4290	Mark 90
4442	8 27.0	52 28	14.5	Sb/SBc	5147	
4671	8 53.1	52 18	13.6	S	4236	pw 4675
NGC 2693	8 53.3	51 33	13.1	E	4926	
UGC 4749	9 01.0	51 50	13.6	S	4802	Mark 101
4829	9 08.4	46 51	14.3	compact	4265	Mark 102
NGC 2857	9 21.1	49 34	14.3	Sc	4904	N2854 grp
UGC 5225	9 43.3	46 00	14.9	compact	4959	
NGC 2998	9 45.5	44 18	13.3	Sc	4782	Sc I brtst in grp.
UGC 5295	9 49.7	43 05	14.5	SBb/Sb	4780	brtst in grp.
5664	10 19.7	46 30	14.8	Sc	5014	
b) NGC 2683: $4200 < cz_0 < 5200$ km s^{-1}.						
UGC 4047	7 47.0	30 51	14.5	SBb	4317	Sc I (M51 type)
NGC 2532	8 07.0	34 06	12.9	Sc	5217	Sc II–III
IC 2421	8 51.2	32 52	14.9	Sc	4355	SC I (very pretty!)
NGC 2823	9 16.2	34 13	15.7	SBa	4995	pec?
2942	9 36.1	34 14	14.1	Sc	4390	Sc I
3074	9 56.7	35 38	14.8	Sc	5131	Sc I
3126	10 05.4	32 06	13.5	Sb	5123	nearly edge on
2955	9 38.2	36 07	13.9	Sb	7051	Sc I, one pec arm (above redshift interval)

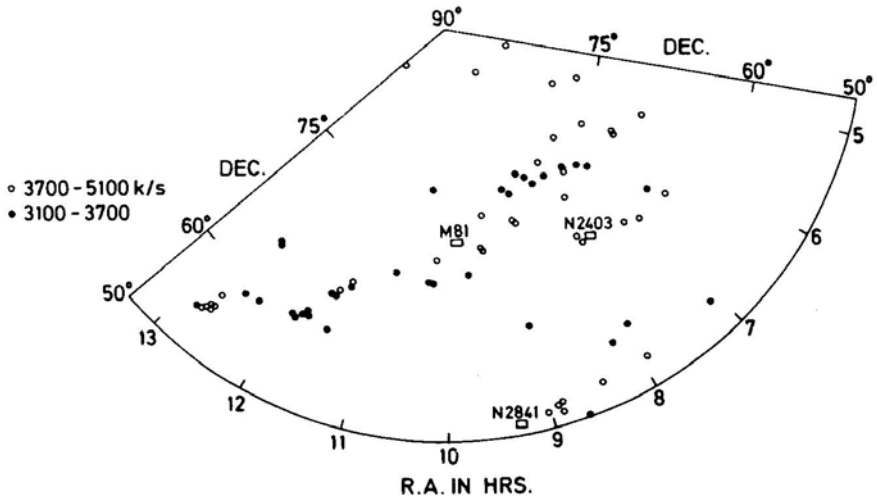

Figure 3. The same plot as in Fig. 1 except the three brightest apparent magnitude galaxies in the region have now been added (see Table 6 for listing of brightest apparent magnitude spirals)

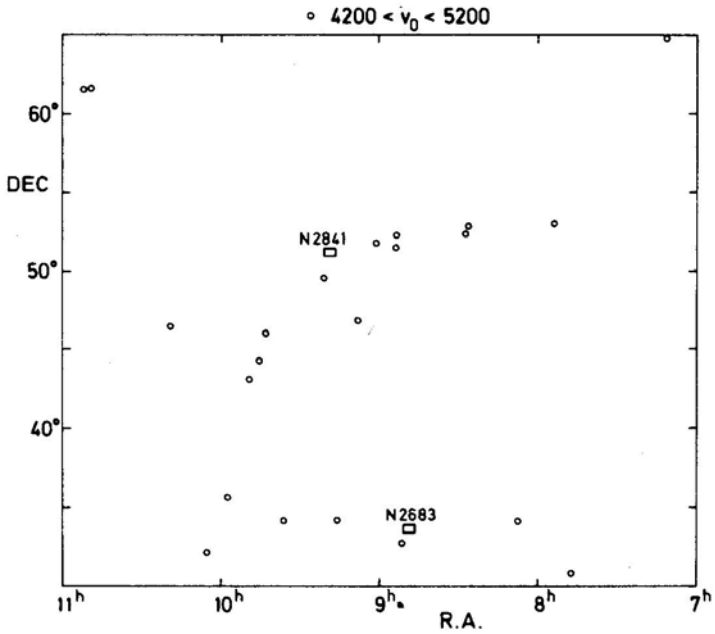

Figure 4. The same plot as in Fig. 2 except the two brightest galaxies in the region have been added.

squares. Again these bright apparent magnitude galaxies fall near the midpoints of the fainter galaxies in the filaments.

3.1 *Small Field Samples*

In Figs 1–4, galaxies obviously sampled only in small areas of the sky have been omitted when plotting from the Rood Catalogue. One such limited region is the Kirshner, Oemler & Schecter (1978) field which falls close to NGC 2403. Fig. 5a shows, however, that when the limits of that field are outlined by a dashed box that only in the top of this field are found galaxies in the redshift range which belong to the NGC 2403 filament. These galaxies form a straight connection across the KOS field from the direction of M81 to NGC 2403. Fig. 5a shows, however, that this is an extraordinary line of galaxies to be found in a fully sampled field. As KOS themselves state: "There are prominent groupings at 4000 and 11000 km s^{-1} . The galaxies in the near grouping are loosely clustered but the 11,000 km s^{-1} galaxies are spread over the entire field." It would be an almost unbelievable coincidence if this straight line of ~ 4000 km s^{-1} galaxies, by accident, just fit exactly into the longer line of similar redshift galaxies that was observed earlier passing from M81 through NGC 2403. The longer line is therefore confirmed by this more complete test in a small sample area.

3.2 *Active Galaxies*

The reality of this line is further reinforced by the fact that special kinds of galaxies of various redshifts appear to define this same line. Fig. 5b shows that the active

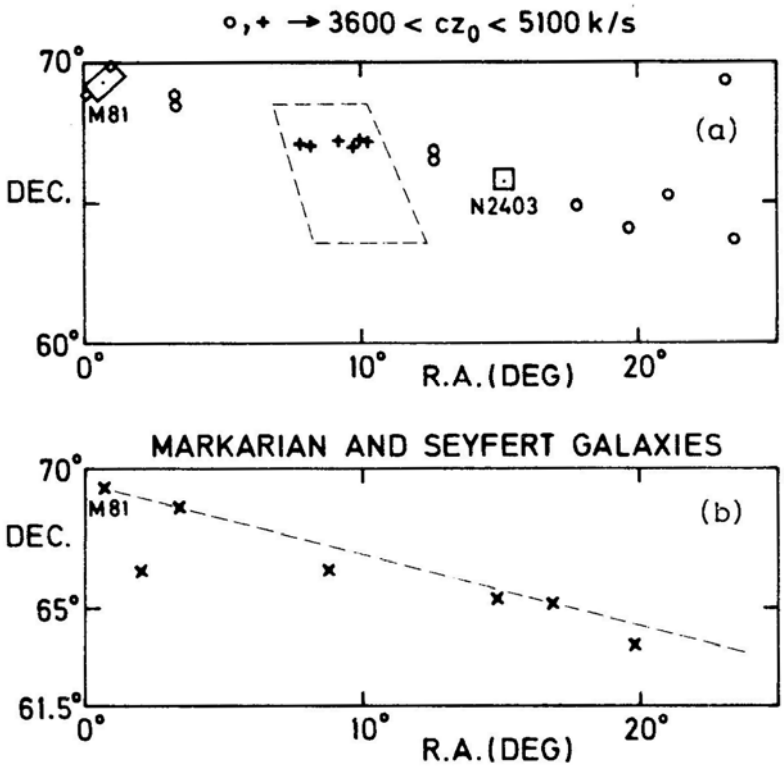

Figure 5. (a) An enlargement of the region southwest of M 81 from Fig. 3. Inside the dashed box a complete measurement of galaxy redshifts has been made (Kirshner, Oemler & Schecter 1978). Galaxies found with $3600 < v_0 < 5100$ kms^{-1} are indicated by plus symbols, (b) A plot of all the known Markarian and Seyfert galaxies in the same area (from Table 3). The line of galaxies from top frame is shown in the lower frame as a dashed line.

Markarian and Seyfert galaxies listed in Nilson (1973) and Veron-Cetti & Veron (1984) fall along this previously defined line. Table 3 lists these individual galaxies.

In fact we will find throughout this paper that the lines of galaxies are characterized by active galaxies. Table 4 shows, for example, that the lines of galaxies through M81, NGC 2403 and NGC 2841 are characteristically composed of peculiar galaxies or

Table 3. Markarian and Seyfert galaxies in M81-NGC 2403 line.

Galaxy	α h m	δ ° ′	mag	Type	Redshift	Comment
M81	09 51.5	69 18	7.01	Sb I–II	124 km/sec	Seyfert 1
NGC 2909	09 40.0	66 13	14.1	pec	3124	Mark 119
UGC 5028	09 23.6	68 39	13.9	pec	3773	Mark 111
4490	08 33.1	66 20	16.0	S . . .	5296	Mark 93
—	07 37.9	65 18	14.6	—	11400	Mark 78, Sey 2
4C65.08	07 19.1	65 11	18.7	compact	0.218	Sey?
0700+63	07 00.8	63 38	16	blue, compact	0.152	Sey 1, X-ray source

Table 4. Peculiarities of galaxies in Figs 1 and 3.

Galaxies	Normal	pec or dbl	Markarian
Non-aligned	6	5	0
Aligned	13	39	18

ultraviolet-rich Markarian galaxies. In fact the startling result shown in Table 4 is that there are more Markarian galaxies than normal galaxies in the long M 81 line! The few galaxies in the regions of the sky pictured in Figs 1–4 which fall off the lines contain no examples of Markarian objects. As we know, Markarian objects are rare kinds of galaxies, and their concentration along the lines demonstrates both the reality of the lines and the active, peculiar, physical state of the galaxies in the lines.

The galaxies extracted from the Rood Catalogue in the relevant redshift range for the broad regions we have been analyzing are individually listed in Tables 1 and 2,

3.3 *Testing for Hubble Relations*

Before we pass on to examination of other regions of the sky we should comment on whether it is possible that these chains of high-redshift galaxies can be physically associated with such bright apparent magnitude, low-redshift galaxies. If they are associated, then the higher redshifts of the galaxies in the chains cannot be indicative of their distances. Of course, there has been evidence accumulating for over two decades that some galaxies have large intrinsic redshifts (see Arp 1982, 1987a and 1990 for reviews). The present chains contain some examples of supposedly normal galaxies, however, and it would be natural to first check whether there is therefore evidence which would argue against the possibility that these chain members could be as near to us in distance as the central, bright apparent-magnitude galaxies.

The only test which could give evidence for this particular group of galaxies being at its redshift distance would be to see them define a Hubble relation. Fig. 6 plots redshift versus apparent magnitude for all the galaxies in the M81 superfilament which was pictured in Figs 1 and 3. Obviously there is no Hubble relation present between the redshift and apparent brightness of these galaxies.

One might argue that because of the restricted redshift interval that there could be a Hubble relation which was masked by a large range in intrinsic luminosities. But Fig. 6 shows the Sb's (filled circles) and Sc's (crosses) separately obey no such redshift-apparent magnitude relation. In fact the behaviour of all these galaxies in the Hubble plane is to have about the same redshift until the faintest apparent magnitudes and then curve up slightly to higher redshift. This is just the behaviour of fainter galaxies in physical groups which was attributed to increasing components of intrinsic redshift in the analysis of Arp (1990). But regardless of whether the behaviour of their parameters in Fig. 6 can be used to *disprove* that the galaxies are at conventional redshift distances, the diagram clearly demonstrates that there exists no proof whatsoever that these particular higher redshift galaxies are in fact *at* their redshift distances.

If these galaxies belong to an alignment and that alignment belongs to M81, then they must be 5 to 7 magnitudes less luminous than M81. Therefore their intrinsic

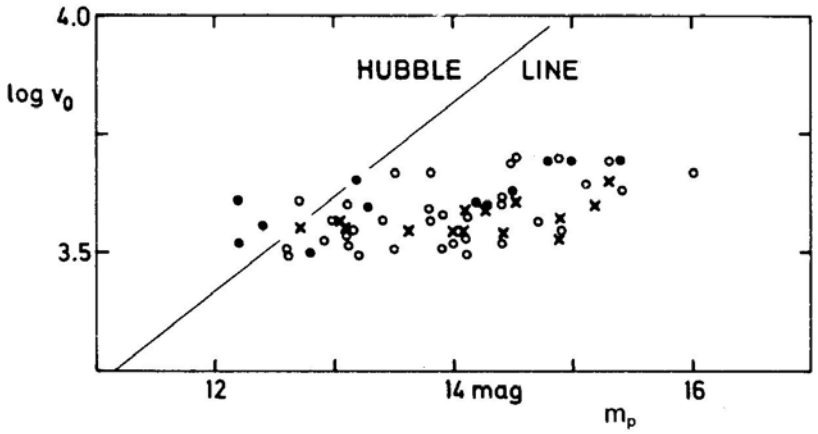

Figure 6. The redshift–apparent-magnitude plot for all the galaxies plotted in Figs 1 and 3.The filled circles represent galaxies of class Sb and the crosses class Sc. Open circles represent remaining galaxy classes.

redshift must increase as their luminosities decrease, roughly mimicking the behaviour of galaxies of the same luminosity seen at increasing distance. This is the only sense in which they obey a Hubble relation. It is very rough, however, essentially only a qualitative agreement in the direction of fainter apparent magnitude occurring with higher redshift.

3.4 *Differences of Galaxies in Different Lines*

If the $3100 < cz_0 < 5100$ km s^{-1} galaxies aligned through M81 are physically associated they must be at the same distance as M81 despite their much higher redshift. Companions with similar intrinsic redshifts around central galaxies which are more distant than M81 should appear fainter in apparent magnitude. This will be an important point to check as we go on to study other examples of these alignments. The true distances of these other alignments will be difficult to judge, however, because of the doubt which has now been cast on the redshift as a distance criterion.

One aspect which is in principle distance-independent, however, is the morphological and spectral types of the galaxies in the various lines which have been identified. It has been shown that in the long M81 alignment and the shorter NGC 2403 and NGC 2841 alignments that galaxies have a marked tendency to be peculiar or double or have ultraviolet-rich (Markarian-type) spectra. This is a strong confirmation that the alignments are not chance arrangements of unrelated galaxies. In the case of chance alignment the aligned galaxies would be like an average galaxy, not spectroscopically and morphologically unusual as they are observed to be.

But as we continue to investigate different alignments we shall find the constituent galaxies more different in some lines than in others. The aligned galaxies will be different from that of the average background, but present marked differences from line to line. A good example of this shown in Table 2b. The galaxies aligned through NGC 2683 consist of a startling majority of Sc I spirals. (The classification of thin arm spiral was made by the author from Palomar Sky Survey prints.) The Sc I classification

is relatively rare among spirals (Sandage & Tamman 1981). The fact that there is such a high percentage of Sc I spirals in the NGC 2683 alignment may be connected to the fact that NGC 2683 is a bright apparent magnitude Sb of abnormally low redshift. It has been argued (Arp 1990) that the Sc I luminosity class is a very low luminosity, nearby class of galaxy. The faint Sc I companions to NGC 2683 support this previous result.

Finally we shall see when we come to analyze the Local Group of galaxies that high redshift companions in the M31–M33 alignment are extremely peculiar in yet another way: small, high surface brightness, often interacting galaxies. Apparently it is characteristic to have a line, or lines, of high-redshift galaxies radiating from a bright apparent-magnitude spiral. The fact that different lines have different kinds of peculiarities makes it more difficult to understand the cause of the phenomenon. But the repetition of the phenomenon strongly reinforces the reality of the filaments.

Of course the existence of the filaments of galaxies is not difficult to accept. As pointed out earlier, they are like the Perseus-Pisces and other galaxy alignments which are now widely recognized. The difficult point is the apparent association of these much higher redshift galaxy filaments with bright apparent magnitude, very low redshift galaxies. Because of the extreme importance of this association if real, all the bright apparent magnitude galaxies which are accessible will now be carefully examined.

4. Examining a complete sample of bright apparent magnitude galaxies

4.1 *M101*

Still postponing the discussion of Local Group galaxies, we consider the next brightest apparent magnitude galaxy after M81, namely M101. Table 5 lists the Rood galaxies

Table 5. Rood galaxies centred on M101 ($12^h30^m < \alpha < 15^h30^m$; $+40 < \delta < +70$).

Object	α h m	δ ° ′	m mag	v_0 km s^{-1}
NGC 5109	13 18.9	+57 55	13.6	2271
DDO 175	13 23.5	58 05	15.6	1661
NGC 5169	13 26.0	46 56	14.7	2585
5173	13 26.3	46 51	13.5	2498
5205	13 28.2	62 46	13.5	1940
	13 31.8	60 39	—	2226
DDO 178	13 33.7	46 11	15.3	1551
DDO 177	13 34.2	46 28	15.2	2540
UGC 8639	13 37.0	51 41	15.5	1834
A 1339	13 38.7	54 35	14.4	2172
NGC 5297	13 44.3	44 07	12.3	2507
NGC 5301	13 44.4	46 22	13.0	1601
	13 44.8	60 38	17.0	2222
UGC 8714	13 44.8	60 39	16.5	2219
NGC 5308	13 45.4	61 13	12.5	2201
	13 46.5	43 39	14.6	2447
	13 48.5	62 59	—	2299

Table 5. Continued

Object	α h m	δ ° ′	m mag	v_0 km s^{-1}
NGC 5336	13 50.1	43 29	13.6	2401
	13 50.7	44 04	16.0	2388
NGC 5350	13 51.3	40 36	12.4	2410
5353	13 51.4	40 31	11.8	2391
5354	13 51.4	40 32	12.3	2507
5355	13 51.6	40 35	14.0	2462
5362	13 52.8	41 33	13.2	2276
5376	13 53.6	59 45	12.9	2237
5379	13 54.0	59 59	14.1	1889
NGC 5377	13 54.3	47 29	12.5	1905
5389	13 54.5	59 59	13.2	1996
5452	13 54.5	78 28	14.2	2272
5383	13 55.0	42 05	12.5	2384
	13 55.1	42 02	16.5	2481
	13 56.0	57 15	15.6	1901
	13 56.4	63 39	16.5	1943
5422	13 58.9	55 24	13.1	1914
5443	14 0.5	56 03	13.2	2177
5448	14 01.0	49 25	12.7	2154
5473	14 03.0	55 08	12.5	2208
5480	14 04.5	50 39	12.6	1987
5481	14 04.9	50 59	13.5	2230
5485	14 05.5	55 15	12.4	2137
5486	14 05.7	55 20	14.0	1559
VV 125	14 09.6	50 27	15.1	2044
NGC 5631	14 25.0	56 49	12.4	2115
5660	14 28.0	49 50	12.2	2483
5667	14 29.0	59 42	13.1	2176
5673	14 29.8	50 10	14.0	2231
5678	14 30.6	58 09	12.1	2101
I 1029	14 30.7	50 07	13.7	2530
NCC 5676	14 31.0	49 40	11.7	2265
5682	14 33.0	48 53	15.1	2439
DDO 193	14 33.2	59 34	15.5	2097
NGC 5687	14 33.3	54 42	13.3	2283
NGC 5689	14 34.4	48 47	14.5	2423
5693	14 35.8	48 51	17.0	2463
NGC 5714	14 36.4	46 51	14.2	2382
	14 39.9	59 30	17.0	2510
NGC 5783	14 51.9	51 17	14.0	2497
	14 56.9	59 04	15.5	2461
	15 09.8	65 05	15.7	2448
	15 24.7	41 55	16.0	2491
$200 < v_0 < 500$ km s^{-1}.				
NGC 4605	12 37.8	61 35	10.8	279
4736	12 48.6	41 23	8.7	368
DDO 165	13 04.5	67 58	14.1	201
	13 05.8	47 07	17.0	314
NGC 5023	13 10.0	44 18	13.2	484
DDO 167	13 11.2	46 35	17.0	259
DDO 168	13 12.2	46 11	14.0	291

Table 5. Continued.

Object	α h m	δ ° ′	m mag	v_0 km s^{-1}
DDO 169	13 13.3	47 46	15.6	358
NGC 5204	13 27.7	58 40	11.7	346
	13 28.8	55 10	14.8	202
NGC 5229	13 32.0	48 10	14.6	476
5238	13 32.7	51 52	14.2	368
DDO 181	13 37.8	41 00	15.3	287
A 1353	13 52.9	54 09	14.2	283
NGC 5457	14 01.5	54 36	8.7	379
5474	14 03.3	53 54	11.9	423
5477	14 03.8	54 42	14.5	461
5585	14 18.2	56 57	11.7	466
DDO 190	14 22.8	44 44	13.9	281
DDO 194	14 33.9	57 29	17.0	393
Supplemented Rood galaxies near M 101 $1600 < v_0 < 2700$ km s^{-1}; $\delta > 35°$.				
	12 44.0	64 50	15.0	2445
4814	12 53.2	58 36	12.4	2618
—	13 34.8	45 09	15.5	2741
5289	13 43.0	41 45	13.5	2609
5290	13 43.1	41 58	13.0	2673
—	13 47.4	39 09	17.0	2352
5313	13 47.6	40 14	12.4	2627
5322	13 47.6	60 26	11.3	1788
5320	13 48.2	41 37	13.1	2709
DDO 183	13 48.7	38 16	15.4	273
NGC 5326	13 48.7	39 49	12.9	2613
5371	13 53.5	40 24	11.5	2653
5541	14 14.4	39 49	13.4	1869
	14 15.3	56 07	17.5	2044
	14 23.3	39 45	14.8	1551
5630	14 25.6	41 29	13.6	2777
DDO 198	14 59.7	52 48	15.2	2594
NGC 5894	15 10.6	60 00	13.2	2679
5899	15 13.2	42 14	12.6	2706
5900	15 13.2	42 24	15.0	2703
5929	15 24.3	41 51	13.7	2680
5930	15 24.8	40 44	14.0	2774
	15 29.0	41 30	17.0	2746

Between $1500 \leqslant cz_0 \leqslant 2500$ km s^{-1} in a wide region around M101. Fig. 7 plots these galaxies.

The outstanding aspect of Fig. 7 is that the filled circles increase strongly in density toward the centre of the plot. They are very sparse on the edges of the region but increase steadily to the centre, to the position where M101 is located. It is difficult to see how this could be any kind of selection effect since galaxies of both higher and lower redshift are scattered more or less uniformly throughout the area. Moreover, these galaxies form lines radiating from the position of M101 outwards. Fig. 7 shows

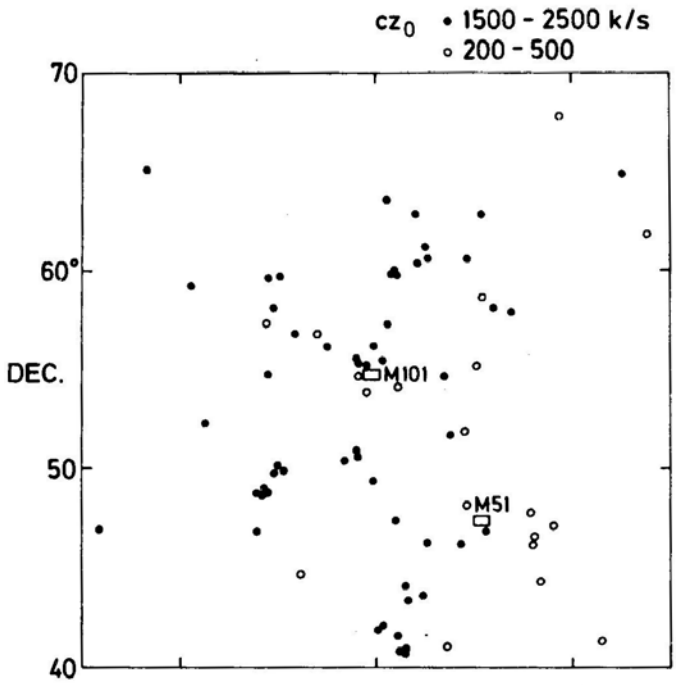

Figure 7. All galaxies listed in the Rood redshift catalogue between $1500 < v_0 < 3500$ km s^{-1} are shown as filled circles. Additional galaxies of low redshifts similar to that of M101 are shown by open circles. The two brightest galaxies in the area are shown by boxes.

that the line radiating to the north-east from M101 is the most marked but there are also indications of a line running NW to SE through the position of M101.

Low-redshift galaxies, $200 \leqslant cz_0 \leqslant 500$ km s^{-1}, are plotted as open circles in Fig. 7. These galaxies are close to the redshift of M101 at cz_0 =379 km s^{-1} and tend to confirm the physical reality of the NE–SW line as defined by the higher redshift galaxies. In other linear associations, the low-redshift galaxies, which we conventionally believe to be physically associated, confirm the alignments of the higher redshift members of the chain. This will be commented on particularly in the case of M31 and M33 as discussed later. We also see evidence in Fig. 7 for more than one line emerging from M101. This too is precedented since the M81 to NGC 2403 filament (Fig. 5) emerges at a different angle from M81 than the longer filament which stretches out on either side of M81.

4.2 *M51*

If M101 is the 4th brightest galaxy in the northern sky it is obvious that the 8th brightest, M51, lies a relatively short distance to the southwest and is also involved with some higher redshift companions. If we change our interval of plotted redshift slightly as in Fig. 8, we see a conspicuous line of galaxies emerging from M51 with redshifts in the range $2300 \leqslant cz_0 \leqslant 2800$ km s^{-1}. It is striking to note that there is now a gaping hole around the position of M101. This furnishes vivid evidence that it is

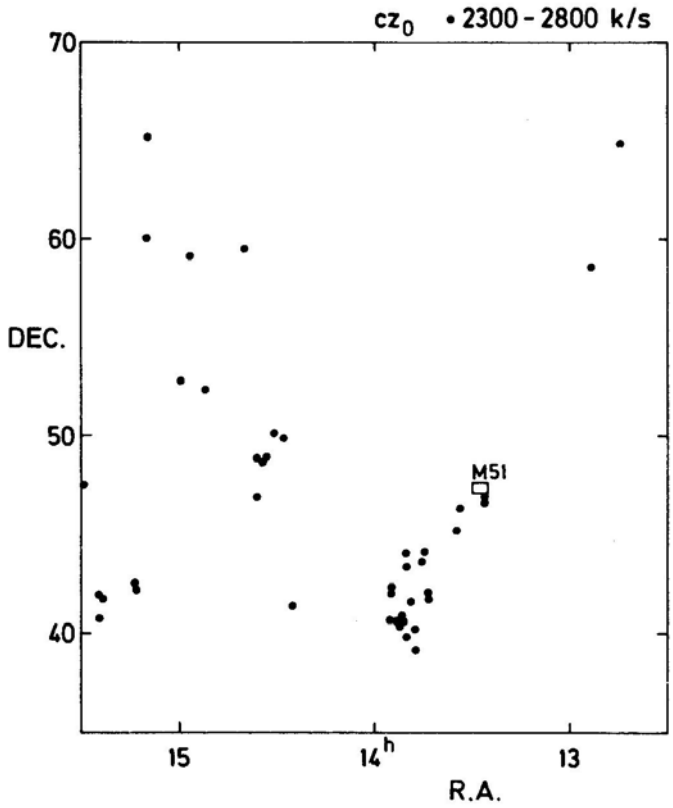

Figure 8. The same region as pictured in Fig. 7 but now a slightly higher range in redshift is plotted. Notice the 'hole' rather than concentration around M101 now and the strong line of galaxies originating from the position of M51.

almost entirely galaxies of redshift $1500 \leqslant cz_0 \leqslant 2300$ km s^{-1} which cluster around M101. There is some overlap in redshift, but it is just the galaxies of slightly greater redshift which then so strikingly emerge from the position of M51.

Of course the much different distribution on the sky of galaxies so close together in redshift, as shown in Figs 7 and 8, demonstrates that these associations cannot be due to a selection effect of observers only measuring galaxies in certain portions of the sky.

5. The line from NGC 6946

The 9th brightest apparent magnitude galaxy in the northern sky is NGC 6946. Although at low galactic latitude, Fig. 9 shows that there is a well-defined line of galaxies emerging from that position in the sky. Because of low latitude absorption from our own galaxy it is possible that the line continues on the other side of NGC 6946 but that we do not see those galaxies. Searching all along this line with hydrogen receivers tuned to the $2600 \leqslant cz_0 \leqslant 5300$ km s^{-1} redshift range would probably be rewarding.

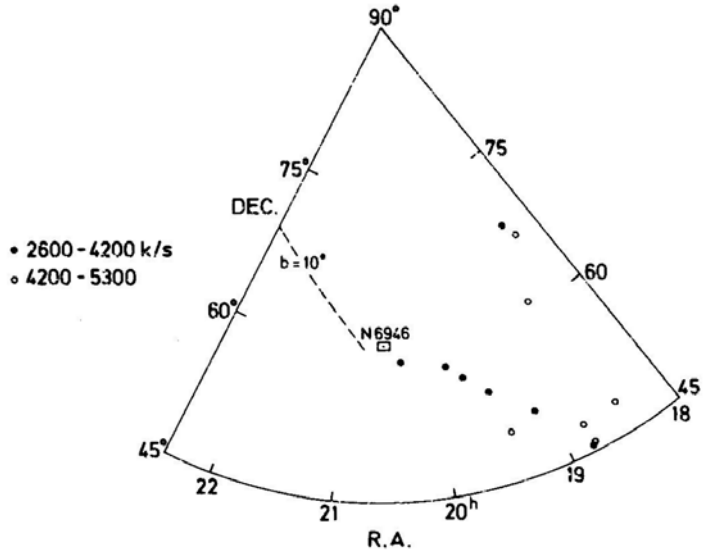

Figure 9. All Rood galaxies in area of sky surrounding NGC 6946. Area to upper left mostly obscured by Milky Way.

6. NGC 2903, NGC 7331 and the remaining brightest apparent magnitude galaxies

Other bright apparent magnitude galaxies have apparent alignments through them. NGC 2903 (not plotted here) is involved in a fairly conspicuous alignment. Those galaxies have a range of redshifts with perhaps best delineation between $2000 < cz_0 < 4100$ km s^{-1}.

NGC 7331 has a very conspicuous association of somewhat higher redshift, $5500 < cz_0 < 7000$ km s^{-1}, galaxies (Fig. 10). But NGC 7331 has the highest redshift of parent galaxies in the 20 brightest apparent magnitude galaxies of the present paper. (See Table 6 and summary Fig. 18). The NGC 7331 association is either a broad, elongated distribution centred on the large galaxy or possibly several lines radiating from NGC 7331. But these galaxies as a whole are so isolated from adjoining regions that they form a very conspicuous concentration around NGC 7331 as shown in Fig. 10. This is similar to the concentration around M101 shown in Fig. 7.

As reinforcement for the striking association of high redshift companions shown in the diagram of Fig. 10, we show here in Fig. 11 (see art plate) an enlargement of the centre of this region. The photograph, taken at the prime focus of the KPNO 4-m reflector, shows a region of about 1 degree in diameter around NGC 7331. The companions which group so conspicuously around the low redshift NGC 7331 and NGC 7320— the latter being the low redshift member of Stephan's Quintet—are just in the redshift range of Fig. 10, $5700 < cz_0 < 6800$ km s^{-1}.It is interesting that these groupings have been evident for as long as wide field photographs around NGC 7331 have been available (see for *e.g.* Arp 1972). But the evident associations have been dismissed because redshifts were believed to be inviolable measures of distance

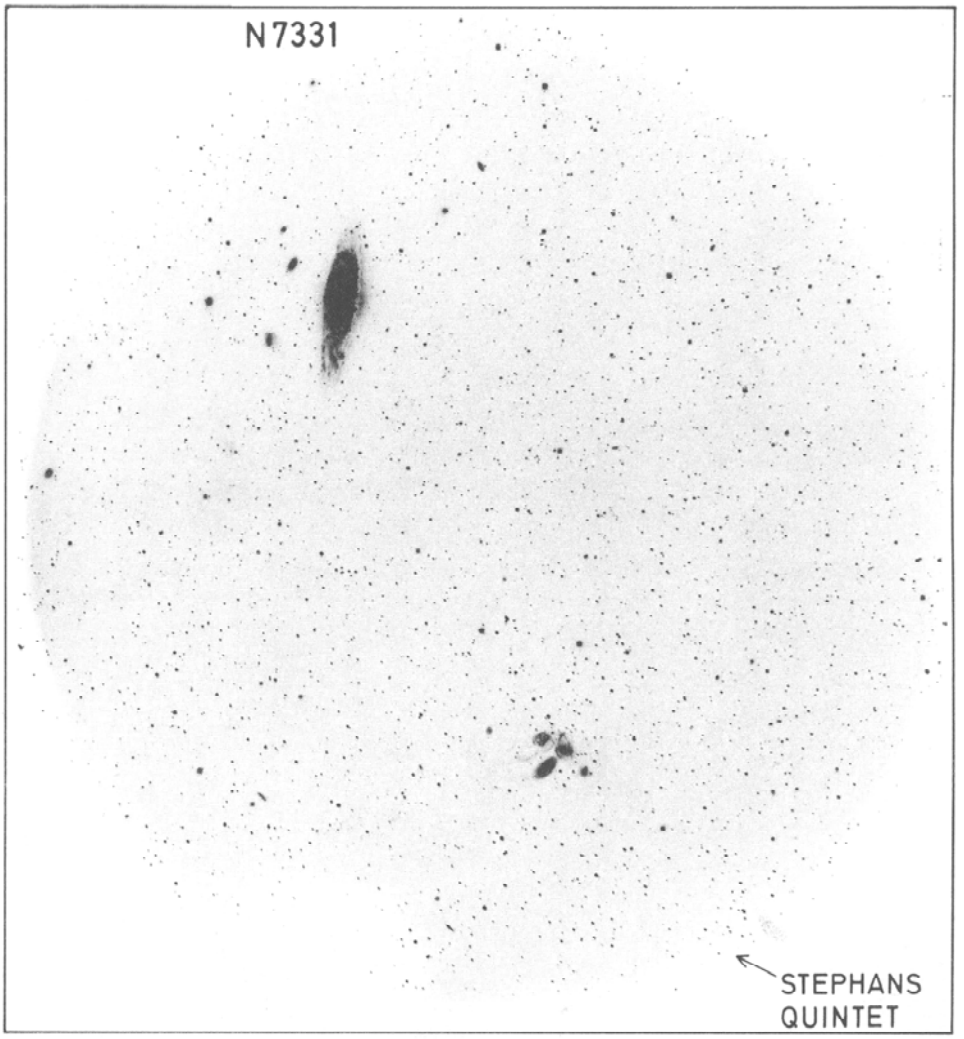

Figure 11. Limiting exposure on IIIa–J emulsion with KPNO 4-m reflector by Arp. The grouping of small, high-redshift companions around the large Sb, NGC 7331 is obvious. Also the grouping of similarly high-redshift companions around the low redshift member of Stephan's Quintet in the lower part of the field is apparent. H. ARP

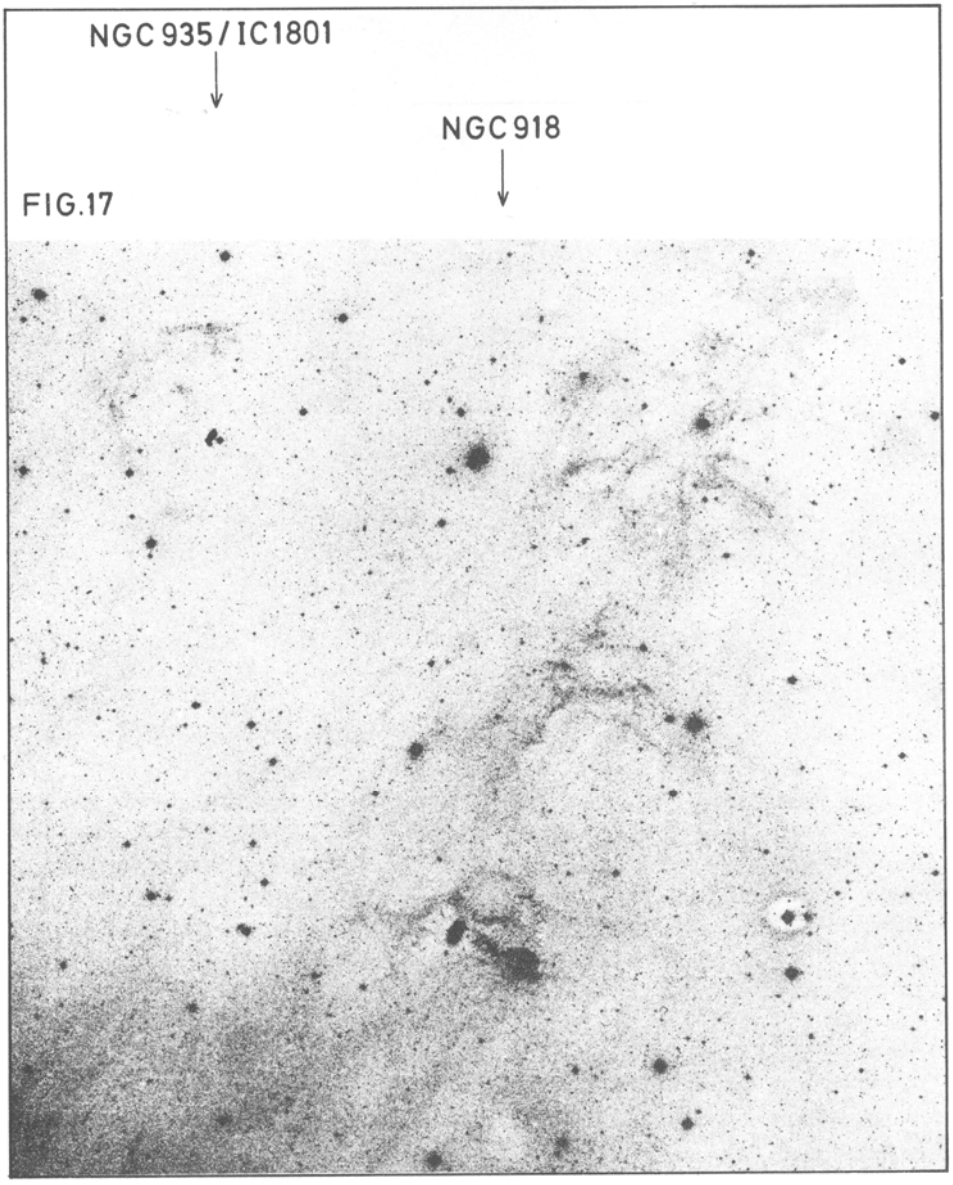

Figure 17. Contrast enhanced print of Palomar Sky Survey print E-443. Nebulous material seen interacting with NGC 918 (lower middle) and nebulous arc centred on NGC 935/IC 1801 (upper left). H. ARP

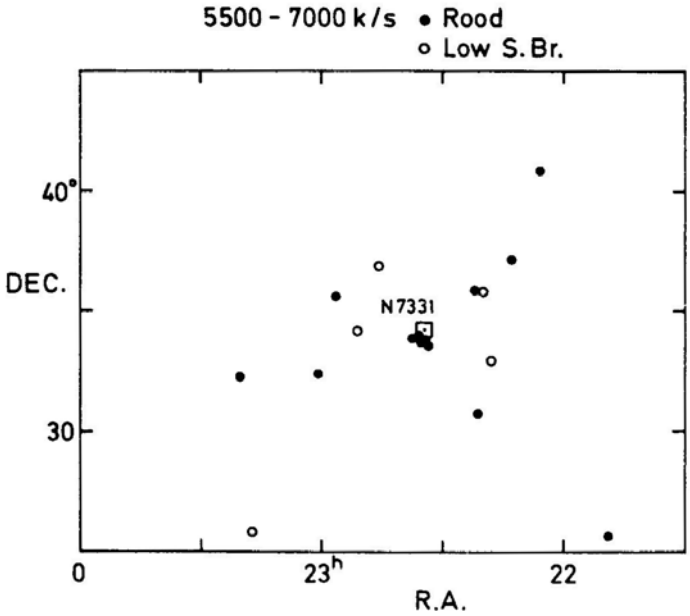

Figure 10. All rood galaxies in area around NGC 7331 Shown by filled circles. Supplementary redshifts Bouthn, Beers & Mould's (1985) survey of low surface brightness galaxies shown by open circles.

Table 6. Brightest spiral (Sb, Sc) galaxies in apparent magnitude—summary of alignment.

Galaxy	α h m	δ ° ′	$B_T^{0,i}$ mag	Type	cz_0†	Remarks
M31	00 40.0	+41 00	3.1	Sb	−86	Low b, Figs 13, 15, 16
M33	01 31.0	30 24	5.7	Sc	−10	Alignment Figs 13, 15, 16
M81	09 51.4	69 18	7.0	Sb	89	Alignment Figs 1, 3
M101	14 01.5	54 36	7.9	Sc	372	Alignment Fig. 7
NGC 4258	12 16.5	47 35	8.0	Sb	524	Broad band, 300–1100 km s^{-1}
NGC 2403	07 32.0	65 43	8.3	Sc	251	Alignment Figs 1, 3, 5
NGC 4736	12 48.6	41 23	8.4	Sab	360	Broad band, 300–1100 km s^{-1}
*M51	13 27.8	47 27	8.6	Sbc	550	Alignment Fig. 8
NGC 6946	20 33.8	59 59	8.8	Sc	294	Alignment Fig. 9
NGC 3521	11 03.3	00 14	8.8	Sb	670	possible alignment
NGC 2903	09 29.3	21 43	8.9	Sc	473	Alignment
NGC 3627	11 17.6	13 16	8.9	Sb	627	} crowded
NGC 4631	12 39.7	32 49	9.0	Sc	631	} region
NGC 4565	12 33.9	26 16	9.1	Sb	1204	near Virgo
NGC 7331	22 34.8	34 10	9.1	Sb	1057	Alignment Fig. 10
NGC 2841	09 18.6	51 11	9.2	Sb	688	Alignment Figs 2, 4
NGC 3623	11 16.3	13 22	9.2	Sa	709	near NGC 3627
NGC 2683	08 49.6	33 37	9.3	Sb	381	Alignment Figs 2, 4
NGC 891	02 19.4	42 07	9.3	Sb	699	Alignment Fig. 14
NGC 628	01 34.0	15 32	9.4	Sc	786	Alignment Figs 12, 13, 15

† values from RSA corrected for solar motion from Arp (1986)
* NGC 4826 crowded region.

Of the remaining bright apparent magnitude galaxies listed in Table 6, NGC 4258 and NGC 4736 lie close together in a crowded region of the sky. Nevertheless together with NGC 4449 and 4490 they fall in a broad, elongated line stretching about 20° NW to SE and consisting of galaxies with $900 \lesssim cz_0 \lesssim 1100$ km s^{-1}. They support the association of higher redshift, fainter galaxies with bright spirals. Because of the possibility of intermingling of lines if they are present, however, these regions are dropped from consideration as test regions in the present paper.

Proceeding down the list in Table 6 we can comment that NGC 3521 has three galaxies of $4300 < cz_0 < 5800$ km s^{-1} forming a line and one falling off. We consider this too sparse to represent anything more than a possibility for further investigation. NGC 3627 and 3623 fall very close together on the sky and may have a concentration of $900 < cz_0 < 1300$ km s^{-1} around them. However they, as well as NGC 4631 and 4565, are excluded from consideration as being in too crowded regions of the sky.

In order to now undertake the analysis of large regions of the sky around the nearest and brightest apparent magnitude galaxies in the sky, M31 and M33, we introduce a survey of low surface brightness galaxies which is more completely sampled over the very large region of the sky that is involved.

7. Low surface brightness galaxies

One recent survey which is complete over the area of the sky covered by the Arecibo antenna ($0^o \lesssim \delta \lesssim 34^0$) is the survey of low surface brightness (LSB) galaxies by Bothun, Beers & Mould (1985). The startling result of that survey is the gross inhomogeneity in galaxies in the redshift range $4500 \leqslant cz_o \leqslant 5300$ km s^{-1} between two direction in the sky . In the half of the the survey centred in the direction $\alpha \simeq 1^h$ there are 58 such galaxies, in the half centred in the direction $\alpha \simeq 11^h$ there are only 13 this is illustrated in Fig. 12.

But as Fig. 12 also shows, the excess in these galaxies in the $\alpha \simeq 1^h$ direction is concentrated primarily around M33, NGC 628 and 3C 120. The first two galaxies are very low redshift and conventionally accepted as being quite nearby. As such, they are further examples of the brightest apparent magnitude galaxies in the sky (M33 is 2nd and NGC 628 is 20th in Table 5) being associated with alignments of galaxies in the $4000 \lesssim cz_0 \lesssim 6000$ km s^{-1} range.

The manner of association, however, is different for M33 and NGC 628. The line of LSB galaxies of which M33 is the centre is rather loose and extends about 20° on either side for a total of about 40° length. The line of LSB galaxies emerging from NGC 628 is only about 10° in extent. Additional galaxies in this redshift range and direction in the sky will be considered in the final sections. But at this point we wish to discuss briefly the most conspicuous grouping of LSB galaxies which was encountered in that survey.

Fig. 12 shows that eleven LSB galaxies fall within a radius of ten degrees of 3C 120, an object previously proposed to be a Local Group member (Arp 1973). Surprisingly, seven radio bright quasars fall within this same radius. These are the same kind of $1.4 \lesssim z \lesssim 2.5$ quasars that are associated with M33 (Arp 1987a). Moreover hydrogen clouds and nebulous filaments which are at least as close as the Local Group of galaxies also appear associated with this group of unusual objects around 3C 120 (for complete analysis see Arp 1987c). The final conclusion is that this tight group of LSB galaxies of $4500 < cz_0 < 5300$ km s^{-1} redshift are associated, along with other objects

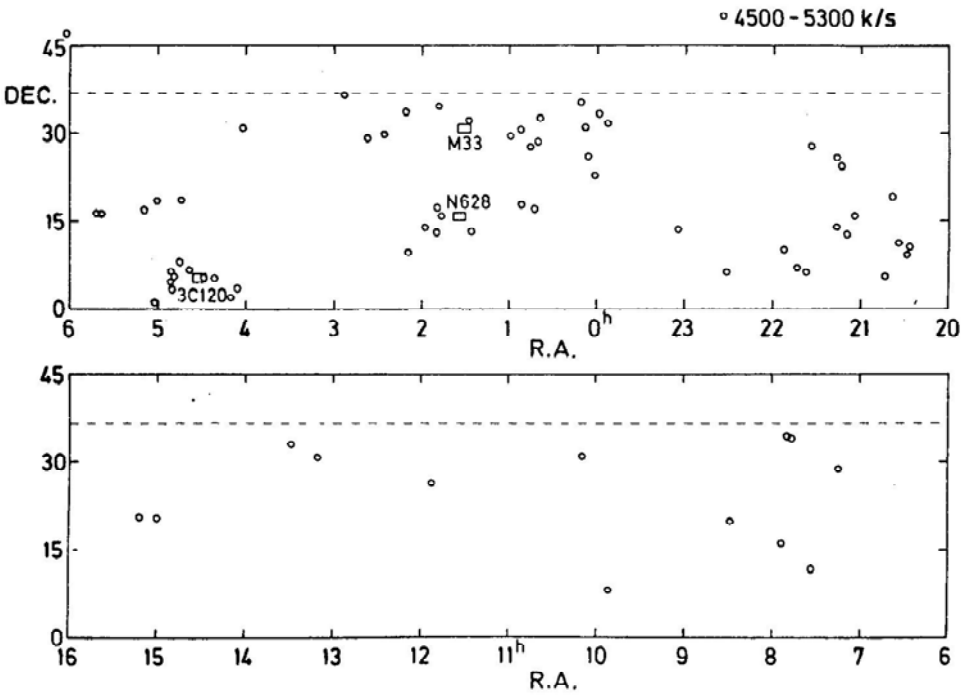

Figure 12. Only galaxies between $4500 < v_0 < 5300$ km s^{-1} are plotted from the complete Arecibo survey of low surface brightness galaxies by Bothun, Beers & Mould (1985). A total of 58 such galaxies fall in $\alpha \simeq 1^h$ the direction of the sky as opposed to only 13 in the opposite direction. In the $\alpha \simeq 1^h$ direction there are alignments with the brightest apparent magnitude galaxies in the area (M33 and NGC 628) and a marked concentration around the peculiar, strong radio source galaxy 3C 120.

of various redshift, with the peculiar Local Group galaxy 3C 120. Placing 3C 120 and these associated objects at the distance of the Local Group reduces the superluminal expansion of 6*c* to a more plausible ~ 12,000 km s^{-1}.

The only remaining major grouping of LSB galaxies in the redshift range being considered is in the $20^h < \alpha < 22^h$ region. As Fig. 12 shows this grouping is much the loosest of any in the survey. The only possible association with a Local Group galaxy would be with NGC 6822. At $\alpha = 19^h\,42^m$ $\delta = -14°56'$, however, NGC 6822 falls outside the frame of Fig. 11. Some Local Group hydrogen clouds are apparently associated over a wide area with NGC 6822 (Arp 1985, Fig. 7) but it would require measures of LSB galaxies in the $4500 < cz_0 < 5300$ km s^{-1} range south of $\delta = 0°$ to investigate this situation further.

In summarizing Fig. 12 we can comment that the LSB galaxies of $4500 < cz_0 < 5300$ km s^{-1} show association, in alignments, with the bright apparent magnitude galaxies M33 and NGC 628. M33 is, of course, one of the defining members of the Local Group and is projected on the sky near its centre. Evidence has been presented that NGC 628 (Arp 1990) and 3C 120 (Arp 1987c) are also members of the Local Group. The striking concentration of LSB galaxies in this redshift range in this half of the sky is then explained as due to the fact that this is the direction in the sky toward the centre of our Local Group of galaxies.

There are, however, large numbers of $4000 \lesssim cz_0 \lesssim 6000$ km s^{-1} galaxies which are not LSB galaxies and also concentrate toward the direction $\alpha \simeq 1^h$ in the sky. We shall see that they exhibit different alignments than the LSB galaxies and, very importantly, that they confirm the association of high redshift galaxies in this range with both M33 and NGC 628.

A complicating factor arises, however, when galaxies north of the LSB survey are considered. For example galaxies from the Rood Catalogue include many galaxies from the Perseus-Pisces superfilament. This filament passes, on the sky, between M31 and M33 and it is not clear to which bright galaxy in the region it belongs or what its distance is. Consideration of this most difficult region has been postponed until the last and will be considered now in the following section.

8. The area in the direction of the Local Group and the problem of the Perseus-Pisces superfilament

Fig. 13 shows all galaxies in the Rood Catalogue which are in the range of redshift $3900 < cz_0 < 5800$ km s^{-1} plotted over the area in the direction of the centre of the Local Group. There are two major difficulties in this region. First, the Local Group centre is so close to our own Milky Way galaxy that associations with M31 and M33 would be expected to stretch over a large apparent angle in the sky. Secondly, the best-defined filament of galaxies in the redshift range in which we are interested starts in the Perseus cluster, extends westward to NGC 891 and then southwest, apparently passing just north of M33. As we have seen in Fig. 12, M33 has LSB galaxies associated with it in the same redshift range as this Perseus-Pisces filament. This situation makes interpretation of the galaxies in this region very difficult.

Let us start with the associations we consider most probable and proceed to those which are most ambiguous.

8.1 *The M31–M33–Southeast Alignment*

Fig. 13 shows that accepted members of the Local Group, M31, NGC 404 and M33 together with the Rood galaxies of redshift $3900 < cz_0 < 5800$ km s^{-1} all form a line going southeast from M31. The same line is evident from the analysis of lower redshift galaxies in this region (Fig. 16). But in the present Fig. 13 we see higher redshift galaxies from the Rood Catalogue also defining this line. This is a confirmatory result in the sense that the low redshift, large galaxies, M81 and NGC 2403, similarly define a line which includes higher redshift ($3700 < cz_0 < 5100$ km s^{-1}) galaxies (Figs 3 and 5 here). Also we have seen in M101 and similar galaxies that dwarfs of slightly higher redshift than the central galaxy outline the same filaments as the higher redshift galaxies do. We will analyze this M31-M33-SE line and its low redshift members further in a following section.

8.2 *The NGC 628 Southeast Line*

Fig. 13 also shows a shorter elongated distribution of $4300 < cz_0 < 5400$ km s^{-1} galaxies coming southeast from NGC 628. It is extremely interesting that this is a

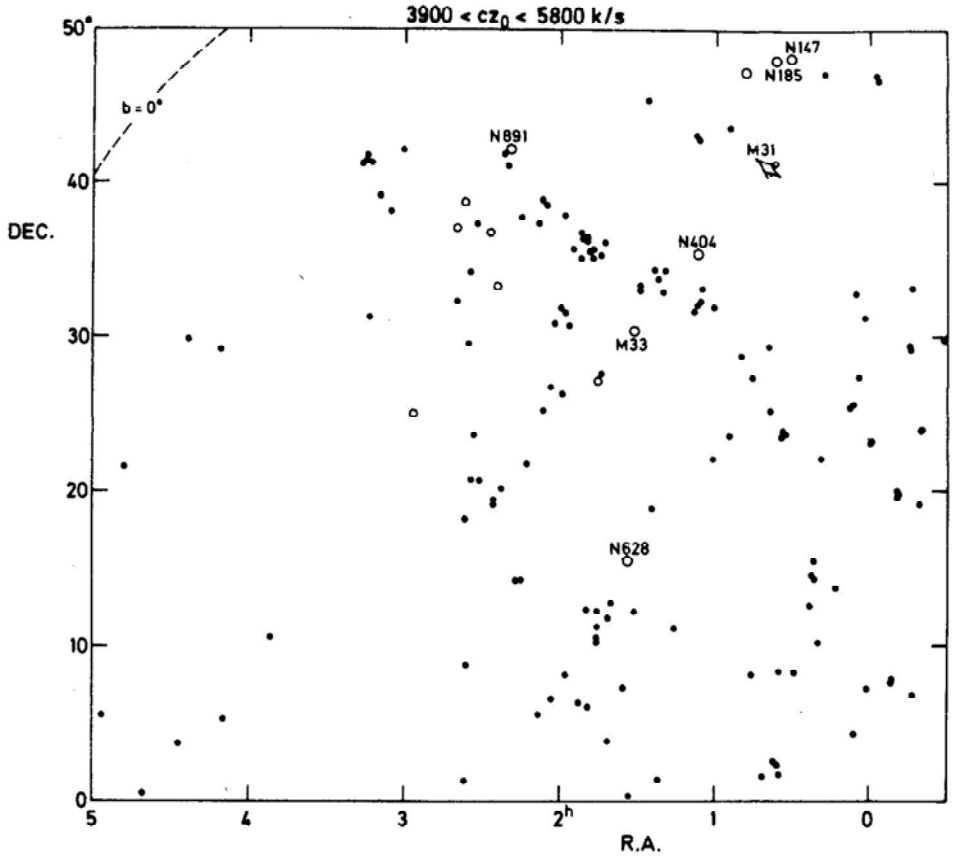

Figure 13. All Rood galaxies with $3900 < v_0 < 5800$ km s^{-1} are considered. Only UGC galaxies are plotted and no E or S0's are plotted. The Perseus-Pisces filament eastward from NGC 891 is therefore not very conspicuous because it is predominantly E and S0. Soutnwestward from NGC 891 the Perseus-Pisces filament is clearly marked because it consists of a greater percentage of spirals. Open circles represent low redshift galaxies. Linear distributions of galaxies southeastward from M33 and NGC 628 are also visible (see also Figs 15 and 16).

different line than the LSB galaxies in Fig. 11 defined. The line in Fig. 13 is about the same length and population but rotated slightly from its position in Fig. 11. The similarity in length, population and direction confirms the fact that lines of galaxies of this redshift originate from NGC 628. But the slight rotation implies that if they arise by ejection from NGC 628, then the ejections took place at slightly different times. In turn this implies that the morphology has evolved (say normal surface brightness to low surface brightness) but the intrinsic redshift has not. This result might be reconciled if the redshifts evolved in discontinuous steps—a result required by quantized galaxy redshifts in general and in particularly the several observed lines of discrete values of intrinsic redshift coming from the same bright galaxy as observed in the present paper.

We will see another, somewhat rotated line of slightly lesser redshift coming from M33 in the next section.

8.3 *The NGC 891 Line and the Perseus Superfilament*

The most conspicuous filament in Fig. 13 appears to originate at NGC 891 and proceed southwestward. This is the so-called Perseus-Pisces filament. Normally one sees this chain of galaxies originating in the Perseus cluster to the east of NGC 891. But Fig. 13 only plots Rood galaxies which are not morphological class E or S0. Therefore the representation from the Perseus cluster, which is richly composed of E and S0 galaxies, is much reduced from a plot which would include such early type galaxies. The filament, interestingly appears to pick up a spiral galaxy representation from about NGC 891 westward.

If one makes a plot of all galaxies without restriction as to morphological type or redshift one obtains a picture like Giovanelli's for the Zwicky Catalogue (shown here in Fig. 14). By comparing Figs 13 and 14 here one can see the Perseus filament proceed strongly from the Perseus cluster westward toward NGC 891, even turning slightly north toward NGC 891 as it approaches that low redshift Sb and then proceeding southwestward from NGC 891, now composed more characteristically of spiral type galaxies. Whether this chain originates in NGC 891 and extends out in almost opposite directions from NGC 891 is difficult to say with certainty. However, in view of the previous evidence in this paper for lines of galaxies of this redshift range emanating from galaxies like NGC 891 (for example M81), it is difficult to reject the reality of the physical association of the Perseus filament with NGC 891. (It is interesting to note that the M81 filament of associated galaxies had a mean of 4100 km s^{-1} . NGC 891 has

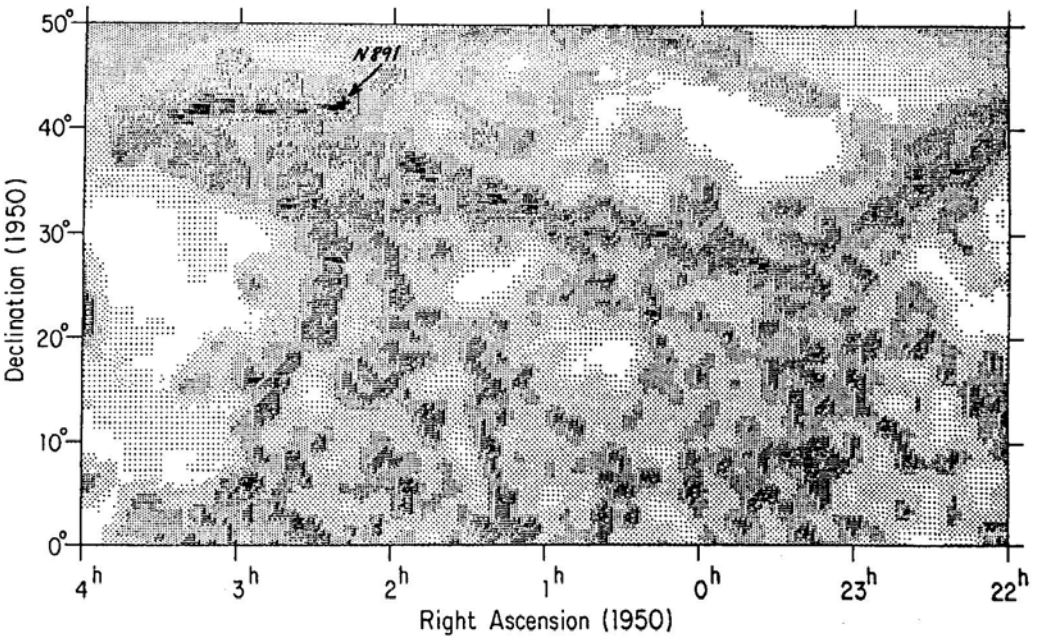

Figure 14. Computer plot of all galaxies in the Zwicky Cataloge (Courtesy R. Giovanelli). Note that Perseus- Pisces filament can be traced over 90^0 arc across the sky and that it is stronger just at its apparent deviation toward the bright appranent magnitude Sb galaxy NGC 891.

a 655 km s^{-1} higher redshift than M81 which would lead us to expect its associated filament at about 4700 km s^{-1} . The mean of the Perseus-Pisces filament is just about 5000 km s^{-1}.) The Perseus-NGC 891 filament then passes southwestward between NGC 404 and M33 (as shown in Fig. 13). At this point the Perseus filament is overlayed with galaxies of similar redshift which lie along the M31-NGC 404-M33 axis. This circumstance makes this region of the sky one of the most difficult to interpret.

We will show later, however, that the high redshift galaxies southeast along the M31–M33 line are very peculiar. Therefore the nearby galaxies in the Local Group of ~ 5000 km s^{-1} redshift can be distinguished morphologically from the presumably more distant members of the Perseus-NGC 891 filament of nearly the same intrinsic redshift. Apparently there are no examples in the Local Group of Perseus filament-like galaxies of ~ 5000 km s^{-1} redshift because they should appear quite bright, with apparent magnitude in the range of 7 to 9. The constituent galaxies in the Perseus filament seem to be unusually luminous for intrinsically redshifted galaxies if they belong to NGC 891 and if NGC 891 is appreciably more distant than M31.

Fig. 15 shows all UGC galaxies, omitting E and SO, in the redshift range $2200 < cz_0 < 4000$ km s^{-1}. This redshift range, somewhat below the ~ 5000 km s^{-1} range we were just considering, shows no marked Perseus-NGC 891 filament but does show an elongated distribution of galaxies coming southeast out of M33. NGC 628 may be a part of this, possibly double, filament of galaxies originating in M33.

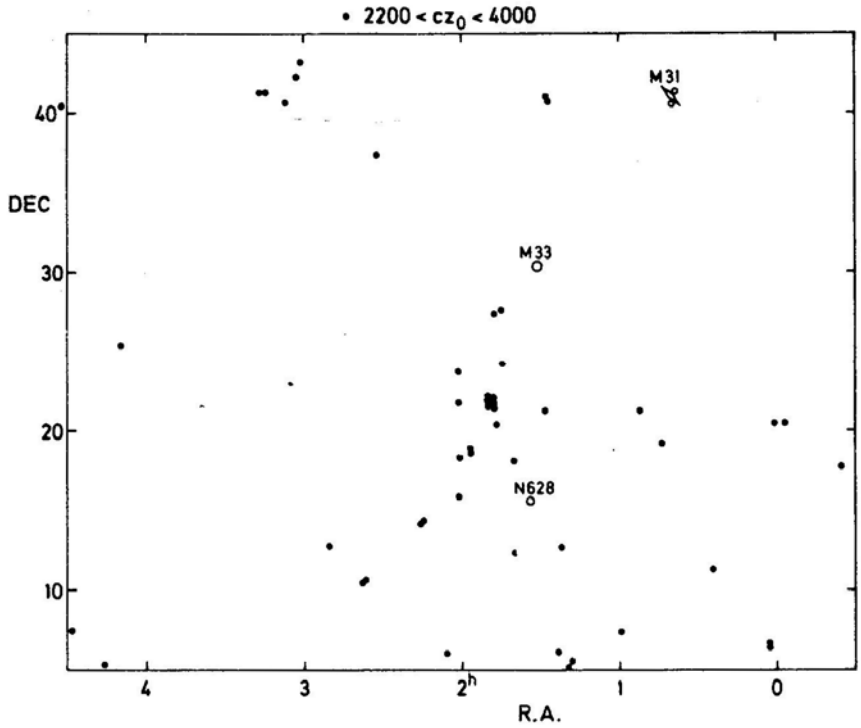

Figure 15 . All Rood Catalogue galaxies $2200 < v_0 < 4000$ km s^{-1} .Only UGC (Nilsen) galaxies are plotted and E and SO are omitted The major concentration is in direction Southeast from M33.

9. Lower redshift galaxies in the direction of the Local Group

Fig. 16 shows the galaxies in the Local Group direction which are of only slightly larger redshift than M31 and M33 ($300 \leqslant cz_0 \leqslant 700$ km s^{-1}). Their concentration in the direction of the centre of the Local Group and their coincidence with the alignment of accepted Local Group members marks these galaxies as belonging to the Local Group (Arp 1987a, c, 1990). It is extremely interesting, therefore, to see much higher redshift galaxies in Fig. 13, $3900 < cz_0 < 5800$ km s^{-1}, extending along this same M31–M33 alignment. In fact these higher redshift galaxies in Fig. 13 extend also down into the $4^h < \alpha < 5^h$ $\delta \sim 0°$ region where the $4300 < cz_0 < 5300$ km s^{-1} LSB galaxies in Fig. 12 cluster around 3C 120 (Arp 1987c). In Fig. 16 some additional, special galaxies are marked by plus symbols. They show apparent involvement with low surface brightness nebulosity and infrared clouds which are presumed to be part of the Local Group. (See Section 9.3 for further discussion.)

9.1 *Nature of the High Redshift Line of Galaxies SE of M33 ($3900 < cz_0 < 5800$ km s^{-1})*

Table 7 lists the 12 galaxies falling most accurately along the line southeast of M33 in Fig. 13. Inspecting these galaxies on sky survey (POSS) prints reveals that they are outstandingly peculiar. The most striking peculiarity is the prevalence of very high surface brightness, compact objects. Next most unusual is the high incidence of distorted galaxies or interacting pairs. The coincidence of this line of peculiar objects with the line of known members of the Local Group which emanates from M33, marks

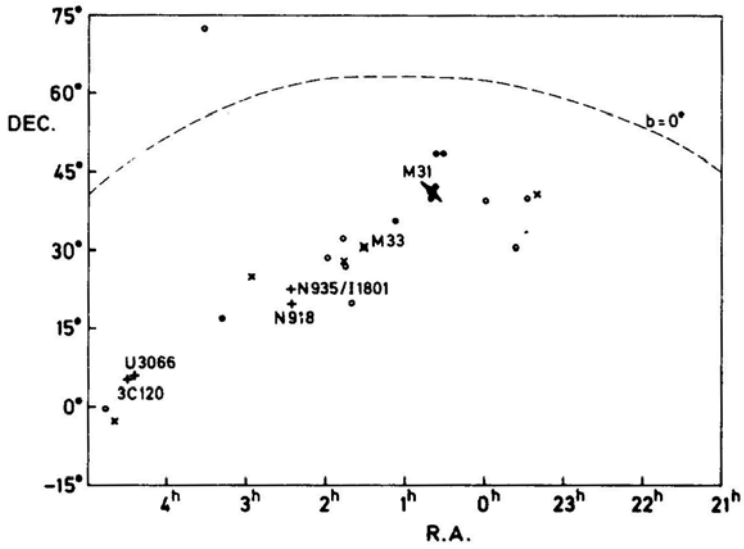

Figure 16. Plotted are all galaxies known with $300 \leqslant v_0 \leqslant 700$ km s^{-1} (crosses are spirals, open symbols dwarfs). Filled symbols represent conventional members of the Local Group ($-86 \leqslant v_0 \leqslant +142$ km s^{-1}). Note coincidence in position and alignment of both sets of galaxies.

Table 7. Line SE of M 33 —Nature of galaxies.

Galaxy	α h m	δ ° ′	m_p	Type	v_0	Remarks
NGC 670	01 44.6	+27 38.1	13.17	Sb:	4023	hi s. br. pec.
672	01 45.1	27 11.1	11.41	SBc III	647	VV 338 (K40)
UGC 1510	01 58.9	26 18	14.4	. . .	5163	v. hi. s. br. I/A pair
1595	02 03.6	26 48	15.5	Sc	5114	small, lumpy, resol. in blue?
1733	02 12.5	21 47	15.6	Sc	4546	shred? p.a. 307°
IC 1797	02 22.7	20 10	15.3	SB . . .	4016	hi s. br. pec.
IC 1801	02 25.4	19 21	14.8	SBb:	4434	⎧ I/A pair ⎫ pec. (K68)
NGC 935	02 25.4	19 22	13.9	Sc	4302	⎩ (VV238) ⎭ cirrus
NGC 976	02 31.2	20 45.4	13.21	Sbc I-II	4550	appears normal
992	02 34.6	20 53	13.5	S?	4244	hi. s. br. lumpy w. plumes
UGC 2140	02 36.3	18 10	14.6	Irr.	4180	Arp 258, v. Pec. I/A irreg.
NGC 918	02 23.1	18 16	14.3	Sc	1625	pec. nebulosity and IR cirrus

them as members of the Local Group despite their higher redshift. The high surface brightness, interacting morphology of these galaxies are in the morphological direction of quasars. Many quasars have been assigned to the Local Group and, of course they are also compact, active objects of large excess redshift (Arp 1987b).

Some of these same kinds of compact galaxies are found on the other side of M33 in a small clump NW as shown in Fig. 13. These include NGC 536 (an interacting triple), NGC 523 (pec. 1/A dbl=Arp 158) and UGC 913 (sm. v. hi s. br.pec.).But this region is also diluted with more normal appearing galaxies from the Perseus-NGC 891 chain. The densest clump, further to the north-northeast of M33 in Fig. 13, is dominated by these more normal types.

9.2 *Quantization in Line SE of M33*

In Arp (1987d) it was shown that the galaxies in this line SE of M33 were quantized in intervals of 72.4 km s^{-1} , up to 14 multiples, or ~ 1000 km s^{-1}. If this implies that the real relative velocity of these galaxies is $\lesssim$ 8 km s^{-1} (the average accuracy both of measurement and observed quantization) then the galaxies could not have been ejected out of M33 with even a few hundreds of km s^{-1}. This is the most difficult paradox in all the observations so far considered. It is almost as if the signal to form a galaxy was ejected but the galaxy actually formed relatively motionless in space with respect to the parent galaxy.

9.3 *Physical Confirmation of the Line SE of M33*

A galaxy with the most peculiar immediate environment I know is NGC 918. Its position along the M31–M33 line is shown in Fig. 16. The Palomar Sky Survey prints show cloudy material surrounding it. The galaxy seems inescapably to be interacting with this nebulous material but the nebulous material is very extended and stretches

several degrees in the northwest direction toward M33. The Schmidt photograph is shown in Fig. 17. IRAS maps (Arp & Sulentic submitted) show this cirrus-like nebulosity is well-detected at 100 μm and confirm the shape of the nebulosity seen on both the 103a–O and 103a–E Schmidt survey plates. About a degree northeast of NGC 918 as shown in Fig. 16 and art plate Fig. 17 is the interacting pair NGC 935/IC 1801 (VV 238). This is the same ~ 4300 km s^{-1} galaxy as listed in Table 6. But this previously identified member of the M31–M33 line also shows an optical and IR semi-circle of nebulous material surrounding it. Clearly both NGC 918 and NGC 935/IC 1801 appear to be interacting with the nebulous material which stretches roughly along the M31–M33 line on the sky.

Both the optical and 100 μm cirrus in this field are what is normally considered to be dust and/or emission nebulosity within our own Milky Way galaxy. Yet the material is at high galactic latitude (b= – 39° and – 38°) and generally outlines a path along the M31–M33 axis through the pictured region. I conclude it must be material in the Local Group and the galaxies under discussion must also be in the Local Group interacting with this material.

It has been argued that there are H I clouds within the Local Group (Arp 1985). Redshifts of such clouds which have so far been discovered are not large and could easily be mistaken for Galactic hydrogen. So I do not see any easy way to rule out the conclusion that the nebulosity pictured in Fig. 17 is not Galactic but exists somewhere within the Local Group. The fact that it is visibly interacting with galaxies that were also concluded to be in the Local Group supports that conclusion.

There is one additional piece of evidence: it is that 3C 120 is the SE terminus of the line of galaxies lying along the M31–M33 axis. It has a nebulous filament pointing at it which is of the same nature as the nebulosity just discussed in connection with NGC 918 and NGC 935/IC 1801 (Arp 1987c). Like the previous two galaxies, 3C 120 and the neighbouring UGC 3066 are imbedded in extensive 100 μm, infrar-ed emission clouds and in addition have 60 μm clouds of about 30 arcmin extent associated with each galaxy. It would appear very unlikely, in four separate instances along this line SE from M33, to just accidentally encounter the same kind of highly unusual nebular interaction with high redshift galaxies.

The astonishing conclusion that high redshift galaxies ($300 < cz_0 < 10{,}000$ km s^{-1}) occur within the Local Group can, it turns out, be checked by observing actual interaction with very low redshift nebulosity within the Local Group. There could be no more important project in astronomy than to map with the highest accuracy possible the complete extent of the infrared cirrus along the line through M33 and compare it to other high latitude regions of the sky. In addition, deep optical continuum and emission mapping of this region should be carried out as well as spectroscopic analyses of these nebulosities. Finally H I surveys which cover a broad range of spatial scales and particularly a large range in H I redshift would be crucial in this area of the sky.

10. Tests of the significance of the apparent association of bright galaxies with higher redshift chains

In practice people tend not to accept a surprising result, no matter how high its improbability of chance occurrence, if it is an isolated event. If the result appears

clearly non-random and is repeated in numerous independent trials, however, its reality is believed. Numerical probabilities are probably not decisive in such final judgements but many scientists nevertheless feel the necessity of quantitative calculations. Therefore we will attempt to calculate a numerical probability that the present associations are real.

We start with the chains of galaxies portrayed in this paper which encompass mean redshifts which range from $1000 < cz_0 \lesssim 7000$ km s^{-1}. Such chains are now well recognized and accepted by extragalactic researchers. The question is asked then:how likely is it that one of the 20 brightest apparent magnitude spiral galaxies in the sky would fall by accident at the centre of, or at the end of such a chain? When a bright galaxy falls centred on a chain we can draw a box around the centre of the chain which represents the area within which the galaxy could fall and still be considered centred. We then consider the much larger area around the chain anywhere within which the galaxy could have fallen if it had no connection with the chain. The ratio of these two areas represents the probability that the bright galaxy falls accidentally in a significant position with the respect to the centre of the chain. These probabilities are listed in Table 8 for each of the 14 brightest apparent magnitude galaxies in Table 6 which occur in uncrowded enough regions of the sky to test. In a few cases the bright galaxy fell somewhere along the chain or near a concentration of higher redshift galaxies Such configurations have a higher probability of being accidental and are listed in the last column of Table 8,

In Table 8 'centred' column two chains have the possibility of one end being partly obscured by low galactic latitude. We do not count these as trials. Of the remaining 12 chains, nine show centred bright galaxies with a probability of being accidental of $p \lesssim 0.02$. Using the binomial probability formula to compute 9 successes in 12 trials we have:

$$P^{9}_{12}(.02) = 1 \times 10^{-13}.$$

We should note that this is an upper limit for the probability because, in fact, each

Table 8. Probability of coincidence of bright galaxies with chains.

	Centred	Near chain or concentration
M31	— (low b)	.08
M33	.02	.08
M81	.01	.13
M101	.01	.15
N 2403	.02 (Fig. 5)	.04 (Fig. 3)
M51	x (not at centre)	.05
N 6946	— (low b)	.06
N 3521	x (possible)	x (possible)
N 2903	.01	.06
N 7331	.01	.09
N 2841	.02	.13
N 2683	.02	.10
N 891	.02 (Fig. 14)	.06 (Fig. 14)
N 628	x (? at centre)	.04

bright galaxy is much better centred than a random position within the box which we used to calculate the acceptable centerings.

We can similarly calculate the accidental probability of a bright galaxy falling only somewhere near the length of a chain or near a concentration of higher redshift galaxies. Table 8 shows we have 13 successes out of 14 trials with $p \lesssim 0.15$, or

$$P_{14}^{13}(.15) = 2 \times 10^{-10}.$$

These calculations vividly illustrate the reason for the usual criterion people have for accepting a result. It shows, namely, that even when an individual result is impressively less probable than .01, that the really overwhelming improbabilities exponentiate rapidly when they are repeated in only a modest number of independent trials.

11. Summary

The present paper has examined large areas of the sky around the brightest apparent magnitude galaxies in the sky. In almost every case where they are not crowded by other bright galaxies, clearly marked lines of higher redshift galaxies have been found going through, or originating from, the positions of these bright apparent magnitude galaxies. Fig. 18 summarizes the redshift ranges of the smaller galaxies in the lines which appear to be associated with the larger galaxies.

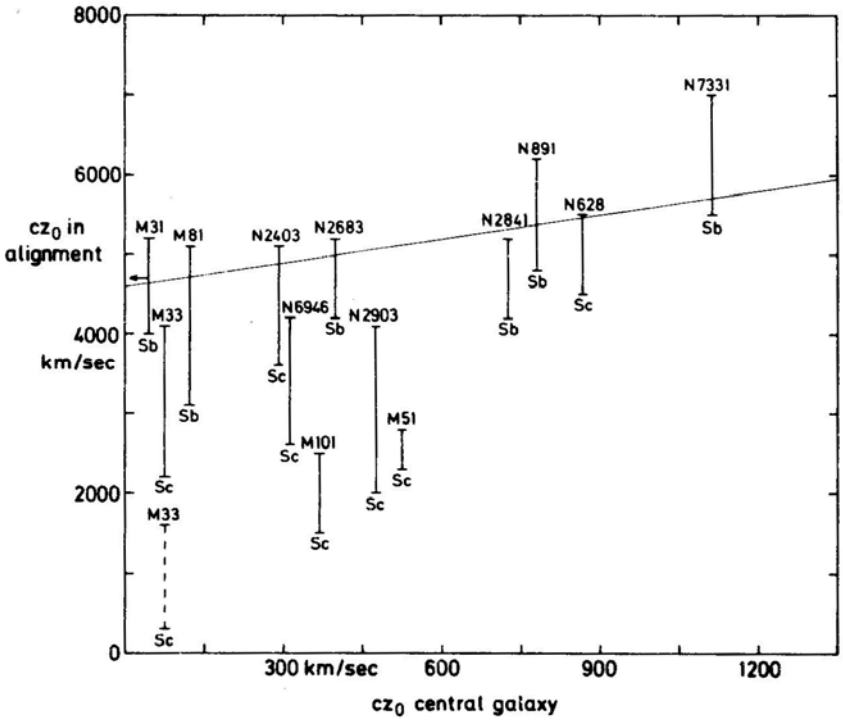

Figure 18. Summary of redshift intervals of galaxies which appear to be aligned with bright apparent magnitude spirals (vertical axis) correlated with the red shift of the bright apparent magnitude galaxy (horizontal axis).

In Fig. 18 it is noticeable that as the central galaxies increase in redshift the associated lines tend to have higher redshift. It is also noticeable that central Sb's tend to have associated lines of higher redshift than do central Sc's. If true, these trends are of interest not only in interpreting this very difficult phenomenon but also in confirming its reality. The latter point is that if the higher redshift galaxies were unrelated to the lower, there would be no way their properties could be correlated to the redshift or morphological type of the lower redshift galaxies.

The analyses made in the present paper were all based on galaxies which had redshifts listed in the Rood Catalogue. The same analyses should now be repeated with larger, more current compilations of redshifts. It is doubtful whether the larger data will contradict the present results because, as explained throughout the present paper, there is no reason for redshift observers to measure along lines in the sky. Moreover, in most cases galaxies of slightly different redshift than in the lines are more or less uniformly spread throughout the areas in question. Larger numbers of galaxies with redshifts can increase the degree of delineation, however, and therefore give more information on the form and content of the lines. The more recent catalogues will include proportionally more high redshift galaxies and it will be important to see if these higher redshift galaxies belong to the lines portrayed here, whether they are uniformly distributed or whether they form new lines or different kinds of lines.

Of course, as redshift catalogues become more complete to fainter apparent magnitudes, tests of all galaxies within a given area can be made. An example of such a test is given in Fig. 1.9. There all the galaxies with $v_0 > 1300$ km s^{-1} listed in the Revised Shapley Ames Catalogue (RSA; Sandage & Tamman 1981) are plotted in a sample area of the sky. The top diagram shows that 19 out of 21 of these galaxies fall in a conspicuous filament of about 45° arc length. Again, as in the M81 filament of galaxies and others discussed in the previous body of this paper, the filament is centred on the brightest galaxy in the chain, which in this case also turns out to be class Sb.

The bottom part of Fig. 19 shows the redshifts in hundreds of km s^{-1}, written near the symbol for each galaxy. It is evident that the redshifts of the apparently fainter galaxies in this filament range up to 3000 km s^{-1} higher than the central Sb. *This is the same kind of result as obtained here in the search of the Rood Catalogue of redshifts around the 20 brightest apparent magnitude spirals.*

The central galaxy in Fig. 19 is NGC 1964, only about one magnitude fainter than the limiting apparent magnitude investigated in Table 5. The redshifts in the line appear to group in a $1600 < v_0 < 2600$ km s^{-1} range and a $3300 < v_0 < 4700$ km s^{-1} range. It is not known how galaxies fainter than the $B_T \simeq 13$ mag limit of the RSA would distribute themselves in this area.

It should be stressed that this is an arbitrary sample of a region in the RSA. The reason this region was investigated was to find out to what association two Sc I galaxies, NGC 2207 and NGC 2223 at 2600 and 2500 km/sec, belonged. In this case these two Sc I's turned out to be associated with the lower redshift Sb (NGC 1964). (In fact in all cases tested the supposedly very luminous Sc I's turn out to be actually low luminosity galaxies physically associated with lower redshift Sb galaxies which dominate groups. Arp 1988, 1990.)

With alignments so extended on the sky there will probably be confusion in many regions due to overlapping of nearby with more distant groups. Perhaps Fig. 19 investigates a fortuitously uncrowded region of the sky. Nevertheless catalogues should be systematically searched with various objective computer algorithms to

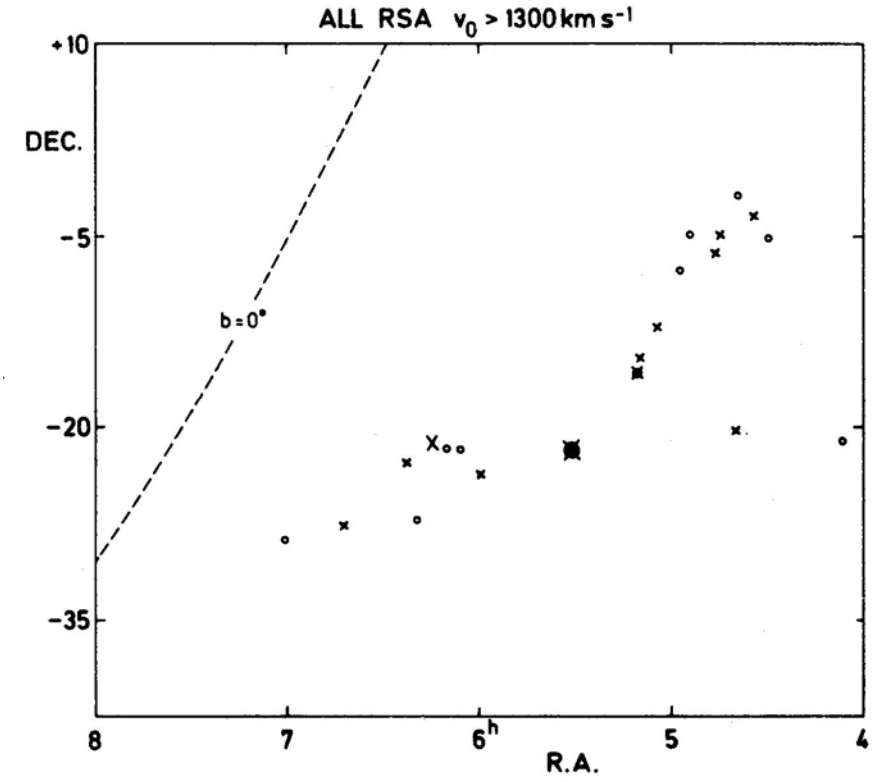
ALL RSA $v_0 > 1300\,km\,s^{-1}$
+10
DEC.
-5
-20
-35
b=0°
8
7
6h
5
4
R.A.

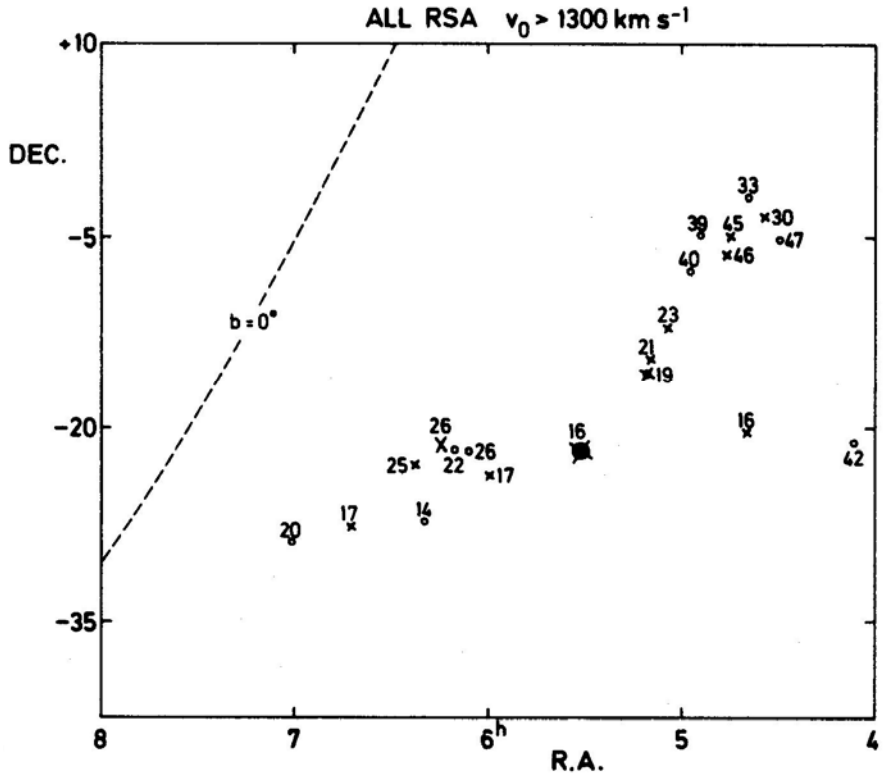
ALL RSA $v_0 > 1300\,km\,s^{-1}$
+10
DEC.
-5
-20
-35
b=0°
33
39
45
30
47
40
46
23
21
19
26
16
25
22
26
17
16
42
17
14
20
8
7
6h
5
4
R.A.

identify significant associations. When the characteristics of these alignment/associations are better understood the question of whether all galaxies belong to them, or whether there is such a thing as an isolated galaxy can be better considered.

12. Discussion

It is now generally accepted that galaxies often exist in chains and filaments in space. What is surprising is to find lines of fairly high redshift galaxies stretching over such large apparent angles on the sky. Even more surprising is to see the brightest apparent magnitude, low redshift galaxies known, occurring at the centres or ends of such lines. If these large galaxies are physically associated with the lines, how can so many small, high redshift galaxies be so much closer to us in space than heretofore believed?

Such associations would require a catastrophic revision of what we currently believe about galaxies. But the question must be settled by appeal to the observations and not to prior assumptions. The test must be the simplest and most fundamental one: do the brightest galaxies in the sky fall in positions in the chains which cannot be due to chance superposition of background and foreground objects? The investigation in the foregoing paper shows that essentially all the uncrowded examples of the brightest apparent magnitude galaxies in the sky fall in lines of, or associated with, smaller galaxies of many thousands of km s^{-1} higher redshift.

The only alternative testing procedure is to start from the configurations which judgement by eye demonstrates to be significant, for example the M81 filament. Then we find independent, confirmatory evidence: the higher redshift galaxies in the lines from the bright apparent magnitude galaxies are systematically peculiar compared to what one would expect from random field galaxies.The galaxies in the M81 and NGC 2403 filaments are predominantly Markarian, double interacting or active Seyferts—as shown in Section 2. The galaxies aligned across NGC 2683 are predominantly Sc I spirals. The galaxies in the M31/M33 line are peculiarly compact and interacting. In the NGC 7331/Stephan's Quintet region we see galaxies in the typical, 5500–7000 km s^{-1} range of the smaller galaxies, actually physically interacting with low redshift galaxies. We also see radio emission involvement of the high and low redshift galaxies (Arp 1987b).

In the M31/M33 line we see an amazing phenomenon. The high redshift galaxies NGC 918 (v_0 = 1625 km s^{-1}) and NGC 935/IC 1801 (VV238, v_0 = 4301 and 4434 km s^{-1}) are actually interacting with low surface brightness nebulosities which are on a scale and placement which must belong to the Local Group of galaxies! This interaction is confirmed by the 100 μm, IR measures of 'cirrus' in the area (Section 9).

Such primary observational evidence backed up by confirmatory, independent evidence should furnish conclusive proof of the phenomenon. Is this Phenomenon unprecedented? Quite to the contrary. It was shown more than 20 years ago (Arp 1968)

Figure 19. (Top) All galaxies in the Revised Shapley Ames Catalogue Sandage & Tamman 1981) which occur in the pictured area are plotted. (v_0 > 1300 km s^{-1}). Crosses are spirals, open circles non-spirals and filled circles with crosses are Sb spirals Size of symbol proportional to apparent magnitude. (Bottom) Redshifts in hundreds of km s^{-1} are written next to the position of each galaxy.

that the brightest radio galaxies in the sky fell in the centre or ends of chains of galaxies. These chains contained fainter galaxies of systematically higher redshift. Some of the chain members had very much higher redshift. Abundant evidence has been presented since then for galaxies with discordant redshifts ranging from $\Delta cz \simeq 72$ to 45,000 km s^{-1} physically interacting with the low redshift galaxies.

Thus it has been previously demonstrated that galaxy redshift is not an unfailing indicator of distance. What assumptions then do the galaxy alignments in the present paper violate? They require for the first time that many galaxies, perhaps even the majority, have intrinsic redshifts and are really at the closeby distances of the brightest apparent magnitude galaxies. Aside from the fact that this is contrary to current astronomical models, could so many galaxies of greatly different redshift actually be significantly associated together on the sky?

One model one might consider is the very small, high space curvature model for the Universe of about 100 Mpc diameter investigated by Fagundes (1985) and Ellis & Schreiber (1986). One could hypothesize that a central galaxy (*e.g.* M81) is seen many times, in slightly different directions at earlier and earlier epochs in its existence. That would naturally give higher redshifts for those images that had travelled through larger distances, a larger number of circuits around this small Universe. In fact this model could in principle account for even quasar (very much higher redshift) alignments with low redshift galaxies without abandoning redshift-distance relations.

Another possibility might involve the quantization of redshifts observed in galaxies and quasars. There is now unavoidable evidence that galaxy redshifts are quantized in redshift intervals of 72 km s^{-1} and quasar redshifts in intervals of $\Delta \log (1 + z)=0.089$. (Arp *et al.* 1990). It is quite possible that, for example, the line southeast of M51 (Fig. 8) represents a quantization at 2500 – 2800 km s^{-1} and that the Perseus-Pisces filament represents a quantization at ~ 5000 km s^{-1}. If redshift quantization is caused by the wave properties of light interacting with the properties of space in the direction of the observed objects then we are pushed toward an explanation of the same type as the small highly curved Universe mentioned above. That is, the observed redshifts need not be intrinsic redshifts of the actual galaxies observed but might represent some deformation of space-time in the direction of the bright objects.

On the other hand, physical interactions of high and low redshift galaxies point to the different redshifts being intrinsic properties of the material in each galaxy. Coincident lines of radio sources, radio material and higher redshift, active galaxies imply that the galaxies along the line arose by ejection from the central galaxy. In that case the higher redshifts of the ejected galaxies would presumably be due to the younger age of their constituent material. The general expectation, however, would be that these younger galaxies should look different than the older central galaxy. Why do so many higher redshift galaxies in the alignments in the present paper look, so far as presently known, much like the central galaxies but only seen at greater distances? The only possible answer would be that low and high luminosity galaxies can appear quite similar—but that the only true examples of high luminosity galaxies we have are those at the centres of the largest alignments like M31, M81 *etc.* (see Arp & Block 1990).

The only way this latter case could be proved is by studying more carefully the higher redshift Sb's in the alignments. If it can be demonstrated that there are at least some significant differences between these higher redshift galaxies and the way galaxies like M31 and M81 would appear at a greater distance, then the view that most of the apparently fainter galaxies are nearby with intrinsic redshifts would be permitted. A

related investigation would be to search for fainter apparent magnitude Sb's that really Were like more distant examples of M31 and M81. Then one could look for shorter, fainter, high redshift lines of galaxies on either side of them—like the M31 and M81 lines viewed at a greater distance. If more distant versions of the M81 chain could be found and if the central Sb's had redshifts which increased with decrease in their apparent magnitude then this would be the first uncontradicted evidence for a redshtft-distance relation in our universe.

Regardless of what the explanation for the phenomenon may be, however, the observational evidence that large numbers of higher redshift galaxies align themselves with the lowest redshift, most nearby galaxies should be confronted and discussed.

References

Arp, H.1972, in *IAU Symp. 44: External Galaxies and Quasi-Stellar Objects,* Ed. D.S. Evans, D. Reidel, Dordrecht, p. 380.

Arp, H. 1973, in *The Redshift Controversy,* Eds G. B. Field, H. Arp, J. N. Bahcall, W. A. Benjamin, Massachusetts.

Arp, H.1982, *Astrophys. J.*, **263,** 54.

Arp, H. 1985, *Astr. J.*, **90,** 1012.

Arp, H.1986, *Astr. Astrophys.*, **156**, 207.

Arp, H. 1987a, in *IAU Symp. 124: Observational Cosmology,* Eds A. Hewitt, G. Burbidge & Lizhi Fang, D. Reidel, Dordrecht, p. 479.

Arp. H. 1987b, in *Quasars, Redshifts & Controversies,* Interstellar Media, Berkeley.

Arp, H.1987c, *J. Astrophys.Astr.,* **8**, 231.

Arp, H. 1987d, *J. Astrophys. Astr.,* **8**, 241.

Arp, H. 1988, in *Proc. Symp. on New Ideas in Astronomy,* Eds F. Bertola, J. W. Sulentic & B. F. Madore, Cambridge Univ. Press, p. 161.

Arp, H.1990, *Astrophys. Sp. Sci.,* **167,** 183.

Arp, H,, Block, D. 1990, *Sky Teles.,* in press.

Arp, H., Bi, H. G., Chu.Y., Zhu, X.1990, *Astr. Astrophys.,* in press.

Bothun, G. D., Beers, T. C, Mould, J. R. 1985, *Astr. J.*, **90**, 2487.

Chincarini, G. L., Giovanelli, R., Haynes, M. P. 1983, *Astr. Astrophys.,* **121**, 5.

Ellis, G. F. R., Schreiber, G. 1986, *Phys. Lett. A.* **115**, 97.

Fagundes, H. V. 1985, *Astrophys. J.,* **291**, 450.

Focardi, P., Marano, B., Vettolani, G. 1986, *Astr. Astrophys.,* **161**, 217.

Giovanelli, R., Haynes, M. P. 1982, *Astr. J.,* **87**, 1355.

Giovanelli, R., Haynes, M. P. 1985, *Astr. J.,* **90**, 2445.

Gregory, S. A., Thompson, L. A., Tifft, W. G. 1981, *Astrophys. J.,* **143**, 411.

Huchra, J., Davis, M., Latham, D., Tonry, J. 1983, *Astrophys. J. Supp.,* **52**, 89.

Kirshner, R. P., Oemler, A., Schecter, P. L. 1978, *Astr. J.,* **83**, 1549.

Nilson, P. 1973, *Uppsala General Catalogue of Galaxies.*

Rood, H. J. 1980, *A Catalogue of Galaxy Redshifts,* (privately circulated).

Sandage, A. R.,Tamman, G.A.1981, *A Revised Shapley-Ames Catalogue of Bright Galaxies,* Carnegie Institution of Washington.

Veron-Cetty, M.-P., Veron, P. 1984, *A Catalogue of Quasars and Active Nuclei,* ESO Sei. Rep.

J. Astrophys. Astr. (1990) **11,** 445–460

The Eccentric Double-Lined Binary BD – 1° 1004

N. Kameswara Rao & B. N. Ashoka* *Indan Institute of Astrophysics, Bangalore, 560034*

C. Lloyd, C. D. Pike & D. J. Stickland *Rutherford Appleton Laboratory, Chilton, UK*

Received 1990 April 18; accepted 1990 August 14

Abstract. A new radial velocity study has been made of the highly eccentric, early-type binary BD –1° 1004 using spectra from the Kavalur Observatory. All available archival material has also been reexamined. An attempt has been made to correct for line 'dragging' by the secondary spectrum to improve the fit of the observed data to the orbital solutions. It is found that an earlier suggestion of apsidal regression is still possible although ω is probably constant within the errors. There remain problems and inconsistencies with other orbital elements, in particular K_1 and γ.

Key words: stars, spectroscopic binaries—stars, radial velocities—stars, individual

1. Introduction

Direct observational studies of stellar structure fall broadly into two camps. The most heavily exploited relies upon measurements of radial and non-radial pulsation to give clues as to the nature of the underlying strata, an approach which has made significant strides in recent years with the development of sensitive instrumentation for stellar seismology led, naturally, by work on the Sun.

The other direction is that of the determination and interpretation of the advance of the line of apsides in binaries with eccentric orbits. Unfortunately, there are selection effects which have prevented this second approach from making a major impact although it has the merit of being applicable to stars considerably fainter than those presently required for seismological investigation (and thus permitting examination of a wider sample of spectral types). The first is that the most accurate measures accrue from eclipsing binaries and these, by dint of their generally relatively small separation, tend to be in circular orbits. On the other hand, apsidal motions derived from spectroscopic orbits generally require a prodigious amount of observing sustained, even if in somewhat staccato fashion, over many years. The latter can also be confounded by uncertainty over the values of ω, especially where the eccentricity is small, as for example in the case of AO Cas (Stickland & Lloyd 1988).

In the case of spectroscopic binaries with large eccentricity, provided that sufficient data exist over an appropriately long baseline—a condition realized with the

*Present address: ISRO Satellite Centre, Bangalore 560017.

availability of IUE archival data (*cf.* Harvey *et al.* 1987), some progress ought to be forthcoming. This appeared to be the case for the massive binary ι Orionis (Stickland *et al.* 1987) where a value of 0.41 ± 0.07 deg / 1000 days was derived, leading to an apsidal constant, K_2, of 0.0023. However, a cautionary note was sounded in that paper concerning the apparently strange apsidal behaviour of a rather similar system, BD – 1° 1004 (= HR 1952, B2 IV, m_v =4.95),in which the published values of ω seemed to decrease with time.

The motivation for this present study was to reexamine the orbital elements for this system, adding in a new set from data secured in the last few years. Along the way, it became apparent that the determination of some of the elements was being confused by the presence of the secondary spectrum and perhaps other effects, and that such manifestations might have wider implications, particularly with regard to the Barr Effect in which there appears a non-random distribution of longitudes of periastron in the catalogues of binary orbital elements.

2. Previous determinations of orbital elements

The binary nature of BD –1° 1004 was established by Frost (1906) who secured four spectrograms at Yerkes Observatory in 1905/6, which showed a range of over 160 km s^{-1} and implied a short period, although with hindsight we note that the observations which lead to this conclusion straddle the sharp change at periastron. He saw no evidence of a secondary although the He I line at 4388 Å gave an anomalous displacement.

Following up their work on ι Ori, Plaskett & Harper (1909) described a study of both systems in an important work which was to foreshadow many problems in the future associated with systems in which the secondary is luminous enough to interfere with measurements of the primary spectrum. They presented orbital elements of BD – 1° 1004 based on 36 spectrograms gathered between the end of 1907 and early 1909 but incorporating Frost's data in order to achieve a better estimate of the period. Unfortunately neither the original measures nor the spectrograms appear to be extant and we have to be content with the 14 normal places given in their paper. As they stood, these data failed to provide a satisfactory solution and recourse was made to using a preliminary solution, fitting a sine wave with the binary period to the residuals, subtracting this from the observations and finding the final set of elements by iteration through four least-squares solutions. While this was effective in reducing the residuals to more accustomed values, the rationale for this method is not obvious and hence the meaning of the derived elements remains unclear. Suffice it to say at this juncture that they obtained a value for ω of 87°, having found 90° in the preliminary solution.

The next study came from Pearce (1953) and depended on 17 spectrograms secured near the nodes during 1941 and which afforded the luxury of measurement of the secondary. Since such spectra presumably did not suffer markedly from the ‘dragging’ which afflicts data taken nearer to the systemic velocity, no mention is made of recourse to the artifice used by Plaskett & Harper; a value of ω of 84.6° ± 3° was obtained. The mass ratio, m_1/m_2, deduced by Pearce was 0.64 with an estimated magnitude difference in the blue of 1.14. Again it is to be regretted that Pearce did not present his measurements for reexamination, and not even the normal points appear in the brief abstract, but fortunately we have been able to borrow, through the kind

offices of Dr. Alan Batten, the original spectrograms; our remeasurement of these is described below.

The final set of published elements for BD — 1° 1004 was derived from 86 plates taken at Haute Provence in the early 1950s and analysed by Mme. Barbier-Brossat (1954), hot on the heels of the work of Pearce and apparently independent of it. Once more only normal points were published but through the generosity of the Director of l'Observatoire de Haute Provence, the spectrograms were available for remeasurement. Mme. Barbier used two least squares iterations, deriving an ω of 76°.

From these determinations, it may be that while a consistent solution can be produced either by careful selection of the data to be used or by *post facto* and somewhat *ad hoc* manipulation, use of the raw measurements in a conventional solution might imply apsidal regression. If the latter is correct, then it needs to be confirmed by observations at a much later epoch; if ω is really constant, then some quantitative explanation needs to be forthcoming for the form of the corrections applied.

3. New observations

An extensive series of new observations has been made at Kavalur Observatory in the period from the end of 1984 to the beginning of 1988. The majority of these plates was taken at a dispersion of 27 Å mm^{-1} and a journal of the observations is given in Table 1. They were scanned with the PDS machine at the Indian Institute of Astrophysics at Bangalore and the tape sent to the Rutherford Appleton Laboratory where measurements were made using the program PICA on the STARLINK computer. In general, even at the higher dispersions and at times of maximum or minimum velocity, signatures of the secondary component were not obvious and consistent asymmetries in all the lines were not readily apparent. For this reason, the lines were measured as

Table 1. Radial-velocity observations of BD – 1° 1004 from Kavalur.

Plate	Disp Å mm^{-1}	HJD 2440000+	RV(all) km s^{-1}	RV(4 lines) km s^{-1}
3118	22	5984.474	+74	+101
3120	22	5985.435	+20	+22
4186	27	6014.108	−67	−56
4187	27	6015.143	−73	−33
4188	27	6096.274	−10	−1
4192	27	6097.208	−34	−16
4219	27	6111.270	+2	+21
4221	27	6113.124	+4	+19
4222	27	6114.200	+5	+31
4224	27	6114.103	+12	+41
4239	27	6117.271	+41	+47
4241	27	6118.269	+64	+63
4244	27	6119.090	+67	+70
4245	27	6119.251	+74	+83
4250	27	6120.089	+89	+90
4251	27	6120.274	+73	+75

Table 1. Continued.

Plate	Disp Å mm^{-1}	HJD 2440000+	RV(all) km s^{-1}	RV(4 lines) km s^{-1}
4255	27	6121.256	+12	+8
4256	27	6121.092	+30	+25
4263	27	6122.100	−53	−48
4264	27	6122.253	−28	−32
4270	27	6123.082	−40	−23
4275	27	6124.128	−40	−35
4278	27	6125.065	−28	−19
4279	27	6127.105	−21	−20
4280	27	6129.095	−20	−8
4281	27	6133.073	+6	+5
4377	27	6135.085	+5	+12
4407	27	6141.073	+21	+33
4408	27	6453.113	−3	+4
4409	27	6454.306	−3	+7
4410	27	6455.244	+1	+6
4411	27	6457.228	+5	+11
4412	27	6460.231	+27	+23
4413	27	6473.226	+79	+82
4414	27	6485.214	+1	+14
4415	27	6485.153	−3	+6
4416	27	6486.195	+9	+3
4417	27	6488.165	+9	+8
4418	27	6489.157	−1	+5
4420	27	6534.110	−25	−13
4421	27	6535.074	−25	−7
318	85	6722.492	−9	−26
353	85	6743.489	+75	+74
399	85	6753.314	+11	+13
410	85	6755.378	+24	+26
474	85	6780.357	+11	+18
475	131	6800.206	−27	+6
544	85	6801.217	−28	−35
545	85	6801.257	+26	+28
547	85	6801.317	+20	+16
548	85	6801.367	−61	−45
551	85	6802.232	−29	−25
552	85	6802.301	−28	−24
682	32	6839.298	−13	−19
1146	32	7039.430	+50	+66
1212	32	7071.484	+29	+37
1213	32	7071.508	+30	+34
1216	32	7072.346	−21	−14
1217	32	7072.378	−8	−10
1222	32	7076.353	−12	−11
1223	32	7076.391	−10	−3
1457	32	7179.140	+67	+99
1460	32	7179.384	+56	+40
1461	32	7180.151	−20	+6
1462	32	7180.289	+10	+30
1519	49	7206.171	+23	+10
1522	49	7208.195	−51	−45
1552	49	7227.151	−81	

Table 2. Lines used in the measurement of Kavalur spectra.

λ	ID	λ	ID	λ	ID
(3797.900)	H	4009.270	He I	(4267.167)	C II
3819.610	He I	4026.140	He I	4340.466	H
3835.386	H	4101.738	H	4387.928	He I
3888.800	H + He I	4120.837	He I	4471.507	He I
3970.075	H	4143.760	He I	(4481.228)	Mg II

Parentheses indicate lines used only occasionally.

though they were single using parabola fitting to set on the cores, the expectation being that this would be most consistent and that the 'dragging' could be treated at a later stage. A list of the lines used is given in Table 2. It will be seen that the lines listed in Table 2 are mainly due to H and He I, the former having profiles with broad wings. It might, therefore, be assumed that the dragging effects would be different for the two types of lines (aside from any adopted wavelength errors). This has been checked by averaging the velocities from the two species separately on each of nine spectra, three taken at each of three different primary velocities (close to the systemic velocity and about 70km s^{-1} on either side of it).The mean (H–He) difference was calculated for each velocity but no trend was apparent as a function of velocity: going from negative, through systemic to positive velocity, the differences were + 1, + 8 and –11 km s^{-1} respectively.

The first action was to try a conventional orbital solution on all the new data. However, it was soon clear that the lower dispersion observations (given the same weight as the higher dispersion ones) were adding considerable scatter to the set, yielding a mean error of 19.5 km s^{-1} for an observation of unit weight. Equally alarming was the value for K_1 derived in this solution: 50 km s^{-1} , far less than the previous determinations. To try to improve the data set, the low-resolution observations were first rejected (*i.e.,* all those lower than 32 Å mm^{-1}). This reduced the mean error to 14.8 km s^{-1} and slightly increased K_1 to 55 km s^{-1}. There still seemed to be excessive scatter and recourse was made to restricting the lines used for the plate averages to just four that appeared to behave well consistently: H I at 4101Å and 4340 A He I at 4388 Å and 4471 Å. This gave only a slight further improvement of the error to 13.9 km s^{-1} and increase of K_1 to 58 km s^{-1}. This final solution, whose elements are given in Table 3, is shown in Fig. 1 where it is clear that the fit is far from adequate; it goes nowhere near the maximum and minimum of the observations and there are notable 'dragging' effects near the systemic velocity.

A further curiosity was that the systemic velocity, +17.5 km s^{-1} for our last solution, was very different from those found by the earlier workers: Plaskett & Harper gave + 26 km s^{-1}, Pearce found + 36 km s^{-1}, and Mme. Barbier recorded + 29 km s^{-1}. This raises the spectre either of systematic errors in the radial velocity zero points from the various spectrographs or of a real variation of the systemic velocity occasioned by a third body. This latter possibility is of interest in connexion with any detection of apsidal regression, being one of its few possible causes.

To investigate further this matter, the Kavalur high dispersion observations were broken down chronologically into a series of runs. Most covered just fragments of cycles but there was a run from JD 2446111 to JD 2446141 which covered nicely a

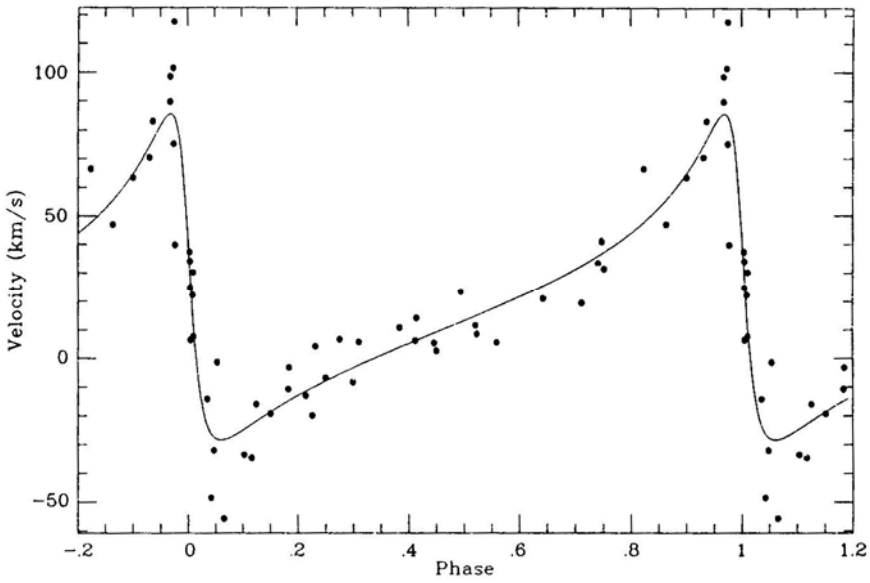

Figure 1. Uncorrected radial velocity data from Kavalur plates and the computed orbit; data falling within 0.2 phase of zero phase are repeated, in this and subsequent figures, to allow these parts of the cycle to be better seen in the context of the remainder of the cycle.

complete cycle and which was sufficient to yield a set of orbital elements of its own (the period being fixed); these are added to Table 3. Interestingly, the mean error of an observation of unit weight in this set was only 5.7 km s^{-1} and K_1 was raised to 66 km s^{-1}. Fitting the other fragmentary runs on to this solution gives some support to the suggestion of a change of the derived systemic velocity or zero point as a function of time, although the origin remains obscure. The change is not obviously monotonic or periodic on the basis of the very limited data: The subset from JD 2446453 to JD 2446535 yields $\gamma = 21.2 \pm 2.5$ km s^{-1}; that from JD 2447071 to JD 2447076 gives

Table 3. Orbital elements from Kavalur data—with no dragging correction.

	High res. all data	High res. short run
P(days)	27.1549 (fixed)	27.1549 (fixed)
T(HJD)	2446120.954	2446120.990
	±.108	.053
K (km s^{-1})	57.9	65.5
	±3.3	3.6
e	0.72	0.75
	±0.04	0.03
ω (degrees)	74.2	74.3
	±5.6	3.9
γ (km s^{-1})	17.5	12.6
	±2.2	1.4
r.m.s. (km s^{-1})	13.9	5.7

γ = 25.2 ± 3.4 km s^{-1}; but that from JD 2447179 to JD 2447180 has γ = 10.6 ± 14.0 km s^{-1}. Therefore it is not feasible to apply corrections to the individual observations.

4. Reexamination of all data

The discussion thus far leaves a rather strong impression that the nature of the data used, in terms of the resolution and its spread in phase, and the approach to treating the non-Keplerian form of the observed points on the radial velocity curve, can give rise to rather disparate sets of orbital elements. Therefore some consistency of method is required if the four collections of observations are to be compared in a meaningful way.

4.1 *Remeasurement of Old Data*

Although Pearce makes reference to 17 plates taken near the nodes we borrowed from DAO 33 plates of BD – 1° 1004 at 25 Å mm^{-1} .These were scanned (arc-star-arc) on the PDS machine at the Royal Greenwich Observatory and measured in the same way as the Kavalur plates *i.e.,* using the interactive PICA programme to set on the line cores rather than using it in the simulation of a Grant-type machine to get a best fit to the whole line profile. (The latter can be very useful in the case of single-lined stars and perhaps even essential in the case of stars with broad lines, but with a double-lined system such as this one, the core fit should give a better representation of the primary motion.) This is important in the present case since this method mimics the measurement of plates made with a long-screw measuring engine, and since the plates

Table 4. Pearce's observations remeasured.

HJD 2400000+	RV km s^{-1}	HJD 2400000+	RV km s^{-1}
29896.049	+32	29994.825	−6
29925.011	+37	29997.823	+19
29927.988	+43	29999.792	+22
29936.077	+123	30006.799	+35
29943.899	+20	30014.779	+87
29945.954	+21	30020.757	−22
29951.941	+37	30023.758	+8
29951.972	+39	30040.636	+73
29962.931	+127	30042.651	+103
29962.946	+126	30042.770	+92
29963.913	+41	30043.690	+113
29963.993	+36	30046.672	−29
29972.806	+22	30046.686	−32
29972.820	+25	30047.632	−18
29975.946	+24	30064.629	+50
29988.847	+109	30065.664	+57
29994.804	−5		

Table 5. Barbier's observations remeasured.

HJD 2430000+	RV km s^{-1}	HJD 2430000+	RV km s^{-1}	HJD 2430000+	RV km s^{-1}
2564.421	+43	4015.451	−2	4033.488	+62
2564.463	+56	4015.467	−5	4313.514	+1
3996.408	+21	4017.367	+6	4313.597	−2
3996.609	+29	4017.399	+3	4667.530	+2
3997.404	+24	4018.387	+17	4667.565	−3
3997.425	+18	4018.402	+3	4670.597	+11
3998.470	+37	4019.393	+9	4673.496	+14
3998.483	+34	4019.408	+13	4673.527	+19
3999.413	+40	4020.417	+17	4739.359	+53
3999.430	+33	4021.441	+9	4739.391	+57
4000.481	+33	4021.457	+17	4741.327	+74
4004.538	+57	4025.432	+25	4741.374	+84
4007.387	+74	4025.445	+23	4742.310	+90
4007.410	+81	4026.355	+21	4742.513	+97
4009.396	+94	4026.373	+31	4743.300	+11
4010.492	−5	4028.431	+40	4743.450	+12
4010.522	−2	4028.472	+30	4743.602	+4
4012.460	−21	4030.413	+34	4744.329	−23
4013.408	−12	4030.434	+40	4744.540	−23
4013.467	−11	4032.381	+49	4750.391	+12
4014.418	−13	4032.397	+42	4750.411	+18
4014.436	−12	4033.473	+54	4751.353	+9
				4751.376	+8

of Plaskett & Harper are not available for study, one needs an approach that would be compatible with their probable technique. Ten photospheric lines of H I and He I were measured and the results are presented with a journal of Pearce's observations in Table 4.

We were also able to remeasure the 38 Å mm^{-1} plates from Haute Provence used by Mme. Barbier. These too were scanned on the PDS at RGO and were measured in a similar fashion although the process was made more efficient by setting up a template to direct the search for line cores so that the fitting could be done automatically. 77 spectrograms were thus examined although ten of these could not be used (due to underexposure, weak arc lines *etc.*)*;* these are reported in Table 5.

4.2 *Reanalysis off Pearce's Observations*

From plots of the various data sets as a function of phase (and the period is long enough that its precise value is inconsequential within each set), it was apparent that Pearce's observations gave the smallest scatter about a smooth (albeit non-Keplerian) curve. Thus it was decided that initial efforts should be concentrated on these data. The first solution is shown in Fig. 2a where, although the cohesion of the observed points can be seen, it is clear that there is marked 'dragging' in the vicinity of the systemic velocity (38 km s^{-1} — see the elements in Table 6). It is also apparent that the observed points and the solution part company at the velocity minimum.

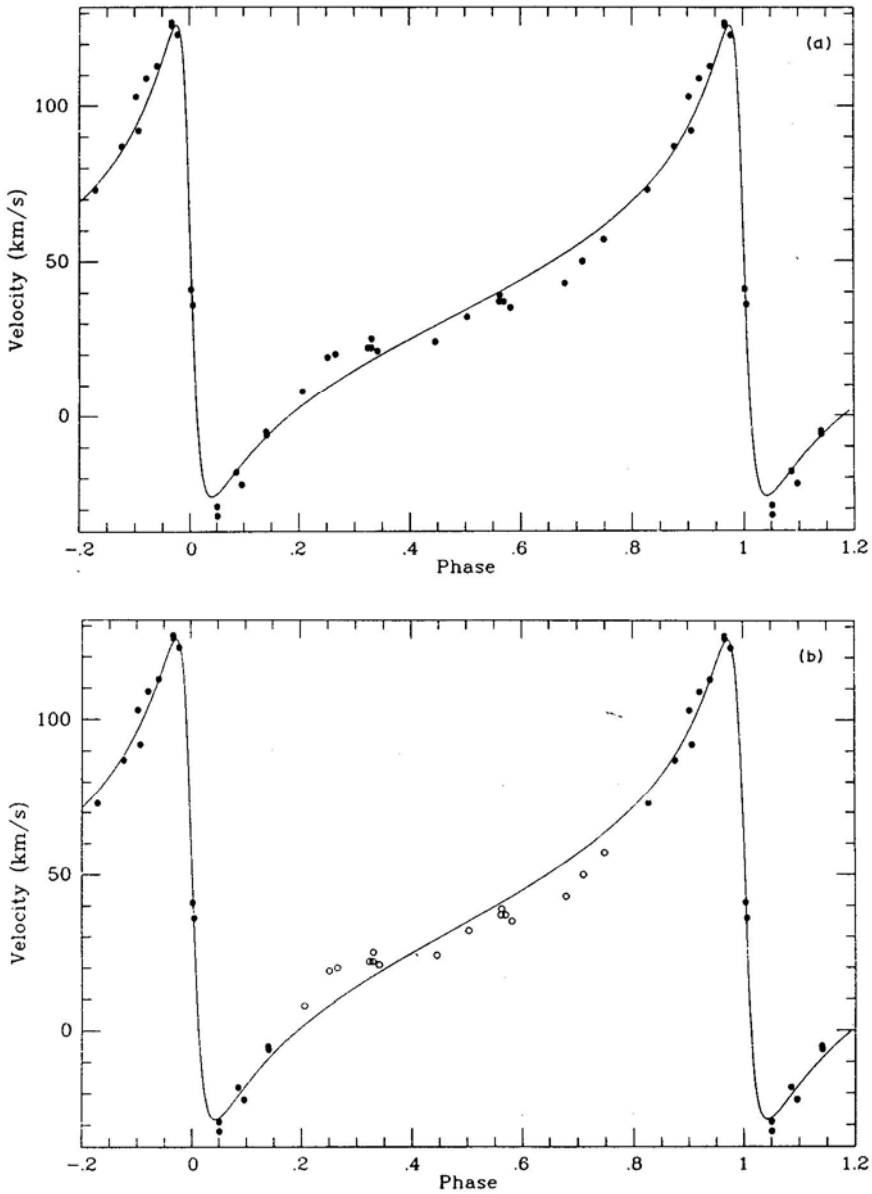

Figrue 2. (a) The orbit using all the radial velocities from the remeasured observation of Pearce (b) The orbit computed using only the extreme velocities (although *all* data points are shown).

Since in Pearce's observations the secondary spectrum can be seen at velocity extrema, one must assume that it is having an effect on measurements of the primary spectrum, to a greater or lesser degree, all the time. However, if one measures the line cores, then there is the prospect that for velocities separated suffciently from the systemic velocity, an accurate estimate of the primary velocity can be obtained. This naturally depends on the line widths, which will be influenced by rotation, and on the

Table 6. Orbital elements deduced from Pearce's observations with corrections.

Solution	1	2	3	4	5
P(days)	27.1546 ±.00006	27.1546 (fixed)	27.1546 (fixed)	27.1546 (fixed)	27.1546 (fixed)
T(2429900+)	91.097 ±.11	90.976 .04	90.984 .03	90.968 .03	90.974 .02
K_1 (km s^{-1})	88.5 ±3.7	76.8 3.0	77.1 1.4	78.7 1.7	81.8 1.6
e	0.73 ±.025	0.77 .02	0.76 .01	0.75 .01	0.76 .01
ω(degrees)	84.6 ±3.0	77.8 2.6	79.4 2.4	78.1 1.7	79.3 1.5
γ(km s^{-1})	+36.2 ±1.4	+37.7 1.0	+38.0 1.3	+36.7 0.7	+38.8 0.6
r.m.s.(km s^{-1})		5.73	4.1	3.6	3.4

Solution 1. Pearce's (1953) elements
2. All remeasured data; uncorrected
3. Extreme velocities only; uncorrected
4. Dragging correction with $\Delta\omega = 0°$
5. Dragging correction with $\Delta\omega$=40°.

resolution of the spectra. From Pearce's own measurements, we can anticipate separations in excess of 200 km s^{-1} at the extrema which corresponds to about 3 Å in the blue spectral region. Thus for a preliminary set of elements unaffected by 'dragging', we have used only those velocities less than 0 and greater than 60 km s^{-1} ; this solution is shown in Fig. 2b with the elements given in Table 6. A plot of the

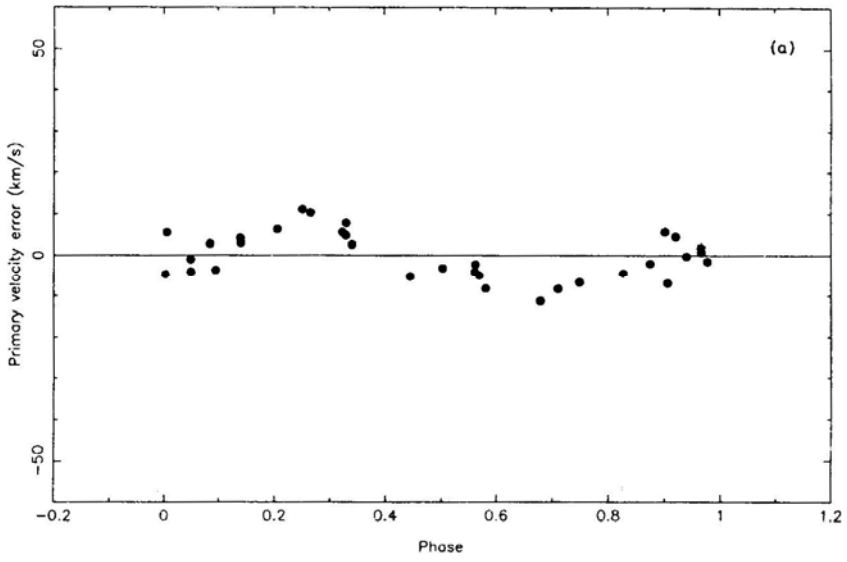

Figure 3. (a) Residuals in the observed data from the solution shown in Fig.2 (b). (b) Observed residuals and theoretical variation of residuals in the presence of 'dragging'computed using a $\Delta\omega$ of 0°. (c) Observed residuals and theoretical variation computed using a $\Delta\omega$ of 40°.

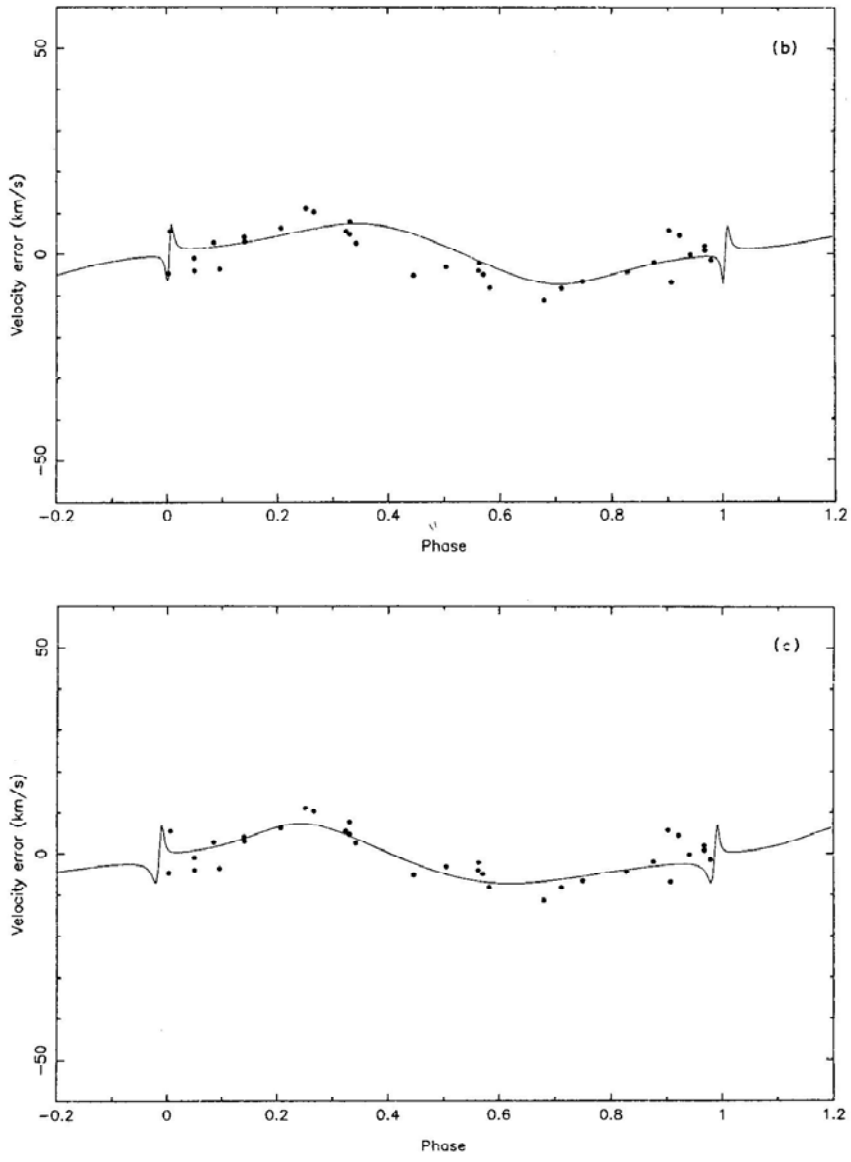

Figure 3. Continued.

residual velocities from such a fit is shown in Fig. 3a. As might be expected,the detailed solution from such a data set is sensitive to exactly which data are included. In order to eliminate this problem it is necessary to correct the blended velocities before solving for the orbital parameters. If this can be done then all observed velocities can be included in the solution.

An attempt to model the deviations from Keplerian motion has been made in the following way—an approach similar to that described by Tatum (1968) and Griffin (1986). A typical spectral line was assumed to have a Lorentz profile with a width of

2 Å; the ratio, R, of secondary:primary line intensities was taken to be 0.30; and the amplitude of the secondary radial velocity curve was deemed to be 120 km s^{-1}. These values are consistent with measurements from the spectra taken at phases with large velocity separations. The simulation consisted of calculating the blended line profile through the range of velocity separations predicted by the preliminary solution and the adopted K_2 and finding the wavelength of minimum intensity. The theoretical residual was computed then as the difference between this wavelength and that of the primary component given by the preliminary solution. The form of the required correction derived for a typical set of orbital elements is shown in Fig. 3b superimposed upon the residuals from Fig. 3a. An important point to note in Fig. 3b is that the theoretical correction is very nearly symmetrical about phase 0.5 as is to be expected from an orbit with ω about 80°. Since these model corrections are dependent on the orbital parameters, a solution for the whole data set must include a recalculation of the model at each iterative correction to the elements. The result of doing this is illustrated in Fig. 4a (with elements given in Table 6) where it is immediately apparent that although the fit is considerably improved it is still not perfect and trends remain in the residuals. This is to be expected from Fig. 3b since it is clear that the asymmetry in the real residuals is not reproduced by the model. A number of experiments was conducted to see if either a change in the parameters of the model or the addition of other effects (third light, asymmetrical or non-Lorenzian line profiles) could better reproduce the observed effect. Any changes to the line profiles, for instance, to take account of the fact that velocities from dissimilar lines are averaged, merely change the amplitude and/or the phase spread of the effect. Asymmetries can be introduced by assuming asymmetrical lines of either component. These are often invoked as manifestations of circumstellar gas streams to explain distorted velocity curves but we were unable to produce a consistent model in this respect. The only way we found to reconcile the data and model corrections was to calculate the model corrections with the correct orbital elements as described above but simply to introduce an offset in the value used for ω. Qualitatively, the best fit was obtained with a $\Delta\omega$ of approximately 40°. Fig. 3c shows a fit of this dragging correction to the residuals shown in Fig. 3a. Fig. 4b shows the final solution when this *ad hoc* correction is applied with iteration; the elements are included in Table 6. Unfortunately, no physical reason comes immediately to mind as to why using a different value from that deduced for the orbital elements should have this effect although one is reminded of the Barr and associated effects when the question of the validity of ω's in binary systems is raised.

If one assumes that this 'solution' to the problem is merely fortuitous it is perhaps possible to gain some insight into its cause by computing the *difference* between the theoretical residuals calculated at the expected ω of 79° and the best fit one of 119° and this is shown in Fig. 5. It has two 'cycles' during the binary period and a peak to peak amplitude of about 10 km s^{-1}. Maximum velocities are reached at phases about 0.2 and 0.75. Although the discrepancy is not truly sinusoidal and its amplitude appears to die away near orbital phase zero, nevertheless it appears that, to within the errors, a quasi-sinusoidal disturbance of this magnitude could be used to bring the observations and the theory into coincidence.

At present we can only speculate on the reality and existence of such a disturbance. One possibility might be a low-amplitude pulsation of the primary star. The spectral type (B2IV) might give it some susceptibility to pulsation (in affiliation to the β CMa

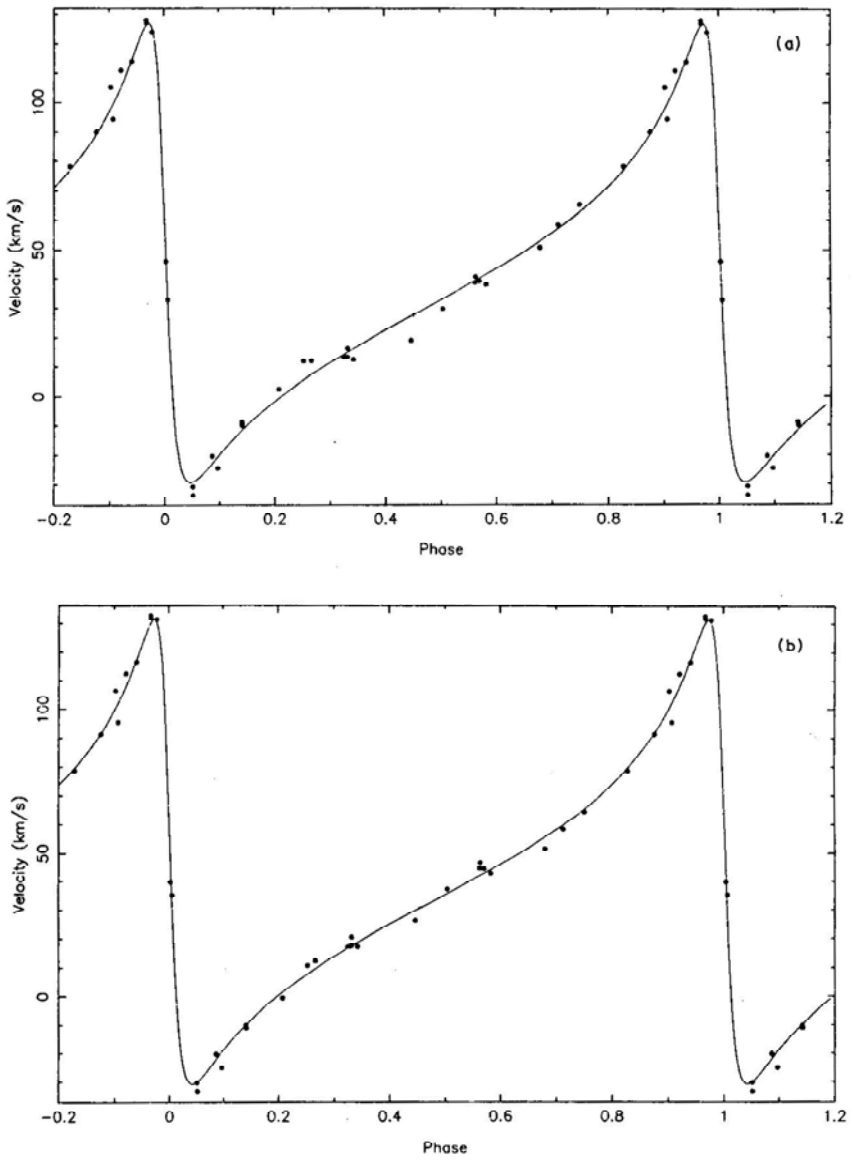

Figure 4. (a) Orbit computed from data corrected for 'dragging' using $\Delta\omega = 0°$; trends are still apparent, (b) As in (a) but with $\Delta\omega$=40°.

stars) but the period of oscillation required (two weeks) is long and clearly rules out a direct link. One might, of course, hypothesize that the driving force is not inherent to the star but rather a gravitational impulse caused by the close encounter at periastron, but if the atmosphere were resonant with such an event, which is of the several-hours timescale, then we would expect the oscillation period to be similarly short.

At present, therefore, we have no explanation for, this discrepancy between the modelled dragging correction and the observed residuals. The measurements from the

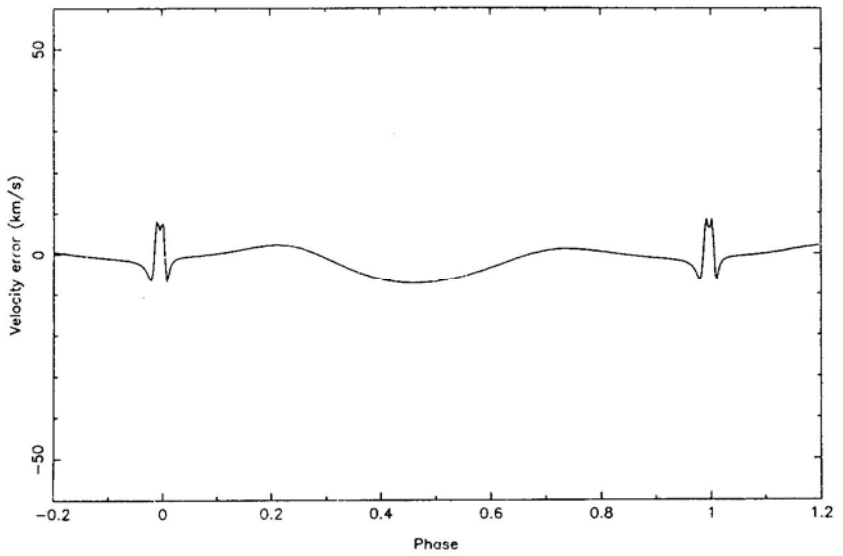

Figure 5. The difference between the theoretical corrections computed with $\Delta\omega = 0°$ and $\Delta\omega = 40°$.

Pearce plates are the only ones we have that have sufficient accuracy to show the effect so in the first instance new observations to confirm its existence would be desirable.

4.3 *Reexamination of Other Data Sets*

On the basis of the work with Pearce's data, we have applied corrections to all of the other data sets in the hope of achieving a consistent collection of orbital elements. Two stages of correction have been applied: the first is the basic dragging correction, *i.e.,* setting $\Delta\omega$ to zero, for which there is some physical justification, and the second is the optimized solution with $\Delta\omega$=40°. It turns out that, in terms of the final derived elements, there is little difference within the formal errors.

The first set to be examined contains the normal points given by Plaskett & Harper. The corrections improve the r.m.s. error from 6.5 to 4.0 km s^{-1} giving elements (Table 7) fairly close to those given by Plaskett & Harper but with somewhat reduced values of K_1 and ω.

The Haute Provence data are rather scattered and the corrections give no improvement over the solution run without them, σ = 6.9 km s^{-1}. Among the elements (Table 7), the most noteworthy problem is with K_1 which is 60 km s^{-1}, only two thirds of the value found from Plaskett & Harper's set and strikingly lower than found by Mme. Barbier herself (75 km s^{-1}). Equally problematical are the data from Kavalur. Like those from Haute Provence, they are rather scattered (σ = 15.2 km s^{-1}) and the elements (Table 7) show little change with the corrections. The whole set of highest resolution observations also give a K_1 of 60 km s^{-1} These two results suggest that our procedure cannot be applied uncritically to data secured by different observers even though the dispersions used are nominally similar.

Table 7. Orbital elements deduced from all data with corrections ($\Delta\omega = 0$).

Solution	1	2	3	4	5
P (days)	27.1546 (fixed)	27.1546 (fixed)	27.1546 (fixed)	27.1546 (fixed)	27.154925 .000043
T(2400000+)	17961.436 ±.036	29990.973 .03	34009.754 .07	46121.054 .10	29990.969 .034
K_1 (km s^{-1})	90.5 ±3.6	78.1 1.7	60.0 1.9	60.5 3.4	68.2 1.4
e	0.78 ±.02	0.76 .01	0.74 .01	0.71 .04	0.74 .01
ω (degrees)	82.7 ±3.3	77.9 1.7	75.1 2.9	73.4 5.5	73.9 1.8
γ (km s^{-1})	+26.3 ±1.3	+37.0 0.7	+25.5 0.8	+15.8 2.5	+38.1* 0.7
r.m.s. (km s^{-1})	4.5	3.8	6.9	15.6	9.2

Solution 1, Plaskett & Harper's data
2. Pearce's data (Solution 4 of Table 5)
3. Haute Provence data
4. Kavalur data
5. All data normalized to $\gamma = +37$ km s^{-1} (Pearce's value).

5. Conclusions

We have described in some detail attempts to model the effects of line dragging in the spectrum of BD –1° 1004 because there is a number of such systems whose orbital elements are astrophysically valuable but for which rather *ad hoc* corrections have been applied in the past. While we feel that some progress in matching the observations has been made, the fitting is not yet satisfactory and further investigation may be desirable. However, the main recommendation is for such systems to be observed at higher resolution and signal-to-noise ratio.

The results presented in Table 7 suggest that the value of ω is constant, within the errors, at about 78°, although one might formally claim a slow regression—see Fig. 6 with $\omega = -0.38° \pm 0.08°$ per 1000 days. The determination of any apsidal motion was a major aim of this work and so it is disappointing to leave the question somewhat open. One comment that can be made, however, concerns the value of comparing ω's from different data sets where different values of e are also produced, the latter being, of course, unacceptable astrophysically. Using a program originating from Dr G. Hill at DAO and made available through Drs Bell and Hilditch at St. Andrews, it has been possible to take a representative set of data and, over a plausible range of parameters, determine the independence (or otherwise) of e and ω. In the present instance, for a run of e from 0.65 through to 0.80, the change in ω was less than 1.5°, smaller than the typical formal error. Thus the finding above regarding apsidal motion cannot be masked by errors in e in the individual solutions.

The matter of the disparate values of K_1 is of some considerable concern and the difference between the original measurements, presumably carried out by eye, and the modern results using a density scan of the spectrum suggests a fundamental difference in what is being measured. It may imply that the eye is better able to pick out the line

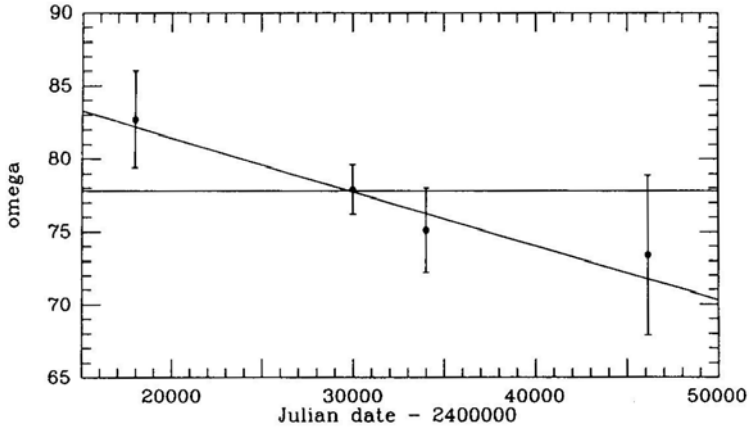

Figure 6. Variation of ω with time.

core which represents the true motion of the primary in the presence of 'dragging' by the secondary. On the other hand, the impartiality of the computer method plus the application of a realistic dragging correction ought to render a correct answer. Further work is clearly needed.

Finally, attention is drawn to the range of systemic velocities found for the various data sets. The span of over 20 km s^{-1} is unacceptably large and raises the spectre of a third body. Fourier analysis of the totality of data has failed to suggest a period for this. Further work including the adequate monitoring of standards will be required to resolve this. For the time being, however, we have merged the data sets by adjusting the velocities to yield γ = + 37 km s^{-1} in each case. The elements from the dragging-corrected solution of this totality of data are given in Table 7, where the main point of interest is the main binary period. It is slightly different from the fixed value of 27.1546 days used for the earlier experiments but within each of the spans of the individual data sets, the difference is immaterial.

References

Barbier-Brossat, M. 1954, *J.Observ.,* **37,** 119.
Frost, E. B. 1906, *Astrophys. J.*, **23,** 264.
Griffin, R. F. 1986, *The Observatory*, **106,** 108.
Harvey, A. S., Stickland, D. J., Howarth, I. D., Zuiderwijk, E. J. 1987,*T he Observatory* ,**107,** 205.
Pearce, J. A. 1953, *Astr. J.,* **58,** 46.
Plaskett, J. S., Harper, W. E.1909, *Astrophys. J.*, **30,** 373.
Stickland, D. J., Pike , C. D., Lioyd , C., Howarth, I. D. 1987, *Astr.Astrophys.,* **184,** 185.
Stickland, D. J., Lloyd, C.1988, *The Observatory,* **108,** 174.
Tatum, J. B. 1968, *Mon. Not. R. astr. Soc.,* **141,** 43.

J. Astrophys. Astr. (1990) **11**, 461–474

Accretion Disc with Dipole Magnetic Field in Linearized Kerr Geometry

P. Bhaskaran, S. C. Tripathy & A. R. Prasanna *Physical Research Laboratory, Ahmedabad*

Received 1990 May 15; accepted 1990 August 16

Abstract. In this paper we discuss the equilibrium configuration of a plasma disc of infinite conductivity around a slowly rotating compact object, and obtain the pressure profiles, and the structure of magnetic field lines for co and counter-rotating discs.

Key words: stars, accretion—stars, magnetic—black holes—magnetohydrodynamics—relativity

1. Introduction

One of the most important aspects in the study of accretion dynamics is to understand the equilibrium and stability of plasma discs in electromagnetic fields around rotating compact objects. Even if initially the central compact object is non-rotating, accretion of matter in the presence of magnetic field can induce rotation due to the transfer of angular momentum effected by magnetic torque. In the frame-work of general relativity, some studies concerning the equilibrium configuration of plasma discs around non-rotating compact objects having nonzero electromagnetic fields have recently been made (see, Prasanna & Bhaskaran 1989, hereinafter PB; Bhaskaran & Prasanna 1989, 1990, hereinafter BP).

In the following, we consider an axisymmetric, stationary plasma disc around a slowly rotating compact object (rotational velocity $\alpha = a/m \ll 1$) which has only the azimuthal component of the spatial three-velocity as non-zero. Further, it is also assumed that the plasma is infinitely conducting and the magnetic field associated has only non-zero poloidal component.

Section 2 outlines the basic theory of accretion disc and their solutions. In Section 3 the solutions are applied to the case of a thin disc. Section 4 presents the results of the calculations and their implication. Section 5 summarizes our conclusion.

2. Formalism

The general equations of structure (PB) for a system having only the azimuthal component of velocity ($V^r = V^\theta = 0$), with the linearized Kerr space-time as the background geometry represented by the metric

$$\begin{aligned} ds^2 = (1-2m/r)dt^2 - (1-2\,m/r)^{-1}\,dr^2 - r^2\,d\theta^2 - r^2\sin^2\theta\,d\phi^2 \\ + 4am\sin^2\theta/r^3\,d\phi\,dt \end{aligned} \tag{2.1}$$

yield the momentum equations:

$$\left[\rho+\frac{P}{c^2}\right]U^{t^2}\left[\frac{mc^2}{r^2}\left(1-\frac{2m}{r}\right)-\frac{2amc}{r^2}\left(1-\frac{2m}{r}\right)\sin^2\theta\, V^{\phi}\right.$$
$$\left.-(r-2m)\sin^2\theta\, V^{\phi^2}\right]+\left(1-\frac{2m}{r}\right)\frac{\partial P}{\partial r}=F^r{}_k J^k, \tag{2.2}$$

$$\left[\rho+\frac{P}{c^2}\right]U^{t^2}\left[-\sin\theta\cos\theta\, V^{\phi^2}+\frac{4am}{r^3}\sin\theta\cos\theta\, V^{\phi}\right]+\frac{1}{r^2}\frac{\partial P}{\partial\theta}=F^{\theta}{}_k J^k, \tag{2.3}$$

and the Maxwell's equations

$$J^r=-\frac{1}{r^2\sin\theta}\frac{\partial}{\partial\theta}\left[\sin\theta\left(1-\frac{2m}{r}\right)B_{\phi}\right], \tag{2.4}$$

$$J^{\theta}=\frac{1}{r^2\sin\theta}\frac{\partial}{\partial r}\left[\sin\theta\left(1-\frac{2m}{r}\right)B_{\phi}\right], \tag{2.5}$$

$$J^{\phi}=\frac{1}{r^4\sin\theta}\frac{\partial}{\partial\theta}\left[\frac{B_r}{\sin\theta}\right]-\frac{1}{r^2\sin^2\theta}\frac{\partial}{\partial r}\left[\left(1-\frac{2m}{r}\right)B_{\theta}\right]$$
$$-\frac{2am}{r^2}\left[\frac{\partial}{\partial r}\left(\frac{E_r}{r}\right)+\frac{1}{r^3\sin\theta}\left(1-\frac{2m}{r}\right)^{-1}\frac{\partial}{\partial\theta}(\sin\theta\, E_{\theta})\right] \tag{2.6}$$

$$J^t=-\frac{1}{r^2}\left[\frac{\partial}{\partial r}(r^2E_r)+\frac{1}{\sin\theta}\left(1-\frac{2m}{r}\right)^{-1}\frac{\partial}{\partial\theta}(\sin\theta\, E_{\theta})\right]$$
$$-\frac{2am}{r^2}\left[\frac{1}{r^3\sin\theta}\left(1-\frac{2m}{r}\right)^{-1}\frac{\partial}{\partial\theta}(\sin\theta\, B_r)-\frac{\partial}{\partial r}(B_{\theta}/r)\right], \tag{2.7}$$

$$\partial B_r/\partial r+\partial B_{\theta}/\partial\theta=0, \tag{2.8}$$

$$\partial E_r/\partial\theta-\partial E_{\theta}/\partial r=0. \tag{2.9}$$

As shown in PB, the ϕ component of the momentum equations and the continuity equation give two constraint equations, which together give two conditions

$$(B_{\theta}J_r-B_rJ_{\theta})=0\rightarrow(B\times J)_{\phi}=0. \tag{2.10}$$

For J_r and J_{θ}= 0, Equation (2.10) gets identically satisfied and further we get a simple solution for B_{ϕ} as

$$B_{\phi}=\frac{K_1}{\sin\theta}(1-2m/r)^{-1}. \tag{2.11}$$

However, with J^r and J^{θ} zero, B_{ϕ} does not enter into any of the dynamical equations. One can for the present case choose it to be zero without any loss of generality. Since the plasma is assumed to be infinitely conducting (σ = 0), the generalized Ohm's law gives the force free condition $F^i_k\, U^k$ = 0, from which one has the electric and magnetic fields related through the expressions

$$E_r=B_{\theta}V^{\phi}/c, \tag{2.12}$$

$$E_{\theta}=-B_rV^{\phi}/c. \tag{2.13}$$

We assume the azimuthal velocity component V_ϕ to be relativistic Keplerian, modified by the effect of frame dragging due to the rotation of the central object, as given by

$$V^\phi = \frac{L}{r^2 \sin^2\theta}(1-2m/r) - \frac{2amc}{r^3 \sin^2\theta}. \tag{2.14}$$

With this definition of V^ϕ, Equations (2.8) and (2.9) are solved for B_r and B_θ and are expressed as:

$$B_r = -Ar^k(1-2b/r)^{-k/2}\sin^{k-1}\theta\cos\theta, \tag{2.15}$$

$$B_\theta = Ar^{k-1}(1-3b/r)\,(1-2b/r)^{(-k/2)-1}\sin^k\theta, \tag{2.16}$$

where A and k are arbitrary constants and b =(1 + ac/L)m. Usingthese in Equations (2.6) and (2.7), the current components J^ϕ and $J_t$are obtained.

In order to appreciate the effects of rotation of the central compact object on the disc dynamics, it is necessary to translate the solutions into the form, as seen by the locally non-rotating observer outside a rotating blackhole. Using the tetrad λ_i^a (LNRF) as given in PB for the linearized Kerr geometry, we rewrite the expressions for the magnetic field components and the current components as:

$$\begin{aligned} J^{(\phi)} = {} & Ar^{k-3}(1-2b/r)^{-k/2}\sin^{k-1}\theta(1-(k-2) \\ & \times(\cos\theta/\sin\theta)^2) - (1-2m/r)^{1/2}\frac{B_{(\theta)}}{r}\Bigg[(k-2) \\ & + \frac{m}{r}(1-2m/r)^{-1} + \frac{3b}{r}(1-3b/r)^{-1} - (k+2)\frac{b}{r}(1-2b/r)^{-1}\Bigg] \\ & - \frac{B_{(\theta)}}{r}(1-2m/r)^{1/2}\Bigg[1 - \frac{m}{r} - \frac{6am}{r^2}(1-2m/r)^{1/2}\sin\theta\, V^\phi/c\Bigg], \end{aligned} \tag{2.17}$$

$$\begin{aligned} J^{(t)} = {} & \frac{-B_{(\theta)}}{r}\frac{L}{(c\,r\sin\theta)}\Bigg[1 - \frac{m}{r} - (6m^2/r^2)\frac{ac}{L}(1-2\,m/r)^{-1}(1+\sin^2\theta)\Bigg] \\ & - (B_{(r)}/r)\frac{4mL}{cr}\frac{ac}{L}(1-2m/r)^{-1}\cos\theta - \frac{V^\phi}{c}(1-2m/r)^{1/2}\frac{B_{(\theta)}}{r} \\ & \times\Bigg[(k-2) + \frac{m}{r}(1-2m/r)^{-1} + \frac{3b}{r}(1-3b/r)^{-1} - (k-2)\frac{b}{r}(1-2b/r)^{-1}\Bigg] \\ & + \frac{V^\phi}{c}Ar^{k-3}(1-2b/r)^{-k/2}\sin^{k-1}\theta[1-(k-2)(\cos\theta/\sin\theta)^2], \end{aligned} \tag{2.18}$$

$$B_{(r)} = -A\,r^{k-2}(1-2b/r)^{-k/2}\sin^{k-2}\theta\cos\theta, \tag{2.19}$$

$$B_{(\theta)} = A\,r^{k-2}(1-2\,m/r)^{1/2}(1-3b/r)\,(1-2\,b/r)^{-(k/2)-1}\sin^{k-1}\theta. \tag{2.20}$$

Similarly the two moment equations are written in terms of LNRF as:

$$\begin{aligned} & (\rho c^2 + P)(1-2m/r)^{-1}(1-(V^{(\phi)}/c)^2)^{-1}\Bigg[\frac{m}{r^2} - \frac{6amc}{r^3}(1-2m/r)^{1/2}\frac{V^{(\phi)}}{c} \\ & - \frac{1}{r}(1-2m/r)\left(\frac{V^{(\phi)}}{c}\right)^2\Bigg] + \partial P/\partial r = (1-2m/r)^{-1/2}B_{(\theta)}\Bigg[J^{(\phi)} - J^{(t)}\frac{V^{(\phi)}}{c}\Bigg], \end{aligned} \tag{2.21}$$

$$(\rho c^2 + P)\left(1-\left(\frac{V^{(\phi)}}{c}\right)^2\right)^{-1}\left(\frac{V^{(\phi)}}{c}\right)^2 \cot\theta - \partial P/\partial\theta = r B_{(r)}\left[J^{(\phi)} - \frac{J^{(t)}V^{(\phi)}}{c}\right], \quad (2.22)$$

where U^i satisfies the orthogonality relation for the four velocity $g_{ij} U^i U^j = 1$ such that

$$U^{t^2} = (1 - 2m/r)^{-1} (1 - V^2/c^2)^{-1}, \quad (2.23)$$

Where

$$V^2 = V^{(r)2} + V^{(\theta)2} + V^{(\phi)2} \quad (2.24)$$

3. Thin disc

As a special case if we consider the disc to be confined to the equilateral plane ($\theta = \pi/2$), we find that P is a function of r only and the expression (2.21) is written as:

$$\partial P/\partial r = -(\rho c^2 + P)(1-2m/r)^{-1}(1-(V^{(\phi)}/c)^2)^{-1}\left[\frac{m}{r^2} - \frac{6amc}{r^3}(1-2m/r)^{1/2}\frac{V^{(\phi)}}{c} - \frac{1}{r}(1-2m/r)\left(\frac{V^{(\phi)}}{c}\right)^2\right] + (1-2m/r)^{-1/2} B_{(\theta)}\left(J^{(\phi)} - J^{(t)}\frac{V^{(\phi)}}{c}\right). \quad (3.1)$$

Since all other physical parameters have been determined except for P and ρ, we need an equation of state along with Equation (3.1) to determine these two quantities uniquely. We consider below two different cases for illustration.

3.1 *IncompressibleFluid*

Considering the case of an incompressible fluid of constant density ($\rho = \rho_0$) Equation (3.1) is written as a differential equation for the variable ($\rho_0 c^2 + P$), as given by the following expression:

$$\frac{d}{dr}(\rho_0 c^2 + P) = -(\rho_0 c^2 + P)(1-2m/r)^{-1}\left[\frac{m}{r^2} - \frac{6amc}{r^3}(1-2m/r)^{1/2}\frac{V^{(\phi)}}{c} - \frac{1}{r}(1-2m/r)\left(\frac{V^{(\phi)}}{c}\right)^2\right] + (1-2m/r)^{-1/2} B_{(\theta)}\left[J^{(\phi)} - J^{(t)}\frac{V^{(\phi)}}{c}\right]. \quad (3.2)$$

which can be integrated numerically for appropriate boundary conditions. The corresponding pressure profiles are shown in Figs 1 to 8.

3.2 *Adiabatic Equation of State*

We assume the equation of state to be of the form

$$P = C_1 \rho^{\gamma} - B^2/8\pi \quad (3.3)$$

where C_1 is a constant and γ is the adiabatic index. Consequently, Equation (3.1)

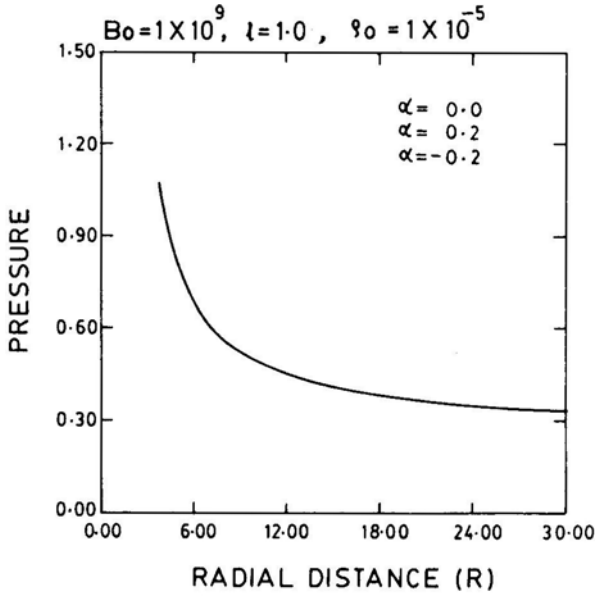

Figure 1. Pressure profiles for $\rho_0 = 10^{-5}$, $\alpha = 0, 0.2, -0.2$.

reduces to,

$$\frac{dP}{dr} = \left[-\left(\rho c^2 + c\rho_1^{\gamma} - \frac{B_{(\theta)}^2}{8\pi} \right)(1-2m/r)^{-1} \left(1 - \left(\frac{V^{(\phi)}}{c} \right)^2 \right)^{-1} \right.$$
$$\times \left(\frac{m}{r^2} - \frac{6amc}{r^3}(1-2m/r)^{1/2} \frac{V^{(\phi)}}{c} - \frac{1}{r}(1-2m/r) \left(\frac{V^{(\phi)}}{c} \right)^2 \right)$$
$$\left. + \frac{d}{dr}\left(\frac{B_{(\theta)}^2}{8\pi} \right) + (1-2m/r)^{-1/2} B_{(\theta)} \left(J^{(\phi)} - J^{(t)} \frac{V^{(\phi)}}{c} \right) \right] \tag{3.4}$$

which contains the arbitrary constant C_1. This is evaluated from the expression for Sound velocity $V_s^2 = \gamma c_1 \rho^{\gamma - 1}$. For known values of V_{s0} and $\rho_{0,}$ the sound velocity and density at the outer boundary of the disc respectively and for different values of γ, the pressure profiles (Figs 8 to 14) are obtained by integrating Equation (3.4) numerical.

4. Results and discussion

As the pressure expression depends on the rotation parameter '*a*' linearly, the case of corotating ($\alpha > 0$; $\alpha = a/m$) discs with respect to the central compact object can be distinguished from that of counter-rotating($\alpha < 0$)discs.We elaborate on this point for the two different cases considered above.

4.1 *Constant Density* ($\rho = \rho_0$)

Figs 1 and 2 show the pressure profiles in the case of an incompressible thin disc for $\alpha = 0, +0.2$, and -0.2 for two different densities. Fig. 1 corresponds to the case of

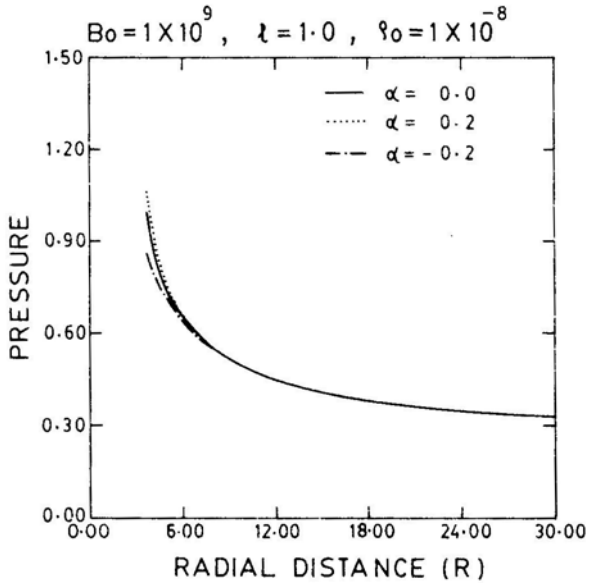

Figure 2. Pressure profiles for $\rho_0 = 10^{-8}$, $\alpha = 0, 0.2, -0.2$.

$\rho_o = 10^{-5}$ gm cm^{-3} (hereafter ρ is expressed in this unit), whereas Fig. 2 corresponds to the case when $\rho_0 = 10^{-8}$. On comparison we find that for lower values of densities, the pressure profile is sensitive to the direction of rotation of the disc and the effect is more prominent in the innermost regions of the disc. But the pressure profiles for higher values of densities do not illustrate this feature. This observation suggests that a corotating disc, for stability, requires higher pressure in the inner region as compared to the counter-rotating disc for a given set of parameters.

The pressure profiles further assert the existence of a critical combination of the surface magnetic field B_0 and density ρ_0 which gives physically reasonable pressure distributions. This was concluded earlier also, for a disc around a nonrotating compact object (BP). Figs 3 and 4 show the pressure profiles for two different magnetic fields for the same values of ρ_0. Fig. 5 gives the pressure profiles for the same values of α and ρ_0 but for different values of magnetic fields. It is clear that for $\rho_0 = 10^{-5}$, the magnetic field should not exceed $\simeq 10^9$ gauss. Figs 6 and 7 show the behaviour of pressure for the case of high magnetic field (10^{10} gauss) but for different values of α for both corotation and counter-rotation. It is interesting to note that in the case of corotation ($\alpha > 0$),the pressure increases towards the inner edge, whereas in the other case ($\alpha < 0$), the pressure decreases signifying the fact that the pressure gradient force in the inner region acts differently for corotating and counterrotating discs.

4.2 $\rho \neq$ *Constant*

The profiles for pressure and density as depicted in Figs 8 and 9 for $B_0 = 10^9$ gauss and $\rho_0 = 10^{-7}$ gm cm^{-3} again show the distinction for different values of α.

Fig. 10 shows the difference in pressure profile as a function of V_{s0} , the sound velocity at the outer edge of the disc. Pressure gradient varies slowly for varying values

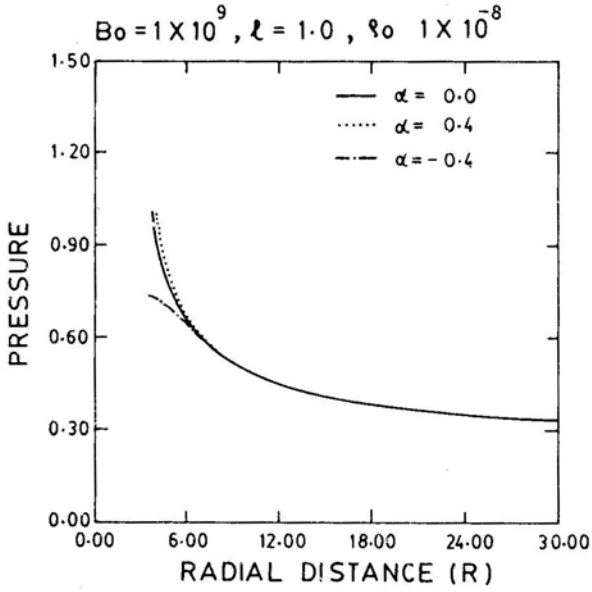

Figure 3. Pressure profiles for $B_0 = 10^9$, α = 0, 0.4, – 0.4

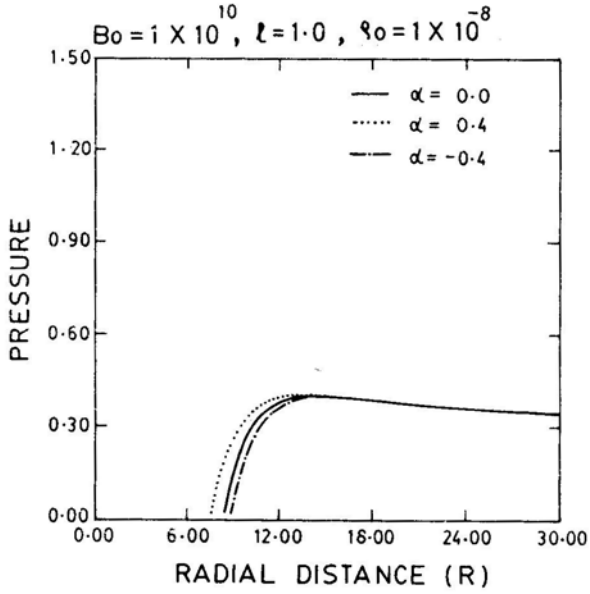

Figure 4. Pressure profiles for $B_0 = 10^{10}$, α = 0, 0. 4, – 0.4.

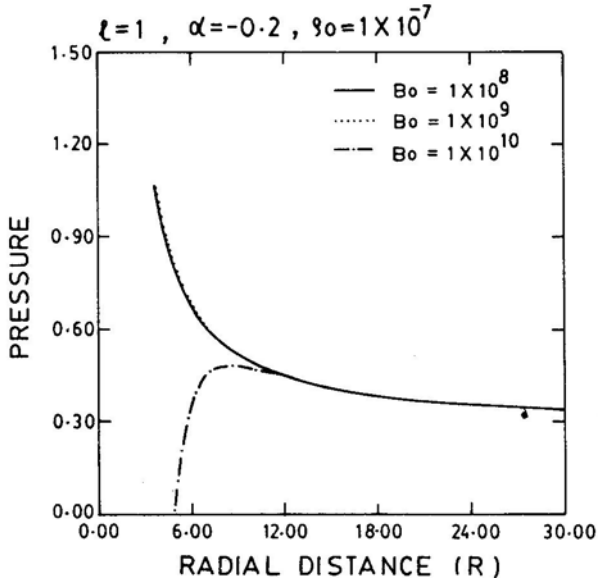

Figure 5. Pressure profiles for different B_0 and $\alpha = -0.2$.

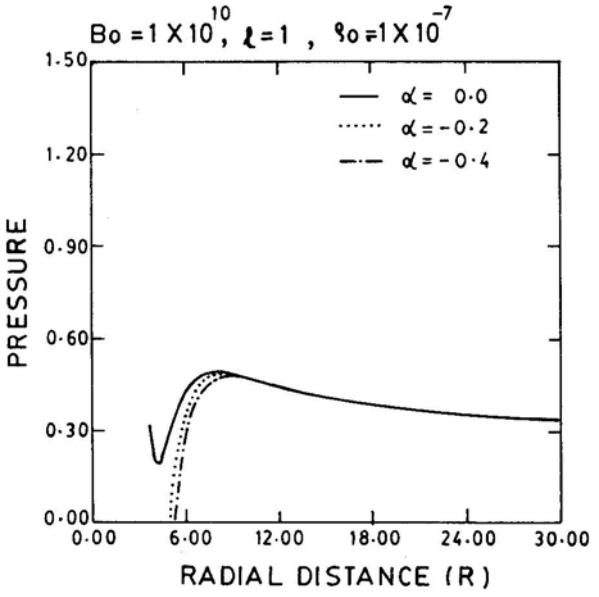

Figure 6. Pressure profiles for different values of α ($\alpha<0$) for $B_0 = 10^{10}$.

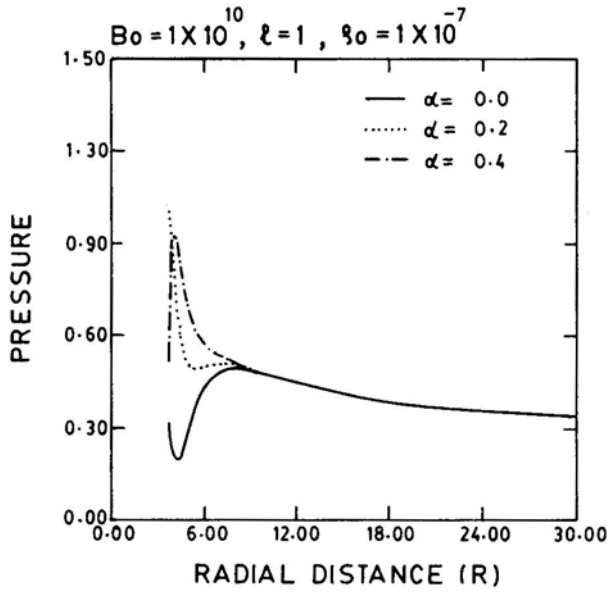

Figure 7. Pressure profiles for different values of α (α > 0) for $B_0 = 10^{10}$.

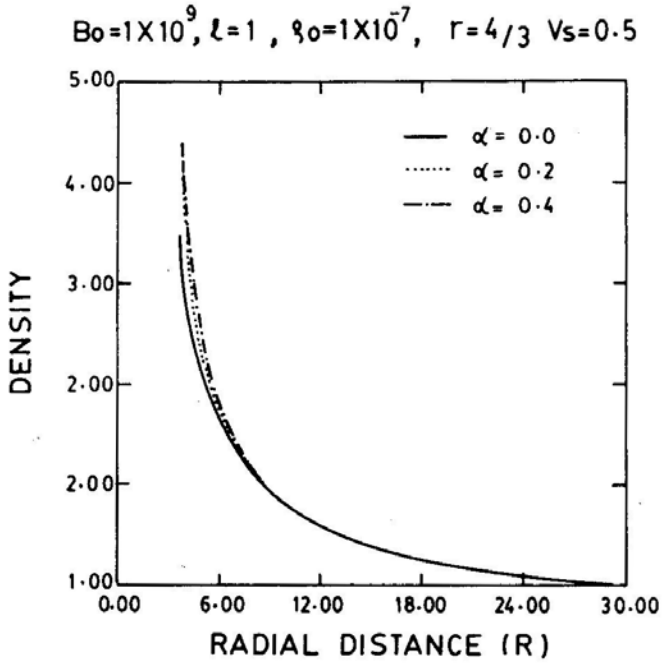

Figure 8. Density profiles for different values of α.

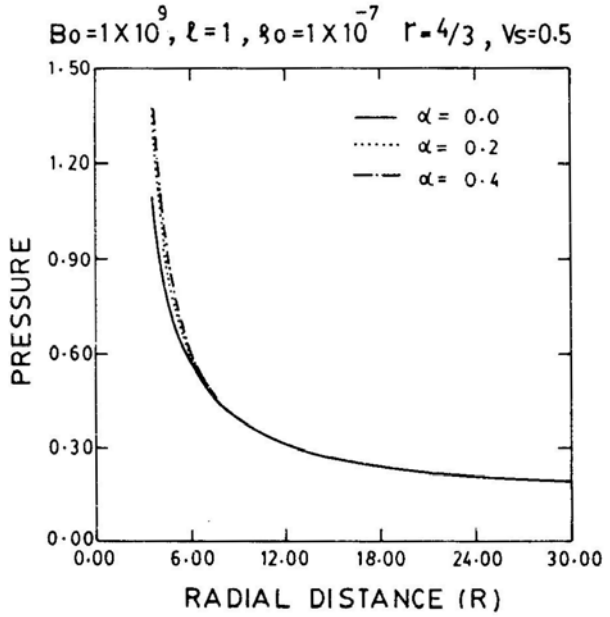

Figure 9. Pressure profiles for different values of α.

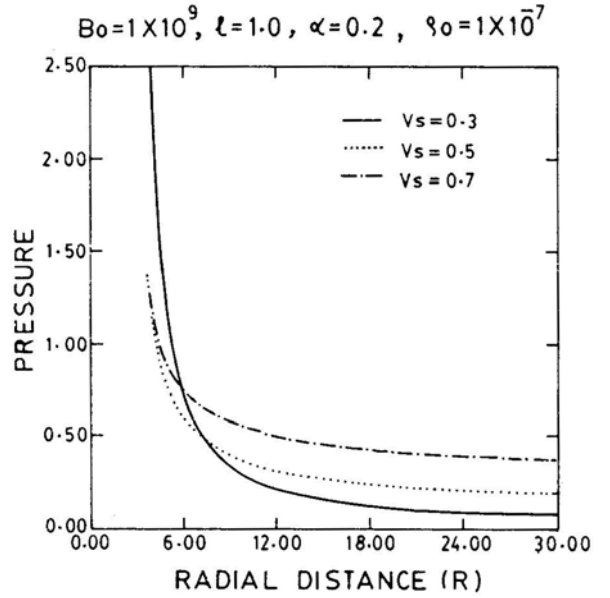

Figure 10. Pressure profiles for different values of V_{s0}.

of V_{s0} , the pressure in the inner region being larger for smaller values of V_{s0}. Fig. 11 shows the pressure profiles for the same value of α but with different values of the adiabatic index γ, whereas Fig. 12 shows the variation with respect to the angular momentum parameter $l(l=L/(cm))$ for $\alpha > 0$. It is to be noted that for low values of $l(l \simeq 0.1)$, the trend in the profile is substantially different from those for higher values. The corresponding case of counter-rotating disc ($l>0$, $\alpha < 0$) is shown in Fig. 13.

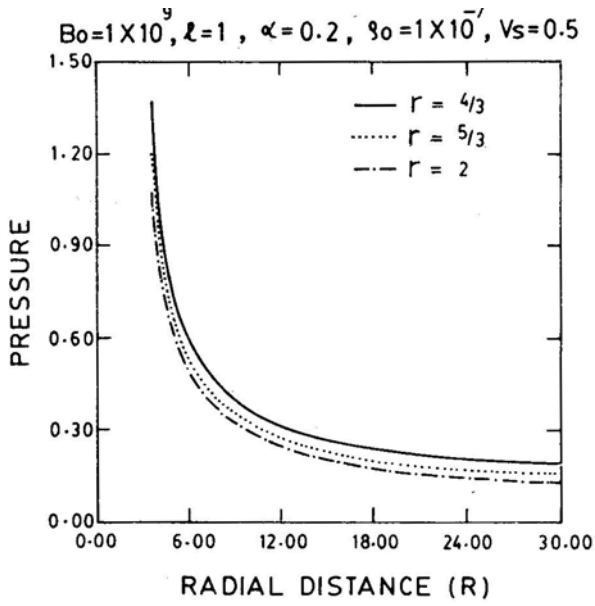

Figure 11. Pressure profiles for different values of γ

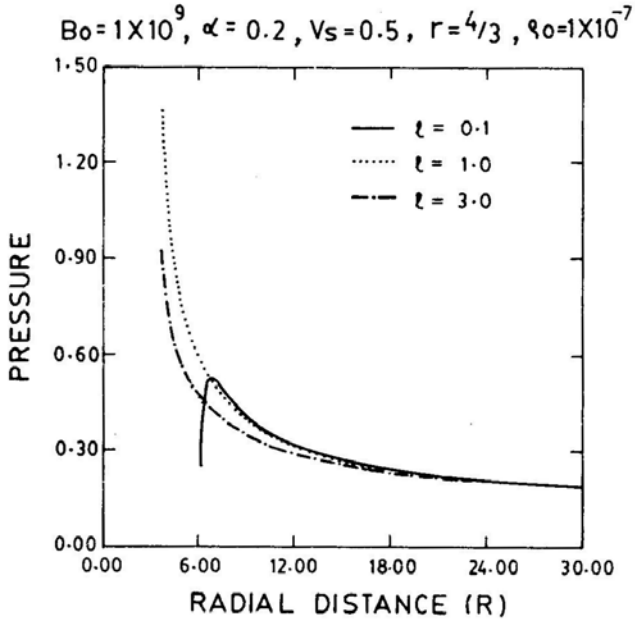

Figure 12. Pressure profiles for different values of l and $\alpha > 0$.

Fig. 14 depicts the behaviour for different initial values of the density for the same surface magnetic field B_0. It is evident that to have a monotonically increasing pressure towards the inner edge of the disc, the density at the outer boundary should be higher than a critical value for a given magnetic field.

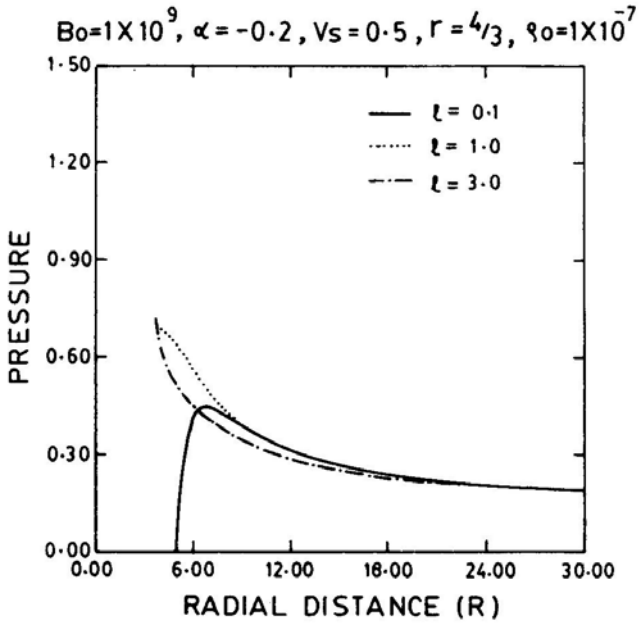

Figure 13. Pressure profiles for different values of l and $\alpha < 0$.

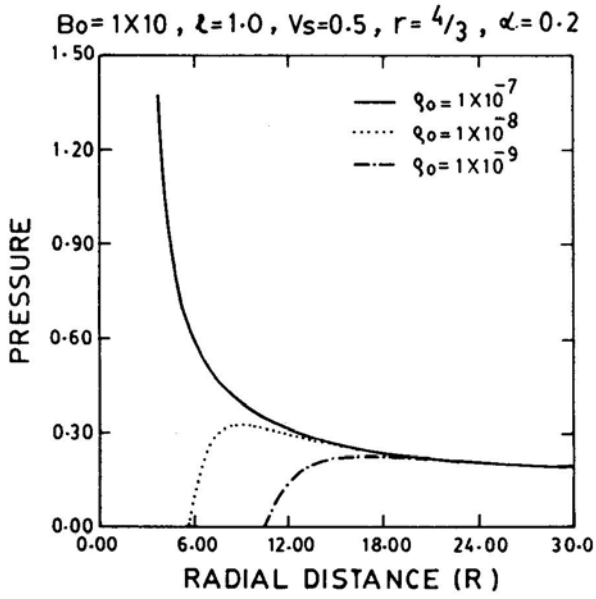

Figure 14. Pressure profiles for different values of ρ_0

4.3 *Structure of the Magnetic Field*

The structure of the magnetic field inside the disc is obtained by matching the interior solutions given by Equations (2.19) and (2.20) with that of the vacuum solutions at the boundary. The structure of magnetic field lines is shown in Figs 15 and 16. Fig. 15

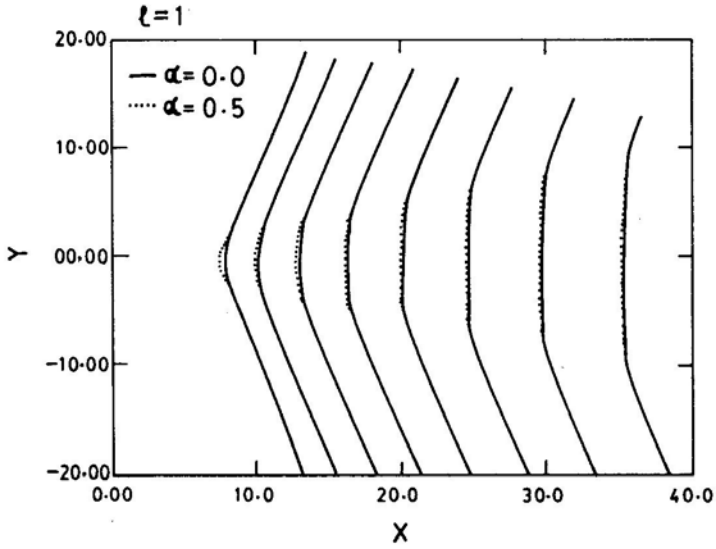

Figure 15. Structure of magenetic field line for corotating disc.

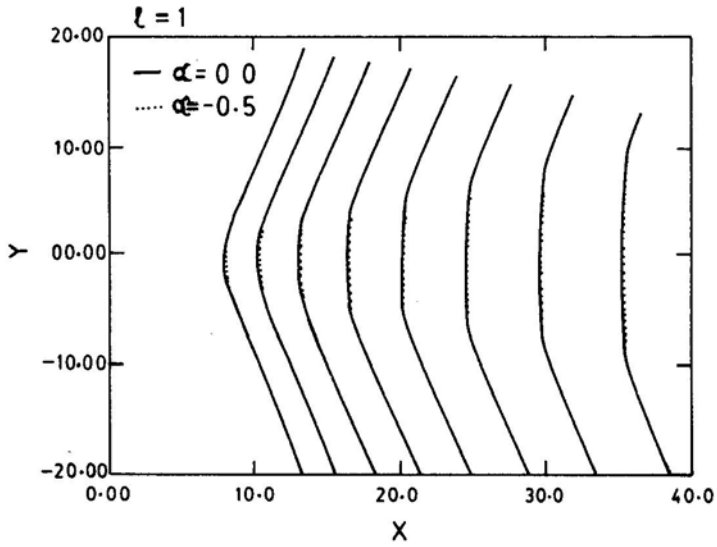

Figure 16. Structure of magenetic field line for counter rotating disc.

shows the field lines for $\alpha = 0$ (static central object) and for $\alpha = 0.5$ (disc crotating with the central object). Fig. 16 shows the same for $\alpha = 0$ and $\alpha = -0.5$ (disc counter-rotating with respect to the central object). It is seen that for the case of corotating disc the field lines are pulled in as compared to that of a disc around a static object, whereas for counter-rotating disc they are pushed out.

5. Concluding remarks

In the case of accretion onto neutron stars through an accretion disc, the role of rotation of the central compact body plays an important role in the establishment of the equilibrium structure. As the effective potential on a single particle does show a good deal of difference between the co and counter-rotating orbits (Prasanna & Dadhich 1982), the momentum balance at the boundary layer between the disc inner edge and the stellar surface does behave differently for the co and counter-rotating discs, as depicted by the pressure profiles at the inner edge. However, the actual dynamics depends on combinations of several parameters like the outer density ρ_0, the surface magnetic field B_0, the angular momentum l and the rotational velocity of the central source a. It is premature to draw any definitive conclusions at this stage. The preliminary studies made above need to be extended to the case of non-zero radial velocity of the plasma ($V^r \neq 0$) and this would definitely bring in more detailed structure of the boundary layer with possible shear due to the interplay of the fluid motion and the effects of inertial frame dragging which definitely depends on the sense of the angular momentum coupling αl. The role of the magnetic field in defining the boundary layer is also very important as the interaction of currents within and outside the disc could have different strength for co and counter-rotating plasma discs. These studies are in progress.

Acknowledgement

We are grateful to A. C. Das for many fruitful discussions.

References

Bhaskaran, P., Prasanna, A. R. 1989, *Astrophys. Sp. Sci*., **159,** 109, (BP).
Bhaskaran, P., Prasanna, A. R. 1990, *J. Astrophys. Astr*., **11**, 49, (BP).
Prasanna, A. R., Bhaskaran, P. 1989, *Astrophys. Sp. Sci.,* **159**, 201, (PB).
Prasanna, A. R., Dadhich, N. 1982, *Nuovo Cim*., **72B**(1), **42**.

J. Astrophys. Astr. (1990) 11, 475– 490

High Resolution Spectroscopy of R Coronae Borealis during the 1988–1989 Minimum

David L. Lambert *Department of Astronomy, University of Texas, Austin, Texas, USA*

N. Kameswara Rao & Sunetra Giridhar *Indian Institute of Astrophysics, Bangalore 560034*

Received 1990 June 14; accepted 1990 August 20

Abstract. Moderate-resolution spectra of the C_2 Swan 0–1 bandhead, the Na I D lines and the K I resonance lines near 7660 Å obtained at minimum light during the 1988–1989 decline of R CrB are discussed and interpreted in terms of a popular model for R CrB declines. High-resolution spectra obtained at maximum light show blue-shifted chromospheric emission in the cores of the Na I D and the Sc II 4246.8 Å lines.

Key words: spectroscopy, R CrB — 1988-1989 minimum

1. Introduction

The class of R Coronae Borealis stars (RCBs) must be among the least well understood peculiar stars. Chief among the puzzling characteristics of RCBs is the origin of the irregularly occurring deep minima. As RCBs in decline are observed spectroscopically with contemporary telescope and instrumentation, one may suppose that novel insights will be gained into the origin of the mysterious declines and the ensuing changes in the atmospheric structure. In this paper, we present and discuss high-resolution high signal-to-noise ratio spectra in intervals containing the C_2 Swan 0–1 bandhead at 5634 Å, the Na I D lines at 5890 and 5896 Å, and the K I resonance lines at 7663 and 7699 Å. The spectra were obtained during the minimum of R Coronae Borealis (R CrB) that began in 1988 July in which the star faded to $m_v \sim 11$ by 1988 September with a recovery to maximum light ($m_v = 5.8$) achieved by the spring of 1989. We observed R CrB twice at minimum in 1988 September–October and again in 1989 February when at $m_v \simeq 7.5$, the star was rising to maximum brightness. In 1990 January, we observed the Na I D lines when R CrB was at maximum. High resolution observations at maximum light were acquired of selected lines to search for chromospheric emission.

Several discussions of spectroscopic monitoring of R CrB through earlier declines have been given in the literature: *e.g.*, Herbig (1949), Payne-Gaposchkin (1963), Rao (1974), and Holm *et al.* (1987). The 1988-1989 minimum was observed intensively by Cottrell, Lawson & Buchhorn (1990, hereafter CLB) in selected spectral intervals at moderate resolution and signal-to-noise ratio. Key spectroscopic signatures of R CrB in decline were noted first by Joy & Humason (1923). These signatures are not peculiar to R CrB for they recur in the extensive spectroscopic (and photometric) study of RY

Sgr conducted by Alexander *et al.* (1972) between 1967 and 1970 including the very deep minimum of 1967-1968 when RY Sgr faded by about 8 mag (see also Spite & Spite 1979).

Specific signatures denote the decline, the minimum, and the recovery to maximum light of an RCB star. Herbig (1949) noted that spectrograms at 75 Å mm $^{-1}$ taken as R CrB faded to $m_v \sim 10$ "showed no perceptible change in the absorption spectrum" relative to spectra taken at maximum light. In the 1948-1949 minimum discussed by Herbig, R CrB faded to a visual magnitude of 14, or 2 to 3 magnitudes below the 1988-1989 minimum. At $m_v \sim 10$, sharp emission lines appeared in the spectrum. In the 1988 decline, CLB's spectra at 0.5 Å resolution and low S/N show sharp emission lines appearing at $m_v \sim 7.7$. CLB assert that photospheric absorption lines, even the C I high-excitation lines, are filled in by emission very early in the decline; their notes indicate this to occur at $m_v \sim 6.6$ or less than a magnitude below the maximum. The emission lines are generally attributed to an extensive chromosphere that IUE observations of the emission lines Mg II 2800 Å and C II] 1335 Å at maximum light show to be most probably a permanent feature of R CrB (Rao, Nandy & Bappu 1981; Holm & Wu 1982). An outstanding characteristic of the sharp emission lines is that, in the decline from maximum light, they are blue-shifted by 10 to 15 k m s $^{-1}$ with respect to the photospheric velocity at maximum light. This velocity difference, which was noted first by Joy & Humason (1923), has been reported for all well-observed minima including that of 1988-1989 (CLB). Additional emission features include the CN violet system band near 3883 Å (Herbig 1949,1968), the C_2 Swan bands (Payne-Gaposchkin 1963), and the [O II] doublet discovered by Herbig (1949). Quantitative spectroscopy of these features has not been reported.

A distinctive set of emission lines is seen at faint magnitudes. Broad (FWHM ~ 200 km s $^{-1}$) emission lines of He I 3889 Å, Ca II H and K, and Na I D lines are seen with approximately parabolic profiles (Rao 1981). These lines, which are unshifted with respect to the photospheric velocity, are sometimes accompanied by blue-shifted absorption at a velocity of 100 to 200 km s $^{-1}$. These emission lines, which were seen first by Joy & Humason (1923) and have been seen at subsequent faint minima of R CrB, have been seen also in RY Sgr at minimum (Alexander *et al.* 1972; Spite & Spite 1979). Even the cool R CrB star U Aqr at minimum shows the broad line at 3889 Å, which is even stronger than the Ca II H and K lines (Bond, Luck & Newman 1979). It is usually supposed (*e.g.*, Feast 1986) that these lines arise from the expanding circumstellar shell.

The photospheric spectrum has been reported to change character at minimum light Herbig (1949) refers to the spectrum as "heavily veiled ", *i.e.*, the lines appear diluted or, perhaps, broadened by a continuous spectrum. Payne-Gaposchkin (1963) refers to the "absorption spectrum, whose line profiles undergo distortion or doubling at times". Herbig noted the onset of veiling to occur at $m_v \sim 10.8$ in the decline. Payne-Gaposchkin(1963)reports that veiling first occurred in the 1960 minimum at $m_v \sim 10.5$ following the initial minimum at $m_v \sim 11.0$ that occurred 50 days earlier with only minor increases in brightness separating the minima. This veiling appears to differ from the weakening and disappearance of lines that occurs with the emergence of the chromospheric lines. The veiled absorption spectrum seems to be that of the normal photosphere, but quantitative descriptions have never been given.

In the following sections, we present and discuss high-resolution spectra in the context of the principal spectroscopic signatures and a popular phenomenological model of the declines that are a unique characteristic of the RCBs.

2. Observations

R Coronae Borealis was observed at the W. J. McDonald Observatory in 1988 September-October when the star was at minimum light (V ~ 10–10.5) following the onset of the decline in early July. Three spectral regions, each about 50 Å wide and at a spectral resolution of 0.2 Å were observed with the coudé spectrometer of the 2.7 m reflector (see Table 1). The detector was a Texas instruments CCD. Since telluric lines contaminate the exposures at 5880 and 7681 Å, a hot rapidly rotating star was observed at these wavelengths and at an airmass similar to that at which R CrB was observed. Then, the ratio of the R CrB spectrum to that of the hot star is almost devoid of telluric lines. The trio of spectra were acquired again in 1989 Feburary when R CrB was at $m_v \sim 7.5$. The interval at 5880 Å including the Na I D lines was observed in 1990 January when R CrB was at maximum light. Spectra of selected lines were obtained in 1990 at a resolving power $\lambda/\Delta\lambda$ ~100,000. In this paper, we discuss high-resolution spectra of the Na I D lines and the strong Sc II line at 4246.8 Å.

The Na I D lines. Emissioninthe Na I D lines is the outstanding feature of the two spectra taken when R CrB was at minimum (Fig. 1). The absorption lines of He I at 5876 Å, C I and Fe I at minimum have profiles similar, but not identical, in strength and shape to those in the spectra taken on the rise to maximum and at maximum. This similarity is shown in Fig. 2 where the illustrated spectra are those obtained by subtracting the spectrum at maximum light from those obtained in the 1988-1989 decline. We refer to these spectra obtained by the subtraction as "differenced" spectra; the continuum of a differenced spectrum is set at unity. The only strong features in the differenced spectra at minimum light are the Na I D lines with their complex profiles. Small residuals appearing at the positions of the photospheric lines are probably due to slight changes in the strength and shape of the photospheric lines. These changes may be unrelated to the occurrence of the deep minimum and may be due to the pulsation of the envelope. Our spectra certainly show that "veiling" did not occur. Veiling at the 1949 and 1960 minima was reported when the star was fainter than the limit reached in this minimum. In order to interpret correctly such small changes of the photospheric lines, it will be necessary to determine the instrumental profile and to

Table 1. Radial velocities (km s^{-1}) during the 1988–1989 decline.

		λ(Å)	C I	Fe I	Others	Na I[a]
1988	Sep 30	5880	23.6 (3)[b]	18.1 ± 2 (6)	20.3 (3)	21[c]
						−115[d]
	Oct 1	7681	22.9 (4)	21.9 (1)	21.5 (4)	
	Oct 2	5616	22.0 (4)	21.5 (3)	21.9 (2)	
	Oct 20	5880				−170[d]
	Oct 21	7681	23.1 (4)	27.4 (1)	21.6 (4)	
1989	Feb 22	5616	21.5 (4)	21.6 (2)	20.4 (3)	
		5880				−174[d]
	Feb 23	7681	22.1 (4)	20.2 (1)	21.0 (4)	

[a] The sharp (interstellar/circumstellar) absorption is at – 22 km s^{-1}.
[b] The number in parentheses is the number of lines contributing to the mean velocity. Estimated errors are less than ± 2 kms $^{-1}$.
[c] Sharp emission.
[d] Broad absorption.

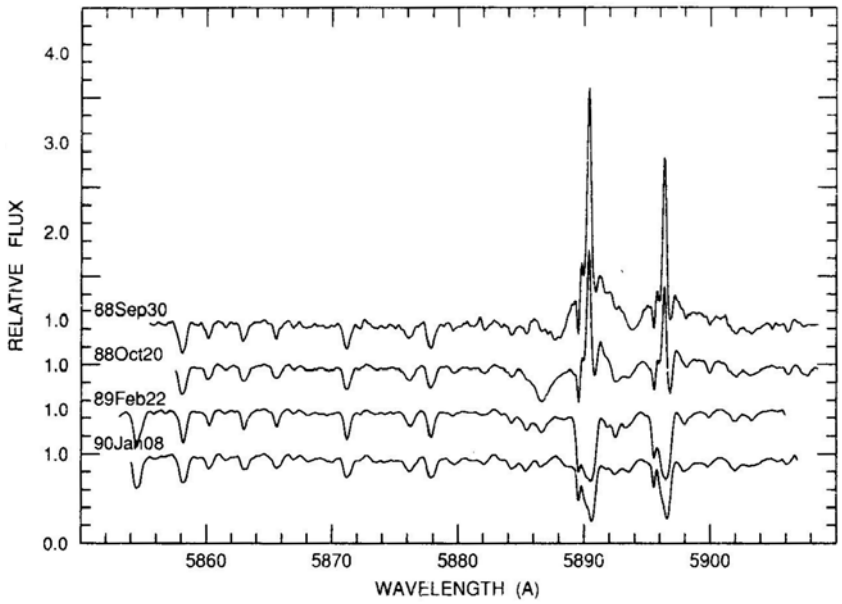

Figure 1. The spectrum of R CrB around the Na I D lines. Three spectra obtained during the 1988–1989 decline and a spectrum at maximum light are shown.

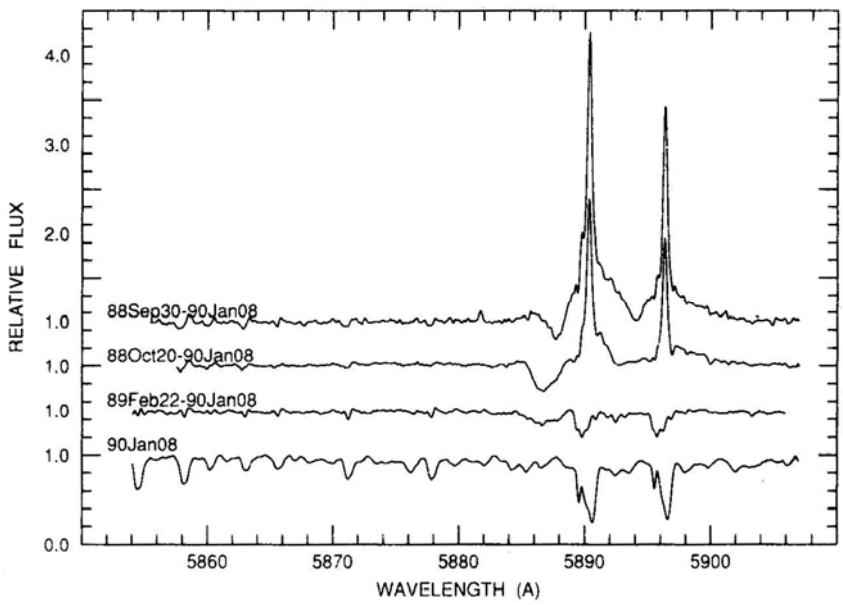

Figure 2. Three "differenced" spectra (see text) of R CrB derived from the spectra shown in Fig. 1. The spectrum at maximum light is also shown.

monitor the lines at maximum light. It should be noted that the photospheric absorption lines were used to set the individual spectra onto a common wavelength scale. Hence, velocity differences from exposure to exposure are ignored in the construction of the differenced spectra. Estimates of radial velocities were made using

either the telluric H_2O lines or hollow cathode (ThAr or FeNe) lines as a reference. These velocities are given in Table 1. Since the small variations are consistent with the known low amplitude velocity variations seen at maximum light (Raveendran, Ashoka & Rao 1986), we assumed that the absorption lines could be shifted into coincidence before the subtraction.

Our spectra show no evidence for broad emission in the He I 5876 Å feature. Such a component at Na I D is obvious in the original and the differenced spectra for 1988 September 30. If the broad 5876 Å profile is assumed to be similar, we may set an upper limit to its flux of about 5 per cent of the continuum flux. Unfortunately, we do not know whether the He I 3889 Å contributed a broad emission line at this minimum. Observations of previous minima would suggest that the latter line must have been present.

The Na I D lines at minimum show a complex profile superimposed on the photospheric spectrum: a sharp intense emission and a weaker broad emission line with a blue-shifted absorption component. Note that the weak, sharp emission component to the blue of the strongest component on 1988 September 30 is the terrestrial Na I D emission. On the assumption that the emitting layers are optically thin in the Na I D lines, the differenced spectra will correctly represent the emission profiles. The assumption is also valid for the case where the optically thick (or thin) emitting layer is not projected onto the photosphere. The blue-shifted (–22km s^{-1}) sharp absorption line seen in the spectrum at maximum light is contributed by circumstellar or interstellar gas. This gas must impose an absorption line on the emission profile that is not removed by the procedure of subtraction: a more refined procedure would allow this line to be removed.

The sharp Na_I emission lines have relative fluxes in the ratio $D_1/ D_2 \sim 0.6$(1988 September and October). Since these are slightly higher than the ratio (0.5) for an optically thin layer, the emitting layer is marginally optically thick. It is unlikely that this condition seriously compromises the use of the differenced spectra. The lines are blue-shifted with respect to the photospheric lines by about 2 km s^{-1} when the mean photospheric velocity of + 23 ± 1 km s^{-1} is adopted for high excitation C I lines. This small shift is in contrast to the shift of about 10 km s^{-1} (CLB) determined from the sharp Ti II and Sc II lines about 50 days earlier (1988 August). CLB's measurements of the Na ID lines appear to confirm that the lines are less blue-shifted than the other lines. The line width (FWHM) of the stronger narrow emission component is about 20 km s^{-1} which is the instrumental width provided by the emission lines of the hollow cathode lamp. The Na I emission lines are substantially narrower than the photospheric absorption lines (FWHM ~ 44 km s^{-1} without correcting for the instrumental width).

The emission component of the broad P Cygni profile is more prominent on 1988 September 30 than on 1988 October 20, but the blue-shifted absorption component is much stronger on the latter date. The half width of the emission at its base is 250 ± 10 km s^{-1} (1988 September 30) (as determined from the redwing of the D_1 line in the differenced spectrum). This value is typical of the broad emission lines seen in the earlier declines of R CrB (Rao 1981). The line is approximately centred on the photospheric velocity.

The differenced spectra show that the blue-shifted absorption component is most prominent on 1988 October 20. On 1988 September 30, the broad absorption was at a velocityof –140 km s^{-1} relative to the photosphere. The absorption on1988 October

20 is centred at about –190 km s $^{-1}$ relative to the photosphere. This absorption component is much weaker on 1989 February 22, but at the velocity observed 4 months earlier. According to CLB high velocity emission was first seen on 1988 July 30 when m_v = 7.9 and the decline was about 3 weeks old. CLB confirm that the absorption was present on 1989 February 2, 17 and 18, but was apparently absent on 1989 March 21. It must be noted, however, that CLB's comments and velocity estimates are based on the observed and not differenced spectra. Furthermore, their spectra are at a modest resolution and S/N. We suggest that examination of differenced spectra is needed to be certain of the first appearance of the high velocity absorption component.

High-resolution spectra of the Na I D lines at maximum light in 1990 May are shown in Fig. 3. These spectra show that the sharp absorption line at – 22 km s $^{-1}$ in the 1990 January 8 spectrum (Fig. 1) consists of two components or possibly a single absorption line with sharp emission superimposed. The sharp Na I D line at –22 km s $^{-1}$ was reported by Keenan & Greenstein (1963), but not resolved by them into two components. Our new spectra show structure in the deep core of the Na I D photospheric lines. Moreover, similar spectra obtained in the earlier months show that this structure is variable. We identify this structure as the blue-shifted chromospheric emission line.

The K I 7664 Å Lines. Examination of our three spectra shows that there are no large changes in the profiles of the K I resonance lines. An absence of strong chromospheric and circumstellar emission in the K I lines at minimum light is not unexpected. The doublet ratio shows that the Na I D lines are not very optically thick. Then, the Na and K emission lines will be roughly proprotional to the elemental abundances. Since the relative abundances of elements heavier than oxygen appear to be solar (Schönberner

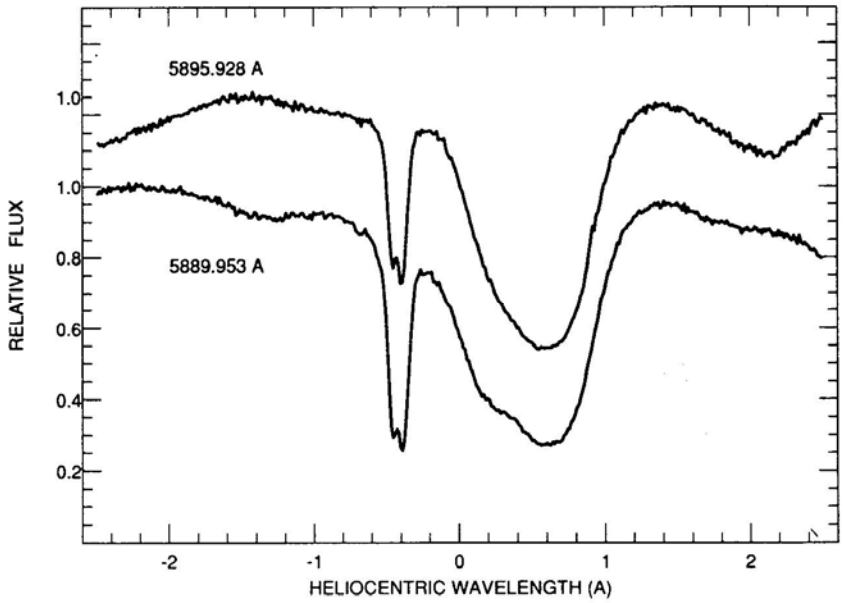

Figure 3. High-resolution spectra of the Na I D lines in the spectrum of R CrB near maximum light.

1975; Cottrell & Lambert 1982), the K I lines will be about a factor of 16 weaker than the Na I D lines. Our observations are consistent with this estimate. Similarly, the absence of high velocity absorption components in the K I lines is due to the low abundance of K.

The C_2 Swan System 0–1 Band. The two spectra of the 0–1 bandhead at 5634 Å are shown in Fig. 4. The C_2 bandhead is appreciably stronger at minimum light. C_2 lines shortward of the blue-degraded head are also strengthened. This is shown with remarkable clarity in the ratioed spectrum in Fig. 4. A ratio of the minimum and maximum spectra is more appropriate for separating the spectrum of the cooler layers giving the C_2 band. However, tests show very little difference between the 'differenced' and the 'ratioed' spectra. The ratioed spectrum is compared in Fig. 5 with a spectrum of the cool RCB WX CrA taken in 1989 July with the Cassegrain echelle spectrometer at the 4 m telescope of the Cerro Tololo Inter-American Observatory. The line for line correspondence between the two spectra is good evidence that the additional C_2 absorption in RCrB at minimum is provided by gas at about the photospheric temperature of WX CrA (~ 4000–5000 K) and not the low temperatures expected in the circumstellar shell. The gas is too cool to contribute absorption lines to the high excitation He I and C I lines and other lines seen in our spectra. The purity of the ratioed spectrum shows that the contributing C_2 molecules have the radial velocity of the photosphere. Such a conclusion was reached by Rao, Giridhar & Ashoka (1990) for the atoms contributing enhanced neutral metal lines in R CrB during the initial decline of an earlier minimum.

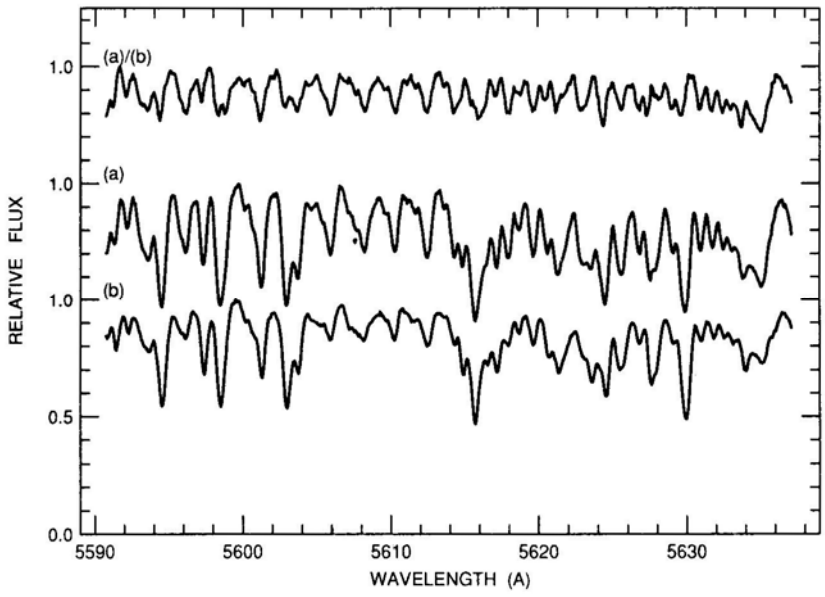

Figure 4. Spectra of R CrB around the C_2 Swan 0–1 bandhead at (a) minimum (1988 October) and (b) near-maximum (1989 February) light together with the "ratioed" spectrum (top spectrum).

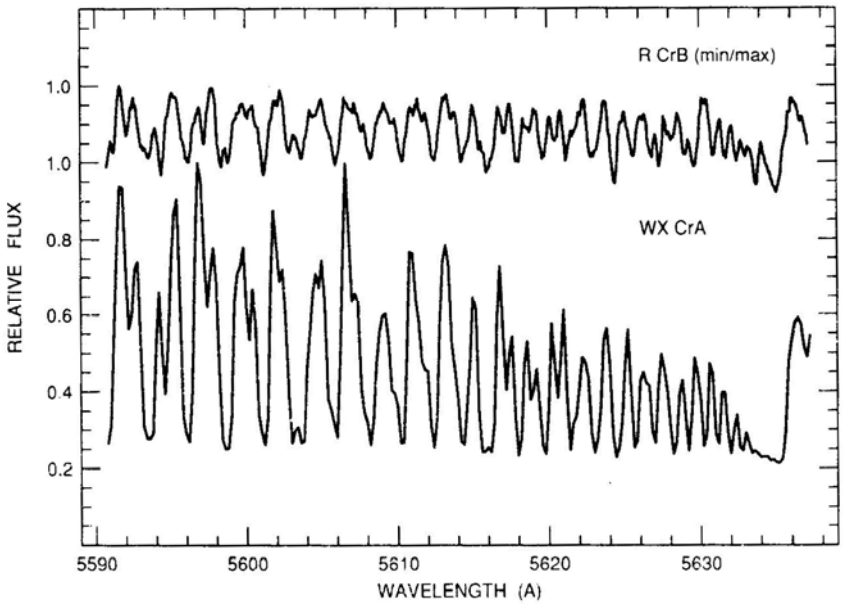

Figure 5. The C_2 0–1 bandhead in the "ratioed" spectrum of R CrB and a spectrum of the cool RCB star WX CrA.

3. Comments on a model of RCB decline

3.1 *A Synopsis of the Model*

The suggestion that the decline of an RCB was due to clouds of carbon dust near the star was made more than 50 years ago (Loreta 1934; O'Keefe 1939). A variety of observations confirms this suggestion. Questions remain unanswered about the location of the dust, and in particular, about the trigger that leads to the production of the dust. In the following remarks, we discuss a popular empirical model that is reviewed by Feast (1986).

This model supposes that an RCB star ejects a puff or spray of dust. At a single ejection dust is ejected into a cone with a semi-angle of about 20°. One or two ejections occur in each pulsation cycle of the RCB. The ejection points are randomly distributed above the stellar surface. Deep minima are caused when an ejection point is on or near the line of sight. The circumstellar shell whose infrared radiation provides an RGB's infrared excess represents the debris of many ejections and emits, therefore, a relatively constant infrared flux. Dust in a fresh ejection and in the circumsteller shell is expelled from the star by radiation pressure. Gas is mixed with the dust and dragged outward at a velocity less than that of the dust. Fadeyev (1988) treated the problem of carbon dust condensation in RCB stars based on the empirical model stated above and could successfully model the light curves.

Can the empirical model account for the key spectroscopic signatures of a decline? Our discussion will be made with reference to Fig. 6. Dust assumed to form at a location P is driven radially outward by radiation pressure and dispersed laterally. In the figure we show the dust cloud as a thin shell. It is possible that dust formation

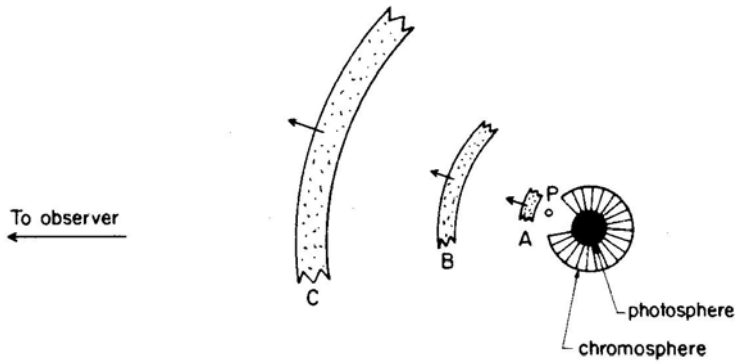

Figure 6. A model for shell formation and ejection around R CrB. Dust formation occurs near point P. Three snapshots are shown of a dust cloud moving away from the star and expanding laterally.

continues for an extended time so that the shell is thick. The location of P is quite uncertain. It is presumably at or above the distance (a few stellar radii) at which the equilibrium temperature of small grains is less than the sublimation temperature. In Fadeyev's model the dust condenses at ~20 R_* from the ejected gas. In Fig. 6, we show the chromosphere to be quenched below P but this is not demanded by the observations. The trigger for dust formation may be related to turbulence or the pulsation of the photosphere. A density enhancement caused by pulsation may lead to dust condensation (Fadeyev 1988). Presence of turbulence is indicated by the large widths of the photospheric lines. Such turbulence may heat the chromosphere. Perhaps a few large (or small) turbulent elements provide the bulk of the heating. As their numbers vary stochastically it may be possible for the chromosphere to cool sufficiently to allow formation of dust. A somewhat similar explanation was proposed by Wdowiak (1975) for dust formation in a granular or supergranular network in R CrB. The carbon grains may initiate further cooling and additional grain formation.

In the early phases of the decline when the leading edge of the dust cloud is at point A (Fig. 6), the principal spectroscopic consequence is, as observed a dimmning of the photospheric spectrum. The photometric consequence of an optically thick cloud spreading across the visible hemisphere is readily shown to be a large dimming for a modest change of colour; *i.e.*, $R = \Delta V/\Delta(B–V)$ is large (Pugach 1984). The star will become bluer as the chromospheric emission lines provide the dominant contribution; CLB refer to this behaviour as a 'blue decline'. If the initially optically thin cloud quickly covers a large portion of the visible photosphere and becomes increasingly optically thick, the star will first become redder as it is dimmed; CLB refer to this as a 'red decline'. The 1988–1989 decline was a 'blue decline' (CLB).

When the dust cloud is at point B, the photosphere appears fully covered and the emission line spectrum from the unobscured portions of the chromosphere must dominate the observed spectrum. An earlier appearance of the emission lines will depend on their brightness relative to the photospheric continuum. CLB reported emission lines at $m_v = 7.4$ in the decline (*i.e.*, the photospheric flux was reduced by a factor of 4.4) and a filling in of the absorption lines was detected even earlier. In the 1949 decline, the sharp emission lines were seen at $m_v \sim 10$, but were not seen on earlier plates at $m_v \sim 8.5$when the photospheric flux was about 10 percent of its normal value.

Continued development of the cloud will lead to obscuration of the chromosphere and to a steady weakening of the chromospheric emission lines. Furthermore, one expects, as is observed (Payne-Gaposchkin 1963; CLB), the character of the emission line spectrum to change as the height above the photosphere of the unobserved area increases.

The slow recovery from the minimum occurs as the dust cloud expands and disperses. It is to be expected that, in the break-up of the cloud, the photosphere and chromosphere will brighten in unison. Therefore, the chromosphere's emission lines will be much less prominent in the recovery phase than in the decline to minimum when areas of the chromosphere are unobscured but the photosphere is obscured. This difference between the decline and the recovery phases is observed—see Rao, Vasundhara & Ashoka (1986), who observed the 1972 minimum of R CrB, and Alexander *et al.* (1972) for RY Sgr. Since the fading to and recovery from minimum light are controlled by different processes, it is not surprising that the timescales for the two phases are different.

3.2 *The Sharp Emission* (*Chromospheric?*) *Lines*

The observed blueshift (about $\leqslant$ 10 km s^{-1}) of the sharp emission lines relative to the mean photospheric velocity suggests an expansion of the region that we term the chromosphere—see Section 3.4. Since such a shift is observed at each minimum, it must be a general property of the chromosphere during a decline. In order to obtain further information about the chromosphere, we searched at maximum light for chromospheric emission in the deep cores of photospheric lines. As noted earlier, the Na I D lines show highly asymmetric cores that we attribute to filling in by blue-shifted chromospheric emission. Confirmation of this identification is provided by observations of a line that is prominent in chromospheric spectra during the decline phase.

High-resolution spectra were obtained of the Sc II 4246.8 Å line. A comparison of the Sc II line in R CrB at maximum light and in the normal F supergiant δ CMa is offered in Fig. 7; δ CMa was shown by Cottrell & Lambert (1982) to be a fair match to R CrB. The core of the Sc II line in R CrB is not that expected of a strong photospheric line. Since the core of this line in δ CMa is smooth and symmetrical, the distorted core in R CrB is probably not due to a blend of photospheric lines. We attribute the distortion to the superposition of a chromospheric emission line on the deep core of the photospheric line with the former shifted relative to the latter by about – l0km s^{-1}. Moreover, as was found for the Na I D lines, the chromospheric contribution is variable. These high-resolution observations suggest that the blue-shifted chromospheric lines seen in a decline are present at maximum light and possibly a permanent feature of R CrB.

If the fluxes of the chromospheric components to the Na I D and Sc II lines are unchanged in a decline, they will equal the photosphere's continuum flux when the photosphere has declined in brightness by a factor of about 10. CLB first recorded "Sc II, Ti II, and Fe II emission" at $m_v \leqslant 7.4$ or 1.6 magnitude below maximum light and on earlier spectra at m_v = 6.8 and 7.3, the photospheric lines were filled in to a noticeable extent. CLB observed first appearance of chromospheric emission lines is roughly consistent with our estimate based on the emission components identified at maximum light.

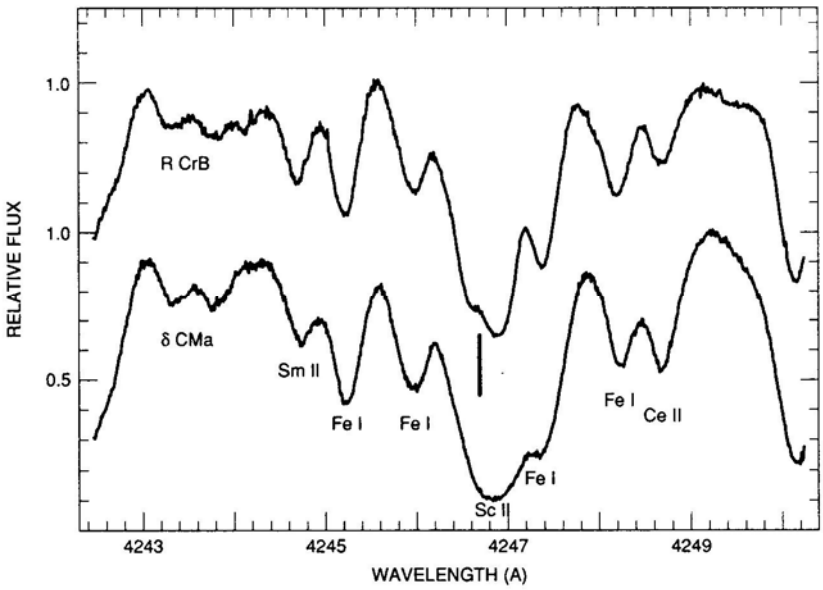

Figure 7. High-resolution spectra near 4247 Å of R CrB near maximum light and the F supergiant δ CMa. The blue-shifted chromospheric emission in the core of R CrB's Sc II 4246.8 Å line is marked by the short vertical line.

One supposes that the blueshift arises from an expansion of the chromosphere. If the chromosphere is approximately spherically symmetric, an optically thin emission line seen from areas unobscured by a cloud at point B or at later times should be unshifted with respect to the photosphere, but broadened by an amount of the order of the expansion velocity. For large optical depths, emission might be expected to come predominantly from the blueshifted gas nearer the observer, but thanks to the velocity gradient along the line of sight, large optical depths in the lines will be difficult to maintain. Accurate line profiles determined from differenced spectra such as those in Fig. 2 would be of real interest. The sharp Na I D lines at the time of our observations show only a very small blueshift and the line profiles are qualitatively consistent with formation in an almost stationary chromosphere.

The onset of dust formation may lead to local changes in the chromospheric structure. If, for example, the chromosphere is quenched below the site of dust formation (point P, Fig. 6), the reduced gas pressure may cause the bordering chromospheric regions to flow into the quenched regions. This flow would lead to a blueshift of the chromospheric lines with a maximum value approximately equal to the sound speed (*i.e.*, about l0 km s^{-1}) . The regions of the quenched chromosphere are presumably the site for the C_2 molecules contributing the enhanced molecular lines. If the chromosphere could be observed at a time when dust was forming at a point on or near the far side of the star, the chromospheric lines may show a redshift This test should be possible, in principle, using the ultraviolet emission lines.

If the site of dust formation is placed in or below the expanding chromosphere, the contrast of the chromospheric line relative to the photospheric continuum will

increase as dust obscures the photosphere. Then, the chromospheric layers projected onto the photosphere will give the dominant contribution to the emission line spectrum and net blueshift will be recorded as long as the chromosphere is expanding. However, this model raises difficult questions: can a chromosphere of high density (Payne-Gaposchkin 1963) be maintained with a substantial content of dust in or above it? Fadeyev (1983) proposed that the sharp emission lines come from a shock front and not a semi-permanent chromosphere.

An enhancement of the photospheric C_2 lines is, in principle, achieveable by an obscuration that is most severe towards the centre of the disc. Under such special circumstances, the photospheric spectrum is primarily that of the limb in which lines of C_2 and other low excitation lines are expected to be enhanced and high excitation lines are weakened. We reject this idea that the enhancement of the C_2 is simply a centre-limb effect because it demands a special geometry with respect to the observer for what appears to be a common property of R CrB declines and because we do not see the predicted weakening of the high excitation lines.

3.3 *The High Velocity Cloud*

The high velocity absorption components seen in the Ca II H and K and Na I D lines are attributed to gas ejected with the dust cloud. If this gas were unrelated to the cloud, the high velocity components should be seen on occasions at maximum light. Such components have never been reported, although an intensive search is yet to be made. It is supposed that the gas is accelerated to speeds of 100 to 200 km s^{-1} by the dust that is driven out by radiation pressure. Detailed observational studies, as yet unavailable, of the development of high velocity components could reveal much about the growth of the dust cloud and particularly because the absorptions can be detected against the bright photospheric continuum that drowns the faint chromospheric emission lines. In the 1988-1989 minimum of R CrB the components in the Na I D lines may have been detected as early as 3 weeks into the decline (CLB). Accurately differenced spectra of the Na I D lines will be needed to detect the onset of weak components that may appear first at low velocity as a deepening and broadening of the photospheric lines. The cloud is probably more easily detected in the Na I D than the Ca II H and K lines because the latter's photospheric lines are broader and deeper and the stellar flux is higher at 5890 Å than at 3930 Å. Early in the decline, the equivalent width of the components will depend on a cloud's projected area. Careful searches for these components in low excitation lines would be valuable in setting limits on the physical conditions in the clouds.

The high velocity absorption components which persist through to the advanced phases of the recovery from minimum are presumed to vanish as the cloud of dust and gas expands so that the column density along the line of sight to the star decreases. This presumption is consistent with the Na I D profiles of 1988 October and 1989 February. The total distance traversed by the cloud in the time that it gives a detectable high velocity component is a small fraction of the radius of the circumstellar shell responsible for the infrared excess. The 1988–1989 cloud moved at about 150 km s^{-1} (relative to the star) for about 200 days if we accept CLB's early detection of the Na I D components; *i.e.*, the distance travelled is about 40 $R_* \simeq 4000\ R_\odot$. The grains contributing the infrared excess must be at about 200 R_* (Hartmann & Apruzese

1976). The radiation emitted by the hot grains in the freshly ejected clouds is at shorter wavelengths and may be detectable on occasions above the photospheric radiation from the obscured star (Shenavrin *et al.* 1979).

Radiation pressure on the grains is considered to drive the mass loss following dust formation. Around cool oxygen-rich luminous supergiants (*e.g.*, Betelgeuse) and asymptotic giant branch stars (*e.g.*, the Mira variables), the stellar wind has an observed expansion velocity of 10 to 20 km s $^{-1}$ These winds have been modelled successfully (Tielens 1983) with radiation pressure on silicate grains as the driving force. It is reasonable to ask why the gas in the temporary wind of a RCB has the much higher expansion velocity of 100 to 200 km s $^{-1}$. (These observed velocities refer to the gas (V_g). The dust grains are driven out at a higher velocity (V_d)). We may note several reasons why higher wind speeds are likely. First, graphite grains present a larger cross-section to photons than silicate grains; Wickramasinghe (1972) estimates the ratio of the radiation to gravitational forces to be approximately 100 times higher for graphite grains. Second, the condensable mass fraction of material (grains) in an RCB atmosphere is higher by a factor of 2 to 4 than that of silicate material in an oxygen-rich giant's atmosphere; this fraction is set by the appropriate elemental abundances, but the actual mass fractions depend on the efficiency of grain formation. Third, the photon supply given approximately by $R_*^2 \quad T_{\rm eff}^4$ is higher for RCB stars. Hartmann & Apruzese (1976) calculate that; in the absence of gas, the graphite grains around R CrB achieve aterminalvelocity of 600 km s $^{-1}$ if formed at $R \sim 300R_*$; this velocity scales as $R^{-1/2}$. The carbon condensation model proposed by Fadeyev (1988) (where the dust condenses from ejected gas at ~20 R_*) shows that the gas is accelerated to velocities ~100 km s $^{-1}$,but the drift velocity between gas and dust never exceeds ~20 km s $^{-1}$ and, hence, grains are most probably not destroyed by sputtering through gas-grain collisions.

A high velocity component to the He I 10830 Å line was seen by Querci & Querci (1978) when the star was rising to maximum following a minimum about 6 months earlier in mid-1977. This absorption component at about – 230 km s $^{-1}$ was seen by Zirin (1982) on a spectrum taken in 1978 July when the star had returned to maximum light. Clearly, the high velocity gas must be hot and dense in order to provide a strong absorption feature at 10830 Å. Zirin's observation suggests that the high velocity feature may be a characteristic of the spectrum near maximum light. Querci & Querci (1978) reported the absorption component to be part of a P Cygni line. Unfortunately, it is unclear from the description of their low resolution spectrum whether the emission component of the P Cygni line is a narrow chromospheric line or a manifestation of the broad emission line seen at He I 3889 Å. We suppose that the latter interpretation is the more likely. Emission was not detected by Zirin.

3.4 *The Broad Emission Lines*

The broad emission lines are undisplaced relative to the photospheric velocity and, hence, the emitting volume is considered to be roughly spherically symmetric about the star. The high velocity absorption components of the same lines are attributed to gas in the new clouds. Later,these clouds will form part of the circumstellar shell giving the infrared excess. Since similar expansion velocities are derived from the velocity of the absorbing clouds near minimum light and the width of the broad emission lines,

the former appears to be a terminal velocity. This velocity is greater than the escape velocity.

The expanding dust shell may also account for the veiling of the photospheric absorption lines seen at the deepest minima of R CrB. At these minima, the absorption spectrum may consist of two components: (1) faint photospheric light transmitted by the new and other clouds along the line of sight, and (2) photospheric light from the entire stellar surface scattered into the line of sight off grains in the circumstellar shell. If the second contribution exceeds the first, the absorption line spectrum will appear washed out; *i.e.*, veiled because the shell's expansion velocity is several times the intrinsic width of the photospheric lines, and hence, the lines in the spectrum of this scattered and Doppler-shifted light will be greatly broadened. Scattering not only broadens the absorption lines, but also introduces a redshift as pointed out by Rao (1974, 1975) and Forrest (1974). The redshift of absorption lines that never go into emission (C I lines) was ~ 5–19 km s $^{-1}$ at the 1960 minimum. Observations at the 1962 minimum were interpreted by Rao (1974,1975) using a Mie scattering model for a cloud of graphite grains and indicate expansion velocities of 40–80 km s $^{-1}$ for the dust.

A key question is whether the broad emission lines are permanent features of the star or appear only at a minimum. The sharp emission spectrum is dominated by low excitation lines of singly ionized metals characterised by $T_e \sim 5000 \pm 500$ K, $N_e \sim 10^{11}$ cm $^{-3}$ (Payne-Gaposchkin 1963; Rao 1974),but no He I sharp emission lines are present even though He I is one of the dominant species showing broad emission lines. IUE low resolution spectra of R CrB show C II] 1335 Å emission at a roughly constant flux during light maximum as well as during minimum (Holm & Wu 1982), Unfortunately, the quality of the available IUE spectra does not permit the sharp and broad components of the C II line to be distinguished. The He I 3889 Å, Ca II H and K broad lines showed asimilar behaviour in the early 1962 light minimumof R CrB: the line flux remained fairly constant even though the equivalent widths varied from 3 to 14 Å (Rao, unpublished observations). This behaviour suggests that the broad emission lines may be permanent features. Even the C III] 1909 Å line seen during the 1983 minimum may belong to the broad emission region. The presence of C III] 1909 Å and the upper limit (1) to the flux ratio of C II] 2325 Å / C II] 1335 Å estimated from the high resolution IUE spectrum obtained by one of us (NKR) at maximum light leads to a $T_e \sim 2 \times 10^4$ K and $N_e \sim 1\,0^{9-10}$ cm $^{-3}$ according to recipes given by Brown & Carpenter (1984).

A question regarding the broad emissions is the excitation mechanism. The fact that even a cool RCB star like U Aqr ($T_{\rm eff} \lesssim 5000$ K) shows He I 3889 Å strongly in emission during the light minimum (even stronger than Ca II H and K lines—Bond, Luck & Newman 1979) indicates radiative excitation is unlikely. Moreover, there is no obvious source of radiation unless the presence of an unseen hot binary component is invoked. Another puzzle about the broad emission line region is the anomaly regarding the He I lines, namely 5876 Å is weaker (in fact, undetected) than 3889 Å and even weaker than 7065 Å (Rao 1981). Such anomalies seem to require the gas to be at $N_e \sim 10^{10}$ cm $^{-3}$ and $T_e \sim 2 \times 10^4$ K and to have high optical depth in the 3889 Å line (Almog & Netzer 1989; Surendiranath, Rangarajan & Rao 1986). A full description of the broad line spectrum from the ultraviolet to the near infrared should be a major goal of observations in a future decline.

The high electron density indicated by the He I lines and by the C II lines (if they belong to the broad line region) suggests that the broad lines may be formed in the

upper layers of an extended expanding chromosphere reminiscent of the models developed for T Tauri stars (Hartmann, Edwards & Avrett 1982) and hybrid supergiants (Hartmann, Dupree & Raymond 1981) where the chromosphere is supported by Alfvén waves. The models have a lower chromosphere that is cool ($T_e \sim 5000$ K), expanding slowly and mildly turbulent and, hence, a plausible site for the sharp emission lines. For a mass loss rate of 2×10^{-8} $M_\odot$ yr^{-1} (*e.g.*, model 1 of Hartmann *et al.* 1982), the temperature increases to about 30,000 K and the wind attains its terminal velocity of about 200 km s^{-1} at a height of 2 to 3 R_*. The He I lines are formed in the hottest layers of the wind. The Na I D lines are formed in the cooler outer reaches of the wind. In these models, the higher the mass loss rate the cooler is the wind temperature.Heating is by the dissipation of Alfvén waves with magneticfields of 300–500 G in high gravity stars (T Tauri stars) and 1–10 G in case of supergiants for mass loss rates of $\sim 10^{-8}$ $M_\odot$ yr^{-1}. The scaling laws suggest that the mass loss rate of R CrB requires a field strength of about 40 G for the wave flux of about 10^5 erg cm^{-2} s^{-1} ($M \sim 1$ $M_\odot$ and $R_* \sim 100$ $R_\odot$ is assumed). This flux is roughly equal to the emitted flux in R CrB's broad emission lines ($\sim 5 \times 10^4$ erg cm^{-2} s^{-1} if $R_* = 100$ $R_\odot$, $d = 1.3$ kpc). The photospheric lines of R CrB are broad and the inferred turbulence of about 20 km s^{-1} may suffice for generations of the waves. In this model the dust may form in the cool outer reaches of the wind where the wind velocity is at its terminal value. It is possible that the primary site for dust formation is, as indicated earlier, above a region where the chromosphere has been temporarily quenched. The trigger for dust formation remains unknown. The [O II] 3727 Å emission discovered by Herbig (1949) may come from the outer reaches of the circumstellar shell or a fossil H II region (Rao & Nandy 1986).

4. Concluding remarks

Our high-resolution spectra taken at minimum light show that the C_2 Swan absorption bands are stronger than at maximum light, The cool gas responsible for the enhancement of the C_2 bands and of low excitation metal lines is stationary with respect to the photosphere. Our spectra extend the earlier finding (Rao, Giridhar & Ashoka 1990) about the line enhancements at minimum light. The Na I D lines at minimum light are strongly in emission with a dominant sharp component and a much broader component. These components and an associated blueshifted absorption component are common features of R CrB in decline. Photospheric lines in the several spectral regions observed at minimum light have profiles that are similar to those observed at maximum light; *i.e.*, the photospheric spectrum was not "veiled".

Further progress in understanding the atmospheric changes occurring during a decline of R CrB requires intensive spectral and temporal coverage. This requirement may be satisfied only through international collaboration. Although the declines deserve especial consideration by observers, our observations of selected lines show that much can still be learned from high resolution spectra taken at maximum light.

We thank Yaron Sheffer for extensive help with the reduction and manipulation of the spectra, Drs V. V. Smith, J. Drake, and J. K. McCarthy for obtaining spectra of R CrB at maximum light, and Drs M. J. Barlow and G. H. Herbig for helpful discussions. This research has been supported in part by the U.S. National Science Foundation (grants AST 8614423 and 8902835).

References

Alexander, J. B., Andrews, P. J., Catchpole, R. M., Feast, M. W., Lloyd Evans, T., Menzies, J. W., Wisse, P. N. J., Wisse, M. 1972, *Mon. Not. R.astr.Soc.,* **158,** 305.

Almog, Y., Netzer, H. 1989, *Mon. Not. R. astr.Soc.,* **238,** 57.

Bond, H. E., Luck, R. E., Newman, M. J. 1979, *Astrophys. J.,* **233,** 205.

Brown, A., Carpenter, K. G. 1984, *Astrophys. J.*, **287**, L43.

Cottrell, P. L., Lambert, D. L. 1982, *Astrophys.J.*, **261,** 595.

Cottrell, P. L., Lawson, W. A., Buchhorn, M. 1990, *Mon. Not. R. astr. Soc.*, **244**, 149 (CLB).

Fadeyev, Yu. A. 1983, *Astrophys. Sp. Sci.*, **95,** 357.

Fadeyev, Yu. A. 1988, *Mon. Not. R. astr. Soc.*, **233,** 65.

Feast, M. W. 1986, in *Hydrogen Deficient Stars and Related Objects,* Eds K. Hunger, D. Schönberner, & N. K. Rao, D. Reidel, Dordrecht, p. 151.

Forrest, W. J. 1974, *PhD Thesis,* Univ.California.

Hartmann, L., Apruzese, J. P. 1976, *Astrophys.J.*, **203**, 610.

Hartmann, L., Dupree, A. K., Raymond, J. C. 1981, *Astrophys. J.*, **246,** 193.

Hartmann, L., Edwards, S., Avrett, E. 1982, *Astrophys. J.*, **261**, 279.

Herbig, G. H. 1949, *Astrophys. J.*, **110**, 142.

Herbig, G. H. 1968, *Mem.* [8] *Soc. R. Sci. Liège,* Cinquieme Series, **17**, 353.

Holm,A.V.,Wu,C.-C.1982, in *Advances in Ultraviolet Astronomy*, EdsY.Kondo, J.M.Mead & R. D. Chapman, NASA Conf. Pub. 2238, p. 429.

Holm, A. V., Hecht, J., Wu, C.-C, Donn, B. 1987, *Publ. astr. Soc. Pacific,* **99,** 497.

Joy, A. H., Humason, M. L. 1923, *Publ. astr. Soc. Pacific,* **35,** 325.

Keenan, P. C., Greenstein, J. L. 1963, *Contr. Perkins Obs.*, *Series II,* p. 197.

Loreta, E. 1934, *Astr. Nach.*, **254,** 151.

O'Keefe, J. 1939, *Astrophys. J.,* **90,** 294.

Payne-Gaposchkin, C. 1963, *Astrophys. J.,* **138,** 320.

Pugach, A. F. 1984, *Sov. Astr.*, **28,** 288.

Querci, M., Querci, F. 1978, *Astr. Astrophys.,* **70**, L45.

Rao, N. K. 1974, *PhD Thesis,* Univ. California.

Rao, N. K. 1975, *Bull. astr. Soc. India,* **3**, 50.

Rao, N. K. 1981, in *Effects of Mass Loss on Stellar Evolution,* Eds C. Chiosi & R. Stalio, D. Reidel, Dordrecht, p. 469.

Rao, N. K., Nandy, K. 1986, *Mon. Not. R. astr. Soc.,* **222,** 357.

Rao, N. K., Giridhar, S., Ashoka, B. N. 1990, *Mon. Not. R. astr. Soc.,* **244,** 29.

Rao, N. K., Nandy, K., Bappu, M. K. V. 1981, *Mon. Not. R. astr. Soc,* **195,** 71P.

Rao, N. K.,Vasundhara, R.,Ashoka,B. N.1986,in*Hydrogen Deficient Starsand Related Objects,* Eds K. Hunger,D. Schönberner& N. K. Rao, D. Reidel, Dordrecht, p. 185.

Raveendran, A. V., Ashoka, B. N., Rao, N. K. 1986, in *Hydrogen Deficient Stars and Related Objects,* EdsK.Hunger,D. Schönberner & N. K. Rao, D. Reidel, Dordrecht, p. 199.

Schönberner, D. 1975, *Astr. Astrophys.* **44,** 383.

Shenavrin, V. I., Taranova, O. G., Moroz, V. I. & Grigorév, A. V. 1979, *Soviet A. J.,* **23,** 567.

Spite, F., Spite, M. 1979, *Astr. Astrophys.,* **80,** 66.

Surendiranath, R., Rangarajan, K. E., Rao, N. K. 1986, in *Hydrogen Deficient Stars and Related Objects,* Eds K. Hunger, D. Schönberner & N. K. Rao, D. Reidel, Dordrecht, p. 199.

Tielens, A. G. G. M. 1983, *Astrophys.J.*,**271,** 702.

Wdowiak, T. J. 1975, *Astrophys. J.*, **198,** L139.

Wickramasinghe, N. C. 1972, *Mon.Not. R.astr.Soc.,* **159,** 269.

Zirin, H. 1982, *Astrophys. J.*, **260,** 685.

J. Astrophys. Astr. 1990 **11**, 491–505

Composite Spectra

Paper 5: Orbital Elements for 30 Systems

R. F. Griffin *The Observatories, Madingley Road, Cambridge, England CB3 0HA*

Received 1990 July 20; accepted 1990 August 23

Abstract. A comprehensive survey of bright composite-spectrum binaries in the northern sky has provided so many radial-velocity data that orbits can now be determined for many objects whose orbits were hitherto unknown or else insecure or actually erroneous. Elements are given for the orbits of 30 such objects, thereby more than doubling the number of composite-spectrum binaries with known orbits.

Key words: composite spectra — spectroscopic binaries — orbits — stars, Individual

1. Introduction

Several years ago Dr. R. E. M. Griffin and I began a comprehensive study of composite-spectrum binary stars in the northern sky. The primary purpose of the project initially was to see whether we could determine the masses of the late-type giant or supergiant primaries by comparing them with those of A- or B-type secondaries. Accomplishment of that objective required the radial velocities of both components (or at least their relative velocities) to be measured with errors small compared with the velocity difference between them. It also required, for each system, a reasonably accurate assessment of the spectral type of the hot star, to serve as the basis for an estimate of that component's mass, so that the mass ratio derived from the radial velocities would then give the mass of the late-type star.

We (Griffin 1986) developed a method, little used previously, of separating the two stars' spectra. We select from a library of spectra of single stars one that is as nearly as possible similar to that of the late-type component of the system under study, and subtract it from the composite spectrum. The spectrum of the hot component is thereby revealed. By performing the subtraction in the rest frame of the cool star, we derive the radial-velocity difference between the components from the wavelength offset of the secondary spectrum that is uncovered by the subtraction process. Very reliable spectral types—a far cry from those estimated from direct observation of composite spectra—can be established by our procedures, making their application worthwhile even in cases (Griffin 1988, 1989) where there is no detectable radial-velocity difference between the components and where, therefore, our original intentions to determine a mass ratio could not be realized. However, the most significant results are still those obtained for systems that show substantial radial-velocity variations and thereby permit determination of the mass ratios from the

relative amplitudes of the variations of the two stars. Obviously, in order to minimize the error of measurement in relation to the size of the velocity difference being measured, it is desirable to observe the spectrum of each object at a time when the velocity difference is near a maximum, *i.e.* near a node of the orbit. Thus there is an antecedent need for knowledge of the radial-velocity behaviour of the systems, and of the orbits in those cases in which they can be determined.

Our observing programme includes all the composite-spectrum binaries known to us that are brighter than about eighth magnitude and whose declinations are above about — 8°, making them accessible to observation with the Cambridge 36-inch telescope and its radial-velocity spectrometer (Griffin 1967). Despite the generally poor observing conditions in Cambridge, the continuous availability of the radial-velocity spectrometer here has allowed us to make reasonably rapid headway in identifying which of the binary systems exhibit significant radial-velocity changes and in establishing the orbits of those that do. Of course, in many cases the time-scale is set by the leisurely nature of the orbits rather than of the observer.

The radial-velocity'spectrometer is particularly well adapted to the observation of composite spectra: having a mask that corresponds to the spectrum of a late-type star, it takes no notice at all of early-type spectra since such spectra have no systematic relationship whatever to the mask. Therefore a star that is hot enough not to show the lines typical of late-type stars in appreciable strength does not register any 'dip', and when observing a composite-spectrum binary that includes such a star one can be certain that the velocity that is measured belongs uniquely to the late-type component, however much the light of that component may be diluted by that of its companion. By contrast, certain sets of published velocities of composite-spectrum binaries seem not to show any particular relationship to the orbits of the relevant systems, and other sets do vaguely follow the orbits but with greatly diminished amplitudes. One wonders whether such measurements are based on a few of the higher Balmer lines (arising from the hot star) plus a few of the strongest metal lines (from the cool star)—an ensemble that would be guaranteed to give very ragged results and to reduce or even conceal the phase-dependence.

Most of the composite-spectrum binaries that are under observation were placed on the programme about the time that Dr. R. E. M. Griffin and I first became committed to such a project in 1981. Other systems have only subsequently come to our attention, often because their composite nature had only just been recognized. On the other hand, some were already under observation on the ordinary Cambridge binary programme before 1981, and several others would have been if it had not been for a report (Bahng 1977) which suggested (inaccurately, as it turned out (Baker 1984; Hendry 1984)) that their orbits had been determined already. Secure, though in some cases preliminary, orbits have now been derived from the observations made in Cambridge (plus a number made with other radial-velocity spectrometers which we have been privileged to use on a guest-investigator basis) for most of the programme stars whose periods are less than about a decade.

The spectroscopic side of the composite-spectrum project requires spectra of high resolution and signal/noise ratio to be obtained at definite orbital phases, near a node of the orbit (preferably both nodes). At first we were fortunate in being accorded Visiting Associate status at Mount Wilson Observatory, whereby we were several times enabled to use the coude spectrograph of the 100-inch reflector to observe composite-spectrum objects at the critical phases. However, with many stars on the

programme, all needing to be observed at different times, progress was bound to be slow when observing runs could not realistically be more frequent than a few per year, and the situation was greatly exacerbated by the sudden closure of the 100-inch telescope in 1985. Since that time, we have been welcomed as visitors at the Dominion Astrophysical Observatory, Victoria, and at Calar Alto Observatory in Spain (operated by MPIA Heidelberg); but Victoria suffers from climatic disadvantages, and our observing time at Calar Alto has been primarily devoted to another, distinct though related, programme (*cf.* Griffin *et al.* 1990).

To provide timely information on the principal results of the radial-velocity work without creating significant duplication of publications or prejudicing future papers which will deal in detail with each system individually, the present paper simply gives the orbital elements derived for 30 composite systems for which either no orbit at all has been published or else the published orbit(s) is or are very insecure or entirely erroneous.

2. Orbits

Table 1 lists the 30 systems whose orbits are reported. The first four columns give the identification of the star according to (1) Hynek's (1938) catalogue of composite spectra, (2) the constellation designation (Bayer 1603; Flamsteed 1725), (3) the HR number (Hoffleit 1982), and (4) the HD number(s) (Cannon & Pickering 1918 –1924). In 19 of the 30 cases the object was recognized as composite when it was classified for the *HD Catalogue,* and in 18 of them the compositeness was sufficiently certain that the object was given two numbers in the *Catalogue.* Where that is so, both are given in the Table, with the second one truncated to the last two digits; the number of the late-type component is given first. Four of the objects (HR 2030, HR 3416, HD 208253 and HD 216572) that were not recognized as composite in the *HD Catalogue* were classified there as A or B types only—no late-type lines were seen at all; nevertheless their orbits have now been determined from the late-type spectra. The fifth and sixth columns of Table 1 give the year in which the author's radial-velocity observations began and the number of those observations utilized in the orbit. It may be assumed that they continue up till the time of writing; indeed, it is intended that they should continue until the work on the relevant system is definitively written up. Where there is a second date in brackets in column 5, it is the year in which the first observation was made; in that case the year given first is the one in which systematic radial-velocity coverage of the orbit commenced. It has been possible to find in the literature some radial-velocity data to assist some of the orbit determinations; where that is so, the number of those data is recorded in column 7. Data that exist in the literature but have not proved useful in refining the orbits are not enumerated in the Table. The last column of Table 1 shows which systems have been observed, to my knowledge (for which I am very largely indebted to the splendid catalogue by McAlister & Hartkopf (1988)), by speckle interferometry, and in that case whether they have yet proved to be resolvable, or not.

Table 2 gives the orbital elements themselves. The Table is largely self-explanatory, apart perhaps from the last two columns. The penultimate column shows the standard deviation of an individual observation from the computed orbital curve, while the last one is an assessment of the 'quality' of the orbit, as discussed more particularly below. The element given in the column headed "T or T_0" is the epoch T of periastron for

Table1. The 30 stars whose orbits are the subject of this paper.

Star identification				R. V. observations			Speckle
Hynek	Name	HR	HD	By the author		Others	Resolution
				Start	No.	No.	
121			4615/16	1983(1982)	68	—	
3		233	4775/76	1981	75	4	Yes
141			16082/83	1979(1978)	56	—	
143			17245/46	1984(1982)	43	—	Yes
11	"g Tau"	958	19926/27	1976	73	9	No
13		1129	23089/90	1980	66	31	Yes
17	36 Tau	1252	25555/56	1983(1981)	32	1	Yes
		1455	29104	1982	50	8	No
180		1736	34533/34	1983(1982)	52	—	
193		2024	39118/19	1981	63	21	
		2030	39286	1979(1977)	66	—	
281			69479/80	1978	49	4	No
		3416	73451	1982	56	—	
40	45 Cnc	3450	74229/28	1981	71	—	No
	14 Ser	5799	139137	1982	54	—	
		7140	175635	1982	65	13	No
478			181658/57	1978	37	—	
84	9 Cyg	7441	184759/60	1981	110	41	Yes
.			190361	1970(1966)	123	—	
512			193350/49	1987(1986)	29	—	
513			193410/11	1986(1983)	40	—	No
518		7895	196753/54	1976(1975)	85	—	No
524			199378/79	1979	61	—	No
			202710	1986(1983)	31	—	
528			203340	1986(1984)	29	—	
			208253	1981	84	—	No
546			213503/04	1983(1982)	52	—	
			216572	1986	55	—	
557			220636/37	1986(1982)	36	—	
			223971	1986	41	—	

orbits which have non-zero eccentricities, and is T_0, the instant of zero mean longitude or nodal passage with maximum positive velocity as defined by Sterne (1941) and recommended by Batten, Fletcher & McCarthy (1989), for circular orbits. The standard deviation of each element is given immediately beneath the value of the element itself. In general, all quantities are given to such a number of significant figures that the standard deviation falls within the range 3 to 25 in units of the least significant digit. The standard deviations in the Table are ranged directly beneath the digits to which they correspond in the respective elements themselves; the decimal points are usually omitted where they are not adjacent to figures printed. Some exceptions to the general conventions have been made for consistency within certain columns.

All the orbits are perfectly secure, in the sense that no increase in the number or quality of the data can do anything more than refine the accuracy of the elements. The 'quality' of each orbit has been assessed after the fashion of the assessments in the

Eighth Catalogue of the Orbital Elements of Spectroscopic Binary Systems (Batten, Fletcher & MacCarthy 1989). Those assessments are inevitably somewhat subjective, but the present author thinks that he has a good impression as to how the quality-scheme is supposed to work, and has followed it quite dispassionately in the ratings of his own orbits in Table 2. There is, however, one point upon which his views do not coincide with those of the authors of the orbit catalogues, and that concerns the reservation of quality *a* for systems whose orbits have been determined more than once. Detectable secular changes are not to be expected in the wide binaries under discussion here, so there seems to be no reason why one sufficiently good determination of an orbit should not be accorded quality *a.* Besides, a continuous and homogeneous set of measurements extending over ten or twenty years is, to say the least, no worse than a couple of independent brief campaigns undertaken ten or twenty years apart, yet the convention adopted in the *Catalogue* would admit an *a* grade for the results of the second short campaign but not for the continuous watch on the star. The author has accordingly allowed himself to flag with an asterisk those *b* ratings that he would have preferred to call *a* if fidelity to the *Catalogue* scheme had not seemed more important. Since all the orbits discussed here are first-time determinations, none could qualify for an *a* rating in the *Catalogue.*

Some notes on individual stars follow the tables, but they refer only to matters connected with the orbits and are not by any means intended to be comprehensive descriptions of the systems.

3. Discussion

A search through the *Eighth Catalogue* (Batten, Fletcher & McCarthy 1989) for composite-spectrum binaries of the sort treated here reveals about 20 such entries with tolerably well-determined (quality *c* or better) orbits. The precise number naturally depends upon the exact criteria used to identify the systems to be counted: cataclysmic binaries, for example, which though showing composite spectra are strongly interacting and dissimilar to those of interest in the present paper, are not included in the count. Of the twenty orbits, three (HR 6902 (Griffin 1986), HD 187299 (Griffin & Radford 1979) and HD 200428/9 (Griffin *et al.* 1976)) are our own work. It may be seen, therefore, that the present programme, and in particular the present paper, has more than doubled the number of orbits known for systems of the type discussed here. It speaks volumes for the neglect of composite-spectrum binaries in the past that so many bright objects, the majority of which were already identified as composite in the *Henry Draper Catalogue* about 70 years ago and some of which are so conspicuous that they even have constellation designations, have had to wait until now to have their orbits determined.

3.1 *These Stars as a Programme for Speckle Interferometry*

The median period of the 30 binaries which feature in this paper is over 1000 days, so it is clear that many of the systems must be widely separated. Without knowing the mass ratios and orbital inclinations one cannot say exactly what the separations of the binaries are, but the observed (late-type) components may ordinarily be expected to be

Table 2. Orbital elements for the 30 stars .

Star	P days	T or T_0 MJD	γ km s^{-1}	K km s^{-1}	e
HD 4615	302.63	46477.1	−0.51	27.54	.435
	.11	.5	.11	.16	5
HR 233	2090.1	45099	−2.40	11.09	.533
	2.0	5	.09	.20	10
HD 16082	3894	45736	−6.92	16.06	.252
	46	27	.16	.19	14
HD 17245	348.9	46902	−5.18	21.87	.101
	.3	5	.17	.23	11
HR 958	115.045	44543.36	−1.75	24.16	0
	6	.13	.12	.16	—
HR 1129	6150	45862	−4.92	15.74	.671
	16	6	.12	.18	7
36 Tau	2802	46110	+10.24	8.9	.693
	4:	10	.13	.3	14
HR 1455	487.63	46259.6	−2.51	25.3	.296
	.25	2.2	.15	.3	8
HR 1736	2570	45512	+15.45	10.15	.351
	13	15	.08	.13	12
HR 2024	1406.5	45823	+19.53	25.88	.300
	1.9	6	.12	.19	7
HR 2030	66.449	45963.47	+3.77	26.13	0
	5	.09	.16	.22	—
HD 69479	90.836	46147.12	−5.52	18.77	0
	6	.12	.10	.14	—
HR 3416	284.93	46755.5	+34.99	20.13	.244
	.14	2.0	.15	.23	10
45 Cnc	1007.5	46637.7	−6.19	19.73	.461
	1.4	2.2	.13	.18	7
14 Ser	259.81	46323.8	−23.81	24.89	.378
	7	.7	.14	.20	7
HR 7140	1583.9	46045	−21.56	16.61	.519
	2.4	4	.09	.16	6
HD 181658	4700	46973	−3.4	13.6	.722
	300	8	.3	.4	13
9 Cyg	1571.76	44299.8	−17.26	22.33	.788
	.15	.5	.07	.17	3
HD 190361	1511.9	43515	−6.18	9.65	.089
	2.1	29	.08	.11	14
HD 193350	1092	47390	−23.43	23.4	.039
	10	40	.25	.3	12
HD 193410	530.4	46962	−7.65	23.45	.086
	.8	8	.13	.19	8

Star	ω deg	$a_1 \sin i$ Gm	$f(m)$ $M_\odot$	σ km s^{-1}	Q
HD 4615	237.3	103.2	0.478	0.8	b*
	.8	.7	9		
HR 233	324.1	270	0.179	0.7	b*
	1.4	5	10		
HD 16082	290	832	1.52	0.9	b
	3	14	9		
HD 17245	13	104.4	0.373	0.8	c
	5	1.1	12		
HR 958	—	38.22	0.168	1.0	b*
	—	.25	3		
HR 1129	137.0	987	1.01	0.8	b
	.8	14	4		
36 Tau	112	247	0.077	0.6	d
	4	10	10		
HR 1455	204.0	162.1	0.716	0.9	b
	1.7	1.9	25		
HR 1736	94.7	336	0.229	0.6	b
	2.4	5	10		
HR 2024	84.0	477	2.20	1.0	b
	1.4	4	5		
HR 2030	—	23.87	0.123	1.2	b
	—	20	3		
HD 69479	—	23.44	0.0624	0.7	b
	—	.18	14		
HR 3416	233	76.5	0.220	1.1	b*
	3	9	8		
45 Cnc	310.5	242.6	0.562	0.8	b
	1.1	2.5	17		
14 Ser	359.2	82.4	0.330	0.9	b*
	1.2	7	8		
HR 7140	13.9	309	0.471	0.7	b*
	1.0	3	15		
HD 181658	222.2	610	0.41	0.6	c
	2.2	40	9		
9 Cyg	139.1	297	0.423	0.8	b*
	.5	3	12		
HD 190361	344	199.9	0.139	0.9	b
	7	2.4	5		
HD 193350	355	351	1.45	0.7	b
	14	5	7		
HD 193410	194	170.4	0.703	0.8	b
	6	1.4	18		

Table 2. Continued.

Star	P days	T or T_0 MJD	γ km s^{-1}	K km s^{-1}	e
HR 7895	371.85	44781.7	+3.21	18.91	0
	.10	.4	.09	.13	—
HD 199378	1201.0	45227	−10.96	16.04	.438
	1.2	3	.09	.17	8
HD 202710	1222	47373.0	−16.76	12.7	.767
	23	2.1	.16	1.2	27
HD 203340	1552	46482	−25.7	16.4	.630
	26	23	.3	.4	10
HD 208253	446.2	46220.4	+2.82	22.69	.288
	.3	1.8	.13	.21	8
HD 213503	2144	47302	−10.73	23.1	.505
	5	4	.13	.3	8
HD 216572	54.723	47269.17	−11.43	72.4	0
	5	3	.21	.3	—
HD 220636	117.58	47236.77	−5.73	21.26	0
	4	.23	.17	.23	—
HD 223971	50.115	47136.74	+3.72	40.83	0
	5	3	.14	.20	—

Notes to Table 2

HD 4615. A photometric campaign around the conjunction of 1988 August revealed no eclipse, though a brief event could have been missed.

HR 233. A spectroscopic orbit with a period of 226 days was published by Hendry (1981b) and later withdrawn (Baker 1984, Hendry 1984). Speckle orbits with periods of 11.420 and 12.17 years were published by Baize (1988) and Balega (1988) respectively, both of whom make comments whose validity is compromised by the fact that the periods are about twice the true one of 5.722 ± 0.006 years. Evidently the quadrants of some of the speckle observations need to be reversed. The fact that there are considerable changes in position angle demonstrates that there is no prospect of an eclipse.

HD 16082. The large mass function shows that either the late-type star is a supergiant or else the secondary is itself double. There has not been an opportunity yet to look for eclipses, but one will arise in 1994 May/June; the object will however not be well placed for observation then.

HD 17245. The orbit is accorded only quality *c* owing to a gap in the phase coverage, unavoidable when the period is so close to one year.

Star	ω deg	$a_1 \sin i$ Gm	$f(m)$ $M_\odot$	σ km s^{-1}	Q
HR 7895	—	96.7	0.261	0.8	b*
	—	.7	5		
HD 199378	37.8	238	0.374	0.7	b*
	1.2	3	13		
HD 202710	313	137	0.069	0.7	d
	3	14	22		
HD 203340	90.4	272	0.33	0.7	c
	2.2	9	3		
HD 208253	346.1	133.3	0.475	1.1	b*
	1.6	1.3	13		
HD 213503	23.3	587	1.75	0.8	b*
	.9	8	8		
HD 216572	—	54.46	2.15	1.5	b
	—	.24	3		
HD 220636	—	34.4	0.117	1.0	b
	—	.4	4		
HD 223971	—	28.14	0.354	0.8	b*
	—	.14	5		

HR 958. The constellation designation is otiose, as the star is now in Cetus. The 115-day period was tentatively suggested by Parsons (1983).

HR 1129. A spectroscopic orbit with a period of 220 days was published by Hendry (1981b) and later withdrawn (Baker 1984; Hendry 1984). Parsons (1983), still relying partly on Hendry's data, suggested revising the period to 212 days. The present author's radial-velocity observations cover only half the 17-year period as yet, but it is the significant half that includes the periastron passage in this very eccentric orbit. The large mass function and (still more) the lack of change of position angle shown by the speckle measurements, which began in 1976 but seem not to have been resumed after the periastron passage of 1984 when the system was too close to be resolved, encourage a search for eclipses. Unfortunately the orbit was not determined until just after the conjunction of late 1986. Radial-velocity traces of this system always show a fairly shallow dip, and if the secondary star were in eclipse that fact would be obvious from the increased depth of the dip. No eclipse was seen in 1986; the maximum interval between successive radial-velocity observations then was five weeks, which is therefore the upper limit to the duration of any eclipse. The next conjunction is due in 2003 September/October.

36 Tau. Sketchy coverage of the rapid decline in velocity in this very eccentric orbit is responsible for its poor quality rating. From my own observations alone the

standard deviation of the period is 80 days; the uncertainty quoted in Table 2 relies entirely upon the single observation published from Victoria (Wright 1952), and may be optimistic. The quadrants of some of the speckle observations need to be reversed. The variation in position angle shows that no eclipse is to be expected.

HR 1455. The secondary is itself a short-period binary system, a fact first pointed out to me by Dr. F. C. Fekel.

HR 2024. A spectroscopic orbit with a period of 209 days was published by Hendry (1981a) and later withdrawn (Baker 1984; Hendry 1984). The huge mass function is due to duplicity of the secondary: the K line is visibly double and changes on a short time-scale. Even so, the mass function is large enough to be interesting; however, a photometric campaign at the 1990 March conjunction showed that there is no eclipse.

HD 69479. An orbit solution with the eccentricity left as a free parameter yields $e = 0.023 \pm 0.008$, $\omega = 206 \pm 18$ degrees. The eccentricity is significant at a level of about 2 per cent, but the author's prejudice (because $P < 100$ days) leads him to favour the circular solution in this statistically marginal case.

HR 3416. The mass function is not large enough to give much hope of an eclipse; photometric observations around the time of the conjunction in 1990 January did not show. one.

45 Cnc. A spectroscopic orbit with a period of 73 days was proposed by Hendry (1981a) and subsequently withdrawn (Baker 1984; Hendry 1984). The large mass function and favourable longitude of periastron encourage a search for eclipses, which was in fact made by four observers at the conjunction in 1989 March but proved definitely negative.

14 Ser. A photometric search was made by Mr. G. Frey for an eclipse at the conjunction of 1988 June, but without positive result.

HR 7140. The next reasonably observable conjunction will occur in 1997 June.

HD 181658. Improved coverage of the abrupt minimum and steep rise of the radial-velocity curve in this very eccentric orbit is needed, but cannot be obtained until 2000.

9 Cyg. A spectroscopic orbit with a period of 1717 days was put forward by Abt & Levy (1976); Morbey & Griffin (1987) showed from Abt & Levy's data that the true period is near 1573 days, as they were able to confirm from their own observations. Another spectroscopic orbit, this time with a period of 215 days, was proposed by Hendry (1978) but was afterwards withdrawn (Baker 1984; Hendry 1984). Yet another orbit with tolerably correct period and eccentricity but entirely erroneous epoch and longitude of periastron, was derived by Baize (1989) from speckle interferometry by others. A photometric search for an eclipse at the very unfavourably timed conjunction of 1989 February was made by Mr. D. Pray; no eclipse was seen. There will be a conjunction on 1993 June 10, a favourable time of year for observation. However, the

speckle observations, despite not having been interpreted correctly yet in terms of the orbit, appear to show variations in position angle which rule out inclinations very close to 90°, so no eclipse is to be expected.

HD 193350. The eccentricity is not quite at the 1-per-cent level of significance. The epoch T_0 is MJD 47406.6 ± 1.6. The very large mass function encourages a search for eclipses in late 1993, but the date of conjunction is not very accurately predicted yet. Alternatively the mass function may be telling us that the hot star is itself double.

HD 193410. Again, the large mass function prompts a search for eclipses; the next conjunction at which the star is reasonably observable is due about 1993 July 14.

HR 7895. The mass function is not very large, and conjunctions have for many years occurred at times when the system is badly placed for observation. The circularity of the orbit at a period as long as one year is intriguing.

HD 199378. Rather sparse photometry around the time of conjunction in 1988 July did not find an eclipse.

HD 202710. The sharp rise and maximum in this very eccentric orbit are not well covered by the radial-velocity observations presently available.

HD 203340. The sudden decline of velocity in this eccentric orbit is not well covered.

HD 208253. Good photometric coverage of the conjunction in 1988 December showed that there is no eclipse.

HD 213503. Once again, an enormous mass function must suggest either a double secondary or a prospect of eclipses, the next of which would occur in 1993 May. A radial-velocity trace fortuitously taken right at the time of the last conjunction (1987 July 5) did not suggest an eclipse.

HD 216572. The extraordinary mass function can hardly be due to duplicity of the secondary, since the period of the observed orbit is too short to admit of it. Radial-velocity traces taken close to conjunction would—but do not—reveal an eclipse in this hot-dominated system. Probably there has been mass exchange and the late-type star is now the less massive one. Photometry shows variations that are seemingly capricious over a range of about $0^m.1$, but may be compromised by the presence of a companion star 8″ distant.

---

the more massive ones and therefore the projected separations should ordinarily be more than twice the values of $a_1 \sin i$ that are found from the orbital elements. The median value of $a_1 \sin i$ is 185 Gm, corresponding to nearly 1.3 AU, so the median projected separation $(a_1 + a_2) \sin i$ may be supposed to be about 3 AU and the median actual separation $(a_1 + a_2)$ to be about 4 AU. Binary systems with such a separation

must be resolvable by speckle interferometry on large telescopes out to distances appreciably beyond 100 pc, especially in view of the fact that the components are guaranteed by the observed composite nature of the spectra to have mutually comparable magnitudes. Thus many of the binaries on this programme are likely to prove significant and rewarding objects for speckle observations, and indeed a few of them have already been resolved, as indicated in Table 1.

3.2 *These Stars as a Search List for New* ζ *, Aurigae Binaries*

Another noteworthy feature of the orbits is the large mass functions associated with many of them. The mass functions ought to give a clue as to which systems are most liable to exhibit eclipses, although other characteristics (in particular, short periods and longitudes of periastron near 270°) offer additional encouragement in those cases that exhibit them. Eclipses are of enormous significance in composite-spectrum binaries: the eclipsing composite systems constitute the select class of stars named after the prototype ζ Aur, and their importance stems from the fact that the hot star acts as a moving light probe against which the absorption spectrum of the late-type chromosphere is seen at times shortly before and after eclipse. At present there are only about eight ζ Aur systems known (again, the exact number depends upon just what criteria one applies to isolate the class). Their periods range from 195 days (HR 2554) to 7430 days (VV Cep), and their mass functions run from 0.31 to 4.6 $M_\odot$ (the same objects again providing the limiting values). The mass function of VV Cep is quite exceptional, like many other characteristics of that system — indeed, even the name of the object seems to have been ordained to remind us that it is a Very Very 'Ceptional star! The next-largest mass functions are two near 1.0 $M_\odot$ (for 31 Cyg and ζ Aur, systems that contain late-type supergiants); then there are three in the range 0.50–0.55 $M_\odot$ (HR 6902, 32 Cyg and 22 Vul), and finally 0.34 and 0.31 (τ Per and HR 2554). For any given pair of stars that constitutes a binary system, the observed mass function is largest if the orbit is viewed edge-on ($i = 90°$), and it decreases in proportion to $\sin^3 i$ as the inclination i decreases. Accordingly, a large mass function implies the likelihood of a high inclination. The distribution of mass functions of the known ζ Aur stars suggests that if a composite-spectrum binary has a mass function as large as 0.3 $M_\odot$ it is liable to be viewed at $i \sim 90°$ and is therefore an eclipse candidate, and if the mass function is as high as 0.5–0.6 $M_\odot$then its candidature is strong—unless the late-type star is a supergiant, in which case the mass function may need to be as much as 1.0 $M_\odot$

When one looks at the mass functions of the 30 binaries whose orbits are disclosed in this paper, one finds that no fewer than 18 of them have mass functions in excess of 0.33 $M_\odot$; nine of them are above 0.55 $M_\odot$, of which six are even above 1 $M_\odot$. Thus one might expect this set of stars to provide a real bonanza of new ζ Aur systems. Unfortunately, that expectation has not been realized—at least not yet—and some promising systems have actually been proved not to show eclipses. As a matter of fact the idea of 'strong candidature' implicit above is too strong: because the mass function is proportional to $\sin^3 i$ it declines only very slowly to begin with as i decreases from 90°—the difference in masses implied by $i = 90^o$ and $i = 80$ is less than 5 per cent whereas the probability of an eclipse declines from 100 per cent at $i = 90^o$ to pretty small at $i = 80^o$.

We have orchestrated a deliberate and systematic campaign, undertaken by amateur astronomers of goodwill who possess appropriate photoelectric photometers, to watch for eclipses around the known times of conjunction of the binaries which form the subject of this paper. Naturally, owing to the long periods of many of the systems, their proclivity for coming to conjunction at seasons inappropriate for observation when they are in the daytime sky, and the vagaries of the weather, relatively few of the systems can be reported definitely as non-eclipsing, though for several others any eclipse must be short in comparison with a central event. The two binaries with the largest mass functions of all, over 2 $M_{\odot}$, are both 'funny' ones: the mass function of HR 2024 is not to be interpreted in the normal way because the secondary star is itself double, while that of HD 216572 is probably misleading on account of mass exchange in that relatively short-period system. There are four other systems with mass functions exceeding 1 $M_{\odot}$, none of which has yet been checked for eclipses and all of which still represent good candidates. One of them, HR 1129, certainly has an orbital inclination near to 90° because it has been resolved by speckle interferometry and has shown changes in separation but not in position angle; but it does not come to conjunction for a long time yet. The present situation regarding the search for eclipses in the various stars is indicated in the notes to Table 2.

3.3 *The Period–Eccentricity Distribution*

In recent years there has been renewed interest in the tidal circularization of binary-star orbits. For any given type of system, it is suggested that there is a period (whose actual value may depend upon the evolutionary state of the group of stars concerned and possibly upon its age) below which orbits will have been circularized and above which they will not. A tendency has also long been noticed for orbital eccentricities to increase with period, even above the circular/eccentric dividing line, but until comparatively recently that tendency was substantiated principally by a comparison of visual with spectroscopic binaries because few of the latter were known to have periods of any considerable length. There may be, therefore, some interest in plotting the eccentricities of the 30 binaries treated here against the logarithms of their respective periods, and that has been done in Fig. 1. Following the lead given by Mathieu, Latham & Griffin (1991), the eccentricities plotted for the orbits adopted as circular in Table 2 are not exactly zero but are those computed with the eccentricity left as a free parameter, so that no suggestion can arise that any conclusion that may stem from the figure is an artifact of the plotted data.

It is seen that the figure does largely confirm current ideas about the relationship it plots. The six orbits of shortest period are all circular or very close to it, whereas all the others, with the curious exception of HR 7895 at P = 372 days and possibly (though probably not) that of HD 193350 at 1092 days, are eccentric. Unfortunately there is a large gap in the period distribution just where the division between circular and eccentric orbits falls, sc one cannot say what the critical period is except that it must lie between 118 days (HD 220636) and 260 days (14 Ser). There is a convincing increase of eccentricity with period. The eight systems with periods above the circular/eccentric division but with log P < 3 all have eccentricities less than 0.5; the thirteen with 3.0 < log P < 3.5 are divided as equally as an odd number can be between systems with

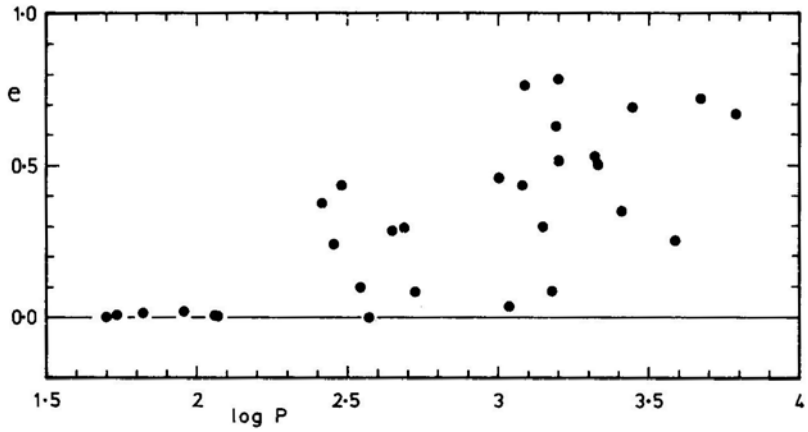

Figure 1. Eccentricity e plotted against the logarithm of the period in days for the 30 new composite-spectrum binary systems.

$e < 0.5$ and $e > 0.5$; and—although there are too few of them to be very significant—two of the three systems with $\log P > 3.5$ have $e > 0.5$.

Acknowledgements

The work reported in this paper is one facet of a programme that has been pursued at Cambridge for the past 25 years. I am very much indebted to the Observatories' whorkshop, currently led by Mr. D. R. Palmer, for making the radial-velocity spectrometer and maintaining it for all that time. Likewise, I am greatly beholden to Mr. D. W. Beggs, who made the electronics of the spectrometer and has maintained them throughout. It is a pleasure to acknowledge the use of other spectrometers on a guest-investigator basis at the Palomar, Dominion Astrophysical and European Southern observatories, and also that of the Geneva Observatory at Haute-Provence. Dr. R. E. M. Griffin collaborated in many of the observations at the overseas observatories, and offered helpful criticisms of drafts of this paper; Dr. J. E. Gunn collaborated in the Palomar observations. Travel expenses were borne by the U.K. Science & Engineering Research Council. Many photometrists have generously donated their time and interest in participating in the (as yet unrewarded) search for eclipses among the composite-spectrum binaries: I am pleased to acknowledge the participation of Messrs. J. Ells[†], P. Ells, G. J. Frey, R. E. Fried, M. B. Houchen, Y. Ito, K. Krisciunas, P. S. Leiker, R. Miles, R. E. Milton, O. Ohshima, D. Pray, K.-P. Schröder, L. Snyder, R. Wasson, J. Watson and D. B. Williams.

References

Abt, H. A., Levy, S. G. 1976, *Astrophys. J.Suppl.,* **30**, 273.
Bating, J. D. R.1977, *Bull. Amer. astr. Soc*, **9,** 142.

[†] Deceased.

Baize, P. 1988, *Astr. Astrophys. Suppl.*, **74,** 507.
Baize, P. 1989, *Astr. Astrophys. Suppl.*, **81,** 415.
Baker, N. H. 1984, *Astr. J.*, **89,** 607.
Balega, Y. Y. 1988, *Sov. Astr. Lett.*, **14,** 393.
Batten, A. H., Fletcher, J. M., MacCarthy, D. G. 1989, *Publ. Dom. astrophys. Obs., Victoria* **17.**
Bayer, J. 1603, *Uranometria*, Augsburg.
Cannon, A. J., Pickering, E. C. 1918–1924, *Ann. Harv. Coll. Obs.*. **91–99.**
Flamsteed, J. 1725, *Historiae Coelestis Britannicae,* Meere, London.
Griffin, R. E. M., Griffin, R. F., Schröder, K.-P., Reimers, D. 1990, *Astr. Axtrophvs,.* **234,** 284.
Griffin, R. F. 1967, *Astrophys. J.,* **148,** 465.
Griffin, R. F., Radford, G. A. 1977, *Observatory,* **97,** 169.
Griffin, R. F., Radford, G. A., Harmer, D., Stickland, D. J. l976, *Observatory,* **96,** 153
Griffin, R. & R. 1986, *J. Astrophys. Astr.*, **7,** 195.
Griffin, R. & R. 1988, *J. Astrophys. Astr.*, **9,** 193.
Griffin, R. & R. 1989, *J. Astrophys. Astr.*, **10,** 433.
Hendry, E. M. 1978, *Astr. J.,* **83,** 615.
Hendry, E. M. 1981a, *Astr. J.,* **86,** 271.
Hendry, E. M. 1981b, *Astr. J.*, **86,** 1540.
Hendry, E. M. 1984, *Astr. J.*, **89,** 607.
Hoffleit, D. 1982, *The Bright Star Catalogue,* Yale Univ. Obs., New Haven.
Hynek, J. A. 1938, *Contr. Perkins Obs.,* **1,** 185.
Mathieu, R. D., Latham, D. W., Griffin, R. F. 1991, *Astr. J.*, submitted.
McAlister, H. A., Hartkopf, W. I. 1988, *Second Cataloa of Interferometric Meaasurements of Binary Stars* (*CHARA Contr.,* no. 2), Georgia State Univ., Atlanta,
Morbey, C. L., Griffin, R. F. 1987, *Astrophys. J.*, **317,** 343.
Parsons, S. B. 1983, *Astrophys. J. SuppL,* **53,** 553.
Sterne, T. E. 1941, *Proc.* [*U.S.*] *Nat. Acad. Sci.*, **27,** 175.
Wright, K. O. 1952, *Publ. Dom. astrophys. Obs.*, *Victoria,* **9,** 167.

Note added in proof

Mr. and Mrs. R. Lines have reported the discovery of eclipses in the HD 223971 system.

J. Astrophys. Astr. (1990) **11,** 507–514

Spatial Velocities of Pulsars

Yu. P. Pskovsky* & O. F. Dorofeyev** *M. V. Lomonosov Moscow State University, Leninskiye Gory, Moscow, 117234, USSR*

Received 1989 January 7; revised 1990 October 1; accepted 1990 October 8

Abstract. Assuming that the orientation of a pulsar's velocity vector is parallel to its spin axis, we have calculated the space velocities of 61 pulsars from their tangential velocities. The mean space velocity of the sample is equal to 267 km s^{-1}. The radial velocities and kinematical ages of 20 pulsars are obtained. The decay time of the magnetic field of pulsars is $\tau_D = 2$ Myr, smaller than previously found.

Key words: pulsars—kinematics—spatial velocity

1. Introduction

The tangential velocities of 33 pulsars are known from their proper motions. The velocities of the scintillations produced by the interstellar medium have also been estimated for 73 radio pulsars; these estimates are proportional to the tangential velocities. These data, among others, are indicative of high velocities of some radio pulsars. However, general methods to estimate the spatial velocities are lacking although the acceleration mechanisms of a pulsar by off-centred magnetic dipole radiation (Harrison & Tademaru 1975) or by anisotropic emission of neutrinos in the URCA processes in a magnetic field (Chugaj 1984; Dorofeyev, Rodionov & Ternov 1984) predict that the acceleration vector of a moving pulsar is directed along the magnetic axis and the resultant spatial velocity vector is parallel to the spin axis (Tademaru 1977). Such an alignment requires that the position angle of the tangential velocity (ϕ_v) and that of the plane of polarization at the pulse centre (ϕ_p) coincide with (Morris, Radhakrishnan & Shukre 1976). The latter angle is supposed to coincide with the projection of the rotation axis on the celestial sphere . The condition $|\phi_v - \phi_p| = 0$ provides an 'angular test' for the asymmetric mechanism of pulsar acceleration. Unfortunately, this test has been contested on observational grounds by Anderson & Lyne (1983), thus undermining the hypothesis of magnetodipole acceleration of pulsars.

On the other hand, Pskovsky & Dorofeyev (1989) have shown that there exists an inverse relation between $|\phi_v - \phi_p|$ and the difference $|\zeta - \beta|$ where ζ is the angle between the light beam and the rotation axis β the angle between the magenetic and rotation axes. In other words, when $|\zeta - \beta|$ is equal to the angular radius of the cone of the radio radiation of the pulsar (the form of the pulse in this case has a sharp

* P. K. Shternberg State Institute of Astronomy
** Physics Department

maximum), $|\phi_v - \phi_p| \sim 0$, as it is expected according to the angular test. But if $|\zeta - \beta| \sim 0$, that is the line of sight intersects the cone near the magnetic axis (the profile of the pulse in this case consists of two or three maxima), $|\phi_v - \phi_p| \sim 90°$. In intermediate cases this difference lies between 0° and 90°. Therefore, it is wrong to assert that ϕ_p and the projection of the rotation axis on the celestial sphere coincide.

In this article we centre our attention on a more descriptive and essentially a scalar test. It is evident that if the spatial velocity V is oriented along the spin axis the tangential velocity V_t is proportional to sin ζ An estimate of ζ is possible in the model of pulsar radiation through the polar cap (Radhakrishnan & Cooke 1969). Further conclusions follow only on the basis of observational confirmation of the acceleration mechanism using the scalar test, ignoring the contradicting results of the angular test.

2. The data

For 26 pulsars having estimates of both V_t and the velocity V_s of the interstellar medium producing pulsar scintillations, we obtain a systematic difference $V_t / V_s = 2.0 \pm 0.1$.The correlation coefficient is equal to 0.81,omitting PSR 0818 – 13 (poor V_t) and PSR 061 + 22, 1933 + 16 and 2303 + 30 with anomalously great V_t / V_s (Cordes 1986). Here and in the following, the calculations of Cordes are used for correcting the tangential velocities of pulsars for galactic rotation.

Table 1 presents the data on 61 pulsars with known V_t, V_s and ζ. The distance D and V_s are generally taken from Cordes (1986), excepting four cases where D is taken from other sources (Gwinn *et al.* 1986; Gordon & Gordon 1977; Bailes *et al.* 1990); and for PSR 1702–19 V_s is taken from Smith & Wright (1985). V_t is the mean weighted value, and V_s is corrected to the scale of V_t with mean weighted square errors (in the case of discrepant values of V_t and V_s, preference is given to the more accurate one, and the omitted estimate is placed in parentheses); the spatial velocity of a pulsar is defined as $V = V_t / \sin \zeta$.

There exist a number of methods for determining ζ and β, some of which use known models of pulsar radiation (Narayan & Vivekanand 1982; Malov 1983). There are systematic differences in different estimates, Malov's method being the most reliable. Hence all values have been corrected to the system of Malov as described below.

For most pulsars statistical methods are applicable. Extensive lists of pulsars have been published by Malov (1986), and Lyne & Manchester (1988). Statistical methods estimate the angular radius of the radiation beam as a function of the pulsation period. All these methods need further development.

A comparison of the estimates of the angle β for 39 pulsars common between the lists of Malov (β_2) and Lyne & Manchester (β_L) indicates the empirical relation (PSR 0611 + 22 is excluded due to its large deviation)

$$\Gamma^{1/5} \sin \beta_2 / \sin \beta_L = (-15.6 \pm 0.8) \sin \beta_L \pm 0.3. \quad (1)$$

Here, Γ is the gradient of the position angle of the projection of the electric vector of the radiation, based mostly on Lyne & Manchester (1988), but in five cases (noted by A) taken from Ashworth (1988) and for PSR 053 + 21 from Malov (1986).

The values β_0, obtained by the model method of Malov (1983), and β_2, obtained by the statistical method (Malov 1986) are related empirically as

$$\beta_2 = (1.32 \pm 0.6)\, \beta_0, (n = \text{ll}, \beta_0 \leqslant 48^{\circ}). \quad (2)$$

The pulsars 0628 – 28, 1747 – 46 and 2021 + 51 are excluded. After making empirical corrections using relations (1) and (2) we used

$$\sin \beta = \Gamma \sin (\zeta - \beta), \tag{3}$$

to get new statistical values of β_2 and ζ_2 in the system of Malov for 33 pulsars (rounded to tenth of a degree) and revised the estimates of Lyne & Manchester (1988) for 21 pulsars (rounded to a degree). In two cases β_2 was derived simply from β_0. For five pulsars the values of ζ and β were found by the method of Malov (noted by asterisk). The system of values for β_2 has, of course, its drawbacks and should be considered as a temporary measure.

3. Pulsar space velocities

The importance of the ζ estimates of Malov (1983), lies in the fact that the values of ζ range from ~ 0° to ~ 90°, enabling a determination of the correlation $V_t \sim \sin \zeta$. Pskovsky & Dorofeyev (1989) have shown that there is a clear tendency for V_t to increase with sin ζ, and thus the models of acceleration of a pulsar along its spin axis and of radiation through the polar cap, previously not known to be related to each other, are seen to be mutually consistent. The spread of points in Fig. 1 indicates that the spatial velocities lie in a broad range. This conclusion follows also from the fact that the mean spatial velocity of the sample of 61 pulsars in Table 1is 267 ± 20 km s^{-1}

Fig. 2 is a histogram of spatial velocities of pulsars. Nine pulsars having velocities greater than 500 km s^{-1} build a little maximum and a tail extending to 1118 km s^{-1}. Most of these nine estimates are ambiguous: four pulsars (0540 + 23, 1905 + 39, 2111 + 46, 2154 + 40) have anomalously high estimates of scintillation velocities. According to the estimates of Cordes (1986), out of 24 pulsars having tangential velocities two have anomalous scintillation velocities. Thus one expects 4 ± 2 such pulsars out of a

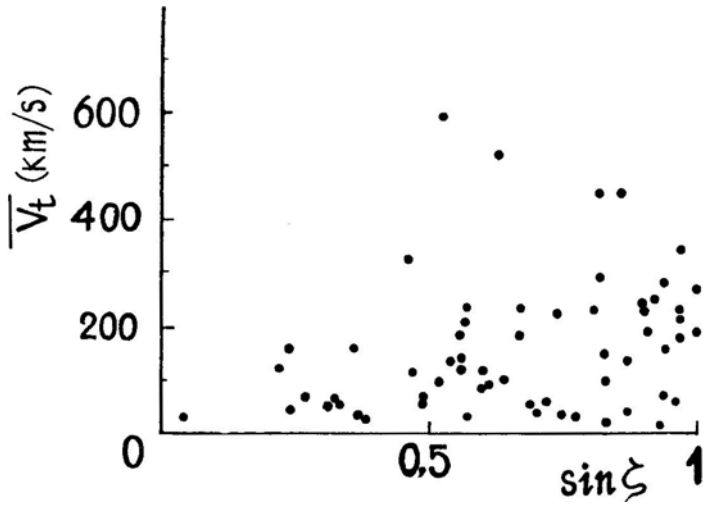

Figure 1. The tangential velocities of pulsars plotted as a function of sin ζ where ζ is the angle between the spin axis and the line of sight.

Table 1. Tangential and space velocities of pulsars.

PSR	D kpc	V_t km s^{-1}	V_s km s^{-1}	$\bar{V}_t$ km s^{-1}	Γ	β_2 deg	ζ_2 deg	V km s^{-1}
(1)	(2)	(3)	(4)	(5)	(6)	(7)	(8)	(9)
0031−07	0.39	<144 D	19±3	38±6	0.5	1.6	4.0	544±86
0138+59	3.00	—	25±3	50±6	9.0	16.4*	18.2	160±19
0301+19	0.56	101±10 L	48±7	99±2	17.0	53.2	56.6	119±2
0320+39	0.87	—	42±6	84±12	20.0 A	35.3*	37.2	139±20
0329+54	2.30	225±10 L	(66±11)	225±10	10.0	44.0	48.0	303±13
0355+54	1.64	66±30 L	(145±26)	66±30	10.0	26.6*	29.4	134±61
0450−18	1.53	—	68±12	136±24	6.0	28.0	33.0	246±44
0525+21	2.00	149±170 L	117±25	234±52	31.0	40.7	42.0	350±79
0531+21	2.00	157±38 RM	—	157±38	1.0 M	87.0 M	71.0	166±40
0540+23	2.51	—	163±23	326±46	9.0	17.6	27.4	708±100
0611+22	3.07	131±56 L	(10±2)	131±56	3.1	50.6	60.2	151±66
0628−28	1.24	<335 D	60±13	120±26	4.2	9.9	12.6	550±120
0656+14	0.41	—	33±12	66±24	1.0	21.0	44.0	95±35
0736−40	1.50	517±62 D	—	517±62	3.6	31.0	39.0	822±99
0809+74	0.18	43±4 L	22±7	43±4	2.0	9.8	13.6	183±17
0818−13	1.46	(221±588) H	75±12	150±24	30.0	50.6	56.6	180±30
0823+26	0.36	193±4 G	65±19	192±6	12.0	87.0 M	90.0	192±6
0833−45	0.50	132±11 BA	53±5	121±16	9.0	12.7	34.3	215±28
0834+06	0.43	105±12 L	84±14	159±9	11.0	19.0	21.0	443±25
0919+06	1.02	—	117±35	234±70	7.0	29.5*	34.6	412±23
0943+10	0.56	115±47 L	—	115±47	2.1	21.0	27.8	274±101
0950+08	0.13 G	25±2 G	32±10	25±3	1.4	13.8	22.5	65±8
1112+50	0.32	—	60±11	120±23	10.0 A	29.7	36.7	201±37
1133+16	0.16	278±6 D	130±32	278±2	12.0	63.9	69.9	296±2
1237+25	0.33	178±5 L	112±20	179±5	50.0	73.8	76.1	184±5
1451−68	0.45 B	88±2 BN	(15±5)	88±2	7.0	30.0	37.3	145±3
1508+55	0.73	346±10 L	(128±23)	346±10	28.0	70.0	76.5	356±10
1541+09	1.34	81±30 L	30±4	61±5	7.0	16.0	19.0	187±15
1604−00	0.36	14±15 L	21±7	28±14	3.0	25.8*	34.8	49±24
1642−03	0.16	20±8 D	(56±9)	20±8	50.0	46.1	56.3	24±10
1702−19	0.74	—	116±23	232±46	14.0	80.0	76.0	240±47
1706−16	0.84	<160 D	36±7	72±14	9.0	60.7	70.3	76±15
1737+13	1.83	—	144±8	288±16	15.0	52.0	55.0	352±20
1738−08	2.76	—	115±20	230±40	15.0	51.0	54.0	284±50
1749−28	1.00	<80 D	15±3	30±6	25.0	40.1	50.2	39±8
1804−08	4.10	—	114±31	228±62	21.0	62.0	64.0	254±69
1818−04	1.50	187±16 L	(69±7)	187±16	13.0 A	62.0	66.0	205±18
1821+05	2.44	—	19±6	38±12	18.0	57.0	60.0	44±14
1822−09	0.65	—	35±5	70±10	50.0	9.9	15.6	260±37
1839+09	1.61	—	31±21	62±42	20.0	18.0	19.0	190±129
1839+56	0.98	—	135±16	270±32	50.0	90.0	89.0	270±32
1905+39	1.00	—	226±53	452±106	15.0	52.0	55.0	552±129
1911−04	3.26	<325 D	125±17	250±34	27.0	65.0	67.0	272±37
1915+13	2.70	—	102±12	204±24	6.0	30.2	34.9	357±42
1919+21	0.36	186±41 GR	65±7	137±19	10.0	26.1	33.8	246±34
1929+10	0.11	55±3 D	36±11	55±2	1.5	18.0	29.1	113±4
1933+16	6.00	(733±110) D	120±16	240±32	50.0	51.4	63.9	267±36
1937+214	5.00	14±12 R	(81±20)	14±12	3.0	79.0	69.0	15±13
1944+17	0.47	20±9 L	18±4	28±8	1.0 A	0.4	2.1	764±218
1952+29	0.21	44±10 L	15±4	35±7	4.0	16.2	22.0	93±19
2003−08	0.93	—	90±28	180±56	4.0	34.0	42.0	269±81

Table 1. Continued.

PSR	D kpc	V_t km s^{-1}	V_s km s^{-1}	$\bar{V}_t$ km s^{-1}	Γ	β_2 deg	ζ_2 deg	V km s^{-1}
(1)	(2)	(3)	(4)	(5)	(6)	(7)	(8)	(9)
2016+28	1.30	15±13 L	20±3	36±9	6.0	42.6	49.0	48±12
2020+28	1.30	97±12 L	47±8	96±1	15.0	29.0	31.0	186±2
2021+51	0.71	59±12 L	(59±12)	59±12	4.0	38.4	46.0	82±16
2044+15	1.41	—	50±10	100±20	11.0	37.0	40.0	156±31
2045−16	0.39	465±78 L	214±51	453±10	30.0	58.0	59.6	525±12
2111+46	4.95	<2340 D	80±13	160±26	6.7	12.0	14.0	661±112
2154+40	2.64	—	298±24	596±48	8.0	29.7	32.2	1118±107
2217+47	1.46	225±41 L	103±22	216±9	26.0	69.8	76.1	223±9
2303+36	1.91	321±54 L	32±8	61±5	9.0 A	66.2	73.2	64±5
2324+60	2.80	—	93±12	186±24	10.0	26.1	33.9	333±43

Reference code to columns 2, 3, 6 and 7

A—Ashworth (1988)
BA—Bailes *et al.* (1989)
BN—Bailes *et al.* (1990)
D—Downs & Raichley (1983)
G—Gwinn *et al.* (1986)
GR—Gullahorn & Rankin (1978)
H—Helfand *et al.* (1980)
L—Lyne *et al.* (1982)
M—Malov (1983)
R—Rawley *et al.* (1988)
RM—Minkowski (1970)

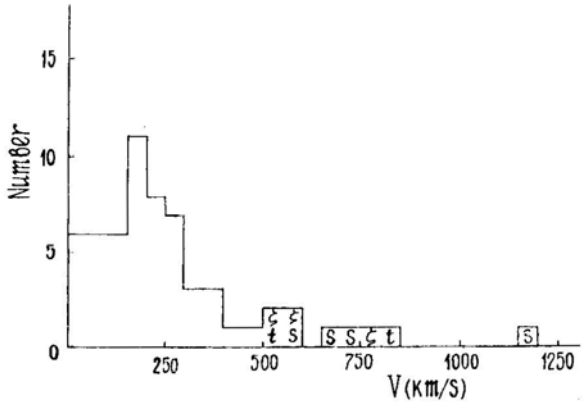

Figure 2. The histogram of spatial velocities of 61 pulsars. High velocities are due to anomalous scintillation velocity (s), anomalous tangential velocity (t), or small value of angle ζ.

sample of 61. Apart from the four indicated above, PSR 0611 + 22 and 2303 + 30, for which we have used only the estimates of tangential velocities, may fall in this category.

PSR 0031 – 07 and 1944 +17 have small values of angle ζ (4° and 2°, respectively) having Standard errors of the same order. Therefore, the determination of their spatial velocities involves great errors. Only for three pulsars, (0628 –28, 0736 –40 and 2045 –16) the spatial velocities are higher than 500 km s^{-1} provided D and ζ for these for these objects are not revised.

4. Pulsar kinematic ages

Having estimates of ζ at our disposal we can calculate the radial velocity of a pulsar, $V_r = V \pm V_t \operatorname{ctg}\zeta$, as well as the z-component of spatial velocity,

$$V_z = \pm V_r \sin b + V_b \cos b - 7.4. \quad (4)$$

Here V_b is the component of the tangential velocity along the galactic latitude and the last term is the z-component of the peculiar velocity of the Sun (in km s^{-1}). Note,that the sign of V_r is not known and therefore both V_z^+ and V_z^- should be considered. From the values of z and V_z we may get two estimates of the kinematic age of the pulsar $t_k^{\pm} = 0.97z / V_z^{\pm}$ (Myr) where z is the height of the pulsar over the galactic plane in pc.

The data on the components V_r and V_b as well as the ages of 22 pulsars are presented in the Table 2. Besides obvious notation, we use $t_c = P/\dot{P}$, the characteristic age of the pulsar. Of 33 pulsars having velocity estimates, 13 had to be rejected:

1) PSR 0525 + 21, 0818 –13, 1604–00, 1933 + 16, 1937 + 214, 1944+17 have large errors in the estimates of V_t and consequently in V_b ;
2) PSR 0329 + 54, 0611 + 22, 1541+ 09, 2045–16 have low-accuracy estimates of V_z ;
3) PSR 0531+ 21 and 0833 – 45 are young and their t_k's are false.

In most cases we obtained two values of t_k, the negative value being excluded. When both values were positive, the value of lower accuracy (PSR 0301 +19 and 2016 + 28)

Table 2. Kinematic and characteristic ages of pulsars.

PSR (1)	z pc (2)	V_r km s^{-1} (3)	V_b km s^{-1} (4)	V_z^+ km s^{-1} (5)	V_z^- km s^{-1} (6)	t_k Myr (7)	t_c Myr (8)	t_k^{LAS} Myr (9)
0301+19	−307	±67±7	−72±16	−104±14	−30±14	2.9±0.4	17.0	3.5
0355+54	+23	±114±51	+89±30	+80±30	+84±30	0.3±0.1*	0.6	2.1
0736−40	−240	±638±84	−193±62	−300±63	−96±63	1.6±0.8*	3.7	—
0809+74	+95	±182±21	−21±6	+70±12	−122±12	1.3±0.2	123.0	4.0
0823+26	+189	0	+54±4	+39±3	+39±3	4.7±0.4*	4.9	2.8
0834+06	+191	±271±16	+51±10	+158±11	−82±11	1.2±0.1	3.0	3.2
0943+10	+383	±167±74	+117±48	+192±62	−36±62	1.9±0.6	4.9	—
0950+08	+90	±60±5	+21±2	+49±4	−33±4	1.8±0.1	17.4	3.5
1133+16	+150	±102±3	−49±5	+71±4	−119±4	2.1±0.1	5.0	0.6
1237+25	+329	±44±1	−83±5	+31±1	−57±1	10.3±0.3	22.9	—
1451−68	−67	±116±4	+22±1	−3±1	+31±1	22.3±0.3	42.6	—
1508+55	+578	±83±0	−341±11	−150±11	−282±11	—	2.3	1.0
1642−03	+70	±128±5	−13±6	−37±6	−75±6	1.8±0.3	3.5	—
1818−04	+123	±86±12	+77±23	+76±23	+62±23	1.7±0.6*	1.5	1.7
1919+21	+22	+279±66	+171±41	+180±41	+146±41	0.14±0.02*	15.8	—
1929+10	−7	±101±2	−35±3	−49±3	−35±3	0.16±0.02*	3.1	4.0
1952+29	+3	±109±27	−40±17	−49±17	−46±17	—	3388.0	2.7
2016+28	−91	±129±112	−6±12	−22±12	−4±12	4.0±2.2	58.9	10.0
2020+28	−106	±165±20	0±2	−21±2	+6±2	4.9±0.5	2.9	1.8
2021+51	−104	±57±11	+16±13	+0.1±13	+17±13	6.0±4.6	2.8	6.0
2217+47	−193	±55±10	−127±44	−134±44	−120±44	1.5±0.5*	3.1	1.5
2303+30	−856	±96±16	−317±54	−334±49	−248±49	2.8±0.4*	8.7	2.4

was excluded. In other cases marked with asterisk the values of t_k were averaged. Column 9 of Table 2 lists the estimates t_k^{LAS} according to Lyne, Anderson & Salter (1982).

5. Decay of magnetic field

In Fig. 3 the relation between log t_k and log t_c is plotted for 20 pulsars. This figure also shows lines for various values of τ_D, the pulsar magnetic field decay time scale (in Myr) in accordance with the following relation

$$t_k = 0.5\ \tau_D \log (1 + 2\ t_c / \tau_D). \quad (5)$$

11 pulsars concentrate around the value $\tau_D = 2$ Myr; the remaining 9 pulsars present considerable scatter, whose origin can be explained in the following way. Consideration of $| z |$-distribution of 330 pulsars (Manchester & Taylor 1981) with allowance for their age yields the average value $|\overline{z}| = 130$ pc. Therefore, nearly half of the pulsars have high starts, that is $| z |$ is greater than 130 pc. These pulsars are PSR 0823 + 26, 1237 + 25, 1508 + 55, 1818–04, 2020 + 28 and 2021 + 51. Three pulsars PSR 0809 + 74, 1919 + 21, 1929 + 10 had high starts even in the other galactic hemisphere.PSR 1952 + 29 is yet to cross the galactic plane. Besides, some of the pulsars might have been accelerated towards the galactic plane and not away from it. It is these factors that

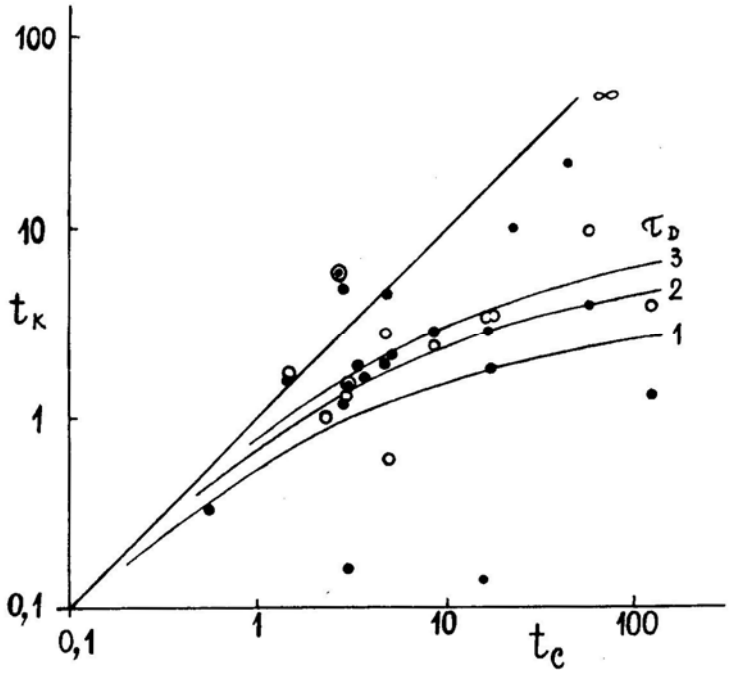

Figure 3. Kinematical and characteristic ages (in Myr) of pulsars. Dark circles correspond to data from Table 1, open ones correspond to data from Lyne *et al.* (1982), and circled dots mark coinciding data. Curves 1, 2, . . . ∞ are theoretical curves obtained from relation (5) for corresponding values of τ_D.

create considerable scatter of points in Fig. 3. Estimates of t_k marked with open circles are given according to Lyne, Anderson & Salter (1982) who calculated V_z in a different way. The derived decay time is smaller than that found by Lyne *et al.* (8 Myr).

The authors express their hope for a further confirmation of the scalar test proposed by them and for making physical characteristic of pulsars more precise.

References

Anderson, B., Lyne, A. G. 1983, *Nature,* **303,** 597.
Ashworth, M. 1988, *Mon. Not. R. astr. Soc,* **230,** 87.
Bailes, M., Manchester, R. N., Kesteven, M. J., Norris, R. P., Reynolds J. E. 1989, *Astrophys. J.*, **343**, L53.
Bailes, M., Manchester, R. N., Kesteven, M. J., Norris, R. P., Reynolds, J. E. 1990, *Nature,* **343,** 240.
Chugaj, N. N. 1984, *Sov. Astr. Lett.,* **10,** 210.
Cordes, J. M.1986, *Astrophys. J.*, **311,** 186.
Dorofeyev, O. F., Rodionov, V. N., Ternov, I. M. 1984, *JETP Lett.,* **40,** 159.
Downs, G. S., Reichley, P. E. 1983, *Astrophys. J. Suppl. Ser.* **53,** 169.
Gordon, K. J., Gordon, C. P.1973, *Astr. Astrophys.,* **24,** 119.
Gullahorn, G. E., Rankin, J. M. 1978, *Astrophys. J.*, **225,** 963.
Gwinn, C. R., Taylor, J. H., Weisberg, J. M., Rawley, L. A. 1986, *Astr. J.*, **91,** 338.
Harrison, E. R., Tademaru, E. 1975, *Astrophys. J.*, **201,** 447.
Helfand, D. J., Taylor, J. H., Bakus, P. R., Cordes, J. M. 1980, *Astrophys. J.*, **237,** 206.
Lyne, A. G., Anderson, B., Salter, M. J. 1982, *Mon. Not. R. astr. Soc.,* **201,** 503.
Lyne, A. G., Manchester, R. N. 1988, *Mon. Not. R. astr. Soc.,* **234,** 477.
Manchester, R. N.,Taylor, J. H. 1981, *Astr. J.*, **86,** 1953.
Malov, I. F. 1983, *Astrophys*., **19,** 95.
Malov, I. F.1986, *Astrophys*., **24,** 507.
Minkowski, R. L. 1970, *Publ. astr. Soc. Pac.,* **82,** 470.
Morris, D., Radhakrishnan, V., Shukre, C. 1976, *Nature,* **303,** 124.
Narayan, R.,Vivekanand, M.1982, *Astr. Astrophys.,***113,** L3.
Pskovsky, Yu. P., Dorofeyev, O. F. 1989, *Nature,* **340,** 701.
Radhakrishnan, V., Cooke, D. J. 1969, *Astrophys. Lett,* **3,** 225.
Rawley, L. A., Taylor, J. H., Davis, M. M. 1988, *Astrophys. J.,* **326,** 947.
Smith, F. G., Wright, N. C. 1985, *Mon. Not. R. astr. Soc.,* **214**, 97.
Tademaru, E. R. 1977, *Astrophys. J.,* **214,** 885.

J. Astrophys. Astr. (1990) **11**, 515–531

Radio Wave Heating of Astrophysical Plasmas

R. T. Gangadhara* & V. Krishan *Indian Institute of Astrophysics, Bangalore 560034*

Received 1990 February 16; revised 1990 August 1; accepted 1990 October 15

Abstract. The coherent plasma process such as parametric decay instability (PDI) has been applied to a homogeneous and unmagnetized plasma. These instabilities cause anomalous absorption of strong electromagnetic radiation under specific conditions of energy and momentum conservation and thus cause anomalous heating of the plasma. The maximum plasma temperatures reached are functions of luminosity of the radio radiation and plasma parameters. We believe that these processes may be taking place in many astrophysical objects. Here, the conditions in the sources 3C 273, 3C 48 and Crab Nebula are shown to be conducive to the excitation of PDI. These processes also contribute towards the absorption of 21cm radiation.

Key words: plasma—parametric instability—quasar—Crab Nebula—anomalous absorption—electromagnetic waves

1. Introduction

One of the fundamental processes in the interaction of intense electromagnetic (e.m.) radiation, of frequency close to plasma frequency, with fully ionized plasmas is the parametric excitation of two new waves. If both the excited modes are purely electrostatic, they are eventually absorbed in the plasma due to collisional and Landau (wave-particle interaction) dampings. Landau damping of excited electrostatic waves occurs when their phase velocity is slightly larger than the thermal velocity of the plasma particles. When the wave dissipates, its energy gets converted into thermal energy of particles. The incident e.m. radiation is anomalously absorbed in the plasma at a rate which is much larger than the collisional absorption rate.

Quasars, Seyfert galaxies and pulsars are among the most luminous objects in the universe, emitting strongly at radio frequencies. Here we study PDI in 3C 273, 3C 48 and the Crab Nebula.

1.1 *Density and Temperature Structure of Broad-line Regions of Active Galactic Nuclei*

The emission line regions of active galactic nuclei (AGN) are commonly separated into a "narrow-line region" (NLR) and a "broad-line region" (BLR). These regions consist

* *Joint Astronomy programme, Department of Physics, Indian Institute of Science, Bangalore* 560012

of photoionized "clouds" moving with large velocities, usually assumed to be embedded in a hot dilute medium providing confinement. It has been recognized for a long time that the intense thermal and/or nonthermal UV and X-ray radiation emitted by AGN is responsible for heating and ionizing the line-emitting regions. The density structure of the BLR is closely related to the ionization structure (Kwan & Krolik 1981). The density deduced in the models has gradually increased from 10^7 cm^{-3} up to 10^{10} cm^{-3}, a value which is now commonly assumed. The absence of broad components in the forbidden lines is interpreted as due to collisional deexcitation, so that the electron density must be greater than 10^7 cm^{-3}. On the other hand the presence of the broad semiforbidden C III] λ1909 line which starts being deexcited at $n_e > 10^9$ cm^{-3} implies $n_e < 10^{10}$ cm^{-3}. Larger densities are however, indicated by some line intensities like those of Fe II. The high ionization zone (H II), facing the central source of ionizing radiation, emits what we call the high ionization lines (HIL) L_α, N v, C IV, He II, C III], *etc.* The temperature of the H II zone varies between about 15000 K and 25000 K according to the values of the density and the ionization parameter. The BLR has a dimension of 0.01–1 parsec, and clouds have electron densities 10^9–10^{10} cm^{-3} and temperatures 1.5×10^4–2.5×10^4 K (Collin-Souffrin & Lasota 1988). The BLR is very close to the active nucleus and therefore is an important diagnostic of the central region of AGN.

Davidson & Netzer (1979) have reviewed some of the heating processes proposed by several workers. Here, we propose one more process for the absorption of radio waves and hence the heating of line-emitting regions: collective plasma process such as PDI driven by intense radio radiation emitted from AGN.

1.2 *The Radio Source*

Most of the radio emission in the quasars is assumed to be emitted from the accretion disc and also from the region interior to the BLR. The radio flux f_ν of 3C 48 at 1400 MHz is 15.63 Jansky and that of 3C 273 is 46.4 Jansky (Lang 1980). The redshift of 3C 48 is $z = 0.367$ and that of 3C 273 is $z = 0.158$. We find the distance d between the observer and quasar using the Hubble distance-redshift relation $d = 5000$ Mpc. The luminosity of 3C 48 and that of 3C 273 at 1400 MHz, determined by using the relation $L_\nu = 4\pi d^2 f_\nu$, are 5.95×10^{34} erg s^{-1} Hz^{-1} and 3.28×10^{34} ergs^{-1} Hz^{-1}, respectively. The total luminosity of Crab Nebula is 10^{38} erg s^{-1}, twelve percent of which is in the radio band. The electron density and temperature at a distance of about 0.03 parsec from pulsar are about 10^7 cm^{-3} and 10^4 K, respectively (Ginzburg & Ozernoy 1966). The excitation of PDI in the emission-line regions of quasar was first discussed by Krishan (1987) and then by Gangadhara & Krishan (1989, 1990). Here, we extend this work to include the new effects associated with strong and broad pump in the three astrophysical objects mentioned above.

2. Parametric decay instability (PDI)

An incident e m. pump wave (ω_0, $\mathbf{K}_0$) excites a high frequency electron plasma wave (ω_e, K $_e$) and a low frequency ion-acoustic wave (ω_i , $\mathbf{K}_i$) such that

$$\omega_0 = \omega_e + \omega_i \quad \text{and} \quad \mathbf{K}_0 = \mathbf{K}_e + \mathbf{K}_i \tag{1}$$

where

$$\omega_0^2=\omega_{pe}^2+k_0^2c^2,\quad \omega_e^2=\omega_{pe}^2+\frac{3}{2}k^2v_e^2\quad\text{and}\quad \omega_i^2=\omega_{pi}^2\left(1+\frac{1}{(k\lambda_{De})^2}\right)^{-1}.$$

$\omega_{pj} = [4\pi n_j e^2/m_j]^{1/2}$, $v_j = [2k_B T_j/m_j]^{1/2}$ and $\lambda_{Dj} = [k_B T_j/4\pi n_j e^2]^{1/2}$ are the plasma angular frequency, thermal velocity and Debye length of jth species ($j = e, i$), respectively. k_B and c are the Boltzmann constant and velocity of light. The density, mass and temperature of jth species are n_j, m_j and T_j, respectively.

We chose $\omega_0 \simeq \omega_e$, $k_0^2c^2 \ll \omega_{pe}^2$ and obtain $K_e \simeq -K_i$. From equation (1), when $k\lambda_{De} \ll 1$, we find the wave number $k_e \simeq k_i = k$ of the excited Langmuir waves to be

$$k=\lambda_{De}^{-1}\left[\left\{\left(\frac{\omega_{pi}}{\omega_{pe}}\right)^2+\frac{2}{3}\left(\frac{\omega_0}{\omega_{pe}}-1\right)\right\}^{1/2}-\frac{\omega_{pi}}{3\omega_{pe}}\right]. \tag{2}$$

The non-relativistic theory of parametric instabilities has been developed by Drake *et al.* (1974) for the case of linearly polarized pumps. The PDI can be described by using the dispersion relation (Liu & Kaw 1976):

$$\frac{1}{\chi_e(\mathbf{K},\omega)}+\frac{1}{\chi_i(\mathbf{K},\omega)+1}=-(\mathbf{K}\cdot\mathbf{V}_0)^2\left[\frac{1}{(\omega-\omega_0)^2\,\varepsilon(\mathbf{K},\omega-\omega_0)}+\frac{1}{(\omega+\omega_0)^2\,\varepsilon(\mathbf{K},\omega+\omega_0)}\right], \tag{3}$$

where w and **K** are the angular frequency and wave vector of the low frequency daughter mode. The quiver velocity of electrons in the pump electric field $\mathbf{E}_0$ is $v_0 = eE_0/m_e\omega_0$. The electron and ion susceptibilities are χ_e and χ_i, respectively. The dielectric function of the plasma is $\varepsilon(\mathbf{K}, \omega \pm \omega_0) = 1 + \chi_e(\mathbf{K}, \omega \pm \omega_0) + \chi_j(\mathbf{K}, \omega + \omega_0)$.

We note that χ_e and χ_i have the following asymptotic forms:

$$\chi_e(\mathbf{K},\omega)=\begin{cases}-\dfrac{\omega_{pe}^2}{\omega^2}\left(1+\dfrac{3}{2}\dfrac{k^2v_e^2}{\omega^2}\right)+i\dfrac{\sqrt{\pi}}{(k\lambda_{De})^2}\dfrac{\omega}{kv_e}\exp\{-\omega^2/(kv_e)^2\} & \text{for } \omega\gg kv_e\\ \dfrac{1}{(k\lambda_{De})^2}\left(1+i\sqrt{\pi}\dfrac{\omega}{kv_e}\right) & \text{for } \omega\ll kv_e\end{cases}$$

$$\chi_i(\mathbf{K},\omega)=\begin{cases}-\dfrac{\omega_{pi}^2}{\omega^2}+i\dfrac{\sqrt{\pi}}{(k\lambda_{De})^2}\dfrac{T_e}{T_i}\dfrac{\omega}{kv_i}\exp\{-\omega^2/(kv_i)^2\} & \text{for } \omega\gg kv_i\\ \dfrac{1}{(k\lambda_{De})^2}\dfrac{T_e}{T_i}\left(1+i\sqrt{\pi}\dfrac{\omega}{kv_i}\right) & \text{for } \omega\ll kv_i\end{cases}$$

The energy density of the pump field E_0 and luminosity of the source are related by

$$\frac{E_0^2}{8\pi}=\frac{L}{4\pi R^2c}$$

where $L = L_{41} \times 10^{41}$ erg s^{-1} and $R = r_{pc} \times 3.1 \times 10^{18}$ cm are the luminosity of the source and the distance between the source and plasma, respectively. Now, the

oscillation velocity of electrons in the pump field is given by

$$v_0 = \frac{eE_0}{m_e \omega_0} = \frac{e}{m_e}\left(\frac{2L}{R^2 c}\right)^{1/2} \frac{1}{\omega_0}. \quad (4)$$

If the pump is strong enough, the normal modes get modified and no more remain linear. An intense pump can cause amplitude dependent shift in the real and imaginary parts of the normal mode frequencies. For $\omega_0 > \omega_e$, PDI occurs due to the parametric decay of a pump wave into an electron and an ion mode. Depending on the pump strength and the ratio T_e/T_i, it can occur through three different routes: PDI-1, PDI-2, PDI-3, discussed below. However, when $\omega_0 < \omega_e$, a purely growing (zero frequency) ion density fluctuation will spontaneously grow from the noise level. As it grows in amplitude, so also does the associated electron plasma wave. This case of parametric instability is called the "oscillating two stream instability" (OTS).

2.1 *PDI-1: Decay of a Pump Wave into an Electron Plasma Wave and an Ion-Acoustic Wave* (ω_{i1})

Here $\omega_0 \simeq \omega_e + \omega_{i1}$. For $k\lambda_{De} \ll 1$ and $\omega_{pi} \gg \omega_i = kc_s$, we neglect $\varepsilon(\mathbf{K}, \omega + \omega_0)$ as being off resonant. Using the asymptotic forms for χ_e and χ_i corresponding to $kv_e \gg w \gg kv_i$ Equation (3) becomes

$$(\omega^2 + i2\Gamma_i\omega - k^2 c_s^2)(\omega - \Delta + i\Gamma_e) + \frac{(\mathbf{K}\cdot\mathbf{V}_0)^2}{2\omega_{pe}}\omega_{pi}^2 = 0 \quad (5)$$

where $\Delta = \omega_0 - \omega_e$ is the frequency mismatch. The ion-acoustic velocity is $c_s = [(k_B T_e + 3k_B T_i)/m_i]^{1/2}$. The damping rate of the electron plasma wave is the sum of the Landau damping rate and the electron collision frequency, given by

$$\Gamma_e = \frac{\sqrt{\pi}}{2}\frac{\omega_{pe}}{(k\lambda_{De})^3}\exp\left\{-\frac{1}{2(K\lambda_{De})^2} - \frac{3}{2}\right\} + \nu_e.$$

The collisional damping rate of the electron plasma wave is $\nu_e = 3.632 n_e$, ln $\Lambda/T^{3/2}{}_e$. The Coulomb logarithm is In $\Lambda \simeq 10$. The damping rate of the ion-acoustic wave is the sum of the Landau damping rate and the ion collision frequency, given by

$$\Gamma_i = \left(\frac{\pi}{8}\right)^{1/2} kc_s\left[\left(\frac{m_e}{m_i}\right)^{1/2} + \left(\frac{T_e}{T_i}\right)^{3/2}\exp\left\{-\frac{1}{2}\left(3 + \frac{T_e}{T_i}\right)\right\}\right] + \nu_i.$$

The collisional damping rate of the ion-acoustic wave is given by $\nu_i = 0.0598 n_i \ln \Lambda / T_i^{3/2}$.

Like electrostatic waves, e.m. waves also experience collisional damping in the plasma medium. If ν_0 is the collisional damping rate of e m. wave, then the rate of energy loss from the e.m. wave ($\nu_0 E_0^2/8\pi$) must balance the rate at which the oscillatory energy of electrons is randomized by the electron-ion scattering, *i.e.*

$(v_0 E_0^2/8\pi) = (\nu_{ei} m_e v_0^2/2)$. Since $v_0 = eE_0/m_e\omega_0$, this power balance gives

$$v_0 = \left(\frac{\omega_{pe}}{\omega_0}\right)^2 \nu_{ei} \tag{6}$$

where $\nu_{ei} \simeq \nu_e$ is the electron-ion collision frequency. The dependence of v_0 on electron temperature T_e is shown in Figs 2(a), 3(a) and 4(a). Krolik, McKee & Tarter (1978) have pointed out that the radio frequency waves can heat the plasma through free-free absorption process.

For $\omega = \omega_{l1} = \omega_{r1} + i\,\gamma_1$, Equation (5) gives two coupled equations cubic in ω_{r1} and γ_1. Using $\omega_{r1} = kc_s$ and $\gamma_1 \ll \omega_{rl}$, we find only one root (ω_{r1}, γ_1) which represents growing mode while the other two roots represent damped modes because their growth rates are negative. The growth rate of growing mode is given by

$$\gamma_1 = -\frac{(\Gamma_e + \Gamma_i)}{2} + \mathrm{Re}\left[\frac{(\mathbf{K}\cdot\mathbf{V}_0)^2}{4kc_s}\left(\frac{m_e}{m_i}\right)^{1/2}\omega_{pi} + \frac{(\Gamma_i - \Gamma_e - i\Delta)^2}{4} + i\frac{\Gamma_e\Delta}{2}\right]^{1/2}. \tag{7}$$

We assume K || E_0, (the electric field of pump wave), $n_i = n_e$ in the hydrogen plasma and $\omega_0 = 1.01\omega_{pe}$. Though we have chosen initially single frequency $\omega_0 = 1.01\omega_{pe}$, as the instability sets up plasma temperatures T_e and T_i go up due to the damping of excited electrostatic waves and so do ω_e and ω_i. Since $\omega_0 = \omega_e + \omega_i$, the resonant pump frequency should also increase. Therefore, a band of pump frequencies satisfies the resonance condition. An inhomogeneity in plasma density will also admit a broad pump. Therefore, we assume that the maximum band width $\Delta\omega \simeq \omega_0$ satisfies the resonant condition of the parametric decay instability. Since γ_1 is the growth rate due to a monochromatic pump at ω_0, the actual growth rate γ_1' due to the broad pump with spectral width $\Delta\omega \gg \gamma_1$ is given by

$$\gamma_1' = \frac{1}{\Delta\omega}\gamma_1^2. \tag{8}$$

Hence due to a broad pump the growth rate of PDI is decreased by a factor of $\Delta\omega / \gamma_1$ (Kruer 1988). The coherence condition is satisfied for $\Delta\omega \leqslant \gamma_1$. Since the resonance condition for the instability is satisfied for the fraction of the band width, i.e., for $\Delta\omega \leqslant \gamma_1$, only a portion of the total luminosity is useful for the excitation of the instability.

The threshold condition obtained by setting γ_1 equal to zero in Equation (7), is given by

$$\frac{(\mathbf{K}\cdot\mathbf{V}_0)^2}{4kc_s}\omega_{pi}\left(\frac{m_e}{m_i}\right)^{1/2} = \Gamma_e\Gamma_i. \tag{9}$$

The threshold is higher for an incoherent pump because incoherency effectively amounts to having more collisions in the system. A partially polarized pump again offers only a part of its luminosity for the excitation of PDI.

We introduce a decay parameter D, defined from Equation (8), as

$$D = \frac{\int_{\nu_1}^{\nu_2} L_\nu d\nu}{4\pi R^2 n_e c} P(\lambda_{De}, k) \tag{10}$$

where the function $P(\lambda_{De}, k)=\frac{k\omega_{pi}}{2c_s(m_e m_i)^{1/2}}\frac{1}{\Gamma_e\Gamma_i}$ expresses the ffect of plasma parameters on the instability. The integration over the luminosity has to be computed over the width $v_2 - v_1 = \Delta\omega/2\pi$. The variation of the function P with respect to T_e for different densities is shown in Fig. l(a). The bending of curves at $K\lambda_{De} \ll 1$ is due to collisional damping. But when $k\lambda_{De} \simeq 0.4$ Landau damping operates which is a strong function of T_e but not of n_e. The strength of P describes if the conditions in the plasma are favourable for PDI to occur. For small pump, PDI is favoured at large P. PDI occur for $D > 1$ and switch off $D \leqslant 1$. for The variation of D with respect to temperature T_e is shown in Fig. l(b). When $D \geqslant 1$ the ionacoustic mode loses its linearity and the instability falls into one or the other three cases discussed below.

2.2 *Resonant Interaction Regions*

The average values of different parameters in the resonant interaction region of radio waves in the different sources, determined observationally, are listed in Table 1. Table 2 shows different values of ion temperature T_i and ω_0 used for each case of PDI.

Electrons being lighter generally heat up before the ions and since the electron-ion collision time is much larger than the excitation time of PDI the inequality in temperature will remain during the instability.

We solve Equation (5) numerically for real and imaginary parts of ω and exhibit the results for PDI-1 in Figs l(c) and 2(a). The region log $T_e > 5.08$ in Fig. l(c) for 3C 273

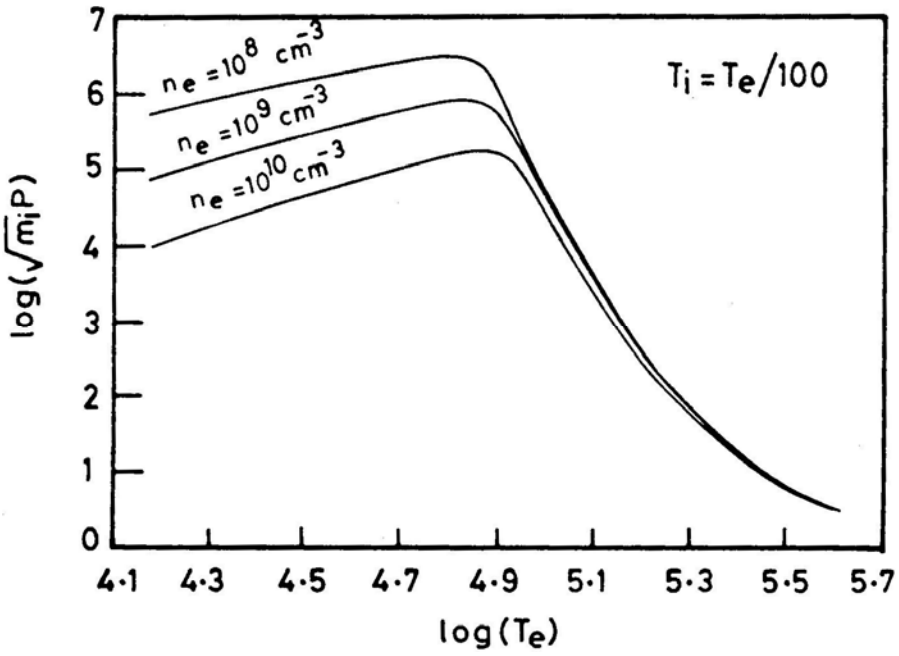

Figure 1. (a) Variation of $\sqrt{m_i}P$ with electron temperature T_e for different electron densities.

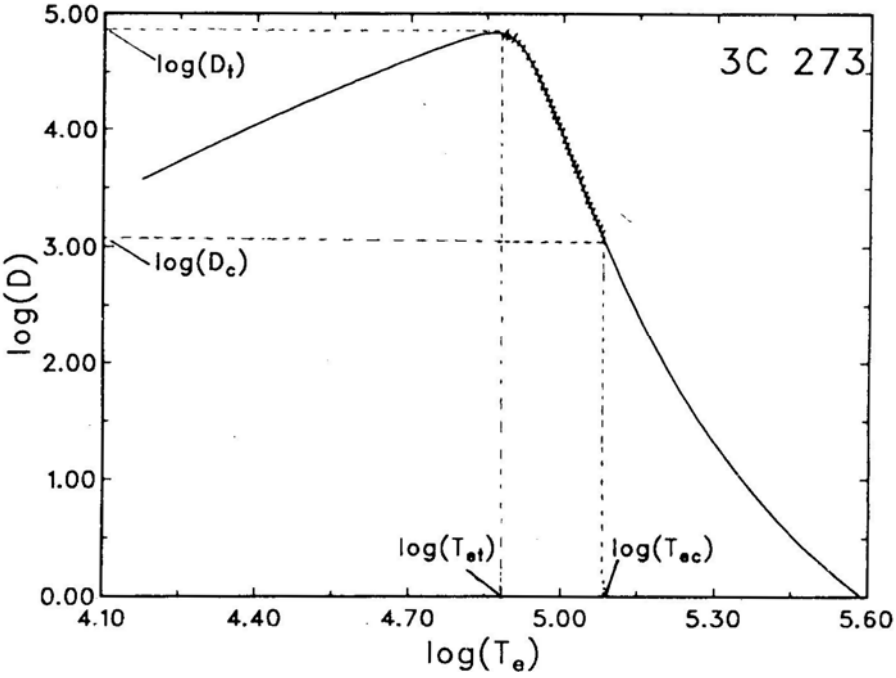

Figure 1. (b) Decay parameter D *vs* T_e in the 3C 273.

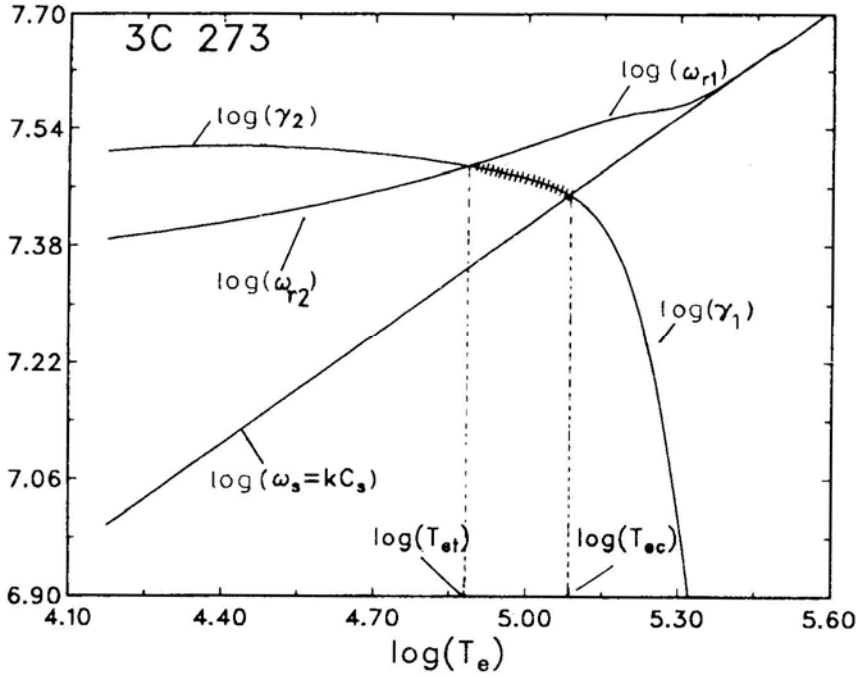

Figure 1. (c) Variation of real of the frequencies of the low frequency daughter mode ω_s, ω_{rj} and its growth rate γ_j (j = 1,2) *vs* T_e in the 3C 273.

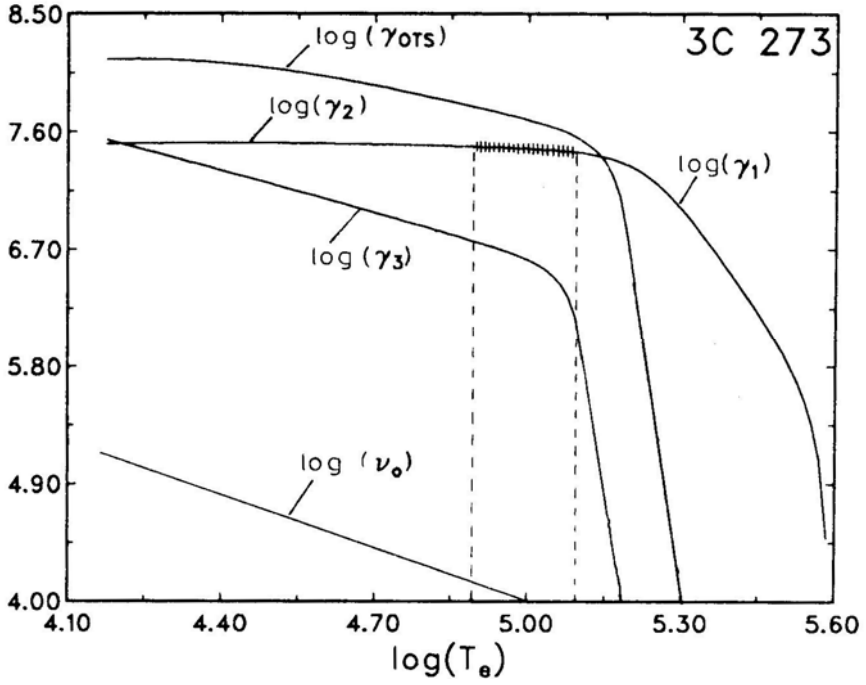

Figure 2. (a) Variation of growth rates $\gamma_j (J = 1,2,3$ and OTS) *vs* T_e for a monochromatic pump at $\omega_0 = 1.01\ \omega_{pe}$ in the 3C 273.

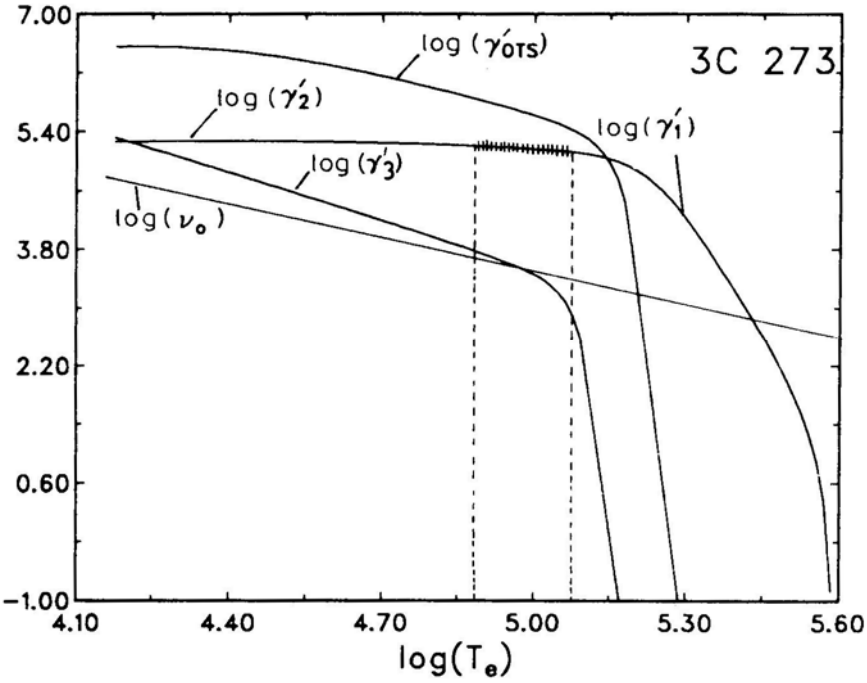

Figure 2. (b) Variation of γ_j' (j = 1, 2,3 and OTS) *vs* T_e using a broad pump in the 3C 273.

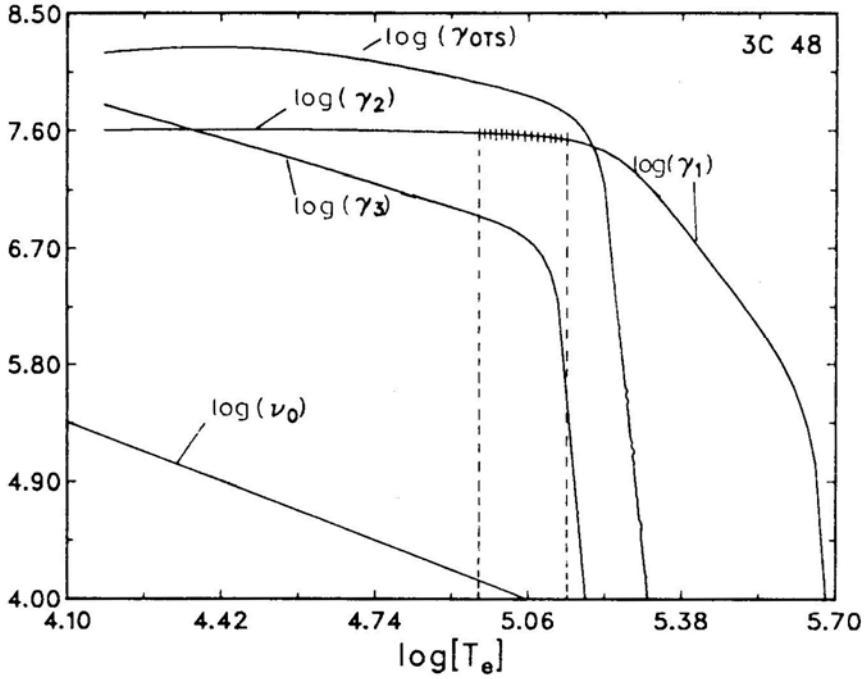

Figure3. (a) Variation of growth rates γ_j (j = 1, 2, 3 and OTS) *vs* T_e for amonochromatic pump at $\omega_0 = 1.01\omega_{pe}$ in the 3C 48.

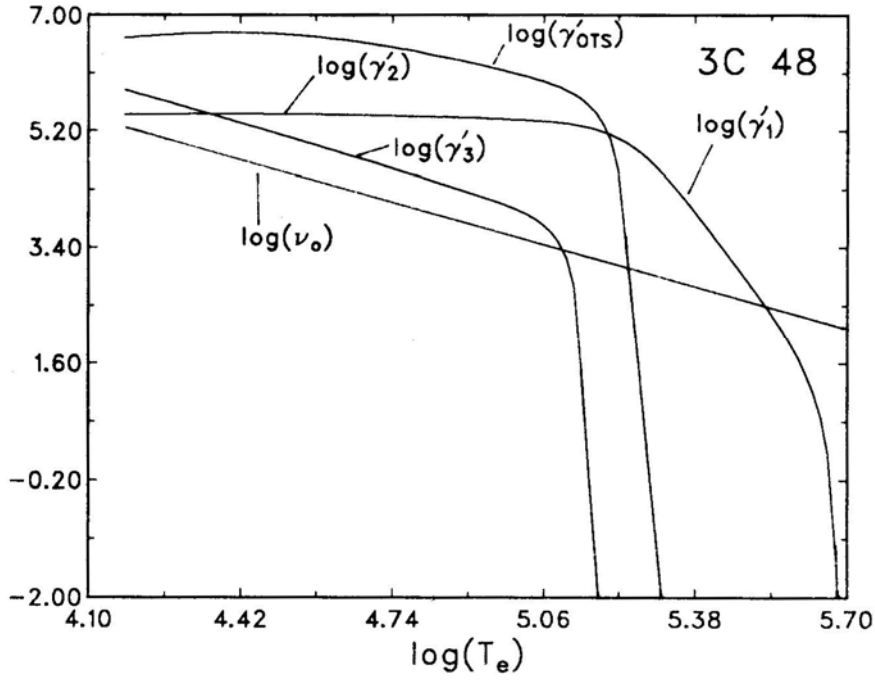

Figure 3. (b) Variation of γ'_j (j = 1, 2, 3 and OTS) *vs* T_e using a broad pump of width, $\Delta\omega = \omega_0$ in the 3C 48.

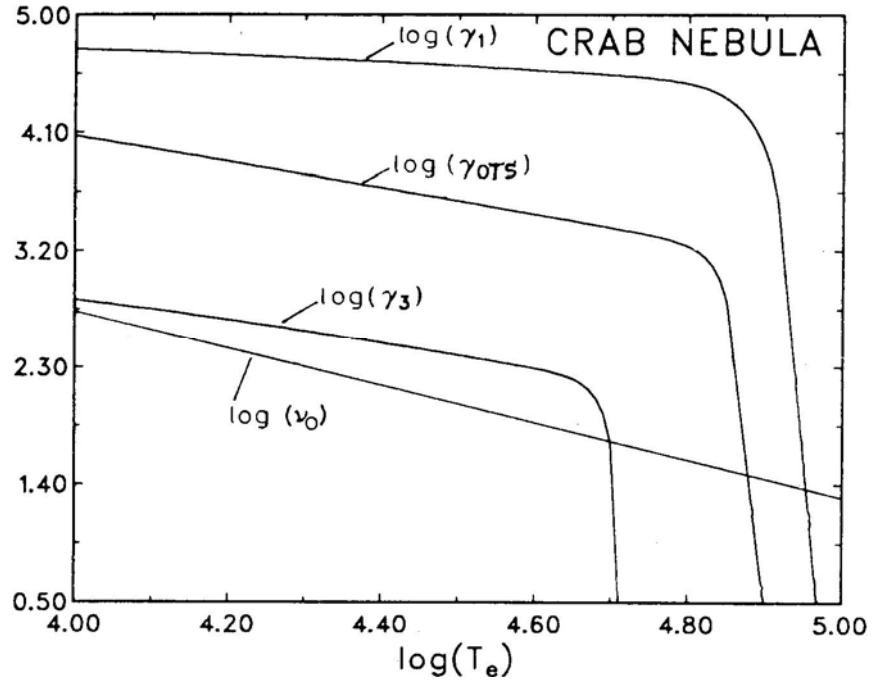

Figure. 4. (a) Variation of growth rates $\gamma_{j;}$(j = 1, 3 and OTS) *vs* T_e for a monochromatic pump at ω= 1.01 ω_{pe} in the Crab Nebula.

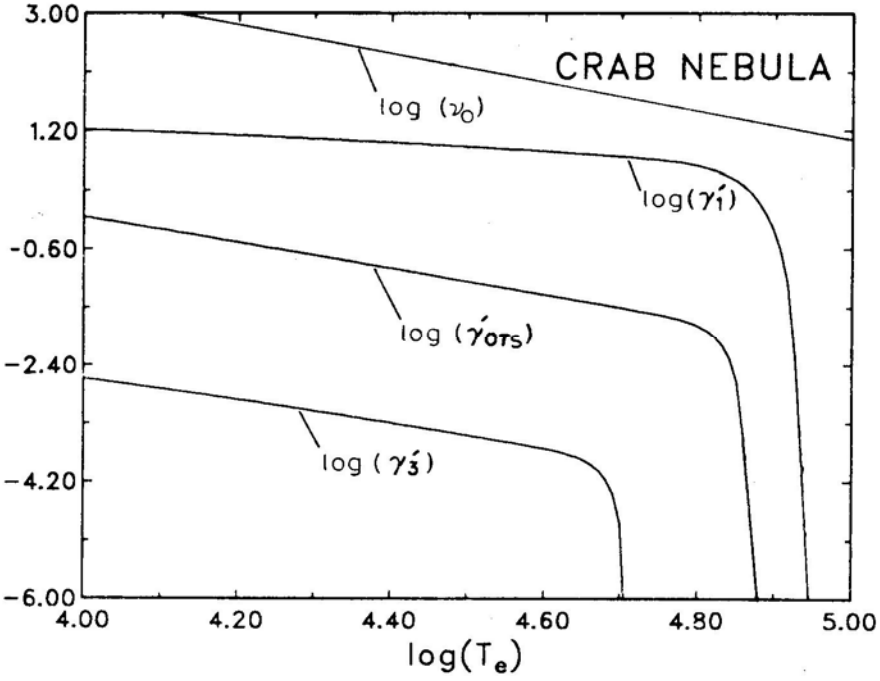

Figure 4. (b) Variation of γ'_j (j = 1, 3 and OTS) *vs* T_e using a broad pump of width $\omega = \omega_0$ in the Crab Nebula. Note that PDI-2 is not excited and also collisional absorption is dominant.

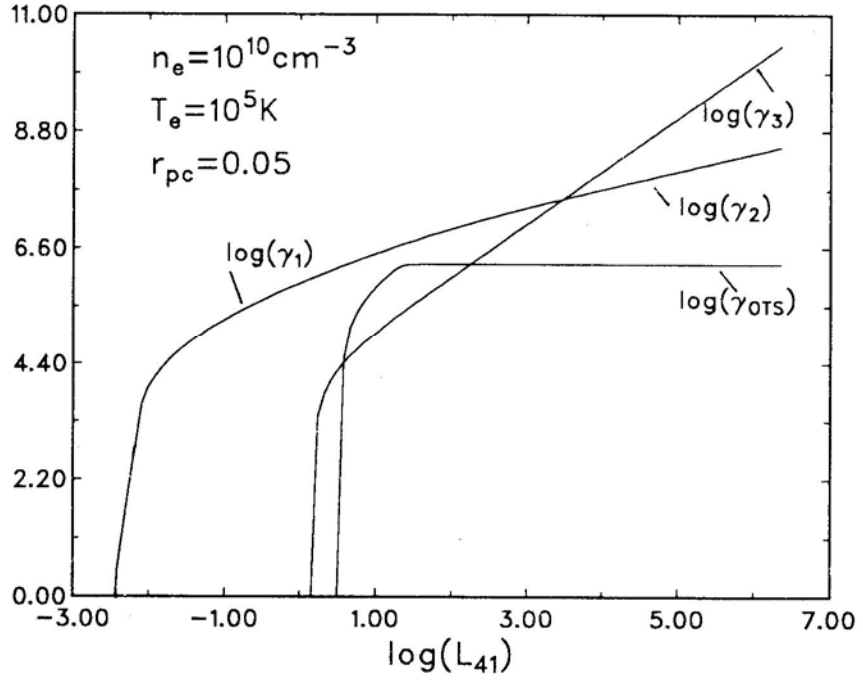

Figure 5. (a) Variation of growth rates γ_j = (j = 1, 2, 3 and OTS) *vs* pump luminosity L_{41} at $\omega_0 = 1.01\,\omega_{pe}$.

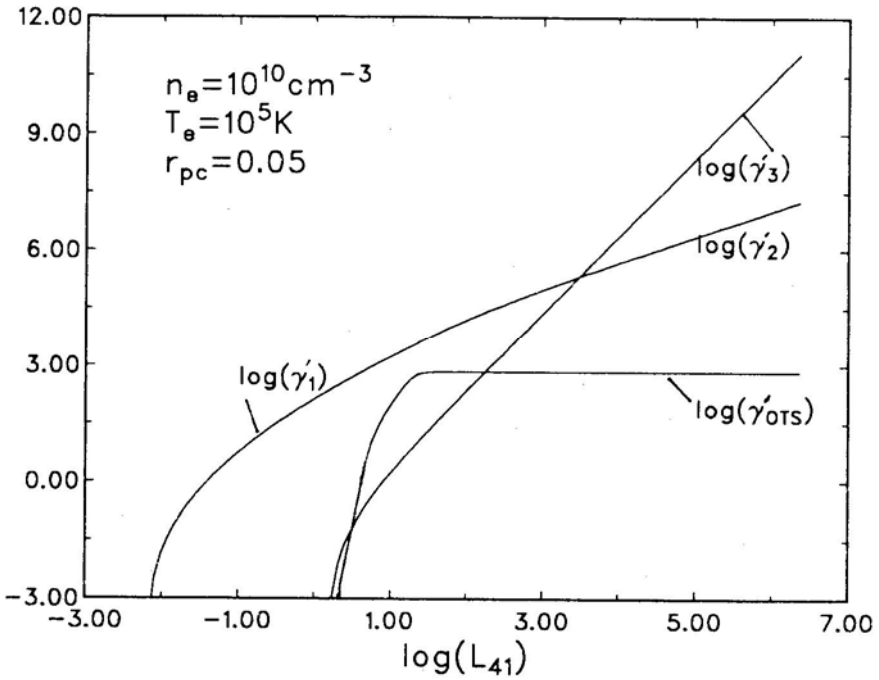

Figure 5. (b) Variation of γ'_j (j = 1, 2, 3 and OTS) *vs* luminosity L_{41} of a broad pump of width $\Delta\omega = \omega_0$.

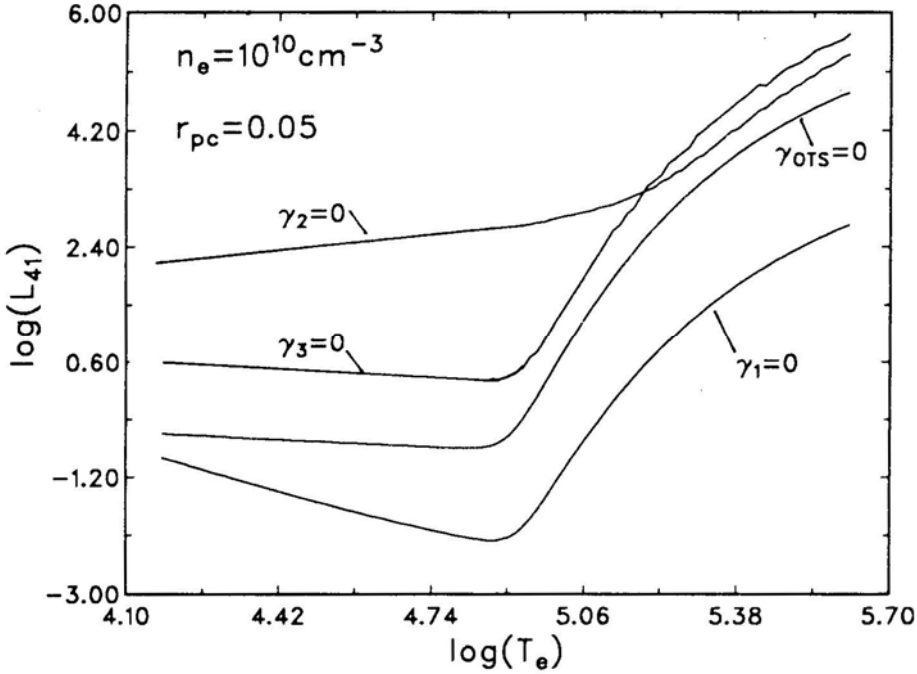

Figure 6. Variation of threshold luminosity L_{41} *vs* T_e for the plasma parameters shown in the figure. (Fluctuations in curves $\gamma_{OTS} = 0$ and $\gamma_3 = 0$ are due to numerical effects)

Table 1. Observed parameters in the resonant interacting region.

Source	n_e (cm^{-3})	minimum T_e (K)	r (pc)	ω_0 (rad s^{-1})	$L_{41}(\Delta\omega=\omega_0)$
3C 273	10^{10}	1.5×10^4	0.05	8.8×10^9	4.59×10^2
3C 48	10^{10}	1.5×10^4	0.05	8.8×10^9	8.33×10^2
Crab Nebula	10^7	1.0×10^4	0.03	1.8×10^8	1.20×10^{-4}

represents PDI-1 where $\omega_{r1} \simeq kc_s$ and $\gamma_1 \ll \omega_{r1}$. The variation of growth rate γ_1 of PDI-1 with respect to T_e due to a monochromatic pump is shown in Figs 2(a) for 3C 273, 3(a) for 3C 48 and 4(a) for Crab Nebula. Similarly, the variation of growth rate γ'_1 of PDI-1 with respect to T_e due to a broad pump of width $\Delta\omega = \omega_0$ is shown in Figs 2(b) for 3C 273, 3(b) for 3C 48 and 4(b) for Crab Nebula. Fig. 2(a) shows that the maximum electron temperature T_e attainable through PDI-1 is $\simeq 10^{5.6}$ K. The maximum Te attained in the 3C 48 is $\simeq 10^{5.7}$ K and in the Crab Nebula is $\simeq 10^5$ K for the values of the parameters indicated in Tables 1 and 2.

The dependence of the growth rate y_1 on monochromatic pump strength is shown in the Fig. 5(a). Similarly, Fig. 5(b) shows the variation of γ'_1 with respect to the strength of a broad pump. Fig 5(a) shows that at just above the threshold (i.e. when $\gamma_1 < \Gamma_i$), γ_1 is proportional to (L_{41}/r_{pc}^2) and at well above threshold (*i.e.* when $\gamma_1 > \Gamma_i$) it is

proportional to $(L_{41}/r_{pc}^2)^{1/2}$. Fig. 6 shows the dependence of threshold luminosity on electron temperature T_e for all cases of PDI together with OTS. The curve $\gamma_1 = 0$, in Fig. 6, shows the dependence of threshold luminosity of PDI-1 on T_e. At $T_e < 10^{4.5}$ K the collisional damping operates and as the temperature goes up Landau damping takes over for $T_e > 10^{5.1}$ K. But in the range $10^{4.5}$ K $< T_e < 10^{5.1}$ K both collisional and Landau damping are small and therefore lower threshold luminosity is needed. The cross marked region in figures represents transition from PDI-1 to PDI-2.

2.3 *PDI-2:* Decay into a Reactive Quasi-Ion Mode (ω_{i2})

For large pump strength and low temperature, the ion mode loses its linearity. We call this ion mode as the reactive quasi-ion mode because its growth rate γ_2 and frequency ω_{r2} are much larger than the ion-acoustic wave frequency ($\omega_s = kc_s$).

Here $\omega_0 = \omega_e + \omega_{i2}$ and $\omega = \omega_{i2} = \omega_{r2} + i\gamma_2$. The variation of ω_{i2} and γ_2 with respect to T_e are shown in the Fig. l(c) where we define $T_e = T_{ec}$ and correspondingly $D = D_c$ (Fig. lb) at the point where γ_1 crosses ω_s. At this point the ion-acoustic mode loses its linearity. For $T_e < T_{ec}$ the imaginary part of ω crosses its real part at $T_e = T_{et}$ and $D = D_t$ (Fig. lb). In Fig. l(c) the range $T_e < T_{et}$ represents the region of reactive quasi-ion mode. The range $T_{et} \leqslant T_e \leqslant T_{ec}$ and $D_t \geqslant D \geqslant D_e$ represents the transition region in which the reactive quasi-ion mode changes into an ion-acoustic mode or vice versa. Figs l(b) and l(c) shows for 3C 273, $T_{ec} = 10^{5.08}$ K, $T_{et} = 10^{4.89}$ K, $D_c = 10^{3.2}$ and $D_t = 10^{4.8}$. Under the coherent pump approximation, the variation of growth rate γ_2 with respect to T_e is shown in Figs 2(a) for 3C 273 and 3(a) for 3C 48. Similarly, using a broad pump of width $\Delta\omega = \omega_0$, the variation of growth rate γ'_2 with respect to T_e is shown in Figs 2(b) for 3C 273 and 3(b) for 3C 48.

For $T_e < T_{et}$ and $D \gg D_t$, $\gamma_2/\omega_{r2} = \sqrt{3}$. The variation of growth rate γ_2 with respect to the luminosity of the pump is shown in the Fig. 5(a). We find that the γ_2 is proportional to (L_{41}/r^2_c) Similarly, the variation of growth rate γ'_2 with the luminosity of a broad pump is shown in Fig. 5(b). The curve $\gamma_2 = 0$ in the Fig. 6 shows the variation of the threshold luminosity with respect to T_e. This mode excites only when $D > D_c$ or $L_{41} > 4\pi R^2 n_e c/P$. We find $L_{41} > 10^{2.38}$ at $T_{ec} = 10^{5.08}$ K for 3C 273. This mode is not excited in the Crab Nebula because the radio luminosity is too low to cross the threshold luminosity $L_{41} = 1.1 \times 10^2$, calculated using parameters given in Tables 1 and 2. We find that PDI2 occurs at the lower temperature $T_e < T_{ec}$ and the collisional damping rate ν_0 of the pump is still much smaller than the growth rate γ_2 of a reactive quasi-ion mode.

Table 2. Model parameters.

Type of instability	minimum T_i (K)	ω_0 (rad s^{-1})
PDI-1	$T_e/100$	$1.01\omega_{pe}$
PDI-2	$T_e/100$	$1.01\omega_{pe}$
PDI-3	$10 \times T_e$	$1.01\omega_{pe}$
OTS	$T_e/100$	$(\omega_e + \omega_{pe})/2$

2.4 *PDI-3: Decay into a Resistive Quasi-Ion Mode* (ω_{i3})

Here $\omega_0 = \omega_e + \omega_{i3}$. For $T_e \leqslant T_i$, the phase velocity of the ion-acoustic mode (c_s) becomes slightly greater than thermal velocity (v_i) of the ions. Therefore, the beat mode (*i.e.* ion mode) of a pump wave and an electron plasma mode undergoes the nonlinear Landau damping over the thermal ions. Since the ion mode is strongly damped, a weak instability is excited compared to other three cases.

From Equation (3), for $\omega = \omega_{i3} = \omega_0 + i\,\gamma_3$, we get

$$\omega_{r3} = \frac{(\mathbf{K}\cdot\mathbf{V}_0)^2}{2\omega_{pe}} \operatorname{Re}\left\{\frac{\chi_e(\chi_i+1)}{\varepsilon(K,\omega)}\right\}\Bigg|_{\frac{\omega}{k}=\frac{\Delta}{k}} + \Delta \tag{11}$$

$$\gamma_3 = \frac{(\mathbf{K}\cdot\mathbf{V}_0)^2}{2\omega_{pe}} \operatorname{Im}\left\{\frac{\chi_e(\chi_i+1)}{\varepsilon(K,\omega)}\right\}\Bigg|_{\frac{\omega}{k}=\frac{\Delta}{k}} + \Delta. \tag{12}$$

Using a coherent pump, the variation of γ_3 with respect to T_e is shown in Figs 2(a) for 3C 273, 3(a) for 3C 48, and 4(a) for Crab Nebula. Similarly, using a broad pump having the width $\Delta\omega = \omega_0$, we have plotted y 3 with respect to T_e in Figs 2(b) for 3C 273, 3(b) for 3C 48 and 4(b) for Crab Nebula. We find $\omega_{r3} \simeq A = \omega_s$ and γ_3 is small compared to ω_{r3}, γ_1, γ_2 and γ_{OTS}.

In the BLR of 3C 273 and 3C 48 the collisional damping rate ν_0 of the pump wave is smaller than γ_3 but it is approximately equal to γ_3 in Crab Nebula. Since width chosen is large, the figure shows that growth rates of all the cases of PDT are smaller than ν_0.

The dependence of γ_3 on the monochromatic pump strength is shown in the Fig. 5(a). We find y, is proportional to (L_{41}/r_{pc}^2). Similarly, the dependence of γ_3' on the broad pump strength is shown in the Fig. 5(b). The curve $\gamma_3 = 0$ in Fig. 6 shows the dependence of threshold luminosity on Te.

2.5 *Oscillating Two-Stream Instability* (*OTS*)

This instability excites when an intense e.m. pump of frequency less than the frequency of electron plasma wave interacts with the plasma. Here $\omega_{pe} < \omega_0 < \omega_e$. The pump e m. wave ($\omega_0$, $\mathbf{K}_0$) couples with a nigh frequency wave (ω_e, $\mathbf{K}_e$) and a non-oscillatory ion mode (0, $\mathbf{K}_i$). We find that $\mathbf{K}_e \simeq -\mathbf{K}_i \equiv \mathbf{K}$. In this case the thermal ion density fluctuations of zero frequency grow along with an electron plasma mode. Since these static ion density fluctuations do not qualify for a normal mode of the plasma, we can not include OTS in the class of parametric decay instabilities. However, it has been considered as a special case of the parametric instability.

Here both the terms $\varepsilon(\mathbf{K}, \omega - \omega_0)$ and $\varepsilon(\mathbf{K}, \omega + \omega_0)$ are resonant. For $\omega = 0 + i\gamma_{OTS}$, Equation (3) gives

$$\frac{1}{1-\dfrac{\sqrt{\pi}\,\gamma_{OTS}}{kv_e}} + \frac{1}{\left(1-\dfrac{\sqrt{\pi}\,\gamma_{OTS}}{kv_i}\right)\dfrac{T_e}{T_i} + (k\lambda_{De})^2} = -\frac{(\mathbf{K}\cdot\mathbf{V}_0)^2\Delta}{(k\lambda_{De})^2\,\omega_{pe}\left\{(\gamma_{OTS}+\Gamma_e)^2+\Delta^2\right\}}. \tag{13}$$

If we simplify Equation (13) for γ_{OTS}, we get

$$a_1\gamma_{OTS}^3+a_2\gamma_{OTS}^2+a_3\gamma_{OTS}+a_4=0, \tag{14}$$

where

$$a_1=\frac{\sqrt{\pi}}{kv_e}+\frac{\sqrt{\pi}}{kv_i}\frac{T_e}{T_i},$$

$$a_2=2\Gamma_e a_1-(k\lambda_{De})^2-\frac{T_e}{T_i}-\frac{(\mathbf{K}\cdot\mathbf{V}_0)^2}{\omega_{pe}(k\lambda_{De})^2}\frac{\pi\Delta}{v_e v_i k^2}\frac{T_e}{T_i}-1,$$

$$a_3=a_1(\Gamma_e^2+\Delta^2)-2\left(1+(k\lambda_{De})^2+\frac{T_e}{T_i}\right)\Gamma_e$$

$$+\frac{(\mathbf{K}\cdot\mathbf{V}_0)^2\Delta}{\omega_{pe}(k\lambda_{De})^2}\left\{\left(\frac{\sqrt{\pi}}{kv_e}+\frac{\sqrt{\pi}}{kv_i}\right)\frac{T_e}{T_i}+\frac{\sqrt{\pi}(k\lambda_{De})^2}{kv_e}\right\}$$

and

$$a_4=-\left(1+(k\lambda_{De})^2+\frac{T_e}{T_i}\right)(\Gamma_e^2+\Delta^2)-\frac{(\mathbf{K}\cdot\mathbf{V}_0)^2\Delta}{\omega_{pe}(k\lambda_{De})^2}\left((k\lambda_{De})^2+\frac{T_e}{T_i}\right).$$

For $k\lambda_{De}\simeq 0.4$, Equation (13) gives

$$\gamma_{OTS}=\pm i\left[\frac{(\mathbf{K}\cdot\mathbf{V}_0)^2}{(k\lambda_{De})^2\omega_{pe}}\Delta\left\{1+\frac{1}{(k\lambda_{De})^2+\frac{T_e}{T_i}}\right\}^{-1}+\Delta^2\right]^{1/2}-\Gamma_e. \tag{15}$$

The γ_{OTS} is real only when $\Delta=\omega_0-\omega_e<0$, *i.e.* $\omega_0<\omega_e$. The expression $\gamma_{OTS}=0$ gives $\Delta=\Delta_{thr}$ while $\frac{\partial\gamma_{OTS}}{\partial\Delta}=0$ gives $\Delta=\Delta_{max}$ corresponding to a maximum growth rate. Now, $\Delta_{thr}=\Delta_{max}$ gives the minimum pump strength at which instability occurs:

$$\left(\frac{v_0}{v_e}\right)^2=2\left\{1+\frac{1}{(k\lambda_{De})^2+\frac{T_e}{T_i}}\right\}\frac{\Gamma_e}{\omega_{pe}}. \tag{16}$$

We solve Equation (14), using $k=8.75$ cm^{-1} for 3C 273 and 3C 48, and $k=6.0$ cm^{-1} for Crab Nebula where k has been determined using the condition $\omega_{pe}<\omega_0<\omega_e$ and the values of parameters given in the Tables 1 and 2. One of the three roots represents a growing electron mode and an ion density fluctuation while the other two represent damped modes. Using $\Delta=\Delta_{max}$ and a monochromatic pump, the growth rate γ_{OTS} is plotted as a function of T_e in Figs 2(a) for 3C 273, 3(a) for 3C 48 and 4(a) for Crab Nebula. Similarly, using a broad pump, γ'_{OTS} is plotted as a function of T_e in Figs 2(b) for 3C 273, 3(b) for 3C 48 and 4(b) for Crab Nebula. The dependence of γ_{OTS} on a monochromatic pump luminosity is shown in the Fig. 5(a). The dependence of γ'_{OTS} on the broad pump luminosity is shown in the Fig. 5(b): The curve $\gamma_{OTS}=0$ in the Fig. 6 shows the variation of threshold luminosity with T_e. Again one notices that the γ_{OTS} is much larger than the collisional absorption rate ν_0, of e m. pump wave.

3. Formation of 21cm absorption line in the emission-line region

The 21-cm absorption line has been observed from several QSO systems. It is believed to originate in the neutral hydrogen clouds in the vicinity of the QSO. This absorption line can also originate when the radiation of frequency 1420 MHz (21-cm) drives the PDI in the plasma having electron plasma frequency close to 1420 MHz. This effect was first considered by Krishan (1988). This process has line character in principle since it occurs only when a frequency matching condition is satisfied. The presence of 21cm absorption line indicates that the electron density in the emission-line region must be $\simeq 2.5 \times 10^{10}$ cm^{-3}, which falls within the range of inferred densities for these regions. The 21-cm radiation luminosities in 3C 273 and 3C 48 are sufficient to drive PDI.

For comparison, the standard expression (Krishan 1988) for absorption rate for the spin flip transition is given by

$$K(\omega) = 2.58 \times 10^{-15} \frac{f(\omega) N}{T_K} \text{ cm}^{-1}$$

where T_K is the temperature which characterizes the population distribution between the two atomic states, $f(\omega)$ is the line shape function normalized to unity and N is the number of hydrogen atoms cm^{-3}. Using some standard values of the different parameters we find absorption rate due to PDI in the ionized region is much larger than the absorption rate for spin flip transition in the neutral hydrogen region.

4. Results and conclusions

(1) An incident e.m. pump wave drives purely electrostatic oscillations at two frequencies close to ω_{pe} and ω_{pi}.

(2) A parametric amplification occurs for drive frequencies $\omega_0 \geqslant \omega_{pe}$ and for driver amplitude exceeding a certain critical threshold.

(3) Instability is maximum when $\mathbf{K} \parallel \mathbf{E}_0$ and zero for $\mathbf{K} \perp \mathbf{E}_0$.

(4) For circularly polarized pumps the general picture remains unchanged, since growth rates are again determined by the component of $\mathbf{K}_0$ parallel to $\mathbf{K}$.

(5) The absorption rate of e.m. wave depends on the ratio (L_{41}/r_{pc}^2) and it is much larger than the free-free absorption rate ν_0.

(6) Electron temperature T_e and ion temperature T_i increase by multiples of tens for moderate radio luminosities.

Compared to all other processes reviewed by Davidson & Netzer (1979), PDI is a faster process. The excited Langmuir wave will heat the plasma when it undergoes Landau damping. Apart from damping it can undergo many other processes: $\omega_e + \omega_e \rightarrow \omega'_0$, $\omega_e \rightarrow \omega'_e + \omega'_i$, *etc.* In the first process, two electron plasma waves combine together to produce an e m. wave. In the second case, it drives PDI, and produces electron and ion-acoustic waves. Therefore, an incident e m. energy can heat the plasma medium, as well as get reprocessed to other frequencies.

The growth rates indicate the rates at which the plasma medium and the radio radiation try to attain equilibrium with each other. The threshold condition (Equation (9), Fig. 6) ensures those values of plasma parameters like density and temperature for which the fast process of PDI does not occur and the equilibrium is

reached. Decay instability may be the mechanism for the formation of hot lower density corona adjoining each photoionized dense region. The dip in the spectrum of 3C 273 at 5.0×10^9 Hz (Cowsik & Lee 1982) may be due to the anomalous absorption of radio waves through PDI. Since PDI is an efficient process, it cannot be ignored while accounting for the observed value of radio luminosity which is less than that obtained by extrapolation from the high frequency part of the spectrum.

Acknowledgment

Discussions with Prof. Paul J. Wiita during this work are gratefully acknowledged.

References

Collin-Souffrin, S., Lasota, J. P. 1988, *Publ. astr. Soc. Pacific*, **100,** 1041.
Cowsik, R., Lee, Y. C. 1982, *Proc. R. Soc. London Ser.* **A383,** 409.
Davidson, K., Netzer, H. 1979, *Rev. Mod. Phys.*, **51,** 715.
Dobrowoniy, M., Ferrori, A. 1976, *Astr. Astrophys.*, **47,** 97.
Drake, J. F., Kaw, P. K., Lee, Y. C., Schmidt, G., Liu, C. S., Rosenbluth, M. V. 1974, *Phys. Fluids*, **17**, 778.
Gangadhara, R. T., Krishan, V. 1990, in *I AU Symp. 142: Basic Plasma Processes on the Sun*, Eds E. R. Priest & V. Krishan, D. Reidel, Dordrecht (in press).
Gangadhara, R. T., Krishan, V. 1990, in Proc. Atlanta meeting on *Variability of Active Galactic Nuclei*, Eds D. Miller & P. J. Wiita, Cambridge Univ. Press, (in press).
Ginzburg, V. L., Ozernoy, L. M. 1976, *Astrophy. J.*, **144,** 599.
Krishan, V. 1987, *Mon. Not. R. astr. Soc.*, **226,** 629.
Krishan, V. 1988, *Mon. Not. R. astr. Soc.*, **231,** 353.
Krolik, J. H., McKee, C. F., Tarter, C. B. 1978, in Proc. Pittsburgh Conf. on *BL Lacertae Objects*, Ed A. Wolfe, Univ. Pittsburgh. p. 277.
Kruer, W. L. 1988, in *The Physics of Laser-Plasma Interactions*, Addison-Wesley, New York, p. 70.
Kwan, J., Krolik, J. H. 1981, *Astrophys. J.*, **278,** 558.
Lang, K. R. 1980, *Astrophysical formulae*, Springer-Verlag, Berlin, p. 195.
Liu, C. S., Kaw, P. K. 1976, *Advances in plasma physics*, **6,** 83.

J. Astrophys. Astr. (1990) **11,** 533–540

Spectroscopic Binaries near the North Galactic Pole
Paper 18: HD 118670

R. F. Griffin *The Observatories, Madingley Road, Cambridge, England CB3 0HA*

Received 1990 June 6; accepted 1990 October 22

Abstract. Photoelectric radial-velocity measurements show that HD 118670 is a double-lined spectroscopic binary in an orbit which is not quite circular and whose period is about 48 days. Spectral types of K0 V and K7 V would satisfy the photometry and the mass ratio; the mass function would then suggest the possibility of eclipses. However, actual spectral classification indicates a luminosity somewhat above the main sequence.

Key words: radial velocities—spectroscopic binaries—orbits—stars, individual—HD 118670

1. Introduction

This is the fourth successive paper in this series to report the discovery of a double-lined spectroscopic binary with a period of about 50 days. The star concerned here is a comparatively bright object, seventh magnitude, and is to be found on the eastern border of Bootes about 40′ preceding the fifth-magnitude star 2 Boo. Although it is not bright enough to feature in the *Bright Star Catalogue* (Hoffleit 1982) it does appear in the *Supplement* (Hoffleit, Saladyga & Wlasuk 1983) to that *Catalogue.* lt is shown there as having a magnitude and ($B - V$) colour of $7^{m}.02$ and $0^{m}.94$ respectively; those data are presumably drawn from Häggkvist & Oja (1973). No spectral type is given for HD 118670 in the *Supplement,* although a type of K1 IV was published a long time ago by Keenan (1940). Fehrenbach *et al.* (1987) observed the star for radial velocity, by the objective-prism technique; they gave a mean velocity of -45 ± 3.8 km s^{-1} from four measurements. One velocity, obtained with the spectrometer (Fletcher *et al.* 1982) at the Dominion Astrophysical Observatory, Victoria, has been published by Yoss, Neese & Hartkopf (1987); the same authors derived from DDO-style photometry a pseudo-spectral type of K0 III–IV, but the interpretation of the photometry may have been confused by the unrecognized duplicity of the object.

2. Photometry

The photometry of Häggkvist & Oja (1973) has been corroborated and extended to the U band by observations kindly made at my request by Mr. R. Fried at the privately operated Braeside Observatory near Flagstaff, Arizona. On eight nights HD 118670 was measured against 2 Boo as the comparison star and HR 5102 as the check star; of

those two stars, only HR 5102 has a known U magnitude. The magnitude and colours derived differentially from HR 5102, whose own values were taken as $V = 6^{m}.11$, $(B - V) = 0^{m}.96$, $(U - B) = 0^{m}.70$ (Hoffleit 1982), are $V = 7^{m}.01$, $(B - V) = 0^{m}.95$, $(U - B) = 0^{m}.75$.

3. Radial velocities and orbit

HD 118670 was first observed for radial velocity at Cambridge in 1973, but a second observation was not made for 11 years. After the large amplitude was discovered in 1985, intensive observations in the spring of the following year determined the period, which proved to be about 48 days. Efforts were made with integrating spectrometers to see if the system were double-lined; those efforts were rewarded by the discovery of a very weak secondary dip with an intensity only about a tenth of that of the primary (Fig. 1). Altogether 63 photoelectric velocity measurements (including the one by Yoss, Neese & Hartkopf (1987)), have been made of the primary star, and five show the secondary; they are all listed in Table 1. The published one has been adjusted by +1.2 km s^{-1} to take account of the zero-point difference implied by Scarfe, Batten & Fletcher (1990) between the 'DAO RVS' system and the Cambridge reference stars. A referee has expressed surprise at how few measurements are available for the secondary. The reasons are that the secondary dip is altogether too weak to be visible on Cambridge traces, from which two-thirds of the primary velocities have been derived; and on the majority of traces obtained with other spectrometers, with which the trace can be integrated until an arbitrarily high S/N ratio is achieved, the secondary is either masked by blending with the primary or else is so far separated as to be partly or wholly beyond the end of the scan.

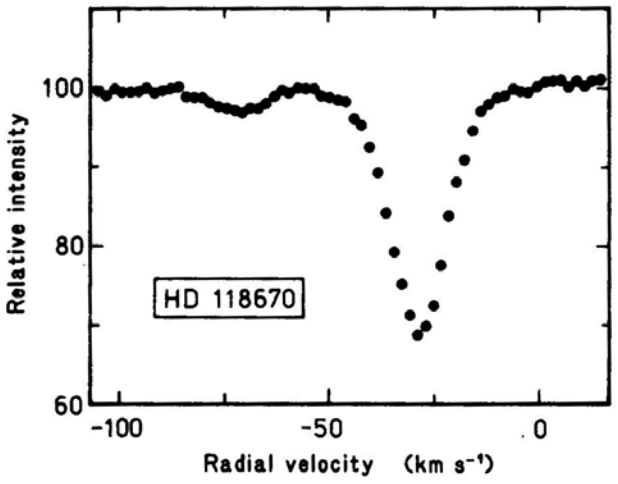

Figure 1. CORAVEL radial-velocity trace of HD 118670, taken on 1989 April 28 and illustrating the double-lined nature of the object. Each point in the graph represents an independent photon count; the number of photons is of the order of 100,000 per point.

Table 1. Photoelectric radial-velocity measurements of HD 118670 (made at Cambridge and by the author extent where otherwise noted).

Date	MJD	Velocity km s^{-1}	Phase	$(O-C)$ km s^{-1}
1973 Feb 26.25*	41739.25	−16.7	0.435	+1.1
1982 Mar 27.03	45055.03	−46.0	69.575	−15.7
31.03	059.03	−51.0	.658	−6.6
May 13.91	102.91	−34.0	70.573	−4.0
15.90	104.90	−49.0	.615	−12.4
1984 May 1.04	45821.04	−26.4	85.548	+0.1
1985 Feb 24.16	46120.16	−67.3	91.785	+0.1
June 1.96	217.96	−72.7	93.824	+0.3
1986 Mar 17.33†	46506.33	−74.9	99.837	−0.4
Apr 10.10‡	530.10	−21.0	100.333	+0.5
May 5.99	555.99	−77.3	.872	+0.5
13.04	563.04	−72.7	101.019	+1.2
13.97	563.97	−72.1	.039	−0.7
16.93	566.93	−60.3	.101	+0.6
25.92	575.92	−26.2	.288	+0.3
26.94	576.94	−24.1	.309	−0.2
27.92	577.92	−22.6	.330	−0.9
28.99	578.99	−19.2	.352	+0.7
30.91	580.91	−17.0	.392	+1.0
June 3.96	584.96	−20.2	.477	−0.6
10.94	591.94	−37.5	.622	+0.4
11.95	592.95	−40.5	.643	+1.1
14.90	595.90	−51.4	.705	+1.8
29.94	610.94	−73.3	102.018	+0.8
Aug 23.83‡	665.83	−48.4	103.163	+0.2
28.83‡	670.83	−29.5	.267	0.0
Nov 23.55§	757.55	−65.7	105.075	−0.1
Dec 12.29	776.29	−18.7	.466	+0.3
1987 Jan 30.15	46825.15	−21.1	106.485	−0.9
Feb 1.17	827.17	−23.4	.527	+0.6
21.18	847.18	−80.0	.944	−0.4
Mar 3.13‡	857.13	−51.6	107.152	−0.8
20.08	874.08	−22.7	.505	−0.9
May 7.99	922.99	−23.2	108.525	+0.6
9.00	924.00	−26.8	.546	−0.5
June 3.96	949.96	−64.0	109.087	−0.6
22.94	968.94	−21.1	.483	−1.1
24.93	970.93	−23.2	.525	+0.6
July 5.91	981.91	−62.9	.754	−0.7
17.97¶	993.97	−74.9	110.005	+0.7
1988 Jan 8.23	47168.23	−41.4	113.639	−0.6
23.52‖	183.52	−79.4	.958	−0.3
31.50‖	191.50	−56.1	114.124	+0.3
Mar 11.18‡	231.18	−79.8	.951	−0.4
12.06‡	232.06	−78.6	.970	−0.1
14.00‡	234.00	−75.3	115.010	−0.3
17.04‡	237.04	−65.7	.074	+0.2
23.11	243.11	−42.0	.200	−0.8

Table 1. Continued.

Date		MJD	Velocity km s^{-1}	Phase	$(O-C)$ km s^{-1}
Apr	9.93	47260.93	−31.5	.572	−1.7
	13.94	264.94	−44.4	.655	−0.5
May	19.97	300.97	−18.2	116.407	−0.5
June	6.93	318.93	−66.9	.781	−0.1
	12.94	324.94	−79.7	.906	−0.2
	22.91	334.91	−57.5	117.114	+0.8
Nov	5.22‡	470.22	−79.8	119.936	−0.1
1989 Feb	11.22	47568.22	−78.1	121.979	−0.2
Mar	25.14‡	610.14	−76.1	122.853	+0.1
	25.99‡	610.99	−77.7	.871	0.0
Apr	28.02‡	644.02	−28.0	123.560	+0.1
May	28.89	674.89	−41.2	124.203	−0.6
June	4.95	681.95	−19.8	.351	+0.2
1990 Jan	31.19‡	47922.19	−19.2	129.360	+0.2
Feb	12.40¶	934.40	−36.4	.615	+0.2
	14.40¶	936.40	−44.1	.656	0.0
Mar	13.35‖	963.35	−38.1	130.218	−0.3
Apr	5.03	986.03	−50.2	.691	+0.4
	29.03	48010.03	−42.6	131.192	+0.2
1987 July	17.97¶s	46993.97	−16.1	110.005	−1.6
1988 Jan	23.52‖s	47183.52	−10.2	113.958	0.0
1989 Mar	25.99‡s	47610.99	−10.4	122.871	+1.5
Apr	28.02‡s	644.02	−70.8	123.560	+0.6
1990 Jan	31.19‡s	47922.19	−82.3	129.360	−0.4

* Observed with the Cambridge instrument by Dr. (then Mr.) G. A. Radford.
† Observed at DAO by Yoss, Neese & Hartkopf (1987).
‡ Observed with 'Coravel' at Haute-Provence (Baranne *et al.* 1979).
§ Observed, in collaboration with Dr. J. E. Gunn, with the 200-inch telescope (Griffin & Gunn 1974).
¶ Observed with 'Coravel' at ESO.
‖ Observed with the Dominion Astrophysical Observatory 48-inch telescope (Fletcher *et al.* 1982).
s Observation of the secondary star.

In the orbit determination, all velocities that are not explicitly of the secondary have been attributed to the primary. Those that are near the γ-velocity must be affected to some extent by blending with the secondary, but owing to the weakness of the latter the effect is too small significantly to spoil the fit of the computed velocity curve. It was found in preliminary orbital solutions that the Cambridge radial velocities were on average less accurate than the others by about a factor of two in terms of their r.m.s. residuals (a factor four in variance), so they have been weighted 1/4 in the solution below. However, they are not at all bad: their r.m.s. residuals are only 0.7 km s^{-1}. Radial velocities of the secondary star were weighted 0.1. The final orbit is illustrated in

Fig. 2 and has the following elements:

P	$= 47.9578 \pm 0.0022$ days	$(T)_{113}$	$=$ MJD 47137.6 ± 0.7
γ	$= -47.80 \pm 0.07$ km s^{-1}	T_0	$=$ MJD 47109.856 ± 0.025
K_1	$= 31.07 \pm 0.10$ km s^{-1}	$a_1 \sin i$	$= 20.48 \pm 0.06$ Gm
K_2	$= 37.2 \pm 0.6$ km s^{-1}	$a_2 \sin i$	$= 24.5 \pm 0.4$ Gm
q	$= 1.199 \pm 0.020$ $(= m_1/m_2)$	$f(m_1)$	$= 0.1491 \pm 0.0014\ M_\odot$
e	$= 0.034 \pm 0.003$	$f(m_2)$	$= 0.257 \pm 0.013\ M_\odot$
ω	$= 208 \pm 5$ degrees	$m_1 \sin^3 i$	$= 0.864 \pm 0.023\ M_\odot$
		$m_2 \sin^3 i$	$= 0.721 \pm 0.015\ M_\odot$

R m.s.residual (weight l)= 0.35km s^{-1}

The true period (measured in the rest frame of the system) is 47.9654 ± 0.0022 days.

The eccentricity, though small, is very significant: not only is it many times its own standard deviation, but an orbit in which it is set to zero is obviously and systematically ill-fitting, and the sum of the squares of the deviations from it is getting on for three times the sum found for the orbit given above. This orbit has one of the smallest definitely non-zero eccentricities to have been established from spectroscopic observations, although all too often the statistical significance or otherwise of a small departure from zero eccentricity is not made clear. Among orbits published by the present author, only that of HD 207739 (Griffin *et al.* 1990), with $e = 0.027 \pm 0.004$, has a smaller value. HD 105341, discussed in Paper 3 of the present series (Griffin 1982), has an eccentricity of 0.027 ± 0.012, but in that case there is a possibility of 5–10 per cent that the apparent eccentricity arises by chance and that the orbit is actually circular The distinction between orbits that are exactly circular and those that are not

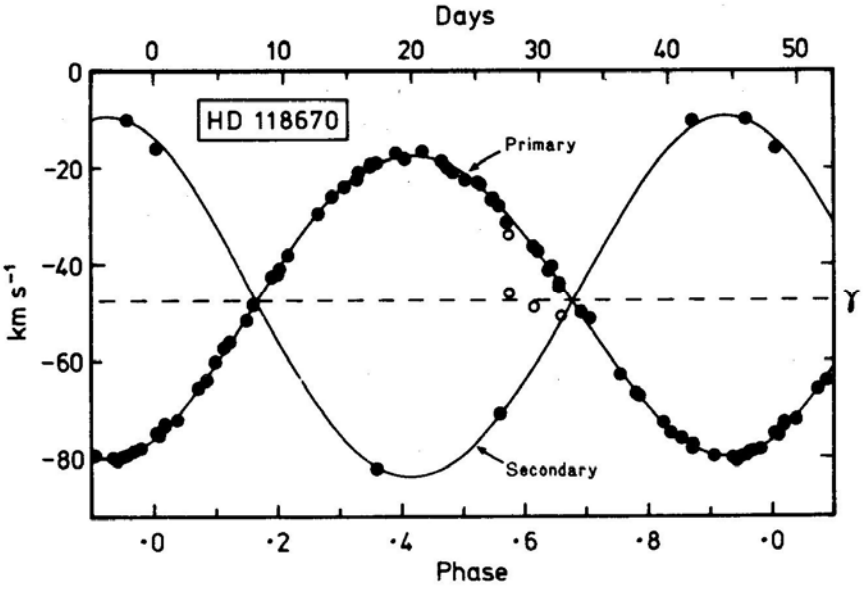

Figure 2. The computed radial-velocity curves for HD 118670, with the measured radial velocities plotted. The four open circles represent the objective-prism radial velocities of Fehrenbach *et al.* (1987); they were not taken into account in the orbital solution.

has assumed a good deal of importance in recent years, since the former are thought to have been circularized by tidal processes whose effectiveness is related to the separations, sizes and internal construction of the stars concerned. Thus the existence of an exactly circular orbit tells us that tidal dissipation is, or at some time in the past has been, important in the system.

4. Discussion

The most natural model for a binary system that contains two late-type stars with a substantial difference in brightness and a moderate disparity in mass is a main-sequence pair, and it seems worthwhile to explore the applicability of such a model despite the subgiant classification by Keenan (1940). It is to be recalled that not only was the classifier less experienced then than he is now, but the MK classification system (Morgan, Keenan & Kellman 1943) that he was using was then under development and was not unveiled until three years later. It is also to be remarked that HD 115968, which was treated in Paper 2 of this series (Griffin 1981) and whose large proper motion makes a luminosity above the main sequence improbable (though not impossible), is also accorded luminosity class IV in the same paper (Keenan 1940); so is HD 108078 (Griffin 1980a), which three subsequent authors have considered to have luminosity class III.

Owing to the disparity seen on radial-velocity traces in the dip areas given by the two components of HD 118670, to be interpreted largely in terms of a disparity in luminosities, the magnitude and colours of the primary star must not be very different from the observed quantities for the system as a whole. At first sight it is impossible to match the colours by a main-sequence model, because Allen (1973) shows a star of type K0V, whose $(B - V)$ colour is $0^m.89$—a good starting point for modelling the primary—to have a $(U - B)$ colour of $0^m.47$, far too blue to match HD 118670. However, a colour–colour plot for the K dwarfs in the *Bright Star Catalogue* shows a considerable spread, whose overall envelope interpolated at the $(B - V)$ colour $0^m.89$ ranges from $0^m.48$ to $0^m.67$ in $(U - B)$. If we adopt for the primary a $(B - V)$ colour of $0^m.91$, corresponding in Allen (1973) to a type about K0.5 V but shown by the *Bright Star Catalogue* to be well within the ranges occupied by types K0, Kl and even K2 V, we could also adopt a $(U - B)$ colour of $0^m.71$, corresponding to the upper boundary of the observed colour–colour distribution. Then if we adopt the observed colours of 61 Cyg B (K7 V; the only K dwarf later than K5 in the *Bright Star Catalogue*) to represent the secondary, we obtain the model set out in Table 2 which represents

Table 2. Model for HD 118670.

	Spectral type	Absolute magnitude V m	B m	U m	Colour index $(B-V)$ m	$(U-B)$ m	Mass $M_\odot$	Mass ratio q
	K0.5 V	6.0	6.91	7.62	0.91	0.71	0.77	1.23:
Model	K7 V	8.0	9.37	10.70	1.37	1.23	0.62:	
	K0.5 V + K7 V	5.85	6.81	7.56	0.96	0.75	1.39:	
HD 118670 (observed)					0.95	0.75	>1.59	1.20

HD 118670 as well as could be desired. Thus the model is a fully satisfactory representation of the photometry of HD 118670. The mass ratio of the model depends upon exactly how one interpolates between K5 and M0 the very non-linear relationship given by Allen between mass and spectral type, but the ratio of 1.20 observed for HD 118670 is right in the middle of the range of possible values.

If the subgiant spectral classification of HD 118670 is to be taken seriously—and it is supported by the DDO-style 'photometric classification', although that is perhaps of dubious validity especially in a case of unrecognized compositeness—it is no use merely increasing the luminosities of both the components in the model and leaving everything else unchanged, since no stars of type K7 IV exist. It would still be necessary to suppose that the disparity in dip areas on radial-velocity traces arises from the luminosity difference, but the colour of the secondary would be almost unconstrained, so types of K0 or K1 IV and K0 V might be as good as any to represent the components. In that case the mass ratio, which accords so neatly with the main-sequence model, is just fortuitous, since very little is known observationally about the masses of subgiant field stars.

The minimum masses are perhaps the most interesting feature of the orbital elements given in the table above: they are 0.86 $M_{\odot}$ for the primary and 0.72 $M_{\odot}$ for the secondary. Those masses (with the caveat given above in relation to the secondary) are about 12 per cent greater than stars of types K0 V and K7 V are supposed to have (Allen 1973). That is not at all fatal to the idea that HD 118670 is a main-sequence pair, because a good deal of evidence has accumulated (Batten & Wallerstein 1973; Griffin 1978, 1980b, 1988; Griffin & Gunn 1978; Griffin, Mayor & Gunn 1982; Griffin *et al.* 1985; McClure 1982) that the tabulated masses for late-type stars are too small by amounts of the same order as the excess found here.

A referee, Dr. D. M. Popper, considers my quotation of Allen's (1973) *Astrophysical Quantities* to be rather naive, which is understandable since he is himself the author (Popper 1980) of a substantial and distinguished work on stellar masses. However, in that work Dr. Popper wisely refrained from committing himself to a tabular summary of his results, so individual readers of his review need to draw their own conclusions, which may not be mutually identical; the merit of Allen is that he provides a concrete (if questionable) starting point for discussion. Dr. Popper has also kindly pointed out that the eclipsing binaries that he has studied include additional examples of stars with super Allen masses (Popper *et al.* 1986).

Since the minimum masses found here for the components of HD 118670 are so large, even when the $\sin^3 i$ factor in the mass function is set to unity, there is clearly little scope for that factor to be appreciably less than unity: the implication is that the orbit is seen at an inclination very close to 90° and therefore may exhibit eclipses. Because the orbit has such a small eccentricity, eclipses are almost equally likely at the two conjunctions. Unfortunately, it happens that the interval between conjunctions, like the period, is close to an integral number of days, so the zone of terrestrial longitude from which the system may be observed at conjunction shifts only a little during any one observing season. During the 1990 season it was centred over the western Pacific Ocean, where there are relatively few observers, and for them the weather did not coöperate. Observations made in Japan by Mr. O. Ohshima of the conjunction of 1990 Jan 21 were hampered by cloud and were not conclusive. The late Mr. J. Ells of Bexleyheath, England, observed on the occasions of the conjunctions of 1989 May 3, May 26 and July 21, but daylight prevented his measurements from starting until

about an hour after the predicted times of conjunction, which are themselves uncertain by about two hours; no eclipses were in progress during his observations.

In 1991 conjunctions will be observable from the Americas, and the existence or otherwise of eclipses ought to be definitely established. Conjunctions are due on Jan 17.29, Feb 9.36, Mar 6.25, Mar 29.32, Apr 23.21, May 16.27, June 10.16 and July 3.23. The uncertainty in timing is still about two hours, and a central eclipse could last up to nine hours, even if the primary star is on the main sequence. Alternate conjunctions starting with the first listed are with the primary behind the other. If the system consists of a main-sequence pair and shows eclipses, at those conjunctions the eclipse could be up to several tenths of a magnitude deep, because the difference in luminosity between K0 V and K7 V stars is due largely to the disparity in surface brightness rather than in diameter; if the primary star is a subgiant then neither eclipse is likely to be more than a tenth of a magnitude deep.

I am very grateful to the Geneva, Dominion Astrophysical, European Southern and Palomar observatories for the use of their equipment, without which the secondary star in HD 118670 would not have been detected; and to Messrs. Ells, Fried and Ohshima for their willing response to my call for photometric observations of the system, as well as to Dr. D. M. Popper for a helpful referee's report. Dr. A. Duquennoy kindly retrieved from the CORAVEL data tape the numbers that form the basis of Fig. 1.

References

Allen, C. W. 1973, *Astrophysical Quantities* (third edition), Athlone, London, pp. 206, 209.
Baranne, A., Mayor, M., Poncet, J.-L. 1979, *VistasAstr.,* **23,** 279.
Batten, A. H., Wallerstein,G.1973. *Publ. Dom. astrophys. Obs.,* Victoria, **14,** 175.
Fehrenbach, C., Duflot, M., Burnage, R., Mannone, C., Peton, A., Genty, V. 1987, *Astr. Astrophys. Suppl.,* **71,** 275.
Fletcher, J. M., Harris, H. C., McClure, R. D., Scarfe, C. D. 1982, *Publ. astr. Soc. Pacific,* **94,**1017.
Griffin, R. F. 1978, *Observatory,* **98,** 257.
Griffin, R. F. 1980a, *Observatory,* **100,** 1.
Griffin, R. F. 1980b, *Observatory,* **100,** 113.
Griffin, R. F. 1981, *J. Astrophys. Astr.,* **2,** 309.
Griffin, R. F. 1982, *J. Astrophys. Astr.,* **3,** 1.
Griffin, R. F. 1988, *J. Astrophys. Astr.,* **9,** 205.
Griffin, R. F., Gunn, J. E. 1974, *Astrophys. J.,* **191,** 545.
Griffin, R. F., Gunn, J. E. 1978, *Astr. J.,* **83,** 1114.
Griffin, R. F., Gunn, J. E., Zimmerman, B. A., Griffin, R. E. M. 1985, *Astr. J.,* **90,** 609.
Griffin, R. F., Mayor, M., Gunn, J. E. 1982, *Astr. Astrophys.,* **106,** 221.
Griffin, R. F, Parsons, S. B., Dempsey, R., Bopp, B. W. 1990, *Publ. astr. Soc. Pacific,* **102,** 535.
Häggkvist, L., Oja, T. 1973, *Astr. Astrophys. Suppl.,* **12,** 381.
Hoffleit, D. 1982, *The Bright Star Catalogue* (fourth edition), Yale Univ. Obs., New Haven.
Hoffleit, D., Saladyga, M., Wlasuk, P. 1983, *A. Supplement to the Bright Star Catalogue,* Yale Univ. Obs., New Haven.
Keenan, P. C. 1940, *Astrophys. J.,* **91,** 506.
McClure, R. D. 1982, *Astrophys. J.,* **254,** 606.
Morgan, W. W., Keenan, P. C., Kellman, E. 1943, *An Atlas of Stellar Spectra with an Outline of Spectral Classification* (Univ. of Chicago, Chicago).
Popper, D. M. 1980, *Ann. Rev. Astr. Astrophys.,* **18,** 115.
Popper, D. M., Lacy, C. H., Frueh, M. L., Turner, A. E. 1986, *Astr. J.,* **91,** 383.
Scarfe, C. D., Batten, A. H., Fletcher, J. M. 1990, *Publ. Dom. astrophys. Obs.,* Victoria, **18,** 21.
Yoss, K. M., Neese, C. L., Hartkopf, W. I. 1987, *Astr. J.,* **94,** 1600.

Erratum

An observational constraint on the Existence of Proto-Superclusters at z = 3.3

Ravi Subramanya & G. Swarup
J. Astrophys. Astr. (1990) 11, 237–253

Dates of receipt and acceptance were inadvertantly left out. They should read:

Received 1989 September 26; accepted 1990 April 17